

BIROn - Birkbeck Institutional Research Online

Enabling Open Access to Birkbeck's Research Degree output

Using low-cost remote sensing data for geohazard modelling and analysis in Small Island Developing States (examples of Dominica and Cape Verdes).

<https://eprints.bbk.ac.uk/id/eprint/47303/>

Version: Full Version

Citation: Mickson, Michael (2021) Using low-cost remote sensing data for geohazard modelling and analysis in Small Island Developing States (examples of Dominica and Cape Verdes). [Thesis] (Unpublished)

© 2020 The Author(s)

All material available through BIROn is protected by intellectual property law, including copyright law.

Any use made of the contents should comply with the relevant law.

[Deposit Guide](#)
Contact: [email](#)

**Using Low-Cost Remote Sensing Data for Geohazard Modelling
and Analysis in Small Island Developing States (Examples of
Dominica and Cape Verdes).**

PhD Geology

Michael Mickson BSc. MSc.

**Submitted to Department of Earth and
Planetary Sciences, Birkbeck University of
London**

July 2021.

Abstract

Geohazards such as flooding and debris flows pose serious threats to livelihood, the physical and built environment especially in mountainous Small Island Developing States (SIDS). Geohazards cause an economic loss of over \$2 billion and approximately 300 to 600 deaths and injuries across the Caribbean and Pacific SIDS annually. To mitigate the negative impacts of flooding and debris flow, it is necessary to model and map areas that are susceptible to these hazards and to inform local officials about the potential risk.

The study was undertaken on selected localities in two SIDS, specifically Dominica and the Cape Verde. These islands lie on the Atlantic Hurricane Line and are prone to hazards such as flooding and debris flow. A typical example is the 2017 Hurricane Maria that triggered landslides, debris flows and flooding in Dominica, causing substantial loss of life, destruction of properties and economic losses. These islands are SIDS and so they face major challenges in tackling these hazards due to limited financial and human resources coupled with lack of technological advancement.

This study utilised low-cost remote sensing data such as drone-derived DEMs and orthophotographs in RAMMS and HEC-RAS to model and map areas vulnerable to debris flow and flooding hazards. Movement of boulders during Hurricane Maria aggravated the level of damages to properties and infrastructures. Therefore, drone-derived orthophotographs were applied in ImageJ to analyse size of boulders moved in relation to the damages and fatalities recorded. Results of the study demonstrated that these methods can be applied in other SIDS to mitigate impact of geohazards such as floods and debris flow.

Keywords

Geohazards, GIS, Remote Sensing, SRTM, ALOS PALSAR, Floods, Debris Flow, DJI Phantom 4 Pro Drone, SIDS, Dominica, Cape Verde, Agisoft Metashape, Hurricane Maria, ImageJ, RAMMS and HEC RAS.

Acknowledgement

Glory and adoration be unto GOD ALMIGHTY for seeing me through this course successfully.

I would like to extend my gratitude to my family for their love, prayers and support throughout my studies.

Special thanks to my supervisors Professor Hilary Downes, Dr. Simon Day and Dr. Richard Teeuw for their support, encouragement and guidance throughout this project.

I would also like to thank Dr. Robert Rall, Dr. Robert Watts and Mr. Kennedy Ferguson for assisting during my fieldworks in Dominica and Cape Verde.

Many thanks to Swiss Federal Institute for Forest, Snow and Landscape Research WSL for providing RAMMS software free of charge for a year.

Disclaimer

The enclosed project is entirely the work of the postgraduate student and any opinions expressed are not necessarily those of any member of the staff of the School of Earth and Environmental Sciences, Birkbeck, University of London. The text does not show any corrections of fact or calculations, and significant errors and omissions are possible. Any external reader or user of this report does so entirely at his own risk and responsibility, and neither the Department of Earth and Planetary Sciences nor the Birkbeck, University of London can be held responsible for anything contained within this report.

Table of Contents

Contents

Abstract.....	ii
Acknowledgement	iii
Disclaimer.....	iv
Table of Contents.....	v
List of Figures	ix
List of Tables	xv
CHAPTER ONE	1
Geohazards in Small Island Developing States (SIDS).....	1
1.0 Introduction	1
1.1 Understanding geohazards and risk reduction capacities in small island developing states	1
1.2 Research Aims and Objectives	2
1.3 Challenges Encountered by SIDS in Tackling Natural Disasters.....	2
1.4 A brief introduction to natural disasters.....	6
1.5 Background to Geohazards in Dominica and Cape Verde	10
1.6 Research Work Applications; GIS, Remote Sensing, Unmanned Aerial Vehicle (UAV) (Drone), Agisoft Metashape Professional, ImageJ, RAMMS and HEC-RAS 2D.....	13
1.6.1 Geographic Information Systems (GIS) and Remote Sensing	13
1.6.2 Application of Unmanned Aerial Vehicle (UAV) (Drone) in Geoscience	14
1.6.3 Photogrammetry and Agisoft Metashape Professional.....	15
1.6.4 ImageJ	16
1.6.5 Hydrologic Engineering Centre – River Analysis Systems (HEC-RAS).....	17
1.6.6 Rapid Mass Movement Simulation (RAMMS).....	18
1.7 Structure of Thesis	19
CHAPTER TWO	21
The Study Areas	21
2.0 Introduction	21
2.1 Location and geography of Dominica Island.....	21
2.2 Dominica Geological Setting	24
2.3 Dominica Topography, Climate, Hurricanes and Vegetation.....	27
2.4 Fogo Study Area	35
2.4.1 Location and Description of Fogo Island.....	35
2.4.2 Fogo Geology	37
2.4.3 Fogo Climate and Vegetation.....	39

CHAPTER THREE	43
Methodology.....	43
3.0 Introduction	43
3.1 Desk Study, Data Source, Collection Procedure and Software Used.....	43
3.2 Digital Elevation Models (DEMs).....	45
3.3 ALOS PALSAR and SRTM DEMs Corrections.....	50
3.4 Terrain Analysis.....	55
3.4.1 Shaded Relief Analysis	56
3.4.2 Slope Steepness Analysis	57
3.4.3 Aspect Analysis.....	58
3.4.4 Contour Analysis	59
3.5 Drainage Network Analysis.....	59
3.3 Dominica Fieldwork and Unmanned Aerial Vehicle (UAV) Survey	63
3.4 Cape Verde, Fogo Fieldwork and UAV Survey	71
3.5 UAV (Drone) Data Acquisition Techniques and Processing	75
3.6 BOULDER ANALYSIS.....	78
3.6.1 Introduction to ImageJ Software	78
3.6.2 Input Data and Plugins	78
3.6.3 Boulder Analysis Workflow in ImageJ	79
3.7 RAMMS DEBRIS FLOW METHODOLOGY	83
3.7.1 Introduction to RAMMS Software	83
3.7.2 RAMMS Debris Flow Module Equations	84
3.7.3 RAMMS Debris Flow Module Input Data and Parameters	86
3.7.4 RAMMS Debris Flow Simulation Workflow	87
3.7.5 Sensitivity Analysis	92
3.8 HEC-RAS Flood Modelling Methodology.....	93
3.8.1 HEC-RAS Background and Description.....	93
3.8.2 HEC-RAS 2D Unsteady Flow Hydrodynamics and Hydraulic Equations	94
3.8.3 HEC-RAS 2D Unsteady Flow Input Data and Input Parameters	97
3.8.4 Unsteady Flow Simulation Procedure.....	98
CHAPTER FOUR	108
Results.....	108
4.0 Introduction	108
4.1 Corrected ALOS PALSAR and SRTM DEM.....	108
4.2 Terrain Analysis Results	110

4.2.1 Hillshade Analysis Results	110
4.2.2 Slope Angle Analysis Results	110
4.2.3 Slope Aspect Analysis Results	111
4.2.4 Contour Analysis Results.....	112
4.3 Drainage Network Analysis Result	117
4.3.1 Flow Direction Analysis Result	117
4.3.2 Flow Direction Analysis Result	117
4.3.1 Flow Direction Analysis Result	118
CHAPTER FIVE	122
Results Of Field Work and Boulder Analysis, Processed Drone Images, Dominica and Fogo	122
5.0 Introduction	122
5.1 Impact of Hurricane Maria Events on Selected Study Areas in Dominica	122
5.2 ImageJ Boulders Size and Distribution Analysis Results	143
5.3 Boulders in Ribeira Santo Domingo, Fogo, Cape Verde.....	154
5.4 Processed Drone-Derived DSMs and Orthophotographs	157
CHAPTER SIX.....	172
Modelling Results.....	172
6.0. Results of RAMMS Debris Flow Modelling.....	172
6.1 Sensitivity Analysis.....	173
6.1.1 Sensitivity Analysis of Turbulent Coefficient (ξ).....	174
6.1.2 Sensitivity Analysis of Friction Coefficient (μ).....	177
6.1.3 Sensitivity Analysis of Earth Pressure (Lambda) (λ)	180
6.2. Model Calibration	183
6.2.1 Coulibistrie Debris Flows Simulation.....	184
6.2.2 Delice Debris Flows Simulation	189
6.2.3 Layou Debris Flows Simulation	194
6.2.4 Pagua Debris Flows Simulation	199
6.2.5 Pointe Michel South Debris Flows Simulation	203
6.2.6 Pointe Michel North Debris Flows Simulation	208
6.2.7 Soufriere Debris Flows Simulation	213
6.2.8 Ribeira Domingo Santo Debris Flows Simulation.....	217
6.3 HEC-RAS 2D Unsteady Flow Results.....	221
6.4 Model Calibration Results.....	221
6.4.1. Coulibistre HEC-RAS 2D Unsteady Flow Simulation Results	222
6.4.2 Delice HEC-RAS 2D Unsteady Flow Simulation Results.....	226

6.4.3 Layou HEC-RAS 2D Unsteady Flow Simulation Results	230
6.4.4 Pagua HEC-RAS 2D Unsteady Flow Simulation Results.....	234
6.4.5 Pointe Michel HEC-RAS 2D Unsteady Flow Simulation Results	238
6.4.6 Soufriere HEC-RAS 2D Unsteady Flow Simulation Results.....	242
6.4.7 Ribeira Santo Domingo HEC-RAS 2D Unsteady Flow Simulation Results	246
CHAPTER SEVEN.....	250
Discussion.....	250
7.0 Introduction.....	250
7.1 Main Features of Geohazards Experienced During Hurricane Maria In Dominica.....	250
7.2 Vulnerability of Dominica To Geohazards.....	253
7.2.1 Validation of Models.....	253
7.2.2 Comparison of RAMMS Debris Flow Model Results with Google Earth Images.	254
7.2.3 Analysis of Results	264
7.2.4 HEC-RAS 2D Unsteady Flow and Hydraulic Modelling	265
7.2.5 Assessment of Debris Flow and Flood Hazards in Study Localities.....	268
7.3 Implication of Research Work For Managing Geohazards in Other SIDS.....	271
7.3.1 Fogo, Cape Verde Example.....	271
7.3.2 Evaluation of Usefulness of Drones.	272
7.3.3 Recommendations For Geohazards Risk Management	277
7.4 Limitations of Research Work.....	283
7.4.1 Uncertainties and Errors.....	283
7.4.2 Problems Associated with SRTM and ALOS PALSAR DEMs.	289
7.4.3 Sensitivity Analysis of RAMMS Debris Flow Module.....	293
7.4.4 Further Work	295
CHAPTER EIGHT.....	297
Conclusion.....	297
8.0 Conclusion.....	297
REFERENCES.....	300

List of Figures

FIGURE 1.1 A LIST OF THE SMALL ISLANDS DEVELOPING STATES (SIDS). SOURCE: UN SUSTAINABLE DEVELOPMENT GOALS KNOWLEDGE PLATFORM (WWW.SUSTAINABLEDEVELOPMENT.UN.ORG). 5

FIGURE 1.2: MAIN AND CASCADING GEOPHYSICAL AND HYDRO-METEOROLOGICAL HAZARDS (AUTHOR’S OWN IMAGE). 9

FIGURE 2.1A SKETCH MAP OF LESSER ANTILLES ISLANDS, SHOWING LOCATION OF DOMINICA WHICH CAN BE CONSIDERED AS THE NORTHERNMOST ISLAND IN THE WINDWARD ISLANDS OR THE SOUTHERNMOST ISLAND IN THE LEEWARD ISLANDS (HUGH ET AL, 2018). 22

FIGURE 2.1 B: GEOGRAPHIC AND LOCATION MAP OF DOMINICA (RESEARCHER’S IMAGE CREATED IN ARCMAP 10.7). 23

FIGURE 2.2: DOMINICA GEOLOGICAL MAP (SMITH ET AL, 2004). 26

FIGURE 2.3: SHADED RELIEF MAP OF DOMINICA SHOWING LOCATION OF FATALITIES (DEAD AND MISSING PEOPLE) (RESEARCHER’S IMAGE CREATED IN ARCMAP 10.7). 31

FIGURE 2.4: DOMINICA RAINFALL MAP SHOWING ANNUAL RAINFALL DISTRIBUTION ACROSS THE ISLAND (CDEMA, 2018). 32

FIGURE 2.5: DOMINICA VEGETATION MAP SHOWING TYPES OF VEGETATION ACROSS THE ISLAND (CDEMA, 2018). 33

FIGURE 2.7: GEOGRAPHIC MAP OF FOGO, WITH INSET SHOWING LOCATION OF FOGO IN CAPE VERDE (RESEARCHER’S IMAGE CREATED IN ARCMAP 10.7). 36

FIGURE 2.8: FOGO GEOLOGICAL MAP (TORRES ET AL, 1997) 38

FIGURE 2.9. FOGO PRECIPITATION DATA (WORLD CLIMATE AND WEATHER INFORMATION, 2020) 42

FIGURE 2.10. FOGO TEMPERATURE DATA (WORLD CLIMATE AND WEATHER INFORMATION, 2020). 42

FIGURE 3.1A: DIFFERENCE BETWEEN DSM AND DTM. SOURCE: WWW.GISRESOURCES.COM 47

FIGURE 3.1B: DIFFERENCE BETWEEN DSM AND DTM. SOURCE:WWW.GISRESOURCES.COM 47

FIGURE 3.2: DIFFERENCE BETWEEN RASTER AND VECTOR LAYERS. SOURCE: 48

FIGURE 3.3 A: REMOTE SENSING TECHNIQUE FOR ACQUIRING DEM. SOURCE: 48

FIGURE 3.3 B: OPTICAL (PASSIVE) AND ACTIVE (RADAR) REMOTE SENSING METHODS. SOURCE: WWW.CRISP.NUS.EDU.SG 49

FIGURE 3.4: SRTM DEM CORRECTION WORKFLOW IN ARCMAP. 51

FIGURE 3.5: UNCORRECTED SHUTTLE RADAR TOPOGRAPHIC MISSION DEM. (RESEARCHER’S IMAGE CREATED IN ARCMAP 10.7) 52

FIGURE 3.6: ALOS PALSAR CORRECTION WORKFLOW IN ARCMAP 53

FIGURE 3.7: UNCORRECTED ALOS PALSAR DEM. (RESEARCHER’S IMAGE CREATED IN ARCMAP 10.7). 54

FIGURE: 3.8: WORKFLOW FOR DEM TERRAIN ANALYSIS IN ARCGIS. 55

FIGURE: 3.9: WORKFLOW FOR EXTRACTING HILLSHADE FROM A DEM IN ARCMAP. 56

FIGURE: 3.10: WORKFLOW FOR CALCULATING SLOPE ANGLE FROM A DEM IN ARCMAP. 57

FIGURE: 3.11: WORKFLOW FOR CALCULATING ASPECT FROM A DEM IN ARCMAP 58

FIGURE: 3.12: WORKFLOW FOR GENERATING CONTOUR MAP FROM A DEM IN ARCMAP. 59

FIGURE 3.13: WORKFLOW USED TO CREATE FLOW DIRECTION MAP 60

FIGURE 3.14: WORKFLOW USED TO CREATE FLOW DIRECTION MAP 61

FIGURE 3.15: WORKFLOW USED TO CREATE FLOW ACCUMULATION MAP. 62

FIGURE 3.16: WORKFLOW USED TO CREATE DRAINAGE MAP 62

FIGURE 3.17: MAP OF DOMINICA SHOWING SELECTED STUDY LOCATIONS FOR GROUND-TRUTHING AND DRONE SURVEY. (RESEARCHER’S IMAGE CREATED IN ARCMAP 10.7). 67

FIGURE 3.18: GOOGLE EARTH MAP OF DELICE AREA WHERE A DRONE SURVEY WAS CONDUCTED..... 68

FIGURE 3.19: GOOGLE EARTH MAP OF SOUFIERE AREA WHERE A DRONE SURVEY WAS CONDUCTED. 68

FIGURE 3.20: GOOGLE EARTH MAP OF POINTE MICHEL AREA WHERE A DRONE SURVEY WAS CONDUCTED. 69

FIGURE 3.21: GOOGLE EARTH MAP OF PAGUA AREA WHERE A DRONE SURVEY WAS CONDUCTED. 69

FIGURE 3.22: GOOGLE EARTH MAP OF LAYOU AREA WHERE A DRONE SURVEY WAS CONDUCTED..... 70

FIGURE 3.23: GOOGLE EARTH MAP OF COULIBISTRIE AREA WHERE A DRONE SURVEY WAS CONDUCTED. 70

FIGURE 3.24: GOOGLE EARTH MAP OF EASTERN FOGO SHOWING THE UPPER RIBEIRA AREA, FROM PONTO ALTO DO SUL TO THE ROAD FROM CIDREIRA TO MONTE GRANDE..... 73

FIGURE 3.26: GOOGLE EARTH MAP OF WESTERN FOGO SHOWING AREA OF LOWER RIBEIRA IN SAO FILIPE. 74

FIGURE 3.27: GOOGLE EARTH MAP OF WESSTERN FOGO SHOWING COMPLETE OVERVIEW OF RIBEIRA COMPLEX FROM “RIBEIRA SANTO DOMINGO” AT ITS SOURCE IN PONTO ALTO DO SUL TO ITS END “RIBEIRA DO TRINDADE” IN SAO FILIPE. 74

FIGURE 3.28: WORKFLOW USED TO PROCESS DRONE AERIAL PHOTOGRAPHS IN AGISOFT METASHAPE PROFESSIONAL..... 77

FIGURE 3.29: IMAGEJ BOULDER ANALYSIS WORKFLOW. 80

FIGURE 3.30: 2 M ROD USED AS SCALE FOR MEASURING BOULDER SIZE, DEPLOYED IN DOMINICA.	81
FIGURE 3.32: CARTESIAN COORDINATE SYSTEM IN RAMMS, Z IS TOPOGRAPHY, X AND Y ARE HORIZONTAL COORDINATES (CHRISTEN ET AL, 2010).	84
FIGURE 3.33 A: RASTER COORDINATE SYSTEM PROJECTION WORKFLOW IN ARCGIS.	87
FIGURE 3.33 B: RASTER COORDINATE SYSTEM PROJECTION IN ARCGIS.	87
FIGURE 3.34: PRESELECTION OF INPUT DATA DIRECTORY IN RAMMS.	88
FIGURE 3.35: PROJECT WIZARD SHOWING INFORMATION OF IMPORTED DEM IN RAMMS.	88
FIGURE 3.36: IMPORTED DSM AND ORTHOPHOTOGRAPH IN RAMMS.	89
FIGURE 3.37 A AND B: SIMULATION PARAMETERS.	90
FIGURE 3.38 A: DIAGRAMMATIC PRESENTATION OF COMPUTATIONAL MESH IN HEC-RAS 2D (US ARMY CORPS, 2019).	96
FIGURE 3.38 B: COMPUTATIONAL MESH 2D FLOW AREA GENERATED FROM DSM IN HEC-RAS.	96
FIGURE 3.39: MAIN HEC-RAS 5.0.7 WINDOW.	99
FIGURE 3.40: HEC-RAS OVERVIEW AND FUNCTIONALITIES	99
FIGURE 3.41: NEW PROJECT WINDOW FOR HEC-RAS SOFTWARE.	100
FIGURE 3.42 RAS MAPPER WINDOW SHOWING UPLOADED DSM (DELICE RIVER, DOMINICA).	101
FIGURE 3.43 A: RASTER COORDINATE SYSTEM PROJECTION WORKFLOW IN ARCGIS. (RESEARCHER'S IMAGE)	102
FIGURE 3.43 B: RASTER COORDINATE SYSTEM PROJECTION IN ARCGIS.	102
FIGURE 3.44: RAS MAPPER WINDOW SHOWING UPLOADED SPATIAL COORDINATE PROJECTION.	103
FIGURE 3.45 A: RAS MAPPER WINDOW SHOWING UPLOADED LANDCOVER DATA LAYER.	104
FIGURE 3.45 B: RAS MAPPER WINDOW SHOWING MANNING ROUGHNESS COEFFICIENTS BASED ON LANDCOVER DATA.	104
FIGURE 3.46: GEOMETRY DATA WINDOW SHOWING 2D FLOW AREA AND BOUNDARY LINES USING AN EXAMPLE FROM THIS STUDY (DELICE, DOMINICA).	105
FIGURE 3.47 A: UNSTEADY FLOW DATA UPSTREAM WINDOW USING DATA FROM THIS STUDY.	106
FIGURE 3.47 B: UNSTEADY FLOW DATA DOWNSTREAM WINDOW.	107
FIGURE 4.1: CORRECTED DEM OF DOMINICA WITH BACKSCATTER VALUES. (RESEARCHER'S IMAGE CREATED IN ARCMAP 10.7).	109
FIGURE 4.2: HILL SHADED RELIEF MAP EXPOSING THE RUGGED TOPOGRAPHY OF DOMINICA.	113
FIGURE 4.3: SLOPE ANGLE (STEEPNESS) MAP SHOWING FLAT AREAS (0° - 30°), MODERATE SLOPE AREAS (31° - 45°) AND HIGH SLOPE AREAS (46° - 75°).	114
FIGURE 4.4: SLOPE ASPECT (ORIENTATION) MAP SHOWING DIRECTION OF DOWNSLOPE MOVEMENT.	115
FIGURE 4.5: CONTOURS OVERLAID ON HILLSHADE MAP SHOWING CHANGES IN ELEVATION.	116
FIGURE 4.6: FLOW DIRECTION MAP SHOWING SURFACE WATER FLOW DIRECTION WHERE 1 IS EAST, 2 IS SOUTH-EAST, 4 IS SOUTH, 8 IS SOUTH-WEST, 16 IS WEST, 32 IS NORTH-WEST, 64 IS NORTH AND 128 IS NORTH-EAST.	119
FIGURE 4.7: FLOW ACCUMULATION MAP SHOWING TEN ACCUMULATED STREAMS.	120
FIGURE 4.8: DRAINAGE NETWORK MAP SHOWING DENDRITIC DRAINAGE PATTERN.	121
FIGURE 5.1 A: FIELD IMAGE SHOWING CLUSTER OF BOULDERS (0.4-1.5 M) AND TREE DEBRIS (1-3 M) IN THE CHANNEL BED AT COULIBISTRIE (DOMINICA).	124
FIGURE 5.1 B: GOOGLE EARTH IMAGE BEFORE THE HURRICANE MARIA EVENT FOR COULIBISTRIE (DOMINICA).....	125
FIGURE 5.1 C: GOOGLE EARTH IMAGE SHOWING POST-HURRICANE MARIA EVENT DEVASTATION AT COULIBISTRIE (DOMINICA) ...	125
FIGURE 5.1 (D): POST-HURRICANE MARIA DRONE-DERIVED ORTHOPHOTOGRAPH SHOWING DAMAGE CAUSED BY HURRICANE MARIA AT DELICE (DOMINICA).	126
FIGURE 5.2 A: FIELD IMAGE SHOWING COBBLES (0.06-0.2 M), BOULDERS (0.4-2 M) AND TREE DEBRIS (0.5-3 M) DEPOSITED LATERALLY IN THE CHANNEL BED AT DELICE (DOMINICA).	127
FIGURE 5.2 B: PRE-HURRICANE MARIA GOOGLE EARTH IMAGES FOR DELICE (DOMINICA)	128
FIGURE 5.2 C: GOOGLE EARTH IMAGE SHOWING POST-HURRICANE MARIA DEVASTATION AT DELICE (DOMINICA)	128
FIGURE 5.2 D: DRONE-DERIVED ORTHOPHOTOGRAPH SHOWING DAMAGE CAUSED BY HURRICANE MARIA AT DELICE (DOMINICA).	129
FIGURE 5.3 A: FIELD IMAGE SHOWING DEPOSIT OF MUD-LADEN DEBRIS AND HYDROTHERMALLY ALTERED BOULDERS (0.5-1.5 M) AT LAYOU (DOMINICA).	130
FIGURE 5.3 B: GOOGLE EARTH IMAGES BEFORE THE HURRICANE MARIA EVENT FOR LAYOU (DOMINICA)	131
FIGURE 5.3 C: GOOGLE EARTH IMAGE SHOWING POST-HURRICANE MARIA EVENT DEVASTATION AT LAYOU (DOMINICA).	131

FIGURE 5.3 D: DRONE-DERIVED ORTHOPHOTOGRAPH SHOWING DAMAGE CAUSED BY HURRICANE MARIA AT LAYOU (DOMINICA).	132
FIGURE 5.4 A: FIELD IMAGE SHOWING DEEP-SEATED GIANT BOULDER (10 M), SMALL TO MEDIUM BOULDERS (0.4-7 M) AND SUPERVISOR WITH 2 M ROD AS SCALE AT PAGUA (DOMINICA).	133
FIGURE 5.4 B: GOOGLE EARTH IMAGES BEFORE HURRICANE MARIA FOR PAGUA (DOMINICA).	134
FIGURE 5.4 C: GOOGLE EARTH IMAGE SHOWING POST-HURRICANE MARIA DEVASTATION AT PAGUA (DOMINICA).	134
FIGURE 5.4 D: POST-HURRICANE MARIA DRONE-DERIVED ORTHOPHOTOGRAPH SHOWING DAMAGE CAUSED BY HURRICANE MARIA AT PAGUA (DOMINICA).	135
FIGURE 5.5 A: FIELD IMAGE SHOWING DEPOSIT OF TREE DEBRIS (0.5-2 M) AND CLUSTER OF BOULDERS (0.5-1.5 M) AT POINTE MICHEL (DOMINICA).	136
FIGURE 5.5 B: GOOGLE EARTH IMAGES BEFORE HURRICANE MARIA FOR POINTE MICHEL (DOMINICA).	137
FIGURE 5.5 C: GOOGLE EARTH IMAGE SHOWING POST-HURRICANE MARIA DEVASTATION AT POINTE MICHEL (DOMINICA).	137
FIGURE 5.5 D: DRONE-DERIVED ORTHOPHOTOGRAPH SHOWING DAMAGE CAUSED BY HURRICANE MARIA AT POINTE MICHEL (DOMINICA).	138
FIGURE 5.6 A: FIELD IMAGE SHOWING DEPOSIT OF TREE DEBRIS (0.5-2 M) AND CLUSTER OF BOULDERS (0.5-1.5 M) AT SOUFRIERE (DOMINICA).	139
FIGURE 5.6 B: GOOGLE EARTH IMAGES BEFORE HURRICANE MARIA FOR SOUFRIERE (DOMINICA).	140
FIGURE 5.6 C: GOOGLE EARTH IMAGE SHOWING POST-HURRICANE MARIA DEVASTATION AT SOUFRIERE (DOMINICA).	140
FIGURE 5.6 D: DRONE-DERIVED ORTHOPHOTOGRAPH SHOWING DAMAGE CAUSED BY HURRICANE MARIA AT SOUFRIERE (DOMINICA).	141
FIGURE 5.9: RESULTS OF IMAGEJ BOULDERS ANALYSIS FOR LAYOU (DOMINICA) SHOWING THE SIZES (M) AND NUMBER OF BOULDERS.	145
FIGURE 5.11: RESULTS OF IMAGEJ BOULDERS ANALYSIS FOR POINTE MICHEL (DOMINICA) SHOWING THE SIZES (M) AND NUMBER OF BOULDERS.	146
FIGURE 5.12: RESULTS OF IMAGEJ BOULDERS ANALYSIS FOR SOUFRIERE (DOMINICA) SHOWING THE SIZES (M) AND NUMBER OF BOULDERS.	146
FIGURE 5.13: RESULTS OF IMAGEJ BOULDERS ANALYSIS FOR ALL STUDY AREAS IN DOMINICA SHOWING THE SIZES (M) AND NUMBER OF BOULDERS.	147
FIGURE 5.14: COULIBISTRIE RIVER FIELD PHOTOGRAPH SHOWING WEATHERED GIANT BOULDERS (0.7-3.3 M IN DIAMETER) AT THE SOUTH BANK OF THE RIVER WITH A 2 M ROD AS SCALE AND RIVER FLOWING LEFT TO RIGHT. MOST BOULDERS CAME DOWN AS ROCKFALL AND PROBABLY PRE-DATED HURRICANE MARIA.	148
FIGURE 5.15: DELICE RIVER FIELD PHOTOGRAPH SHOWING LATERAL DEPOSITION OF BOULDERS (0.5-3.4 M IN DIAMETER) FROM THE RIVERBANK FAILURE CAUSED BY EXCESSIVE FORCE OF THE FLOW AND HYDRAULIC TOE EROSION UNDERCUTTING THE RIVER-BANK DURING HURRICANE MARIA. RIVER FLOWS FROM RIGHT TO LEFT FROM THE VIEWER.	149
FIGURE 5.16: LAYOU RIVER FIELD PHOTOGRAPH SHOWING DEPOSIT OF HYDROTHERMALLY ALTERED BOULDERS (0.4-7.3 M DIAMETER).	150
FIGURE 5.17: PAGUA RIVER FIELD PHOTOGRAPH SHOWING DEEP-SEATED GIANT BOULDER (0.5-10 M IN DIAMETER) IN THE RIVER-BED AND 2 M ROD AS SCALE. THE BOULDER IS A CONGLOMERATE OF PUMICE AND VOLCANIC CLASTS AND RIVER FLOWS FROM LEFT TO RIGHT. THE BOULDER PRE-DATED HURRICANE MARIA BUT MAY BLOCK THE STREAM FLOW WHEN TREE DEBRIS AND OTHER SEDIMENTS PILE-UP BEHIND IT WHICH MAY RESULT IN OVERBANK FLOODING.	151
FIGURE 5.18: POINTE MICHEL FIELD PHOTOGRAPH SHOWING HURRICANE MARIA DEBRIS FLOW DEPOSIT OF BOULDERS (0.4-4.5 M IN DIAMETER).	152
FIGURE 5.19: SOUFRIERE FIELD PHOTO SHOWING HURRICANE MARIA DEBRIS FLOW DEPOSIT OF CLUSTER OF HYDROTHERMALLY ALTERED BOULDERS (0.4-7.3 M IN DIAMETER) MIXED WITH CLAY, TREE DEBRIS AND COBBLES.	153
FIGURE 5.20 A, B AND C: FIELD PHOTOS OF THE WESTERN PART OF RIBEIRA DOMINGO SANTO (FOGO), SHOWING SETTLEMENTS SITUATED LATERALLY ON THE EDGE OF CHANNEL'S LEFT BANK. THE BUILDINGS ARE ON AN UNSTABLE SLOPE MADE OF LAYERS OF BOULDERS (0.5-1 M) WHICH ARE BEING ERODED AND DEPOSITED INTO THE CHANNEL BED. DIRECTION OF THE CHANNEL AND BUILDINGS IS NORTH TO SOUTH OF RIBEIRA SANTO DOMINGO (CAPE VERDE, FOGO).	156
FIGURE 5.21: DRONE-DERIVED DIGITAL SURFACE MODEL (DSM) FOR COULIBISTRIE SHOWING AREAS OF LOW ELEVATION IN DARK AND HIGH ELEVATION IN GREY.	159
FIGURE 5.22: DRONE-DERIVED ORTHOPHOTOGRAPH FOR COULIBISTRIE, SHOWING DESTRUCTION CAUSED BY HURRICANE MARIA.	160

FIGURE 5.24: DRONE-DERIVED ORTHOPHOTOGRAPH FOR DELICE, SHOWING DEVASTATION OF HURRICANE MARIA ON INFRASTRUCTURE AND FARMLANDS.	162
FIGURE 5.25: DRONE-DERIVED DSM FOR LAYOU SHOWING AREAS OF LOW ELEVATION IN DARK AND HIGH ELEVATION IN GREY	163
FIGURE 5.26: DRONE-DERIVED ORTHOPHOTOGRAPH FOR LAYOU, SHOWING POST-HURRICANE MARIA DESTRUCTION	164
FIGURE 5.27: DRONE-DERIVED DSM FOR PAGUA, SHOWING AREAS OF LOW ELEVATION IN DARK AND HIGH ELEVATION IN GREY...	165
FIGURE 5.28: DRONE-DERIVED ORTHOPHOTOGRAPH FOR PAGUA, SHOWING DAMAGE CAUSED BY HURRICANE MARIA.	166
FIGURE 5.29: DRONE-DERIVED DSM FOR POINTE MICHEL, SHOWING AREAS OF LOW ELEVATION IN DARK AND HIGH ELEVATION IN GREY.	167
FIGURE 5.30: DRONE-DERIVED ORTHOPHOTOGRAPH FOR POINTE MICHEL SHOWING DESTRUCTION CAUSED BY HURRICANE MARIA.	168
FIGURE 5.31: DRONE-DERIVED DSM FOR SOUFRIERE SHOWING AREAS OF LOW ELEVATION IN DARK AND HIGH ELEVATION IN GREY.	169
FIGURE 5.32: DRONE-DERIVED ORTHOPHOTOGRAPH FOR SOUFRIERE, SHOWING POST-HURRICANE MARIA DEVASTATION.	170
FIGURE 5.33: (A) DRONE-DERIVED DSM FOR RIBEIRA SANTO DOMINGO SHOWING AREAS OF LOW ELEVATION IN DARK AND HIGH ELEVATION IN GREY, (B) DRONE-DERIVED ORTHOPHOTOGRAPH FOR RIBEIRA SANTO DOMINGO, SHOWING CURRENT STATE AND FEATURES OF THE TERRAIN.	171
FIGURE 6.1 A: SENSITIVITY ANALYSIS OF RAMMS SIMULATIONS FOR DEBRIS FLOW RUNOUT DISTANCE FOR 200 M/S ² AND 400 M/S ² TURBULENT COEFFICIENT (ξ) VALUES (EXAMPLE OF PAGUA RIVER, DOMINICA).....	175
FIGURE 6.1 B: SENSITIVITY ANALYSIS OF RAMMS SIMULATIONS FOR DEBRIS FLOW RUNOUT DISTANCE FOR 600 M/S ² AND 800 M/S ² TURBULENT COEFFICIENT (ξ) VALUES (EXAMPLE OF PAGUA RIVER, DOMINICA).....	176
FIGURE 6.2 A: RESULTS OF RAMMS SENSITIVITY ANALYSIS SIMULATIONS OF DEBRIS FLOW RUNOUT DISTANCE FOR 0.05 AND 0.10 FRICTION COEFFICIENT (μ) VALUES (EXAMPLE OF PAGUA RIVER, DOMINICA)	178
FIGURE 6.2 B: RESULTS OF RAMMS SENSITIVITY ANALYSIS SIMULATIONS OF DEBRIS FLOW RUNOUT DISTANCE FOR 0.15 AND 0.20 FRICTION COEFFICIENT (μ) VALUES (EXAMPLE OF PAGUA RIVER, DOMINICA).....	179
FIGURE 6.3 A: RESULTS OF SENSITIVITY ANALYSIS OF RAMMS DEBRIS FLOW MODELLING, SHOWING VARIATIONS IN THE RUNOUT DISTANCE FOR 0.25 AND 0.50 EARTH PRESSURE (LAMBDA) (λ) VALUES.....	181
FIGURE 6.3 B: RESULTS OF SENSITIVITY ANALYSIS OF RAMMS DEBRIS FLOW MODELLING, SHOWING VARIATIONS IN THE RUNOUT DISTANCE FOR 0.75 AND 1 EARTH PRESSURE (LAMBDA) (λ) VALUES.....	182
FIGURE 6.4: RESULTS OF RAMMS DEBRIS FLOW MODELLING FOR COULIBISTRIE (DOMINICA), (A) VARIATIONS IN FLOW HEIGHT (IN M); (B) FLOW VELOCITY (IN M/S) OVER THE WHOLE DRAINAGE AREA.....	186
FIGURE 6.4: RESULTS OF RAMMS DEBRIS FLOW MODELLING FOR COULIBISTRIE (DOMINICA), (C) FLOW PRESSURE (IN KPA), (D) FLOW ENTRAINMENT (IN M ³) OVER THE WHOLE DRAINAGE AREA.	187
FIGURE 6.4: RESULTS OF RAMMS DEBRIS FLOW MODELLING FOR COULIBISTRIE (DOMINICA).; (E) FLOW DEPOSITION (IN M ³) AND (F) FLOW MOMENTUM (IN M/S) OVER THE WHOLE DRAINAGE AREA.....	188
FIGURE 6.5: RESULTS OF THE RAMMS DEBRIS FLOW SIMULATION OF DELICE (DOMINICA), (A) VARIATIONS IN FLOW HEIGHT (IN M); (B) FLOW VELOCITY (IN M/S) OVER THE WHOLE DRAINAGE AREA.	191
FIGURE 6.5: RESULTS OF THE RAMMS DEBRIS FLOW SIMULATION OF DELICE (DOMINICA), (C) FLOW PRESSURE (IN PA); (D) FLOW ENTRAINMENT (IN M ³) OVER THE WHOLE DRAINAGE AREA.....	192
FIGURE 6.5: RESULTS OF THE RAMMS DEBRIS FLOW SIMULATION OF DELICE (DOMINICA), (E) FLOW DEPOSITION (IN M ³) AND (F) FLOW MOMENTUM (IN M/S) OVER THE WHOLE DRAINAGE AREA.....	193
FIGURE 6.6: RESULTS OF RAMMS DEBRIS FLOW SIMULATION OF LAYOU (DOMINICA), (A) VARIATIONS IN FLOW HEIGHT (IN M); (B) FLOW VELOCITY (IN M/S) OVER THE WHOLE DRAINAGE AREA.....	196
FIGURE 6.6: RESULTS OF RAMMS DEBRIS FLOW SIMULATION OF LAYOU (DOMINICA), (C) FLOW PRESSURE (IN PA), (D) FLOW ENTRAINMENT (IN M ³) OVER THE WHOLE DRAINAGE AREA.....	197
FIGURE 6.6: RESULTS OF RAMMS DEBRIS FLOW SIMULATION OF LAYOU (DOMINICA), (E) FLOW DEPOSITION (IN M ³) AND (F) FLOW MOMENTUM (IN M/S) OVER THE WHOLE DRAINAGE AREA.	198
FIGURE 6.7: RESULTS OF RAMMS DEBRIS FLOW SIMULATION OF PAGUA (DOMINICA), (A) VARIATIONS IN FLOW HEIGHT (IN M); (B) FLOW VELOCITY (IN M/S) OVER THE WHOLE DRAINAGE AREA.....	200
FIGURE 6.7: RESULTS OF RAMMS DEBRIS FLOW SIMULATION OF PAGUA (DOMINICA), (C) FLOW PRESSURE (IN PA), (D) FLOW ENTRAINMENT (IN M ³) OVER THE WHOLE DRAINAGE AREA.....	201
FIGURE 6.7: RESULTS OF RAMMS DEBRIS FLOW SIMULATION OF PAGUA (DOMINICA), (E) FLOW DEPOSITION (IN M ³) AND (F) FLOW MOMENTUM (IN M/S) OVER THE WHOLE DRAINAGE AREA.	202

FIGURE 6.8 : RAMMS DEBRIS FLOW SIMULATION OF POINTE MICHEL SOUTH (DOMINICA), (A) VARIATIONS IN FLOW HEIGHT (IN M); (B) FLOW VELOCITY (IN M/S) OVER THE WHOLE DRAINAGE AREA.	205
FIGURE 6.8: RAMMS DEBRIS FLOW SIMULATION OF POINTE MICHEL SOUTH (DOMINICA); (C) FLOW PRESSURE (IN PA), (D) FLOW ENTRAINMENT (IN M ³) OVER THE WHOLE DRAINAGE AREA.	206
FIGURE 6.8: RAMMS DEBRIS FLOW SIMULATION OF POINTE MICHEL SOUTH (DOMINICA), (E) FLOW DEPOSITION (IN M ³) AND (F) FLOW MOMENTUM (IN M/S) OVER THE WHOLE DRAINAGE AREA.	207
FIGURE 6.9: RAMMS DEBRIS FLOW SIMULATION OF POINTE MICHEL NORTH (DOMINICA), (A) VARIATIONS IN FLOW HEIGHT (IN M); (B) FLOW VELOCITY (IN M/S) OVER THE WHOLE DRAINAGE AREA.	210
FIGURE 6.9: RAMMS DEBRIS FLOW SIMULATION OF POINTE MICHEL NORTH (DOMINICA), (C) FLOW PRESSURE (IN PA), (D) FLOW ENTRAINMENT (IN M ³) OVER THE WHOLE DRAINAGE AREA.	211
FIGURE 6.9: RAMMS DEBRIS FLOW SIMULATION OF POINTE MICHEL NORTH (DOMINICA), (E) FLOW DEPOSITION (IN M ³) AND (F) FLOW MOMENTUM (IN M/S) OVER THE WHOLE DRAINAGE AREA.	212
FIGURE 6.10: RESULTS OF RAMMS DEBRIS FLOW SIMULATION OF SOUFRIERE (DOMINICA), (A) VARIATIONS IN FLOW HEIGHT (IN M); (B) FLOW VELOCITY (IN M/S) OVER THE WHOLE DRAINAGE AREA.	214
FIGURE 6.10: RESULTS OF RAMMS DEBRIS FLOW SIMULATION OF SOUFRIERE (DOMINICA), (C) FLOW PRESSURE (IN PA), (D) FLOW ENTRAINMENT (IN M ³) OVER THE WHOLE DRAINAGE AREA.	215
FIGURE 6.10: RESULTS OF RAMMS DEBRIS FLOW SIMULATION OF SOUFRIERE (DOMINICA), (E) FLOW DEPOSITION (IN M ³) AND (F) FLOW MOMENTUM (IN M/S) OVER THE WHOLE DRAINAGE AREA.	216
FIGURE 6.11: RAMMS DEBRIS FLOW SIMULATION OF RIBEIRA SANTO DOMINGO (FOGO), (A) VARIATIONS IN FLOW HEIGHT (IN M); (B) FLOW VELOCITY (IN M/S) OVER THE WHOLE DRAINAGE AREA.	218
FIGURE 6.11: RAMMS DEBRIS FLOW SIMULATION OF RIBEIRA SANTO DOMINGO (FOGO), (C) FLOW PRESSURE (IN PA), (D) FLOW ENTRAINMENT (IN M ³) OVER THE WHOLE DRAINAGE AREA.	219
FIGURE 6.11: RAMMS DEBRIS FLOW SIMULATION OF RIBEIRA SANTO DOMINGO (FOGO), (E) FLOW DEPOSITION (IN M ³) AND (F) FLOW MOMENTUM (IN M/S) OVER THE WHOLE DRAINAGE AREA.	220
FIGURE 6.12 A: RESULTS OF HEC-RAS UNSTEADY FLOW SIMULATION FOR COULIBISTRIE (DOMINICA), SHOWING VARIATIONS IN FLOW DEPTH ACROSS THE FLOODPLAIN (IN M).	223
FIGURE 6.12 B: RESULTS OF HEC-RAS UNSTEADY FLOW SIMULATION FOR COULIBISTRIE (DOMINICA), SHOWING VARIATIONS IN DAILY FLOW DEPTH OVER A MONTH (IN M).	223
FIGURE 6.12 C: RESULTS OF HEC-RAS UNSTEADY FLOW SIMULATION FOR COULIBISTRIE (DOMINICA), SHOWING VARIATIONS IN FLOW VELOCITY ACROSS THE FLOODPLAIN (IN M/S).	224
FIGURE 6.12 D: RESULTS OF HEC-RAS UNSTEADY FLOW SIMULATION FOR COULIBISTRIE (DOMINICA), SHOWING VARIATIONS IN FLOW VELOCITY ALONG THE CHANNEL (IN M/S).	224
FIGURE 6.12 E: RESULTS OF HEC-RAS UNSTEADY FLOW SIMULATION FOR COULIBISTRIE (DOMINICA), SHOWING VARIATIONS IN WATER SURFACE ELEVATION ACROSS THE FLOODPLAIN (IN M).	225
FIGURE 6.12 F: RESULTS OF HEC-RAS UNSTEADY FLOW SIMULATION FOR COULIBISTRIE (DOMINICA), SHOWING COMPARISON BETWEEN WATER SURFACE ELEVATION AND TERRAIN ELEVATION (IN M).	225
FIGURE 6.13 A: RESULTS OF HEC-RAS UNSTEADY FLOW SIMULATION FOR DELICE (DOMINICA), SHOWING VARIATIONS IN FLOW DEPTH ACROSS THE FLOODPLAIN (IN M)	227
FIGURE 6.13 B: RESULTS OF HEC-RAS UNSTEADY FLOW SIMULATION FOR DELICE (DOMINICA), SHOWING VARIATIONS IN DAILY FLOW DEPTH OVER A MONTH (IN M).	227
FIGURE 6.13 C: RESULTS OF HEC-RAS UNSTEADY FLOW SIMULATION FOR DELICE (DOMINICA), SHOWING VARIATIONS IN FLOW VELOCITY ACROSS THE FLOODPLAIN (IN M/S)	228
FIGURE 6.13 D: RESULTS OF HEC-RAS UNSTEADY FLOW SIMULATION FOR DELICE (DOMINICA), SHOWING VARIATIONS IN FLOW VELOCITY ALONG THE CHANNEL (IN M/S)	228
FIGURE 6.13 E: RESULTS OF HEC-RAS UNSTEADY FLOW SIMULATION FOR DELICE (DOMINICA), SHOWING VARIATIONS IN WATER SURFACE ELEVATION ACROSS THE FLOODPLAIN (IN M).	229
FIGURE 6.13 F: RESULTS OF HEC-RAS UNSTEADY FLOW SIMULATION FOR DELICE (DOMINICA), SHOWING COMPARISON BETWEEN WATER SURFACE ELEVATION AND TERRAIN ELEVATION (IN M)	229
FIGURE 6.14 A: RESULTS OF HEC-RAS UNSTEADY FLOW SIMULATION FOR DELICE (DOMINICA), SHOWING VARIATIONS IN FLOW DEPTH ACROSS THE FLOODPLAIN (IN M)	231
FIGURE 6.14 B: RESULTS OF HEC-RAS UNSTEADY FLOW SIMULATION FOR LAYOU (DOMINICA), SHOWING VARIATIONS IN DAILY FLOW DEPTH OVER A MONTH (IN M).	231

FIGURE 6.14 C: RESULTS OF HEC-RAS UNSTEADY FLOW SIMULATION FOR LAYOU (DOMINICA), SHOWING VARIATIONS IN FLOW VELOCITY ACROSS THE FLOODPLAIN (IN M/S).	232
FIGURE 6.14 D: RESULTS OF HEC-RAS UNSTEADY FLOW SIMULATION FOR LAYOU (DOMINICA), SHOWING VARIATIONS IN FLOW VELOCITY ALONG THE CHANNEL (IN M/S).	232
FIGURE 6.15 A: RESULTS OF HEC-RAS UNSTEADY FLOW SIMULATION FOR PAGUA (DOMINICA), SHOWING VARIATIONS IN FLOW DEPTH ACROSS THE FLOODPLAIN (IN M).	235
FIGURE 6.15 B: RESULTS OF HEC-RAS UNSTEADY FLOW SIMULATION FOR PAGUA (DOMINICA), SHOWING VARIATIONS IN DAILY FLOW DEPTH OVER A MONTH (IN M).	235
FIGURE 6.15 C: RESULTS OF HEC-RAS UNSTEADY FLOW SIMULATION FOR PAGUA (DOMINICA), SHOWING VARIATIONS IN FLOW VELOCITY ACROSS THE FLOODPLAIN (IN M/S).	236
FIGURE 6.15 D: RESULTS OF HEC-RAS UNSTEADY FLOW SIMULATION FOR PAGUA (DOMINICA), SHOWING VARIATIONS IN FLOW VELOCITY ALONG THE CHANNEL (IN M/S).	236
FIGURE 6.15 E: RESULTS OF HEC-RAS UNSTEADY FLOW SIMULATION FOR PAGUA (DOMINICA), SHOWING VARIATIONS IN WATER SURFACE ELEVATION ACROSS THE FLOODPLAIN (IN M).	237
FIGURE 6.15 F: RESULTS OF HEC-RAS UNSTEADY FLOW SIMULATION FOR PAGUA (DOMINICA), SHOWING COMPARISON BETWEEN WATER SURFACE ELEVATION AND TERRAIN ELEVATION (IN M).	237
FIGURE 6.16 A: RESULTS OF HEC-RAS UNSTEADY FLOW SIMULATION FOR POINTE MICHEL (DOMINICA), SHOWING VARIATIONS IN FLOW DEPTH ACROSS THE FLOODPLAIN (IN M).	239
FIGURE 6.16 B: RESULTS OF HEC-RAS UNSTEADY FLOW SIMULATION FOR POINTE MICHEL (DOMINICA), SHOWING VARIATIONS IN DAILY FLOW DEPTH OVER A MONTH (IN M).	239
FIGURE 6.16 C: RESULTS OF HEC-RAS UNSTEADY FLOW SIMULATION FOR POINTE MICHEL (DOMINICA), SHOWING VARIATIONS IN FLOW VELOCITY ACROSS THE FLOODPLAIN (IN M/S).	240
FIGURE 6.16 D: RESULTS OF HEC-RAS UNSTEADY FLOW SIMULATION FOR POINTE MICHEL (DOMINICA), SHOWING VARIATIONS IN FLOW VELOCITY ALONG THE CHANNEL (IN M/S).	240
FIGURE 6.16 E: RESULTS OF HEC-RAS UNSTEADY FLOW SIMULATION FOR POINTE MICHEL (DOMINICA), SHOWING VARIATIONS IN WATER SURFACE ELEVATION ACROSS THE FLOODPLAIN (IN M).	241
FIGURE 6.16 F: RESULTS OF HEC-RAS UNSTEADY FLOW SIMULATION FOR POINTE MICHEL (DOMINICA), SHOWING COMPARISON BETWEEN WATER SURFACE ELEVATION AND TERRAIN ELEVATION (IN M).	241
FIGURE 6.17 A: RESULTS OF HEC-RAS UNSTEADY FLOW SIMULATION FOR SOUFRIERE (DOMINICA), SHOWING VARIATIONS IN FLOW DEPTH ACROSS THE FLOODPLAIN (IN M).	243
FIGURE 6.17 B: RESULTS OF HEC-RAS UNSTEADY FLOW SIMULATION FOR SOUFRIERE (DOMINICA), SHOWING VARIATIONS IN DAILY FLOW DEPTH OVER A MONTH (IN M).	243
FIGURE 6.17 C: RESULTS OF HEC-RAS UNSTEADY FLOW SIMULATION FOR SOUFRIERE (DOMINICA), SHOWING VARIATIONS IN FLOW VELOCITY ACROSS THE FLOODPLAIN (IN M/S).	244
FIGURE 6.17 D: RESULTS OF HEC-RAS UNSTEADY FLOW SIMULATION FOR SOUFRIERE (DOMINICA), SHOWING VARIATIONS IN FLOW VELOCITY ALONG THE CHANNEL (IN M/S).	244
FIGURE 6.17 E: RESULTS OF HEC-RAS UNSTEADY FLOW SIMULATION FOR SOUFRIERE (DOMINICA), SHOWING VARIATIONS IN WATER SURFACE ELEVATION ACROSS THE FLOODPLAIN (IN M).	245
FIGURE 6.17 F: RESULTS OF HEC-RAS UNSTEADY FLOW SIMULATION FOR SOUFRIERE (DOMINICA), SHOWING COMPARISON BETWEEN WATER SURFACE ELEVATION AND TERRAIN ELEVATION (IN M).	245
FIGURE 6.18 A: RESULTS OF HEC-RAS UNSTEADY FLOW SIMULATION FOR RIBEIRA DOMINGO SANTO (FOGO), SHOWING VARIATIONS IN FLOW DEPTH ACROSS THE FLOODPLAIN (IN M).	247
FIGURE 6.18 B: RESULTS OF HEC-RAS UNSTEADY FLOW SIMULATION FOR RIBEIRA DOMINGO SANTO (FOGO), SHOWING VARIATIONS IN DAILY FLOW DEPTH OVER A MONTH (IN M).	247
FIGURE 6.18 C: RESULTS OF HEC-RAS UNSTEADY FLOW SIMULATION FOR RIBEIRA DOMINGO SANTO (FOGO), SHOWING VARIATIONS IN FLOW VELOCITY ACROSS THE FLOODPLAIN (IN M/S).	248
FIGURE 6.18 D: RESULTS OF HEC-RAS UNSTEADY FLOW SIMULATION FOR RIBEIRA DOMINGO SANTO (FOGO), SHOWING VARIATIONS IN FLOW VELOCITY ALONG THE CHANNEL (IN M/S).	248
FIGURE 6.18 E: RESULTS OF HEC-RAS UNSTEADY FLOW SIMULATION FOR RIBEIRA DOMINGO SANTO (FOGO), SHOWING VARIATIONS IN WATER SURFACE ELEVATION ACROSS THE FLOODPLAIN (IN M).	249
FIGURE 6.18 F: RESULTS OF HEC-RAS UNSTEADY FLOW SIMULATION FOR RIBEIRA DOMINGO SANTO (FOGO), SHOWING COMPARISON BETWEEN WATER SURFACE ELEVATION AND TERRAIN ELEVATION (IN M).	249

FIGURE 7.1 A AND B: COMPARISON OF RAMMS DEBRIS FLOW SIMULATION RESULT AND GOOGLE EARTH IMAGE OF OBSERVED DEBRIS FLOW DEPOSITS FROM HURRICANE MARIA FOR COULIBISTRIE (DOMINICA).	255
FIGURE 7.2 A AND B: COMPARISON OF RAMMS DEBRIS FLOW SIMULATION AND GOOGLE EARTH IMAGE OF OBSERVED DEBRIS FLOW EVENT AFTER HURRICANE MARIA FOR DELICE (DOMINICA).	257
FIGURE 7.3 A AND B: COMPARISON OF RAMMS DEBRIS FLOW SIMULATION RESULT AND GOOGLE EARTH IMAGE OF OBSERVED DEBRIS FLOW EVENT POST-HURRICANE MARIA FOR LAYOU IN DOMINICA.	258
FIGURE 7.4 A AND B: COMPARISON OF RAMMS DEBRIS FLOW SIMULATION RESULT AND GOOGLE EARTH IMAGE FROM POST-HURRICANE MARIA FOR PAGUA (DOMINICA).	260
FIGURE 7.5 A AND B: COMPARISON OF RAMMS DEBRIS FLOW SIMULATION RESULT AND GOOGLE EARTH IMAGE OF REAL-LIFE DEBRIS FLOW EVENT POST-HURRICANE MARIA FOR POINTE MICHEL IN DOMINICA.	262
FIGURE 7.6 A AND B: COMPARISON OF RAMMS DEBRIS FLOW SIMULATION RESULT AND GOOGLE EARTH IMAGE OF OBSERVED DEBRIS FLOW EVENT POST-HURRICANE MARIA FOR SOUFRIERE IN DOMINICA.	263
FIGURE 7.7: DIAGRAMMATIC PRESENTATION OF FACTORS THAT TRIGGER DEBRIS FLOW AND RELATED HAZARDS (USGS).....	279
FIGURE 7.8: DIAGRAMMATIC PRESENTATION OF RAINFALL INDUCED LANDSLIDE SOURCED DEBRIS FLOW (USGS)	286
FIGURE 7.9: DIAGRAMMATIC PRESENTATION OF LANDSLIDE INITIATED DEBRIS FLOW, AND CHANNEL-BED FAILURE AND EROSION INITIATED DEBRIS FLOW (SHEN ETAL, 2018).	286
FIGURE 7.10 A AND B: (A) COMPARISON OF HIGH RESOLUTION AND UP TO DATE DRONE-DERIVED DSM OF SOUFRIERE WITH (B) ERRONEOUS LOW RESOLUTION AND OUTDATED SRTM DEM OF DOMINICA.	292

List of Tables

TABLE 2.1 DOMINICA AVERAGE MONTHLY TEMPERATURES (DES, 2019).....	27
TABLE 2.2 DOMINICA AVERAGE MONTHLY PRECIPITATION (DES, 2019)	28
TABLE 2.3 HURRICANES IN DOMINICA OVER THE PAST FORTY YEARS (DES, 2019).	29
TABLE 3.1: DATASET USED FOR RESEARCH WORK	45
TABLE 3.2: SOFTWARE USED FOR THE RESEARCH WORK.	45
TABLE 3.3: STUDY LOCALITIES, DISTANCES AND LAND AREAS COVERED BY DRONE SURVEY IN DOMINICA	65
TABLE 3.4: RANGE OF VALUES USED FOR SENSITIVITY ANALYSIS IN RAMMS DEBRIS FLOW MODULE.....	92
TABLE 5.1: PROCESSED DRONE AERIAL IMAGES TOTAL AREA COVERED AND DIGITAL SURFACE MODELS (DSMS) RESOLUTIONS FOR ALL STUDY AREAS IN DOMINICA AND CAPE VERDE. ..	158
TABLE 6.14: TOTAL AREA AND DSM RESOLUTION FOR EACH LOCALITY USED FOR THE UNSTEADY FLOW SIMULATION.	221
TABLE 6.1: MODEL CALIBRATION AND INPUT PARAMETERS USED FOR SENSITIVITY ANALYSIS OF RAMMS SIMULATIONS FOR EXAMPLE OF PAGUA RIVER (DOMINICA).	173
TABLE 6.2: MODEL CALIBRATION AND INPUT PARAMETERS USED FOR SENSITIVITY ANALYSIS IN RAMMS SIMULATIONS FOR PAGUA RIVER (DATA IN TABLE 6.1).	174

TABLE 6.3: MODEL CALIBRATION AND INPUT PARAMETERS USED FOR RAMMS SENSITIVITY SIMULATION FOR FOUR DIFFERENT VALUES OF THE FRICTION COEFFICIENT.	177
TABLE 6.4: MODEL CALIBRATION AND INPUT PARAMETERS USED FOR RAMMS SENSITIVITY ANALYSIS SIMULATIONS FOR FOUR DIFFERENT VALUES OF EARTH PRESSURE (LAMBDA) (λ).	180
TABLE 6.5: MODEL CALIBRATION AND INPUT PARAMETERS USED FOR RAMMS DEBRIS FLOW SIMULATION FOR ALL STUDY AREAS.	184
TABLE 6.6: COULIBISTRIE RAMMS SIMULATION RESULTS SHOWING RUNOUT DISTANCE, FLOW HEIGHTS, FLOW VELOCITIES AND FLOW PRESSURE OF VARIOUS AREAS OF THE CHANNEL.	185
TABLE 6.7: DELICE RAMMS SIMULATION RESULTS SHOWING RUNOUT DISTANCE, FLOW HEIGHTS, FLOW VELOCITIES AND FLOW PRESSURE IN DIFFERENT PARTS OF THE CHANNEL.....	189
TABLE 6.8: LAYOU RAMMS SIMULATION RESULTS SHOWING RUNOUT DISTANCE, FLOW HEIGHTS, FLOW VELOCITIES AND FLOW PRESSURE OF VARIOUS AREAS OF THE CHANNEL.....	194
TABLE 6.9: PAGUA RAMMS SIMULATION RESULTS SHOWING RUNOUT DISTANCE, FLOW HEIGHTS, FLOW VELOCITIES AND FLOW PRESSURE OF VARIOUS AREAS OF THE CHANNEL.....	199
TABLE 6.10: POINTE MICHEL SOUTH RAMMS SIMULATION RESULTS SHOWING RUNOUT DISTANCE, FLOW HEIGHTS, FLOW VELOCITIES AND FLOW PRESSURE OF VARIOUS AREAS OF THE CHANNEL.	203
TABLE 6.11: POINTE MICHEL NORTH RAMMS SIMULATION RESULTS SHOWING RUNOUT DISTANCE, FLOW HEIGHTS, FLOW VELOCITIES AND FLOW PRESSURE OF VARIOUS AREAS OF THE CHANNEL.	208
TABLE 6.12: SOUFRIERE RAMMS SIMULATION RESULTS SHOWING RUNOUT DISTANCE, FLOW HEIGHTS, FLOW VELOCITIES AND FLOW PRESSURE OF VARIOUS AREAS OF THE CHANNEL.	213
TABLE 6.13: RIBEIRA SANTO DOMINGO (FOGO) RAMMS SIMULATION RESULTS SHOWING RUNOUT DISTANCE, FLOW HEIGHTS, FLOW VELOCITIES AND FLOW PRESSURE OF VARIOUS AREAS OF THE CHANNEL.	217

CHAPTER ONE

Geohazards in Small Island Developing States (SIDS)

1.0 Introduction

Chapter one gives details about the study background, problem statement, previous literature in the subject area, research objectives and structure of thesis.

1.1 Understanding geohazards and risk reduction capacities in small island developing states

This section reviews the problems of geohazards specific to Small Island Developing States (SIDS) and the application of geoinformatics in geohazard analysis. The term “SIDS” refers to island nations that are confronted with environmental and socio-economic constraints and susceptibilities (Gomes, 2014). Many SIDS are in unstable geological settings and may also consist largely of mountainous terrain. Geohazards, defined here as including hurricanes, tsunamis, landslides, flooding, earthquake, liquefaction, debris flow and mudslide, severely disturb these regions almost on annual basis. Such hazards occurrence in these regions contribute to about 30% decline in Gross Domestic Product (GDP), deaths, fatalities, loss of money and damage of properties (Mata-Lima et al, 2013). Furthermore, these natural disasters hinder the socio-economic development of these regions by degrading the physical and built environment.

Efforts have been made over the past decades by governmental institutions, Non-Government Organisations (NGOs) and other stakeholders to implement mitigation strategies to control the impact of natural disasters. However, these strategies and disaster management systems have not effectively controlled the risk imposed by these catastrophic events. Factors such as limited research, inadequate human and capital resources, political bureaucracy and lack of advanced technology contribute to the inability of SIDS to control the effects of natural hazards. This study therefore seeks to address these issues by developing effective hazard monitoring and

modelling techniques. These techniques will help to make appropriate and precise evaluation of the hazards and their impact on these regions and mitigating their effects in the long term.

1.2 Research Aims and Objectives

The main aim of this thesis is to identify, map and model debris flow and flood hazard-prone zones of selected localities in Dominica and Cape Verde, using transferable low-cost remote sensing data in RAMMS and HEC-RAS 2D respectively. As part of this, the study will analyse size of boulders moved during Hurricane Maria in relation to damages caused. The following objectives have been identified to address these issues:

1. To identify and map areas susceptible to flooding and debris flow hazards in selected study sites in Dominica and Cape Verde.
2. To analyse the movement of boulders during Hurricane Maria in relation to damages caused.
3. To identify suitable modelling techniques for analysing flooding and debris flows risks.
4. To make use of Hurricane Maria post-disaster knowledge and apply it in pre-disaster reduction programmes in a selected study area in Cape Verde.

1.3 Challenges Encountered by SIDS in Tackling Natural Disasters.

There are 38 SIDS (Table 1.1) that are recognised as being among the two-thirds of nations that have the potential to be massively affected by catastrophic natural disasters (Thomas et al, 2017). These catastrophic events have long-lasting adverse impacts on the socio-economic growth, infrastructure and population of these states and it takes over a decade to recover from these disasters. Over the past five decades, approximately \$1.9 billion was lost annually across the Caribbean and Pacific SIDS due to tropical cyclones alone (Thomas et al, 2017).

Mountainous SIDS are particularly vulnerable to dangerous geological hazards with limited or no resources to tackle these challenges. Both study areas are mountainous volcanic islands, with thinly distributed rural populations and a few larger urban areas. The vulnerability of a nation is how the resources, structures and system of the country predict, manage, resist and recover from catastrophic events (Wisner, 2004). SIDS are more susceptible to natural disasters than developed nations (Toya and Skidmore, 2007; World Bank and United Nation, 2010). This is due to the fragile nature of their environment and limited human, financial and technological resources to control or recover from the damage caused by these natural disasters. The influencing factors such as small size, geographical isolation, unprotected coastal zones, global warming and rapid sea rise make SIDS vulnerable to geohazards (Pelling and Uitto, 2001; Mimura et al, 2007; Meheux et al, 2007). Small economies with low per capita income, high rates of urbanization and population growth coupled with political ideologies such as economic systems, form of government and ethical ideals also contribute to the susceptibility of SIDS to disasters (Girvan, 2006; ECLAC, 2009). Although developed countries suffer greater economic losses due to destruction of properties and infrastructures, the availability of resources to alleviate or recover from disasters makes them less vulnerable.

Developing countries also encounter economic losses just like the developed countries, however although the actual loss is small when compared with developed countries, the proportional cost can be enormous. For instance, the 1991 earthquake in Costa Rica resulted in drastic decline of approximately 9% of the value of goods and services produced (Bommer and Rodriguez, 2002). From 1960 to 1985, the value of goods and services produced by most developing countries in Caribbean and Latin America reduced by about 3% because of the occurrence of geological hazards (Mora, 2007).

This was a huge economic loss to the affected developing countries but when, compared with developed countries such as USA or Canada over the same timeframe, the economic loss was only 1%. Moreover, there were about 3 million deaths recorded worldwide caused by geological hazards over three decades and typical example is the 2004 earthquake in Indonesia which resulted in 227, 989 deaths (Goff et al, 2006). Out of the 3 million deaths, only 21,000 people were killed in developed countries whilst 2.2 million people were killed in developing countries and the remaining 729,000 people were killed in moderately developed countries.










A distinctive characteristic as well as a challenge for most SIDS is geographical isolation and their size makes them vulnerable to geohazards (U.N., 2011; U.N., 2013; Shultz et al, 2016). This is because there is high cost in delivery of vital services, products and other infrastructure such as healthcare, education, communication, transportation and energy, due to their small size and geographical remoteness. Also, the small population of SIDS usually results in reduction in the human resource needed to tackle the geohazards facing them. Small population leads to less productivity and subsequently low per capita income and limited capital resources required to tackle the challenges posed by catastrophic events such as earthquakes, hurricanes, tsunamis and volcanoes (U.N., 2011; U.N., 2013; McIver et al, 2016; Shultz et al, 2016).

Lack of technological advancement, inadequate education and training of qualified personnel are some of the obstacles faced by SIDS in their fight against geohazards (U.N., 2011; U.N., 2013; McIver et al, 2016; Shultz et al, 2016). SIDS do not have the latest technological equipment to monitor and mitigate the impacts of geohazards. A typical example is disaster management in Caribbean and Pacific SIDS relies on international networks such as US Hurricane Centre for information about incoming hurricanes because they do not have the facilities to monitor this impending catastrophic phenomenon. Also, there are insufficient trained personnel in SIDS capable of using these advanced technological tools if they were able to obtain them (U.N., 2011; U.N., 2013; Shultz et al, 2016). This makes it difficult to conduct

















essential research work within the SIDS themselves about these geohazards and mitigate their effects.

UN MEMBERS (38)

Atlantic, Indian Ocean, Mediterranean and South China Sea (AIMS) (9)

 Bahrain	 Cabo Verde	 Comoros
 Guinea-Bissau	 Maldives	 Mauritius
 Sao Tomé and Príncipe	 Seychelles	 Singapore

Caribbean (16)

 Antigua and Barbuda	 Bahamas	 Barbados
 Belize	 Cuba	 Dominica
 Dominican Republic	 Grenada	 Guyana
 Haiti	 Jamaica	 Saint Kitts and Nevis
 Saint Lucia	 Saint Vincent and the Grenadines	 Suriname
 Trinidad and Tobago		

Pacific (13)














 Fiji	 Kiribati	 Marshall Islands
 Micronesia (Federated States of)	 Nauru	 Palau
 Papua New Guinea	 Samoa	 Solomon Islands
 Timor-Leste	 Tonga	 Tuvalu
 Vanuatu		

Figure 1.1 A list of the Small Islands Developing States (SIDS). Source: UN Sustainable Development Goals Knowledge Platform (www.sustainabledevelopment.un.org).

1.4 A brief introduction to natural disasters

Natural disasters are naturally occurring phenomena as a results of Earth's dynamic processes which poses threat to livelihood and properties (Figure 1.2) (Wisner et al, 2004). The impact of natural hazards on lives, properties and infrastructures annually is estimated to be \$138 billion economic loss globally (CRED, 2018). Any phenomenon that occurs naturally which poses danger to lives, properties and the built environment is termed a "geohazard" (Varnes, 1984). Furthermore, hazards often show a cascade of effects, for example the cascading effects of earthquakes are tsunami, liquefaction, landslides, floods and debris flow (Figure 1.2) (Blaikie et al, 2005). The term "hazard" is anything that can harm or disrupt human livelihood, the built and physical environment (Wisner et al, 2012). The fatalities, destructions and losses caused by a hazard are called a "disaster" (Wisner et al, 2012). An alternative definition of disaster is an event whose damaging consequences exceed the capacity of an area to cope with on its own (Blaikie et al, 2005; Wisner et al, 2012). The extent of damage or loss caused by a disaster is termed the "risk" (Wisner et al, 2004; Blaikie et al, 2005).

Some geohazards such as earthquakes, volcanic eruptions and tsunamis can occur abruptly without any warning. Events such as rockfall, landslide and erosion that develop slowly may show some indications before they occur. There is an argument in the literature about natural disasters. Some studies suggest that the only thing natural about disasters is the causing factor; hence disasters are hazards with a natural triggering factor. For example, hurricane is the natural trigger of disasters such as flooding, landslides, debris flows and mudslide (Comfort et al, 1999; O'Brien and Leichenko, 2000; Turner et al, 2003; Wisner et al, 2004; Kelman, 2008; Gaillard, 2010; Wisner et al, 2014). Tropical cyclones (hurricanes) can also result in catastrophic events such as landslides, flooding and debris flows that cause harm to agriculture, human lives and the built environment. The dangers and fatalities associated with these natural disasters have led to an increase in the study of these phenomena over the past decades.

Geohazards pose a great threat to the built environment, properties and lives especially in SIDS due to their unpredictable nature and abrupt occurrence. It is difficult to analyse the risk of multiple geological hazards occurring in the same geographical area and how they interact with each other. The occurrence of one geohazard often triggers other disasters which can multiply their damages and make it more difficult to control (Dilley et al, 2005). Cascading hazards are events that are triggered by primary hazards (Figure 1.2), a typical example is the occurrence of landslide after torrential rainfall or earthquake (Dilley et al, 2005). Although efforts have been made to quantify geological processes, understanding the dynamics of the Earth still remains a difficult task. For example, the occurrence of cyclone and torrential rainfall may trigger flooding as was seen in Mozambique on 25 March 2019, killing over 100,000 people (UNICEF, 2019). The 14 August 2017 torrential rainfall in Sierra Leone induced flooding, mudslides, debris flows and landslides which resulted in about 1,142 fatalities (UNDAC, 2017). Another example is the 12 April 2019 magnitude 6.1 Luzon earthquake in Philippines which caused 18 deaths and \$10.5m economic loss (NDRRMC, 2019).

Although earthquakes and volcanic eruptions can cause landslides and debris flows, this study concentrated on landslides and debris flows induced by hurricanes and torrential rainfall, which are the most common catastrophic events that cause landslides and debris flows to occur in the study areas. A typical example is the September 2017 Hurricane Maria event in Dominica which caused intense rainfall and resulted in numerous rainfall-induced landslides and subsequent debris flows that caused major devastation to livelihood, the natural and built environment (Teeuw et al, 2018; Teeuw et al, 2019). Hurricane Maria also resulted in flooding, landslides and debris in Puerto Rico which caused severely destruction and fatalities across the island (Bessette-Kirton et al, 2019). Other example Madeira where human activities coupled with flash floods cause flooding, landslides and debris which results in major devastation and fatalities in the island (Baioni, 2011; Fragoso et al, 2012).

Although torrential rainfall was the main triggering factor in Dominica, other influencing factors were the steep unstable slopes, variable lithological units in the underlying geology and geotechnical properties of the soil and rocks (Teeuw et al, 2018; Teeuw et al, 2019). The ruggedness and steep unstable slopes in Dominica exposed the island to landslides and debris flows during hurricanes (Teeuw et al, 2018; Teeuw et al, 2019). Dominica's lithological units and associated geotechnical parameters such as cohesion, unit weight and friction angles must have an impact on the occurrence of landslides and debris flows. However, due to lack of geotechnical parameter data, it was difficult to determine which lithologies are more susceptible to landslides and debris flows.

The mechanisms influencing the occurrence of landslides and debris flows depend on the different triggering factors (Wieczorek, 1996; Zhang and Li, 2011) such as earthquakes, volcanoes, hurricanes and torrential rainfall. Landslides and debris flows triggered by these phenomena have different characteristics and influencing factors (Zhang and Li, 2011). Seismic waves from earthquakes causes shaking of the ground and subsequently the occurrence of landslides in unstable slope areas due excess stress greater than the strength of the base rocks and soil (Newmark,1965; Munier et al, 2007; Zhang and Li, 2011). Earthquake landslides and debris flow occur at steeper slopes (35° and above) and are characterised by abrupt ejection and movement of mass, dust and liquefaction which moves debris down slope (Newmark,1965; Zhang and Li, 2011; Lee, 2012).

Volcanic-induced landslides and debris flows mainly occur in mountainous areas where slopes are weakened and eventually collapse and move downslope as lahars (Scott et al, 2001; Study.com, 2013). Debris flows caused by volcanoes are muddy, cohesive and have a low volume of sediment usually below 30% (Scott et al, 2012; Vallance et al, 2015). Hurricane- or rainfall-induced landslides occur when unstable slopes are saturated with water and yield to gravitational force acting on the slope (Zhang and Li, 2011; Piciullo et al, 2018; Dikshit et al,

2019). Rainfall-induced landslides and debris flows contain over 60 volume% sediment; they show rapid movement and their deposits are matrix-supported and they often form levees (Pierson, 2005; Zhang and Li, 2011; Vallance et al, 2015; Piciullo et al, 2018; Dikshit et al, 2019). Slope angle and geotechnical properties of the soil and rocks are factors that affect occurrence of landslides and debris whether they are induced by rainfall, volcanic activities or earthquakes (Pierson, 2005; Zhang and Li, 2011; Vallance et al, 2015; Piciullo et al, 2018; Dikshit et al, 2019). This is because the steeper the slope angle is (over 20°), the more an area is susceptible to landslides and debris flows regardless of the trigger (Varnes, 1984; Pierson, 2005; Zhang and Li, 2011; Dikshit et al, 2019). Geotechnical properties such as cohesion, friction angle and unit weight of rocks and soil affects debris flow and landslides since cohesion and friction angle determines the shear strength and resistance of the soil and rocks to stress (Iverson et al, 1997; Chen et al, 2006; Picarelli et al, 2008, Iverson, 2015).

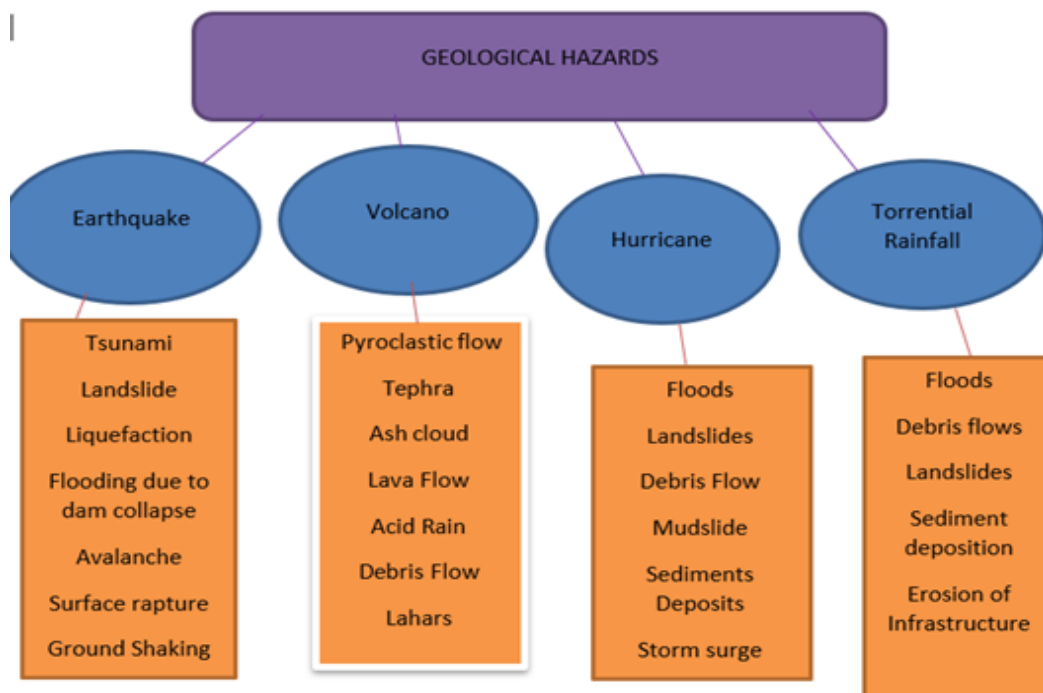


Figure 1.2: Main and cascading geophysical and hydro-meteorological hazards (Author’s own image).

1.5 Background to Geohazards in Dominica and Cape Verde

Dominica is the most volcanically active region among the Lesser Antilles states with five active volcanoes across the country. The country is highly susceptible to volcanic hazards with approximately 20% of the populace living in active volcano zones (GOCD, 1999). However, there have not been any fatalities because of volcanic eruption in the past century (Rowley, 1992). Findings by Rowley (1992) indicated that many people live in volcanic hazard zones across the island. Although there is an argument by the populace that there have not been any volcanic eruption for many years, the housing and planning department of government must take the risk of volcanic activities into consideration when granting building permissions. Although Dominica lies on the Eastern Caribbean subduction zone, where the Atlantic plate thrusts beneath the Caribbean plate, risk of seismic hazards is thought to be minimal, although in 2004 an earthquake in Portsmouth destroyed the Ville Case Catholic cathedral (Zahibo et al, 2006). Research work by Zahibo et al (2006) suggested that the risk of earthquake hazards in Dominica is minimal but measures should be put in place mitigate its effects. Most studies conducted in Dominica over past years usually concentrated on volcanic hazards at the expense of hydro-meteorological and geological hazards such as hurricane, landslides, flooding and debris flows (UNDP, 2009).

Situated along the Atlantic Hurricane line, Dominica is prone to dangerous tropical cyclones and related hazards such as flooding, landslides, debris flow and sediment deposition. The most recent one to hit the island was Hurricane Maria, which occurred on 20 September 2017, aggravating the damage caused by Hurricane Irma approximately two weeks earlier. Much infrastructure was damaged, people were displaced, over 100 deaths recorded and an estimated economic loss of \$90 billion across the Caribbean (NCEI, 2019).

About 19 hurricanes have occurred on the island from 1890 to date (NCEI, 2019). These events have severely damaged the built environment and socio-economic activities of the island

(Benson and Clay, 2010). Geohazards have a significant economic impact on the island, both directly and indirectly. Destruction of physical assets such as buildings, roads, hospitals, factories, livestock, crops and other raw materials constitute a direct cost caused by disasters (Benson and Clay, 2010). Loss of jobs, shortage in supply of goods and services, high cost of living, injuries and fatalities are indirect costs that result from natural hazards. Implementation of strategic methods is required to mitigate their impact on the island. Furthermore, Dominica is vulnerable to landslide risks attributable to the hurricanes and torrential rainfall. About 3% of the land in Dominica is affected by landslides and debris flows (De Graff, 1987; De Graff et al, 1989). Flash floods, storm surge and tsunamis are other hazards that Dominica is susceptible to, but they are often considered as hazards with small effects although this is not always the case (De Graff, 1987; De Graff et al, 1989). The recent Hurricane Maria in Dominica triggered flooding, landslides, debris flows and deposition of sediments across the island. Hurricane Maria severely damaged the island, resulting in about \$90 billion economic loss, 68 casualties, displacement of people and destruction of over 80% of the infrastructure (ACAPS, 2018; IFRRCS, 2017; UN, 2017).

Cape Verde is a volcanic archipelago that is very vulnerable to numerous hazards (Plesner et al, 2003). There are inadequate publicly available records of geohazards in Cape Verde, mainly because of the limited studies on the archipelago and lack of proper hazard monitoring system. This is a major problem which makes it difficult to analyse and mitigate the risks the island faces. Out of the ten islands in Cape Verde, Fogo and Santo Antao have the most active volcanoes over the past 500,000 years (Siebert et al, 2011). Eight historic eruptions have been recorded with the last eruption occurring in 2014-2015 (Day et al, 1999; Heleno et al, 1999; Richter et al, 2016). Although no volcanic eruption has occurred in Brava in historic times, the island is seismically active (Heleno and Fonseca, 1992; Fonseca et al, 2003). The most recent earthquake in Brava occurred on 4th August 2016, no deaths or fatalities were recorded but

people were evacuated (Grevemeyer et al, 2004). Most studies undertaken in the Cape Verde concentrate on volcanic and seismic hazards at the expense of other dangerous hazards such as hurricanes, flooding, landslides, tsunamis and debris flows (Amelung et al, 2002; Fonesca, 2003; Cappello et al, 2016).

The governmental departments or organization responsible for monitoring and mitigating impacts of geohazards in Dominica and Cape Verde are Office of Disaster Management and National Institute of Metrology and Geophysics, respectively. Both islands also get help from Red Cross Society during an emergency. One common problem faced by these organizations is the lack of adequately trained personnel to oversee a smooth operation of their activities. This is due to poor educational facilities in these islands which means staff have to get their training in the developed western world which is very expensive.

Funding is also another problem facing these islands which makes it difficult to undertake projects that will help put essential measures in place to tackle risks posed by geohazards. They often depend on foreign aid and money from organizations such as United Nations and World Bank to undertake these important projects. As a result of limited capital resources, they are unable to purchase the latest technology required to monitor and mitigate the effects of geohazards on the islands. Therefore, they rely on organizations such as United States Geological Survey (USGS), United States Hurricane Centre (USHC) and Geological Survey of Portugal (GSP) for information or warning on an impending geohazard.

1.6 Research Work Applications; GIS, Remote Sensing, Unmanned Aerial Vehicle (UAV) (Drone), Agisoft Metashape Professional, ImageJ, RAMMS and HEC-RAS 2D.

1.6.1 Geographic Information Systems (GIS) and Remote Sensing

Geoinformatics involves the application of science and technology to capture, store, process and present geological information to solve problems in geosciences, geography and cartography (Tomlinson, 1962). Geoinformatics are useful for mapping, analysing, mitigating and managing natural disasters (Buechele et al, 2006; Dawson et al, 2009). Global Positioning Systems, Geographic Information Systems, Remote Sensing, Digital Cartography are all components of Geoinformatics (Tomlinson, 1962). However, only Remote Sensing and Geographic Information Systems was used for this study.

Geographic Information Systems (GIS) is a software for gathering, storing, processing and presenting information that has been referenced geographically (Tomlinson, 1962). The first computerized GIS was developed in 1960 (Tomlinson, 1962). GIS provides a platform for integrating geoscience and socio-economic datasets when examining the impacts of hazards in a geographic area. The spatial analytical toolset of GIS helps to simulate geological hazards to get better understanding of the causative factors and effective mitigation measures to implement (Buechele et al, 2006; Dawson et al, 2009).

Remote Sensing involves sensing and recording spatial information without any physical contact with the Earth. Analysing and mapping of natural disasters before and after a catastrophic event can be done by remote sensing (Ziel, 2003; Kelmelis, 2006). To monitor hazards during daytime and cloud-free conditions, multispectral optical sensors are used to sense infrared and visible wavelengths (Teeuw, 2007). Also, monitoring of flooding, debris flows, landslides and other disasters during the night and cloudy conditions is done by using radar sensors (Teeuw, 2007). For quick assessment of damage during a disaster, remote

sensing techniques are used especially when it is difficult to undertake ground surveys (Zhang et al, 2008). An example is the 2018 Kilauea volcano eruption in Hawaii where remote sensing techniques were used to gather information and assess level of damage (Cozzens, 2018).

1.6.2 Application of Unmanned Aerial Vehicle (UAV) (Drone) in Geoscience

There has been a surge in the use of drones in many disciplines for different purposes (Watts et al, 2012; Madjid et al, 2018) in recent times. The advantage of cost effective, time, portability and high resolutions makes the use of unmanned aerial vehicles appealing to many users (Madjid et al, 2018). The technique of most research surveys in archaeology, geohazards, ecology, hydrology and other geosciences has been revolutionised by the emergence of drones (De Reu et al, 2016; Faye et al, 2016; Bandini et al, 2017; Mateos et al, 2017; Madjid et al, 2018). Airborne surveys, mapping and monitoring can be undertaken for a large area within a short time (Jordan, 2015). Accessibility is another advantage of drones, areas that are too dangerous access manually can be surveyed using drones (Jordan, 2015).

Even with all the benefits of drones, there are three main challenges that affects their usage (Jordan, 2015). Weather conditions, technological limitations and legal permissions are factors affecting the smooth operation of drones (Jordan, 2015). This is because drones cannot be operated when wind speed is above 30 km/h and when it is raining (Jordan, 2015). Drone flights are restricted by their battery duration, each flight last only 30 minutes per battery which can delay survey works (Jordan, 2015). Legal permissions from a country or region's aviation authority are sometimes required to be able to operate a drone, which can be a tedious and bureaucratic process (Jordan, 2015).

Despite the widespread use of drone for geological survey and other research works, the use of drones in Dominica and Cape Verde has not been exploited much. There are only few research works in Dominica and Cape Verde that involved the use of drone (Heidarzadeh et al, 2018;

Teves, 2018; Leidig et al, 2019; Schaefer et al, 2020). Therefore, this study used drone for the survey works in Dominica and Cape Verde to help address this omission.

1.6.3 Photogrammetry and Agisoft Metashape Professional

Over the past years, there has been rapid advancement of photogrammetry due to the ever-increasing availability of satellite sensors and demand for DEMs (Ahmadi and Ebadi, 2009; Sechin, 2014; Laporte-Fraute et al, 2019; Lastilla et al, 2021). Photogrammetry involves creating 3D models such as Digital Elevation Models (DEMs) and orthophotographs through the process of analysing, evaluating and interpreting aerial images via electromagnetic radiation (Ahmadi and Ebadi, 2009; Sechin, 2014; Laporte-Fraute et al, 2019; Lastilla et al, 2021). Visualisation of the 3D models is made possible by georeferencing and orthorectifying aerial images and then draping the georeferenced and orthorectified images on a Light Detection and Ranging (LiDAR) sensor. The ability to remotely sense a terrain data for surveying, mapping and modelling makes photogrammetry appealing to many fields of geoscience (Laporte-Fraute et al, 2019; Lastilla et al, 2021). The science of photogrammetry enables the processing of 3D models from geographically referenced aerial satellite images using photogrammetry software (Laporte-Fraute et al, 2019; Lastilla et al, 2021). With an interactive bundle modification technique, the software computes the locations and directions of the images and align them according to their coordinate systems (Laporte-Fraute et al, 2019; Lastilla et al, 2021).

There are various photogrammetry software which are either freely available or needs a license to run. MicMac, VisualSfM are freely available whilst Pix4Dmapper and Agisoft Metashape are licensed. Based on previous research, Agisoft Metashape produces more accurate results with few to no errors in comparison to MicMac, VisualSfM and Pix4Dmapper (Pyka, 2018; Vacca et al, 2018; Kingland, 2020). Agisoft Metashape is based on Structure from Motion (SfM) technique which processes satellite images into DEMs, orthophotographs, tiled models

and dense clouds (Lastilla et al, 2021). Structure from Motion (SfM) is a technique used in photogrammetry to generate 3D models from 2D image structures that may be disrupted by motion signals (Ullman, 1979). Structure from Motion (SfM) is mostly applied in rugged terrains where laser scanning is affected by roughness of the topography of the terrain which can result in loss of data (Javernick et al, 2014; Del Soldado et al, 2018). Based on previous literature, Agisoft Metashape produces more realistic results than any other photogrammetry software (Pyka, 2018; Vacca et al, 2018; Kingland, 2020). Another advantage of Agisoft Metashape is in the cooperation of georeferencing and ground control points into the image processing (Pyka, 2018; Vacca et al, 2018; Kingland, 2020). For these reasons, Agisoft Metashape Professional photogrammetric software was used for this research work.

1.6.4 ImageJ

Over the past decade, there has been a surge in technological developments of scientific imagery computing (Schneider et al, 2012). Imagery analysis involves the process of characterizing 2D and 3D digital images either quantitatively or qualitatively to obtain essential information using computers (Blaschke et al, 2008; Solomon and Breckon, 2011). Image analysis software demand has been on the rise in almost all disciplines in recent times (Schneider et al, 2012). The ability to critically analyse images in detail within a short time makes such technologies very essential. Developed by National Institute of Health (NIH), ImageJ has the capabilities of processing and analysing different images from different academic disciplines (Collins, 2007; Schneider et al, 2012).

However, it was mainly developed for the health sector to process and analyse biomedical images (Collins, 2007; Schneider et al, 2012). Due to the ever-increasing improvement of the acquisition of images by remote sensing, the demand in geoscience for image analysis software has increased in recent years. The cost and complicated plugins of most image analysis software make it difficult for geoscientists to undertake research using such works but the

availability of software such as ImageJ provides an alternative means of image analysis (Barboriak et al, 2005).

ImageJ was used in this study to analyse drone-derived orthophotographs to examine boulder sizes moved and damages caused by their movements during Hurricane Maria. This helped to determine how effective and suitable the software is geoscience research works.

1.6.5 Hydrologic Engineering Centre – River Analysis Systems (HEC-RAS)

The frequency of flood events in recent times globally has prompted the development of models for modelling, mapping and monitoring flood hazards to mitigate their effects (Knebl et al, 2005; Forsee and Ahmad, 2011; Bhandari et al, 2017). There are many hydraulic models which have been used to model potential flood events to help predict and control their impact. Developed by the United States of America Army Corps Engineers, Hydrologic Engineering Centre – River Analysis Systems (HEC-RAS), has been used in many research works to simulate flood events (Collins et al, 2014; Bhandari et al, 2017; Forlie, 2019; Ikromi and Wardhana, 2020). HEC-RAS can be used to perform 1D (steady flow) and 2D (unsteady flows) simulation of river systems (Bhandari et al, 2017).

Steady flow refers to when the quantity of water flowing through a stream per second and all related conditions such as pressure and velocity along the flow channel are constant (USACE, 2016; Bhandari et al, 2017). With steady flow, flow pressure and velocity are considered as equal on both sides of the flow channel (USACE, 2016; Bhandari et al, 2017). On the other hand, unsteady flow is when the amount of water flowing through a stream per second is not constant and there are fluctuations in flow velocity and pressure at any part of the channel (USACE, 2016; Bhandari et al, 2017). To replicate the real-life flooding that occurred during Hurricane Maria, the 2D unsteady flow model was used at the expense of the 1D steady flow because the actual flow was unsteady. HEC-RAS 1D needs to be used together with HEC-GeoRAS in ArcGIS and requires detailed information of a river's geometry (Bhandari et al,

2017). HEC-RAS 2D is used solely and does not require information of geometry of the channel nor Manning roughness coefficients as this is computed from the DEM and landcover data respectively (Bhandari et al, 2017). RAS Mapper which is within HEC-RAS 2D has the capabilities of performing animated simulation of flow and results are presented as flow depth, flow velocity and water surface elevation (Bhandari et al, 2017). This functionality of HEC-RAS 2D enables geospatial visualisation of results to easily identify areas susceptible to flood hazards.

Even though HEC-RAS is freely available, it has not been applied for flood mapping in Dominica or Cape Verde islands prior to this study. Therefore, this research work exploited the capabilities of HEC-RAS to model unsteady flow analyses at selected study areas in Dominica and Cape Verde which devastated by flooding during the 2017 Hurricane Maria events. Outcomes of the simulation helped to determine how vulnerable these areas are to flooding and what measures should be implemented to mitigate the impact of flooding.

1.6.6 Rapid Mass Movement Simulation (RAMMS)

Rapid Mass Movement Simulation debris flow module is a numerical geohazard model developed by Swiss Federal Institute for Forest, Snow and Landscape Research to simulate debris flow movement (Christen et al, 2010; Hussin, 2011). The model can predict debris flow volume, height, runout distance, velocity, entrainment and impact pressure (Christen et al, 2010; Hussin, 2011; Hussin et al, 2012) in both 2D and 3D. Debris flow simulation in RAMMS is based on Voellmy rheology method (Voellmy, 1955; Salm, 1993; Hussin, 2011, Hussin et al, 2012). This implies that a debris flow is based on a hydraulic depth-average continuum model where flow resistance is made of friction coefficient (μ) and turbulent coefficient (x) (Christen et al, 2010; Hussin, 2011; Hussin et al, 2012).

RAMMS debris flow module has been applied in many research works with success to model debris flow run-out (Cesca and D'Agostino, 2006; Kowalski, 2008; Christen et al, 2010; Hussin, 2011; Hussin et al, 2012). Despite the success of RAMMS in other studies (Issler et al, 2012) is critical of the Voellmy model and suggests that the Random Kinetic Energy model produces better results. Regardless of the criticism, the Voellmy Rheological methodology has deemed suitable for modelling not only debris flow but avalanches as well (Christen et al, 2010; Hussin, 2011; Hussin et al, 2012). Numerous landslide-triggered debris flows occurred during 2017 Hurricane Maria events in Dominica. Six study areas which were devastated by these events were chosen to model and map their vulnerability to debris flow should there be an event like Hurricane Maria or even worse. RAMMS debris flow module 1.7.2 version was used to model, map and monitor the susceptible of selected study areas in Dominica and Cape Verde to debris flow hazards. This will help to put strategic measures in place to control the impact of debris flow hazard in these areas.

1.7 Structure of Thesis

This thesis was organized into eight different chapters, summarised below:

Chapter one outlined the background of thesis, focusing on the problem statement, research objectives, previous literature in the subject area and structure of thesis.

Chapter two focuses on the background of study area in terms of the location, geology, climate, vegetation and how these factors make the islands vulnerable to natural hazards. The reasons behind the choice of these places as study areas are also discussed in this chapter.

Chapter three outlines the methodologies used for the study, focusing on the type of data, source of data, data collection techniques and data processing. Also, the procedure used to

analyse boulders moved during Hurricane Maria is elaborated in this chapter. Flood and debris flow hazards modelling techniques adopted for the study and the workflows are explained.

Chapter four presents results of Shuttle Radar Topographic Mission (STRM) and ALOS PALSAR Digital Elevation Models (DEMs) corrections. Also, terrain and drainage analysis results which influenced the decision to use drone-derived DEMs for this study are presented.

Chapter five presents the fieldwork results for the selected study areas in Dominica, this involved detail description of the impact of Hurricane Maria on these localities. Image analysis of sizes of boulders moved during Hurricane Maria and damage caused by their movement was presented in this chapter. Also, results of the photogrammetry processed aerial images captured with unmanned aerial vehicle are presented.

Chapter six presents the results of the debris flow and flood modelling including sensitivity analysis for all study areas in Dominica and Cape Verde.

Chapter seven involves in-depth discussion and interpretation of the results for study areas in both Dominica and Cape Verde. Review of the data uncertainties, problems associated with ALOS PALSAR and SRTM DEMs, evaluation of results, validation of models to ascertain accuracy of modelling results and further works are presented.

Chapter eight focuses on general conclusions based on outcomes of the thesis and recommendations for future works.

All research articles, journals and books used and cited in the thesis are listed under the reference section.

CHAPTER TWO

The Study Areas

2.0 Introduction

This chapter gives a detailed description of Dominica and Fogo (Cape Verde) in terms of the location, geology, climate and vegetation and also the reason for choosing the study areas.

2.1 Location and geography of Dominica Island

The Commonwealth of Dominica is the largest island in the Lesser Antilles, situated about 94 km northwest of Martinique and about 96 km southeast of Guadeloupe. Its geographic coordinates are 15° 20 N, 61°22 W (Figure 2.1). Dominica is approximately 26 km wide and 47 km long with a land cover of about 750 km² and a coastline about 148 km long. Its highest point is Mount Morne Diablotins at 1447 m above sea-level. The major urban and populated towns are the capital city Roseau and the northern town of Portsmouth with a population of 14,725 and 4,167 respectively. English is the official language, although Creole is widely spoken. The island has a population of 74,000 people, according to the 2016 census, with a population growth of 0.3 % annually (National Statistics Division, 2016).

Dominica's economy heavily depends on agriculture and tourism, and it has one of the lowest per capita GDP especially after Hurricane Maria in 2017 (World Bank, 2018). Dominica was chosen as the study area because it is a SIDS with limited human and financial resources yet prone to numerous geological hazards such as landslides, debris flows and flooding. Researching into the hazard distribution across the island will help to develop a methodology framework for monitoring and controlling the impact of these hazards on the island.

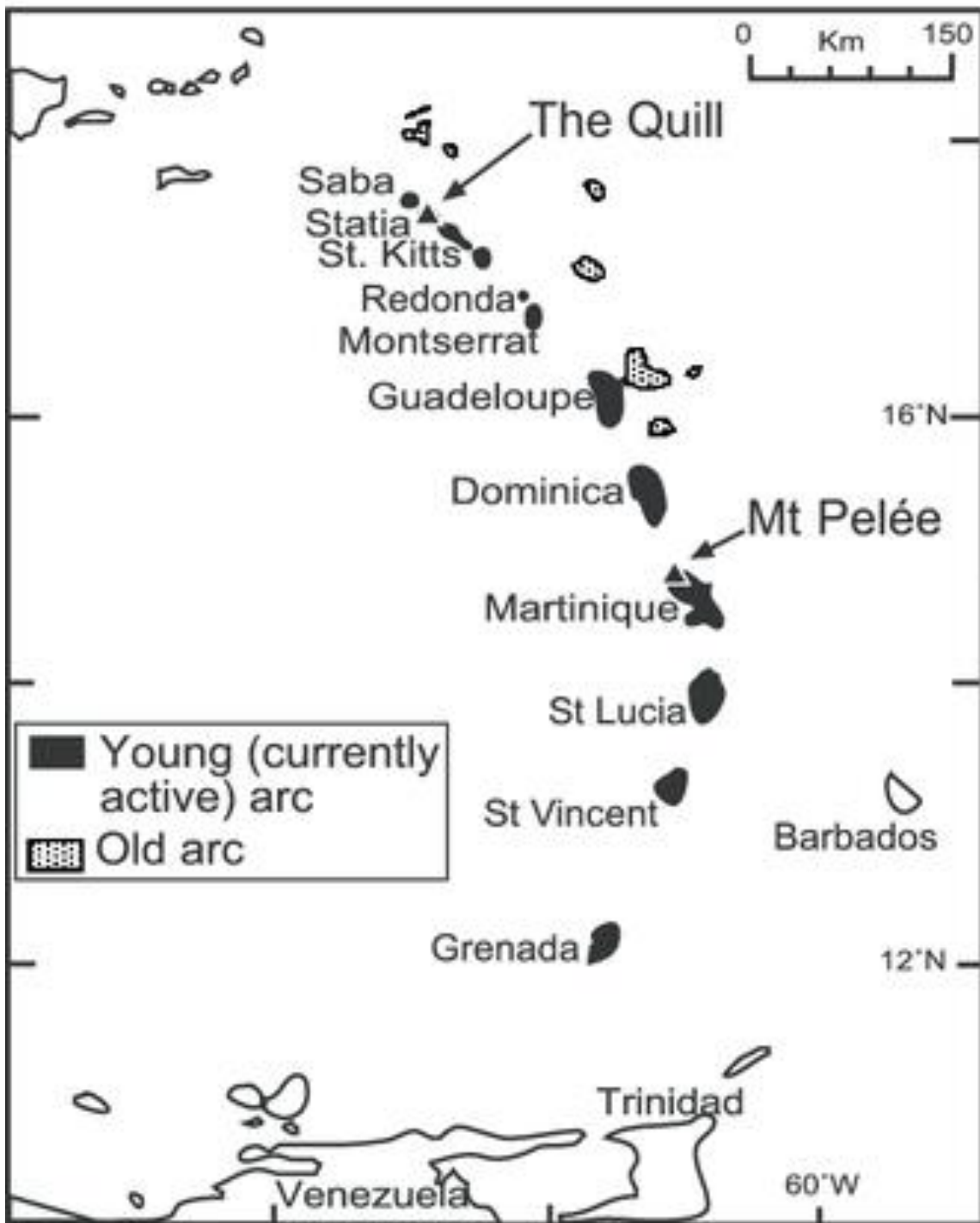


Figure 2.1A Sketch map of Lesser Antilles islands, showing location of Dominica which can be considered as the northernmost island in the Windward Islands or the southernmost island in the Leeward Islands (Hugh et al, 2018).

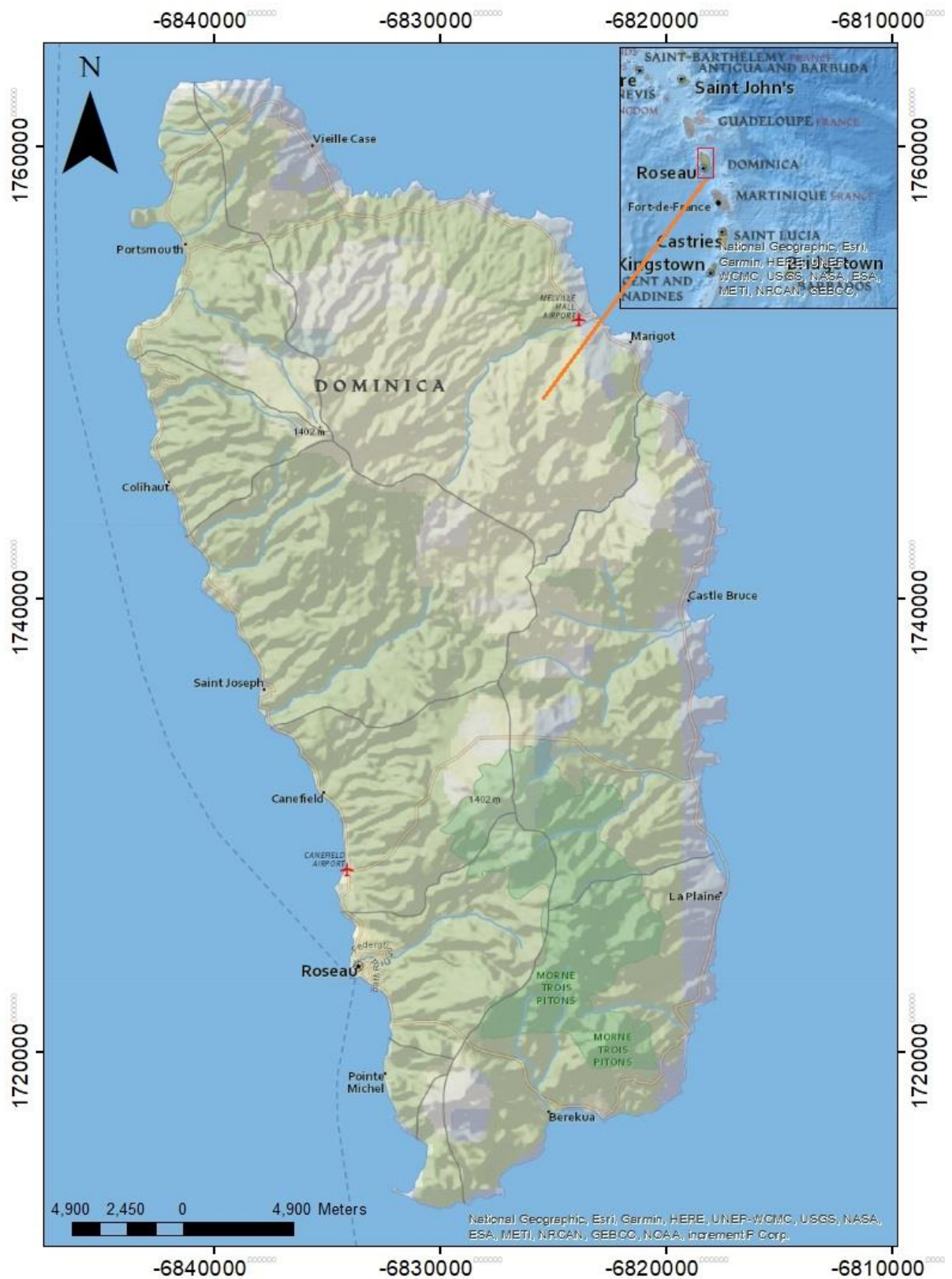


Figure 2.1 B: Geographic and location map of Dominica (Researcher’s image created in ArcMap 10.7).

2.2 Dominica Geological Setting

Figure 2.2 shows the general geology of Dominica (Smith et al., 2004). Although there have been no volcanic eruptions in the island since 1880, there are still indications of volcanism in Dominica (Lindsay, 2005; Lindsay and Robertson, 2018). This is evident in the Boiling Lake generated by the heat originating from the magma chamber underneath the lake coupled with geothermal activities and the sulphurous Valley of Desolation with volcanic vents and hot springs is another evidence of volcanism in Dominica (Lindsay, 2005; Lindsay and Robertson, 2018). The volcanic deposits from Morne Plat Pays Pelean eruption in the southwest are the youngest dated deposits (Robool et al, 2004; Lindsay et al, 2005). There have been two phreatic eruptions in Dominica, one in 1880 and another in 1997 which both occurred at the Valley of Desolation geothermal area (Robool et al, 2004; Lindsay et al, 2005)

Dominica is predominantly composed of basalt, andesite and dacite rocks formed by past volcanism and their weathered equivalents, coupled with conglomerates formed in Pleistocene and ignimbrite (Robool et al, 2004; Lindsay et al, 2005). The south, southwestern and central parts of Dominica are made of Pleistocene shield basalts. The north and north-eastern parts of the island are composed of basaltic andesite volcanic deposits dated at 20,000 to 50,000 years (Robool et al, 2004; Lindsay et al, 2005).

Dominica was largely formed in the Pliocene and Miocene epochs (Martin-Kaye, 1960; Sigurdsson et al, 1991). The south-eastern area of the island is composed of deeply weathered basaltic rocks with an age of 6.92 Ma and dissected by younger andesitic dykes dated at 3.35 Ma (Monjaret, 1985; Bellon, 1988). The south-central part of the island is made of basaltic pillow lavas, old submarine volcanic breccias and younger subaerial andesitic lavas interbedded with pyroclastic deposits (Demanage, 1985; Monjaret, 1985; Bellon, 1988). Morne Trois Pitons, Morne Micotrin and Plat Pays volcanic complex in the south of Dominica were formed in the late Pleistocene (Gurenko et al, 2005; Halama et al, 2006).

The northern part of the island is formed of stratovolcano andesitic rocks. It has experienced volcanism in the early Pleistocene which resulted in the formation of the Morne Diablotins stratovolcano and the Morne Aux Diablies lava dome complex (Smith et al, 2013). Plat Pays volcanic complex is the only volcano in Dominica that is well studied (Wadge, 1985; Le Friant et al, 2002; Lindsay et al, 2003, 2005).

Ignimbritic rocks composed of lithics, pumice and volcanic ash are distributed across the island suggesting numerous Plinian eruptions (Lindsay et al, 2005; Smith et al, 2013). Over the past 10,000 years, there have been a voluminous ignimbrite deposits across the island. The first ignimbrite deposit from Morne Diablotins, Morne Micotin and Morne Trois Piton was found in Roseau (Roseau Tuff). This is approximately a 3 km³ volume of ignimbrite that filled the Roseau valley (Sigurdsson, 1972). The island also shows deposits of very angular giant boulders and sub-angular to rounded conglomerates cobbles at base of the slopes, cliffs, and valleys. Rockfall landslides, lava dome collapse, debris flows, pyroclastic flows, block and ash flows are all factors that contributed to the distribution of boulders and cobbles in Dominica.

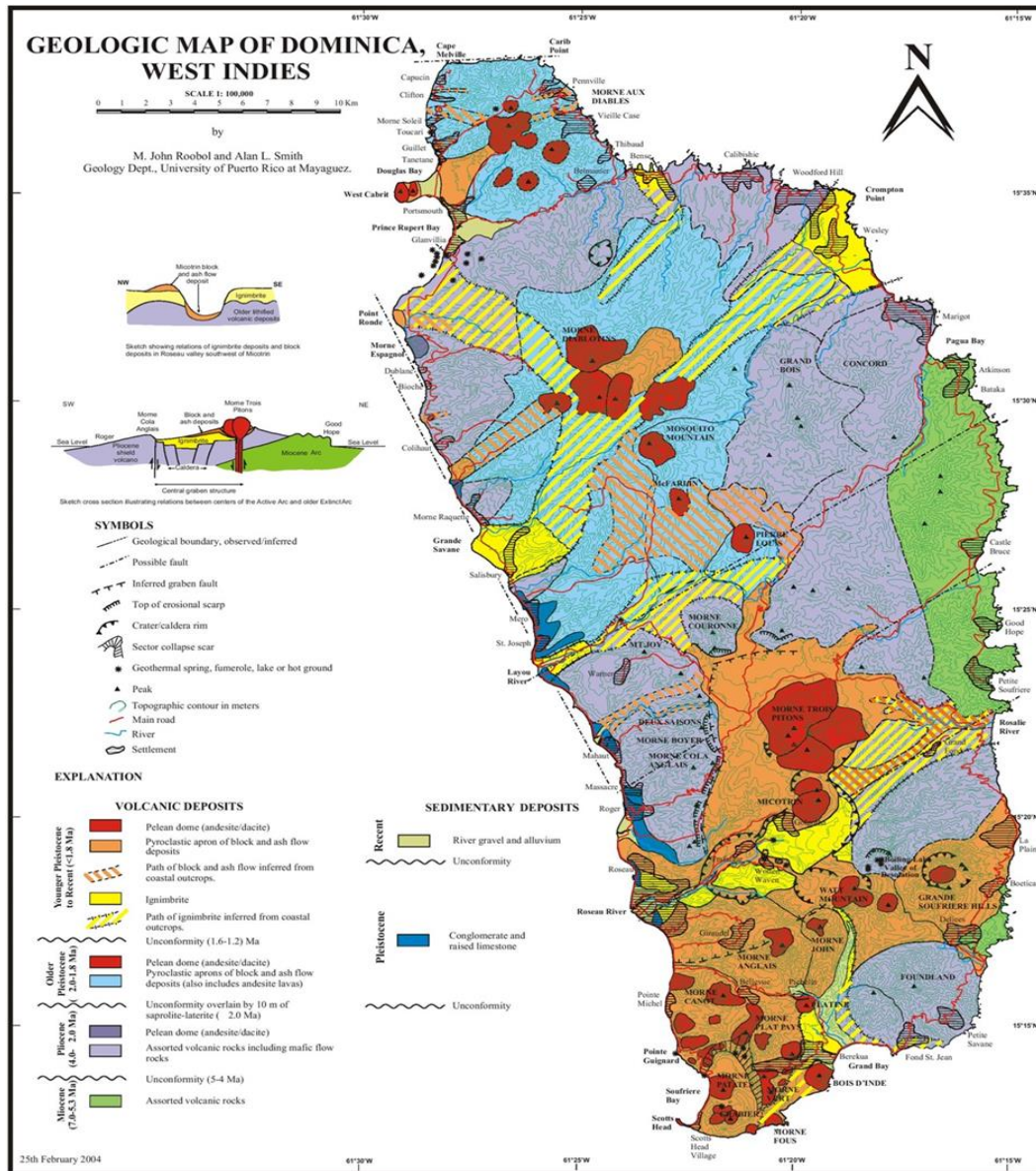


Figure 2.2: Dominica geological map (Smith et al, 2004).

2.3 Dominica Topography, Climate, Hurricanes and Vegetation

Past volcanic activity in the island accounts for the rugged topography and very steep slopes.

Most of the island is occupied by rainforest experiencing high rainfall throughout the year with annual rainfall of 8000-10000 mm (CDEMA, 2018) (Figure 2.4). It has a tropical maritime climate with average daily temperatures of 26°C in coastal areas and 19°C in mountainous areas (CDEMA, 2018). There are mild seasonal variations although the island only experiences dry and wet season throughout the year.

Dominica has tropical climate which is characterized by hot temperatures and high humidity all year round, as a result it is largely covered by rainforest vegetation (DES, 2019) (Table 2.1). From January to May, Dominica is relatively cool and dry with little to no rains, whilst from June to December it is hot, humid and rainy (DES, 2019) (Table 2.1). During the cool and dry period, the northeast Trade Winds blows regularly with low intensity and the temperature decreases. During the humid and rainy period, the Northeast Trade Winds blows irregularly with high intensity and temperature increases (WCG, 2018).

Month	Jan	Feb	March	April	May	June	July	Aug	Sept	Oct	Nov	Dec
Min (°C)	22	22	22	23	24	25	25	24	24	23	23	22
Max (°C)	28	28	28	29	30	30	30	31	30	29	30	29

Table 2.1 Dominica Average Monthly Temperatures (DES, 2019).

Rainfall is experienced in Dominica throughout the year even the dry period especially in the mountainous areas (WCG, 2018; DES, 2019) (Figure 2.4). There is little rainfall from February to April with about 65 mm of rainfall per month on the average (Table 2.2). The heaviest period of rainfall occurs from July to November with average rainfall of 200 mm per month (Table

2.2) (WCG, 2018; DES, 2019). The annual rainfall in the western part of the island is about 2000 mm (Figure 2.4). The eastern part of the island gets more rainfall with about 2500 mm which greater than the western part due to the exposure to trade winds (WCG, 2018; DES, 2019) (figure 2.4). Precipitation in the central part of the island is very frequent due to the high lands and thick vegetation (Figure 2.5). Torrential rainfall associated with hurricane activities which results in flooding and landslides are major problems the island is faced with.

Month	Jan	Feb	March	April	May	June	July	August	Sept	Oct	Nov	Dec
Rainfall mm	125	75	75	60	95	200	275	260	225	200	225	160

Table 2.2 Dominica Average Monthly Precipitation (DES, 2019)

The location of Dominica makes the island vulnerable to tropical cyclones and storms. Over the past fifty years the island has been affected massively by hurricanes such as Hurricane David in 1979, Tropical Storm Erica in 2015 and Hurricane Maria in 2017. Torrential rainfall during Hurricane David initiated landslides, debris flows and floods (Lawrence, 1979). Roseau in the southwest was the most devastated area of the Island (Fontaine, 2003). Approximately 80% of homes were damaged leaving 75% of the Dominican populace homeless (Lawrence, 1979; Fontaine, 2003). The agriculture industry was severely damaged by Hurricane David, 75% of the crops were blown away by the strong winds (Lawrence, 2003). About 56 people were reported dead and 136 people were reported injured (Lawrence, 1979; Herbert, 1980).

Tropical Storm Erica occurred almost four decades after Hurricane David and was characterised by torrential rainfall which resulted in flash flooding, landslides and mudflow (Richard and Andrew, 2016). During Tropical Storm Erica, 30 people were killed, 20 injured and 574 people were reported misplaced (Richard and Andrew, 2016). The economic loss (\$482.8 million) caused by Erica amounted to 90% of Dominica’s GDP (IFRC, 2016).

Hurricane Maria was the worst hurricane to ever hit Dominica due to the excessive damages caused. Over 90% of the country’s buildings were destroyed by strong winds and filled with sediments (IFRC, 2017; Mathew, 2017). Facilities such as electricity, communication network and water supply were disrupted during Hurricane Maria. The economic loss caused by Hurricane Maria was about \$1.3 billion which amounted to 226% of Dominica’s 2016 GDP (CARICOM, 2018). Dominica’s rainforest vegetation was severely destroyed by the strong winds during Hurricane Maria, exposing the terrain to landslides, erosion and debris flows (Phipps, 2018). A total of 65 fatalities (Figure 2.3) were recorded with 30 people confirmed dead and 35 injured (CARICOM, 2018). Table 2.3 below lists the hurricanes that have affected the island over the past forty years.

Hurricane	Category	Year	Damage Estimate (\$)
Hurricane David	5	1979	1.54 billion
Tropical Storm Erica	1	2015	511.4 million
Hurricane Maria	5	2017	91.61 billion

Table 2.3 Hurricanes in Dominica over the past forty years (DES, 2019).

The vegetation of Dominica is that of a rainforest with trees and creepers in the valleys (Figure 2.5). Thick forest and woodland cover about 60% of the island. The east coast of the island is characterised by tropical rainforest whilst the west coast is characterised by dry grassland. Flat and arable land amounts to 22.6% of the island with fertile volcanic soil for agricultural activities and water covers the remaining 17.4% (CDEMA, 2018) (Figure 2.5 and 2.6). Agriculture contributes to 20% of Dominica's GDP and 40% of the population are farmers. Aside agriculture, some the lands are used for settlement and most lands in Dominica are reserved and protected (Figure 2.6).

The 2017 category 5 Hurricane Maria had a massive impact on the vegetation of Dominica. The thick vegetation of the island was significantly defoliated (Cozzens, 2018). Many trees were destroyed by the strong winds, with sustained wind speed of 280 km/h and moved around as tree debris (Hu and Smith, 2018). The bare land was then exposed to landslide, erosion and debris flows hazards. According to Hu and Smith (2018), the vegetation fully recovered within two months. This statement is not entirely true, because although the vegetation was growing, it was creepers and opportunistic plants growing around the dead trees which was evident during the fieldwork in February 2019. This indicates that the trees do not have roots to hold the soil together, hence there is the possibility of further landslide and debris flow should torrential rainfall or another hurricane event occur.

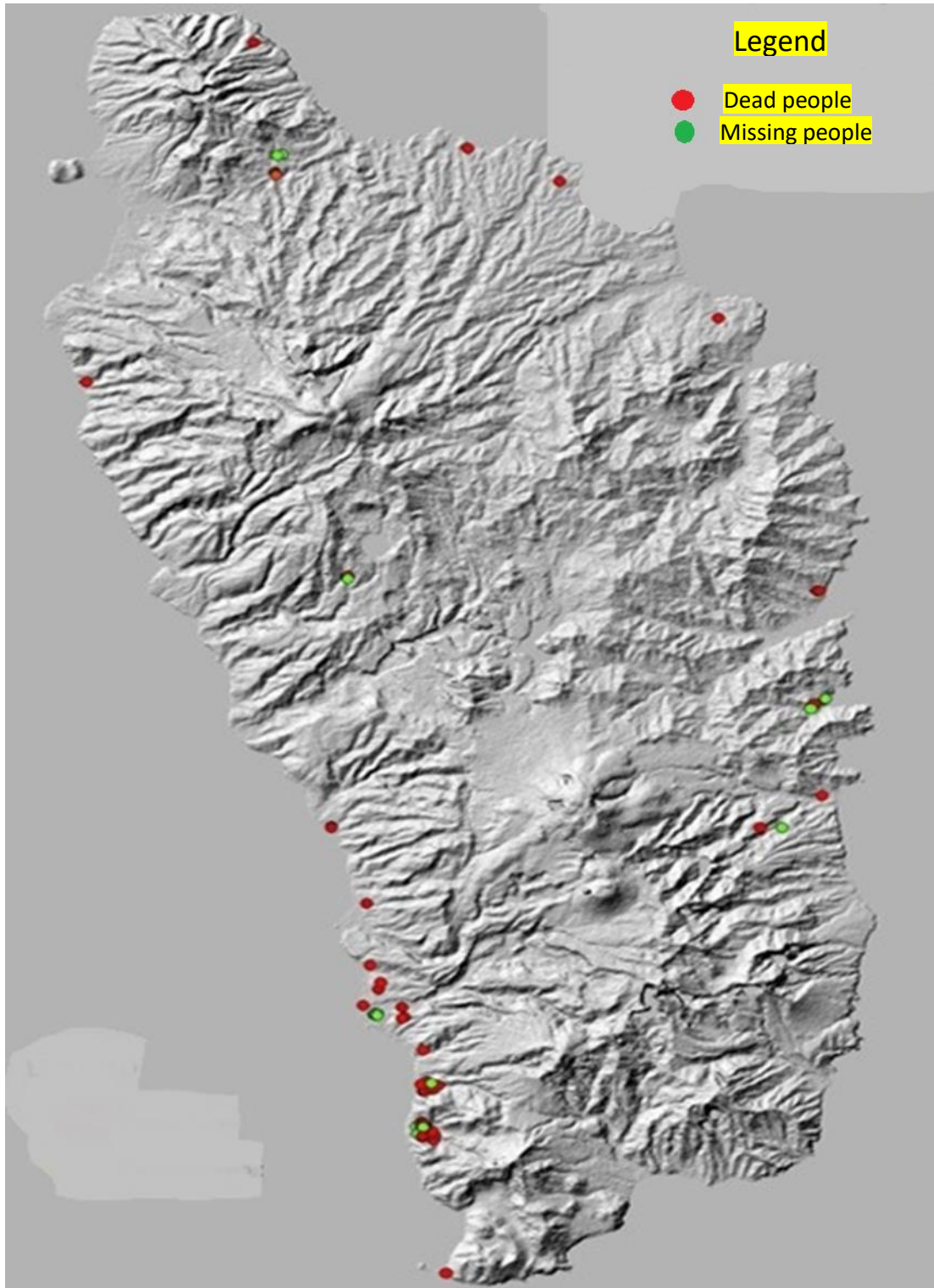


Figure 2.3: Shaded Relief Map of Dominica Showing location of fatalities (dead and missing people) (Researcher's image created in ArcMap 10.7).

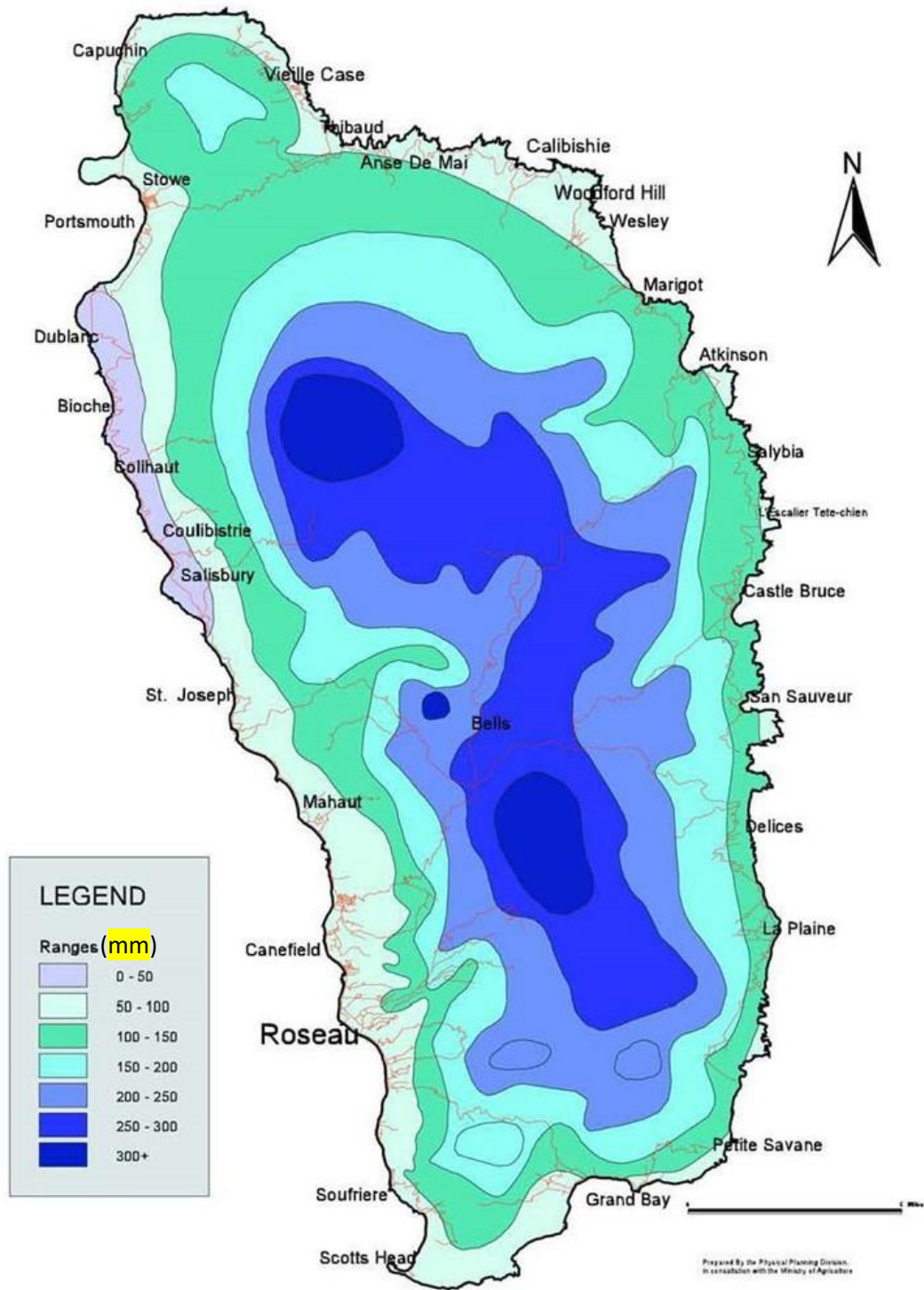


Figure 2.4: Dominica rainfall map showing annual rainfall distribution across the island (CDEMA, 2018).

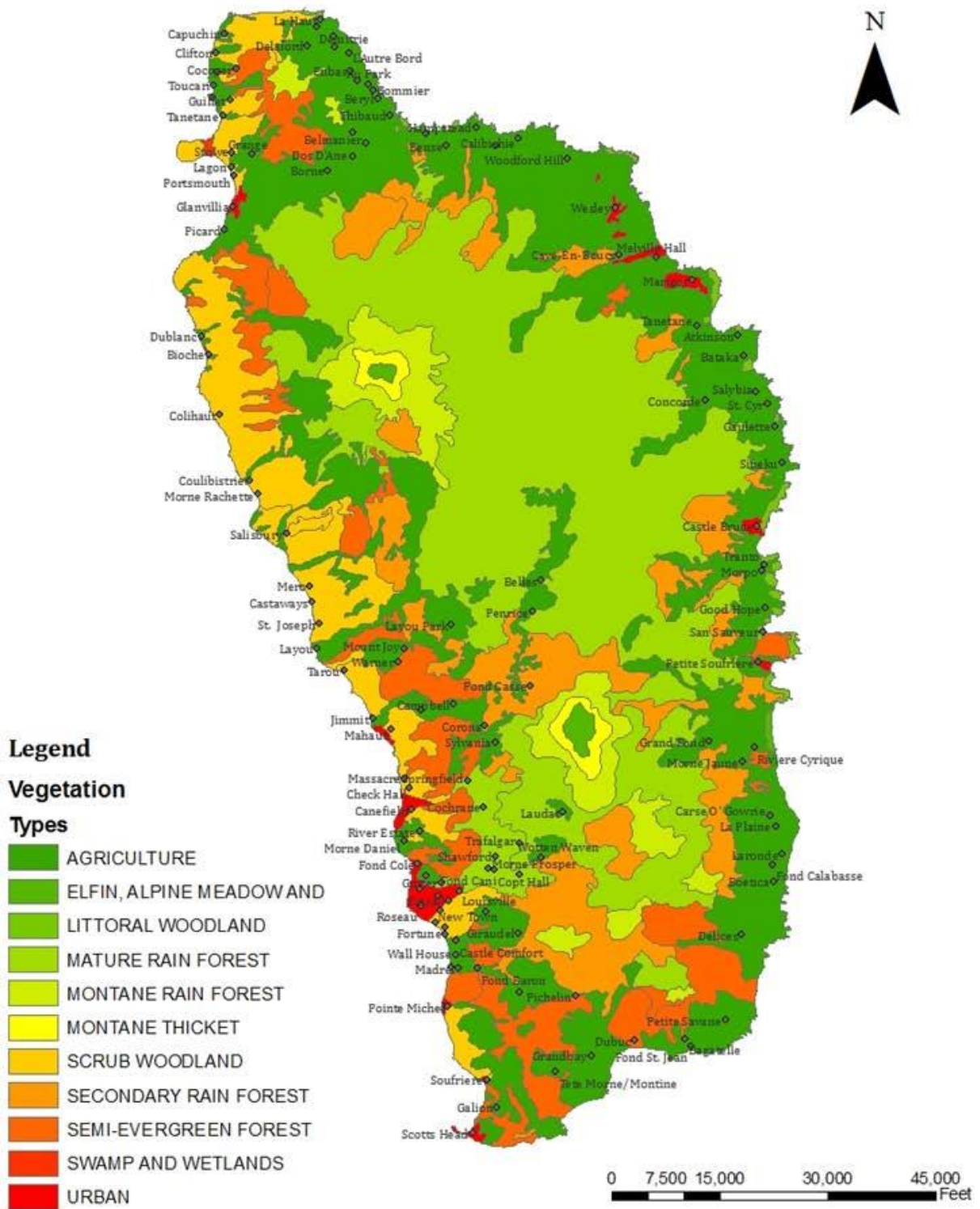


Figure 2.5: Dominica vegetation map showing types of vegetation across the island (CDEMA, 2018).

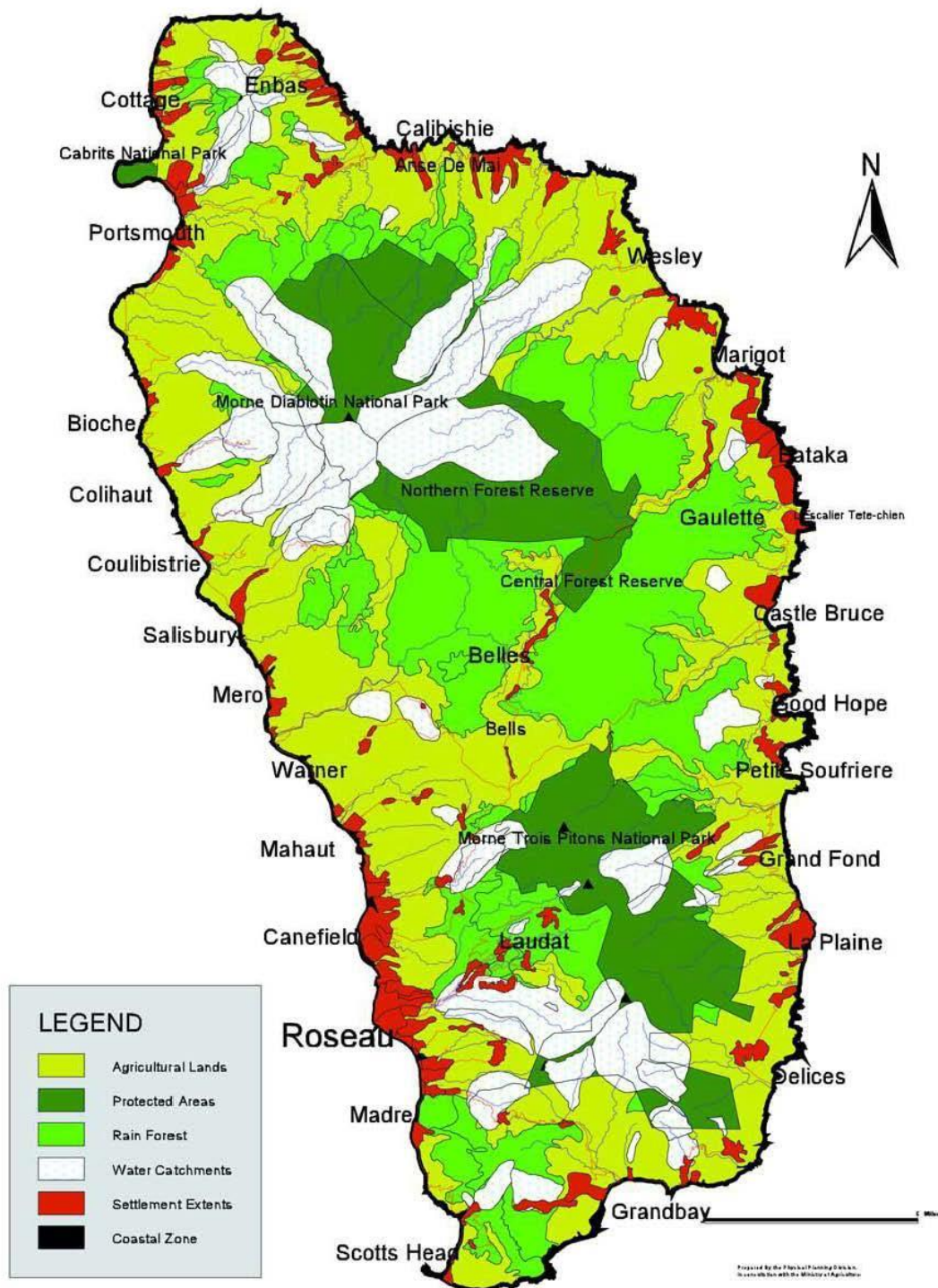


Figure 2.6: Dominica land use map showing landcover of the island (CDEMA, 2018).

2.4 Fogo Study Area

This section gives a detailed description of Fogo (Cape Verde) in terms of the location, geology, climate and vegetation and also the reason for choosing the study area.

2.4.1 Location and Description of Fogo Island

Cape Verde is situated in the Atlantic Ocean about 450 km east of Senegal in West Africa, 1600 km south of the Canary Islands and 800 km west of the Mid-Atlantic Ridge. Cape Verde is a volcanic archipelago composed of 10 main islands and 8 islets (Figure 2.7). The distribution of the islands and islets give a horseshoe-like (Figure 2.7) appearance to the archipelago. Cape Verde is located between latitude 14° and 18°N, and longitudes 22° and 26°W and is part of the Macaronesia ecoregion (Masson et al, 2008). The archipelago is divided into Windward Islands and Leeward Islands. The Windward Islands are Boa Vista, Santa Luzia, Santo Antao, Sao Vicente, Sao Nicolau and Sal, whilst Brava, Fogo Maio and Santiago constitute the Leeward Islands (Figure 2.7) (Peace Corps, 2017).

Santiago is the largest island in Cape Verde with a total area of 991 km². Praia, the capital city, is situated on Santiago and has the biggest population of all the islands with over 294,300 people (NIS, 2015). Boa Vista, Maio and Sal are relatively flat, arid and sandy whilst Fogo, Brava, Santo Antao, Sao Luzia, Sao Nicolau, Santiago and Sao Vicente are mountainous with rugged topography and vegetated (Peace Corps, 2017). The main economic activities in Cape Verde are agriculture, fishing and tourism. The study will be undertaken in Fogo and the rationale for the selection is susceptibility of the areas to natural hazards such as flooding, debris flow and landslides. Accessibility for data acquisition was also a factor taken into consideration in selecting the study area.

Fogo is one of the southernmost islands in the archipelago, located between Santiago and of Brava (Figure 2.7). Its maximum altitude is 2.83 km above mean sea level at Pico Do Fogo. It has a circular shape, being 26.3km long and 23.9 km wide with a total area of 476 km² (Figure

2.7). Pico Do Fogo is an active volcano (Madeira et al, 1997; Day et al, 1999; Jenkins et al, 2017). Fogo has a population of 35, 837 according to the 2015 census. It has fertile agricultural soil due to volcanism and the main economic activities are agriculture, fishing and tourism. The transport system consists of the domestic Sao Filipe Airport, the inter-island Vale de Cavaleiros Port with ferry services to and from Brava and Santiago, and a local road network.

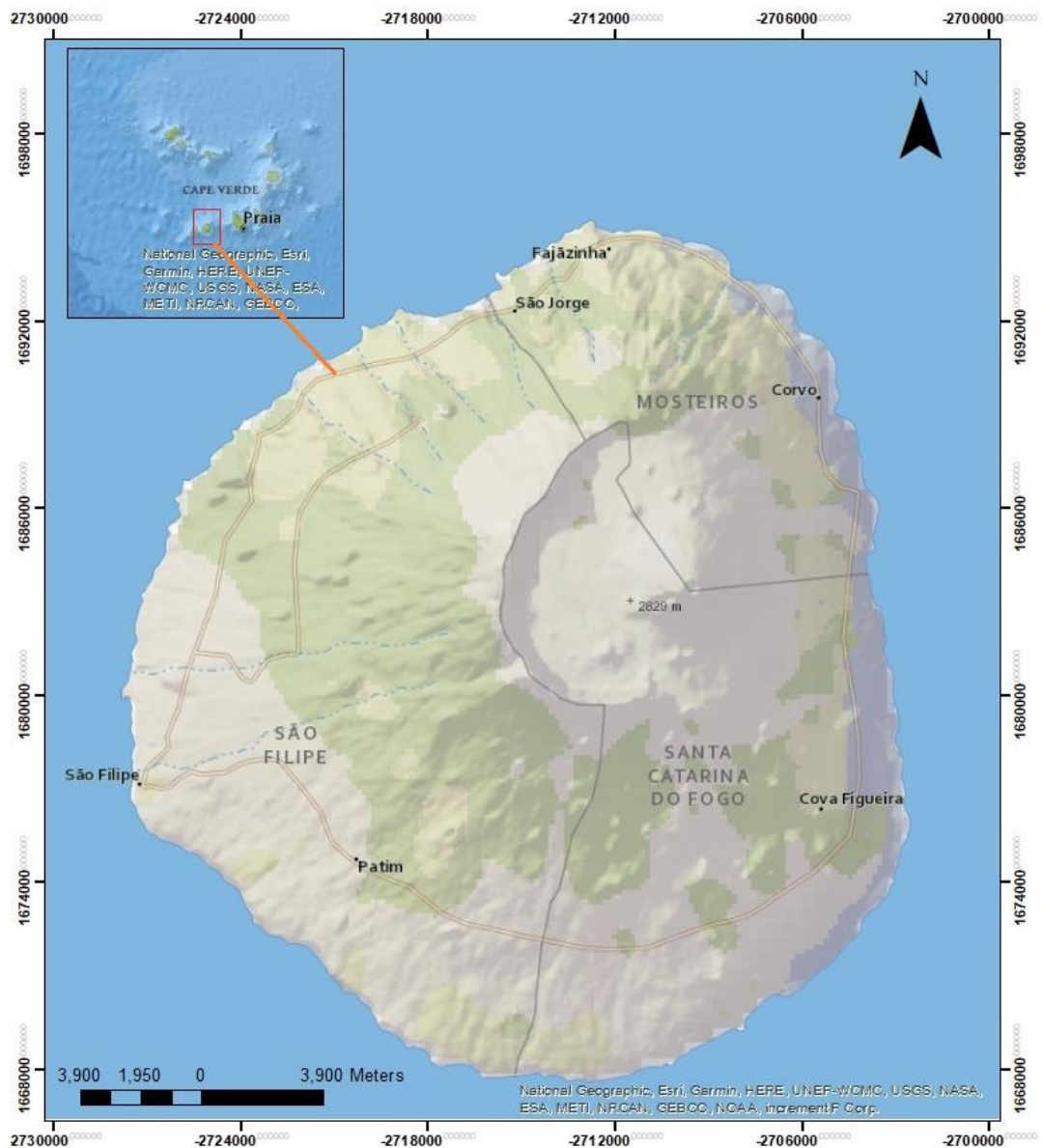


Figure 2.7: Geographic map of Fogo, with inset showing location of Fogo in Cape Verde (Researcher’s image created in ArcMap 10.7).

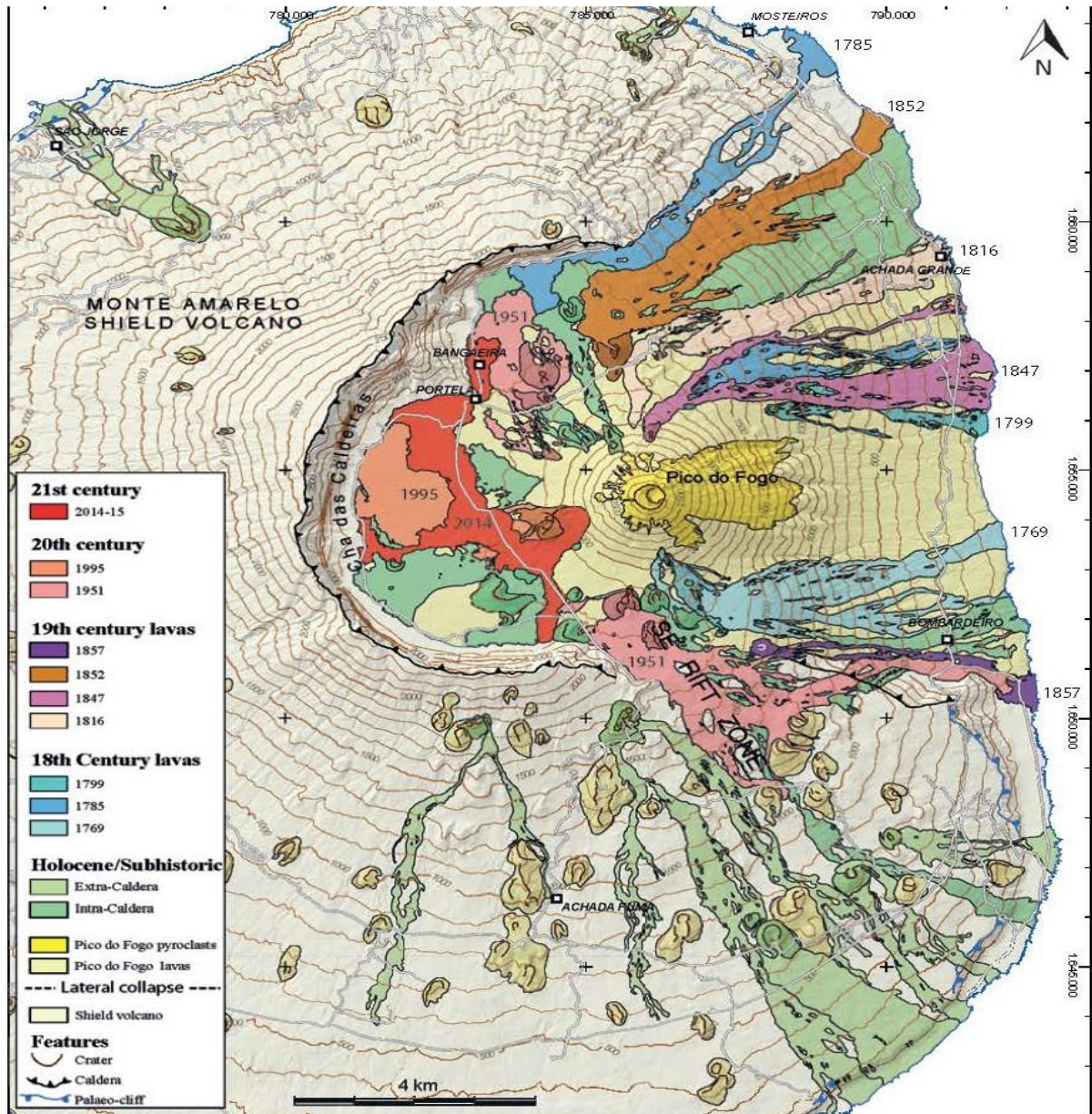
2.4.2 Fogo Geology

The Cape Verde Rise is believed to have resulted from hot upwelling of an underneath mantle plume (Holm et al, 2008; Pim et al, 2008). Volcanism started in the archipelago around late Oligocene and early Miocene (Torres et al, 2002). The geologic age of the oceanic crust on which Cape Verde is built is around 122 Ma to 150 Ma, as pillow lavas with characteristics of Mid-Ocean Ridge Basalt (MORB) are the oldest igneous rocks found in the Cape Verde Rise (Anderson et al, 1992). Most volcanic activity occurred in 16 Ma to date and the age of the volcanism decreases from east to west of the archipelago (Stillman et al, 1982; Mitchell et al, 1983; Plesner et al, 2002; Holm et al, 2006, 2008; Ramalho et al, 2010a, 2010b). Fogo, Sao Vicente and Santo Antao are the only islands that have experienced volcanism in the past 500 ka (Plesner et al, 2002; Holm et al, 2006, 2008). However, recent volcanic activity has taken place in Fogo in 1951, 1995 and 2014-15 (Madeira et al, 1997; Day et al, 1999; Jenkins et al, 2017).

Fogo came into existence through volcanism over millions of years. From the sea floor, Fogo rises approximately 6000 m to about 2829 m above mean sea level (Figure 2.8) (Ribeiro, 1960; Torres et al, 1997; Jenkins et al, 2017). Fogo is a shield oceanic island with a diameter of approximately 27 km (Figure 2.8) which is still in the process of shield-building. Until the collapse of Monte Amarelo shield volcano and volcanism at Pico do Fogo, Monte Amarelo was the highest elevation in Fogo reaching an estimated height of approximately 3500 m (Ribeiro, 1960; Torres et al, 1997; Jenkins et al, 2017). The collapse of Monte Amarelo was caused by a giant landslide which resulted in a caldera-like depression Cha das Caldeiras (Figure 2.8). The depression was later filled with basaltic rocks from subsequent volcanic eruptions which resulted in the formation of a 2829 m stratovolcano known as Pico do Fogo (Figure 2.8) which is predominantly made up of strata of basaltic lapilli.

Since the discovery of Fogo in the 15th century, approximately 30 volcanic eruptions have been recorded with the most recent eruption occurring in November 2014 to February 2015 (Ribeiro, 1960; Torres et al, 1997; Jenkins et al, 2017). Fogo geology has been categorised into four formations (Day et al, 1999; Foeken et al, 2009), namely the Seamount Series, the Monte Barro Group, the Monte Amarelo Group and the Cha das Caldeiras Group. Alkali basalts and carbonatites of the raised seamount are covered by subaerial lavas of the Monte Barro Group (Foeken et al, 2009; Eisele et al, 2015). The Monte Amarelo Group is a 3000 m thick lava and scoria deposits formed of mafic alkaline rocks (Foeken et al, 2009; Eisele et al, 2015). The collapse of Monte Amarelo between 123 ka and 62 ka due to a giant landslide resulted in the formation of the Bordeira cliff which is 1000 m high (Foeken et al, 2009; Eisele et al, 2015). Cha das Caldeiras and Pico do Fogo came into existence after the collapse of Monte Amarelo, Cha das Caldeiras is predominantly made up of lava and scoria deposits which are filling up the depression created by collapse (Foeken et al, 2009; Eisele et al, 2015). Pico do Fogo is predominantly made up of mafic lava and scoria deposits (Foeken et al, 2009; Eisele et al, 2015) which indicates that most volcanic activity was of low intensity although there were phreatomagmatic eruptions as well. The identification of ignimbrite and phonolitic deposits at the base of Bordeira at the eastern flank indicates volcanic activities of high intensity did occur in the past (Foeken et al, 2009; Eisele et al, 2015).

Figure 2.8: Fogo Geological Map (Torres et al, 1997)



2.4.3 Fogo Climate and Vegetation

Located in the Sub-Saharan African climatic region, Fogo has a tropical dry climate with only dry and wet seasons all year round. Fogo's climate is influenced by four distinct systems such as the Canary Maritime Current, Low Equatorial Pressures, Thermal Depression over Africa and the Subtropical Azores (UNFC, 2007). The annual dry season in Fogo lasts for approximately nine months from November to July. The dry season is characterized by extreme drought with practically no rainfall and experiences a microclimate in comparison to other

islands of the Cape Verde archipelago due to the amount of heat the terrain is exposed to (UNFC, 2007; CD, 2020). Intense solar radiation coupled with strong maritime winds results in extremely rapid evapotranspiration (UNFC, 2007).

The rainy season covers a period of only three months, starting in July and ending in October (UNFC, 2007; CD, 2020) (Figure 2.9). This period is characterized by extreme torrential rainfall events and the island's precipitation is influenced by tropical maritime air and Africa east waves during the wet season which blows from north-east (World Climate and Weather Information, 2020). The average annually rainfall in Fogo is 225 mm and precipitation is higher in areas with slopes above 800 m (UNFC, 2007; CD, 2020). The weather in Fogo varies due to the rugged topography of the island. Coastal parts of the island have moderate temperatures (UNFC, 2007; CD, 2020), areas in the middle belt have high temperature and temperature decreases in the highlands with elevation of 800 m and above. Generally, the temperature in Fogo is high with average annual temperature of 20-25° C (Figure 2.10). On average, September is the wettest and warmest month, February is the coolest month and January is the driest month in Fogo (Figure 2.9 and 2.10) (UNFC, 2007; CD, 2020; World Climate and Weather Information, 2020).

In comparison to Dominica, Fogo is less vegetated which makes the island more vulnerable to geohazards such as flooding, debris flows and landslides. Fogo is generally less green and the vegetation is predominantly made of scrub and dry forests (UNFC, 2007; CD, 2020). Most of the island's fauna are restricted in the accessible areas such as steep slopes and mountain peak. Fogo's vegetation type is described as grassland or savannah which is common in tropical and sub-tropical regions depending on altitude (UNFC, 2007; CD, 2020). Flat parts of the island have semi-desert plants and highlands have arid shrubland.

Tropical cyclones rarely affect Fogo and Cape Verde islands, although hurricanes are formed in this region and subsequently move northwest towards the Caribbean and Americas (CT, 2007). The island is sometimes slightly hit by the tropical cyclones (UNFC, 2007; CT, 2020), but these cyclones are still in their tropical depression stage and attain maximum intensity when in mid-ocean.

The change in climate plays a major role in the occurrence of geohazards such as landslides, flooding and debris in Fogo. Although the island is susceptible to these hazards, most of the research works in the island are conducted on geophysical hazards such as lava flow, lahars and earthquake at the expense of hydrometeorological hazards such as floods, debris flows and landslides (UNFC, 2007). Lack of rainfall during the dry season, reduction of vegetation cover and degradation of ecosystem makes the island vulnerable to drought since they do not have adequate water storage facilities during the rainy season (UNFC, 2007). Most of the people of the island use traditional methods of storing water instead of modern water tanks which involves construction of a small rectangular-like structure for water storage. These structures are so small they cannot store enough water for a long time which was evident during the recent fieldtrip in January 2020.

On the other hand, during the rainy season, torrential rainfall exposes the island to extreme flood events, debris flows and landslides. Sometimes a month's worth rain can fall within a day or few hours recording over 200 mm (UNFC, 2007). These hazardous events result in loss of lives, properties and destruction of the built environment since the island have little to no financial and human resources to tackle these geohazards. A typical example is the 1984 tropical cyclone which resulted in extreme flood events causing around 28 deaths in Fogo and destroying lots of arable lands, infrastructure and other essential amenities (UNDHA, 1984; Gilbert, 1984; USAID, 1993; UNFC, 2007). Tropical Storm Fran was one the catastrophic storm to hit the archipelago of Cape Verde on 15th September 1984 (UNDHA, 1984; Clark,

1984; USAID, 1993). This event had wind speed of 100km/h coupled with torrential causing severe damage to infrastructure, agricultural lands and road networks (UNDHA, 1984; Gilbert, 1984; USAID, 1993). Approximately 1094 buildings were destroyed and over 2100 people were made homeless (UNDHA, 1984; Gilbert, 1984; USAID, 1993). In total, over 31 casualties were recorded over £2 million was lost.

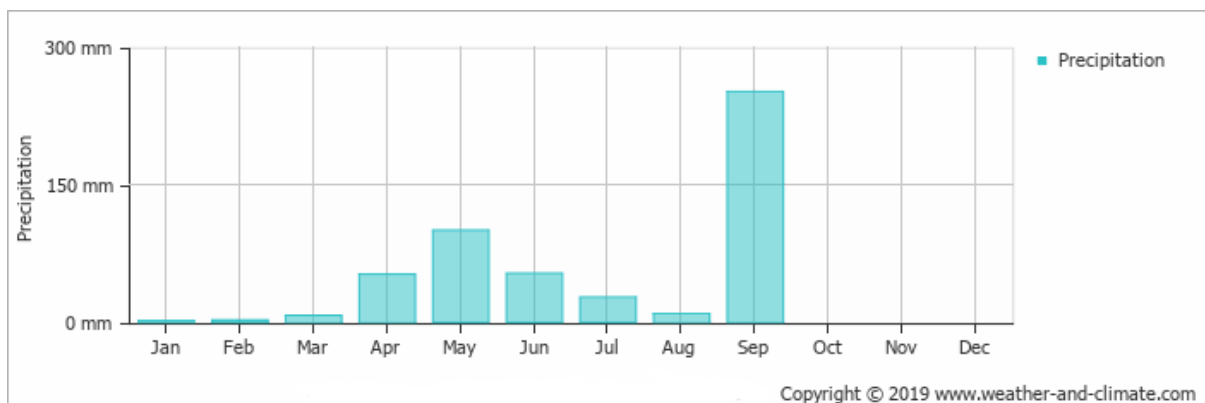


Figure 2.9. Fogo Precipitation Data (World Climate and Weather Information, 2020)

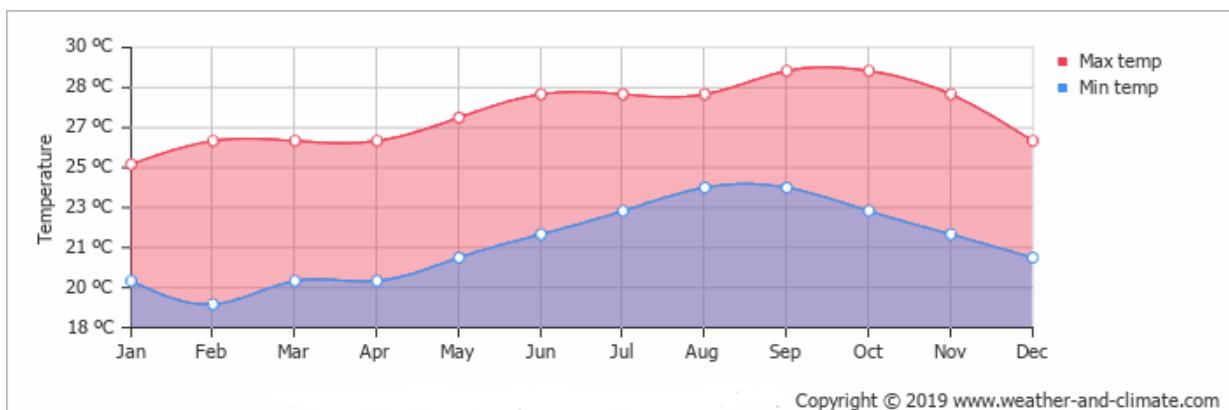


Figure 2.10. Fogo Temperature Data (World Climate and Weather Information, 2020).

CHAPTER THREE

Methodology

3.0 Introduction

This chapter provides detailed descriptions of desk study, data type, source of data, method of data acquisition, data processing and modelling techniques used for the research work. It also describes the step-by-step procedures used to analyse size of boulders, RAMMS 2D debris flow modelling and HEC-RAS 2D flood simulation. Sensitivity analysis conducted in this research work was also presented in this chapter.

3.1 Desk Study, Data Source, Collection Procedure and Software Used

Prior to embarking on fieldworks to collect data, desk study was undertaken to review the available information about the study areas. This was done by looking at previous literature in on the subject area in relation to the study areas. Available google earth images and DEMs for the study areas were analysed to understand features of the terrain and how prone these areas are to geohazards.

The initial plan was to use freely available Shuttle Radar Topographic Mission (SRTM) DEM and acquired from Advanced Land Observation Satellite Phased Array type L-band Synthetic Aperture Radar (ALOS PALSAR) together with drone-derived DSMs for this research work. However, this plan was abandoned due to certain issues with SRTM and ALOS PALSAR DEMs. Firstly, the latest freely available SRTM and ALOS PALSAR DEMs dates back to 2011 which is a decade ago. Therefore, using this data will not give a realistic result as there have been many geomorphological and topographical changes since 2011. Another option will have been to purchase current SRTM and ALOS PALSAR DEMs for the study areas. This option was not feasible as it is expensive and would have undermined the purpose of the research, which was to use free or low-cost remote sensing data.

Moreover, the SRTM and ALOS PALSAR were full of voids, backscatter, low resolution and elevation issues. After several attempts of reprocessing of the SRTM and ALOS PALSAR DEMs, there were still errors with the terrain elevation values and discontinuity of river channels. Also, SRTM and ALOS PALSAR DEMs were generic and not specific to the study localities. They were for the whole of Dominica and Fogo and not the selected study areas. Taking all these issues into account, the best option was to use the up-to-date, high resolution and less erroneous drone-derived DSMs for this research.

This study aims to use low-cost remote sensing data and fieldwork data for flood and debris flow mapping and analysis. The decision to use drone-derived remote sensing data was made because SIDS nations such as Dominica and Cape Verde cannot afford to purchase expensive satellite data. The data type, source, date of collection, resolution, sensor and usage are presented in Table 3.1.

Software used for processing remote sensing data and modelling of hazards such as flood, debris flow and spatial analysis of boulders moved during Hurricane Maria in relation to damage caused are presented in Table 3.2. Agisoft Metashape is photogrammetry software that is used to process remote sensing data into orthophotographs and Digital Elevation Models (DEMs) for geoinformatics studies. Rapid Mass Movement Simulation (RAMMS) is a Swiss developed application used for simulating and analysing mass movements such as debris flows, snow avalanche and rockfalls. For this study, RAMMS was used to model debris flow hazard. ArcMap is a component of ArcGIS which was used to process and transform DEMs, orthophotographs and landcover data. Hydrologic Engineering Centre and River Analysis System (HEC-RAS) is a hydraulic software used for simulation of flow of water through natural rivers and other channels. ImageJ is an image analysis software that was used to analyse the spatial movement of boulders moved during Hurricane Maria. For this study, ArcMap 10.7.1, HEC-RAS 5.0.7, ImageJ 1.52a and RAMMS 1.7.20 versions were used.

Data Type	Source	Resolution	Sensor	Date	Purpose
Landcover Data	Charimgeonode.net (Dominica) USGS (Cape Verde)	5 m	49 SIR-C/X-SAR	1/11/2018	For geospatial analysis
Rainfall Data	US National Hurricane Centre			17/03/2018	For hydrological analysis
Unmanned Aerial Vehicle (UAV) (Drone) derived Orthophotographs and DEMs	DJI Phantom Drone operated by Researcher	3 – 15 m	1" 20 MP sensor	29/05/2019 - 12/06/2019 (Dominica) 04/01/2020 - 18/01/2020 (Fogo, Cape Verde)	For geospatial analysis
ALOS PALSAR DEM	ALF	12.5 - 30 m	PRISM/AVNIR-2/PALSAR	01/01/2018	For geospatial analysis
SRTM DEM	USG	30 – 90 m	SIR-C/X-SAR	01/01/2018	For geospatial analysis

Table 3.1: Dataset used for research work.

Processing Software	Modelling Software
Agisoft Metashape (Drone Aerial Images)	RAMMS (Debris Flows Hazard Simulation)
ArcMap (DEM and orthophotographs)	ImageJ (Boulders Size Analysis)
	HEC-RAS (Flood Hazard Modelling)

Table 3.2: Software used for the research work.

3.2 Digital Elevation Models (DEMs)

A Digital Elevation Model (DEM) is a 3-dimensional representation of the surface of a terrain which encompasses both Digital Surface Models (DSM) and Digital Terrain Models (DTM)

(Figures 3.1a and b) (Li et al, 2004; Balenovic et al, 2016). DEMs are available as raster data or vector data (Figure 3.2). Raster DEMs appear in a grid with each pixel containing a value terrain and vector DEMs appears in triangular irregular network (TIN) with each vertex containing a terrain value (Figure 3.2) (Ronald, 1987; Jakubowski et al, 2013).

It is fundamentally important to understand the difference a DSM and a DTM. A DSM is a digital presentation of the Earth's surface including all natural and man-made features. The DTM is a digital presentation of the Earth's surface without any features (Figures 3.1A and B) (Li et al, 2004; Balenovic et al, 2016). A DSM is used for landscape and infrastructure modelling whilst a DTM is used for hydrogeological modelling (Balenovic et al, 2016).

DEMs are derived from passive (optical) and active (radar) remote sensing techniques such as drone aerial orthophotographs, radar and lidar altimetry and interferometric synthetic aperture radar (Figures 3.3a and b) (Guth, 2006; Gesch et al, 2007). DEMs from topographic contour maps were coarse with low resolutions but the recent DEMs such as drone-derived DEM, SRTM DEM and ALOS PALSAR DEM are of better quality with high resolution (Tobler, 1969; Hancock et al, 2006). The quality of a DEM depends on the source of data, data capturing technique used and interpolation. Most remotely-sensed DEMs are generated with errors with sinks in DEMs which may be due to insufficient data and inappropriate interpolation methods (Wise, 2011). Surface noise is another problem encountered during DEM generation and it is necessary to reduce the noise before running any analysis on DEMs (Lee, 1980; Lee, 1998; Rahmes et al, 2006).

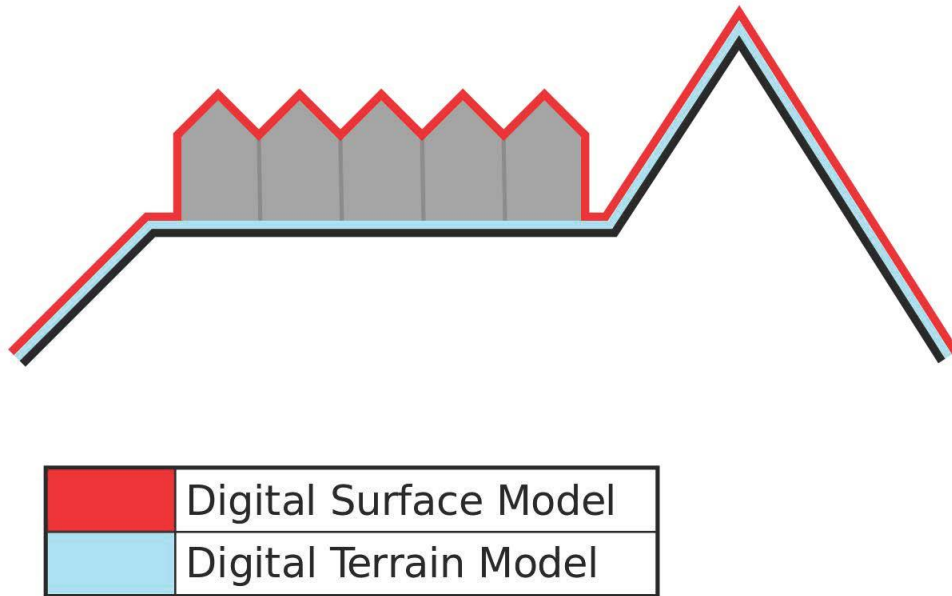


Figure 3.1A: Difference between DSM and DTM. Source: www.gisresources.com

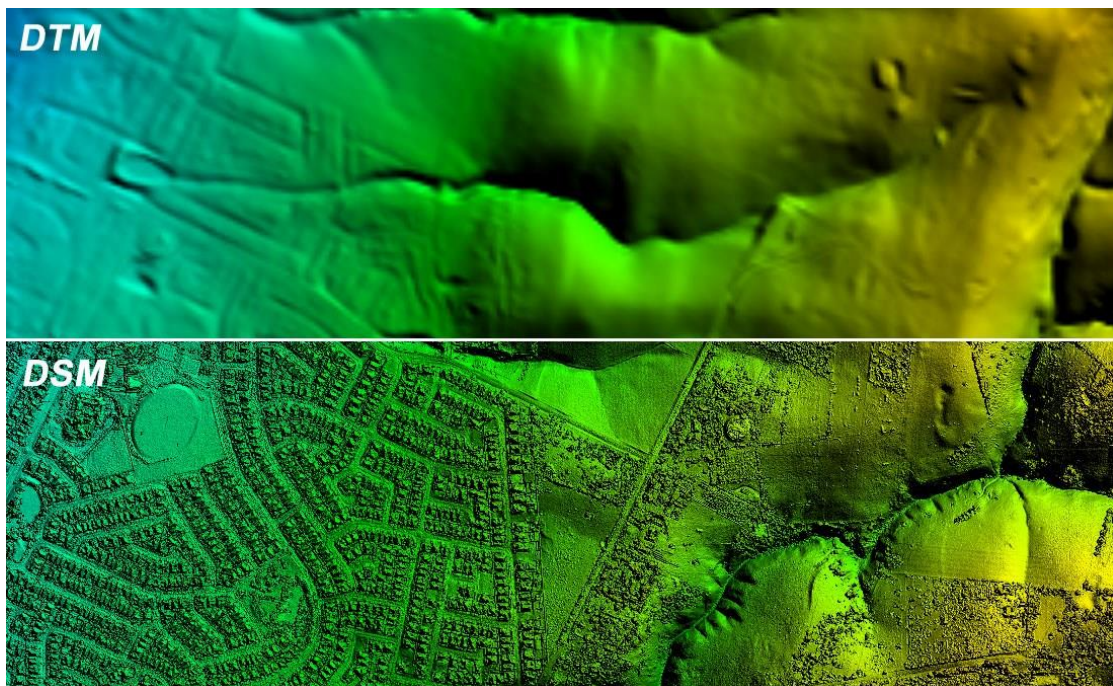


Figure 3.1B: Difference between DSM and DTM. Source: www.gisresources.com

Methods of representing geographic space

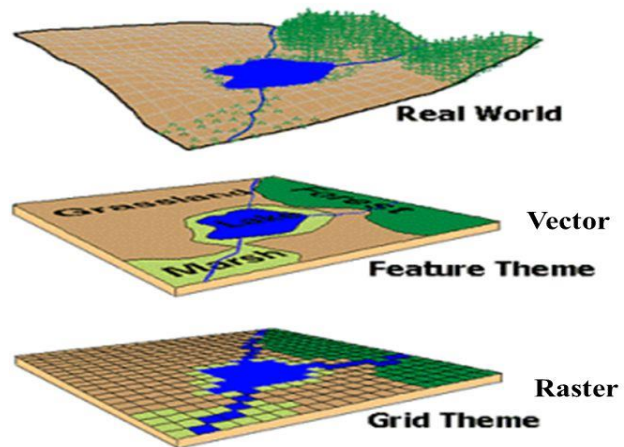


Figure 3.2: Difference between Raster and Vector layers. Source: www.gisresource.com

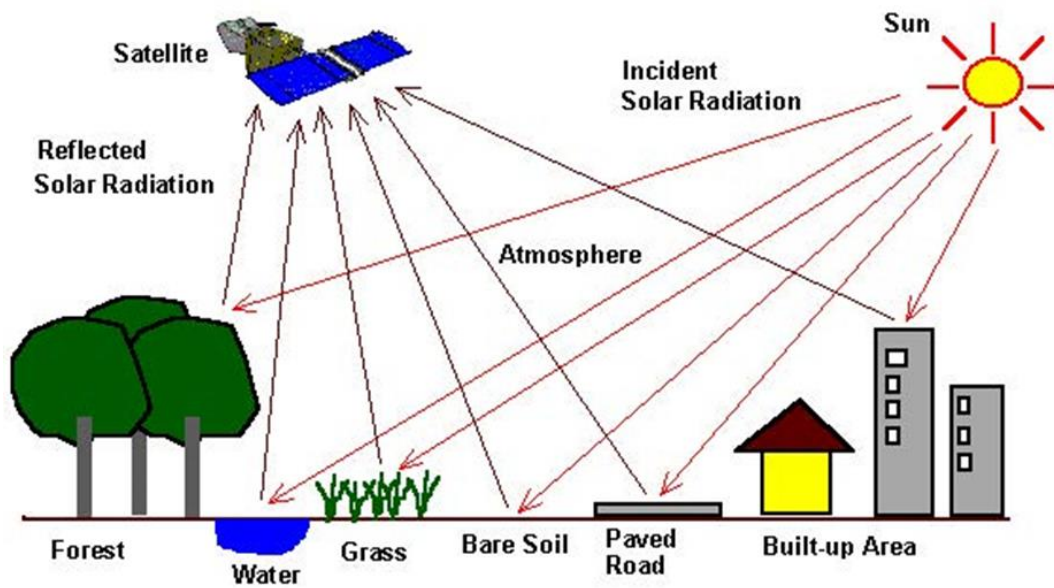


Figure 3.3 A: Remote sensing technique for acquiring DEM. Source: www.crisp.nus.edu.sg

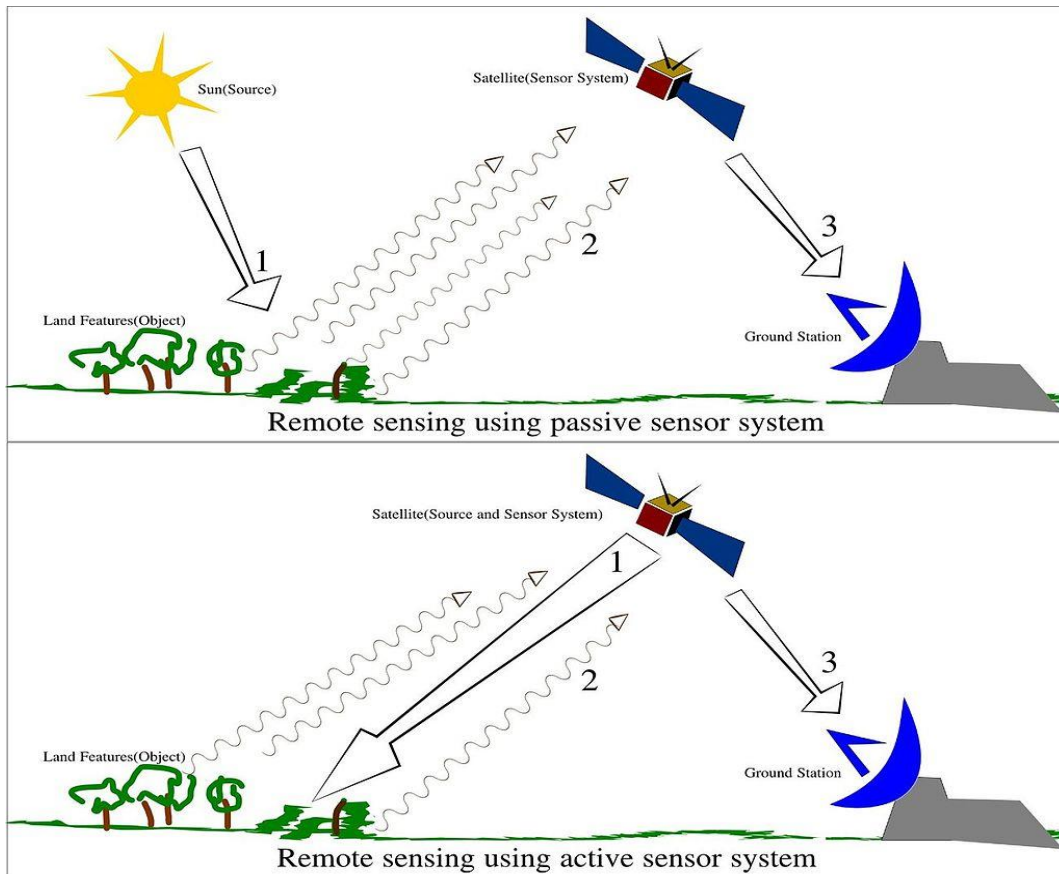


Figure 3.3 B: Optical (Passive) and Active (Radar) Remote Sensing methods. Source: www.crisp.nus.edu.sg

3.3 ALOS PALSAR and SRTM DEMs Corrections

One of the factors that affect the quality of a DEM is the topography of the terrain. A mountainous and rugged topography affect the backscatter values of the satellite due to the side-looking geometry of the satellite radar (Sun et al, 2002; Sinha et al, 2015; Das et al, 2015). Also, vegetation affects accuracy of satellite DEMs because some satellites are not able to penetrate through thick vegetation (Baugh et al, 2013). Pre-processing of DEMs for relatively flat terrains is not usually required since the backscatter value are not affected (Rauste et al, 2007; Parihar et al, 2011). The correction of a terrain's faulty DEM requires another DEM of the same area from a different source which shows the steepness and direction of the terrain (Das et al, 2015).

The correction of a faulty DEM involves radiometric and terrain corrections. Removal of the topographic influence on backscatter values refers to radiometric correction (Figure 3.4) (Loew et al, 2007; ASF, 2014). The satellite reflection from steep slopes causes errors in the backscatter values and correcting the errors helps to show actual terrain surface by adjusting the pixels (Sowter, 2010; ASF, 2014). Sometimes DEMs are generated with geolocation errors and the process of correction the geometrical distortion in DEMs is called terrain geocoding (Sowter, 2010; ASF, 2014). The side-looking radar satellite coupled with rugged topography causes the geometric distortion (Julea et al, 2006). Orthorectification helps to align the pixels properly in a spatial reference frame and corrects the shape and geolocation of the terrain features (Schlapfer et al, 2002).

A 30 m SRTM DEM (Figure 3.5) acquired from USGS was pre-processed to correct the gaps and no value backscatter. The DEM is showing negative values with appearance white spots (Figure 3.5) which indicates errors in the DEM. DEM backscatter values start from zero (0) which represents bodies of water; hence any negative value proves there is inaccuracy with the DEM even if the white spots (no values fields) are not visible. To obtain accurate results from

the DEM, it is very important to correct these errors before running any analysis. The correction was done in GIS using ArcMap 10.6.1 version. Figure 3.4 is the workflow procedure used to fill the gaps and no value backscatter in the DEM. The 30m DEM was input to ArcMap using the Spatial analyst toolbox hydrology toolset. The “fill sink” function under the hydrology toolset was used to manipulate the DEM to fill all the gaps and places where there are no values of backscatter (Figure. 3.4).

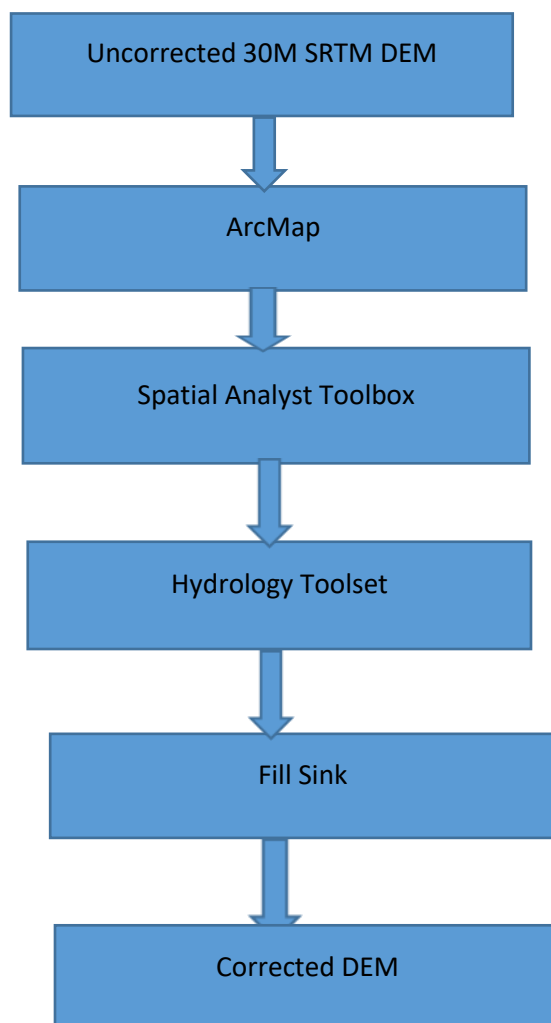


Figure 3.4: SRTM DEM correction workflow in ArcMap.

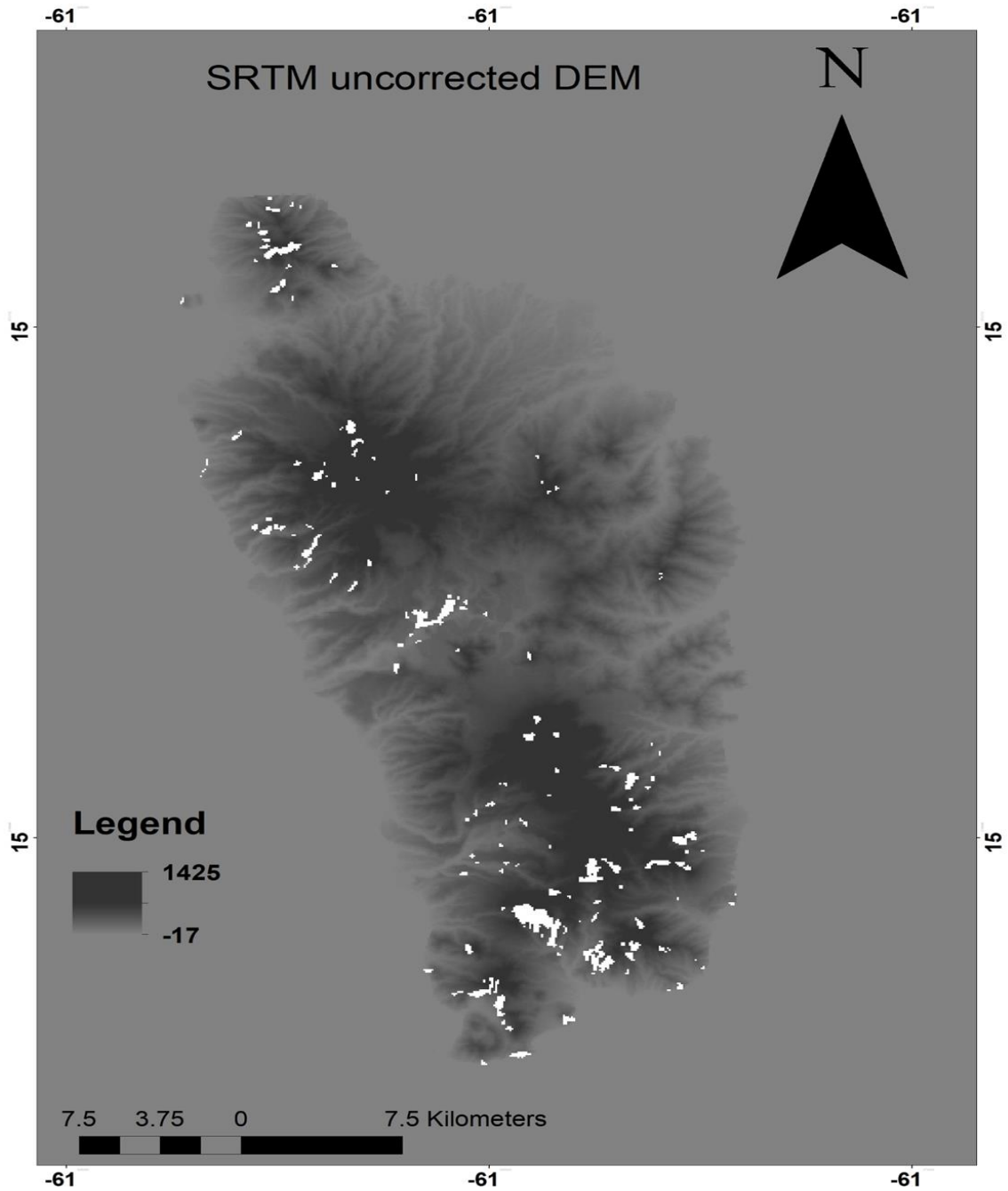


Figure 3.5: Uncorrected Shuttle Radar Topographic Mission DEM. (Researcher's image created in ArcMap 10.7)

The next stage after correction of the 30m pixel SRTM DEM involves integrating it into the 12.5 m pixel ALOS PALSAR DEM of Dominica (Figure 3.7). The gaps in the 12.5 m pixel ALOS PALSAR DEM were filled with data from the 30 m pixel SRTM DEM. The ALOS PALSAR DEM shows minimum pixel value of -30 m which indicates that there are errors in the DEM because it shows the lowest elevation is -30 m below sea level. The no data values appear as tiny white spots on the DEM (Figure 3.5 and 3.7). The no data gaps in the DEM were filled with neighbouring values using statistical information. Spatial analyst toolset such as map algebra (raster calculator) and neighbourhood (focal statistics) were used to fill gaps in the DEM. Using ArcGIS 10.6.1 version, the DEM was input into ArcMap and spatial analyst tools, raster calculator and focal statistics were used to run the code syntax (`IsNull("raster"), FocalStatistics("raster", NbrRectangle(5,5, "CELL"), "MEAN"), "raster"`).

Figure 3.6 shows the workflow used to correct the ALOS PALSAR DEM.

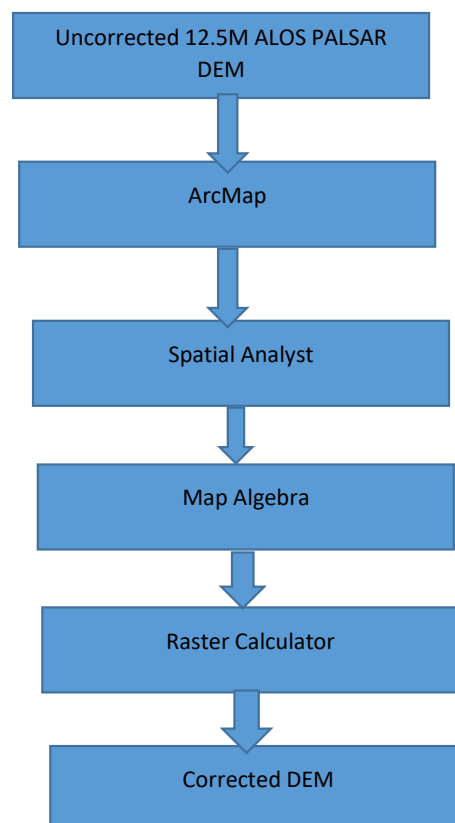


Figure 3.6: ALOS PALSAR correction workflow in ArcMap.

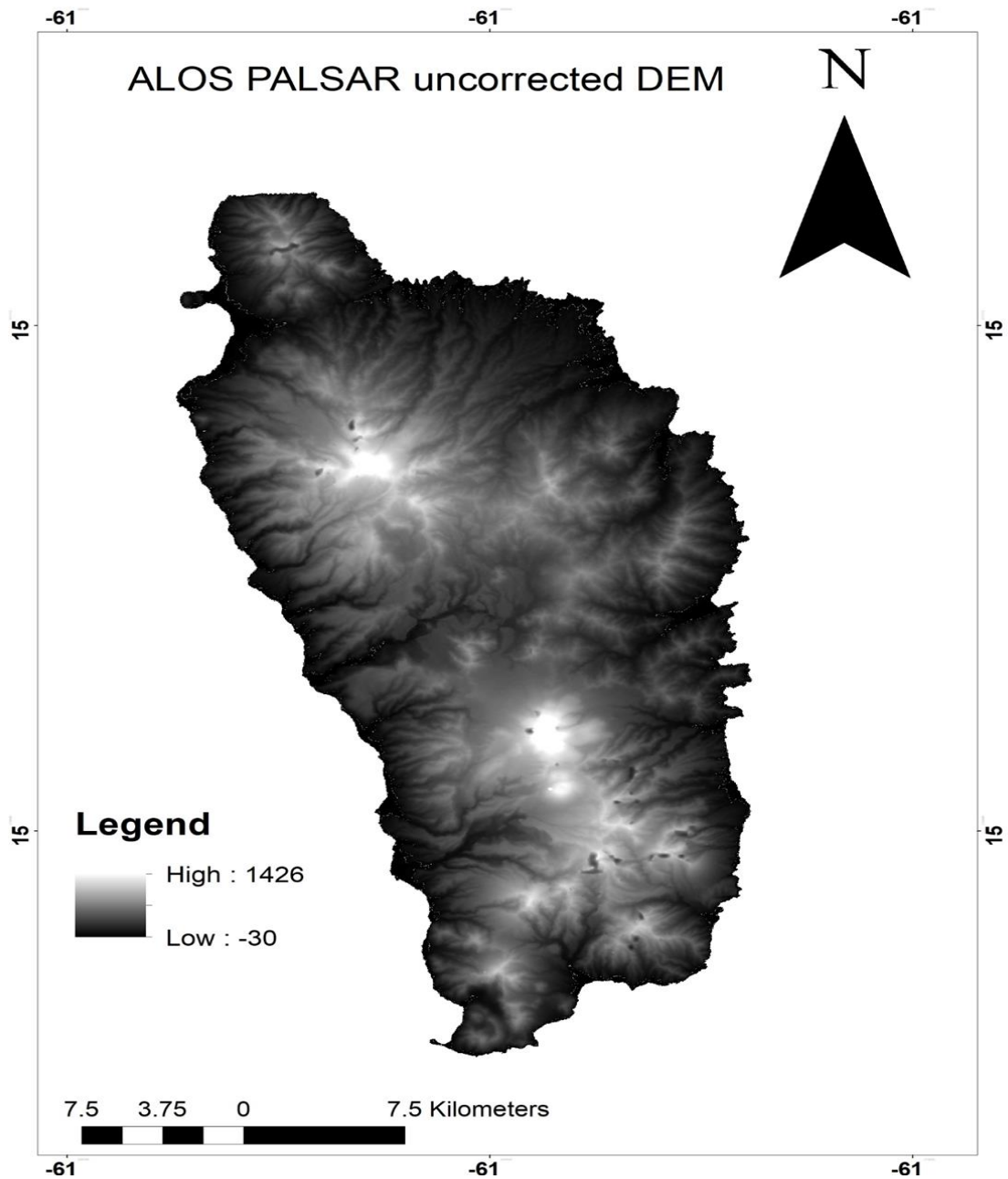


Figure 3.7: Uncorrected ALOS PALSAR DEM. (Researcher's image created in ArcMap 10.7).

3.4 Terrain Analysis

Terrain has a major influence on atmospheric processes and shape of the Earth's surface (Hutchinson et al, 2000; Salvacion, 2016). Knowing the characteristics of a terrain helps to understand the processes that shape the topography (Wilson, 2012). The procedure used for analysing and interpreting topographic features such as elevation, slope, aspect and contours is termed as terrain analysis (Deng et al, 2008; Zhou et al, 2013). The technological advances in remote sensing led to the introduction of DEMs for terrain analysis in late 20th century (Garbrecht et al, 2000; Pike et al, 2008; Schillaci et al, 2015). The availability of DEMs helped geoscience researchers to undertake quantitative and qualitative spatial analysis and visualization of the Earth's surface (Wilson, 2012; Florinsky, 2016).

Digital terrain analysis involves extracting topographic features such as slope, elevation, aspect, curvature and contours from a DEM (Wilson, 2012; Zhou et al, 2013; Salvacion, 2016). The features of a terrain such as slope, aspect and curvature help to understand the geomorphology of the landscape (Zhou et al, 2013; Salvacion, 2016). Understanding the terrain can help to help to predict the impact of natural and human processes on the terrain. The occurrence of landslides and debris flows in a terrain is massively influenced by slope, aspect and elevation (Dragicevic et al, 2015). Application of DEM in GIS helps to assess slope stability and predicting mass movements (Wieczorek and Snyder, 2009; Zakerinjad and Maeker, 2014). The spatial analyst tool surface in ArcMap is used for DEM terrain analysis. Figure 3.8 is the basic workflow for digital terrain analysis in ArcMap 10.6.1 version.

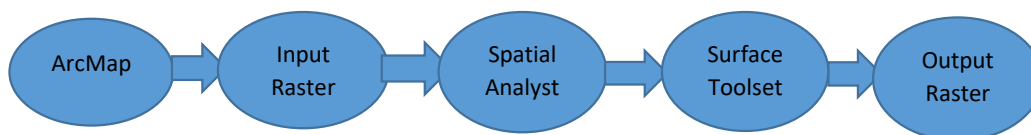


Figure: 3.8: Workflow for DEM terrain analysis in ArcGIS.

3.4.1 Shaded Relief Analysis

The hillshade tool under the surface toolset and in the spatial analyst toolbox of ArcMap was used to create a shaded relief raster from the 12.5m pixel ALOS PALSAR raster DEM. The shaded relief map was generated considering the azimuth angle and shadows. This methodology helps to determine the illumination values of each cell in the raster DEM. Illumination values of each cell enhances the presentation and visualisation of a surface for detail surface analysis. The hillshade analysis helps to determine raster cells that will be covered in other cells shadow. Cells that are covered in shadows of other cells are assigned a value of zero whilst the remaining cells have shaded relief values of 1 to 255. Therefore, the dark areas in the output raster are cells in other cells shadow and have an illumination value of 0 whilst light areas in the output raster are cells that not covered in shadow and have illumination values ranging from 1 to 255.

To create the shaded relief map from the 12.5m pixel ALOS PALSAR DEM acquired from (<https://www.asf.alaska.edu/sar-data/palsar/>), input data was uploaded into ArcMap 10.6.1 version using the add data function. The in-built spatial analyst tool surface was used to generate the shade relief output raster by running the hillshade function. Figure 3.9 indicates the workflow used to produce the hillshade map. Visualisation of the output raster clearly shows the ruggedness of the topography. Greater number of raster cells were exposed to the illumination, hence only a small part of the surface raster was covered in the shadow. The minimum illumination value of the output raster was 0 and the maximum illumination value was 254. The hillshade analysis indicates that, the angle direction of sun was illuminated from a declination of 315° NW and an inclination of 45°.

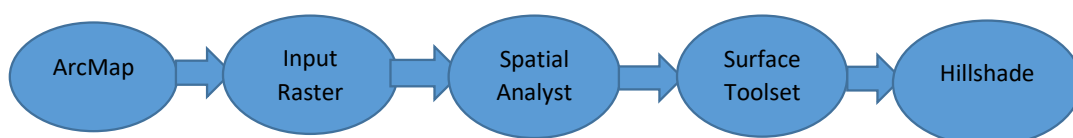


Figure: 3.9: Workflow for extracting hillshade from a DEM in ArcMap.

3.4.2 Slope Steepness Analysis

Slope steepness is an integral part of terrain analysis which determines the change in elevation from one cell to another from a surface raster DEM. Low slopes indicates flat terrain whilst high slopes indicate rugged terrain. Slope angle output raster is expressed in either degrees or percentage. The slope tool calculates the rate of change in a cell's value to its neighbour which determines its steepness downhill. Slope angle analysis was calculated with a 12.5 m pixel ALOS PALSAR DEM obtained from (<https://www.asf.alaska.edu/sar-data/palsar/>). The analysis was done using ArcMap 10.6.1 version, where surface raster data was input using the add data function. The readily available spatial analyst tool such as "surface", was used to calculate slope steepness of the DEM by running the slope function. Figure 3.10 is the procedure used to calculate the slope angle map from the 12.5m pixel ALOS PALSAR DEM in ArcMap.

Slope steepness analysis helps to determine slope stability in mapping and prediction of areas susceptible to the occurrence of landslide and debris flow. Although not all high slopes are unstable, slope steepness analysis helps to detect slopes that are likely to fail. The output raster shows areas with low, moderate and high slopes. The types of slopes are classified in colours, areas showing green colour are classified as flat, moderate slopes areas are depicting yellow colour and areas with high slopes are red in colour.



Figure: 3.10: Workflow for calculating slope angle from a DEM in ArcMap.

3.4.3 Aspect Analysis

Aspect analysis of a terrain categorises the direction that each downhill slope is facing. Each cell in the surface raster has a value which determines the direction it is facing. Aspect is measured in degrees in clockwise direction from 0° to 360°. Cells with no downslope movement are assigned a -1 value which indicates that the terrain is flat. The input data for the aspect analysis was a 12.5 m pixel ALOS PALSAR DEM which was downloaded from (<https://www.asf.alaska.edu/sar-data/palsar/>). The input surface raster DEM was analysed with ArcMap 10.6.1. version. Surface tool under spatial analyst the surface raster was input to ArcMap. The aspect map was extracted from the raster DEM by running the aspect function. Figure 3.11 is the workflow used to create the aspect map.

The slope aspect of a terrain determines the sun illumination the terrain receives, south-facing slopes receive more sunlight than north-facing slopes. (Williams, 2018). As a result, north-facing slopes are cooler with less green vegetation whilst the south-facing vegetation experience warm temperature with greener vegetation. Slope aspect therefore influence vegetation cover and soil moisture of a terrain (Guerrero et al, 2016). Aspect analysis helps to identify areas that are prone to surface runoff, high mobility flows and mass movement.

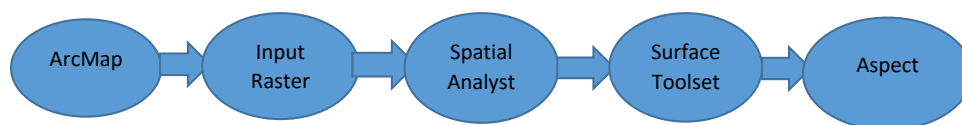


Figure: 3.11: Workflow for calculating aspect from a DEM in ArcMap.

3.4.4 Contour Analysis

Contour analysis helps to detect areas of same altitude above sea level in a surface raster. The contour lines connect cells of the same value in raster DEM. The analysis on contour lines reveals the changes in height from cell to another across the surface raster DEM of a terrain. Widely spaced contour lines indicate a small change in height whilst closely spaced contours lines indicate great change in height.

The 12.5 m pixel ALOS PALSAR DEM acquired from (<https://www.asf.alaska.edu/sar-data/palsar/>) was used for the contour analysis. ArcMap 10.6.1 version, was used to extract the contours of the terrain. The already available spatial analyst tools integrated in ArcMap makes it possible to run the contour analysis from the DEM. The DEM was uploaded into ArcMap using the add data button. The DEM was then analysed using the surface tool contour to extract the contour map. Figure 3.12 is the procedure used to generate the contour map from the 12.5m pixel DEM in ArcMap 10.6.1 version.

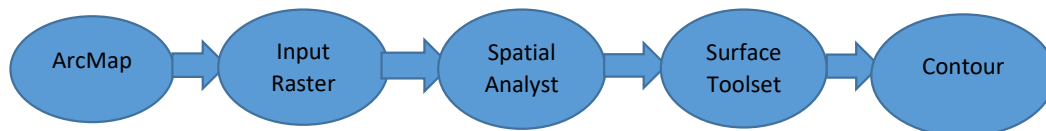


Figure: 3.12: Workflow for generating contour map from a DEM in ArcMap.

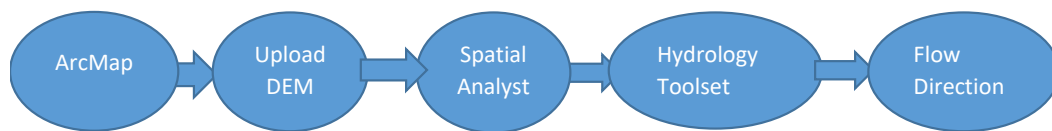
3.5 Drainage Network Analysis

Over the past decade, there has been considerable improvement in application of remote sensing data and geographic information systems for hydrological modelling (Tarboton,1997;

Maidment and Djokic, 2000; Maidment, 2002). Hydrological analysis of an area helps to understand the drainage network and the interaction of a terrain's geomorphology and water (Mani et al, 2014). Application of DEMs in GIS facilitates the process of identifying pathway of groundwater and also mapping areas susceptible to flooding (Houston et al, 20011; Mani et al, 2014). With the aid of spatial analyst tools in GIS, flow direction, flow accumulation and drainage network of terrain are extracted from a surface raster DEM. Flow direction and flow accumulation create the basis for hydrology analysis of a terrain drainage network.

The primary input data for GIS hydrological analysis is DEM and for this study, a 12.5 m pixel ALOS PALSAR DEM acquired from (<https://www.asf.alaska.edu/sar-data/palsar/>) was used for the analysis. The spatial analyst toolset in ArcMap 10.6.1 version, was used for the analysing the flow direction, flow accumulation and drainage network of Dominica. Figure 3.13 is the workflow used to generate the flow direction, figure 3.14 is the workflow used to create flow accumulation and figure 3.15 is the workflow used to create drainage network from the 12.5m pixel DEM.

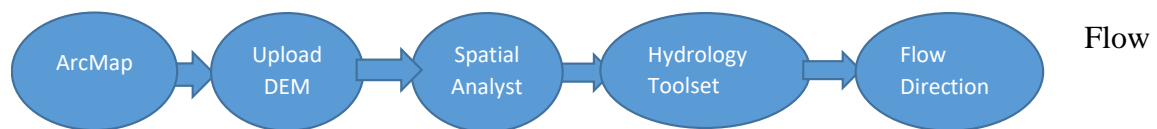
Figure 3.13: Workflow used to create flow direction map.



Flow direction map was generated by uploading the DEM into ArcMap by using the add data button (Figure 3.14). The hydrology toolset under the spatial analyst toolbox was selected for the analysis. The flow direction algorithm was then run to generate the flow direction map. Flow direction shows the direction that each cell within the raster DEM flow. It is presented in

an eight-direction flow model, south, east, west, north, north-east, south-west, north-west and south-east. These orientations of each cell within the DEM are presented in colours in the output map with each colour presented in numbers. The number 1 indicates that cell is flowing eastward, number 2 indicates that cells are flowing towards south-east, number 4 shows cells are flowing towards the south and number 8 indicates that cells are flowing in south-west direction. Likewise, number 16 shows cells that flowing westward, number 32 indicates cells that are flowing towards north-west, number 64 shows cells that are flowing towards the north and number 128 shows cells that are flowing towards north-east. It is important to know the direction flow of a terrain's surface water especially in flood hazard modelling.

Figure 3.14: Workflow used to create flow direction map.



accumulation is the next step in drainage network analysis. Flow direction forms the basis for generating flow accumulation map as it shows where the small streams flow to. The method for generating flow accumulation map is similar to the method used to create flow direction map. The flow accumulation map was extracted from the surface raster DEM using the flow direction map. The flow accumulation algorithm under the hydrology toolset was run using the flow direction raster to create the flow accumulation map. Figure 3.15 shows the procedure used to create the flow accumulation map. Cells that have small accumulation values represents small streams contributing to big streams, cells with higher accumulation values indicates the concentration of the flow.

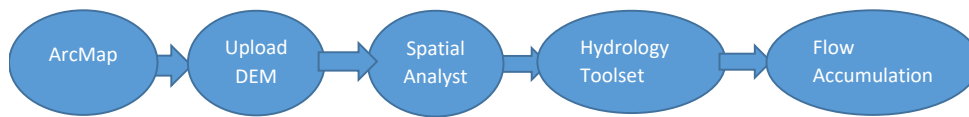


Figure 3.15:

Workflow used to create flow accumulation map.

The drainage network map was calculated from flow accumulation using map algebra tool raster calculator. The drainage network was extracted from the DEM by combining both map algebra tools and hydrology tools, all under spatial analyst toolbox. After producing the flow accumulation map, it was used to create the drainage network by running the raster calculator on it using a deterministic syntax. The syntax (`con (log10flowaccum ≥ 2, log10flowaccum)`) was used in raster calculator extract the drainage network from the flow accumulation. Figure 3.16 is the procedure applied in creating the drainage network map.

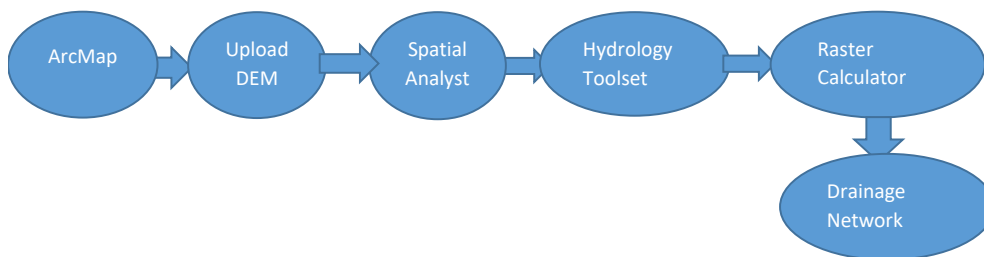


Figure 3.16: Workflow used to create drainage map.

3.3 Dominica Fieldwork and Unmanned Aerial Vehicle (UAV) Survey

Based on initial fieldwork undertaken in Dominica after Hurricane Maria by my supervisors Dr. Simon Day and Dr. Richard Teeuw in early 2018, six principal study locations were chosen for ground-truthing. Some other sites of potential interest had to be discarded after initial reconnaissance because of accessibility issues and ongoing engineering works that had destroyed the evidence of the effects of Hurricane Maria (Figures 3.17 - 3.23). The selected locations are Soufriere and Pointe Michel in south-west, Delice in south-east, Pagua in north-east, Coulibistrie in northwest and Layou in the west respectively (Figures 3.17 - 3.23).

The fieldwork was undertaken to: (1) ground-truth the desk study undertaken prior to the field survey; (2) capture remote sensing data for debris flow and flood hazard modelling, (3) assess devastations caused by events of Hurricane Maria and (4) investigate movements of boulders during Hurricane Maria in relation to damages caused. Ground-truthing in remote sensing basically refers to data collected at a study site in comparison to satellite data (Pickles, 1995). The ground-truthing exercise was conducted to validate the remote sensing data in relation to the on-ground terrain data. This helps to determine the accuracy of remote sensing data by comparing the results with on-site reality. Results of some studies conducted after Hurricane Maria in Dominica were found to be inaccurate due to lack of ground-truthing. A typical example is the vegetation index analysis by Hu et al, (2018) which indicated that the Dominica's vegetation has recovered within two months after Hurricane Maria. This was not true because, what was considered as vegetation were actually creepers growing on dead trees. The spatial distribution and characteristics of boulders moved during Hurricane Maria differs from one study location to another, hence the ground-truthing was conducted to understand differences in spatial distribution of boulders and influencing factors behind such differences. Also, the impact of movement of boulders during Hurricane Maria on the people, the built and

physical environment differ from one study site to another, so ground-truthing was done to validate the hypothesis that fatalities were high in areas that had large movement of boulders.

The fieldwork trip was embarked on 29th January 2019 to 20th February 2019 and I was accompanied by my supervisor Dr. Simon Day and field-assistant Dr. Robert Watts. The three-week fieldwork trip was undertaken for ground-truthing of desk-study and for collection of data after Hurricane Maria and possibly Tropical Storm Erica. Deposits of boulders by Hurricane Maria for each locality were documented taking pictures with mobile phone, recording location with GPS and writing fieldnotes. Movement of boulders from unstable slopes during Hurricane Maria killed many people and destroyed many residential and commercial buildings. Understanding the mechanisms influencing the movement of boulders and their spatial distribution is necessary in attempt to mitigate the negative effects they have on livelihood, properties and the built environment.

A second period of two-week fieldwork was undertaken on 29th May 2019 to 12th June 2019 to conduct the drone survey and assisted by Mr. Kennedy Ferguson and Dr. Robert Watts. Aerial photographs of selected areas (Figures 3.17-3.23) massively affected by events of Hurricane Maria were taken using DJI Phantom 4 PRO V2.0. For this research work, a DJI Phantom 4 Pro V2.0 drone was used for data capture.

Although planned for a fortnight, the fieldwork itself took only 11 days to complete, despite various challenges such as, constant rainfall, strong winds, thick vegetation, needing a permit to fly in drone-restricted areas and captured images not aligning in Agisoft. The ruggedness of the terrain and thick vegetation made it difficult to access some areas, especially the inner parts of Delice, Layou, Coulibistrie and Pagua (Figures 3.18, 3.21, 3.23 and 3.22). The distance and landcover of each locality in Dominica where aerial photos were captured with the drone are summarised in Table 3.3.

Locality	Distance (km)	Area (km²)
Coulibistrie	0.5	2.8
Delice	0.7	2.5
Layou	1.2	1.7
Pagua	1.7	2.3
Pointe Michel	1.5	1.6
Soufriere	1.2	1.3

Table 3.3: Study localities, distances and land areas covered by drone survey in Dominica

A reconnaissance survey was undertaken on 30th May 2019 to get a good understanding of the terrain and to identify vantage points that will be suitable for operating the drone before conducting the main survey. After the reconnaissance survey, the main survey work began on 1st June 2019 because it rained heavily on 31st June 2019. Mr. Kennedy Ferguson and Dr. Robert Watts assisted with spotting the drone whilst I was operating it, to ensure it did not go out of sight.

Delice (Figure 3.18) was surveyed first from 1st June 2019 but the interior was not surveyed due to the ruggedness of the topography and limited accessibility. Most the images captured during the first flight did not align properly during image processing in Agisoft Metashape Professional. It took another survey was undertaken on 2nd June 2019, to get all missing images to fill the gaps and for images to align properly in the image processing. The survey of Soufriere (Figure 3.19) was undertaken on 3rd June 2019, although issues of battery failure were encountered. All aerial photos needed were captured with good overlaps and accurate alignments.

Drone survey of Pointe Michel (Figure 3.20) was carried out on 4th June 2019 and just like Soufriere, all aerial photos were captured within a day with good overlaps and perfect alignments. From 5th to 7th June 2019, aerial photos for layou were captured with enough overlaps and accurate alignments. The drone was nearly lost at Layou (Figure 3.21) due to strong winds and thick vegetation obstructing spotter's vision. Flight missions was undertaken at Coulibistrie (Figure 3.23) on 11th June and all photos taken aligned accordingly. It took 3 days to survey Pagua (Figure 3.22) due to intensive rainfall interrupting flights on first 2 days. Aerial photos capture was completed on the third day, so 8th to 10th June was spent at Pagua. In total about 2000 aerial photos were captured from approximately 113 flight missions in 11 days in Dominica.

The aerial photographs were processed into orthophotographs and high resolution DSMs using Agisoft Metashape Professional. The DSMs and orthophotographs generated was applied in ImageJ for boulders size analysis, RAMMS for debris flow modelling and HEC-RAS for flood hazard simulation. Outcomes of the various modelling will help to identify, map and monitor areas susceptible to debris flow and flood hazards

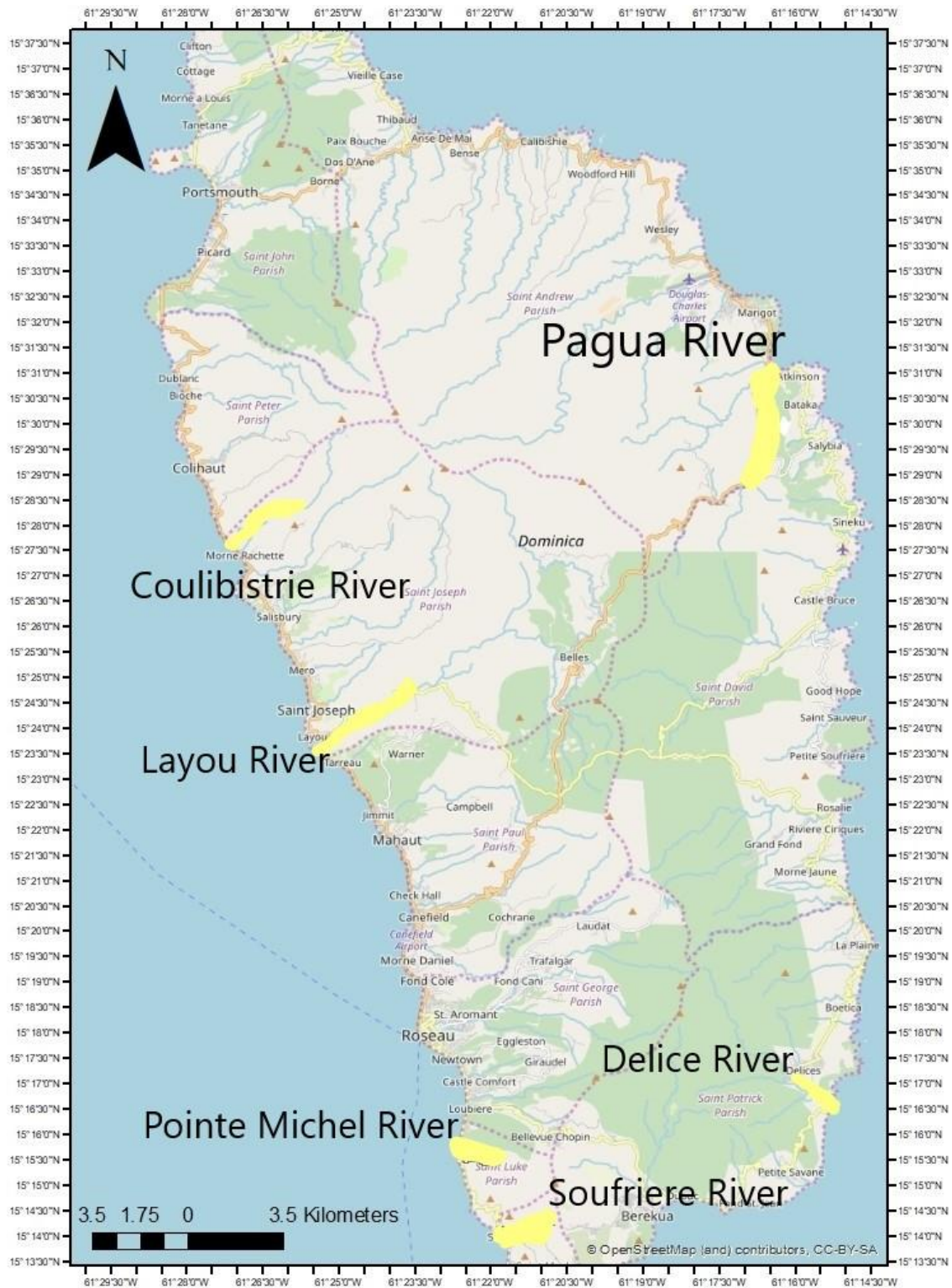


Figure 3.17: Map of Dominica showing selected study locations for ground-truthing and drone survey. (Researcher’s image created in ArcMap 10.7).



Figure 3.18: Google Earth Map of Delice area where a drone survey was conducted.



Figure 3.19: Google Earth Map of Soufriere area where a drone survey was conducted.

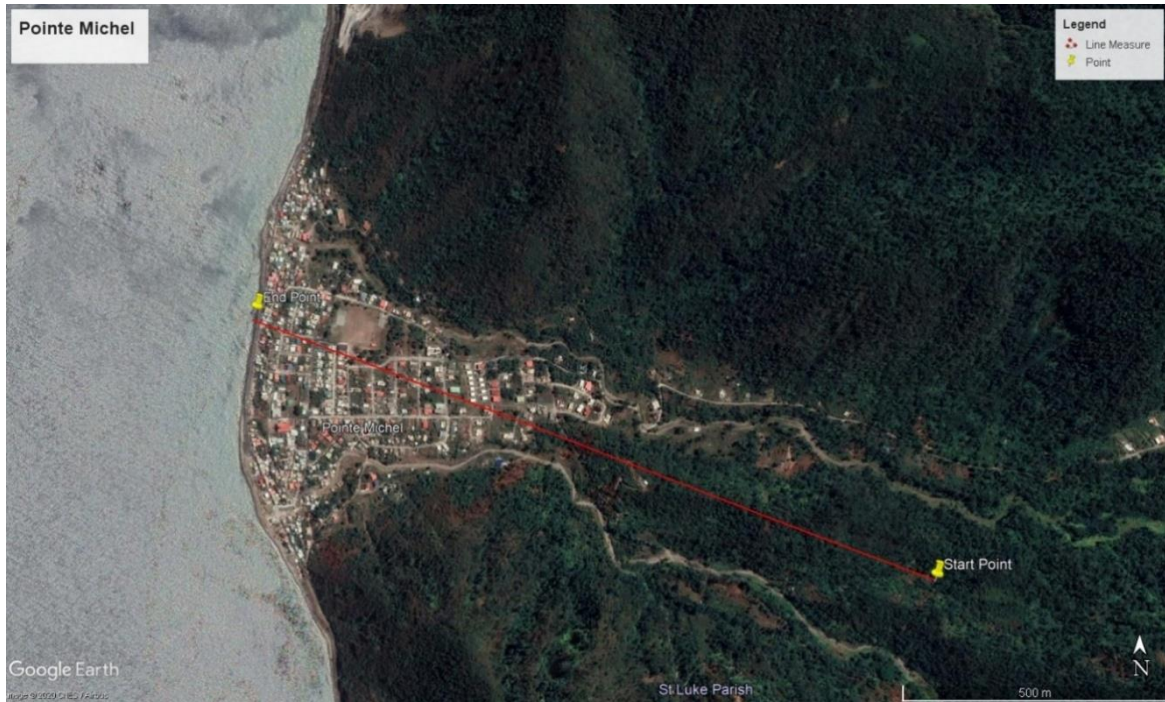


Figure 3.20: Google Earth map of Pointe Michel area where a drone survey was conducted.

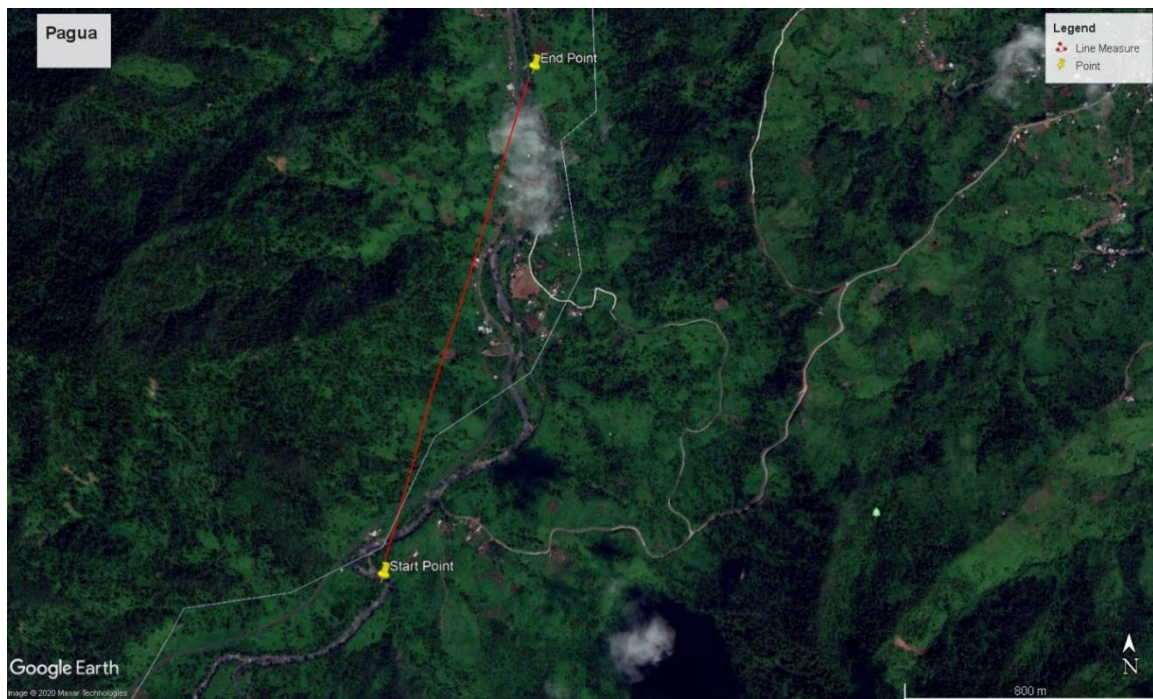


Figure 3.21: Google Earth Map of Pagua area where a drone survey was conducted.



Figure 3.22: Google Earth Map of Layou area where a drone survey was conducted.



Figure 3.23: Google Earth Map of Coulibistrie area where a drone survey was conducted.

3.4 Cape Verde, Fogo Fieldwork and UAV Survey

Two weeks of fieldwork in Fogo (Cape Verdes) was undertaken in January 2020, accompanied by Professor Hilary Downes (supervisor) and Mr. Robert Rall. The study area was the dry river valley system (locally termed “ribeira”) that runs down the eastern part of the island from Ponto Alto do Sul through the island’s capital, Sao Felipe, and into the Atlantic Ocean (Figures 3.24, 3.25, 3.26, 3.27). This ribeira system has different names in different parts, including “Ribeira Domingo Santo” and “Ribeira do Trindade”. The main objective of the fieldwork was to capture aerial photos of the Ribeira system with a drone and ground-truth the desk-study conducted such as terrain analysis using Fogo’s DEM in ArcMap. For this research work, a DJI Phantom 4 Pro V2.0 drone was used for data capture.

The aerial photos of the ribeira system captured by the drone were processed into DEMs and orthophotographs using Agisoft Metashape Professional. The Agisoft-derived DEMs and orthophotographs are the input data required for debris flow and flood hazard modelling in RAMMS and HEC-RAS, respectively. Outcomes of the various modelling will help to identify, map and monitor areas susceptible to debris flow and flood hazards.

Although planned for a fortnight, the fieldwork itself took only ten days to complete, despite various challenges such as needing a permit to fly in drone-restricted areas, captured images not aligning in Agisoft, locals being concerned about walking through their farms and taking images of their residence without their consent. The ruggedness of the terrain made it difficult to access some areas, especially the upper part of the ribeira system (Figure 3.24). The length of the ribeira from Ponto Alto do Sul to Sao Felipe is approximately 13 km with a total area of 86 km², hence the fieldwork was divided into three sections namely: Upper Ribeira (2 km long), Middle Ribeira (5 km long) and Lower Ribeira (7 km long) (Figures 3.24-3.27).

A reconnaissance survey was undertaken on January 5th 2020, to get a good understanding of the terrain and to identify vantage points that will be suitable for operating the drone before

conducting the main survey. After the reconnaissance survey, the main survey work began on the January 6th 2020. Mr Robert Rall assisted with spotting the drone whilst I was operating it, to ensure it did not go out of sight.

The Upper Ribeira was surveyed first from 7th to 9th January 2020 and was the most difficult of all the parts surveyed due to the ruggedness of the topography and limited accessibility. Most the images captured during the first three flights did not align properly during image processing in Agisoft Metashape Professional. It took three more days and surveys to get all missing images to fill the gaps in the Upper Ribeira and for images to align properly in the image processing.

The Lower and Middle Ribeiras were in part within drone flight restriction areas, so we had to obtain permission from the Sao Filipe Airport Authority. This required an authorised letter from the airport supervisor to be sent to DJI to remove the restriction. The Lower Ribeira was surveyed and completed on 11th January 2020 and all images captured aligned perfectly during the image processing in Agisoft Metashape. The Middle Ribeira was the last part to be surveyed on 13th to 17th January 2020. During the image processing, all captured images aligned perfectly and did not require any more surveys. In summary, it took one day to survey the Lower Ribeira, four days to survey the Middle Ribeira and six days to survey the Upper Ribeira. About 7000 images were captured covering a total area of 86.7 km².

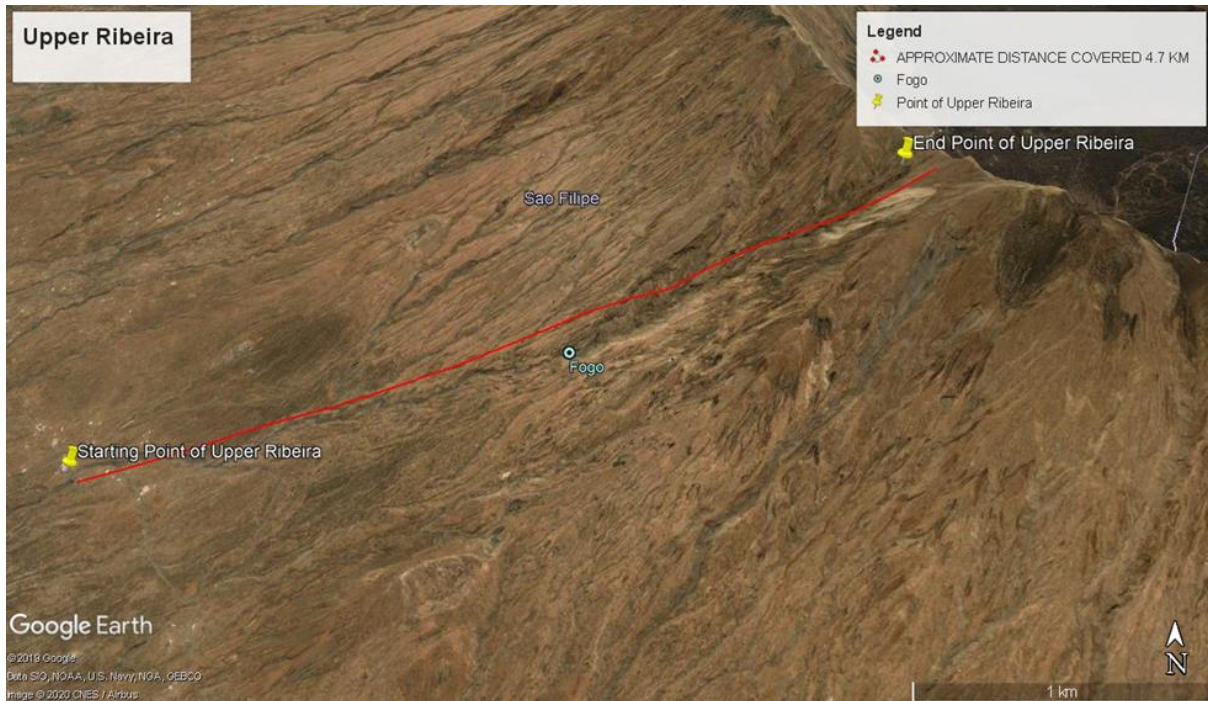


Figure 3.24: Google Earth Map of eastern Fogo showing the Upper Ribeira area, from Ponto Alto Do Sul to the road from Cidreira to Monte Grande.



Figure 3.25: Google Earth Map of eastern Fogo showing area of Middle Ribeira.

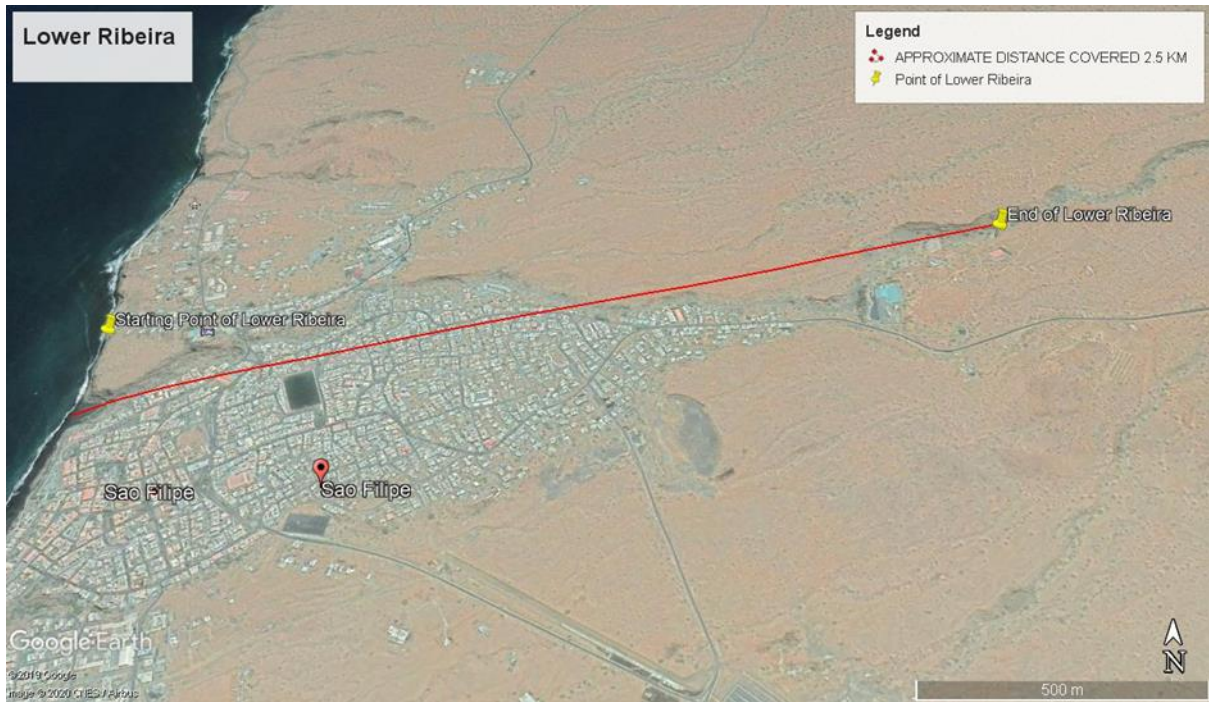


Figure 3.26: Google Earth Map of Western Fogo showing area of Lower Ribeira in Sao Filipe.

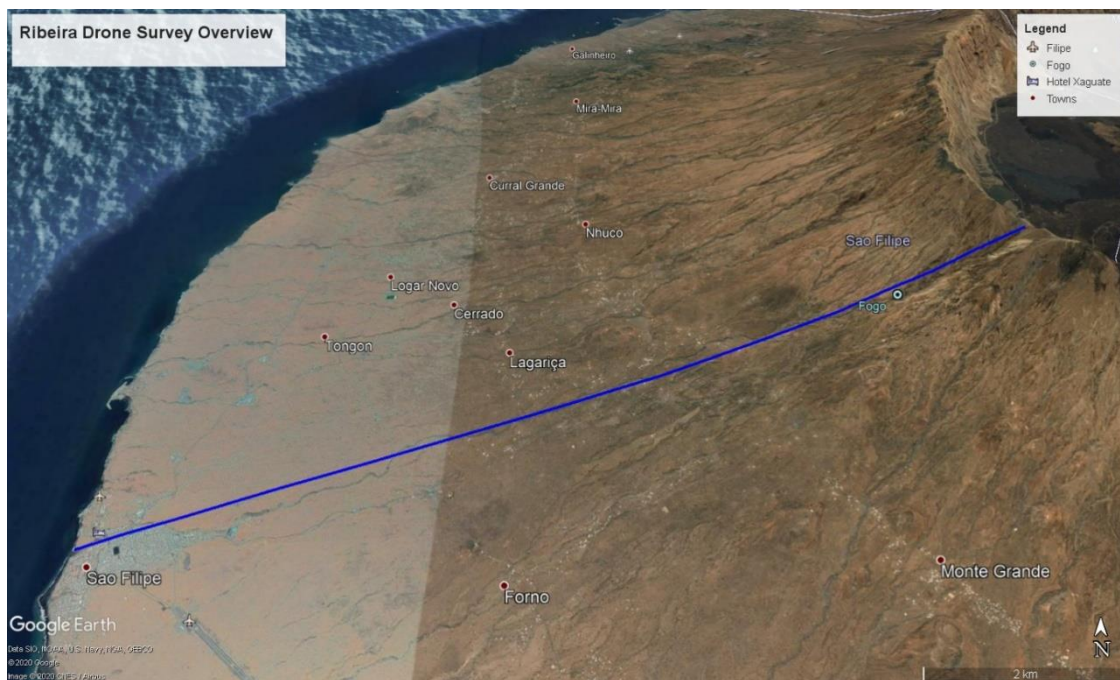


Figure 3.27: Google Earth Map of Western Fogo showing complete overview of ribeira complex from “Ribeira Santo Domingo” at its source in Ponto Alto do Sul to its end “Ribeira doTrindade” in Sao Filipe.

3.5 UAV (Drone) Data Acquisition Techniques and Processing

Drone survey usually requires a competent operator, a good understanding of the terrain, vantage flying and landing spots, and a competent spotter. Before any flight, the gimbal compass must be calibrated to enable the drone to recognise the terrain and avoid crashing it. Having sufficient working batteries is essential since one battery only lasts 20-30 minutes per flight. On both fieldtrips, we had six batteries, but for the Fogo field work one battery was not working, hence we had to make do with 5 batteries, providing only 2.5 hours of flights per day. It takes up to 2 hours to charge one battery and remote controller, hence overnight charging is needed when undertaking field survey.

Having a constant signal between remote controller and drone is essential as it limits the possibility of losing or crashing the drone. During the survey work, the signal was lost a number of times but I managed to bring it back and land safely because my spotter always had it in view. For this study, most surveys were done by flying the drone 150 m above ground level to ensure a good overview of the study areas and their surroundings were captured and avoid crashing the drone into any obstacles. After every survey in a day, the captured aerial images are transferred from the drone into a laptop or hard drive, freeing up space for the next survey and not mixing images from different surveys.

To ensure efficient overlap and to enhance accuracy in results, 700-1000 images were captured in a day. Consistent overlapping between images and passes are essential factors that influence the outcome of drone-derived DEMs and orthophotographs. Generally, the minimum recommended overlap between images is 75% frontal overlap and 60% side overlap but for vegetated and dense forest terrains overlap between images is 85% frontal overlap and 70% side overlap. For this survey work, the general overlap was used because Fogo is less vegetated compared to Dominica with no dense forests.

The aerial photographs were captured using a 20-megapixel sensor DJI Phantom 4 Pro V2.0 drone. Before flying the drone, calibration was done each time to ensure proper orientation of the platform. The take-off area was always in the centre of the terrain as this helps to effectively cover the whole terrain. Flying of the drone and capturing of the aerial photographs were done manually with the camera facing downward, this helps to capture high quality images in a rugged terrain such as Dominica. A total of 313 flight missions were carried out, capturing over 8,000 images and covered a combined area of 12.2 km² in Dominica and 86.7 km² in Fogo, Cape Verde over a month with six drone batteries and each battery has a maximum 30 minute flight time.

The data was processed using the Structure From Motion (SFM) technique to generate accurate orthophotographs and DEMs from the aerial photographs (Turner et al, 2012; Westoby, 2012). Due to large size of the data, processing can take hours to days to complete. Figure 3.28 is the workflow used to process aerial photographs into DEMs and orthophotographs.

The first step for processing aerial photographs with Agisoft Metashape involves uploading all related images into Agisoft. This is followed by aligning all images to ensure proper positioning according to the coordinate system of the terrain since images are automatically georeferenced by the DJI Phantom 4 Pro V2.0. The WGS 84 coordinate system was used for this study. After aligning the images, the dense cloud was built to help correct any distortion and classify data source points for mesh creation. A polygonal mesh was then built from the dense cloud data and was followed by building the texture to give a 3D visual presentation of the terrain. The work is then saved as a psx file to enable processing it to DEM and orthophotograph.

The saved work was then used to build the DEM and Orthophotograph using the “Build DEM and orthomosaic” algorithm. The generated DEM and orthophotographs were then exported and saved as TIFF files. All DEMs generated for this study were DSMs, DTMs were not

generated. This because unlike satellites used by NASA, the drone was not equipped with laser sensor camera to penetrate through thick vegetation and other features on the terrains.

The generated orthophotographs were applied in ImageJ to analysis spatial distribution of boulders during Hurricane Maria and comparing with pre-Hurricane Maria google earth images to understand the changes that occurred. This was done to test the hypothesis that, areas where large fatalities were recorded had movement of boulders. Analysing the movements and characteristics of boulders in terms of size, shape and rock type will also help to understand how they blocked stream channels to cause overbank flooding in some areas. The drone-derived DEMs were used to model flood and debris flows to enhance accurate prediction of areas susceptible to these hazards. Identifying areas susceptible to flooding and debris flows will help to control their impact on people, the physical and built environment through proper settlement and infrastructure planning.

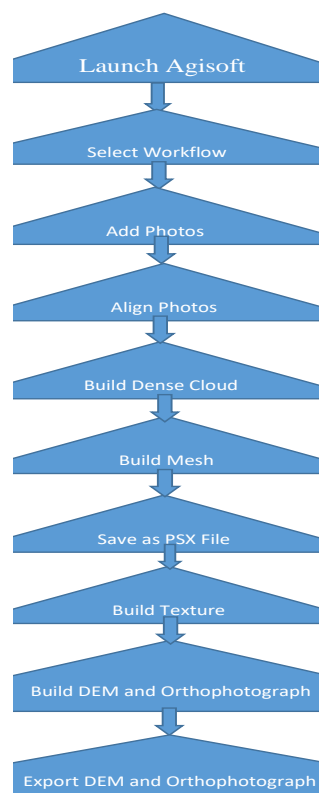


Figure 3.28: Workflow used to process drone aerial photographs in Agisoft Metashape Professional

3.6 BOULDER ANALYSIS

This section gives background information about ImageJ, the procedure involved in analysing the boulders and purpose of using the software.

3.6.1 Introduction to ImageJ Software

ImageJ is an open-source java software developed by National Institute of Health (NIH) which is used for processing and analysing images (Collins, 2007; Schneider et al, 2012). Although initially developed for the health sector for medical purposes, many academic sectors including geoscience have utilized the software. The software is capable of displaying, editing and saving 8 bit, 16 bit, 32 bit and 42 bit grayscale and colour graphics (Collins, 2007; Schneider et al, 2012). ImageJ software is able to process any format of images such as TIFF, GEOTIFF, GIF, JPEG, PNG, BMP, DICOM and FITS (Collins, 2007; Schneider et al, 2012). The software can analyse sizes, shapes and distances of particles in images and the results can be saved in excel and displayed in graphs and charts.

3.6.2 Input Data and Plugins

The main input data for boulder analysis in ImageJ is a geographically referenced orthophotograph of the study area. Due to the large size of the orthophotographs, modern and powerful computers are required to run the analysis. The data were acquired using manually operated DJI Phantom 4 Pro Drone in the field. The UAV-derived images were processed in Agisoft Metashape Professional to generate orthophotographs, which were imported into ImageJ to analyse boulder movement. Another important input parameter is the plugins, plugins such as analyser, graphics and 3D must be updated before undertaking any analysis. The ImageJ software was used to analyse boulders which were moved during Hurricane Maria, including their sizes, distances moved and their impact on the livelihood, infrastructures and properties in selected localities in Dominica. Aside from understanding the mechanisms behind the boulder movement and the effects on livelihood, boulder analysis can help to detect potentially hazardous rapid mass movement, monitor hazardous boulder movements and

understand rockfall landslides. The main objective of the boulder analysis in this study was to test the hypothesis that most of the casualties and damages recorded during Hurricane Maria were caused by boulder movements. To determine which boulders were moved and damages caused during Hurricane Maria, Google Earth images taken prior to Hurricane Maria were compared with drone-derived high resolutions orthophotographs taken on the ground after Hurricane Maria.

3.6.3 Boulder Analysis Workflow in ImageJ

Figure 3.12 shows the workflow involved in using Image J for analysing boulders. The initial step is to launch the application and install all important plugins needed for the analysis (Figure 3.29). The next stage involves importing the image for analysis. All orthophotographs in Agisoft Metashape Professional are generated in Red, Green and Blue (RGB colour) image type. However, when this is imported into ImageJ, the image becomes distorted. To correct this and make it analysable, the image must be converted into 8 bit colour (Figure 3.31).

The next stage involves setting up a scale for measuring the boulders since ImageJ needs to know the scale of the boulders. To set a scale, the “straight-line” tool is used to draw a line on one of the boulders to get the diameter. The scale of most of the boulders were taken during the field survey and ground truthing (Figure 3.30) which helped in setting the scale in ImageJ. The “analyse” function is used to determine the size of the boulder and this is used as the scale for analysing all boulders in the image. To analyse the boulder sizes, the “free-hand” tool is selected to accurately draw around and across the boulder and measured using the “analyse” function to determine the size and diameter of boulders. To ensure accuracy in measurement of distance between boulders, the “magnifier” tool was used for a clearer view. Using the “straight-line” tool, a line was drawn between boulders and measured to determine the distance between them using the “analyse” function. To ensure that previously analysed boulders are

not repeated, and to enhance accuracy in results, analysed boulders were highlighted in distinctive colours using the “edit and fill” tool. The procedure was repeated on all orthophotographs of six selected study localities and the results were saved and exported in Excel format. The exported results in Excel will undergo further analysis and final results will be displayed in charts and graphs.

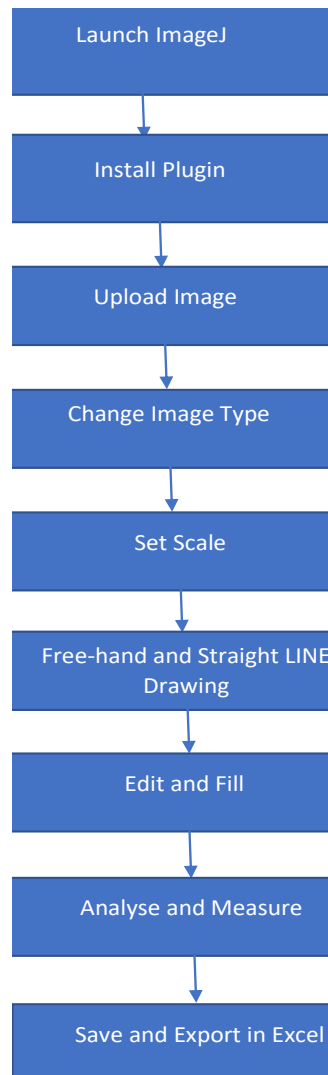


Figure 3.29: ImageJ Boulder Analysis workflow.

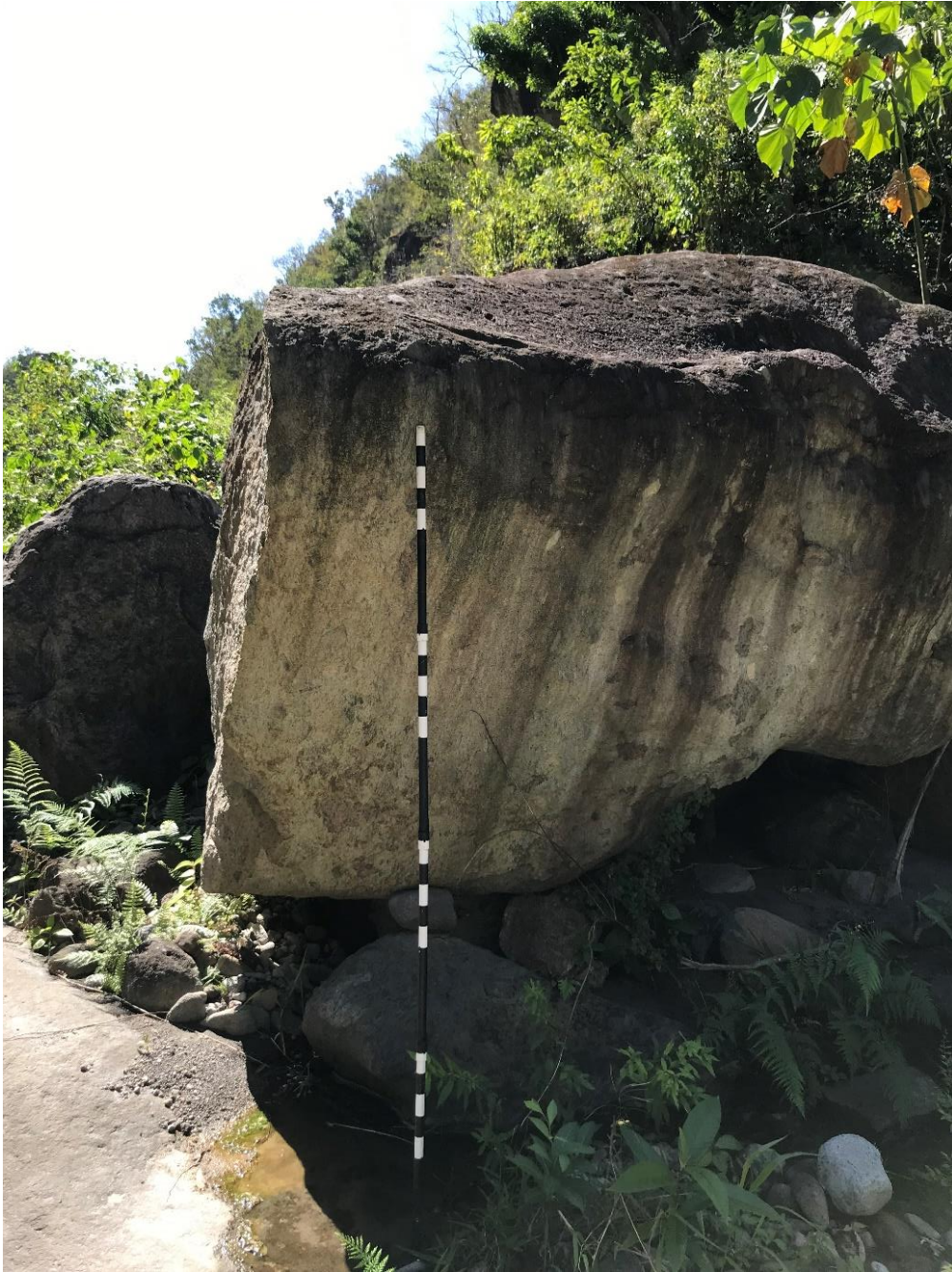


Figure 3.30: 2 m rod used as scale for measuring boulder size, deployed in Dominica.

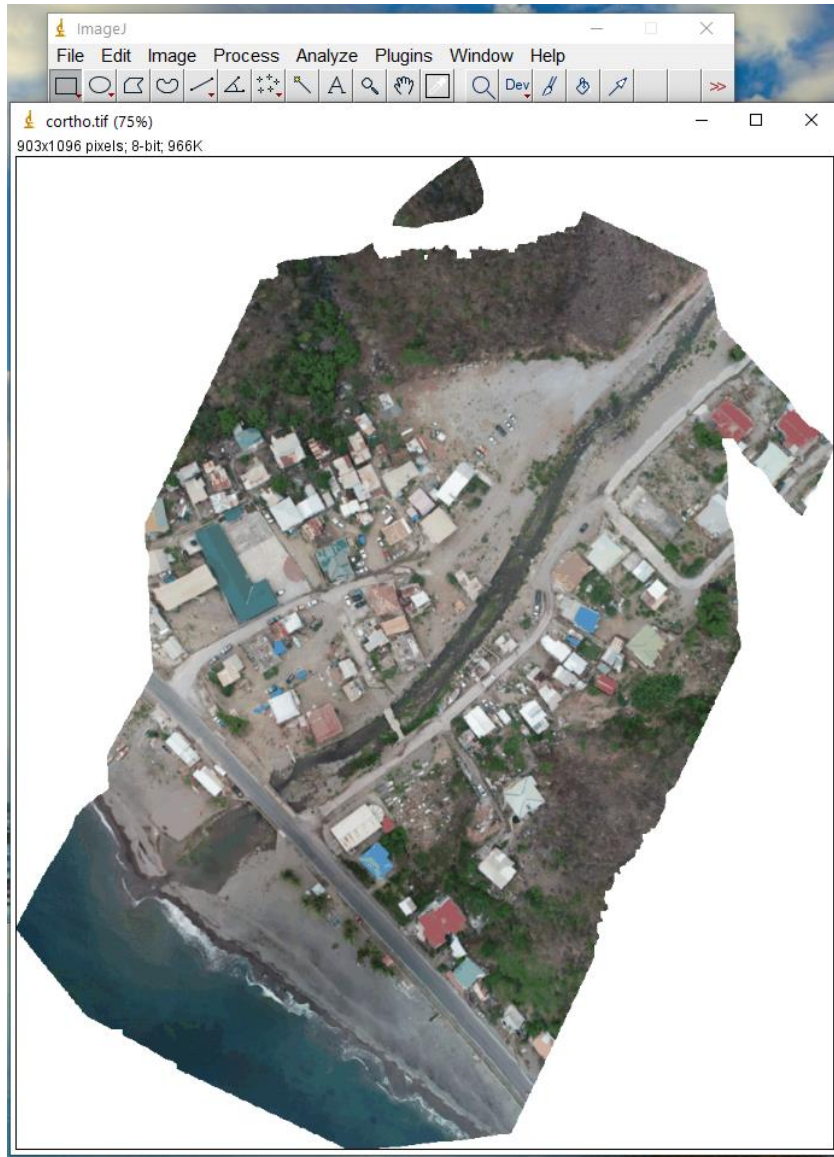


Figure 3.31: Window of ImageJ showing orthophotograph of Coulibistrie study area in Dominica.

3.7 RAMMS DEBRIS FLOW METHODOLOGY

This section gives background information about RAMMS debris module, the governing equations, input data and procedure involved in simulating debris flows and purpose of using the software.

3.7.1 Introduction to RAMMS Software

RAMMS (Rapid Mass Movement System) debris flow module is a licensed application developed by the Swiss Federal Institute (SWL) Institute for Snow and Avalanche Research (SLF) (Christen et al, 2008; Christen et al, 2010; Hussin, 2011). The numerical modelling software was initially developed for mass movement simulation of avalanche runout (Christen et al, 2008; Christen et al, 2010; Hussin, 2011; Bartelt et al, 2013). The software was later modified to include mass moving hazards such as debris flow and rockfall (Cesca and D'Agostino, 2006; Kowalski, 2008; Hussin, 2011; Bartelt et al, 2013). RAMMS was developed using Interactive Data Language (IDL), which is a programming language mostly applied in data analysis (Sovilla et al 2006; Hussin, 2011).

The RAMMS debris flow module is used extensively in both academic and industrial research work for accurate mapping and analysis of debris flow hazards. It has the capacity to identify runout path, and to estimate flow velocity, flow height, impact pressure and runout distance (Christen et al, 2008; Christen et al, 2010; Hussin, 2011; Bartelt et al, 2013) in a three-dimensional terrain. Its visualization functionality enables draping aerial photos over DEMs. The debris flow module is based on the fluid flow model (Voellmy, 1955) which considers a debris flow as a hydraulic-continuum model (Salm, 1993). The model states that dry-Coulomb friction and viscous resistance turbulent friction together make up the flow resistance (Voellmy, 1955; Salm, 1993). Debris flow equations of mass and momentum are solved in the RAMMS debris flow module using the second-order and cell-centered finite flow method (Kowalski, 2008; Christen et al, 2010; Hussin, 2011).

3.7.2 RAMMS Debris Flow Module Equations

The model is setup on three dimensions of the topographic surface coordinates of the DEM in Cartesian coordinate system (x, y, z) (Figure 3.32) (Christen et al, 2010; Bartelt et al, 2013), where x and y show the runout direction and the vertical elevation is $z(x, y)$. The gravitational acceleration vector is expressed as $g = (g_x, g_y, g_z)$ and time is (t) in three-dimensional surface topography (Christen et al, 2010).

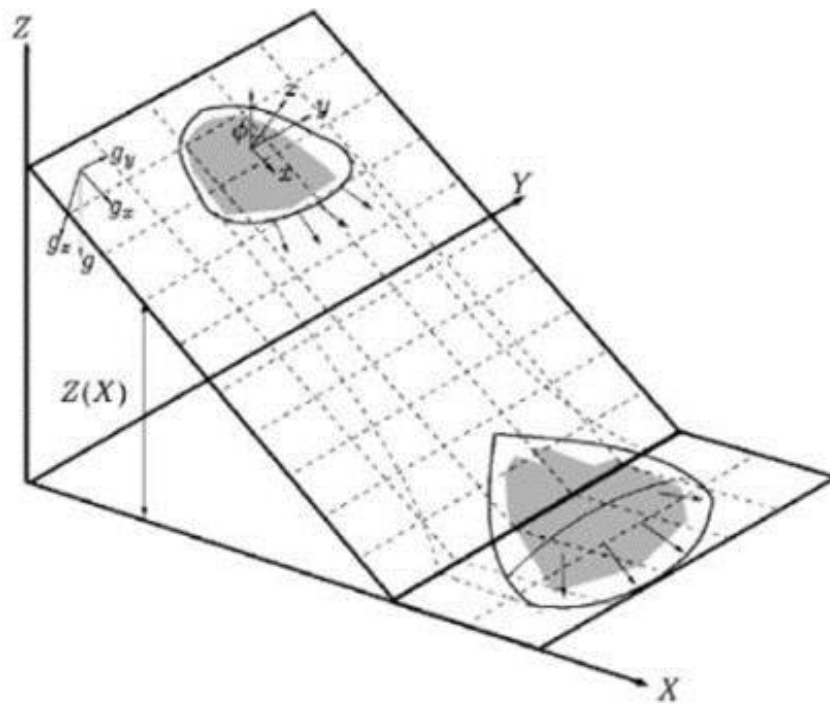


Figure 3.32: Cartesian Coordinate System in RAMMS, Z is topography, x and y are horizontal coordinates (Christen et al, 2010).

Debris flow runout is sporadic and uneven in RAMMS, characterised by flow height $H(x, y, t)$ measured in m and flow velocity $V(x, y, t)$ measured in m/s (Christen et al, 2010). Below are the governing equations of the RAMMS debris flow module (Voellmy, 1955; Salm, 1993; Christen et al, 2010).

$$U(x, y, t) = (U_x(x, y, t), U_y(x, y, t))^T \quad \text{Equation 1: Flow Velocity.}$$

U_x and U_y represent the velocity of the flow in the direction of x and y and the matrix of mean velocity is transposed with T .

$$\|U\| = \sqrt{U_x^2 + U_y^2} \quad \text{Equation 2: Magnitude of Flow Velocity}$$

Equation 2 represents the magnitude of flow velocity, where $(\|\cdot\|)$ is the norm of the velocity U , making $\|U\|$ a positive velocity with a certain size in a vector space and the Cartesian coordinate system.

$$n_U = \frac{1}{\|U\|} (U_x, U_y)^T \quad \text{Equation 3: Direction of Flow Velocity}$$

Equation 3 represents the direction of flow velocity which is expressed as a unit vector n_U

$$\partial_t H + \partial_x (H U_x) + \partial_y (H U_y) = Q(x, y, t) \quad \text{Equation 4: Mass Balance}$$

Equation 4 represents mass balance, where H is flow height (m), $Q(x, y, z)$ (kg/m²s) is the mass flow. When $Q = 0$ there is no entrainment or deposition, when $Q > 0$ there is entrainment and when $Q < 0$ there is deposition (Christen et al, 2010).

$$\partial_t (H U_x) + \partial_x \left(c_x H U_x^2 + g_z k_{a/p} \frac{H^2}{2} \right) + \partial_y (H U_x U_y) = S_{gx} - S_{fx}$$

Equation 5: Depth-average Momentum Balance in x direction

$$\partial_t (H U_y) + \partial_y \left(c_y H U_y^2 + g_z k_{a/p} \frac{H^2}{2} \right) + \partial_x (H U_x U_y) = S_{gy} - S_{fy}$$

Equation 6: Depth-average Momentum Balance in y direction

The depth-average momentum balance in the direction of x and y are expressed in equations 5 and 6 respectively. The values C_x and C_y represent the profile shape aspects, g_z represents gravitational acceleration and K_a/p the earth pressure coefficient which is called Lambda in RAMMS. S_{gx} and S_{gy} represent gravitational acceleration ξ in the direction of x and y, respectively, whilst S_{fx} and S_{fy} represent friction in the direction of x and y, respectively. The basal friction in RAMMS comprises the velocity-independent Dry-Coulomb friction coefficient μ (μ) and the velocity-dependent turbulent friction coefficient ξ (ξ) (m/s^2).

3.7.3 RAMMS Debris Flow Module Input Data and Parameters

Digital Elevation Model (DEM) (Digital Surface Model) (DSM) is the main input parameter required for debris flow simulation in RAMMS debris flow module. For this research work, RAMMS 1.7.20 was used for debris flow hazard simulation and analysis. All DSMs used for this study were acquired by drone survey and processed into DSMs using Agisoft Metashape Professional. RAMMS only accepts DSMs and orthophotographs in GeoTIFF and ESRI ASCII format with projected coordinate system such as Cartesian coordinate system. However, the DSMs were generated in Geographic coordinate system such as WGS 84 in Agisoft Metashape Professional. The DSMs and orthophotographs were projected from World Geodetic System (Geographic Coordinate System) to World Behrmann (Projected Coordinate System). This was done in ArcGIS using the data management tool called Projections and Transformations to project raster DSMs and orthophotographs (Figure 3.33 A and B).

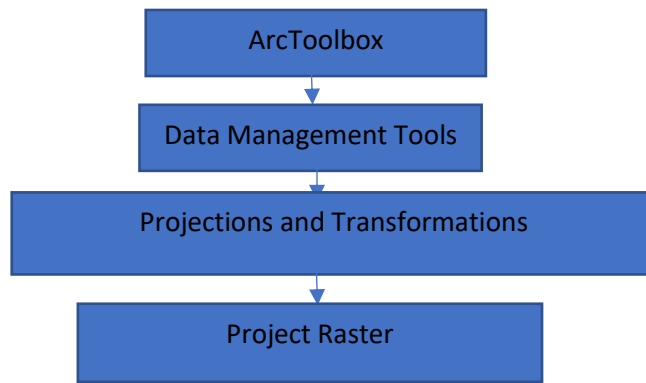


Figure 3.33 A: Raster Coordinate System Projection Workflow in ArcGIS.

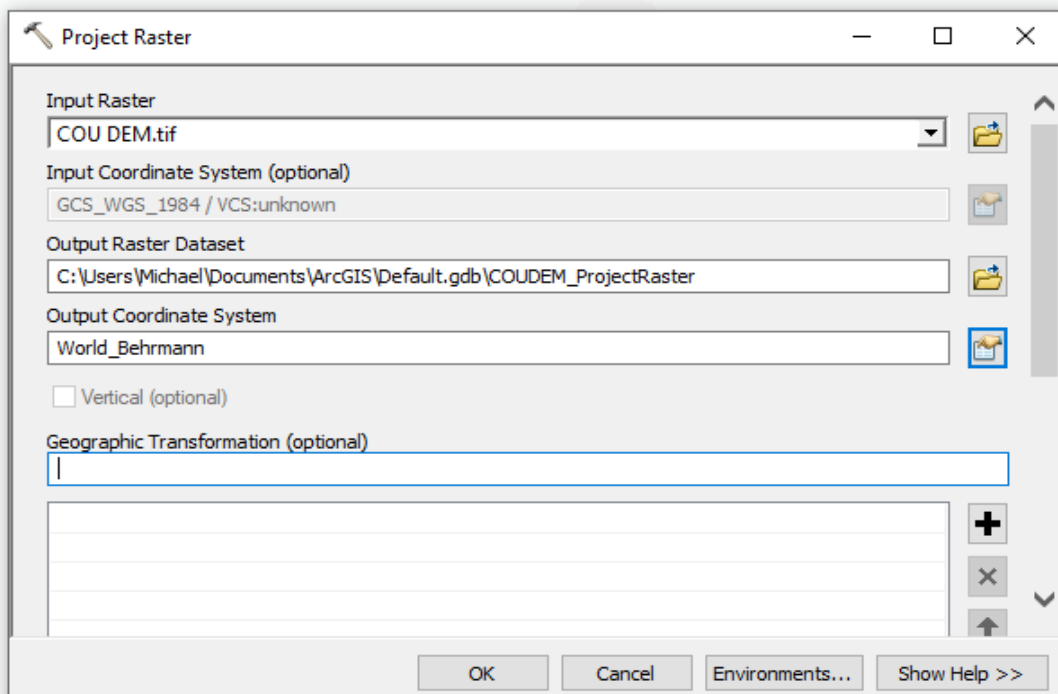


Figure 3.33 B: Raster Coordinate System Projection in ArcGIS.

3.7.4 RAMMS Debris Flow Simulation Workflow

The next stage after projection of raster involves importing DSMs and orthophotographs into RAMMS debris flow module for debris flow simulation and analysis. Before importing input data, the working directory which folders containing DSMs and orthophotographs must be preselected in RAMMS using the Preference tab (Figure 3.34).

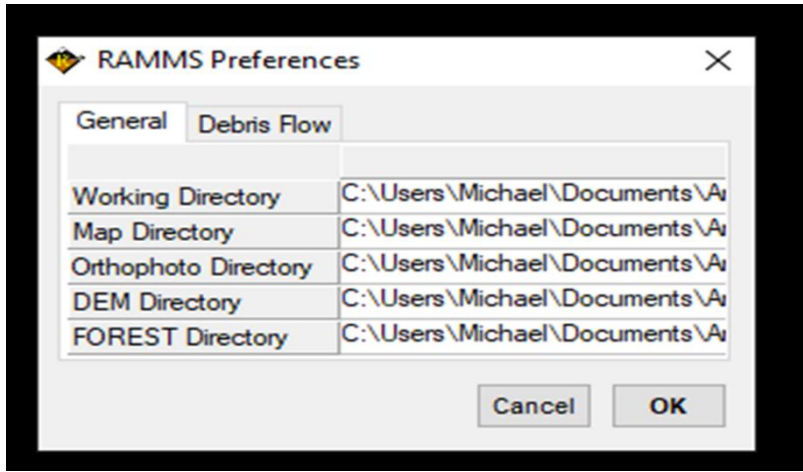


Figure 3.34: Preselection of input data directory in RAMMS.

The DSM was then imported into RAMMS using the Project Wizard tab (Figure 3.35) and the project was named. RAMMS automatically calculates and displays information of the DSM (Figure 3.35).

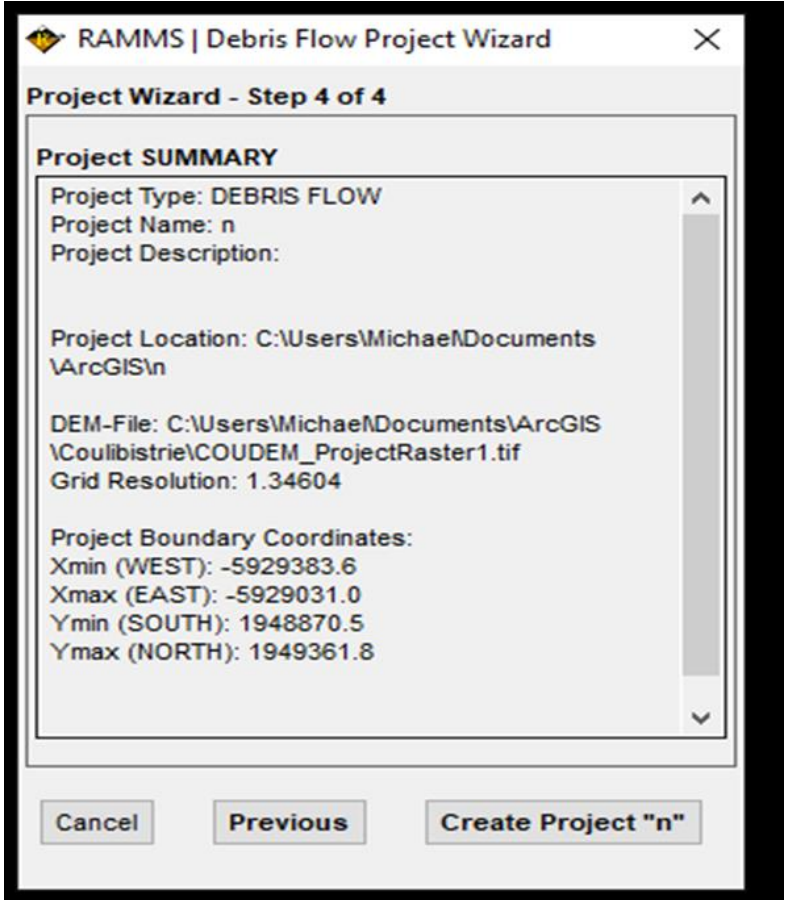


Figure 3.35: Wizard showing information of imported DEM in RAMMS.

Project

The software takes between 1 and 30 minutes to upload a DSM depending on the size of the DSM, the bigger the DSM size the longer it takes to upload and vice versa. After the DSM was uploaded, an orthophotograph was draped over the DSM to enhance visualization and accurate simulation using the add image/map tab (Figure 3.36).

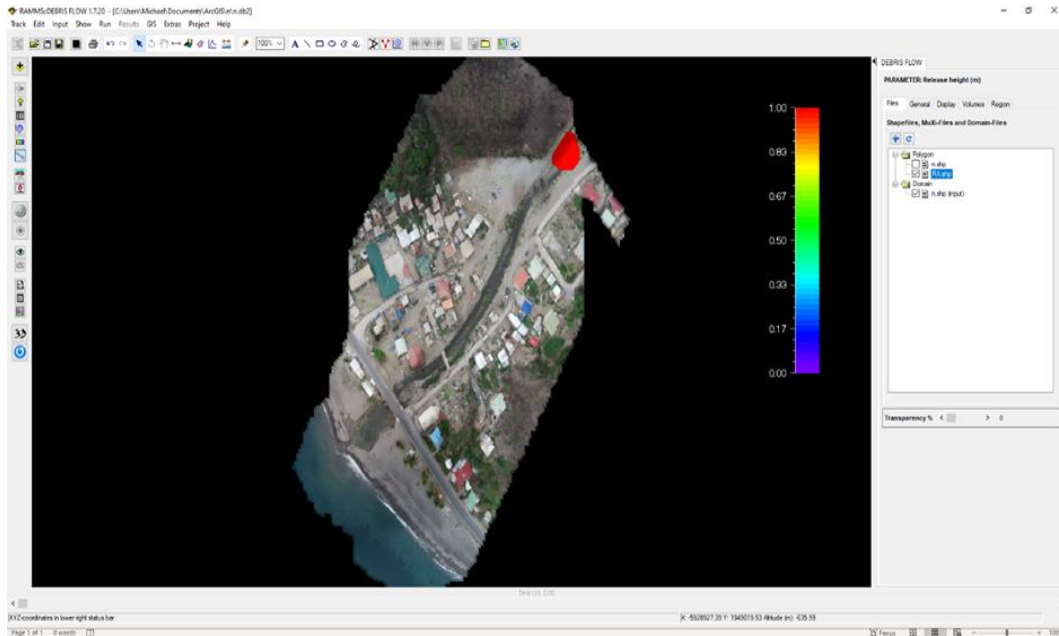


Figure 3.36: Imported DSM and orthophotograph in RAMMS.

After uploading the DSM and orthophotograph, the flow release/initiation area was drawn using the draw release polygon tool. The flow initiation was based on assumption and total surface area of all study areas because the real-life debris flow initiation volume was not known due to lack of original data. The release area polygon was then set as hydrograph since the simulation was for channelized debris flow. The release area height, volume and angle were automatically calculated by RAMMS based on the DSM's topographic surface. By clicking on the Run tab, a drop-down menu is displayed, showing general information of the project, input parameters such as friction, end time, dump steps, earth pressure, DSM resolutions and density (Figure 3.37 A and B). The release area parameters such as volume and depth are also displayed (Figure 3.37C). The end time, impact pressure (λ), friction coefficient and turbulent

coefficient can be defined according to the user's preferences. After entering all input parameters, the Run Simulation button was clicked and simulations take 10 to 30 minutes to finish based on domain and DSM's size and resolution.

RAMMS debris flow module simulation results are the flow initiation area, flow height, flow velocity, impact pressure, flow path, flow time, deposition height and volume. The entire simulation can be exported as image or as an animation video in GIF and other results can be presented in graphs and charts.

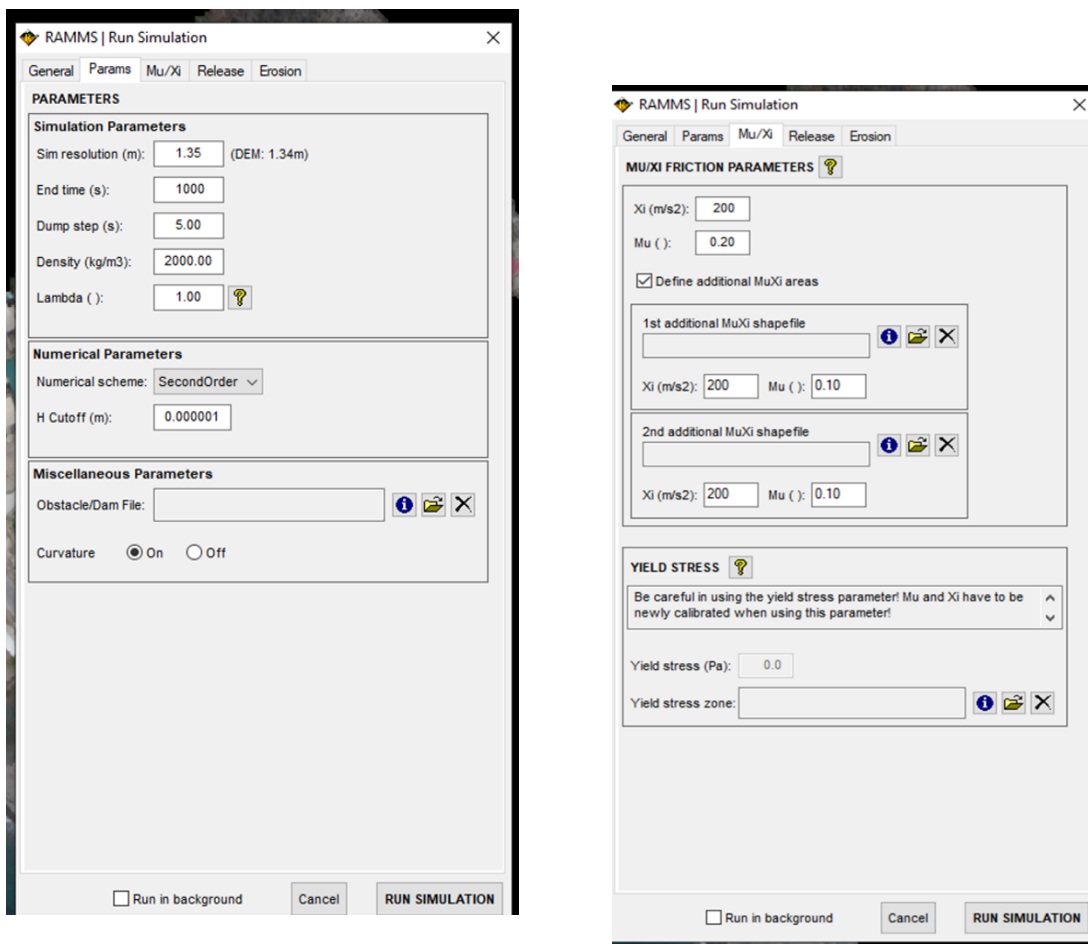


Figure 3.37 A and B: Simulation parameters.

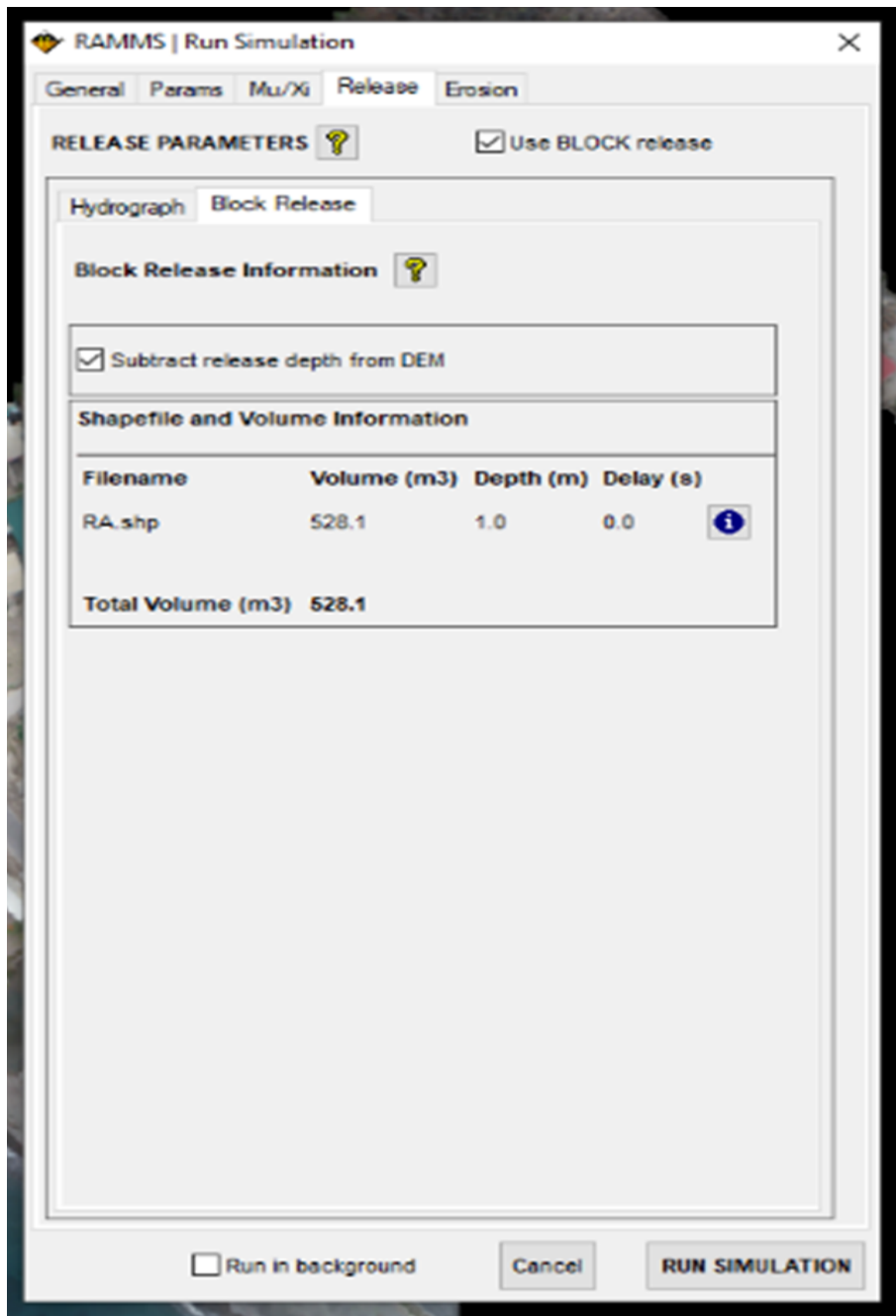


Figure 3.37 C: Simulation parameters

3.7.5 Sensitivity Analysis

Sensitivity analysis is an important technique that helps to determine the impact that changes in input data have on output of the model (Soria et al, 2008). The procedure requires running the simulation multiple times and changing the input parameters whilst others remain constant. Sensitivity analysis provides a wider understanding of how sensitive simulation outputs of RAMMS debris flow model is to variation in input parameters. For this study, sensitivity analysis was conducted for input parameters such as the earth pressure coefficient Lambda (L), friction coefficient (Mv) and turbulent coefficient (Xi).

The three input parameters had their default calibrated value reduced or increased, one at a time whilst the other two remain at their default. This was done to ensure that the sensitivity of the input parameter tested is not affected. Sensitivity analysis was carried out using range of values in table 3.4 and a total of 72 scenarios were simulated for 7 study localities, 1 in Fogo and 6 in Dominica.

Input Parameter	Range of Values
Earth pressure coefficient Lambda	0.25, 0.5 0.75
Friction coefficient	400, 600, 800
Turbulent coefficient	0.05, 0.10, 0.15

Table 3.4: Range of values used for sensitivity analysis in RAMMS debris flow module.

3.8 HEC-RAS Flood Modelling Methodology

This section gives background information about HEC-RAS 2D model, the governing equations, input data and procedure involved in simulating unsteady flows and purpose of using the software.

3.8.1 HEC-RAS Background and Description

Hydrologic Engineering Centre – River Analysis Systems (HEC-RAS) is freely available public domain hydraulic software based on a graphical user interface. It was developed by the US Army Corps of Engineers at their Hydrologic Engineering Centre (US Army Corps, 2019). This numerical modelling software package simulates hydraulic flows through river channels as well as artificial channels (US Army Corps, 2019).

Although predominantly used for channel analysis and flood mapping, HEC-RAS is also used for designing and analysing dams, bridges and culverts (Ray et al, 2011; Lea et al, 2019; US Army Corps, 2019). The software was initially developed for one-dimensional hydraulic simulation only (Yu and Lane, 2006; US Army Corps, 2019) but has since been modified into a two-dimensional hydraulic simulation which considers channel geometry. The latest version of the software is HEC-RAS 5.0.7 (Yu and Lane, 2006; US Army Corps, 2019; Shrestha et al, 2020) which is used in this study.

The 2D HEC-RAS model can simulate both coastal and fluvial floods (Ray et al, 2011; Lea et al, 2019; Shrestha et al, 2020). It uses a computational mesh approach, based on the geometric and hydraulic data of flow channels derived from a DEM (Lea et al, 2019). It also focuses solely on unsteady flow analysis (Lea et al, 2019; Shrestha et al, 2020). The many functionalities of HEC-RAS make it suitable for modelling numerous types of hydrodynamic flows but the model was used for unsteady flow analysis and flood hazard mapping in this research.

3.8.2 HEC-RAS 2D Unsteady Flow Hydrodynamics and Hydraulic Equations

The fundamental principle governing HEC-RAS hydraulic modelling is based on the Diffusion-Wave and Saint Venant momentum equations (Quiroga et al, 2016; Alzahrani, 2017; Maskong et al, 2019). The numerical software computes the water surface elevation at a particular period (Maskong et al, 2019) using either the Diffusion-Wave or Saint Venant momentum equation but Diffusion-Wave was used in this study for simulations. Water movement in the 2D model is both cross-sectional and lateral in x and y directions and velocity in the z direction (Alzahrani, 2017). The 2D unsteady flow model presents the DEM as a topographic surface in a form of mesh which represents the geometry of each cell (Figures 3.38 A and B).

The expression $z(x, y)$ is the elevation of the bottom surface, $h(x, y, t)$ is the depth of water, $H(x, y, t) = z(x, y) + h(x, y, t)$ is the elevation of the water surface and t is time.

The continuity equation for 2D unsteady flow analysis is expressed in Equation 1 (Quiroga et al, 2016; Alzahrani, 2017; Maskong et al, 2019).

$$\frac{\partial H}{\partial t} + \frac{\partial(uh)}{\partial x} + \frac{\partial(vh)}{\partial y} + q = 0$$

Equation 1: Mass Continuity Equation

Where ∂ is the partial derivative, q represents the source of water, h is the depth of water, t is the time and H represents the elevation of water surface. The flow velocity in the direction of x and y are u and v , respectively.

$$-g\nabla H = CfV$$

Equation 2: Pressure Gradient and Base Friction Equation

The symbol g is acceleration due to gravity (m/s^2), ∇ is the vector of partial derivative, H is the surface water elevation (m), V is velocity (m/s) and Cf is basal friction (unitless).

Manning's n value determines the roughness of the continuous surface of the DEM and how it impacts the loss of friction of the flow along an open channel. Manning's roughness coefficient helps to determine the relationship between geometry, slope and friction and flow velocity in a channel (Arcement et al, 1989). The Gauckler-Manning formula was first proposed in 1867 by Gauckler and later modified in 1890 by Manning (Gauckler, 1867; Manning et al, 1890; Arcement et al, 1989). The resistance of flows in open channels and flood plains is depicted in Manning roughness coefficients (Chow, 1959; Arcement et al, 1989).

$$Q = \frac{1.49}{n} * A * R^{\frac{2}{3}} * S^{\frac{1}{2}}$$

Equation 3: Manning's Roughness Coefficient Equation

In Equation 3, the flow rate is Q (cfs), Manning roughness coefficient is n (unitless), A is the flow cross-sectional area (m²), R is the hydraulic radius (m) and S is the slope energy gradient (m/s).

$$\frac{\partial H}{\partial t} - \nabla \cdot \frac{R(H)^{\frac{2}{3}}}{n (\nabla H)^{\frac{1}{2}}} \nabla H + q = 0$$

Equation 4: Diffusion-Wave Momentum Equation

Equation 4 is the main HEC RAS 2D unsteady flow simulation equation used for this study, where ∂ is the partial derivative, H is the water surface elevation (m), ∇ is the vector of partial derivative, t is the time (s), q is the water source, n is the Manning value and R is the hydraulic radius (m).

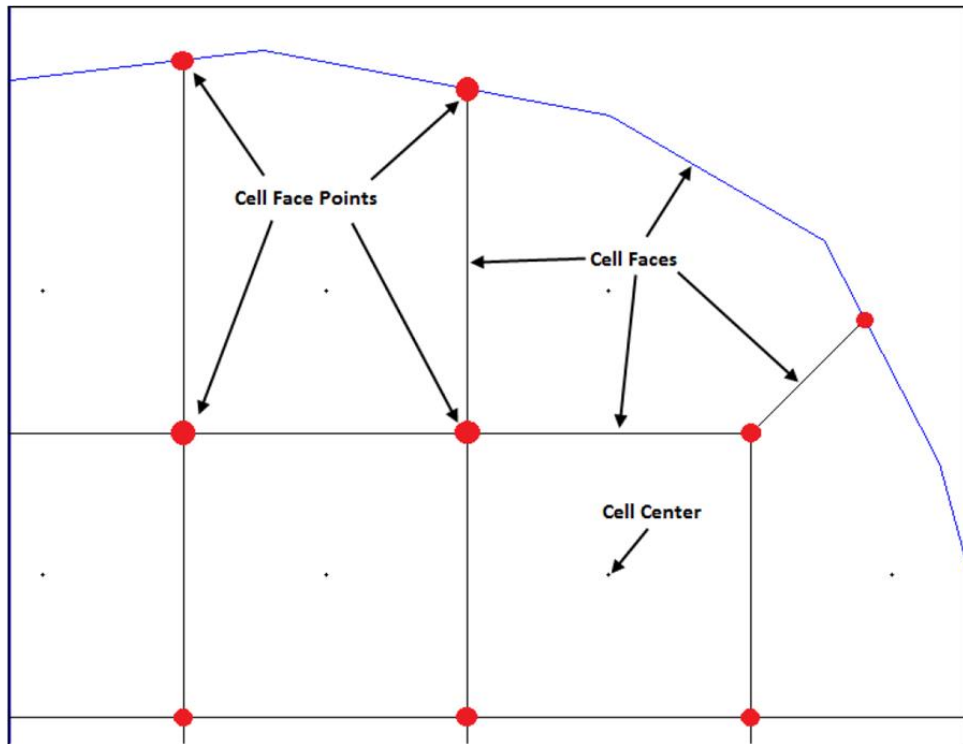


Figure 3.38 A: Diagrammatic presentation of computational mesh in HEC-RAS 2D (US Army Corps, 2019).

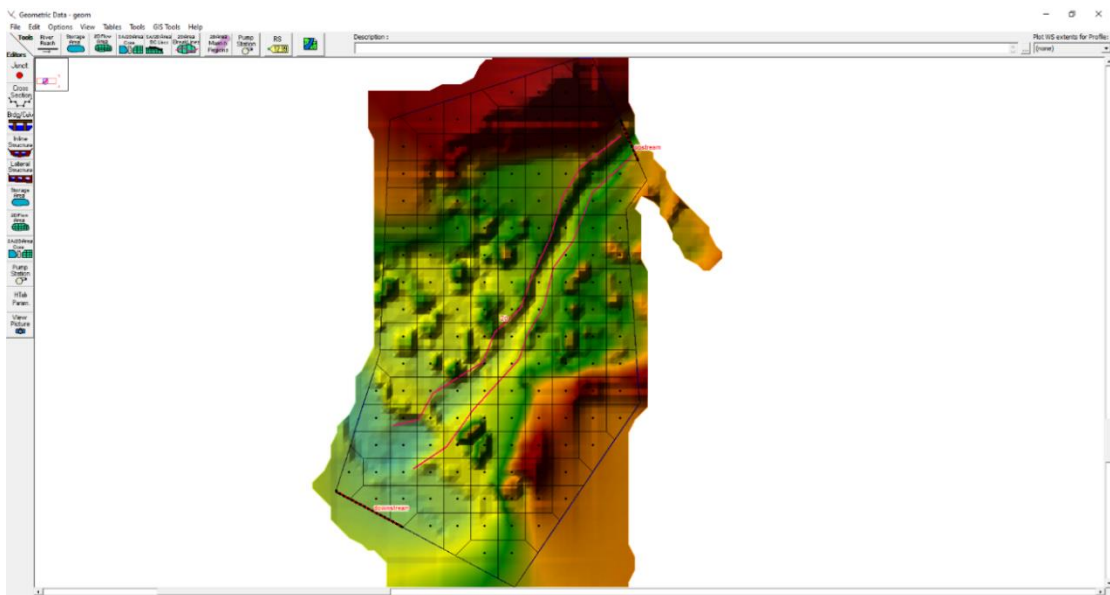


Figure 3.38 B: Computational mesh 2D flow area generated from DSM in HEC-RAS.

3.8.3 HEC-RAS 2D Unsteady Flow Input Data and Input Parameters

The main input data required for HEC-RAS 2D unsteady flow modelling is a DSM of the study area. The accuracy of the model results strongly depends on how detailed and accurate the DSM is (Quiroga et al, 2016; Alzahrani, 2017; Maskong et al, 2019), so having a high resolution and up-to-date DSM is very essential. Although DSMs can be acquired from many sources with different methods, the DSMs used for this study were created in Agisoft Metashape Professional using aerial images acquired from in-field drone surveys. The generated DSMs were projected from GCS_WGS_1984 (Geographic Coordinate System) to WGS_1984_UTM_Zone_20S for Dominica and WGS_1984_UTM_Zone_27S for Fogo (Projected Coordinate System) in the form of grid, which is readable by HEC-RAS. Landcover data is also an important input required by HEC-RAS for unsteady flow analysis. HEC-RAS automatically computes the Manning roughness coefficients from the landcover data, which helps to determine the resistance of flow in open channels and flood plains. The landcover data used for this study was acquired from <http://www.charim-geonode.net> for Dominica and <https://eros.usgs.gov/westafrika/data-downloads> for Cape Verde.

Another important input required for flood analysis is the geometry of the channel which is automatically computed from the DEM in HEC-RAS in a mesh form. Rainfall intensity data, drainage surface area data and runoff coefficient data are needed to calculate the flow discharge rate (Quiroga et al, 2016; Alzahrani, 2017; Maskong et al, 2019). For this study, the rainfall data were acquired from US Hurricane Centre based on the September 2017 Hurricane Maria event. To replicate the real-life floods during Hurricane Maria, the simulation time frame was set for a month since the actual events lasted for a month. Data from Hurricane Maria event used for this research work are not 100% accurate because almost all rain gauges and other data collection equipment were destroyed by the hurricane. Hurricane Maria data published by the US National Hurricane Centre (Pasch et al, 2019) were used for simulation. The drainage

area data were computed from the drone-derived DEMs. The runoff coefficient which ranges from 0 to 1 was determined based on the topography of the terrain. A high runoff coefficient corresponds to areas with low infiltration and low runoff coefficient corresponds to areas with high infiltration. A runoff coefficient was deduced automatically from the landcover data of the study areas.

Flood modelling in HEC-RAS requires certain boundary conditions such as flow hydrograph, normal depth, time of simulation and Manning's roughness coefficient (Hromadka et al, 2010; Quiroga et al, 2016; Alzahrani, 2017; Maskong et al, 2019). The flow hydrograph parameter is the upper-stream of the channel where the flow comes from, whilst the normal depth parameter is the downstream of the channel (Yu and Lane, 2006; Hromadka et al, 2010). Flow hydrograph considers the date, simulation time and flow discharge rate. Normal depth computes slope friction of the flow along the channel (Yu and Lane, 2006; Hromadka et al, 2010). Manning's roughness coefficient is automatically computed from the DEM by HEC-RAS.

3.8.4 Unsteady Flow Simulation Procedure

The HEC-RAS application is started from Windows by double-clicking the icon on the desktop. The main HEC-RAS 5.0.7 window appears without any projects (Figure 3.39). The menu bar contains various function tabs (Figure 3.40) used for unsteady flood simulation and analysis. The "File" tab is used for creating a new project, opening projects, saving projects, deleting projects, importing and exporting data. The "Edit" tab is used for inputting and modifying data such as geometry and unsteady data. The "Run" tab is for calculating hydraulic simulations. The "View" tab allows simulation results to be displayed in both tabular and graphic formats. "Options" enables the user to alter the set-up of the program such as the units system, coordinate systems and parameters. The "GIS Tools" help the user to integrate GIS

functions in HEC-RAS to create model layers. With the “Help” tab, users can go online for further assistance with the software.

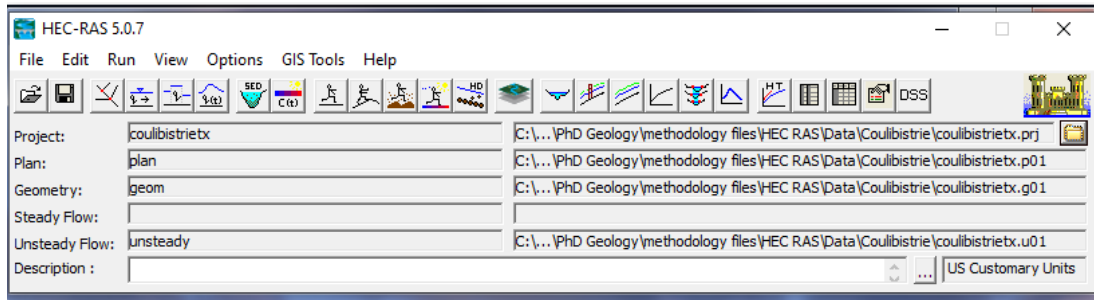


Figure 3.39: Main HEC-RAS 5.0.7 window.

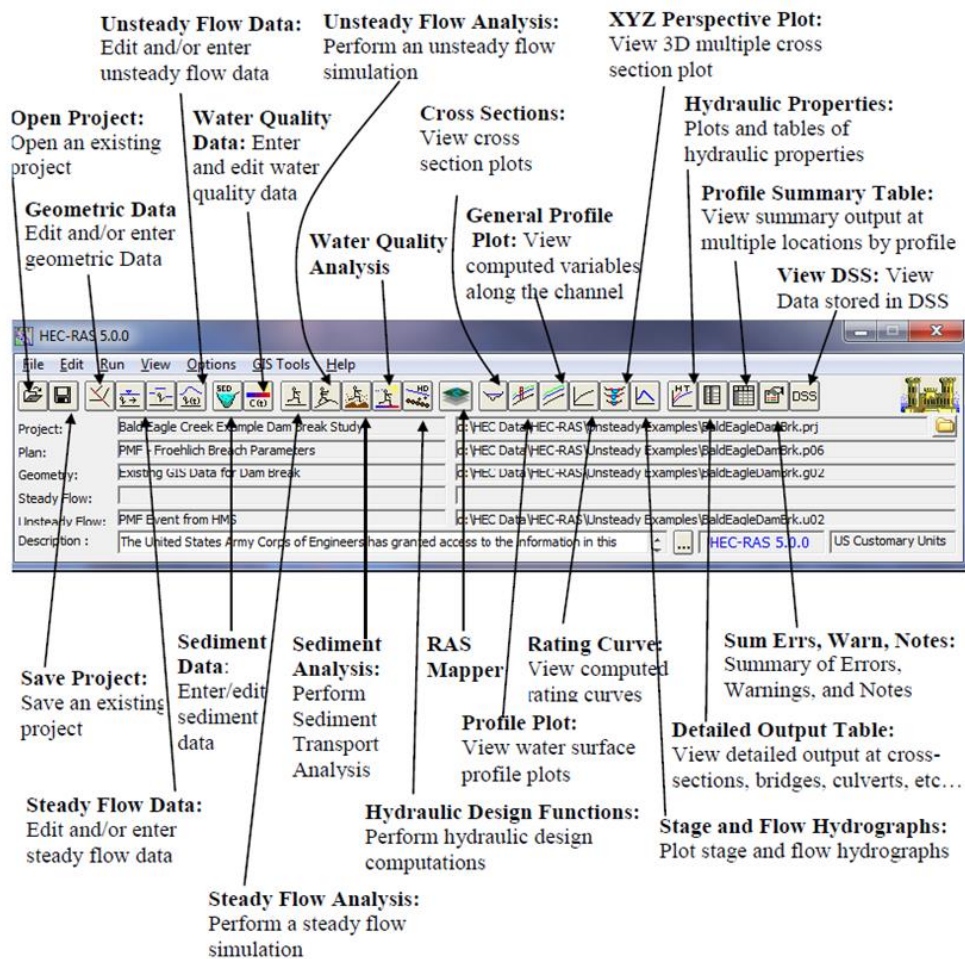


Figure 3.40: HEC-RAS overview and functionalities

Hydraulic 2D model simulation in HEC-RAS 5.0.7 version involves nine stages: (1) creating a project directory folder, (2) creating a new project, (3) uploading DSM data and specifying coordinate system (4) generating flow area and boundary lines, (5) creating the computational mesh, (6) inputting the boundary conditions, (7) entering flow data, (8) undertaking hydraulic calculations and (9) viewing and exporting results. Setting up a project directory folder where all works and data are stored is the first step in the unsteady flow modelling. The next step involves creating and saving a new project (Figure 3.41).

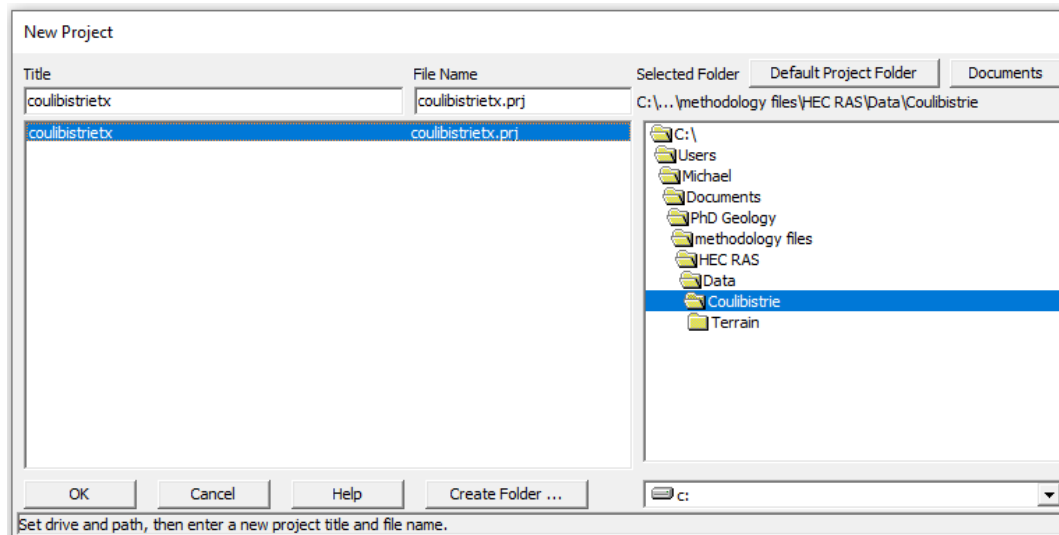


Figure 3.41: New project window for HEC-RAS software.

After creating the project, the DSM data is uploaded to HEC-RAS using the “RAS Mapper” button (Figure 3.42) and navigating to the project directory folder to select and upload the required DSM. All DSMs used for this study were acquired by drone survey and processed into DSMs with Agisoft Metashape Professional. RAS Mapper only accepts DEMs in GeoTIFF format with projected coordinate systems. However, the DSMs were generated in the Geographic Coordinate System (GCS) WGS 84.

The DEMs were then projected from GCS_WGS_1984 to WGS_1984_UTM_Zone_20S for Dominica and WGS_1984_UTM_Zone_27S for Fogo (Projected Coordinate System). This was done in ArcGIS using the data management tool called Projections and Transformations to project raster DSMs (Figure 3.43 A and B). Also, the spatial reference file “prj” (ESRI projection file) which contains information of the coordinate system must be uploaded to RAS Mapper. This was done using by selecting “Set Projection for Project” on the RAS Mapper menu bar. The projection file was then uploaded (Figure 3.44) to obtain the correct position of the terrain data.

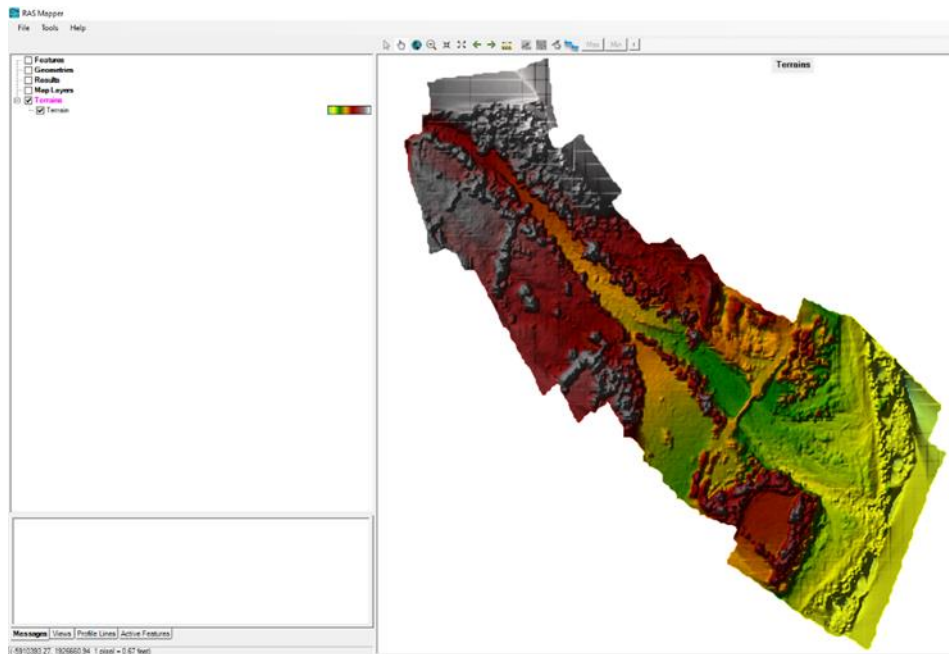


Figure 3.42 RAS Mapper window showing uploaded DSM (Delice River, Dominica).

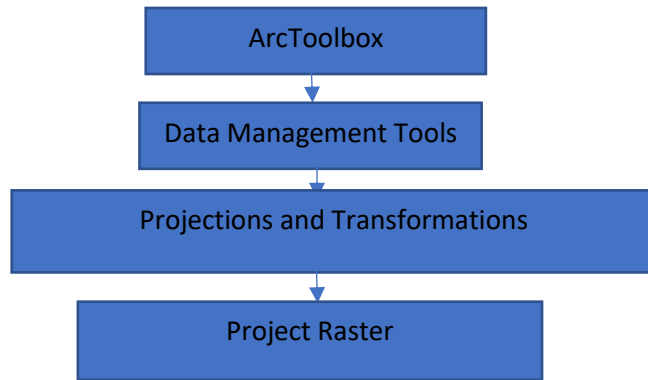


Figure 3.43 A: Raster Coordinate System Projection Workflow in ArcGIS. (Researcher’s image).

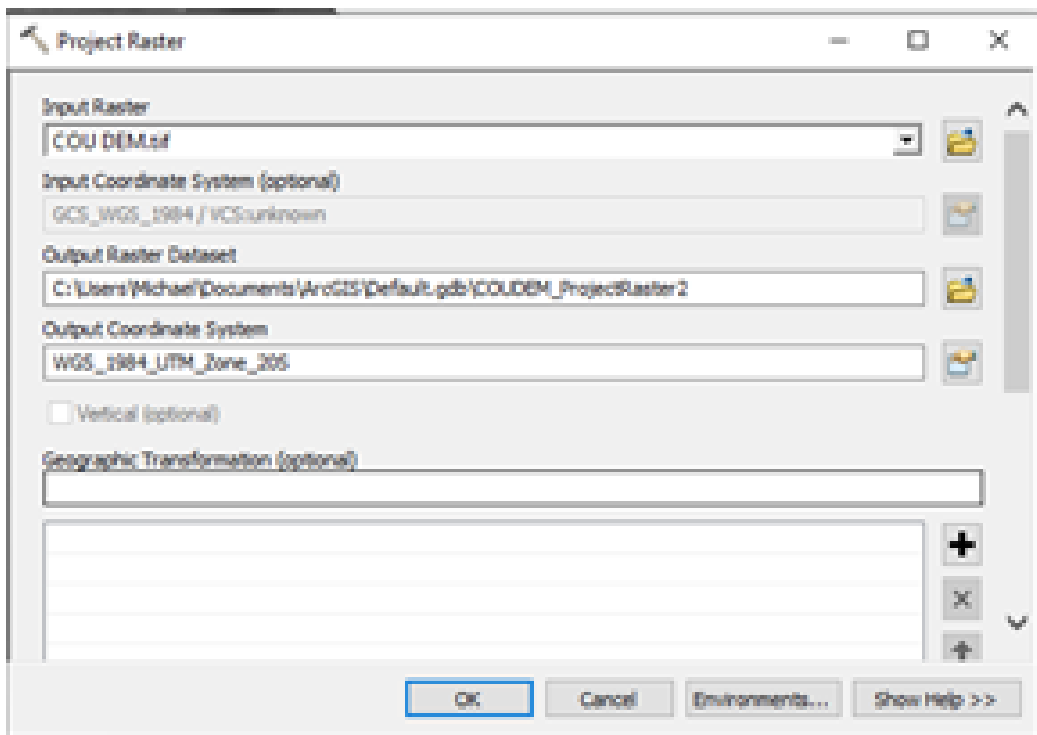


Figure 3.43 B: Raster Coordinate System Projection in ArcGIS.

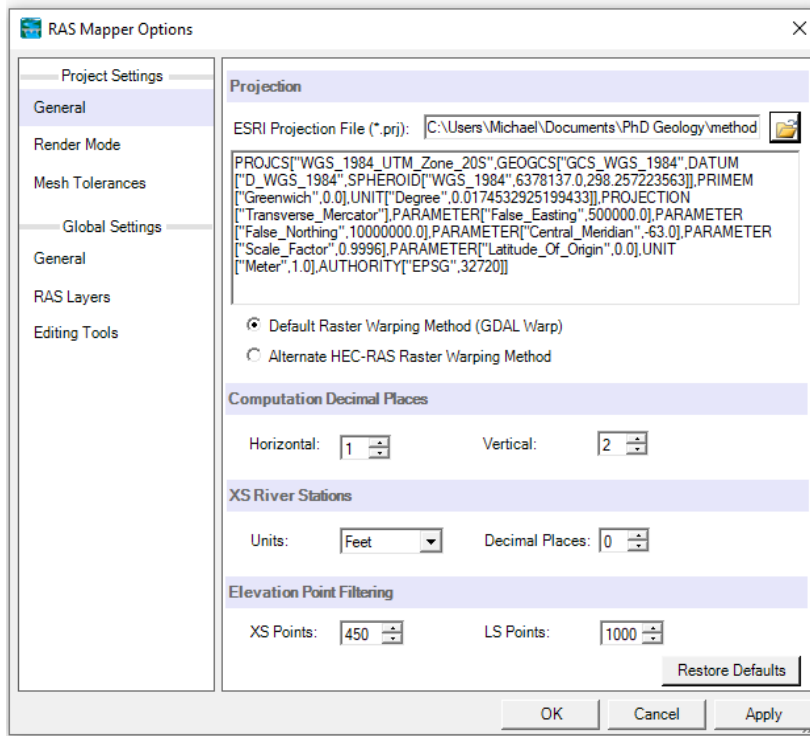


Figure 3.44: RAS Mapper window showing uploaded Spatial Coordinate Projection.

To add the landcover data in the RAS Mapper, the “Add Landcover Layer” was used to open and select the landcover data in RAS Mapper (Figure 3.45A). The landcover cover data was then associated with the terrain data (DSM) and the Manning roughness coefficients for each landuse was automatically computed from the landcover data in the geometry editor (Figure 3.45B).

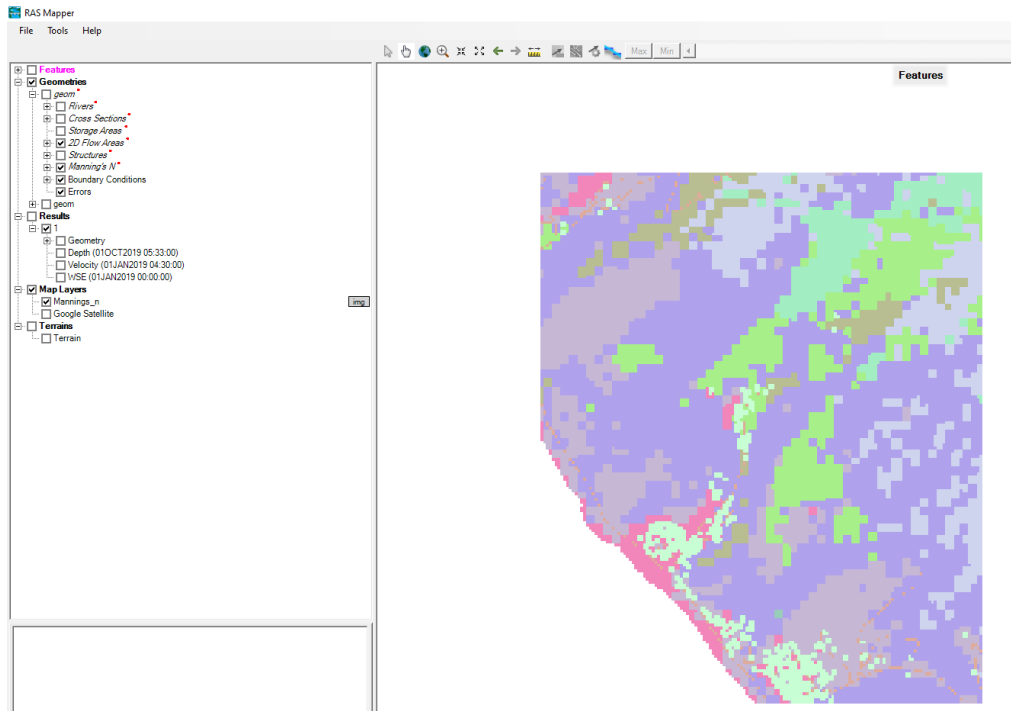


Figure 3.45 A: RAS Mapper window showing uploaded Landcover data layer.

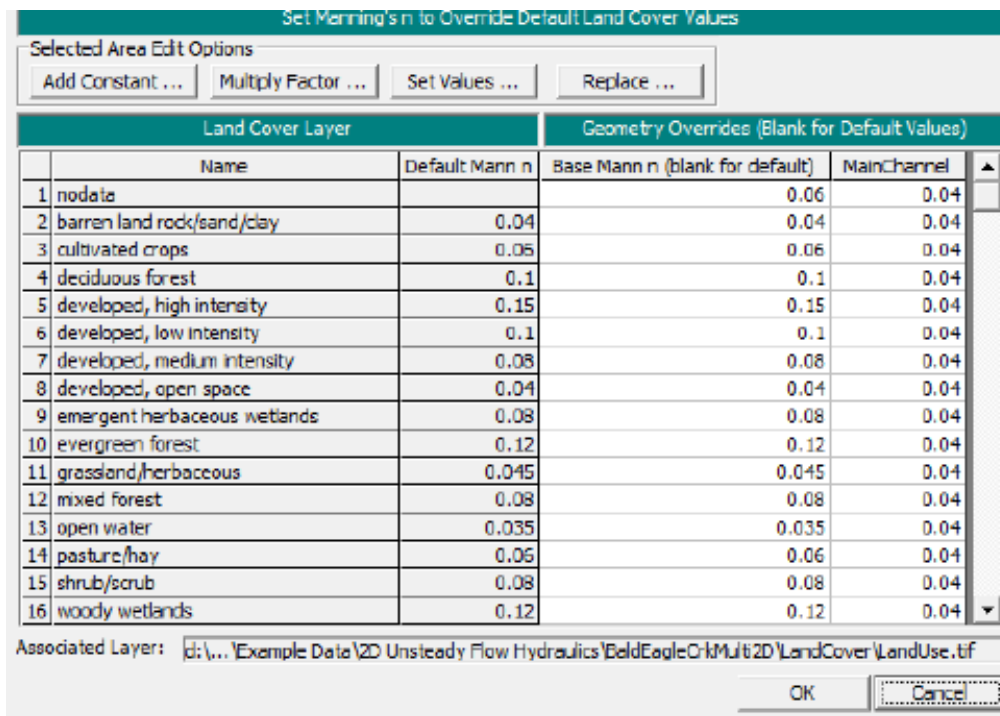


Figure 3.45 B: RAS Mapper window showing Manning roughness coefficients based on landcover data.

To create the 2D flow (Figure 3.33) area and boundary lines, the uploaded DSM was opened in the “Geometric Data” window by selecting the “2D Flow Area” button and drawing an outline around the DSM. The same procedure was used to create the boundary lines along the banks of the channel using the “2D Area Boundary Lines” (Figure 3.46) button.

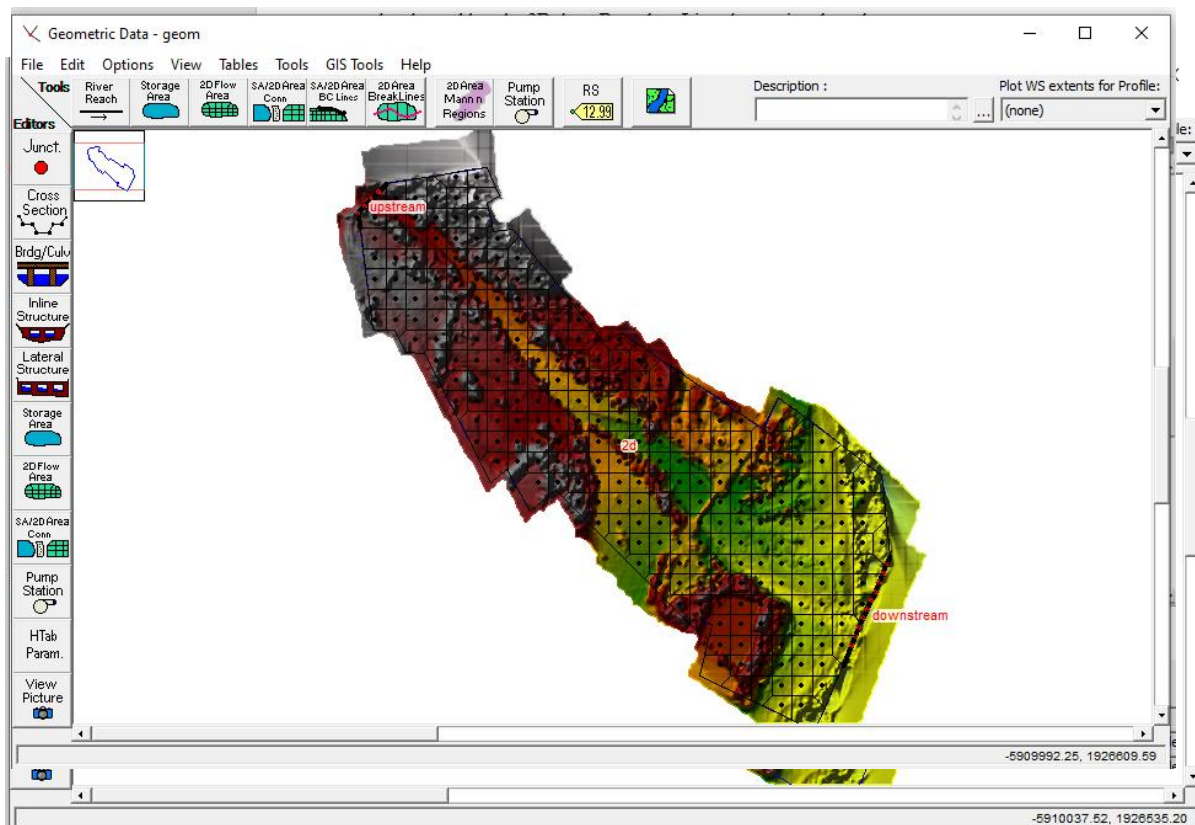


Figure 3.46: Geometry Data window showing 2D flow area and boundary lines using an example from this study (Delice, Dominica).

With the 2D unsteady flow modelling, the geometry data are computed from the topographic surface of the DSM in the form of a computational mesh. To create the computational mesh, the “2D Flow Area Edit” button is selected and all points within the 2D Flow Area are automatically computed from the DSM in HEC-RAS (Figure 3.34). To create the upstream and downstream boundary conditions, the “Storage Area Boundary Line” button is selected and lines for upstream and downstream are drawn and named respectively.

The unsteady flow data for both upstream and downstream boundary conditions are entered by clicking on the “Unsteady Flow data” button. The flow hydrograph data for upstream boundary and the normal depth data for downstream boundary are manually entered (Figures 3.47 A and B).

Flow Hydrograph

SA: 2d BCLine: upstream

Read from DSS before simulation Select DSS file and Path

File:

Path:

Enter Table Data time interval: 1 Day

Select/Enter the Data's Starting Time Reference

Use Simulation Time: Date: 02Jan2018 Time: 00:00

Fixed Start Time: Date: 2Jan2018 Time: 00:00

No. Ordinates

Hydrograph Data			
	Date	Simulation Time	Flow
		(hours)	(cfs)
1	01Jan2018 2400	00:00	0.226
2	02Jan2018 2400	24:00	0.203
3	03Jan2018 2400	48:00	0.295
4	04Jan2018 2400	72:00	0.179
5	05Jan2018 2400	96:00	0.399
6	06Jan2018 2400	120:00	0.295
7	07Jan2018 2400	144:00	0.191
8	08Jan2018 2400	168:00	0.272
9	09Jan2018 2400	192:00	0.208
10	10Jan2018 2400	216:00	0.324
11	11Jan2018 2400	240:00	0.249
12	12Jan2018 2400	264:00	0.255
13	13Jan2018 2400	288:00	0.226
14	14Jan2018 2400	312:00	0.231
15	15Jan2018 2400	336:00	0.26

Time Step Adjustment Options ("Critical" boundary conditions)

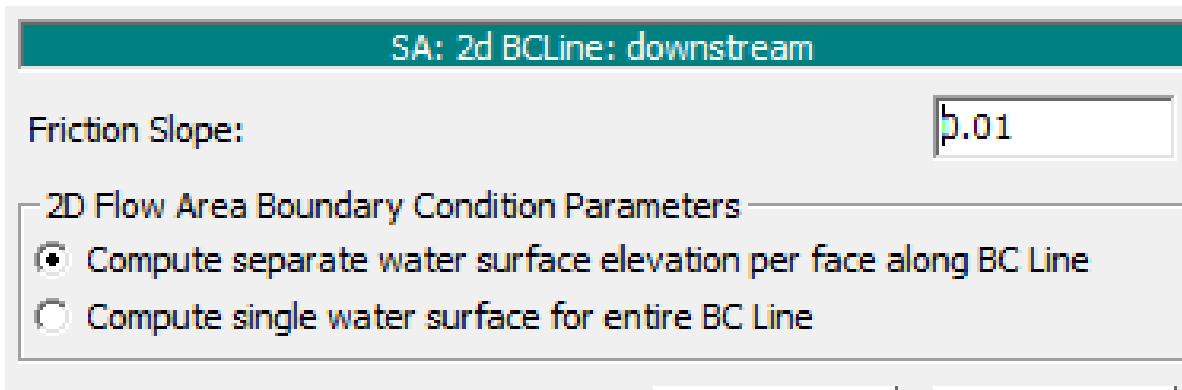
Monitor this hydrograph for adjustments to computational time step

Max Change in Flow (without changing time step):

Min Flow: Multiplier: EG Slope for distributing flow along BC Line: 0.05 TW C

Figure 3.47 A: Unsteady Flow Data upstream window using data from this study

Normal Depth Downstream Boundary



SA: 2d BCLine: downstream

Friction Slope:

2D Flow Area Boundary Condition Parameters

Compute separate water surface elevation per face along BC Line

Compute single water surface for entire BC Line

Figure 3.47 B: Unsteady Flow Data downstream window.

Running the simulation is the final stage of the unsteady flow model. To do this, the “Run” tab was selected and the “Unsteady Flow” analysis option was chosen. All necessary programs such as geometry preprocessor, unsteady flow simulation, post processor and floodplain mapping must be selected before running the model. The simulation time and computation settings can also be manipulated and the “Compute” button runs the simulation. The results of the simulation which show the flow depth, flow velocity, water surface elevation and flood map are viewed in RAS Mapper. Despite the merits of HEC-RAS , the current version is not able to perform sediments and boulders transportaion analysis.

CHAPTER FOUR

Results

4.0 Introduction

This chapter presents results and findings of ALOS PALSAR and SRTM DEMs correction, terrain and drainage network analysis.

4.1 Corrected ALOS PALSAR and SRTM DEM

Most satellite-derived digital elevation models are produced with errors which may be due to the topography of the terrain or illumination angle of the sunlight. Rugged terrains and orientation of sunlight illumination affect the accuracy of digital elevation models. It is therefore necessary to pre-process and correct errors in the DEM to ensure accuracy in analysis. For this reason, the 12.5 m pixel ALOS PALSAR DEM and 30 m pixel SRTM of Dominica was corrected to enhance accuracy with terrain and drainage analysis. The negative backscatter values and null white spots in both DEM were corrected to a more accurate DEM (Figure 4.1).

The erroneous digital elevation models from SRTM and ALOS PALSAR had sea-level values of -30 (Figure 4.2) and -17 (Figure 4.1) respectively. However, after processing the DEMs the sea-level value was corrected to 0, the true value of sea-level (Figure 4.1). Also, each cell within the surface raster DEM had a backscatter elevation value which ranges from 0 to 1426 above sea level (Figure 4.1). The dark-grey areas within the raster DEM indicates areas with lower elevations whilst the light-grey areas of the raster DEM represent areas with higher elevations (Figure 4.1).

Corrected DEM from ALOS PALSAR and SRTM

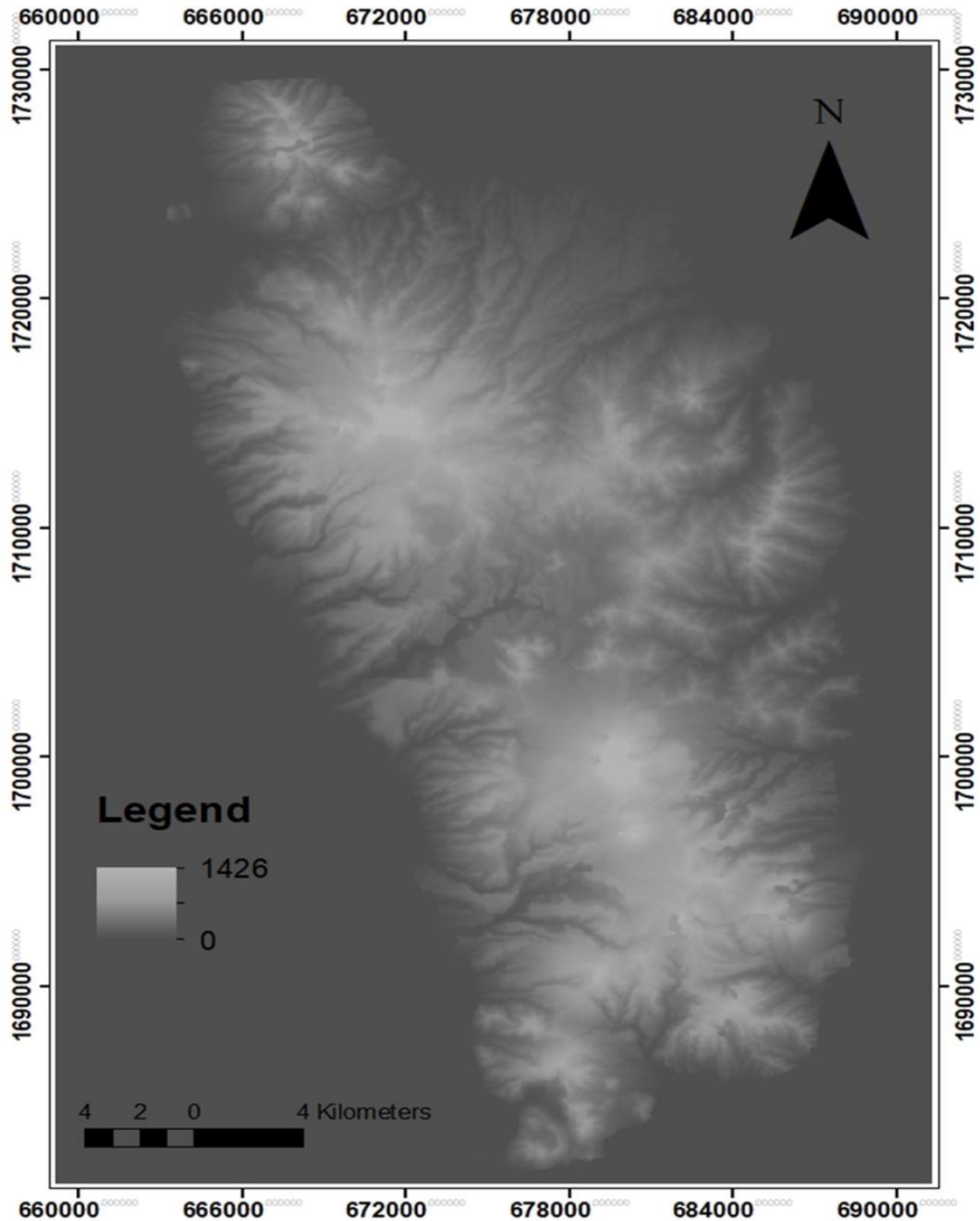


Figure: 4.1: Corrected DEM of Dominica with backscatter values. (Researcher's image created in ArcMap 10.7).

4.2 Terrain Analysis Results

4.2.1 Hillshade Analysis Results

Relief shaded analysis is an important aspect in terrain analysis as it gives a 3D graphical presentation of the terrain surface. The hillshade analysis revealed that the sun illumination was at north-west during the data capture by the satellite radar. The dark-grey areas of the hillshade map (Figure 4.2) have a value of zero and are complete shadows of other relief features that are directly facing the sunlight. The light-grey areas of the hillshade map (Figure 4.2) are relief features that experienced sunlight with illumination values ranging from 1 to 254. The relief analysis exposed the ruggedness of Dominica topography (Figure 4.2). The sharp changes in slopes, evidence of ridges and valleys are clearly visible in the hillshade map (Figure 4.2). The most rugged area of Dominica is the southern part of the island followed by the north-western terrain. The least rugged area is the north-eastern part of the island. In terms of hazard assessment, the hillshade will be used to detect areas with gullies where the risk of surface runoff and mass movement such as debris flows and hyper-concentrated flows are high. Also, the 3D visualisation of the terrain will help to map potential pre-existing landslides by examining the slope morphology at different scales.

4.2.2 Slope Angle Analysis Results

Slope steepness analysis revealed areas that are flat, areas with gentle slope, moderate slopes and steep slopes. The results from the slope analysis showed that the elevation ranges from 0 to 1426 meters above sea level (Figure 4.3). The minimum slope angle was 1° (flat), average slope angle was 42° (moderate slope) and maximum slope angle of 84° (steep slope). Most of the high slopes are found in the south, south-western and north-western parts of the island and most moderate slopes are in the central and north-eastern part of the island (Figure 4.3). Information about elevation is very important because altitude affects the precipitation and temperature of a terrain, higher altitude will experience high amounts of rainfall with low

temperatures (Burisdon et al, 2011; Qing et al, 2011). Also, areas with steep and unstable slopes are susceptible to landslide and debris flow hazards (Dragicevic et al, 2015; Dutta et al, 2015; Chen et al, 2016). Approximately 68% of the slopes in Dominica are very steep, hence making the island vulnerable to landslide hazards. Slope angle is an important input parameter in most geohazard analysis (Lamelas et al, 2009; Cheng et al, 2013; Chen et al, 2016). Knowledge of the steepness of slopes is key in landslide hazard assessment. Slopes with an angle of 30° or more are likely to be unstable, hence the risk of landslide occurrence is high (Lamelas et al, 2009; Cheng et al, 2013; Chen et al, 2016).

4.2.3 Slope Aspect Analysis Results

To determine orientation of the slopes, the aspect map (Figure 4.4) was extracted from the surface raster DEM (Figure 4.1). All the flat areas of Dominica have an aspect value of -1, slopes facing northward have aspect value of 0-22.5 and 337.5-360. Slopes facing north-east, east and south-east direction have aspect values of 22.5-67.5, 67.5-112.5 and 112.5-157.5 respectively. The south and south-west slopes have aspect values of 157.5-202.5 and 202.5-247.5. Aspect values of 247.5- 292.5 and 292.5-337.5 are slopes facing west and north-west respectively. Most of the slopes had downslope movement towards the northwards hence, these slopes receive less sunshine and have cool temperature with greener vegetation (Guan et al, 2013). This was evident during the ground truthing fieldwork in February 2019. In geological hazard mapping, understanding the direction of downslope movement helps to know which areas are susceptible to mass movement such as debris flows and mudflows.

4.2.4 Contour Analysis Results

The contour map (Figure 4.5) was overlaid on the relief shaded map (Figure 4.1) to determine areas with equal elevation above sea. The contour interval used for the analysis to distinguish the distance between contours was 50 m. The contour lines are spaced further apart from each other in the central and north-western parts of the island. This indicates that there were little changes in elevation in these areas. On the other hand, contours lines in the north, north-west and south of the island are very close to each other. This indicates that these areas experience a sharp change in elevation. Comparing the slope map (Figure 4.3), hillshade map (Figure 4.2) and contour map (Figure 4.5), it is clearly visible that all steep slopes are found where there is rapid change in elevation and vice versa. In terms of hazard assessment, spacing of the contours helps to identify toe-slopes where landslide deposits had spread out to form a gentle slope (Crawford, 2011)

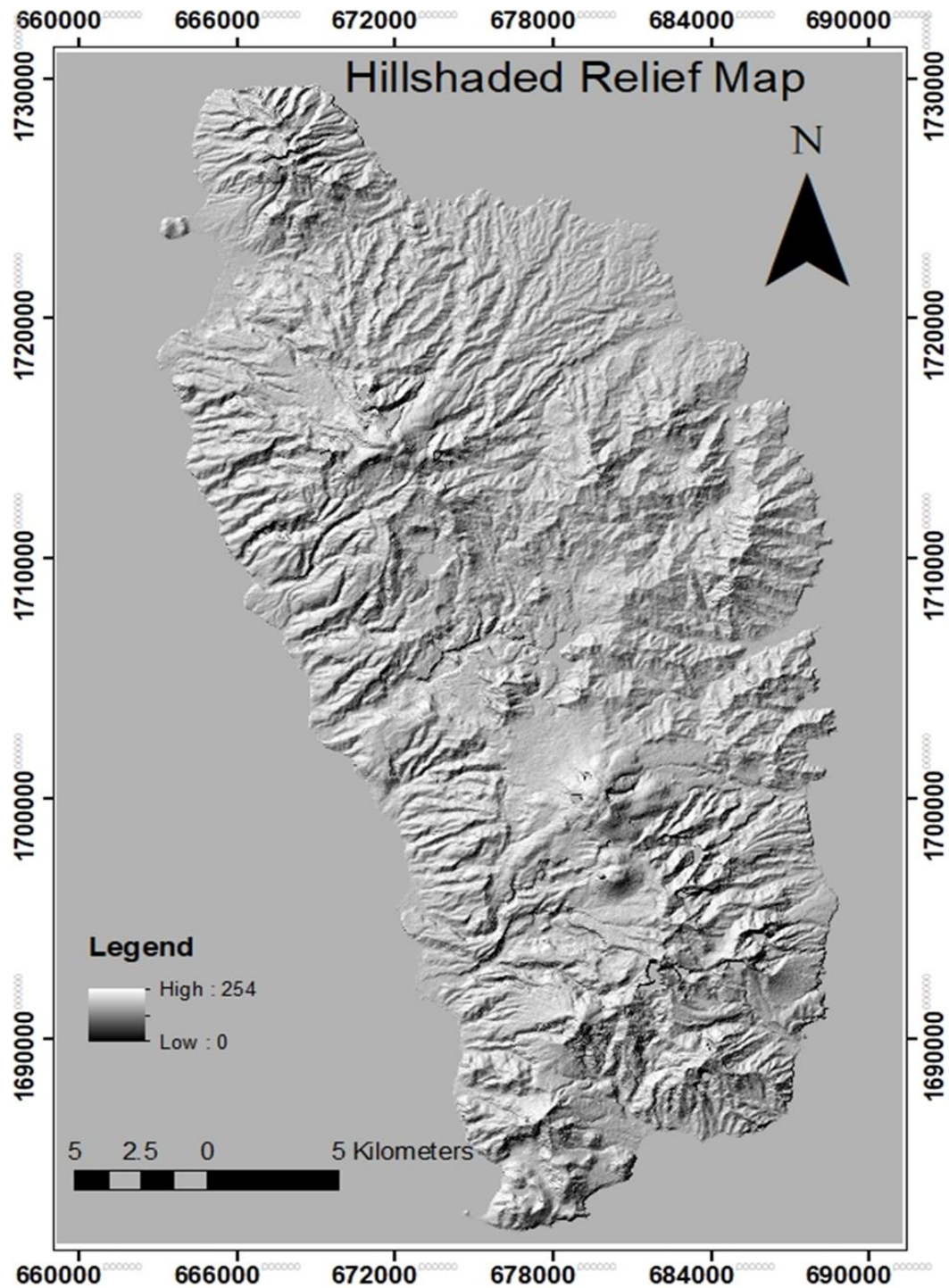


Figure: 4.2: Hill shaded relief map exposing the rugged topography of Dominica.

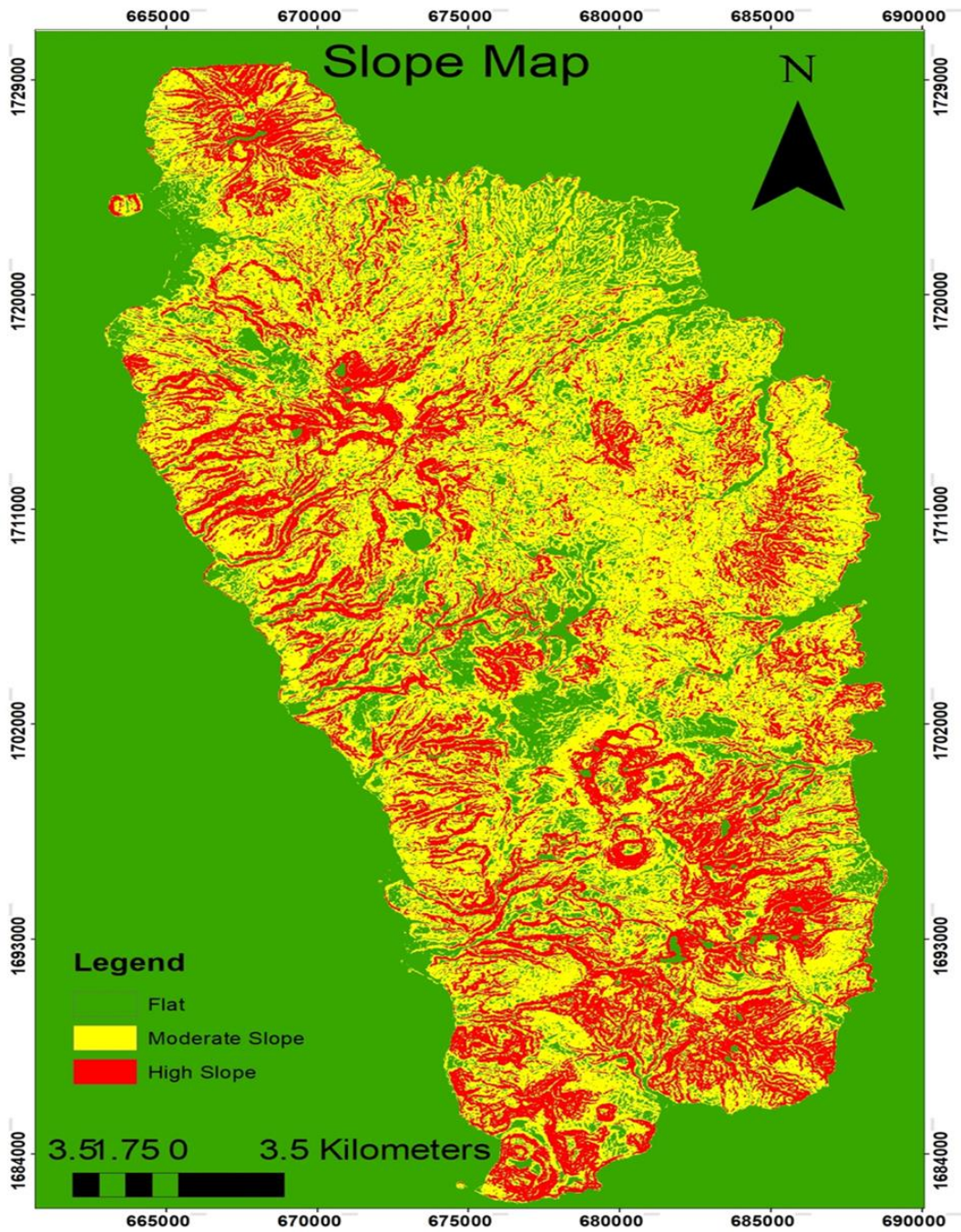


Figure: 4.3: Slope Angle (Steepness) map showing flat areas (0° - 30°), moderate slope areas (31° - 45°) and high slope areas (46° - 75°).

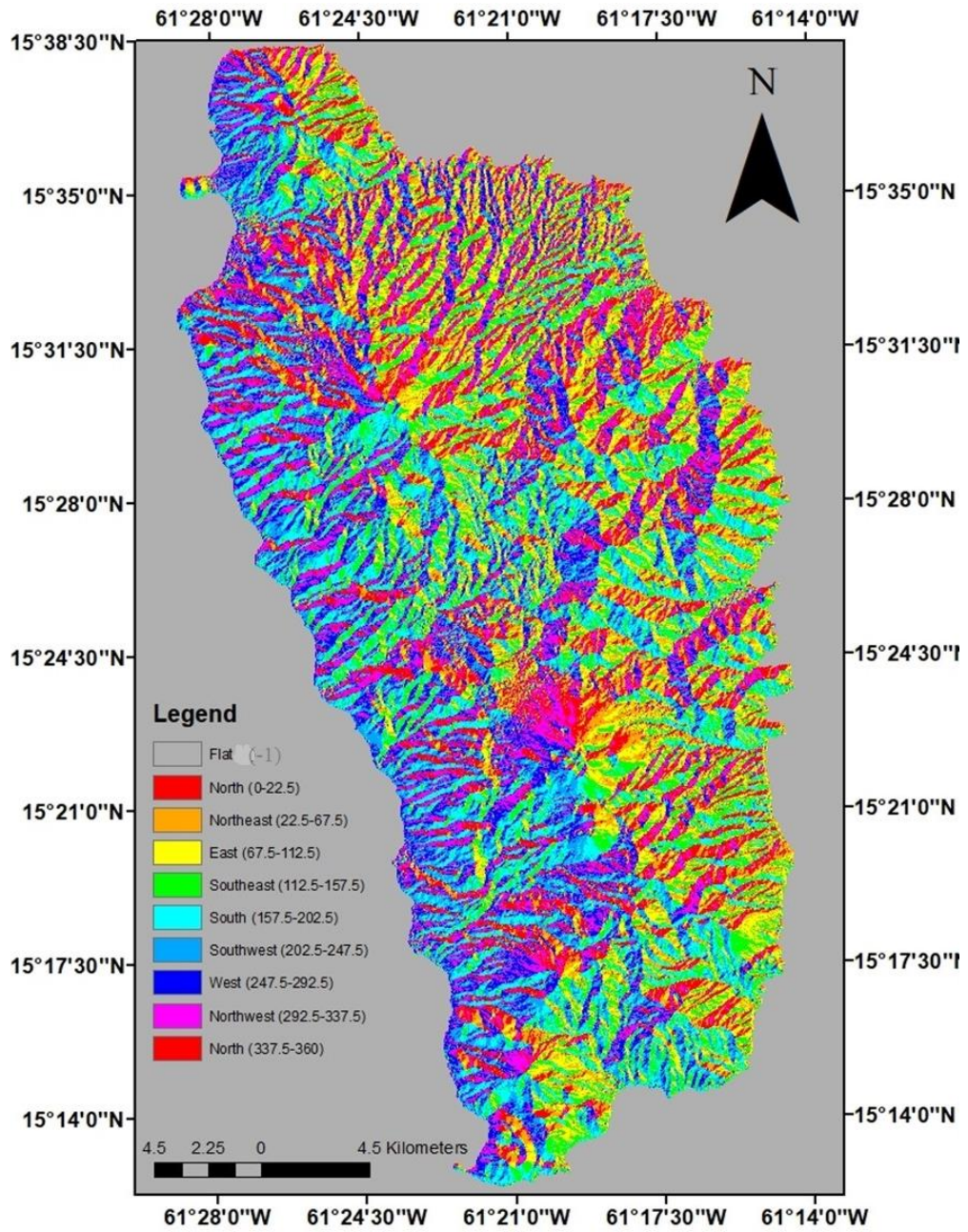


Figure: 4.4: Slope Aspect (Orientation) map showing direction of downslope movement.

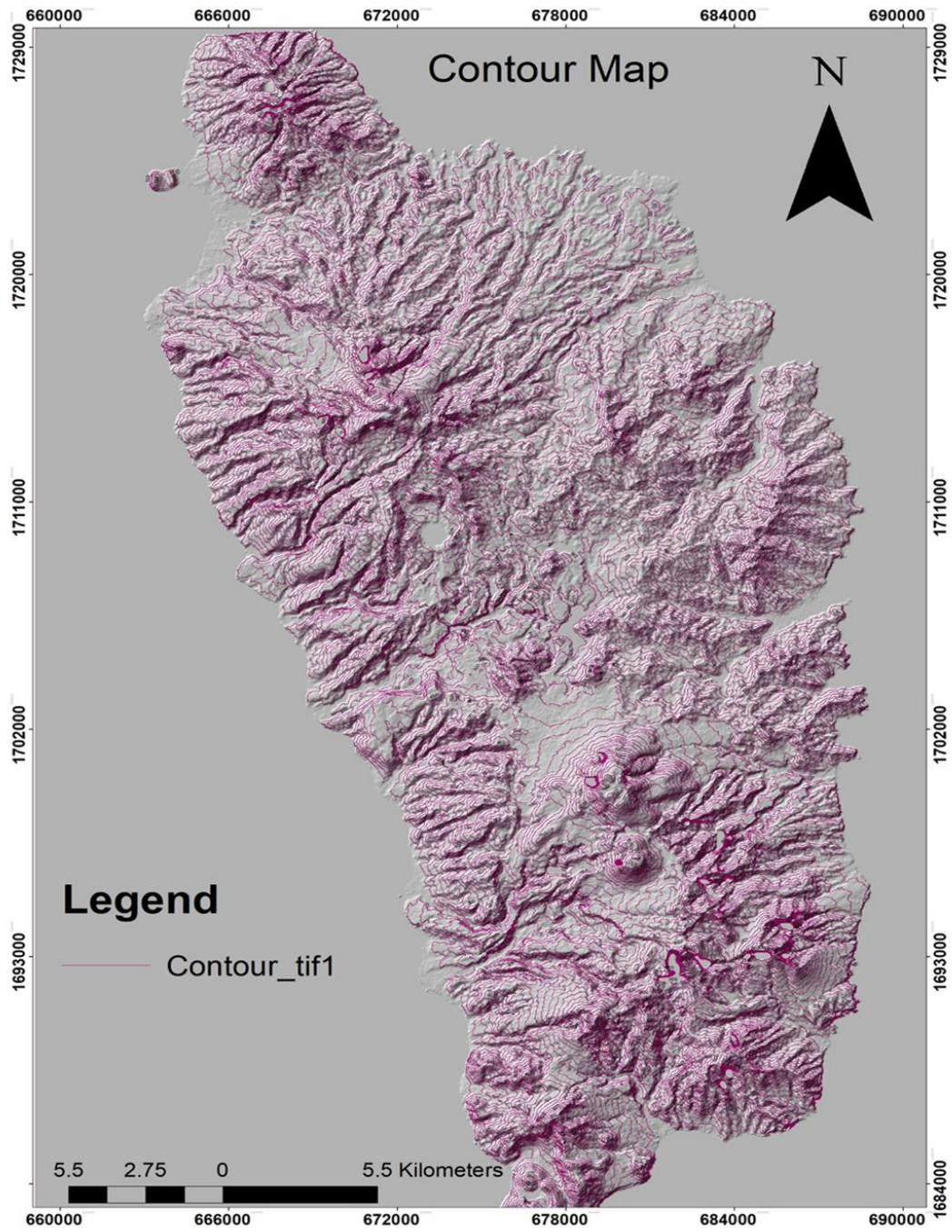


Figure: 4.5: Contours overlaid on hillshade map showing changes in elevation.

4.3 Drainage Network Analysis Result

The first step in analysing drainage network of a terrain is knowing the direction in which the surface water flows. For this reason, flow direction map (Figure 4.6) was extracted from the surface raster DEM (Figure 4.1) spatial analyst tools in ArcMap.

4.3.1 Flow Direction Analysis Result

The flow direction output was presented in eight-direction flow and the direction of flows are presented in numbers (Figure 4.6). The number 1 indicates surface water is flowing east, 2 indicates surface water flowing south-east, 4 indicates surface water flowing south and 8 indicates surface water flowing south-west. Similarly, 16 indicates surface water flowing west, 32 represents surface water flowing north-west, 64 shows surface water flowing north and 128 indicates surface water flowing north-east. There was no dominant direction of surface water flow but most streams west were flowing in south-west direction and most streams in the east showed a south-east flow (Figure 4.6). In hazard mapping, flow direction helps to identify areas that are at high risk of flooding and debris flows by showing the direction in which the flow will go.

4.3.2 Flow Direction Analysis Result

Flow accumulation map (Figure 4.7) showed about 10 accumulated streams in Dominica. These are the big streams that the small streams flow into and there are four accumulated streams in northeast, two in south-east, two in the west and two in northwest. There were breaks in the flow path when there is change in slope even though the DEM was corrected. The drainage network map (Figure 4.8) was generated from the flow direction (Figure 4.6) and flow accumulation (Figure 4.7). In hazard analysis, flow accumulation helps to identify areas where various flows such as floods and debris flow will occur and areas where the risk would be extremely high.

4.3.1 Flow Direction Analysis Result

In flood hazard analysis, drainage network is a major input parameter that is needed to model and predict areas at high risk of flooding. To understand the drainage pattern of Dominica, it was important to analyse the drainage network. The drainage network map (Figure 4.8) clearly shows a dendritic drainage pattern across the whole island. This is characteristic of a terrain with different rock composition but uniform resistance where tributaries join the major streams from all angles forming a tree-like shape (dendritic). This indicates that rocks are impervious, hence influencing the direction of flow. The geology of Dominica is dominated by impervious volcanic rock types such as dacite and andesite which greatly influence the flow of surface water.

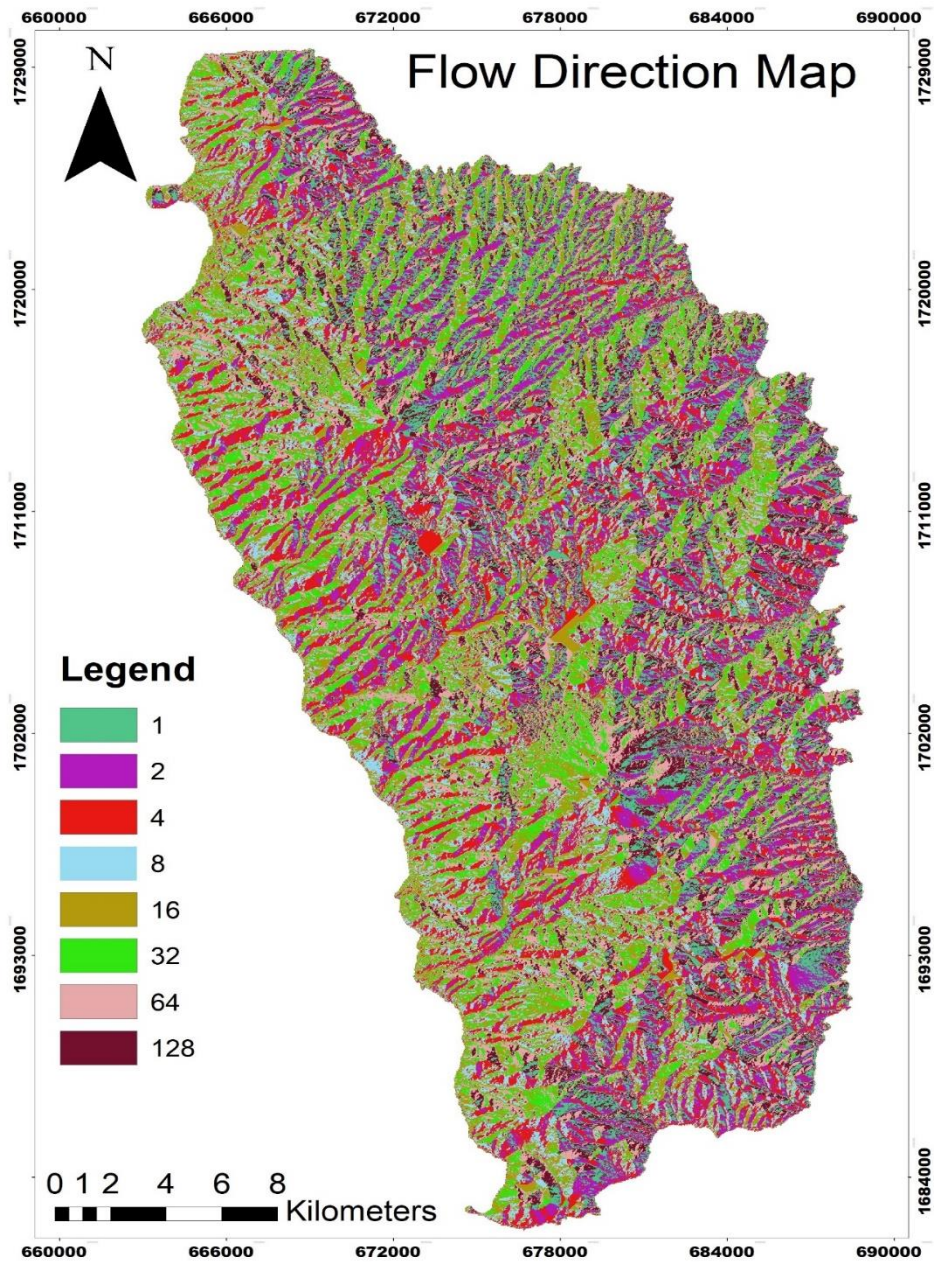


Figure: 4.6: Flow direction map showing surface water flow direction where 1 is east, 2 is south-east, 4 is south, 8 is south-west, 16 is west, 32 is north-west, 64 is north and 128 is north-east.

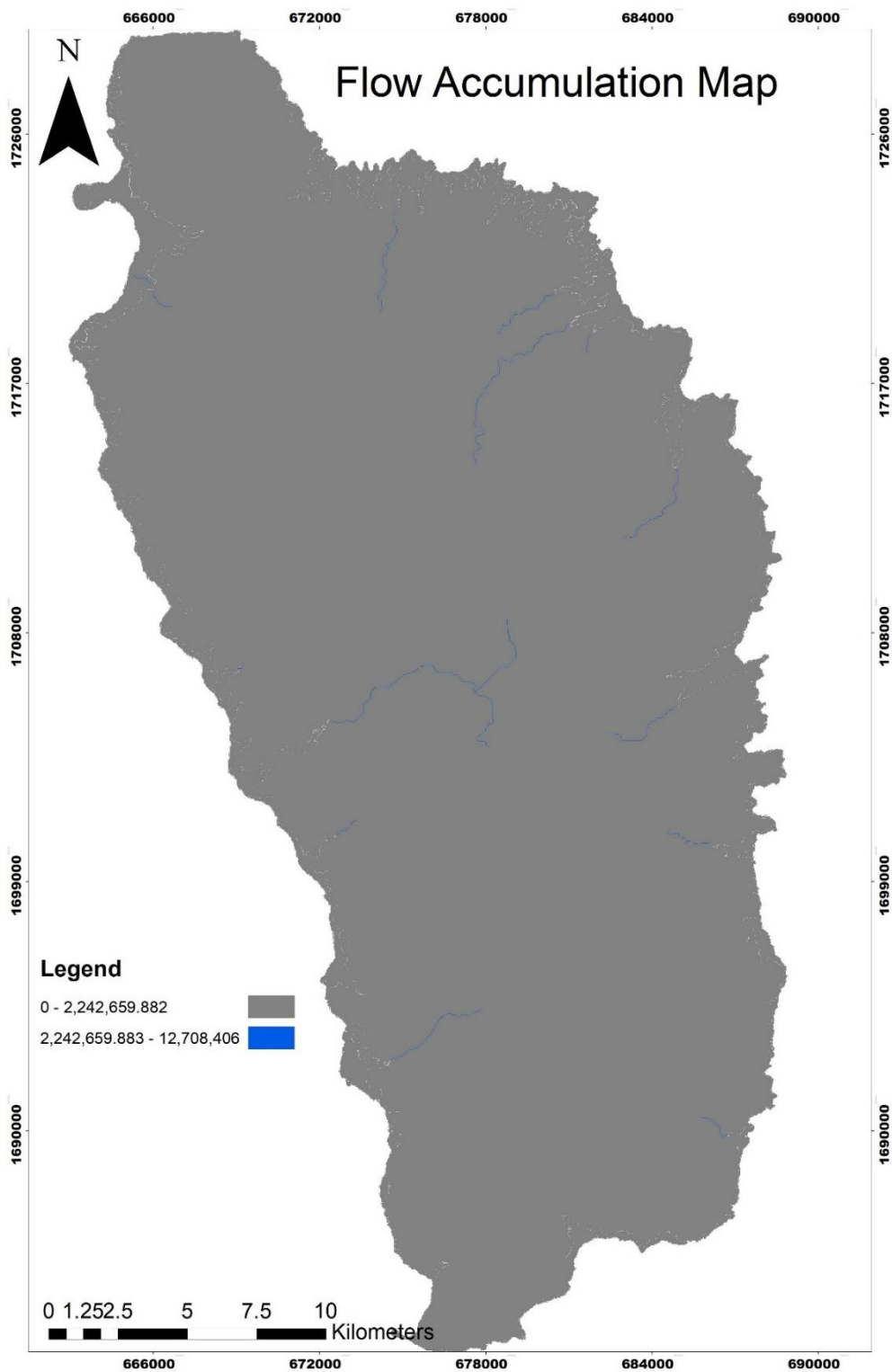


Figure: 4.7: Flow Accumulation map showing ten accumulated streams.

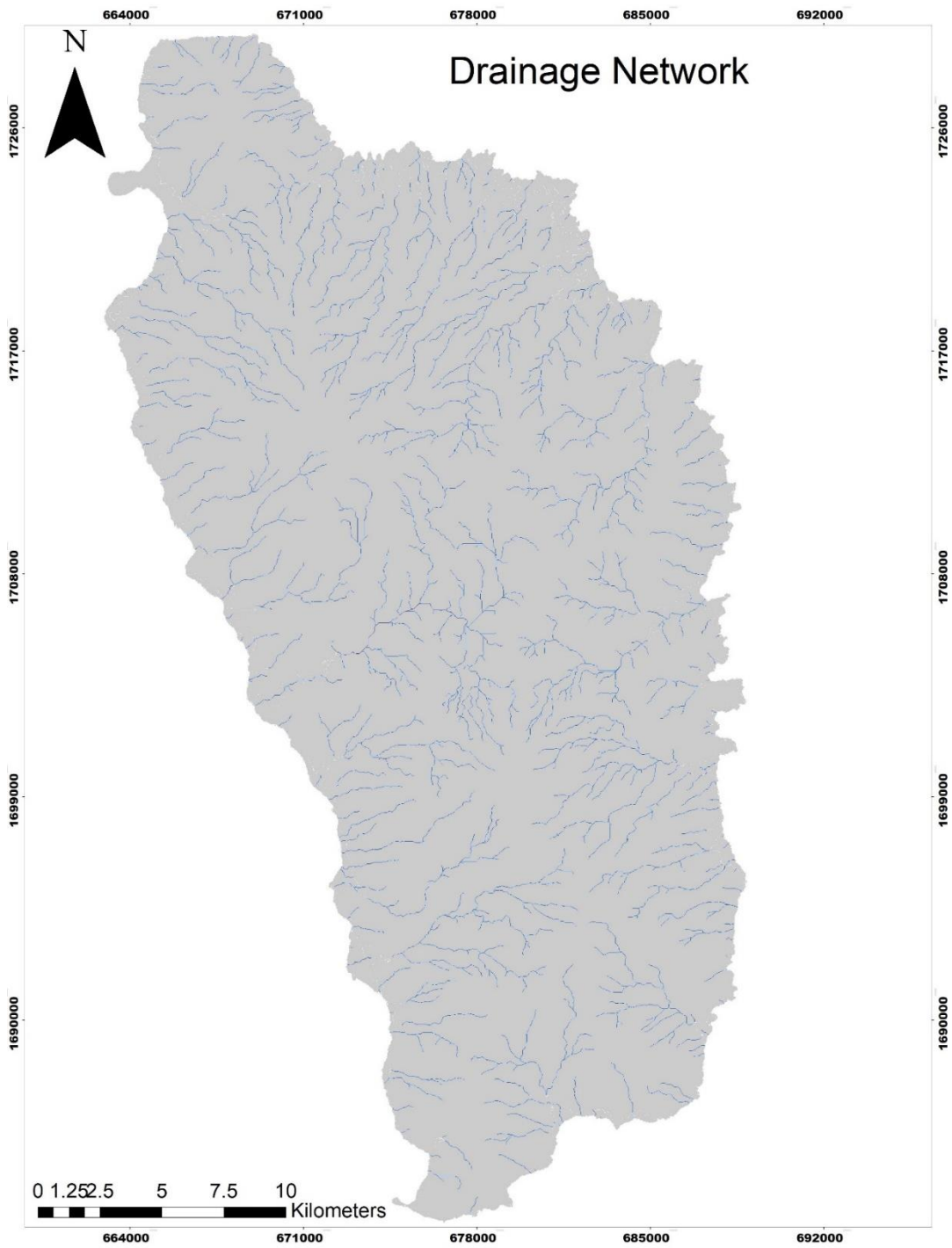


Figure: 4.8: Drainage Network map showing dendritic drainage pattern.

CHAPTER FIVE

Results Of Field Work and Boulder Analysis, Processed Drone Images, Dominica and Fogo

5.0 Introduction

Chapter five presents the comparison of images from before and after Hurricane Maria to determine the impact of the events on livelihood, livestock, infrastructures and the environment. Results of ImageJ analysis of orthophotographs to determine the size of boulders which were moved during the 2017 Hurricane Maria event are also presented. A short section was devoted to observations made in the Ribeira Domingo Santo in Fogo, Cape Verde. Finally, results of processed drone aerial images are also presented in this chapter.

5.1 Impact of Hurricane Maria Events on Selected Study Areas in Dominica

Hurricane Maria caused major devastation across the entire island of Dominica. Strong winds destroyed roofs of most homes and other infrastructures and torrential rainfalls caused many landslides, flooding and debris flows (Talmazan, 2017; Elizondo, 2017 and Weaver et al, 2017). Many lives were lost and properties damaged as a result of this catastrophic event. About 99 fatalities were recorded with 65 deaths and 34 people reported as missing or dead (DNO, 2018). Approximately 80% of Dominica's infrastructures were damaged by Hurricane Maria and 98% of roofs of buildings were destroyed (IFRCRCS, 2017). The island's transport network, water supply systems, schools, hospitals, civil offices and electricity were massively destroyed ((IFRCRCS, 2017). Agriculture, which is Dominica's principal source of income and subsistence for the populace, was completely destroyed as well as farm equipment and large number of livestock was also lost (IFRCRCS, 2017). An estimated value of £998,424,290 was lost as result of this catastrophic event which equivalent to almost 227% of Dominica gross domestic product (GDP) as of 2017 (Caricom, 2018).

Although the whole of Dominica was affected by Hurricane Maria, six localities were chosen for this study due to factors of accessibility and availability of relevant data. These localities are Coulibistrie in north-west, Layou, Pointe Michelle and Soufriere in south-west, Pagua in north-east and Delice in south-east of the island. Damage suffered by these areas can be assessed in detail by comparing images from Google Earth before and after Hurricane Maria and drone-derived orthophotographs.

Coulibistrie township was massively affected by Hurricane Maria, almost all roofs were blown away, buildings submerged in water and filled with sediments, tree debris and boulders (Figure 5.1 A-D). There were many deposits of clustered boulders, cobbles and tree debris among other debris (Figure 5.1A). Comparison of the pre and post Hurricane Maria google earth images clearly shows devastations caused by the catastrophic event (Figure 5.1 B and C). A contributing factor to the flooding was the torrential rainfall coupled with poor drainage networks and jammed bridges causing an overbank flow of water into the settlements (Figure 5.1C). A small bridge connecting the north and south settlements of the town was partially damaged, eroded and jammed with boulders and sediments (Figure 5.1 C and D). A much bigger bridge connecting the south-western part of Dominica to the north-western part of the island was completely destroyed and covered in sediments (Figure 5.1C). Most of the sediments and boulders that filled the buildings were the cascading effects of a giant landslide that occurred 4 km from Coulibistrie and transported downstream as debris flow. All the farm and most livestock were destroyed and the vegetation was washed away. Water and other utility pipelines, telecommunication and electricity lines and poles were severely damaged (Figure 5.1 C and D).



Figure 5.1 A: Field image showing cluster of boulders (0.4-1.5 m) and tree debris (1-3 m) in the channel bed at Coulibistrie (Dominica).



Figure 5.1 B: Google Earth image before the Hurricane Maria event for Coulibistrie (Dominica)

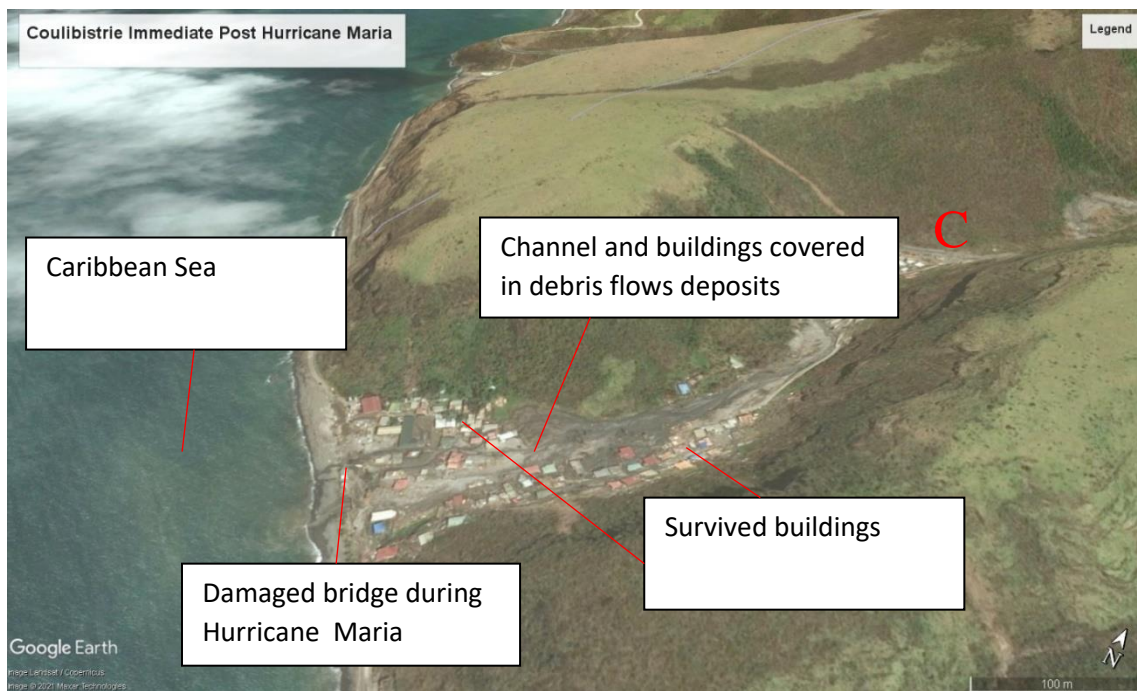


Figure 5.1 C: Google Earth image showing post-Hurricane Maria event devastation at Coulibistrie (Dominica)

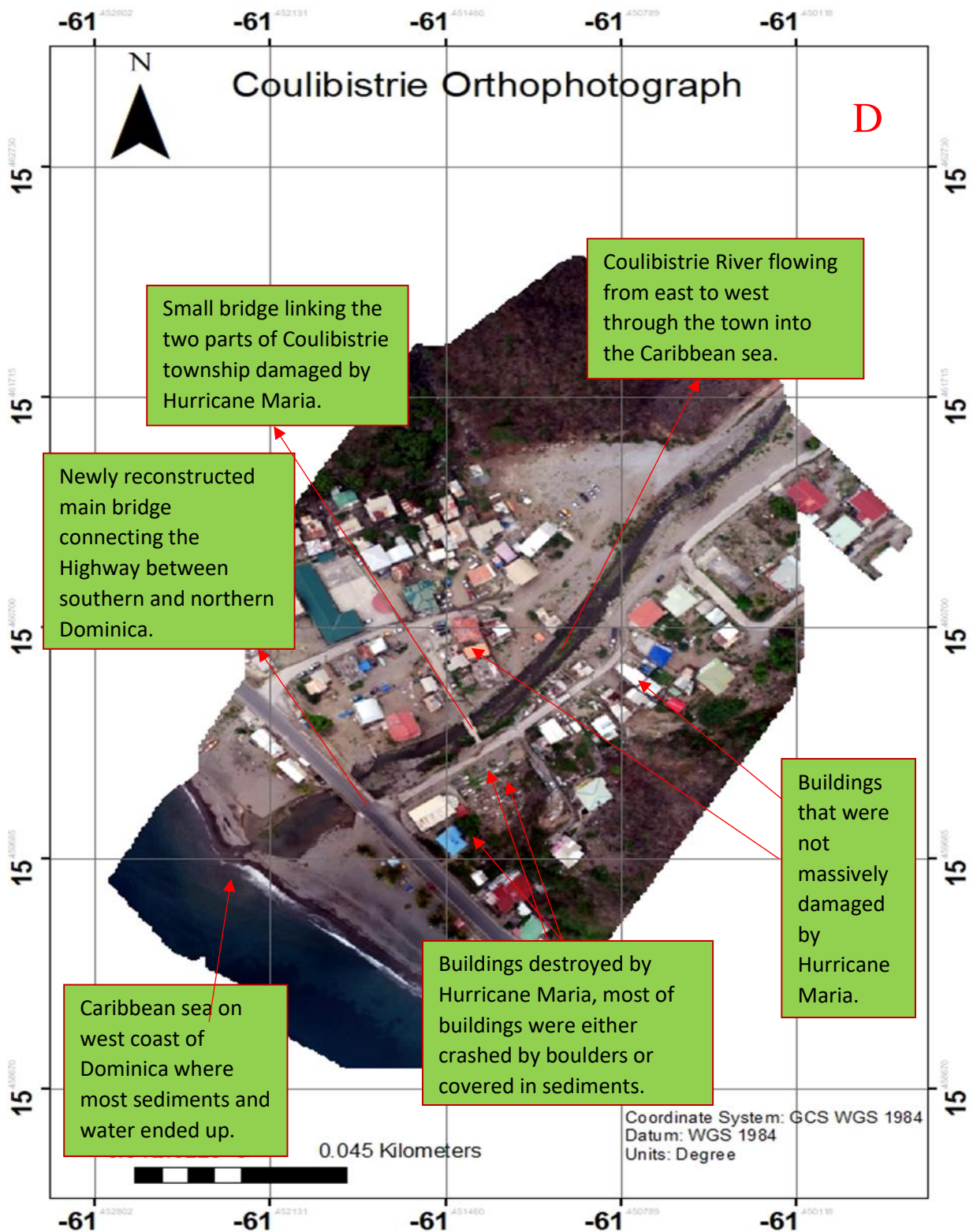


Figure 5.1 (D): Post-Hurricane Maria drone-derived orthophotograph showing damage caused by Hurricane Maria at Delice (Dominica).

Delice is less populated in comparison to Coulibistrie, however there are a lot of agricultural activities. Vegetation and farmlands were completely wiped out by strong winds, high velocity flood, landslides and debris flow (Figure 5.2 A, C and D). Figure 5.2A shows lateral debris flow deposition. Most roofs of buildings in Delice township were blown away by strong winds (Figure 5.2C). Unlike Coulibistrie, houses in Delice were not covered in sediments or submerged in flooding as the settlement is situated on high-grounds. Nevertheless, infrastructure, facilities and social amenities were damaged, leaving the town with no electricity, clean water or transport network to evacuate people to safe grounds. For example, the main bridge linking the road network in Delice to Petite Savannah and other southern towns such as Fond St. Jean, Dubuc and Berekua was damaged by boulders and covered in sediments (Figure 5.5 A, B, C and D).

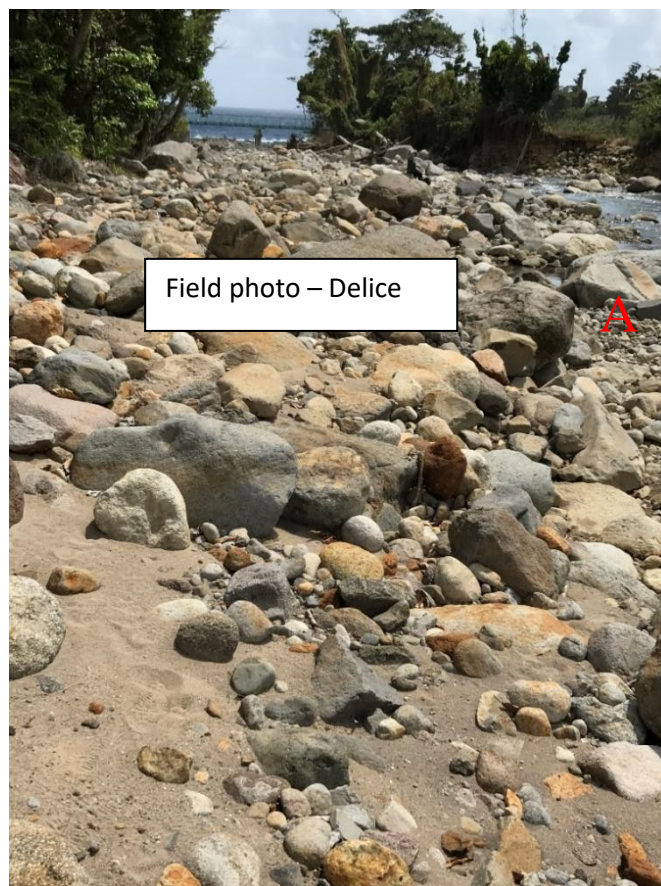


Figure 5.2 A: Field image showing cobbles (0.06-0.2 m), boulders (0.4-2 m) and tree debris (0.5-3 m) deposited laterally in the channel bed at Delice (Dominica).



Figure 5.2 B: Pre-Hurricane Maria Google Earth images for Delice (Dominica)

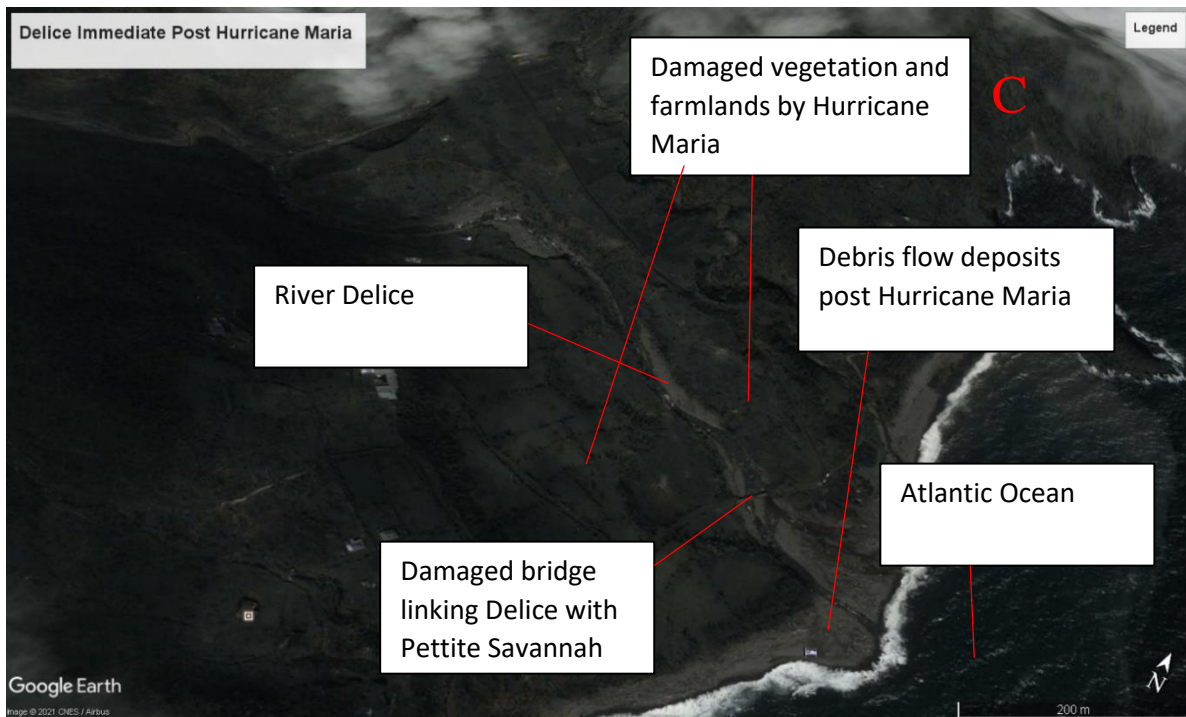


Figure 5.2 C: Google Earth image showing post-Hurricane Maria devastation at Delice (Dominica).

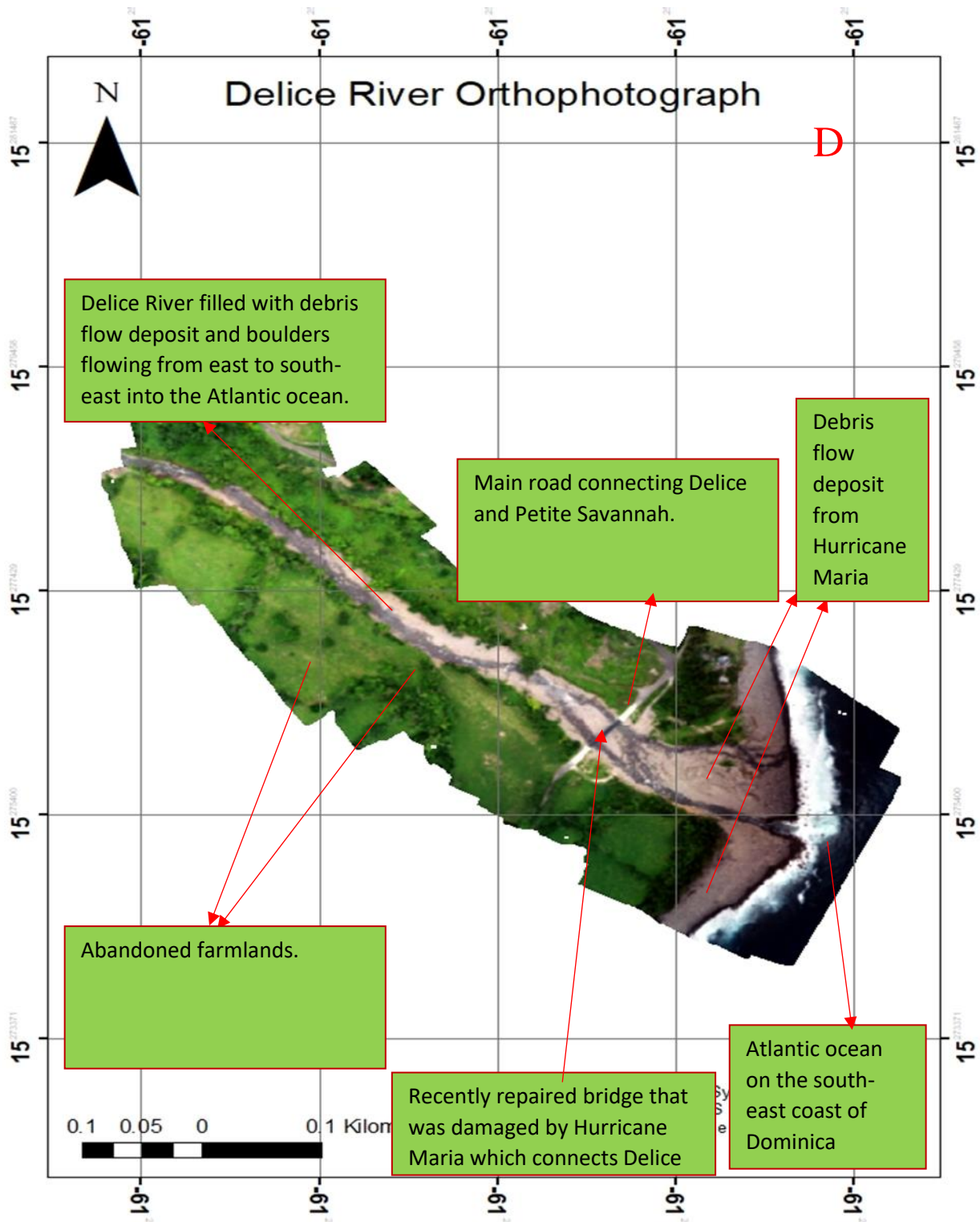


Figure 5.2 D: Drone-derived orthophotograph showing damage caused by Hurricane Maria at Delice (Dominica).

Layou Valley and its environs were devastated by numerous landslides, debris flow and severe flooding. Plantations such as cocoa, banana and other crops were destroyed completely, majority of livestock were killed as well. Situated in low-lying lands, Layou was always susceptible to flooding but torrential rainfall during Hurricane Maria coupled with the collapse of Matthieu Dam meant that Layou was submerged in water and debris. Layou was one the severely damaged towns as most houses were filled with water for days (Figure 5.3 A-D). Roads linking Layou with other towns such as Mero, Mahaut, Warner and St. Joseph were either eroded away or blocked by massive landslides and rockfalls (Figure 5.3 A-D). Just like Delice and Coulibistrie, there was no electricity or supply of clean water and other infrastructures were destroyed.



Figure 5.3 A: Field image showing deposit of mud-laden debris and hydrothermally altered boulders (0.5-1.5 m) at Layou (Dominica).



Figure 5.3 B: Google Earth images before the Hurricane Maria event for Layout (Dominica)

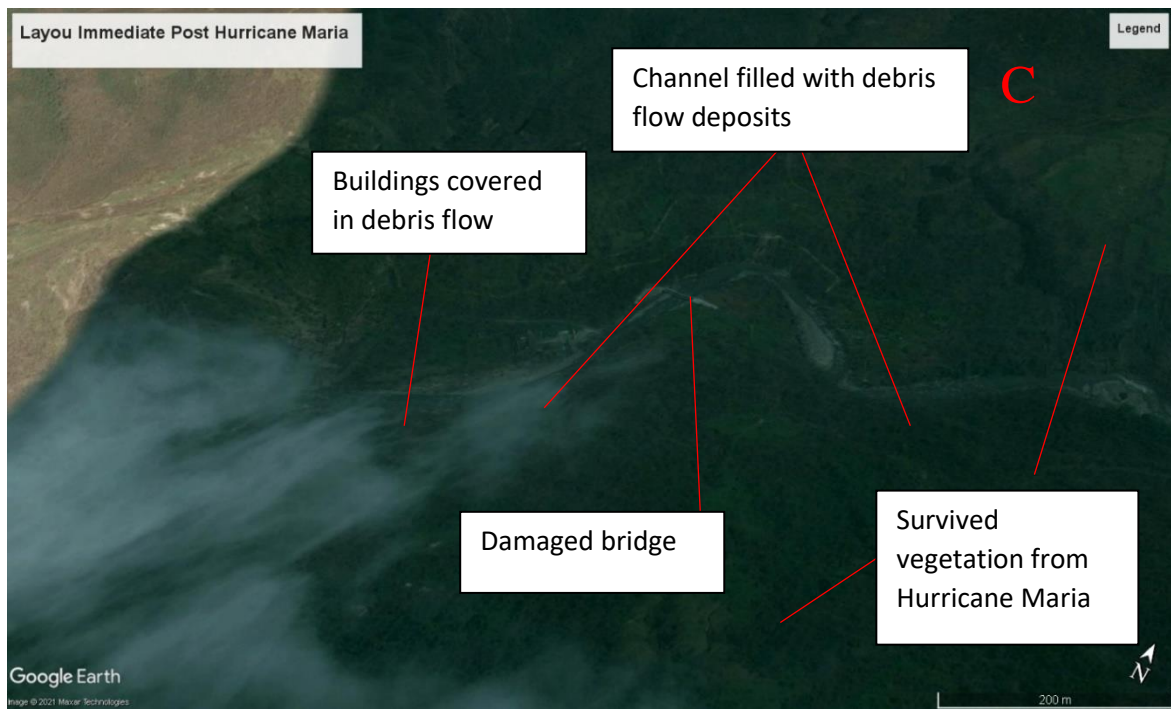


Figure 5.3 C: Google Earth image showing post-Hurricane Maria event devastation at Layout (Dominica).

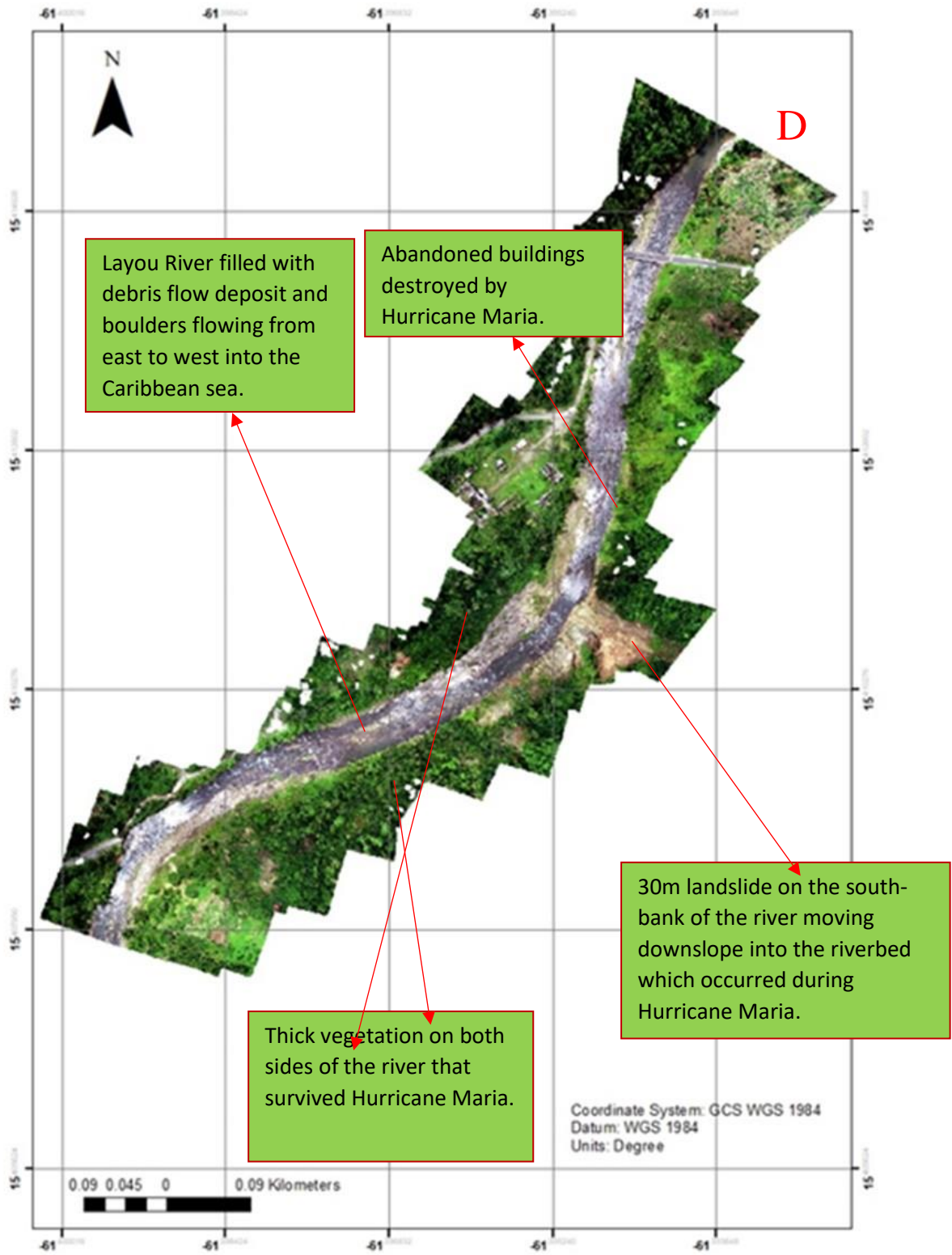


Figure 5.3 D: Drone-derived orthophotograph showing damage caused by Hurricane Maria at Layou (Dominica).

Another area that was affected by Hurricane Maria is Pagua, located at the north-eastern coast of Dominica. In comparison to other towns, Pagua was not severely damaged during Hurricane Maria (Figure 5.4 A-D). There were not much landslides and debris flow activities in Pagua and the vegetation was not completely wiped away. However, most crops, livestock and farmlands were destroyed by Hurricane Maria. Buildings that had aluminium roofing sheets were blown away by the strong winds (Figure 5.4 C and D). Pagua was greatly affected by flooding due to torrential rainfall, although the town was not submerged in water, most buildings and roads were filled with water (Figure 5.4 C and D). This resulted in blockage in transport network, hence it was difficult for emergency agencies to evacuate people quickly. The main road to the largest airport in Dominica runs through Pagua but was not accessible during Hurricane Maria (Figure 5.4A). The water pipes, electrical poles and other utility networks wires were damaged during Hurricane Maria.



Figure 5.4 A: Field image showing deep-seated giant boulder (10 m), small to medium boulders (0.4-7 m) and supervisor with 2 m rod as scale at Pagua (Dominica).

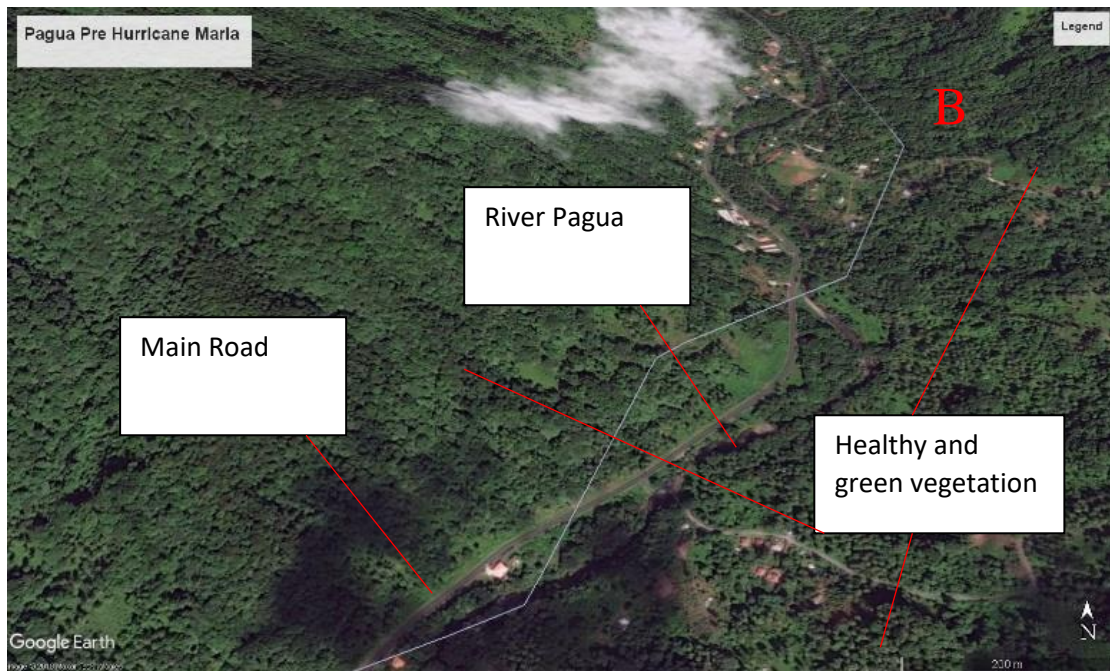


Figure 5.4 B: Google Earth images before Hurricane Maria for Pagua (Dominica).

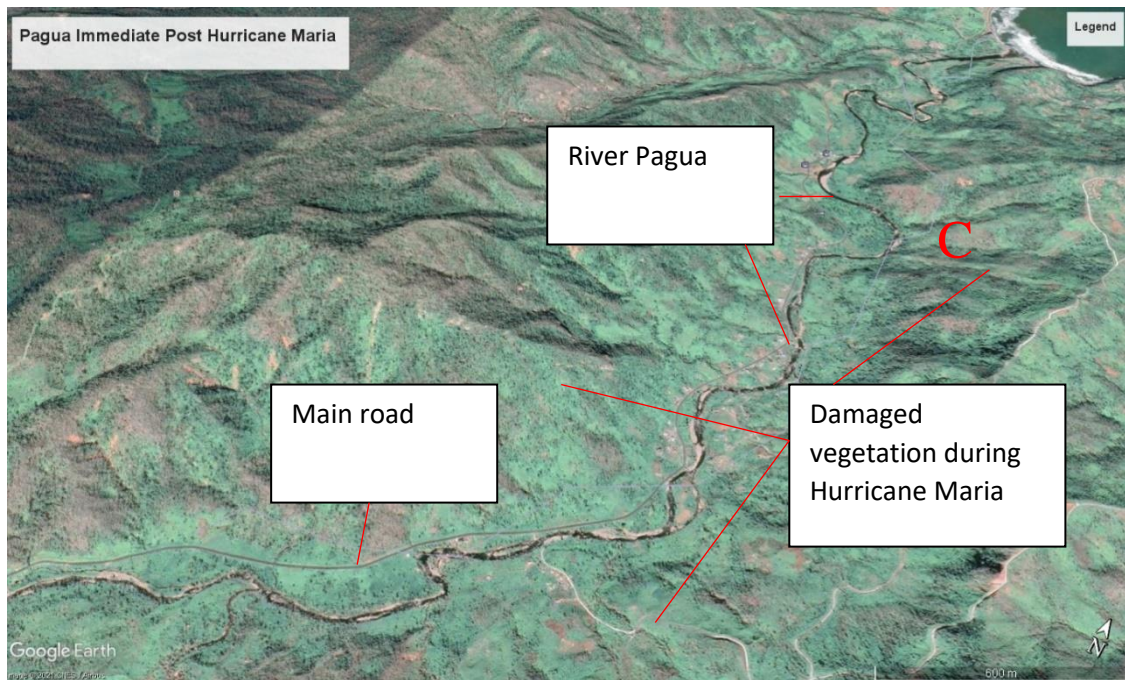


Figure 5.4 C: Google Earth image showing post-Hurricane Maria devastation at Pagua (Dominica).

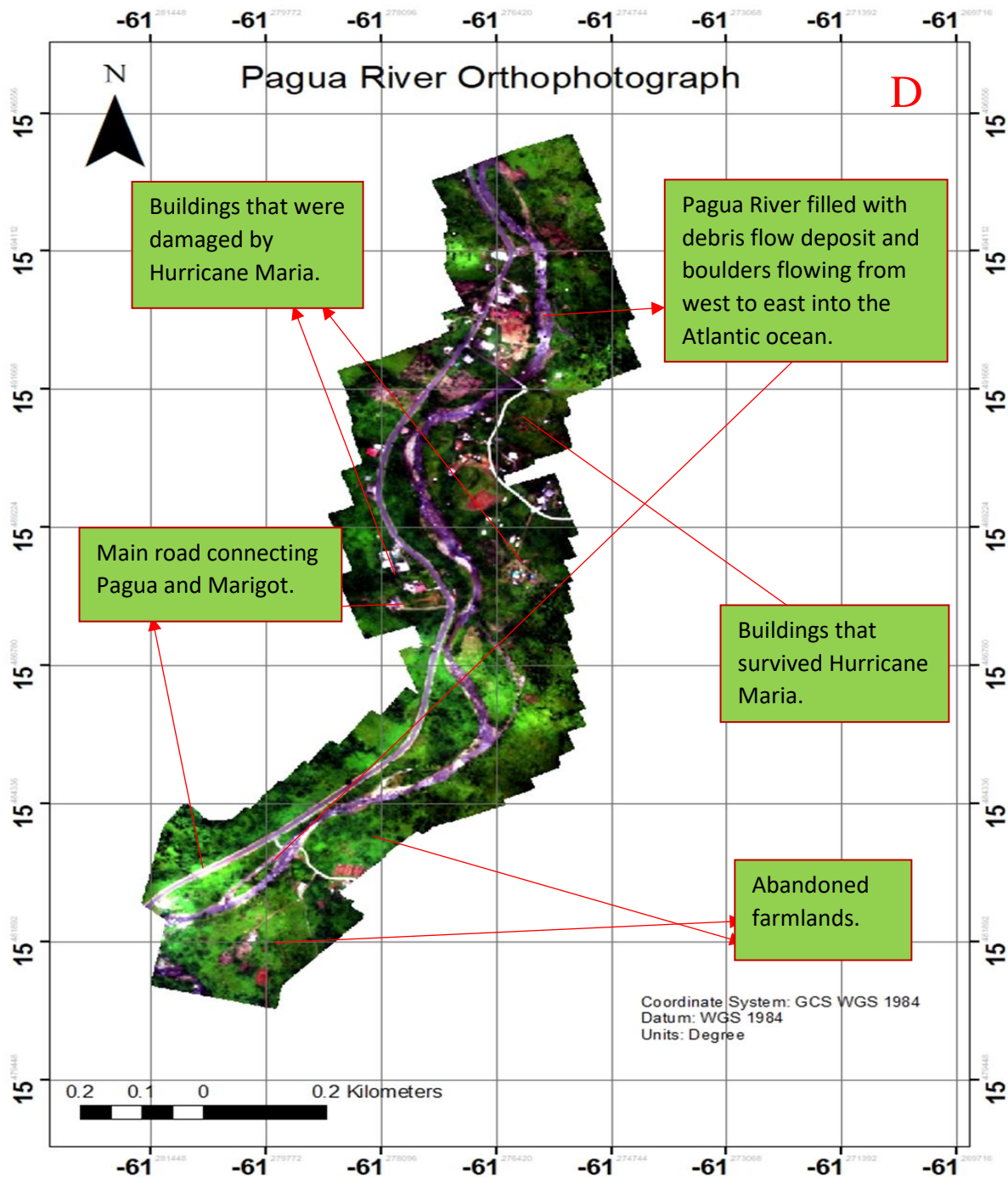


Figure 5.4 D: Post-Hurricane Maria drone-derived orthophotograph showing damage caused by Hurricane Maria at Pagua (Dominica).

Pointe Michel situated at south-western part of the island was the most severely damaged town during Hurricane Maria. Out of the 99 fatalities recorded during Hurricane Maria, 25 of them were reported in Pointe Michel. This can be attributed to the large population of Pointe Michel; it is one the biggest town aside the capital Roseau. Farmlands and livestock were adversely affected. Almost all roofs of buildings were blown away by the strong winds (Figure 5.5 C and D). Settlement at the lower part of Pointe Michel was severely flooded and damaged by debris flows (Figure 5.5C). Most houses at lower Pointe Michel were covered in sediments, boulders and other debris (Figure 5.5 A, C and D). This resulted in casualties and displacement of people. Water pipelines were uprooted, electrical and telecommunication poles and wires were damaged during Hurricane Maria. The main road network linking Pointe Michel to the capital Roseau was damaged as result of the collapse of the main bridge adjoining the roads.



Figure 5.5 A: Field image showing deposit of tree debris (0.5-2 m) and cluster of boulders (0.5-1.5 m) at Pointe Michel (Dominica).

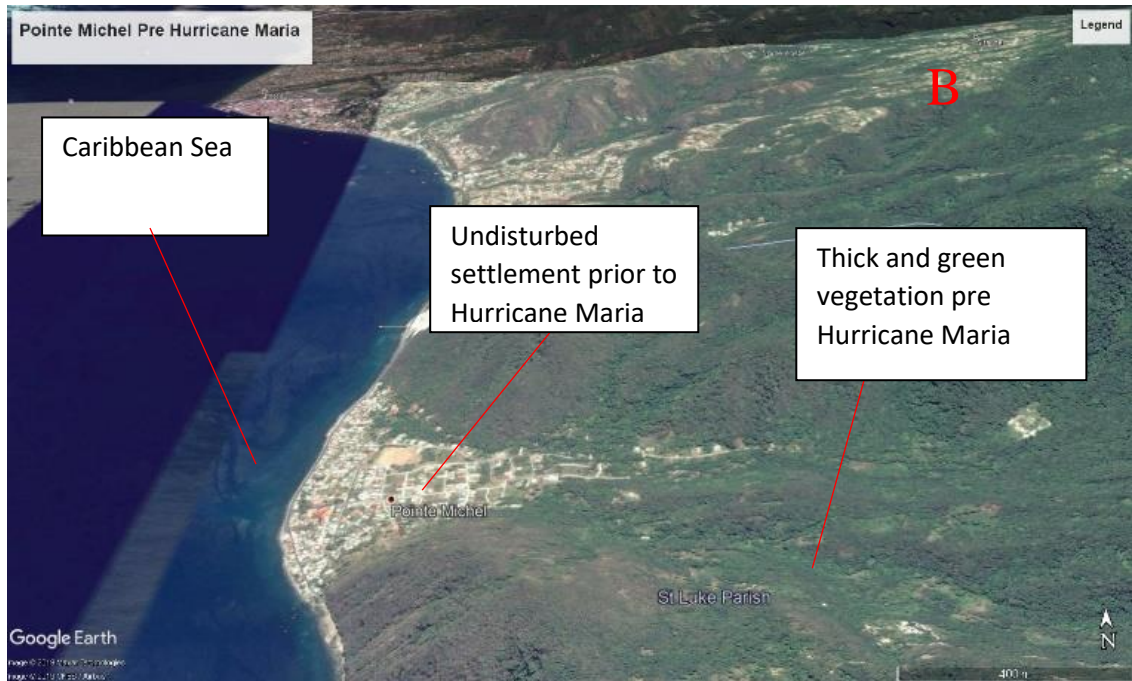


Figure 5.5 B: Google Earth images before Hurricane Maria for Pointe Michel (Dominica).

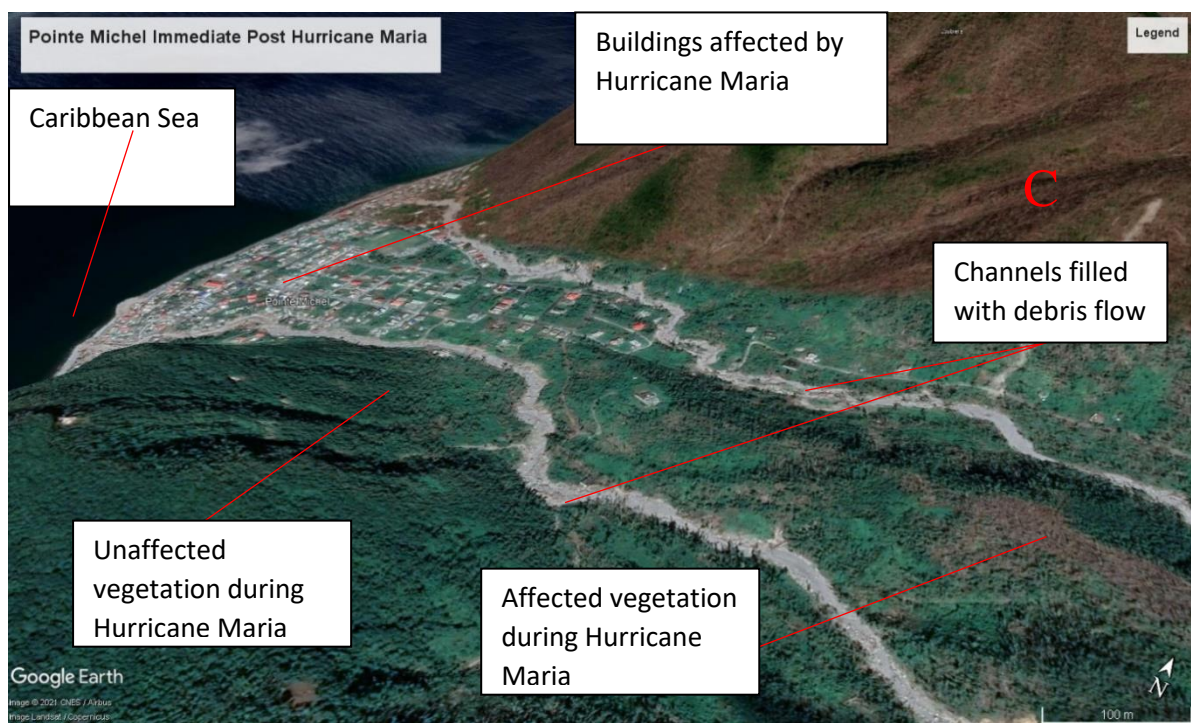


Figure 5.5 C: Google Earth image showing post-Hurricane Maria devastation at Pointe Michel (Dominica).

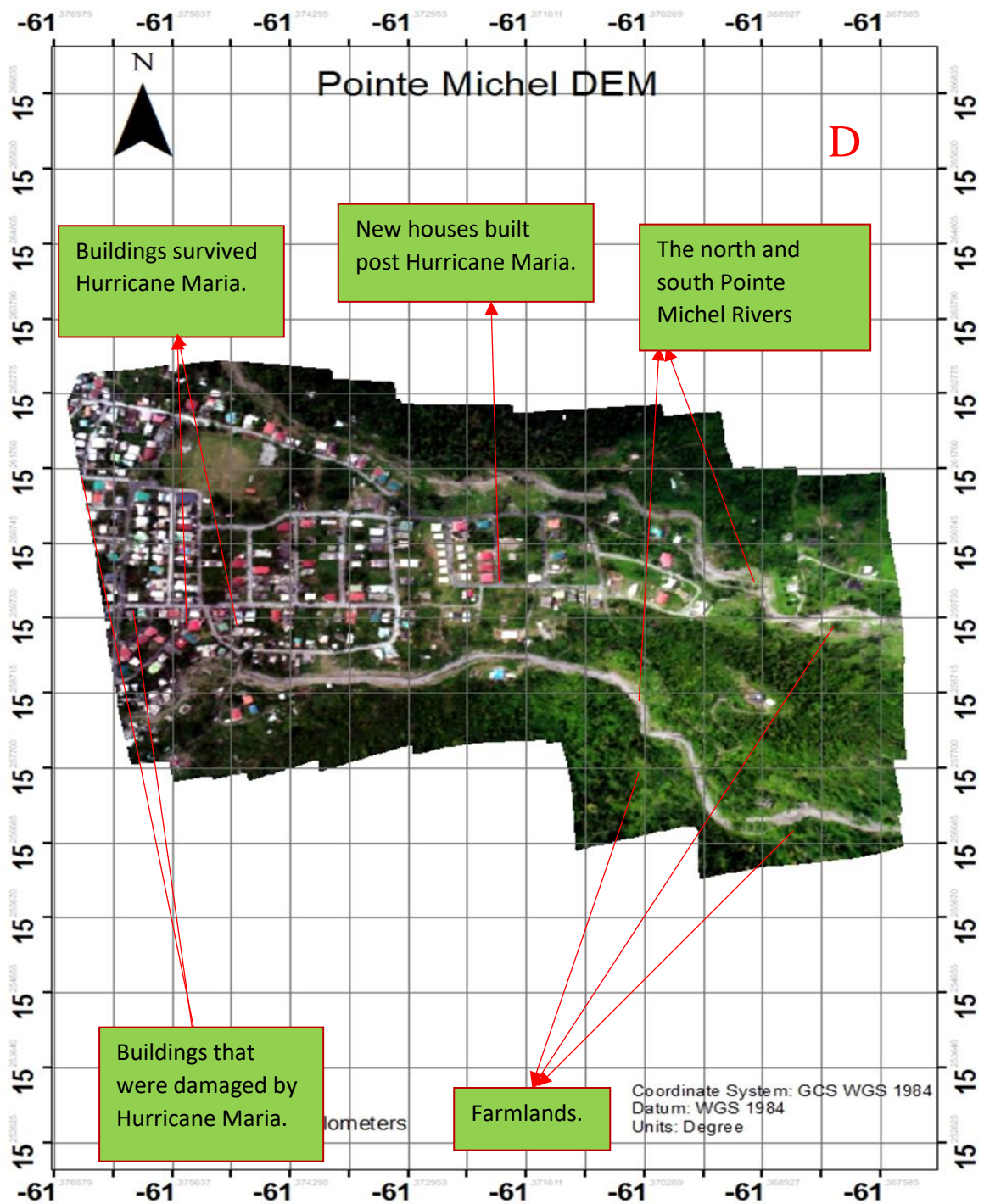


Figure 5.5 D: Drone-derived orthophotograph showing damage caused by Hurricane Maria at Pointe Michel (Dominica).

Soufriere is the southernmost town of all the six localities in Dominica. Just like all the localities, Soufriere was severely damaged by Hurricane Maria. A giant landslide that occurred during Hurricane Maria transported thousands of tonnes of sediments and boulders from the highlands into the settlements on the lowlands in the form of debris flow and rockfall (Figure 5.6A-D). This resulted in a complete wipe of the vegetation, crops and livestock, road networks, buildings and other infrastructure (Figure 5.6A, C, D). Most buildings that were within 1.5 km from the landslide initiation zone were covered in sediments and damaged by giant boulders (Figure 5.6C). Almost all the roofs of buildings were blown away by strong winds during Hurricane Maria (Figure 5.6C). The torrential rainfall that lasted for days also resulted in severely flooding and almost the whole town was submerged in water. Just like the other five localities, all utility networks such water, electricity and telecommunications were destroyed during Hurricane Maria. This made accessibility it extremely difficult for emergency services to go to Soufriere and rescue affected people in time.



Figure 5.6 A: Field image showing deposit of tree debris (0.5-2 m) and cluster of boulders (0.5-1.5 m) at Soufriere (Dominica).

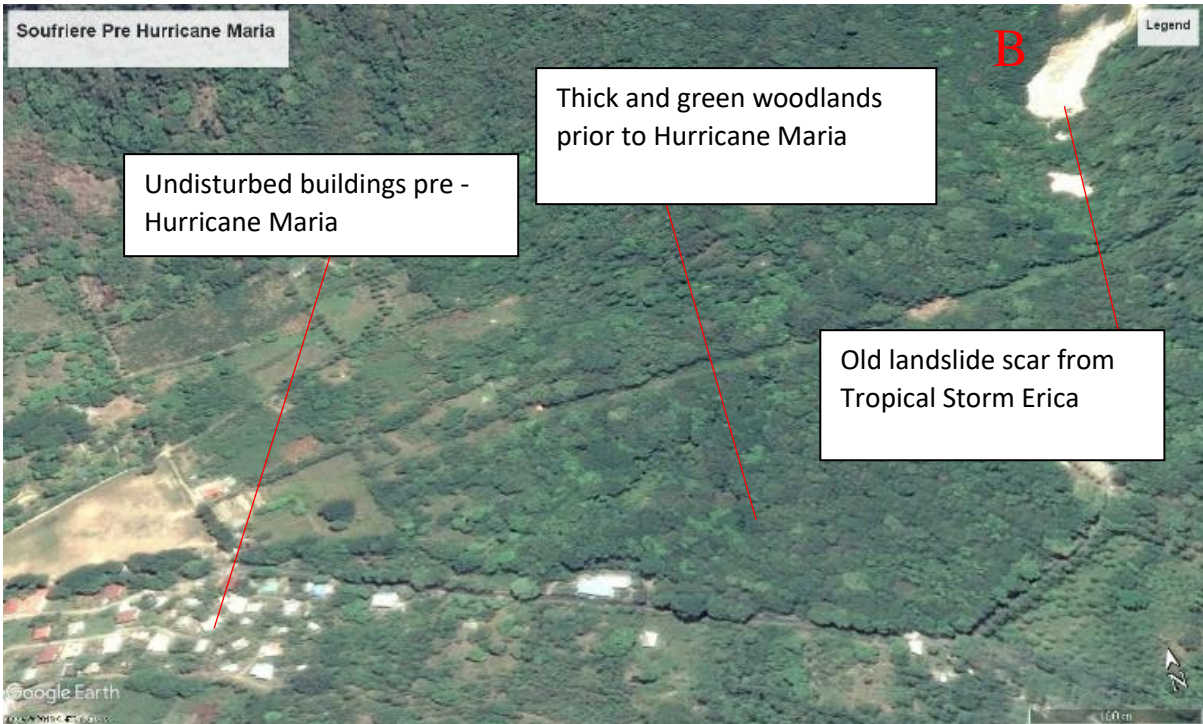


Figure 5.6 B: Google Earth images before Hurricane Maria for Soufriere (Dominica).

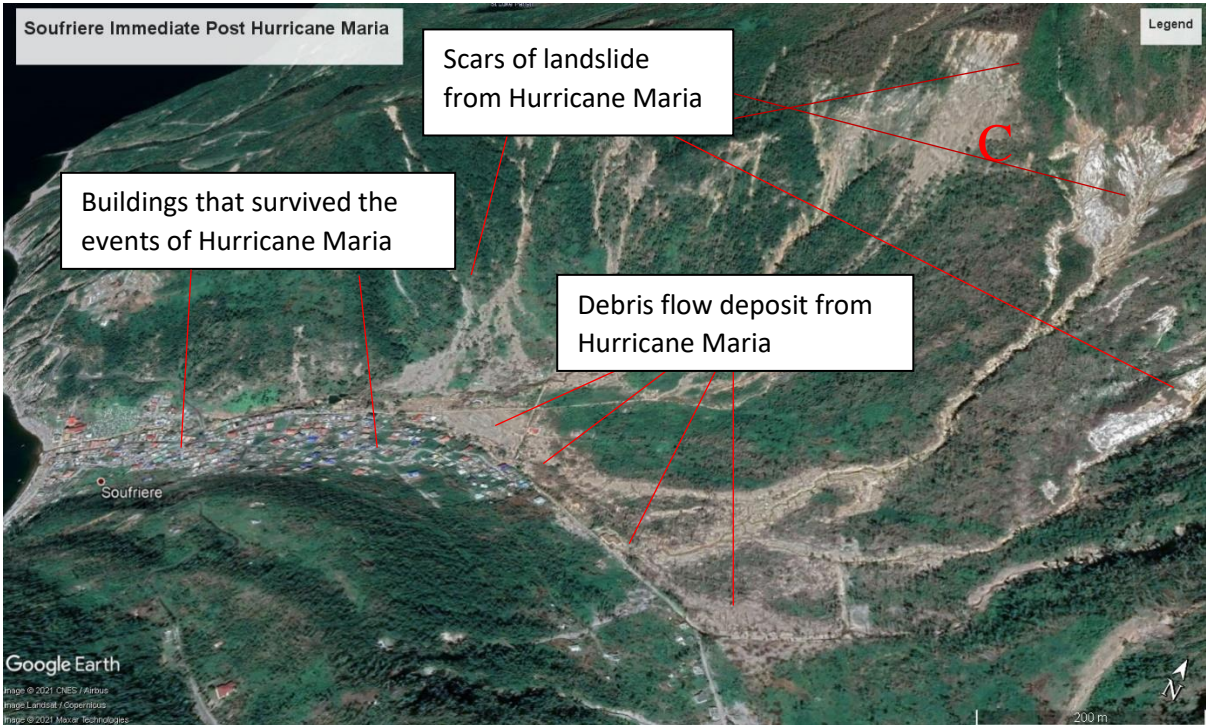


Figure 5.6 C: Google Earth image showing post-Hurricane Maria devastation at Soufriere (Dominica).

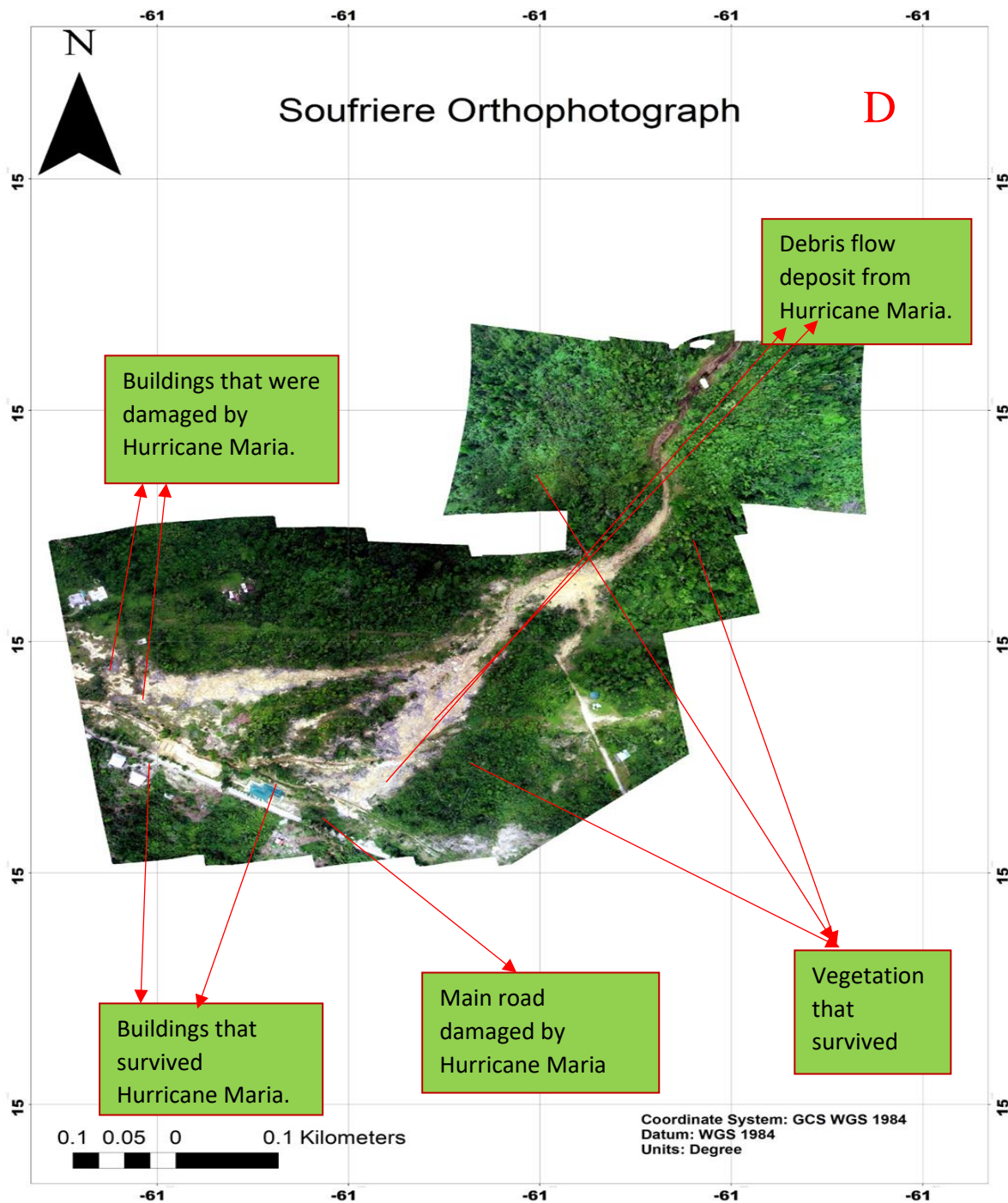


Figure 5.6 D: Drone-derived orthophotograph showing damage caused by Hurricane Maria at Soufriere (Dominica).

Impact of Hurricane Maria resulted in expansion of existing channels and creation of new channels in all six study localities (Figures 5.1-5.6). The expanded and newly created channels were due to entrainment caused by rapid moving water and debris flows. Morphology of these channels were drastically altered during Hurricane Maria (Figures 5.1-5.6). To determine how much the morphology of these channels changed after Hurricane Maria, pre- and post-Hurricane Maria Google Earth images were compared and analysed (Figures 5.1-5.6). A critical analysis of all images clearly shows drastic changes to the morphology of all channels post Hurricane Maria (Figures 5.1-5.6). It was difficult to get accurate data such as length, depth and width of all channels for both pre- and post-Hurricane Maria. However, it clearly evident from the images comparison that old channels were expanded and new channels were created during Hurricane Maria (Figures 5.1-5.6).

Moreover, accounts given by local residents at all localities and other eye-witness evidence confirmed that certainly shape of the channels have been altered after Hurricane Maria. The remains of debris flow deposit, uneven distribution and deposition of boulders and other debris in the channels ascertain the changes (Figures 5.1-5.6). Also, my own observations made during the fieldwork at various localities confirmed changes to the channels as evidence of erosion were clearly visible in the channels. Most of the channels were filled with sediments, tree debris and boulders and had to be excavated to ensure smooth flow of water (Figures 5.1-5.6). Excavation resulted in expansion of the channels and alteration in their morphology.

5.2 ImageJ Boulders Size and Distribution Analysis Results

It was difficult to determine boulders moved during Hurricane Maria and boulders there were already in situ in all localities prior to the event. However, based on the pre and post Hurricane Maria google images comparison, eye-witness evidence and fieldwork observation. A clear distinction was made between in situ boulders and boulders moved during Hurricane Maria. With the exception of Pagua, boulders found in the other five localities experienced movement of boulders during Hurricane Maria. Prior to the fieldwork, comparison of pre- and post-Hurricane Maria revealed that, aside from Pagua, there were little or no boulders in Coulibistrie, Delice, Layou, Pointe Michel and Soufriere before Hurricane Maria. However, after the events of Hurricane Maria, these areas were covered with boulders of different shapes and sizes. Post-Hurricane Maria fieldwork observations and eye-witness evidence confirmed the movements of boulders in all five localities, with exception of Pagua, where some giant boulders did not move.

Size of boulders found in all six localities were determined using an image analysis software called ImageJ to analyse orthophotographs of each locality. Using the Udden-Wentworth grain size scale (Udden, 1912 and Wentworth, 1922) where rocks with diameter > 0.27 m are considered boulders. Results of the analysed size of boulders for each locality are presented as graphs (Figures 5.7 - 5.12). Boulders found in Coulibistrie were relatively small in comparison to other localities. Pagua had giant boulders and was the locality with most big boulders. Boulders were unevenly distributed in all localities; however small boulders were found at the deposition zones whilst medium size boulders were found in transition zones and big boulders were predominantly at the upper parts of the channels. Most boulders were angular in shape indicating recent movements from in situ. Most boulders in all localities were mainly andesite and dacite with dark-grey and pale-grey colours respectively. Only boulders in Soufriere were hydrothermally altered by the hot springs and was brown-yellowish in colour.

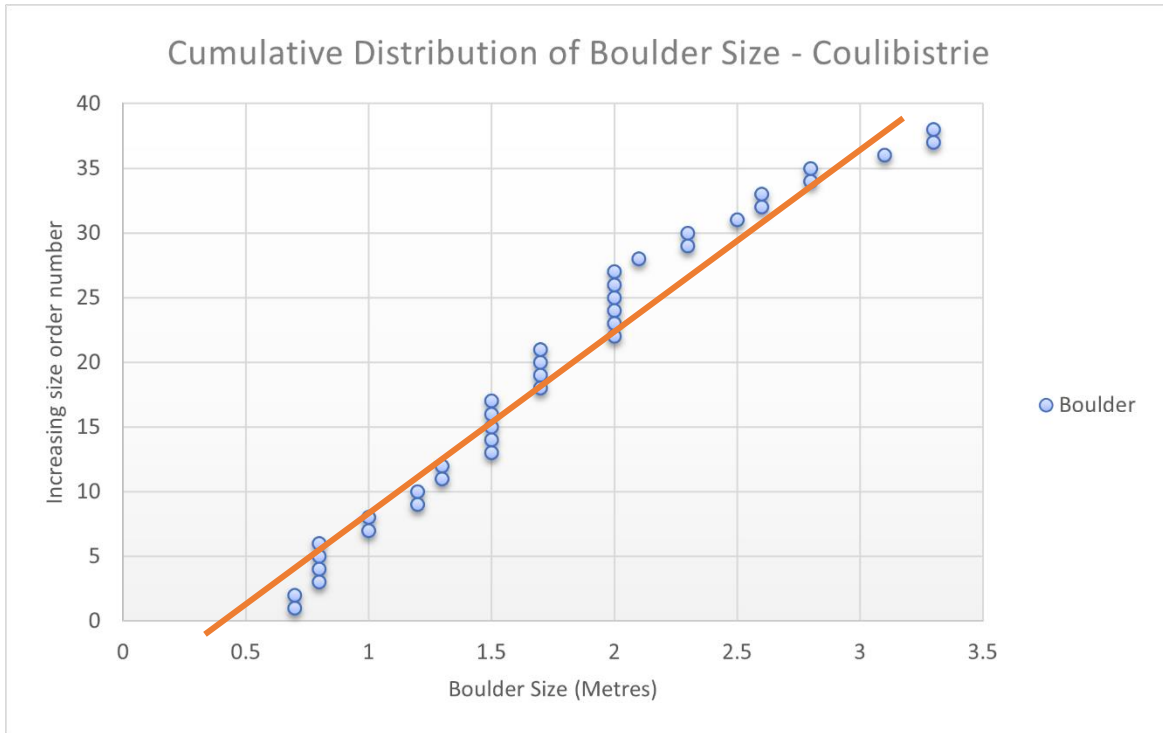


Figure 5.7: Results of ImageJ boulders analysis for Coulibistrie (Dominica) showing the sizes (m) and number of boulders.

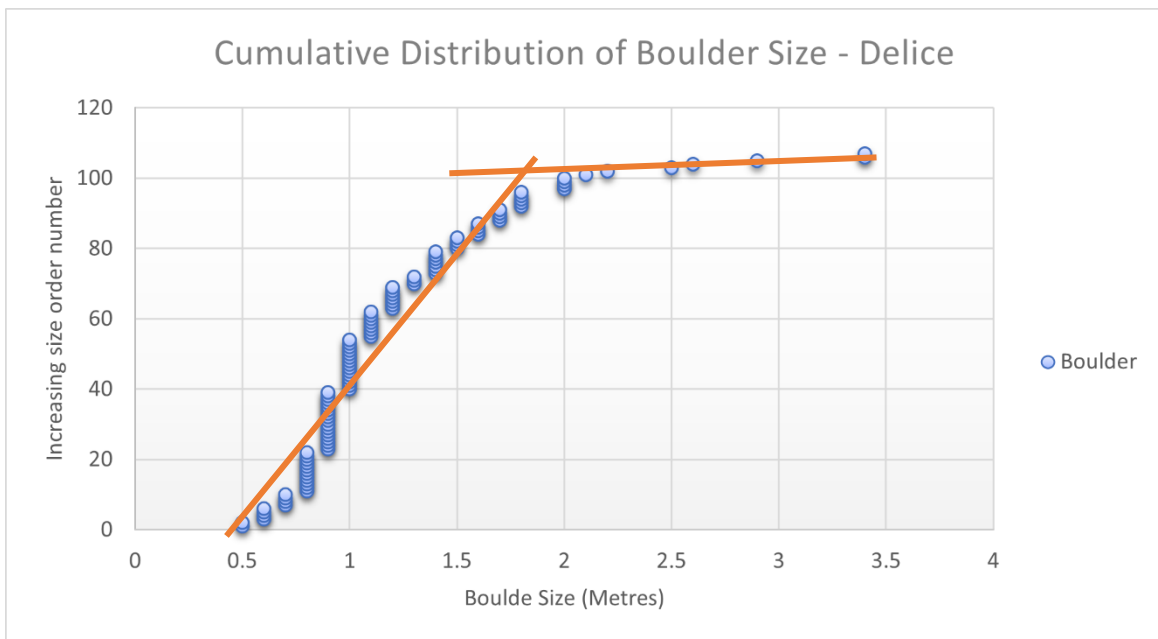


Figure 5.8: Results of ImageJ boulders analysis for Delice (Dominica) showing the sizes (m) and number of boulders.

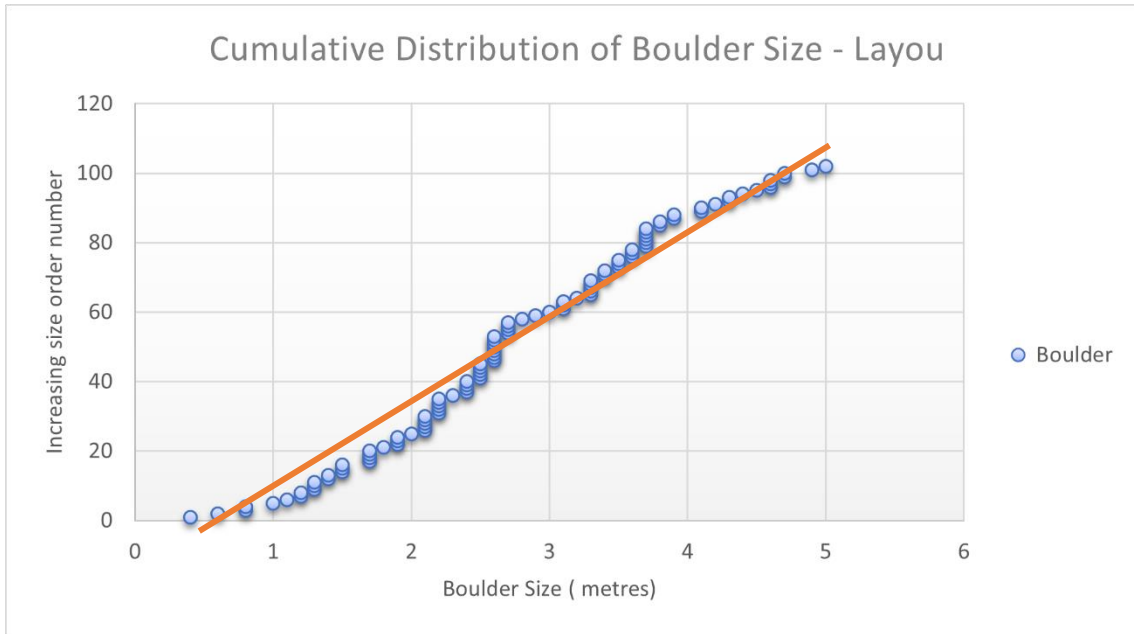


Figure 5.9: Results of ImageJ boulders analysis for Layou (Dominica) showing the sizes (m) and number of boulders.

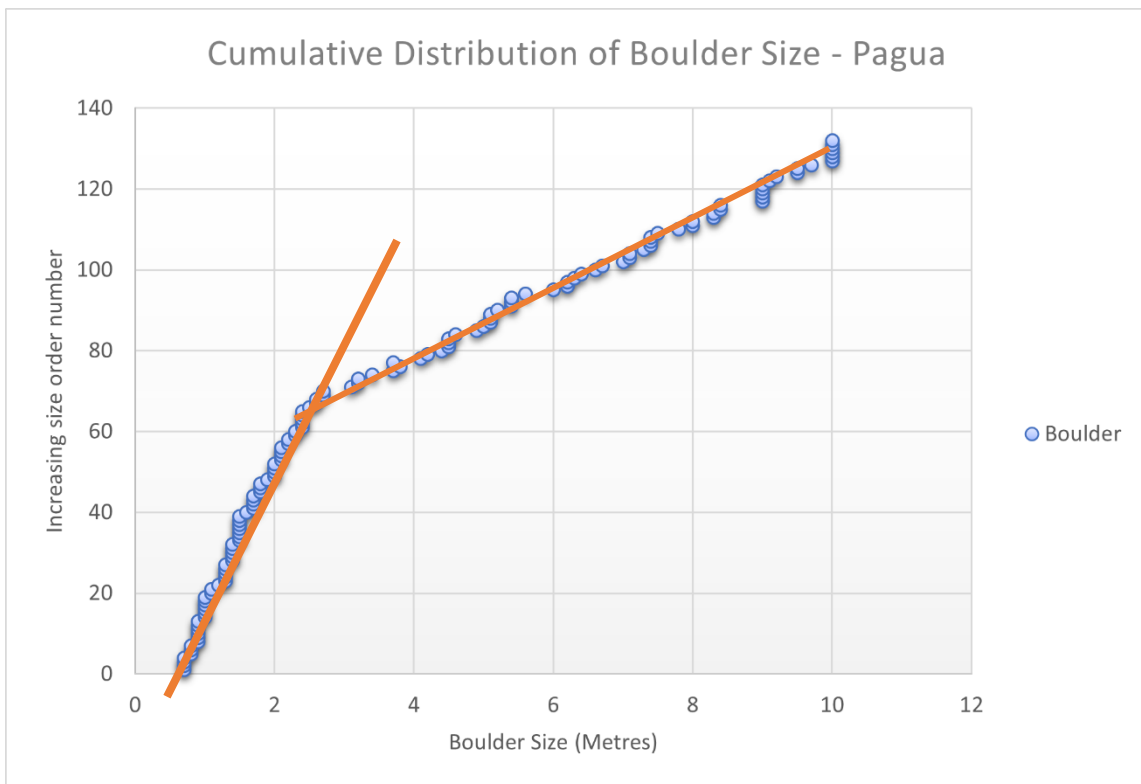


Figure 5.10: Results of ImageJ boulders analysis for Pagua (Dominica) showing the sizes (m) and number of boulders.

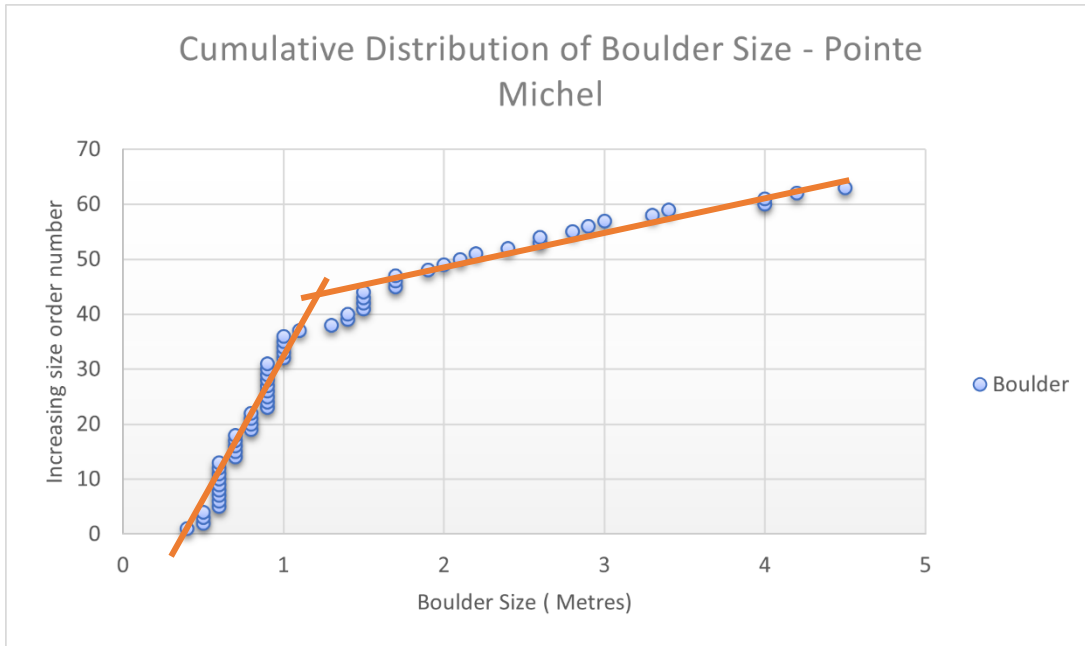


Figure 5.11: Results of ImageJ boulders analysis for Pointe Michel (Dominica) showing the sizes (m) and number of boulders.

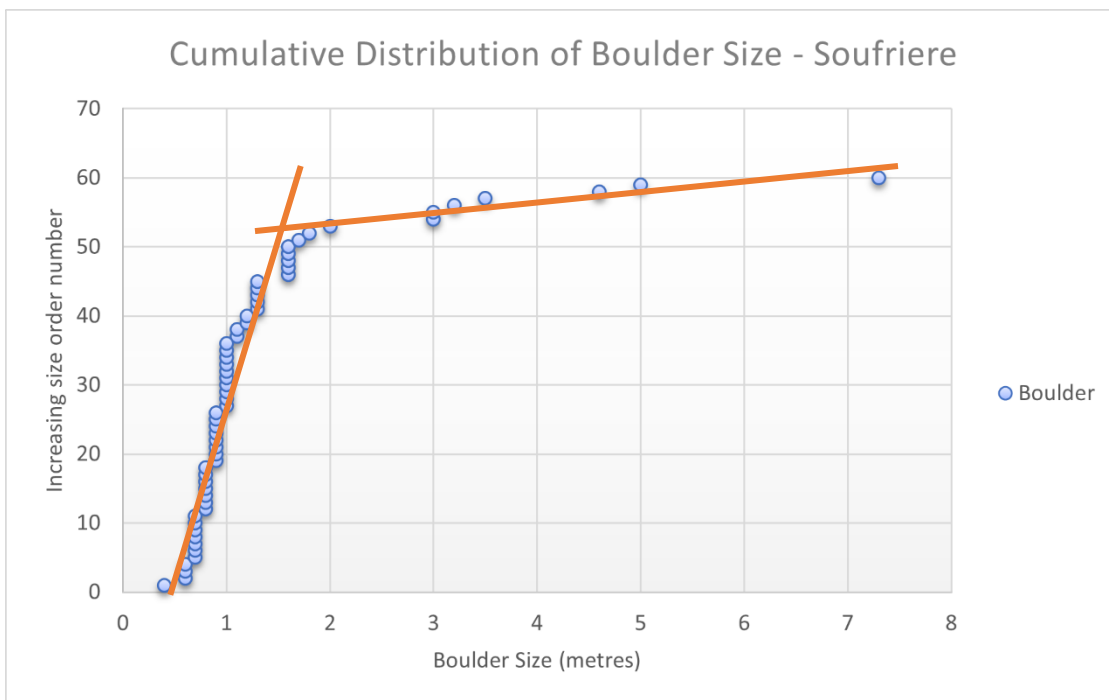


Figure 5.12: Results of ImageJ boulders analysis for Soufriere (Dominica) showing the sizes (m) and number of boulders.

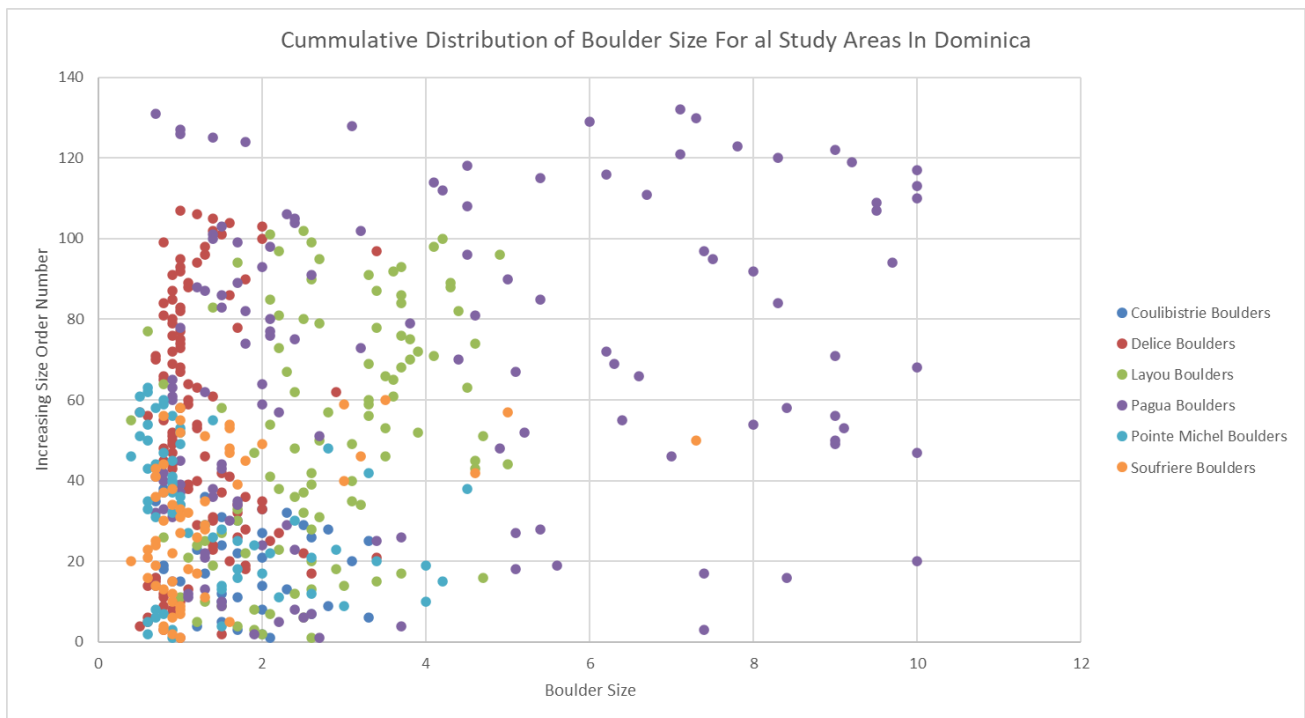


Figure 5.13: Results of ImageJ boulders analysis for all study areas in Dominica showing the sizes (m) and number of boulders.

Figure 5.13 shows all the boulders analysed for all the study localities in Dominica. Majority of boulders found in all study areas had sizes of 0.5-4 m (Figure 5.13). Most of the giant boulders (6-10 m) were recorded in Pagua and most small boulders were found in both Pointe Michel and Soufriere. With 132 boulders, Pagua had the highest numbers of boulders followed by Layou (107) and Delice (102). The least number of boulders were recorded in Coulibistrie (38), Soufriere and Pointe Michel had 60 and 63 boulders, respectively. Only 38 giant boulders (6-10 m) recorded in Pagua that were confirmed to not have moved during Hurricane Maria based on field observation and local eyewitness accounts. It was difficult to confirm whether other boulders in the study areas were in situ or moved during Hurricane Maria because excavation works had been undertaken and destroyed the original data prior to the fieldwork. Therefore, the boulder analysis graphs are not annotated to differentiate between boulders moved during Hurricane Maria and in situ boulders. However, the shape of boulders

distribution on the graphs (Figures 5.7 to 5.12) varies for each study area. The shape of boulders distribution in Coulibistrie (Figure 5.7) and Layou (5.9) is almost linear whilst there is change in shape of boulders distribution in Pagua, Delice, Soufriere and Pointe Michel (Figures 5.8, 5.10, 5.11 and 5.12). The differences in shape boulders distribution can be attributed to the fact that, there was one movement event in Coulibistrie and Layou (Figure 5.7 and 5.9) and two events in Pagua, Delice, Soufriere and Pointe Michel (Figures 5.8, 5.10, 5.11 and 5.12).

Coulibistrie predominantly contains boulders ranging from 0.7 to 3.3 m in size. The boulders (Figure 5.14) are sub-angular to very angular in shape and are laterally distributed along the river channel. Some of the boulders came down as rockfall from the nearby lava dome and some were moved down by flooding and debris flow. Most of the rocks were dacite, andesite and ignimbrite. There were also deposits of fine to coarse sediments behind the boulders mixed with cobbles and conglomerate. There was evidence of tree debris (Figure 5.14), rubber pipes, metallic pipes and plastic debris along the river channel post-Hurricane Maria.

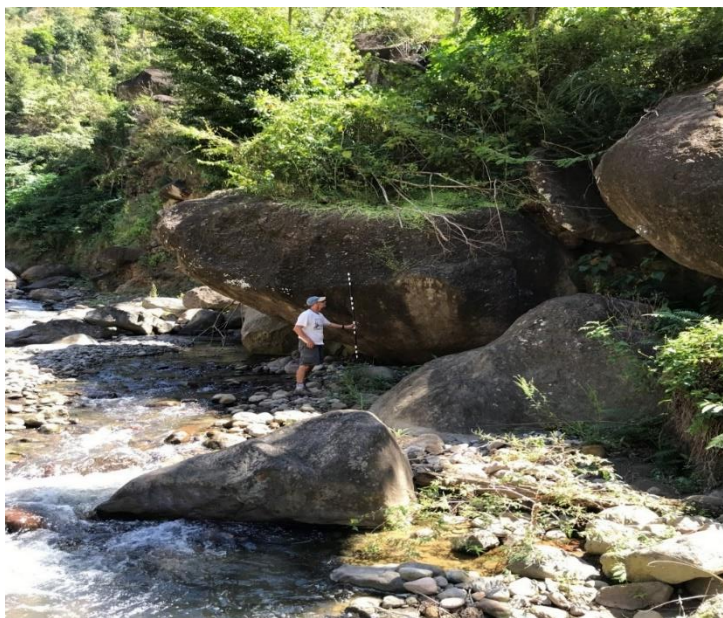


Figure 5.14: Coulibistrie River field photograph showing weathered giant boulders (0.7-3.3 m in diameter) at the south bank of the river with a 2 m rod as scale and river flowing left to right. Most boulders came down as rockfall and probably pre-dated Hurricane Maria.

Delice river contains relatively small boulders in comparison to Coulibistrie about 0.5-3.5 m in diameter. The boulders are laterally distributed along the riverbank (Figure 5.15). Most of the rocks in Delice have undergone hydrothermal alteration hence they have yellowish pink colour. This may be due to the fact that Delice is close to the Boiling Lake and nearby hot springs. Most of the sediment deposits were transported downstream through either debris flow or hyper-concentrated stream flow. Most of the boulders were sub-angular in shape and dark-brown. The sediment deposits were poorly sorted with mixture of gravel, silt, conglomerate and rounded cobbles and transported downstream during Hurricane Maria (Figure 5.15).



Figure 5.15: Delice River field photograph showing lateral deposition of boulders (0.5-3.4 m in diameter) from the riverbank failure caused by excessive force of the flow and hydraulic toe erosion undercutting the river-bank during Hurricane Maria. River flows from right to left from the viewer.

Layou River is one the biggest rivers in Dominica surrounded by a ridge of lava domes on both sides. Most of the rocks found in Layou are from nearby lava domes which came down as rockfall and were transported downstream in debris flows. The boulders were angular in shape, about 0.3 -5 m in diameter and pale-dark in colour. Other sediments found were gravel, silt, conglomerate and cobbles mixed with tree debris (Figure 5.16).



Figure 5.16: Layou River field photograph showing deposit of hydrothermally altered boulders (0.4-7.3 m diameter).

Pagua river is characterised by an uneven and sparse distribution of giant boulders about 100 m apart. The boulders found in Pagua river were about 0.5-10 m in diameter and appeared weathered (Figure 5.17). The boulders were less angular which indicated that they have been moved over a period of time (Figure 5.17). The boulders were dark-grey and had a rough texture (Figure 5.17). It was difficult to determine the rock type due to weathering but it was assumed to be an ignimbrite. Behind the giant boulders was a poorly sorted deposit of gravel, cobbles and conglomerate.



Figure 5.17: Pagua River field photograph showing deep-seated giant boulder (0.5-10 m in diameter) in the river-bed and 2 m rod as scale. The boulder is a conglomerate of pumice and volcanic clasts and river flows from left to right. The boulder pre-dated Hurricane Maria but may block the stream flow when tree debris and other sediments pile-up behind it which may result in overbank flooding.

Unlike Pagua, boulders found in the Pointe Michel river were relatively small about 0.4-4.5 m in diameter. They were less angular in shape and were not evenly distributed. The sediment was poorly sorted with a mixture of gravel, cobbles, pebbles, boulders and tree debris (Figure 5.18). The boulders were angular to subangular, pale-grey and predominantly dacite and andesite.



Figure 5.18: Pointe Michel field photograph showing Hurricane Maria debris flow deposit of boulders (0.4-4.5 m in diameter).

Soufriere was characterised by a rainfall-induced landslide which occurred during Hurricane Maria and turned into a debris flow. The material transported by the debris flow included clay, tree debris, giant boulders, gravels and cobbles (Figure 5.19). Most of the boulders were yellowish, poorly sorted, very angular and about 0.4-7.3 m in diameter (Figure 5.19). Most of the boulders were hydrothermally altered because Soufriere is situated in an area of hot springs which is evident in the yellow colour of boulders. Some of boulders were yellowish-green which may have been altered by degassing of sulphur from fumaroles.



Figure: 5.19: Soufriere field photo showing Hurricane Maria debris flow deposit of cluster of hydrothermally altered boulders (0.4-7.3 m in diameter) mixed with clay, tree debris and cobbles.

5.3 Boulders in Ribeira Santo Domingo, Fogo, Cape Verde.

The mechanism behind the movement and distribution of boulders in Ribeira Santo Domingo in Fogo can be attributed to weathering, erosion and sedimentary processes over the years. Although the boulders are formed from volcanic rocks, all of the processes that have formed and moved them have been sedimentary processes. The boulders are often formed from lava flows that show columnar jointing. Such lava flows originally covered many parts of the region where the ribeira formed. The ribeira was originally a sheet flow, running across the top of the lava flows, but then as erosion continued, it was able to work its way between cooling joints in the lavas, to start forming a river network. Eventually, it could reach depths beneath the lava flows where there were less resistant beds of pyroclastic rocks, which the water then eroded away. Once the less resistant beds were eroded, the edges of the overlying lavas were destabilised and large blocks could fall into the ribeira. Other assumed factors responsible for the movements of boulders in Ribeira Santo Domingo are rockfalls from unstable slopes, debris flows and floods due to torrential rainfalls during the rainy season (July-September). Unlike the study localities in Dominica, boulder size distribution and movement analysis was not performed for the study area in Fogo. This was due to time constraints, not knowing the mechanism behind the boulders movement and distribution, big data size and limited capabilities of the image analysis software (ImageJ).

Unlike in Dominica where boulder movement and distribution were influenced by events of Hurricane Maria, Fogo has not experienced any Tropical Cyclones for approximately three decades since Tropical Storm Fran in 1990. Therefore, it was difficult to determine the exact mechanism or mechanisms that influenced the current boulders distribution in Ribeira Santo Domingo. Nevertheless, it would have been good practice to conduct analysis of the current distribution of boulders to ascertain the susceptibility of livelihood, the built and natural environments to movements of boulders should there be Tropical Cyclones such as Hurricane

Maria in Cape Verde. However, due to the large size of Ribeira Santo Domingo, the drone-derived orthophotograph data was about 2.5 Gb. This data size was too big for the capability of the image analysis software ImageJ. It was not possible to reduce the data size as it reduces the image quality and affects the accuracy of the results. However, images taken during the fieldwork indicated that livelihood, the built and natural environment of Ribeira Santo Domingo are at risk of movements of boulders should there be an event like Hurricane Maria or Tropical Storm Fran (Figure 5.20 A - C).





Figure 5.20 A, B and C: Field photos of the western part of Ribeira Domingo Santo (Fogo), showing settlements situated laterally on the edge of channel's left bank. The buildings are on an unstable slope made of layers of boulders (0.5-1 m) which are being eroded and deposited into the channel bed. Direction of the channel and buildings is north to south of Ribeira Santo Domingo (Cape Verde, Fogo).

5.4 Processed Drone-Derived DSMs and Orthophotographs

All drone aerial images captured at all study localities were processed with Agisoft Metashape Professional photogrammetry software. Outcomes of the photogrammetric processing were DSMs and orthophotographs (Figures 5.21 - 5.33) for all study areas. The coordinate system for all DSMs and orthophotographs for all study localities in Dominica and Cape Verde was WGS 84 (EPSG:4326).

Out of 59 aerial images captured Coulibistrie, only 31 images aligned perfectly during the processing. The results of the processed images in Agisoft Metashape for Coulibistrie are presented as a DSM in Figure 5.21 and as an orthophotograph in Figure 5.22. Resolution of Coulibistrie's DSM and orthophotograph was 5 m covering an area of 2.8 km². About 28 of the 59 images failed to align due to overlapping problems during image capturing process.

At Delice, approximately 103 aerial images were captured but only 72 images aligned accurately during the processing. The remaining 31 aerial images did not have enough overlapping hence were regarded as junk during processing. Processed results of DSM and orthophotograph are presented in figures 5.23 and 5.24 respectively. Delice's generated DSM and orthophotograph had a resolution of 2 m covering a total area of 2.5 km².

Just like Coulibistrie and Delice, there were overlapping issues at Layou as well. This is because, out of the 313 aerial images captured at Layou only 275 images aligned perfectly during processing. Figures 5.25 and 5.26 shows the generated DSM and orthophotograph for Layou study area. The total area covered for Layou was 1.7 km² and the DSM and orthophotograph was resolution of 3 m respectively.

Unlike Coulibistrie, Delice and Layou, all the 573 aerial images captured at Pagua had enough overlapping and aligned perfectly during processing. The processed results are presented in Figures 5.27 and 5.28 as DSM and orthophotograph, respectively. Pagua's DSM and

orthophotograph had 7 m resolution covering an area of 2.3 km². At Pointe Michel, all the 421 aerial images captured also had enough overlap and aligned perfectly during the photogrammetric processing. A total area of 1.6 km² was covered at Pointe Michel and a 7 m resolution DSM (Figure 5.29) and orthophotograph (Figure 5.30) were generated. Approximately 515 were captured at Soufriere covering a total area of 1.3 km². All aerial images aligned perfectly to generate a 6 m resolution DSM (Figure 5.31) and orthophotograph (Figure 5.32). Just like Pagua, Pointe Michel and Soufriere, all 6648 aerial images captured at Ribeira Domingo Santo aligned accurately during processing. The generated DSM (Figure 5.33 A) and orthophotograph (Figure 5.33 B) had a resolution of 15 m and covered a total area of 86.7 km².

Study Areas	Coulibistrie	Delice	Layou	Pagua	Pointe Michel	Soufriere	Ribeira Domingo Santo
Total Area Covered (km²)	2.8	2.5	1.7	2.3	1.6	1.3	86.7
Digital Surface Models (DSMs) Resolution (m)	5	2	3	7	7	6	16
Elevations (m)	-5 - 40	-5 - 54	-10 - 60	0 - 79	0 - 163	22 - 182	0 - 1622

Table 5.1: Processed drone aerial images total area covered and Digital Surface Models (DSMs) resolutions for all study areas in Dominica and Cape Verde.

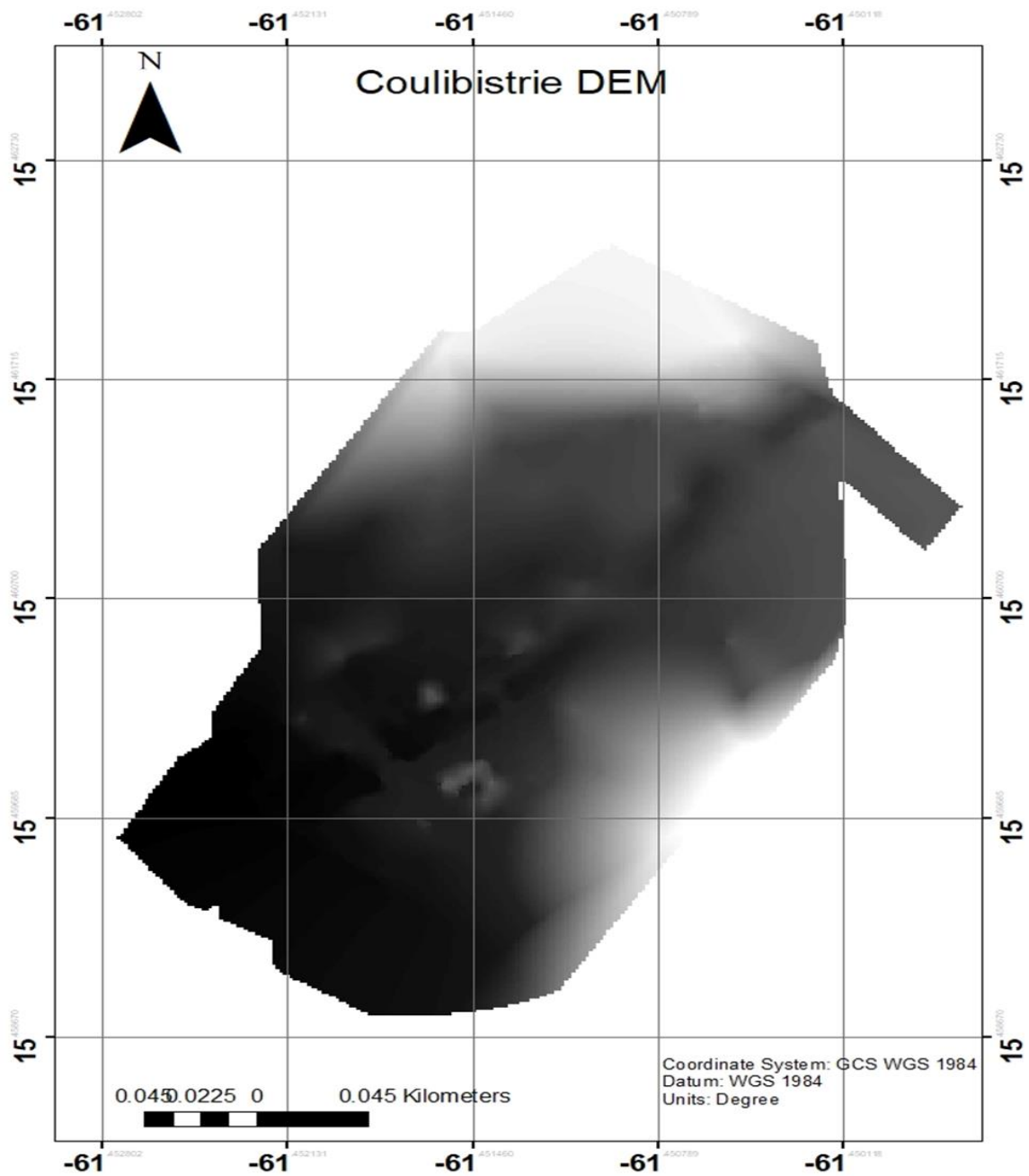


Figure 5.21: Drone-derived Digital Surface Model (DSM) for Coulibistrie showing areas of low elevation in dark and high elevation in grey.

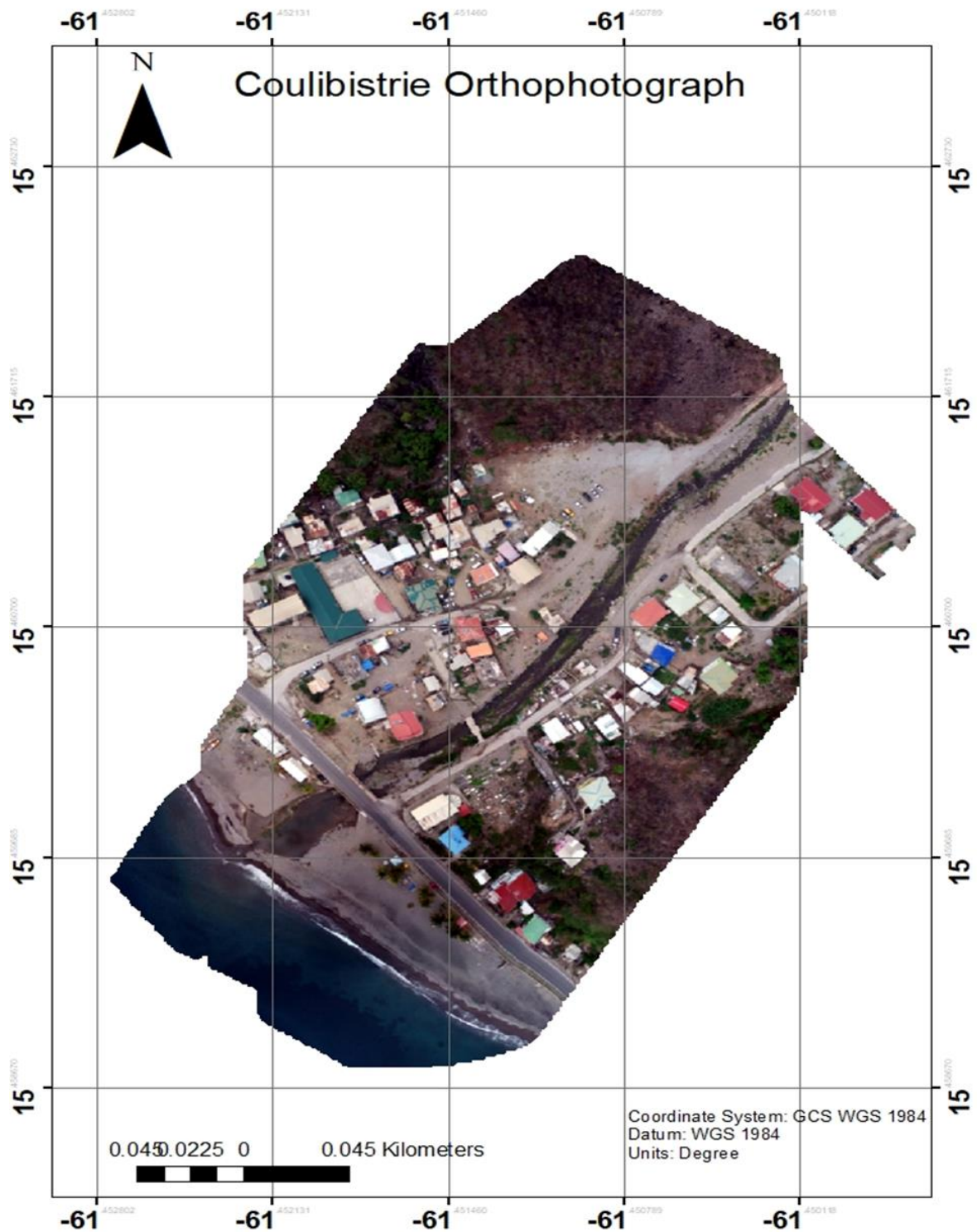


Figure 5.22: Drone-derived orthophotograph for Coulibistrie, showing destruction caused by Hurricane Maria.

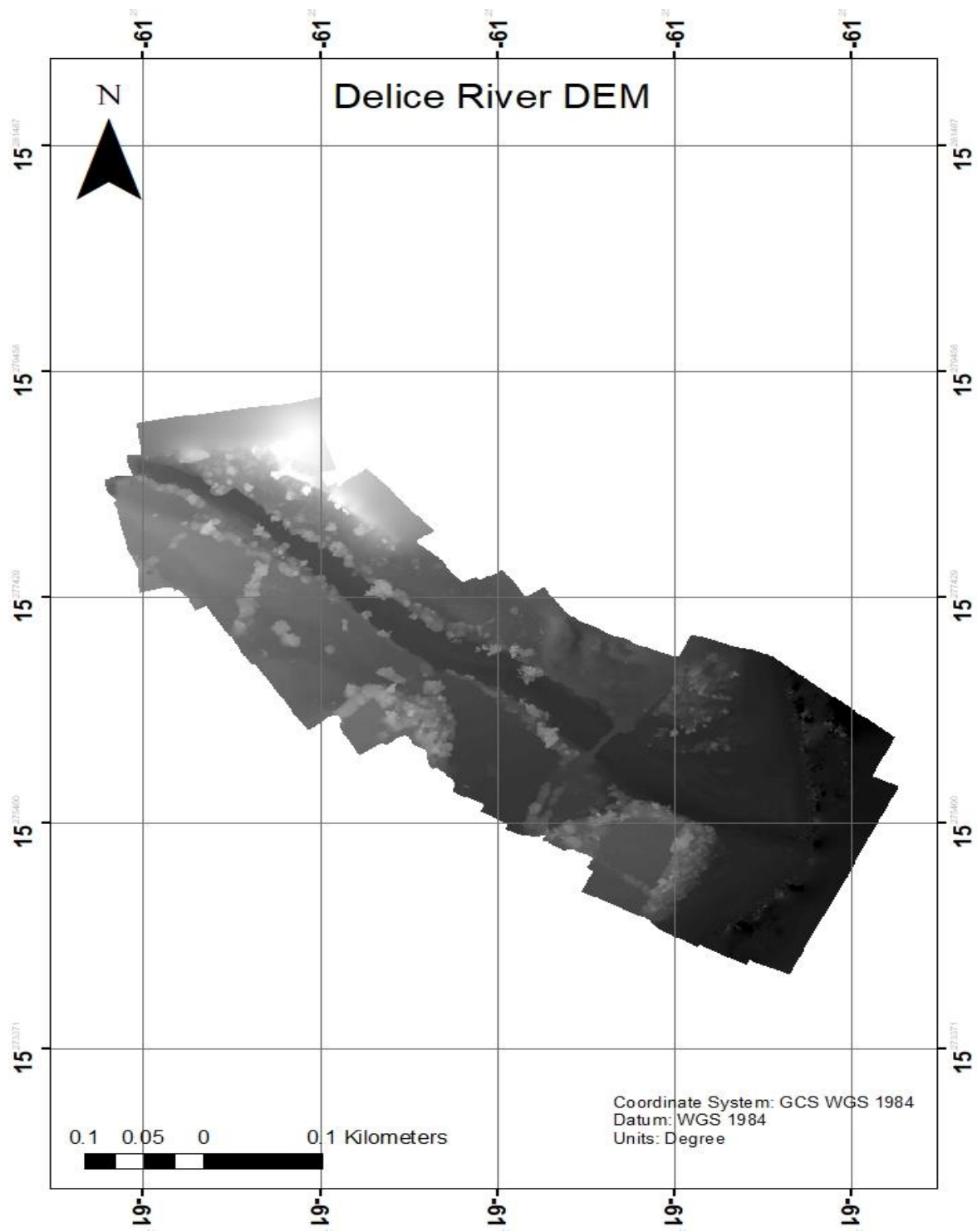


Figure 5.23: Drone-derived DSM for Delice showing areas of low elevation in dark and high elevation in grey.



Figure 5.24: Drone-derived orthophotograph for Delice, showing devastation of Hurricane Maria on infrastructure and farmlands.

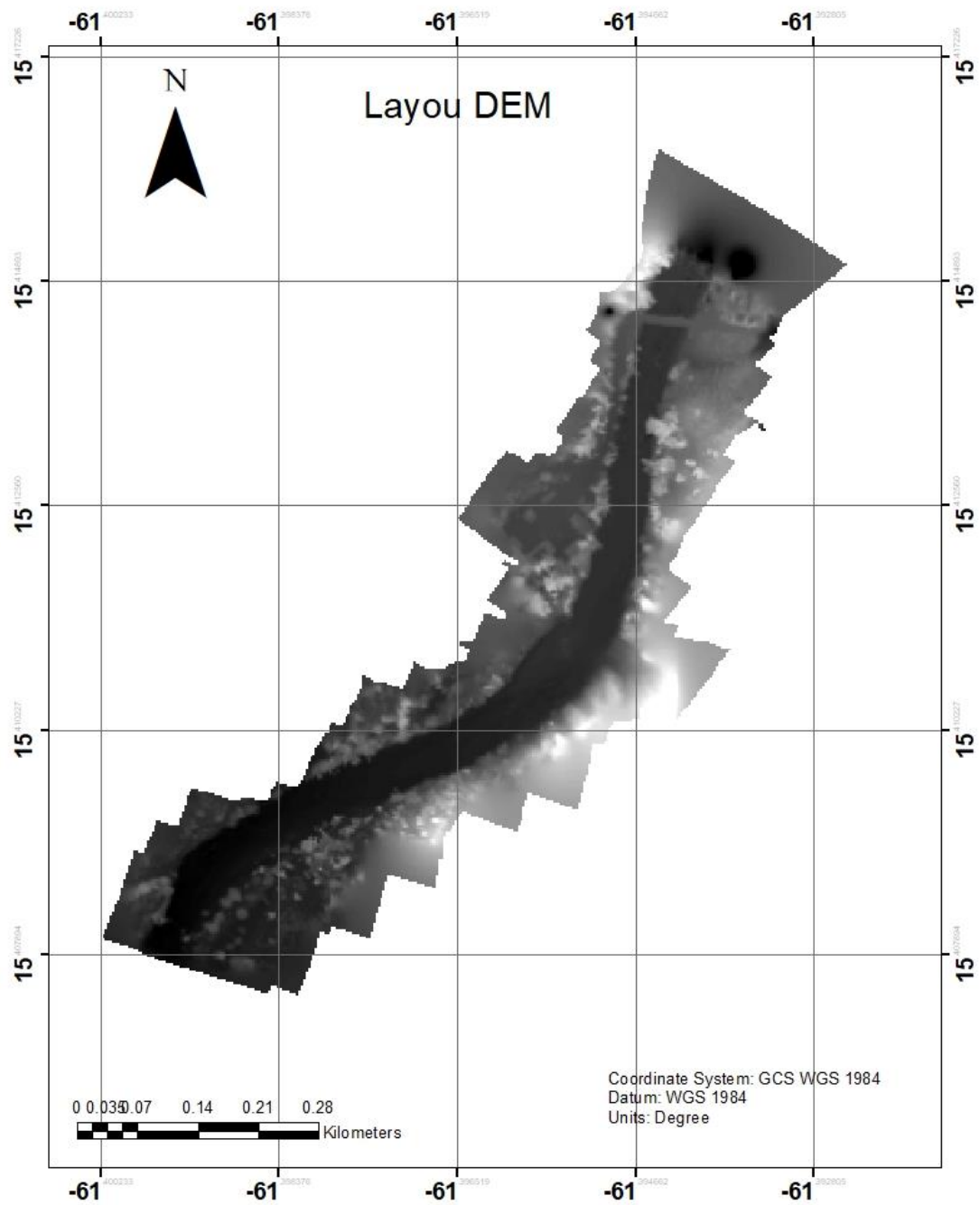


Figure 5.25: Drone-derived DSM for Layou showing areas of low elevation in dark and high elevation in grey.



Figure 5.26: Drone-derived orthophotograph for Layou, showing post-Hurricane Maria destruction

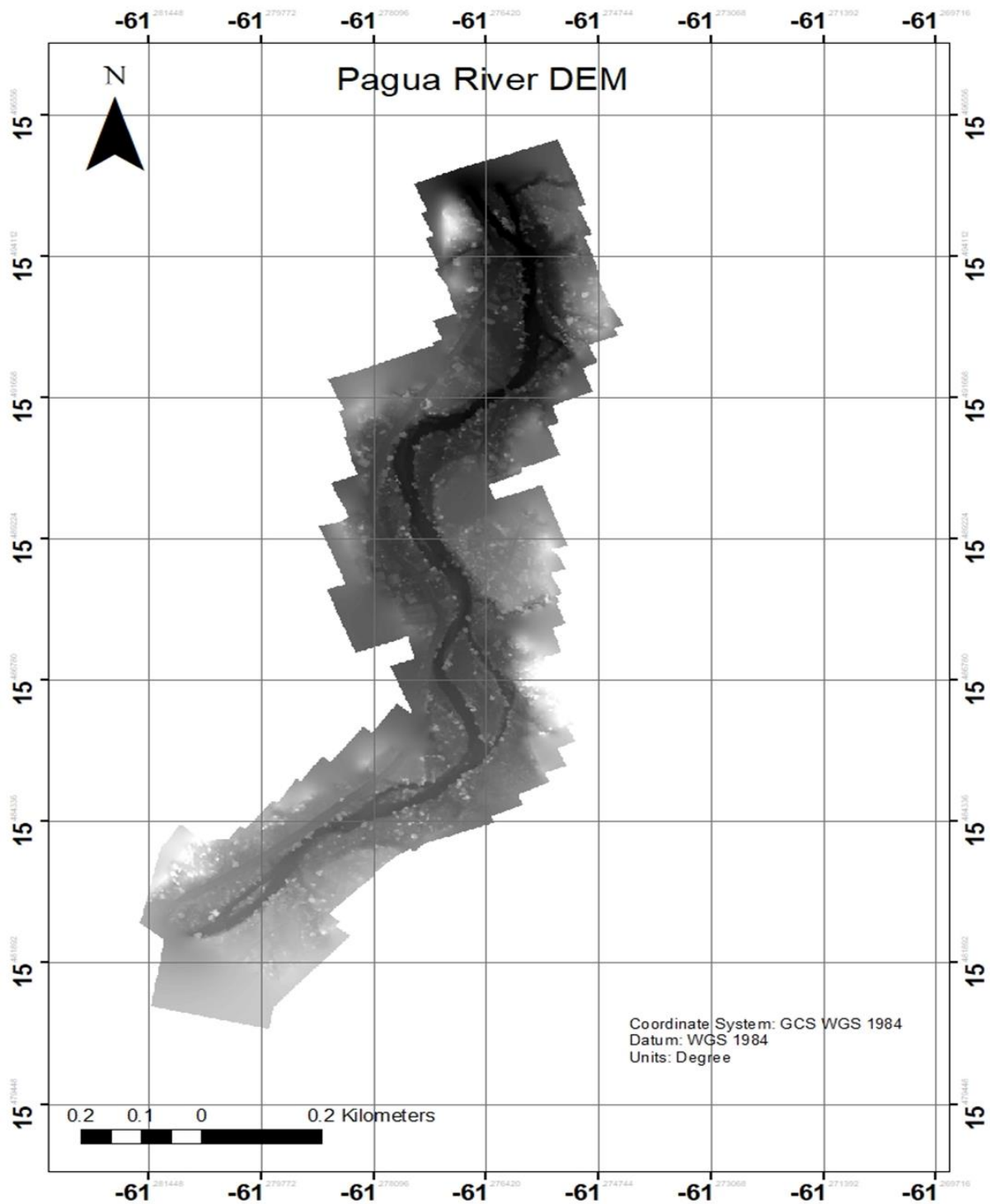


Figure 5.27: Drone-derived DSM for Pagua, showing areas of low elevation in dark and high elevation in grey.

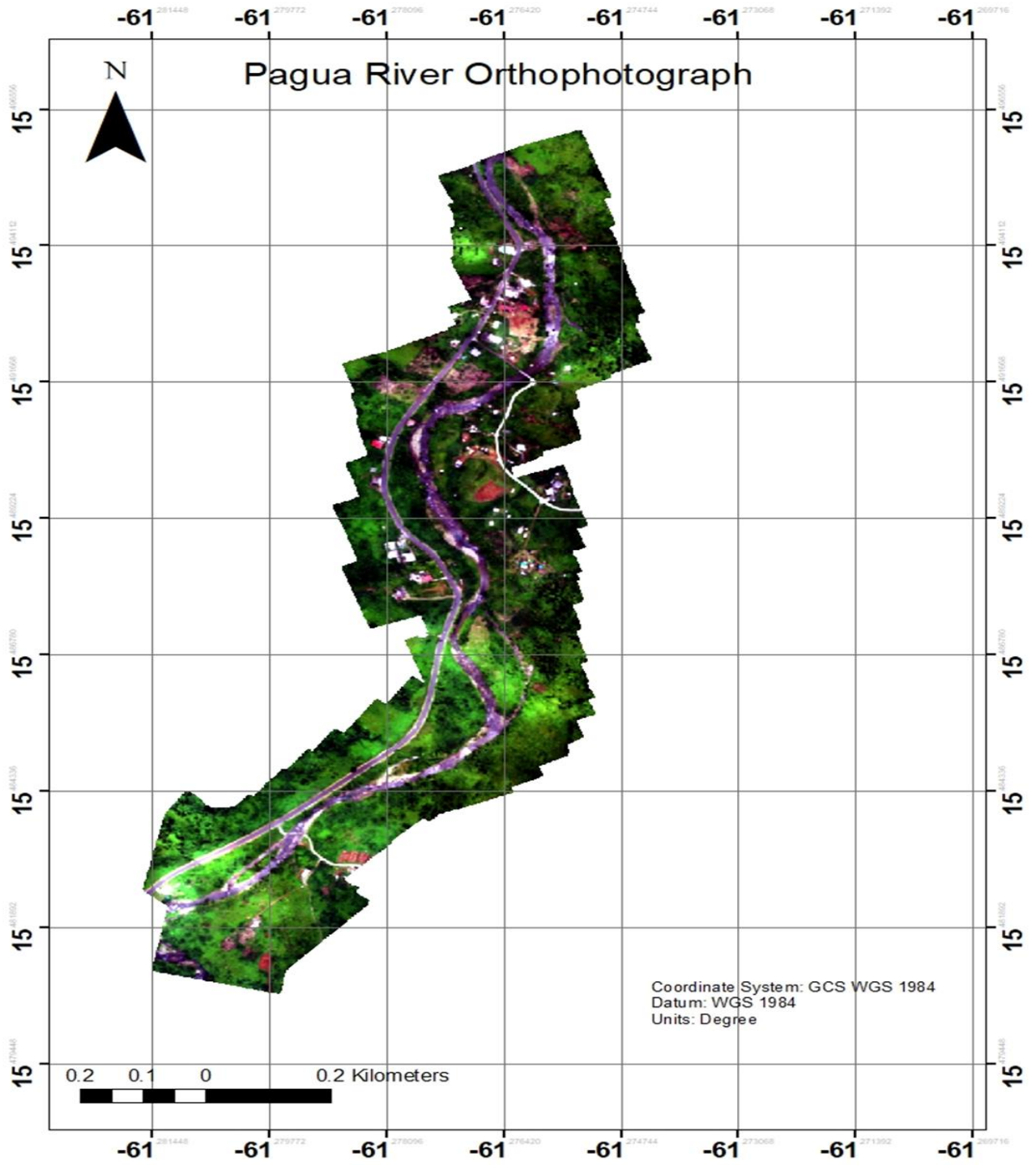


Figure 5.28: Drone-derived orthophotograph for Pagua, showing damage caused by Hurricane Maria.

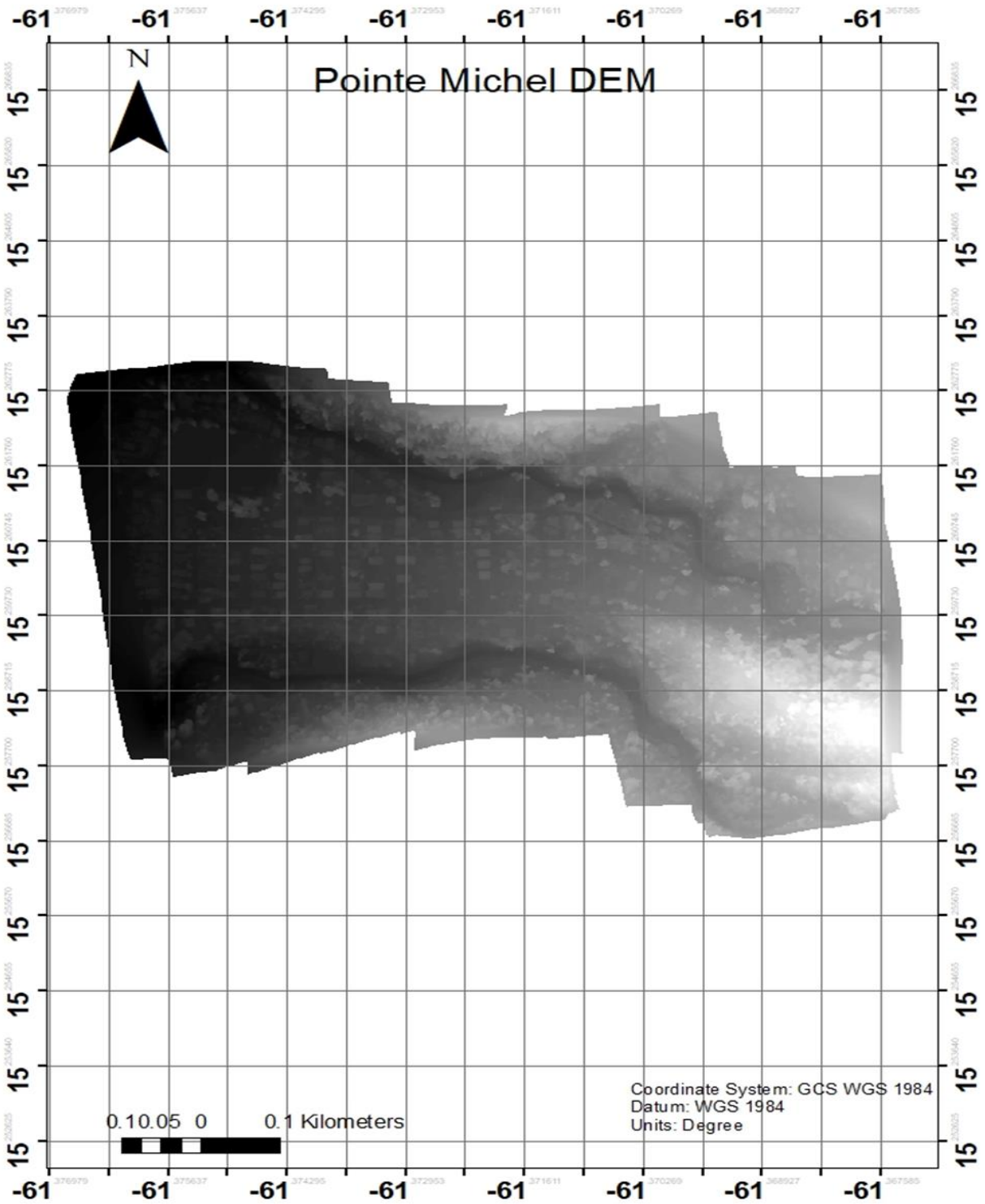


Figure 5.29: Drone-derived DSM for Pointe Michel, showing areas of low elevation in dark and high elevation in grey.

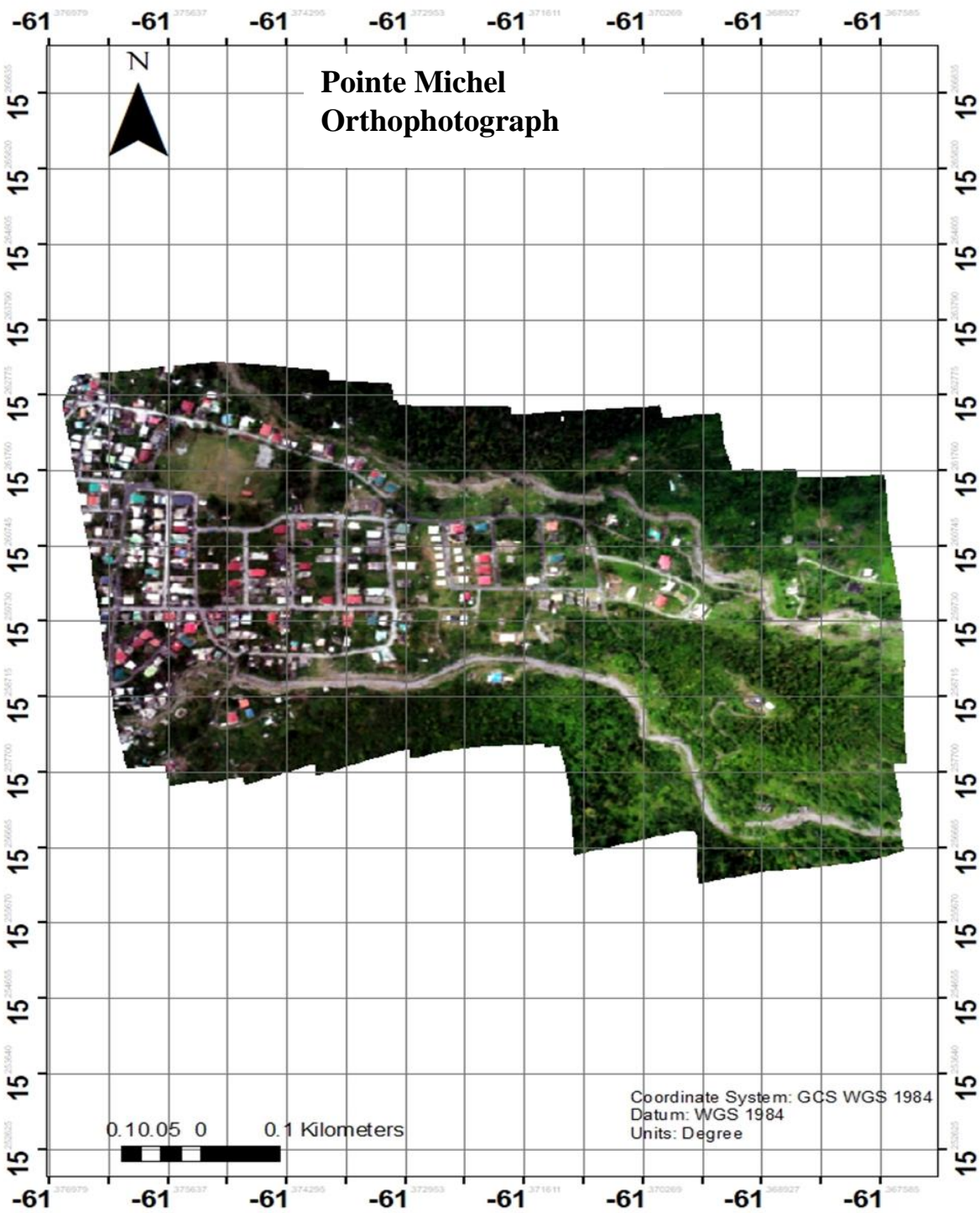


Figure 5.30: Drone-derived orthophotograph for Pointe Michel showing destruction caused by Hurricane Maria.

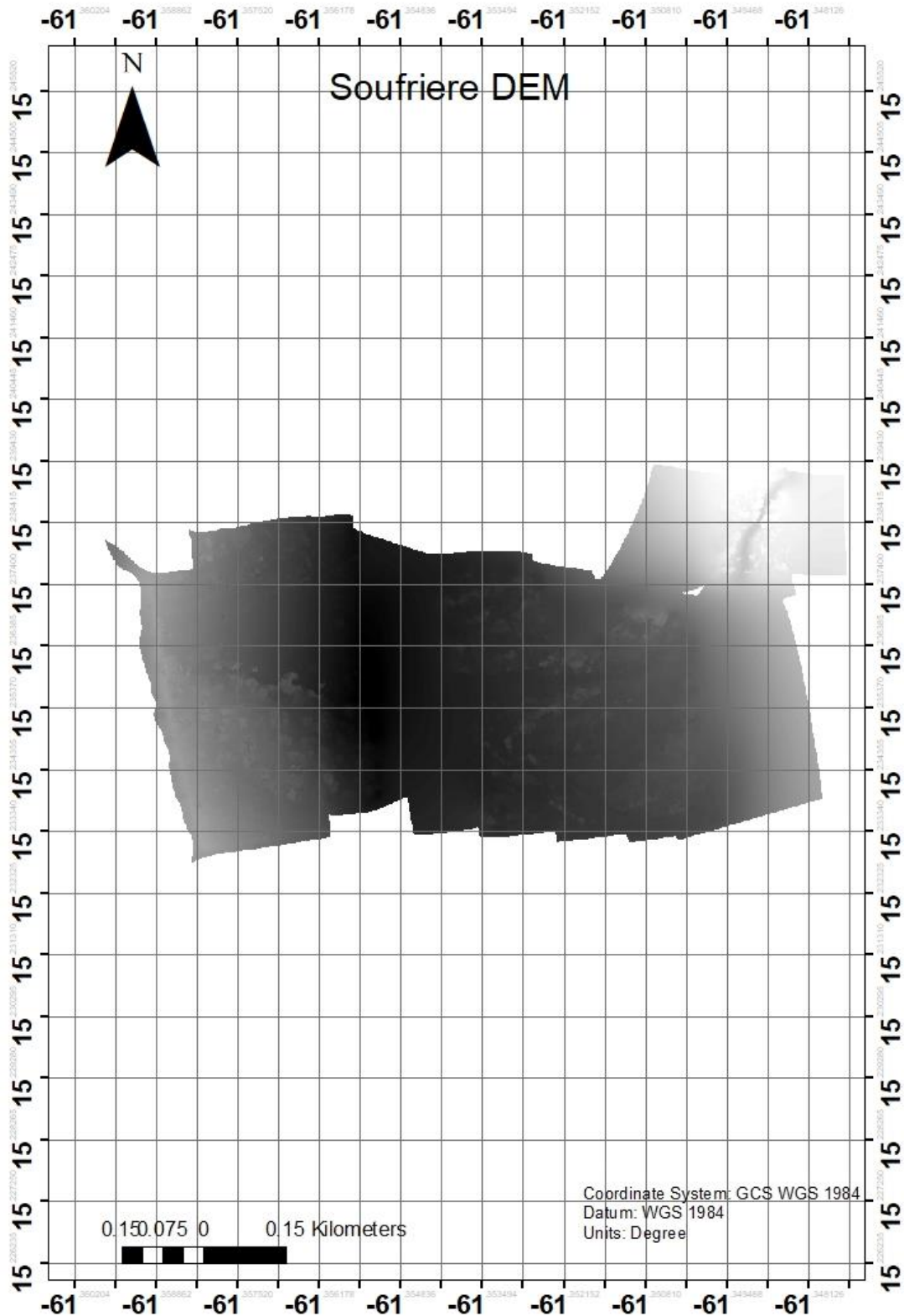


Figure 5.31: Drone-derived DSM for Soufriere showing areas of low elevation in dark and high elevation in grey.

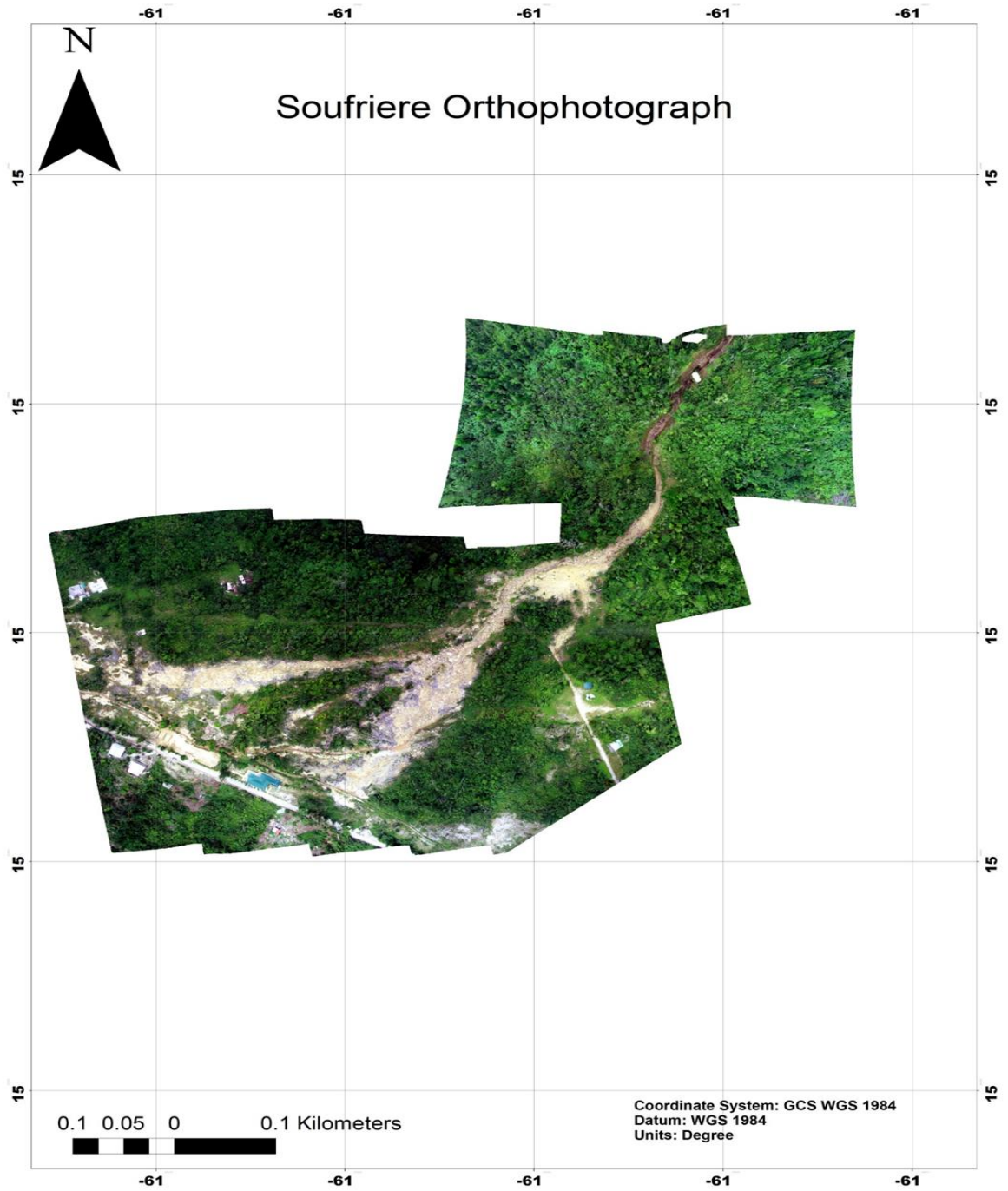


Figure 5.32: Drone-derived orthophotograph for Soufriere, showing post-Hurricane Maria devastation.

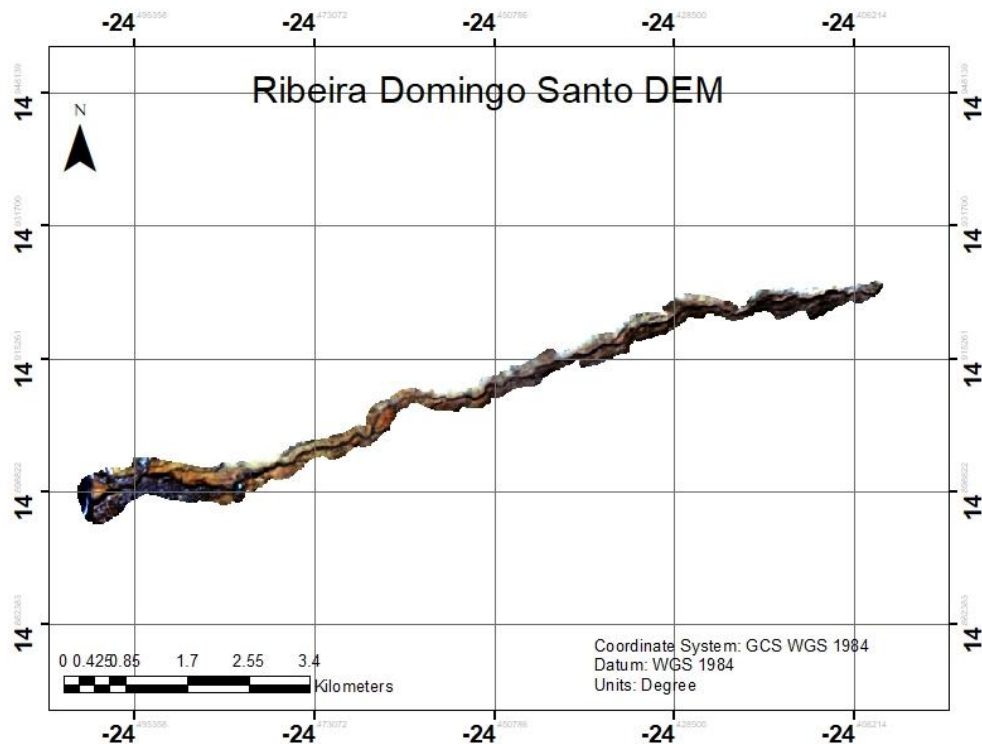
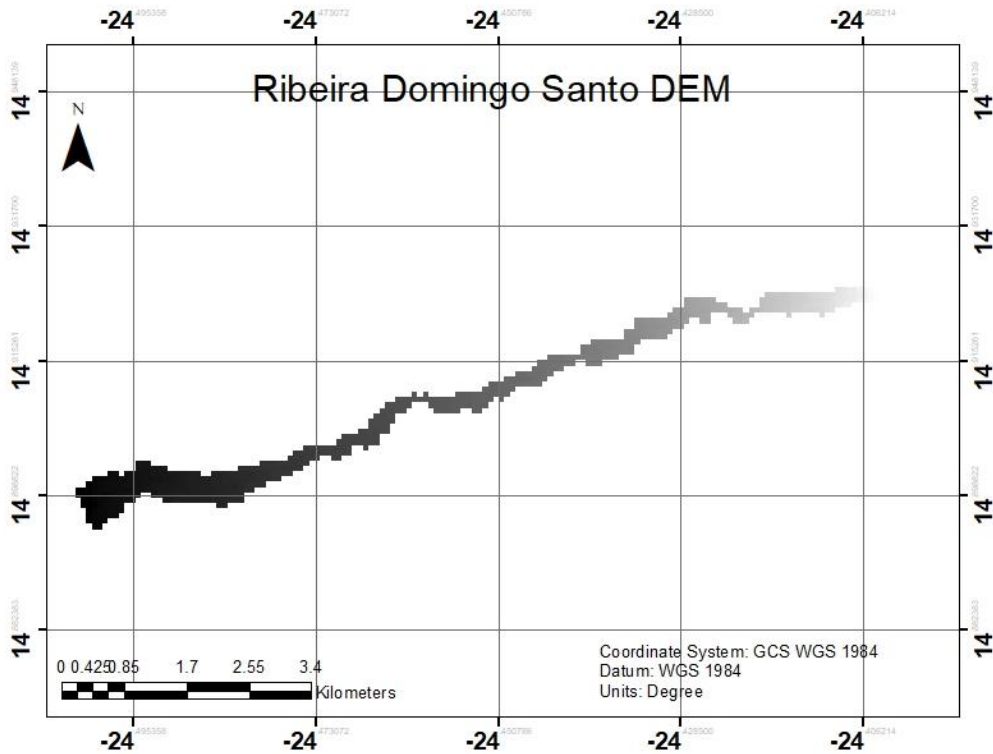


Figure 5.33: (A) Drone-derived DSM for Ribeira Santo Domingo showing areas of low elevation in dark and high elevation in grey, (B) Drone-derived orthophotograph for Ribeira Santo Domingo, showing current state and features of the terrain.

CHAPTER SIX

Modelling Results

6.0. Results of RAMMS Debris Flow Modelling

This chapter presents the results of debris flow simulations using the RAMMS software package. Before presenting the simulations, the results of a sensitivity analysis will be presented.

The sensitivity analysis was undertaken to determine how sensitive the RAMMS model is to changes in input parameters and various factors that affect the occurrence of debris flows. Although developed in Switzerland to simulate debris flows in cold Alpine environments, the developers claim that the application is suitable for debris flow simulation worldwide. To verify this claim for the environment of the studied island volcanoes, RAMMS was used to model debris flows in a single typical locality in Dominica. Changing the input parameters of the model shows how the model's outcomes are influenced by input values. Using a systematic sampling method, the values for the sensitivity analysis were chosen based on the default input parameters.

The main part of this chapter shows the results of debris flow simulations in different drainage systems using the RAMMS debris flow modelling to determine the flow volume, flow height, runout distance and flow pressure, using the DSMs provided by the drone field work in Dominica and Fogo. These simulations used the default input parameters provided by the model. The outcomes of the calibrated simulations help to map-out areas susceptible to debris flow hazard in the different parts of Dominica and in the main area of debris flow hazard in Fogo.

6.1 Sensitivity Analysis

To determine how sensitive RAMMS debris flow modelling is to changes in input parameters, sensitivity analysis was conducted. Friction coefficient (μ), turbulent friction (ξ) and earth pressure (Lambda) (λ) were the input parameters used to perform the sensitivity analysis. These three input parameters values were changed systematically from the default values whilst maintaining the other two parameters constant.

One of the study areas, Pagua River in Dominica, was used to examine how sensitive the RAMMS debris flow module is to changes in input parameters. This region is one of the smaller areas investigated in Dominica, so the length of time required for the simulations was minimised. In total 12 simulations were performed, 4 simulations for friction coefficient (μ), 4 simulations for turbulent coefficients (ξ) and 4 simulations for earth pressure (Lambda λ) (Table 6.1). The default calibrated input parameter value for friction coefficient (μ) was 0.20, turbulent coefficient (ξ) was 200 m/s² and earth pressure (Lambda λ) was 1.0 m/s². The variable input parameters include the entire range of values available in the RAMMS software: Lambda (λ) = 0.25, 0.50, 0.75 and 1; Friction coefficient (μ) = 0.05, 0.10, 0.15 and 0.20; Turbulence (ξ) = 200, 400, 600 and 800 m/s².

Study Location	Projected Area (km ²)	DSM Resolution (m)	Release Volume (m ³)	Release Height (m)	Simulation Time (s)
Pagua	2.3	7	25121	1	415.8

Table 6.1: Model calibration and input parameters used for sensitivity analysis of RAMMS simulations for example of Pagua River (Dominica).

6.1.1 Sensitivity Analysis of Turbulent Coefficient (ξ)

Figures 6.1 A and B and Table 6.2 show the simulation results for different values of the turbulent coefficient (ξ). There are clear trends in the flow runout distance, flow heights and flow volume for each value of ξ even though all simulations were performed with the same flow initiation volume of 24844 m³. The flow runout distance clearly decreases as the turbulent coefficient (ξ) value decreases and vice versa. Also, the flow heights of the simulated debris flow increases when the turbulent coefficient (ξ) value increases. Flow volumes also increase as the turbulent coefficient (ξ) increase (Figure 6.1 A and B; Table 6.2).

Turbulent coefficient (ξ) m/s²	Runout distance (m)	Flow height (m)	Flow volume (m³)	Simulation time (s)
200	652	2.87	25000	1000
400	851	2.96	25750	2500
600	1139	3.04	26700	5000
800	1982	3.07	27944	20000

Table 6.2: Model calibration and input parameters used for sensitivity analysis in RAMMS simulations for Pagua river (data in Table 6.1).

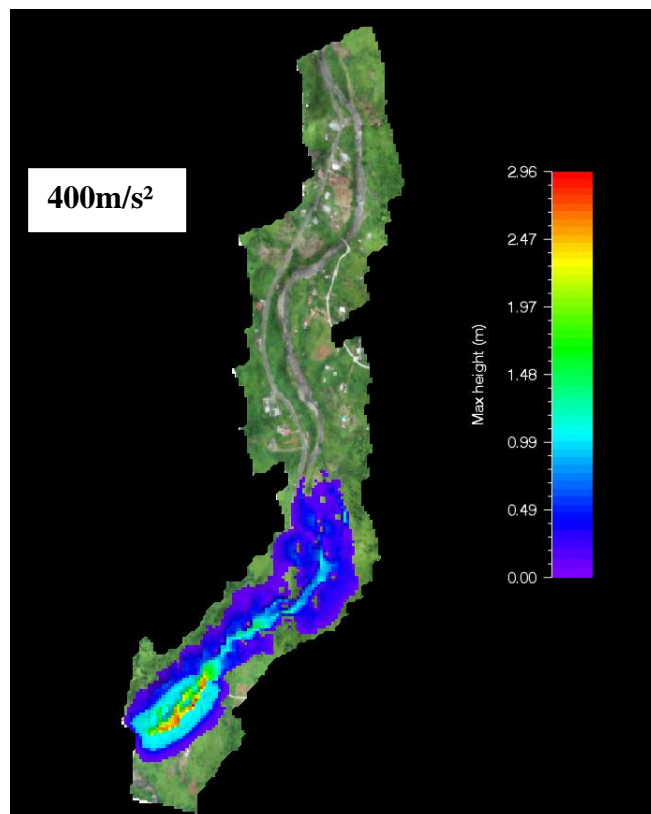
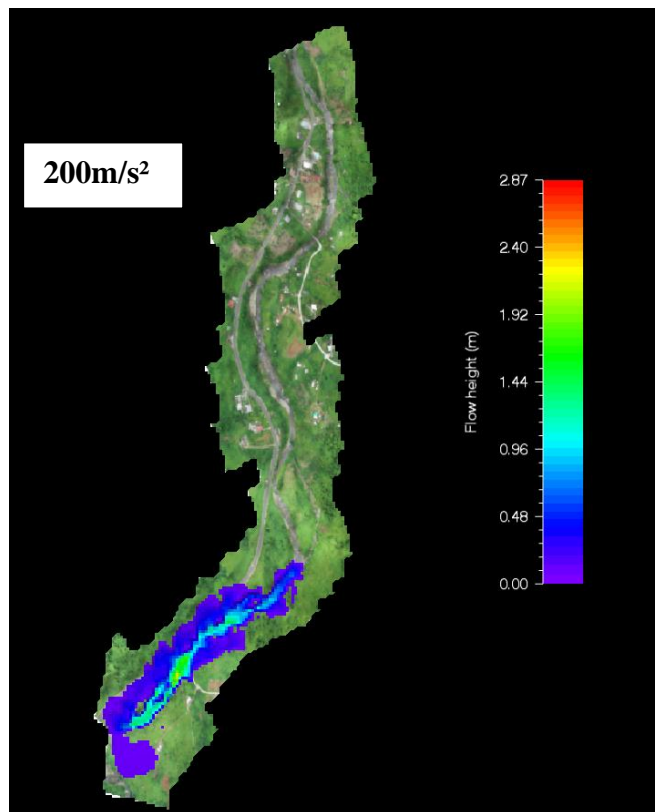


Figure 6.1 A: Sensitivity analysis of RAMMS simulations for debris flow runout distance for 200 m/s² and 400 m/s² turbulent coefficient (ξ) values (example of Pagua River, Dominica)

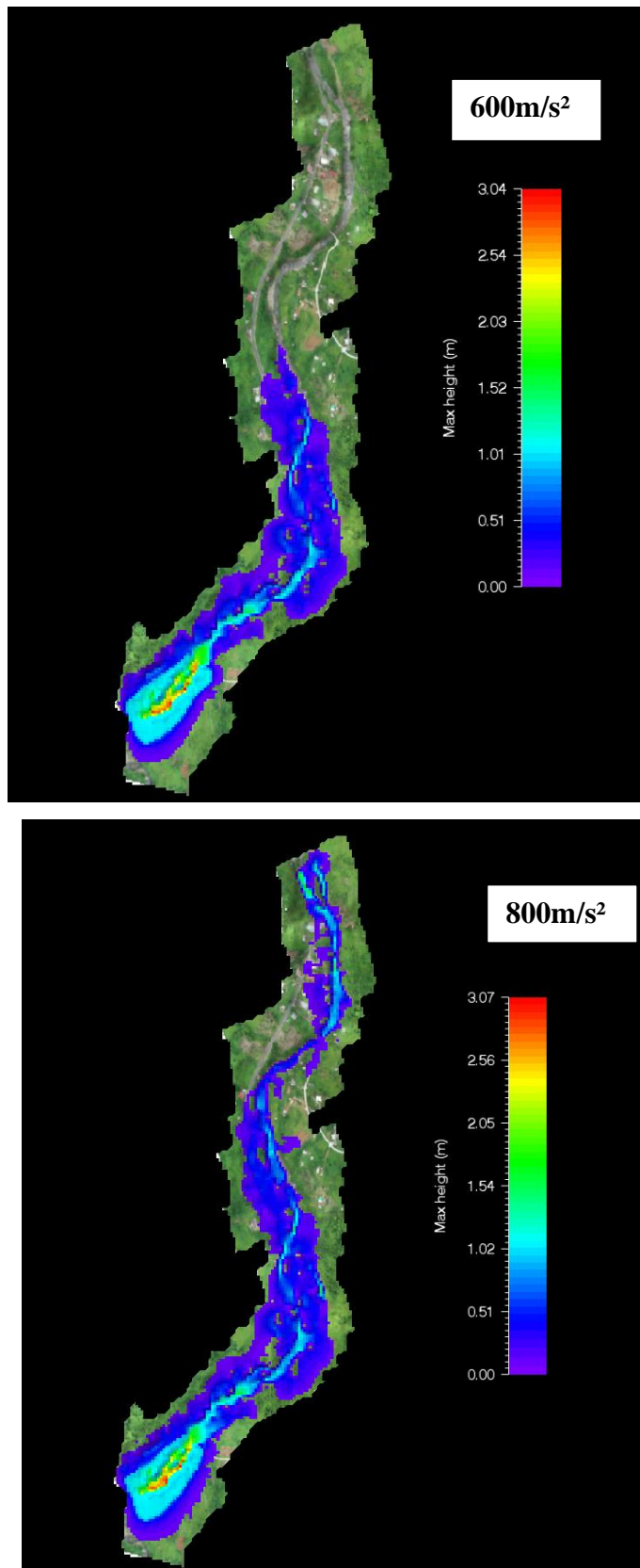


Figure 6.1 B: Sensitivity analysis of RAMMS simulations for debris flow runout distance for 600 m/s^2 and 800 m/s^2 turbulent coefficient (ξ) values (example of Pagua River, Dominica)

6.1.2 Sensitivity Analysis of Friction Coefficient (μ).

Figures 6.2 A and B and Table 6.3 show the simulation results for the four different values of the friction coefficient (μ). There are clear differences in the flow runout distance, flow heights and flow volume for each friction coefficient value, even though all simulations were performed with the same flow initiation volume. The flow runout distance decreases as the friction coefficient (μ) value increases and vice versa. Also, the heights of the simulated debris flow for the four μ values increased when the μ value decreased. Furthermore, the flow volumes increased as μ decreased and vice versa (Figures 6.2 A and B).

Friction coefficient (μ)	Runout distance (m)	Flow height (m)	Flow volume (m^3)	Simulation time (s)
0.05	1980	4.33	27659	50000
0.10	1587	3.63	27389	5000
0.15	831	3.12	27056	2000
0.20	506	2.91	26539	700

Table 6.3: Model calibration and input parameters used for RAMMS sensitivity simulation for four different values of the friction coefficient.

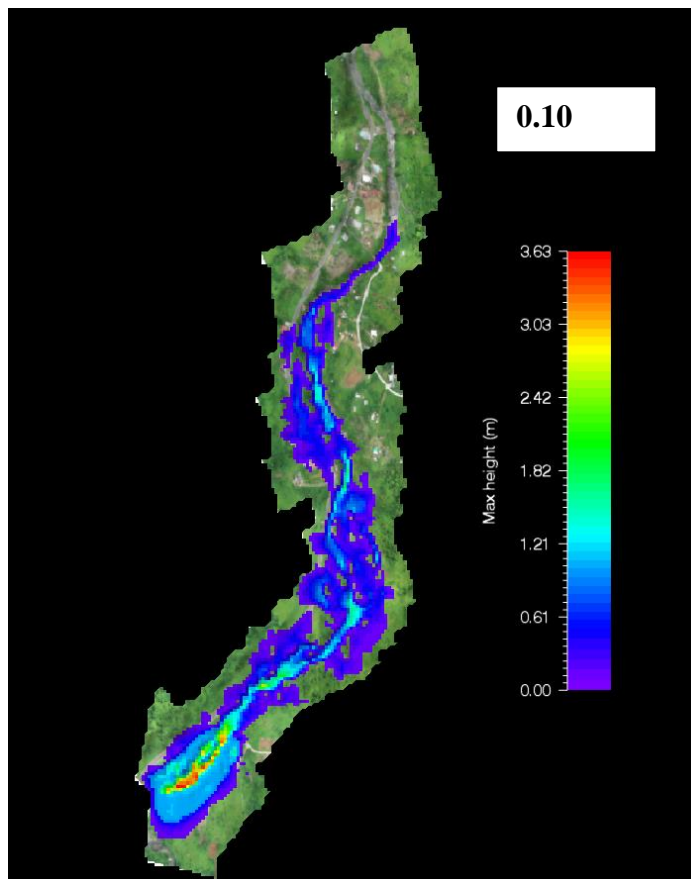
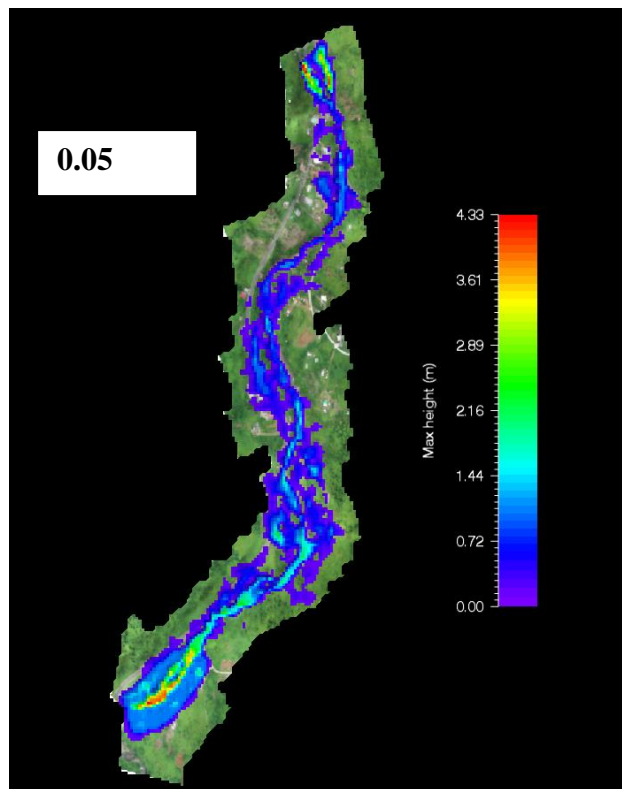


Figure 6.2 A: Results of RAMMS sensitivity analysis simulations of debris flow runout distance for 0.05 and 0.10 friction coefficient (μ) values (example of Pagua river, Dominica)

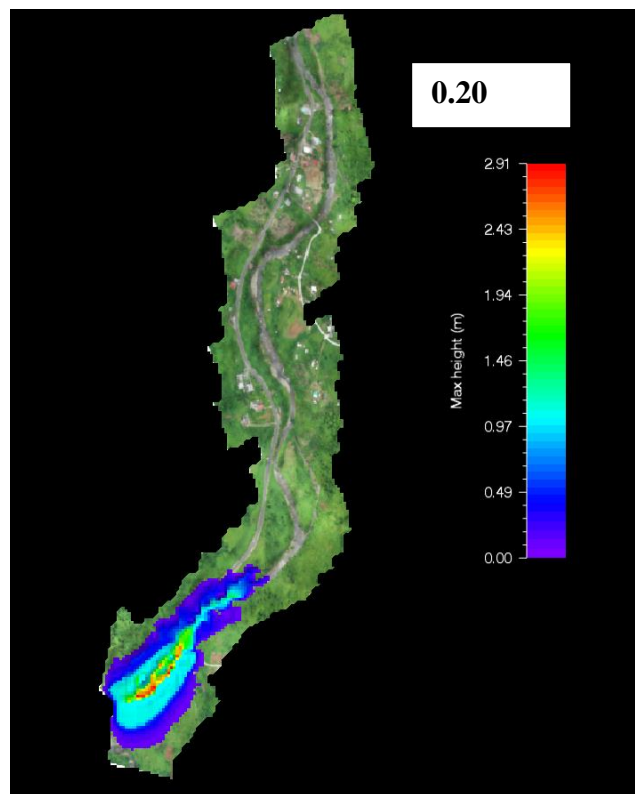
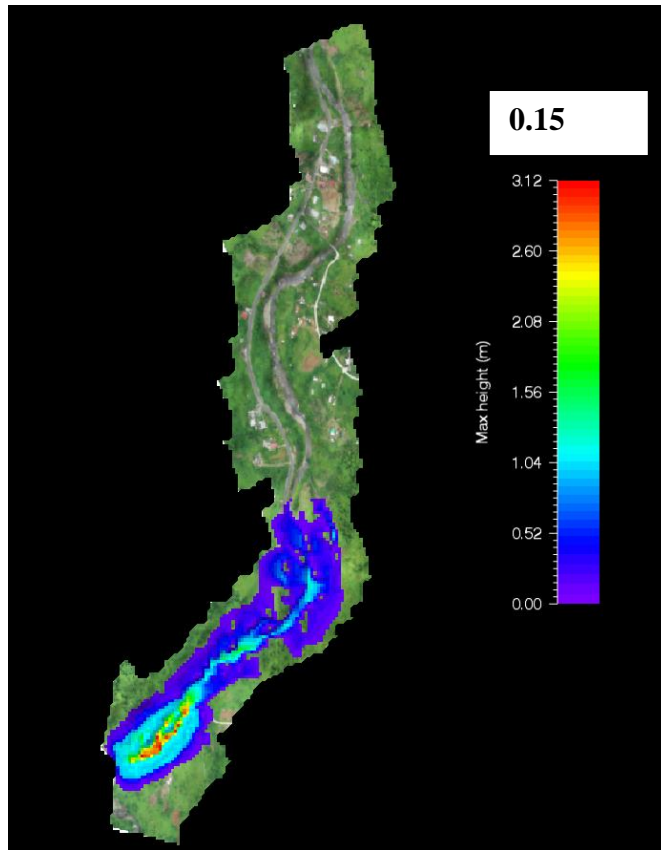


Figure 6.2 B: Results of RAMMS sensitivity analysis simulations of debris flow runout distance for 0.15 and 0.20 friction coefficient (μ) values (example of Pagua river, Dominica)

6.1.3 Sensitivity Analysis of Earth Pressure (Lambda) (λ)

Figures 6.3 A and B and Table 6.4 show the simulation results for different values of earth pressure (Lambda) (λ). Differences were seen in the flow runout distance, flow heights and flow volume for each earth pressure value, even though all simulations used the same flow initiation volume of 25065 m³. The flow runout distance increases as Lambda (λ) decreases and vice versa. Also, the flow heights for the four different earth pressure values are different. The heights of the simulated debris flow increase when the earth pressure (Lambda) (λ) value decreases and vice versa. The flow volumes also increase with increasing earth pressure (Lambda) (λ) (Figure 6.3 A and B).

Earth Pressure (Lambda)	Runout distance (m)	Flow height (m)	Flow volume (m ³)	Simulation time (s)
0.25	746	5.96	29392	5430
0.50	867	3.68	29627	5926
0.75	1992	2.96	29705	25000
1.00	2000	2.88	30188	27000

Table 6.4: Model calibration and input parameters used for RAMMS sensitivity analysis simulations for four different values of earth pressure (Lambda) (λ).

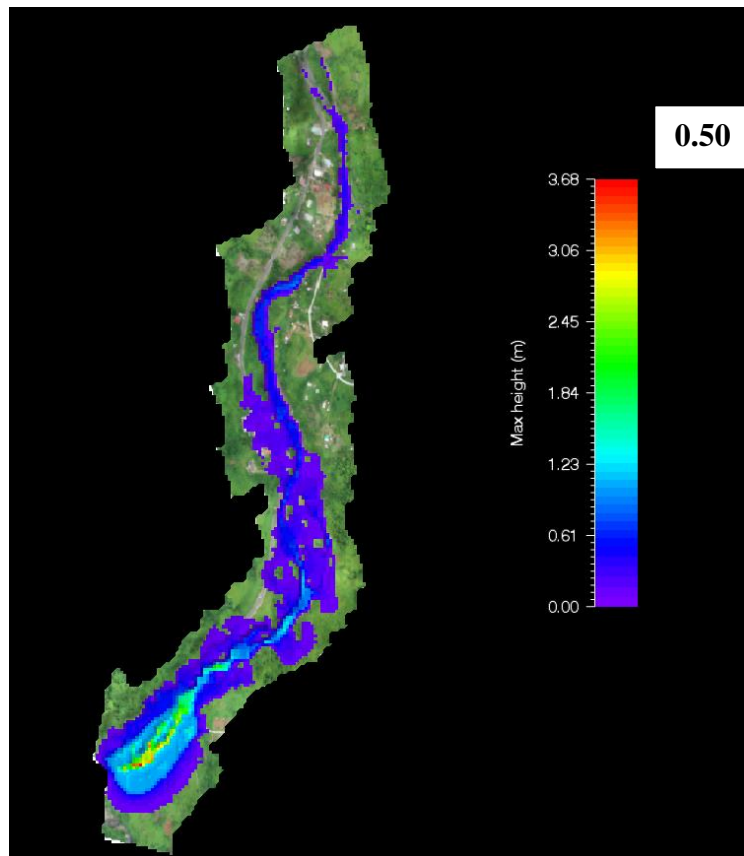
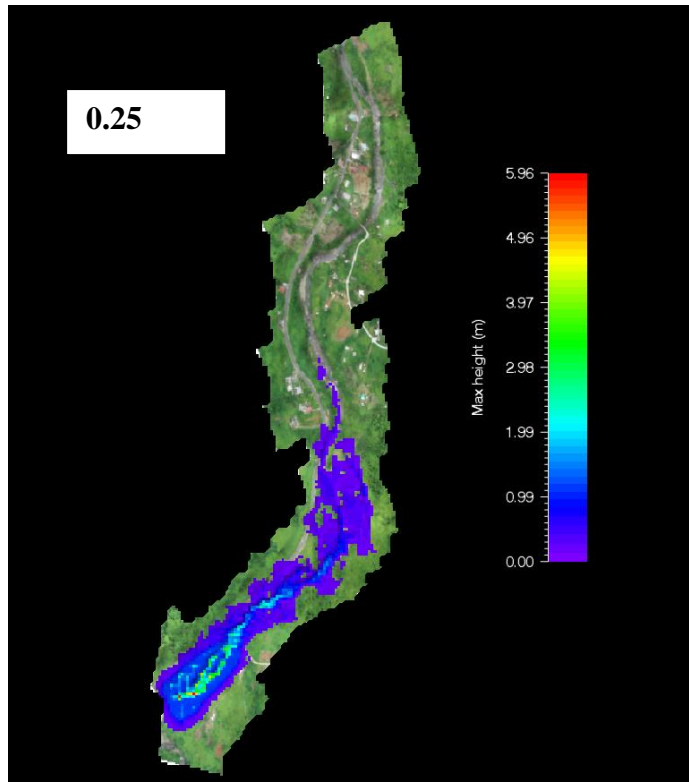


Figure 6.3 A: Results of sensitivity analysis of RAMMS debris flow modelling, showing variations in the runout distance for 0.25 and 0.50 earth pressure (Lambda) (λ) values.

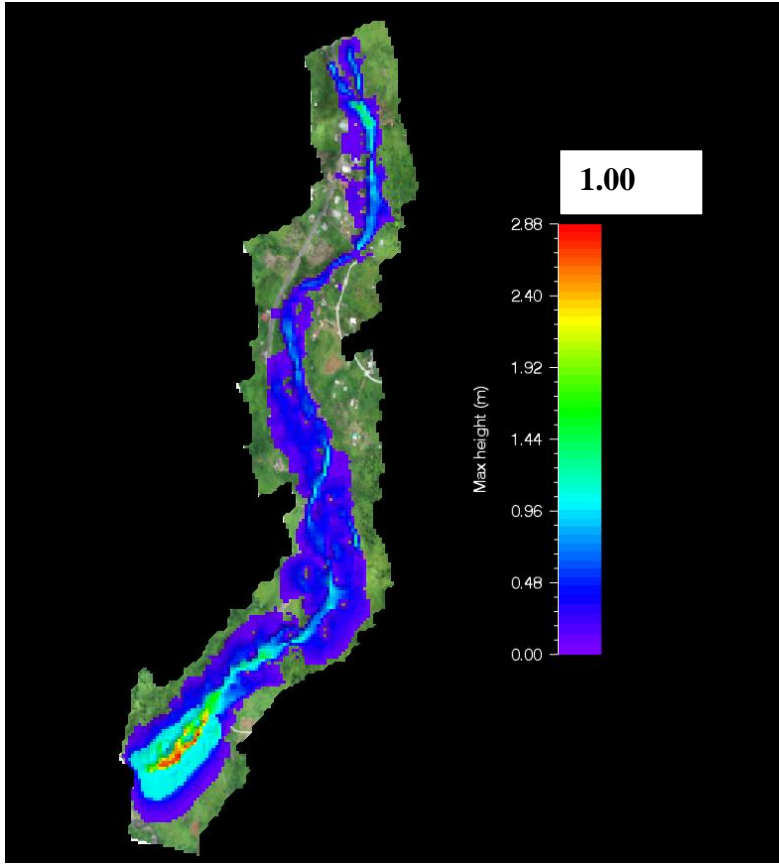
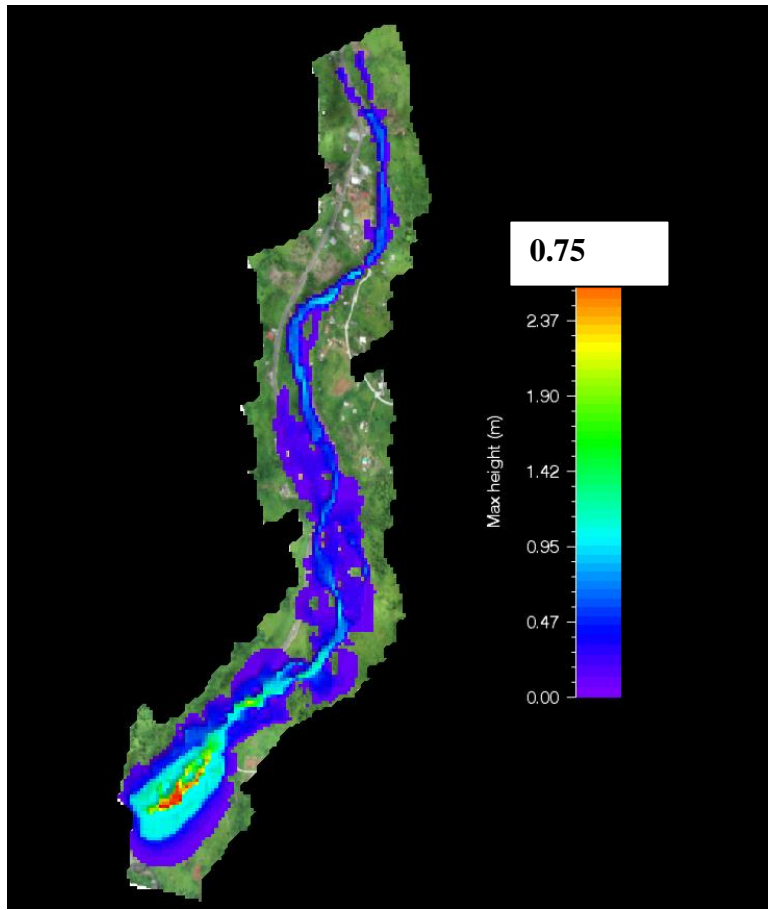


Figure 6.3 B: Results of sensitivity analysis of RAMMS debris flow modelling, showing variations in the runout distance for 0.75 and 1 earth pressure (Lambda) (λ) values.

From the results of the sensitivity analysis described above, it is clear that all of the parameters can affect the outcome of the RAMMS modelling. The default parameter value for friction coefficient (μ) has been set to the highest value (0.20), whereas the default turbulent coefficient (ξ) is set to the lowest value (200 m/s²). The default earth pressure (Lambda) is 1.0, which is the highest value.

6.2. Model Calibration

The calibrated simulations of debris flow for various study localities in Dominica and Cape Verdes (Chapter 3) are presented here. Results of the debris flow simulations are presented as maps and graphs showing flow height, flow velocity, flow pressure, flow direction and flow volume. Also, simulation time, DSM resolution, initiated flow volume, density and region projection for all study areas are presented (Table 6.5). Due to the lack of past debris flow data, release flow volume was chosen based on the total area of each locality as any volume larger than the terrain's DEM will not work in RAMMS. Also, the input hydrograph release method was used because all the study areas had channelised debris flow which is suitable for the model unlike the block release which is more appropriate for unchanneled debris flows. For all simulations, the input parameters were: Lambda = 1; friction (ξ) = 0.20; turbulent (μ) = 200 m/s². RAMMS has never been used for debris flow modelling in Dominica or other Lesser Antilles volcanic islands so it was difficult to choose a suitable calibration for the study. However, the default calibrated input parameters were used for this study because other research works in volcanic terrains used the same calibration for debris flow simulation (Frey et al, 2016; Rodriguez-Morata et al, 2019).

Study Location	Area (km ²)	DSM Resolution (m)	Release Volume (m ³)	Release Height (m)	Simulation Time (s)	Slope angle (°)
Coulibistrie	2.8	5	1576	1	515	23
Delice	2.5	2	17733	1	5859	15
Layou	1.7	3	20700	1	29000	11
Pagua	2.3	7	25121	1	416	32
Pointe Michel North	1.6	7	8755	1	1000	35
Pointe Michel South	1.6	7	8158	1	2435	30
Soufriere	1.3	6	22532	1	2000	55
Ribeira Santo Domingo (Fogo)	86.7	15	127650	1	2371	66

Table 6.5: Model calibration and input parameters used for RAMMS debris flow simulation for all study areas.

6.2.1 Coulibistrie Debris Flows Simulation

All results for the RAMMS modelling of debris flows in Coulibistrie are shown in Figure 6.4 and Table 6.6. Flow height was highest in the flow release area in the upper part of the channel and decreased gradually in the middle to the lower parts of the channel (Figure 6.4A). Flow velocity diminished down the channel, high velocities were recorded at the flow release area and low velocities at the flow deposition area (Figure 6.4B). Flow velocity was highest in the channel-bed and north-west of the channel (Figure 6.4B). The areas with highest pressure are seen in the upper part of the channel, specifically the right bank of the river channel (Figure 6.4C). Most of the impact pressures were within the channel bed with activities at the right bank and inland. Flow pressure drastically decreased downstream (Figure 6.4C).

Channel Parts	Runout Distance (m)	Flow Height (m)	Flow Velocity (m/s)	Flow Pressure (kPa)
Upper channel	47	2.2 - 2.7	3.54 - 5.31	11.83 – 56.48
Middle Channel	86	1.2 - 2.2	1.77 - 3.54	0.7 – 11.83
Lower channel	320	0.01 - 1.2	0.01 - 1.77	0.01 - 0.7

Table 6.6: Coulibistrie RAMMS simulation results showing runout distance, flow heights, flow velocities and flow pressure of various areas of the channel.

Total eroded volume after the simulation was 20 m³ and entrainment predominantly occurred at the flow initiation area (Figure 6.4D). Entrainment occurred mainly in the channel bed, at the upper part of the channel. Each cell contains basal shear stress which determines the rate at which sediments are eroded during the simulation. Small debris flows with low velocity are unlikely to cause entrainment unless the critical shear stress of the surface is reached. The channel contained sand, gravels, cobbles and boulders coupled with tree debris and concrete blocks. Total depositional volume of the simulation was 1535 m³ with a total runout distance of 452 m (Figures 6.4 E and F). This is a decrease of 55 m³ from the total flow volume of 1595 m³ representing 0.3% of the flow volume. Flow direction was north-west of the channel. Most of the flow went under the bridge and deposited downstream into the sea forming an alluvial fan (Figure 6.4E). Some material was deposited behind the bridge and top of the bridge as a result of debris blocking the bridge. The rest of the flow was deposited around the inland buildings, northwest of the channel. Momentum of the flow decreased with time (Figure 6.4F).

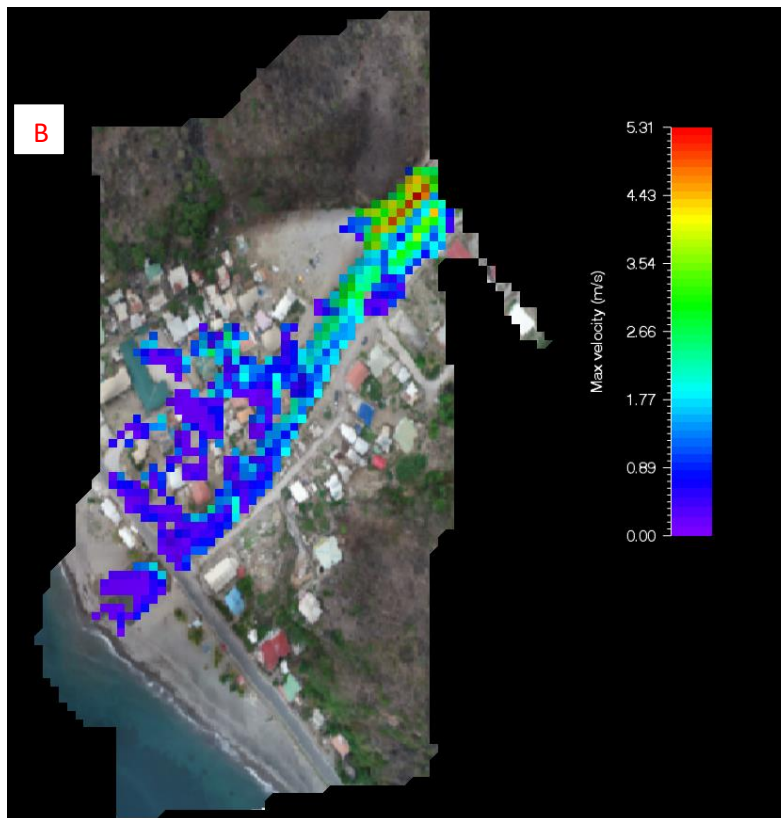
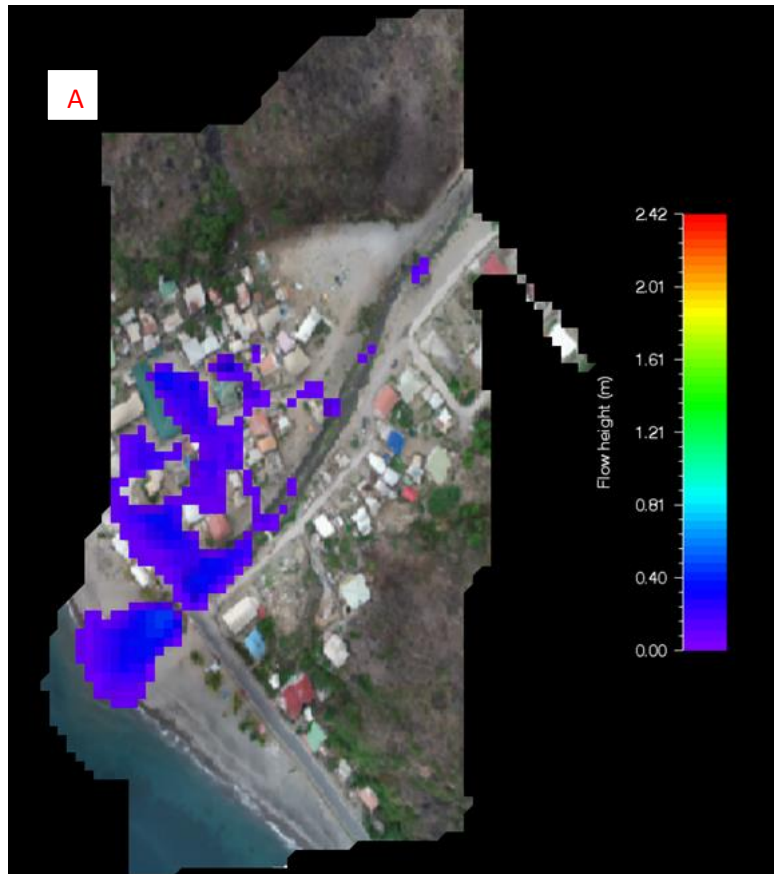


Figure 6.4: Results of RAMMS debris flow modelling for Coulibistrie (Dominica), (A) Variations in flow height (in m); (B) flow velocity (in m/s) over the whole drainage area.

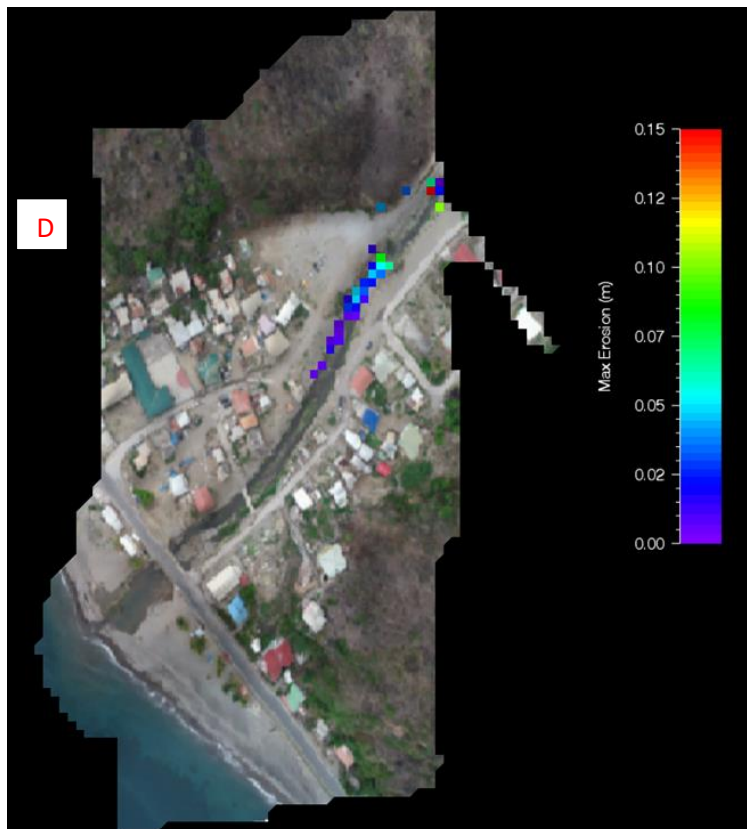
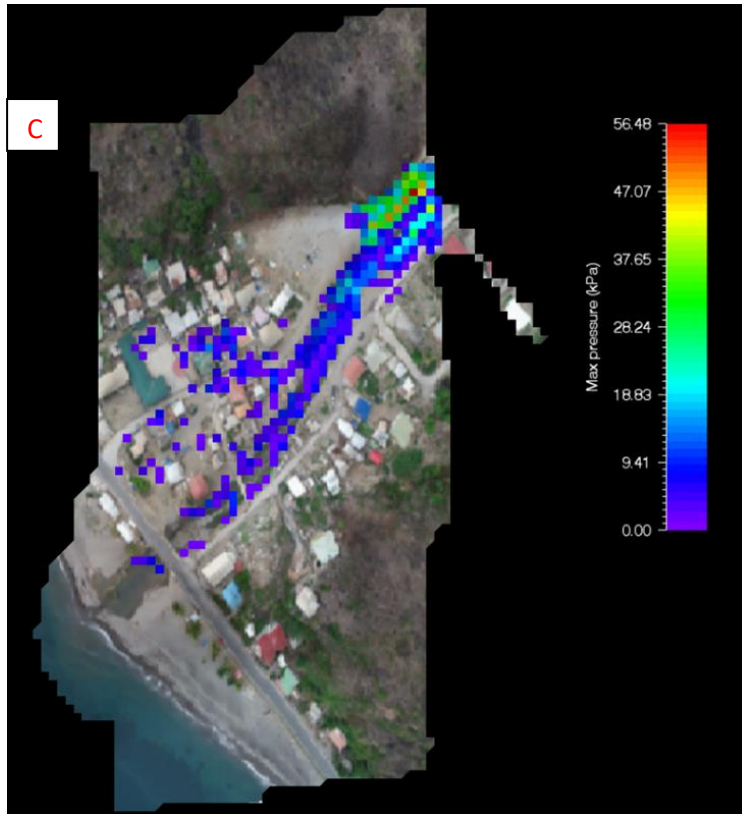


Figure 6.4: Results of RAMMS debris flow modelling for Coulibistrie (Dominica), (C) flow pressure (in kPa), (D) flow entrainment (in m³) over the whole drainage area.

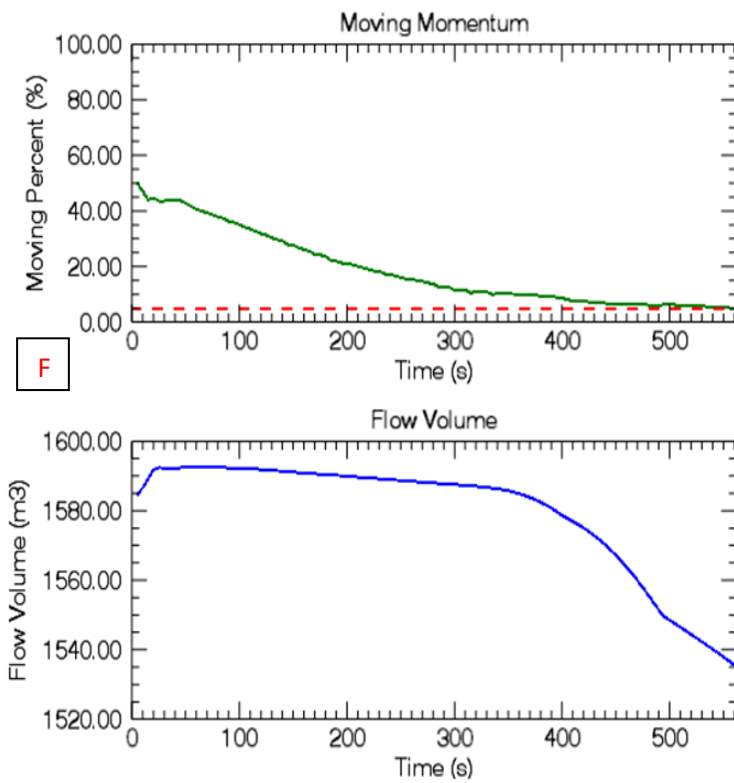
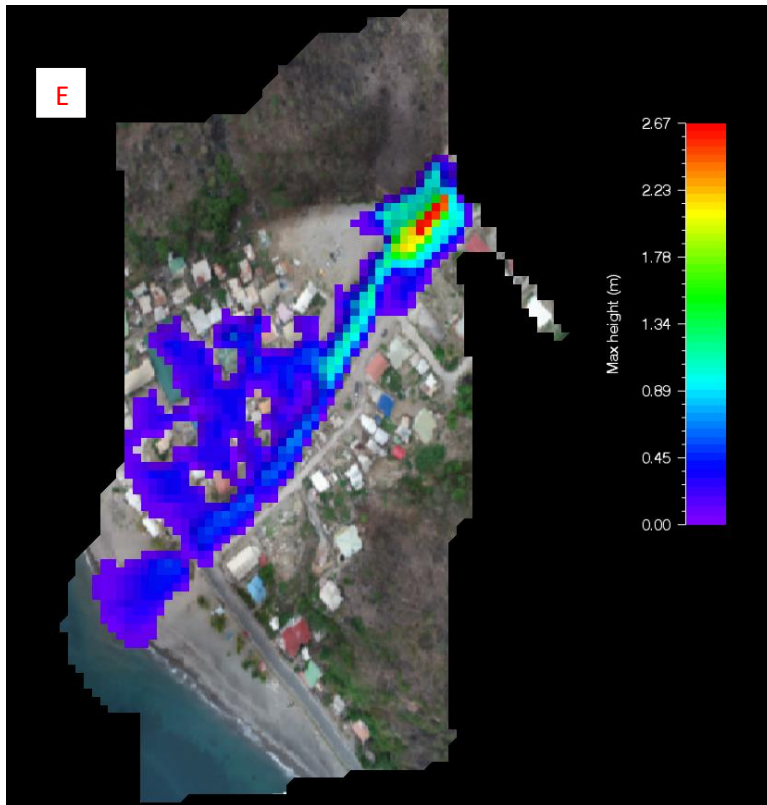


Figure 6.4: Results of RAMMS debris flow modelling for Coulibistrie (Dominica); (E) flow deposition (in m³) and (F) flow momentum (in m/s) over the whole drainage area.

6.2.2 Delice Debris Flows Simulation

Results for the Delice debris flow simulations are given in Figure 6.5 and Table 6.7. The flow height of simulation was maximum at the flow deposition area downstream. Flow height was minimum at the flow transition zone (Figure 6.5A). Velocity of the flow diminished as the flow went down the channel. High velocities were recorded at the flow release area and the low velocities were recorded at the flow deposition area (Figure 6.5B). Flow velocity was highest in the upper part of channel and direction of the velocity was south-west of the channel. High pressure areas were at the upper part of the channel, specifically the left and right banks of the channel. The highest impact pressures areas were around the floodplains and banks of the channel with minor activities in the river-bed (Figure 6.5C).

Channel Parts	Flow Distance (m)	Flow Height (m)	Flow Velocity (m/s)	Flow Pressure (kPa)
Upper channel	136	2.4 - 5.5	4.6 - 13.8	64 - 255
Middle channel	306	0.01 - 2.4	2.3 - 4.6	23 - 64
Lower channel	200	11 - 17.6	0.01 - 2.3	0.01 - 23

Table 6.7: Delice RAMMS simulation results showing runout distance, flow heights, flow velocities and flow pressure in different parts of the channel.

Total entrainment volume after the simulation was 17204.3 m³ and entrainment activities mainly occurred at the flow transition zone, mainly in the channel bed in the middle of the channel (Figure 6.5D). The channel contained sand, gravels, cobbles and boulders coupled with tree debris and hydrothermally altered clay.

Depositional volume of the simulation was 7,639 m³ and total flow volume of 34,937 m³ (Figure 6.5E). That is a decrease of 27,298 m³ from the total flow volume of 34,937 m³ representing 22% of the total flow volume (Figure 6.5E). The flow direction was south-west

of the channel. Most of the flow was deposited behind the bridge as a result of debris blocking the bridge. Some sediments went under the bridge and deposited downstream into the Atlantic Ocean. A volume of 296 m³ of the flow was deposited at the right floodplain of the channel at flow release area.

Momentum of the flow decreased and increased with the flow down the channel (Figure 6.5F). The flow momentum was high at the release zone, decreasing at the transition zone and rising at the deposition zone. The flow volume also increased rapidly from 18,000 m³ to 31,000 m³ within 300s (Figure 6.5F). The flow volume was high at the flow initiation zone, decreasing through the transition zone and then remaining relatively unchanged to the point of deposition.

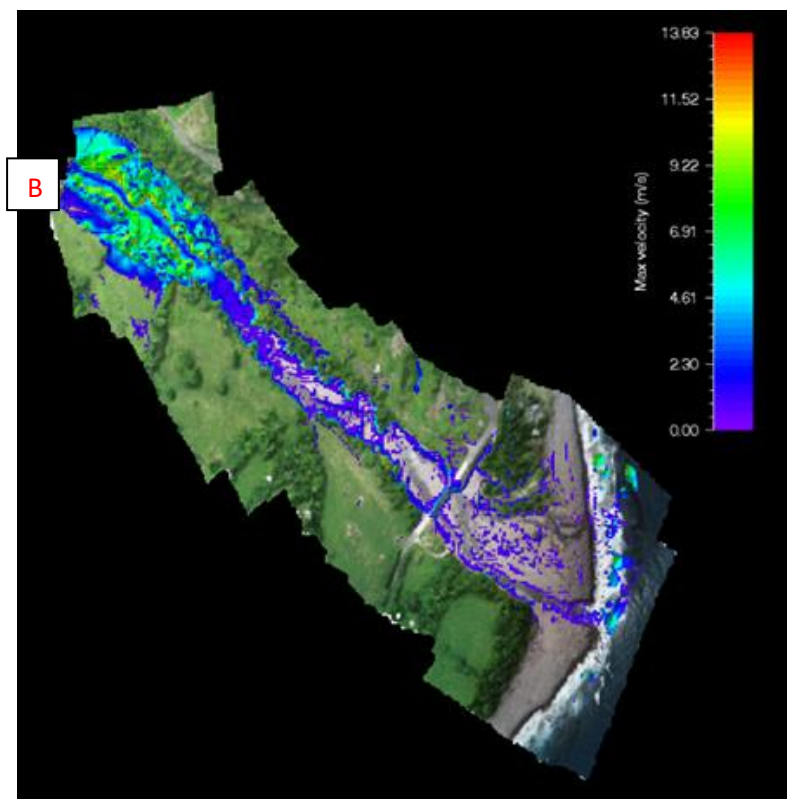
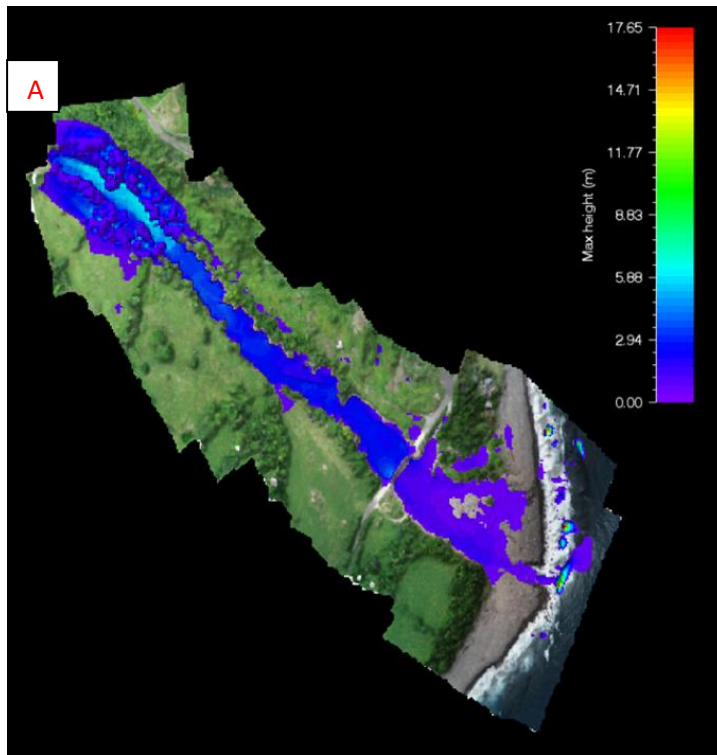


Figure 6.5: Results of the RAMMS debris flow simulation of Delice (Dominica), (A) Variations in flow height (in m); (B) flow velocity (in m/s) over the whole drainage area.

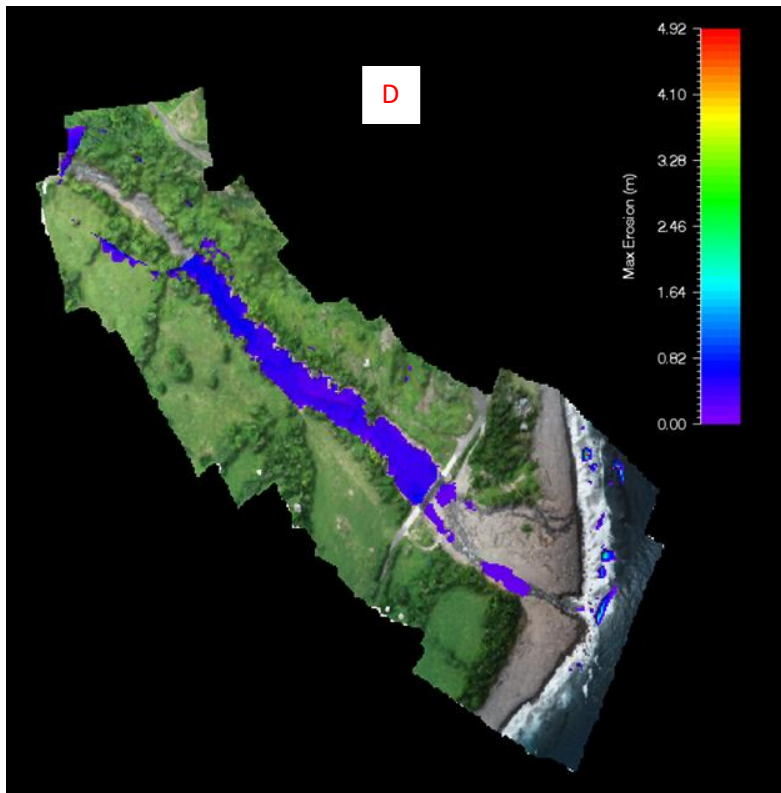
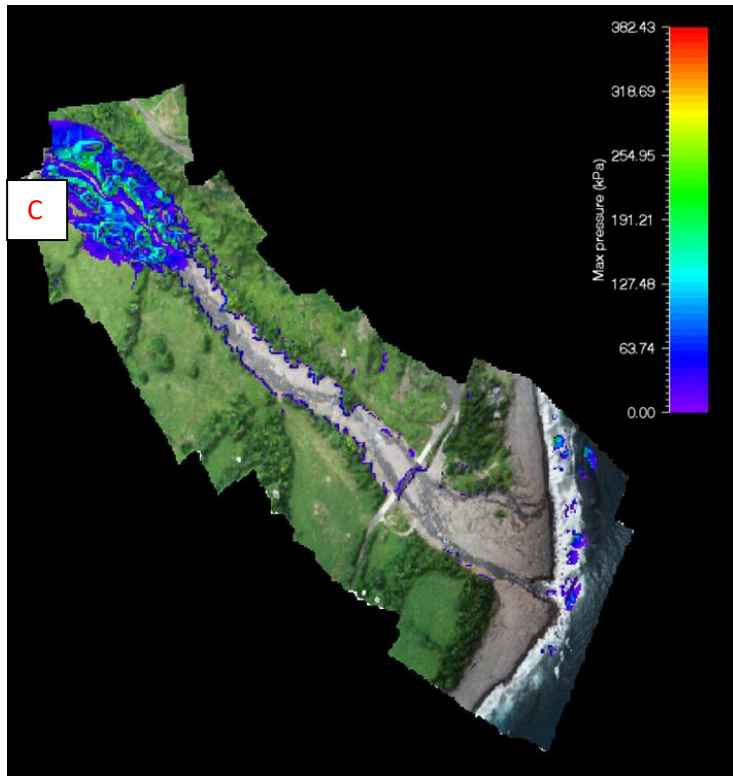


Figure 6.5: Results of the RAMMS debris flow simulation of Delice (Dominica), (C) flow pressure (in Pa); (D) flow entrainment (in m³) over the whole drainage area.

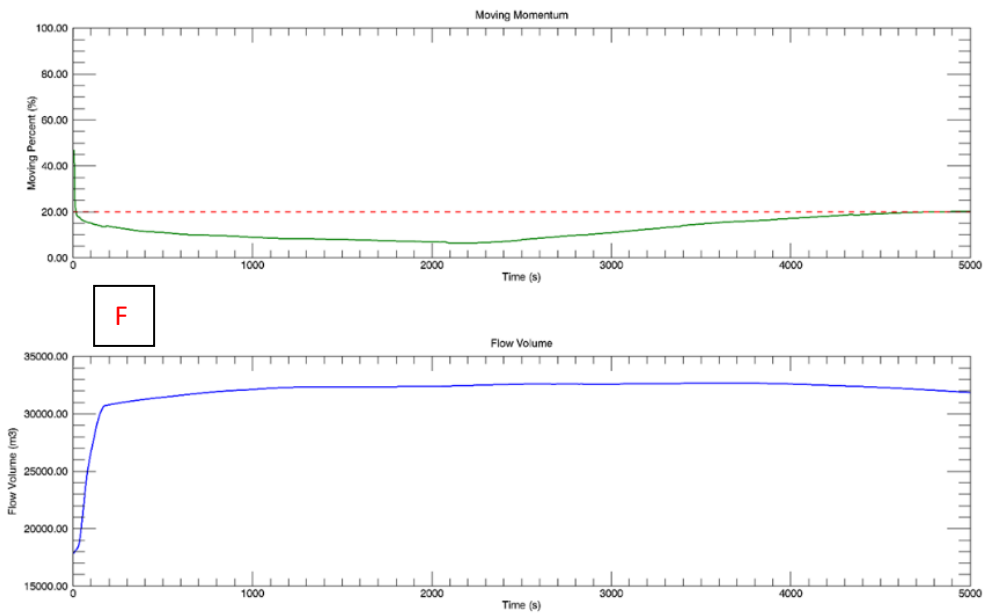
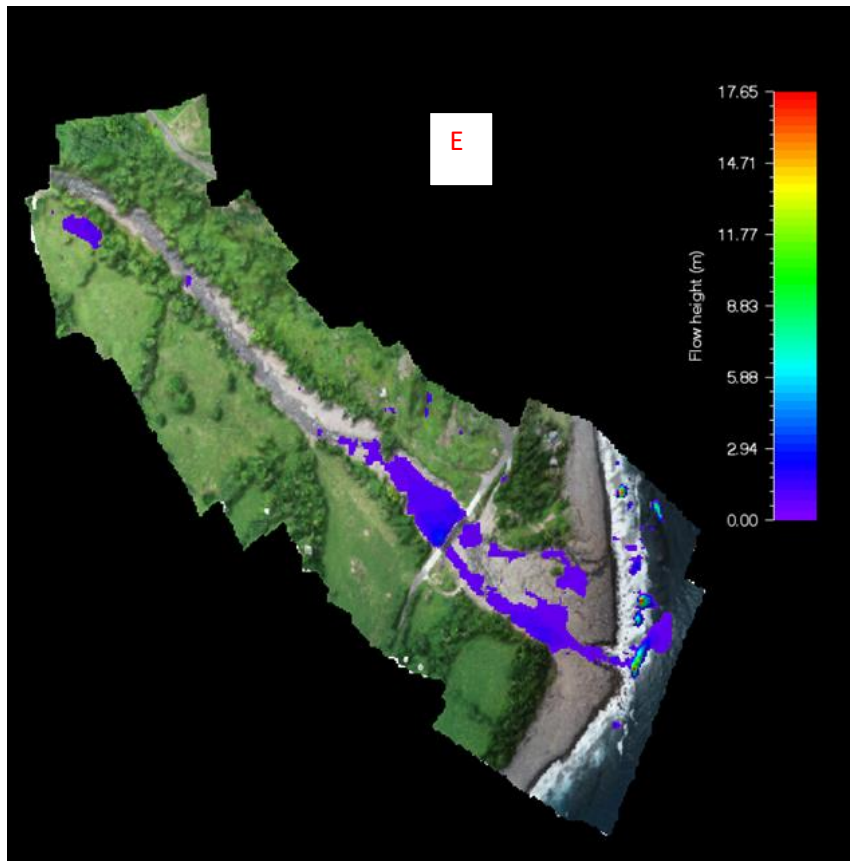


Figure 6.5: Results of the RAMMS debris flow simulation of Delice (Dominica), (E) flow deposition (in m³) and (F) flow momentum (in m/s) over the whole drainage area.

6.2.3 Layou Debris Flows Simulation

Figure 6.6 and Table 6.8 show the results for the Layou debris flow modelling. Flow in the simulation was highest at the flow release area in the upper part of the channel (Figure 6.6A). Height of flow decreased down the channel with flow height of 2.2-1.2 m covering a distance of 417 m (Figure 6.6A). Lower part of the channel had lower flow heights. Velocity of the flow diminished drastically as the flow went down the channel. The highest velocity was recorded at the flow release area and lowest velocity was recorded at the flow deposition area (Figure 6.6B). There was little to zero velocity in the river-bed from the bridge to downstream (Figure 6.6B). Flow velocity was highest in the upper part of the channel to the bridge and direction of the velocity was north-west of the channel (Figure 6.6B). Areas showing highest pressure appeared at the upper part of the channel, specifically the right bank of the channel. Most of the areas of highest impact pressures were around the right and left banks of the channel (Figure 6.6C).

Channel Parts	Flow Distance (m)	Flow Height (m)	Flow Velocity (m/s)	Flow Pressure (kPa)
Upper channel	96.9	4 - 13.3	4.50 - 13.48	60.6 - 363.5
Middle Channel	416.7	2 - 4	2.20 - 4.50	21.4 – 60.6
Lower channel	580.2	0.1 - 2	0.01 - 2.20	0.01 – 21.4

Table 6.8: Layou RAMMS simulation results showing runout distance, flow heights, flow velocities and flow pressure of various areas of the channel.

Total eroded volume after the simulation was 417 m³ and entrainment predominantly occurred in the river-bed underneath the bridge downstream (Figure 6.6D). Sediments were eroded in the upper part of channel, just before the bridge and 350 m downstream (Figure 6.6D). The channel contained sand, gravels, cobbles and boulders coupled with tree debris.

Depositional volume of the simulation was 2,887 m³ (Figure 6.6E). That is a decrease of 17813 m³ from the total flow volume of 20700 m³ representing 14% of the released flow volume (Figure 6.6 E). Flow direction was north-west of the channel. Most of the flow was deposited behind the bridge due to debris blocking the bridge. Some of the material in the flow was deposited inland on the buildings on the right side of the channel. The rest of the flow was deposited downstream at the very end of the channel. Flow momentum was high at the release zone and steadily decreased to the deposition zone (Figure 6.6 F). Flow volume also decreased as the flow moved downstream to the point of deposition after the simulation ceased decreased as the flow moved downstream to the point of deposition after the simulation ceased (Figure 6.6 F).

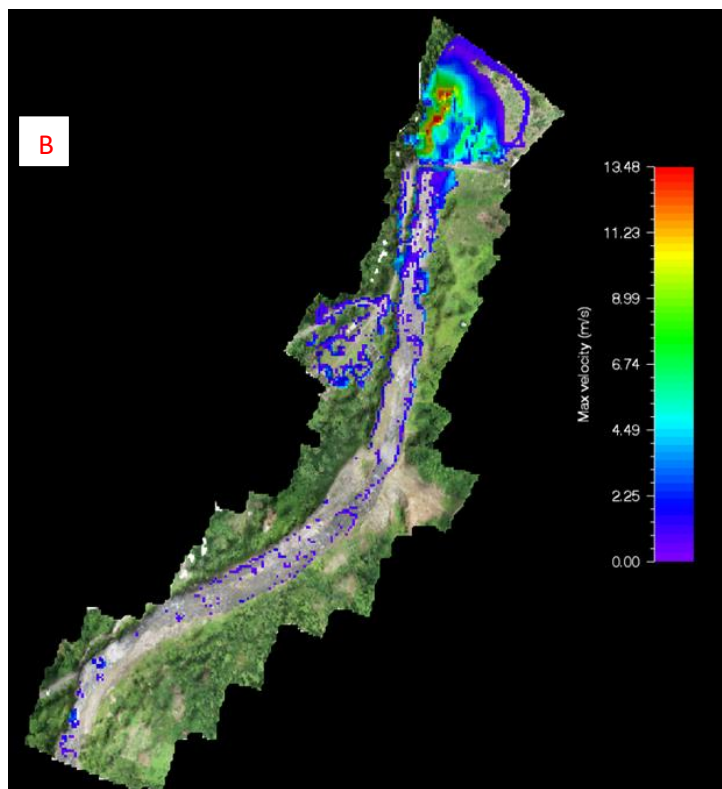
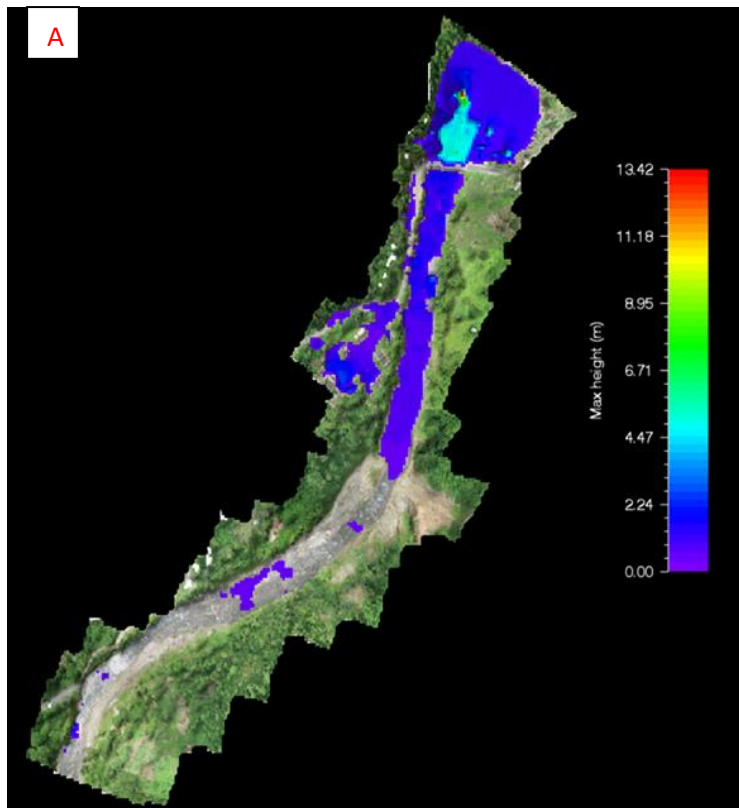


Figure 6.6: Results of RAMMS debris flow simulation of Layou (Dominica), (A) Variations in flow height (in m); (B) flow velocity (in m/s) over the whole drainage area.

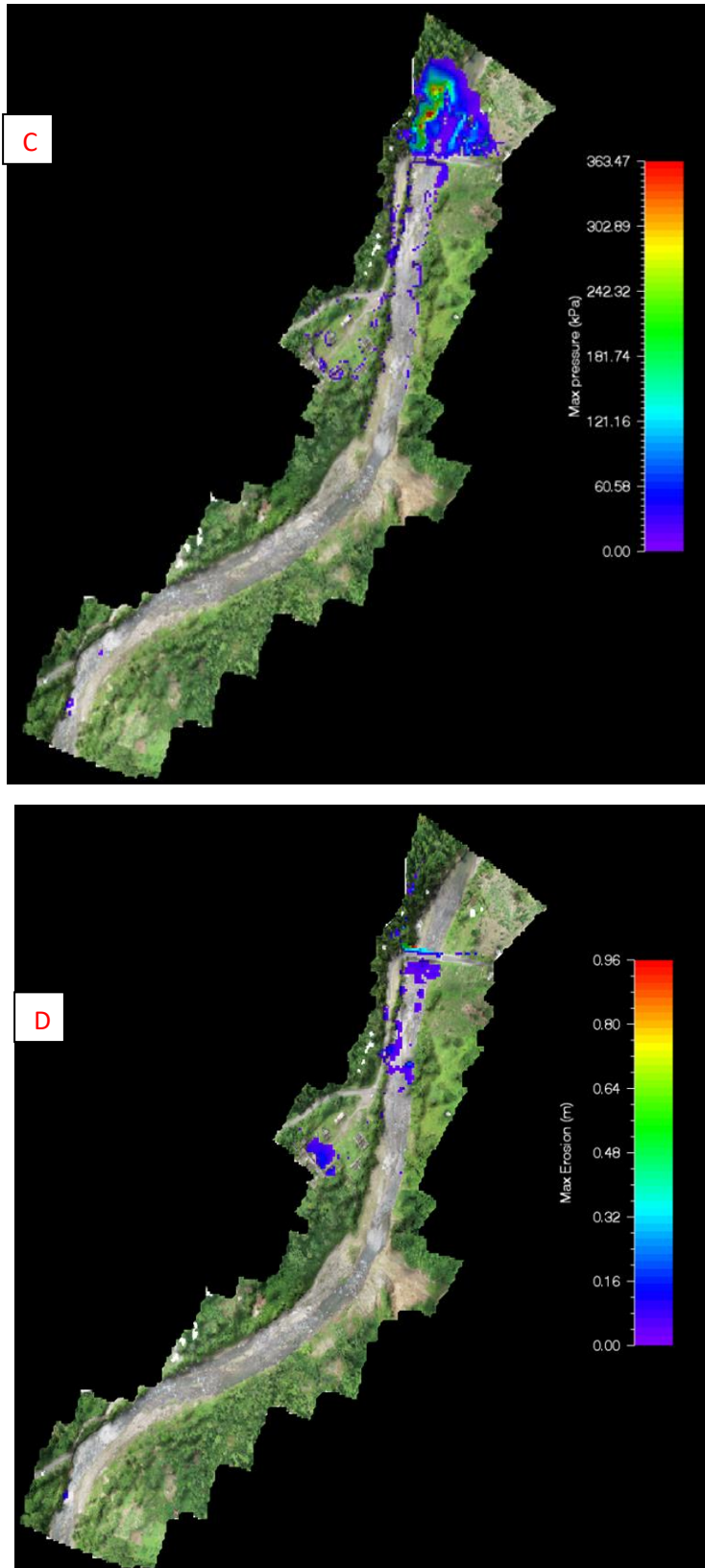


Figure 6.6: Results of RAMMS debris flow simulation of Layou (Dominica), (C) flow pressure (in Pa), (D) flow entrainment (in m³) over the whole drainage area.

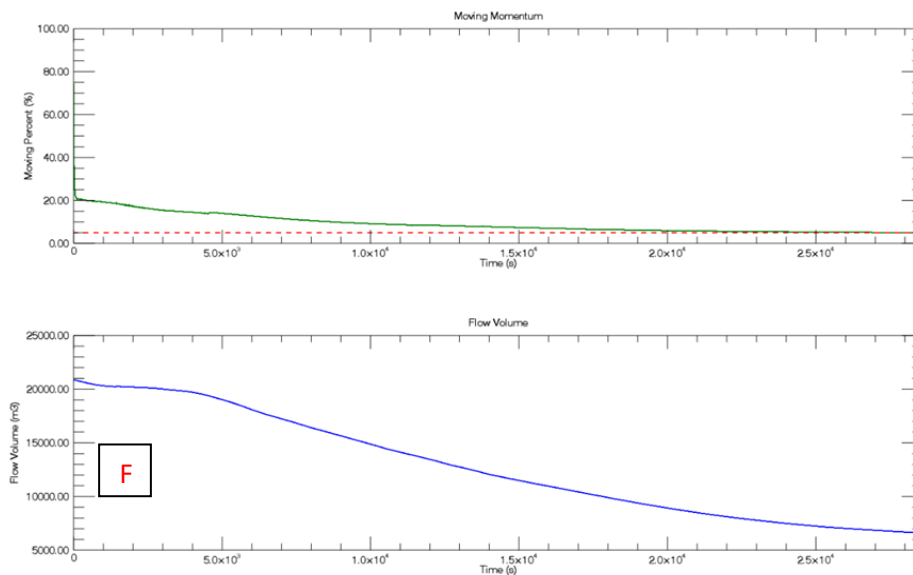
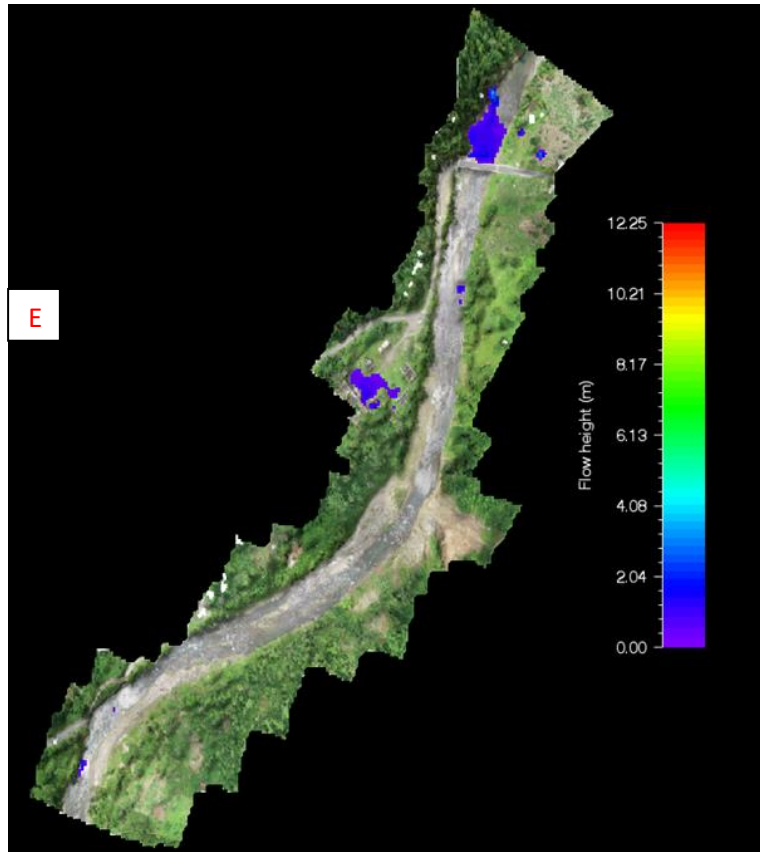


Figure 6.6: Results of RAMMS debris flow simulation of Layou (Dominica), (E) flow deposition (in m³) and (F) flow momentum (in m/s) over the whole drainage area.

6.2.4 Pagua Debris Flows Simulation

Modelling results for debris flows in Pagua are given in Figure 6.7 and Table 6.9. The maximum flow height of simulation was at the flow release area and depositional area and minimum at transition area. Height of flow decreased at the transition zone and increasing at the deposition zone (Figure 6.7 A). There was alternation of flow velocities throughout the channel with high velocities recorded at the flow release, transition and deposition areas. Flow velocity was highest at the flow release area and flow deposition area of the channel and direction of the velocity was north-east of the channel (Figure 6.7 B). High pressure areas were at the upper part of the channel, specifically at the channel-bed. The highest impact pressures were within the channel-bed and floodplains on both sides of the channel (Figure 6.7 C).

Channel Parts	Flow Distance (m)	Flow Height (m)	Flow Velocity (m/s)	Flow Pressure (kPa)
Upper channel	723	3.0 – 6.7	3.5 – 7.6	38.9 – 116.9
Middle Channel	500	1.5 – 3.0	2.0 - 3.5	19.9 – 38.9
Lower channel	769	0.1 – 1.5	0.01 – 2.0	0.01 – 19.9

Table 6.9: Pagua RAMMS simulation results showing runout distance, flow heights, flow velocities and flow pressure of various areas of the channel.

Eroded volume after the simulation was 974 m³ and entrainment mainly occurred 210 m from the flow release area and at the flow deposition area (Figure 6.7 D). Entrainment occurred mainly in the channel bed at the upper and lower parts of the channel covering a distance of 1778 m. The channel contained sand, gravels, cobbles and boulders coupled with tree debris.

Depositional volume of the simulation was 4886 m³. That is a decrease of 21,653 m³ from the total flow volume of 26,539 m³ representing 8.6% of the flow volume. Flow direction was north-east of the channel. Most of the material in the flow was deposited downstream at the

lower parts of the channel. Momentum of the flow dropped, rose and eventually dropped again as the flow moved down the channel (Figure 6.7 F). Flow volume was steady along the channel to the point of deposition.

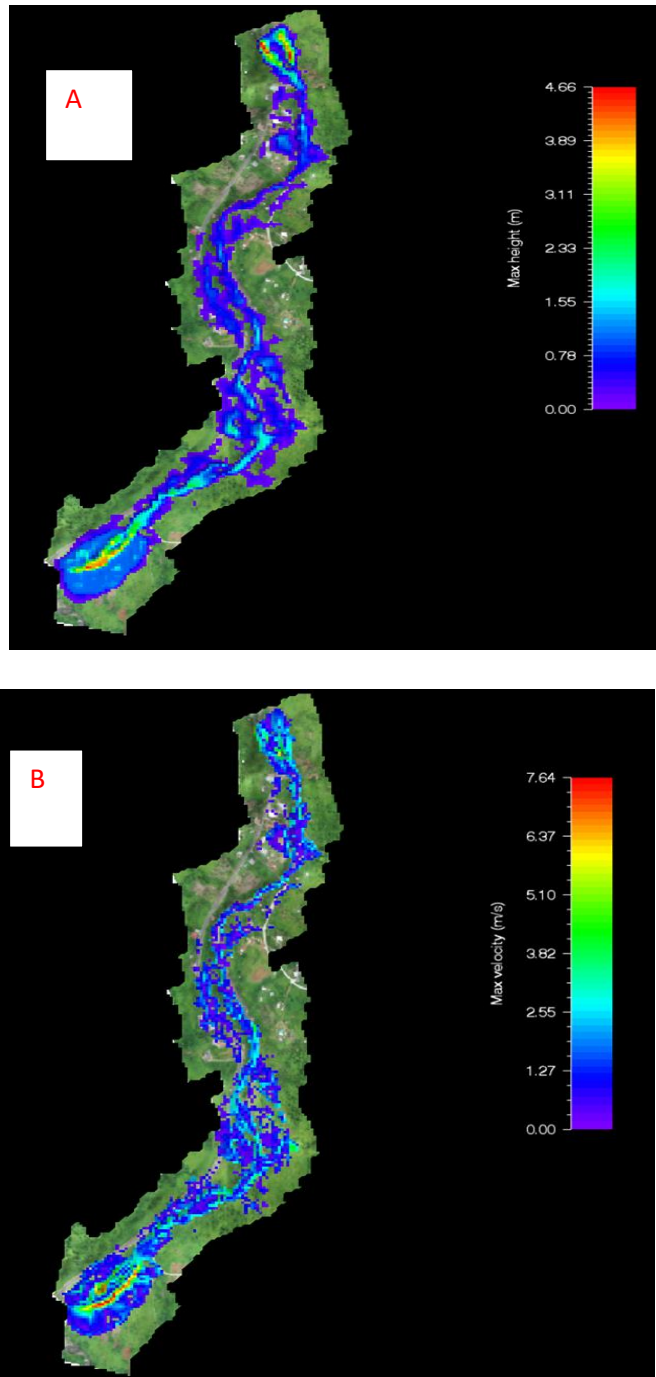


Figure 6.7: Results of RAMMS debris flow simulation of Pagua (Dominica), (A) Variations in flow height (in m); (B) flow velocity (in m/s) over the whole drainage area.

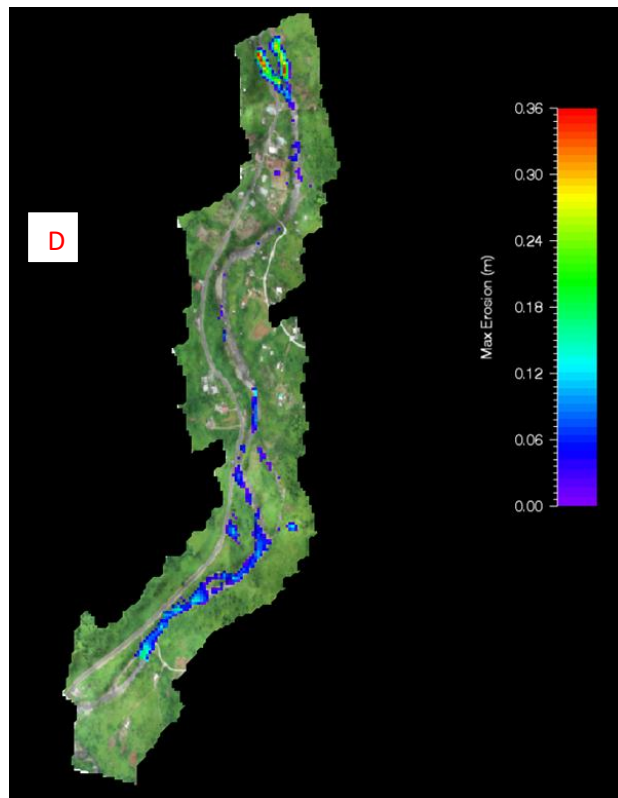
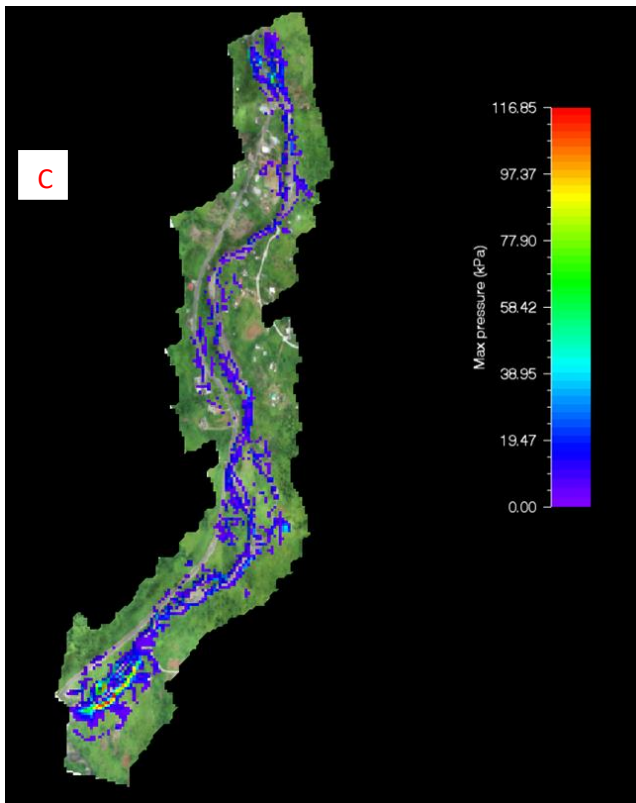


Figure 6.7: Results of RAMMS debris flow simulation of Pagua (Dominica), (C) flow pressure (in Pa), (D) flow entrainment (in m³) over the whole drainage area.

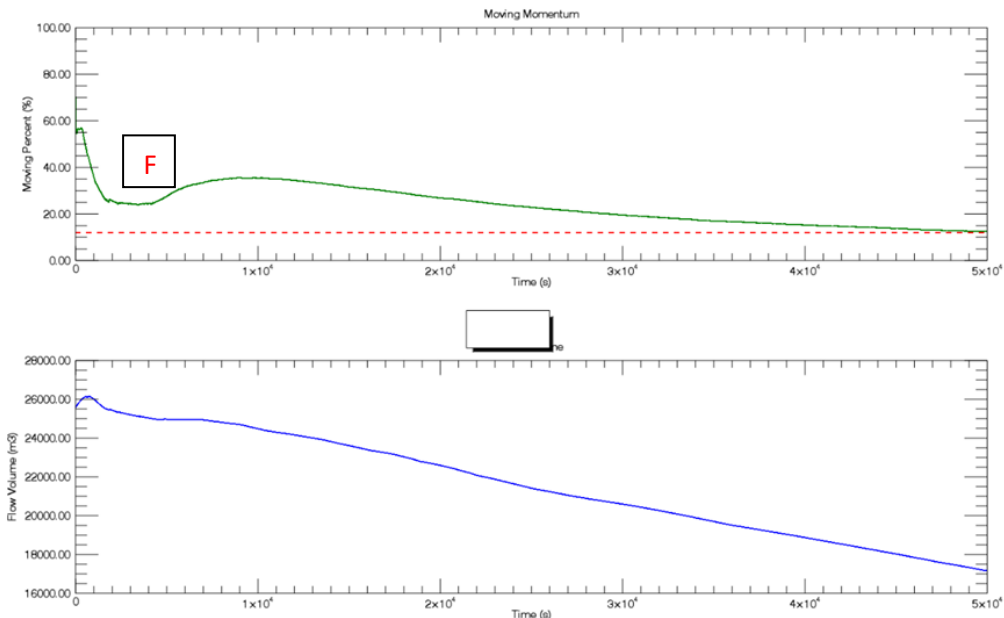
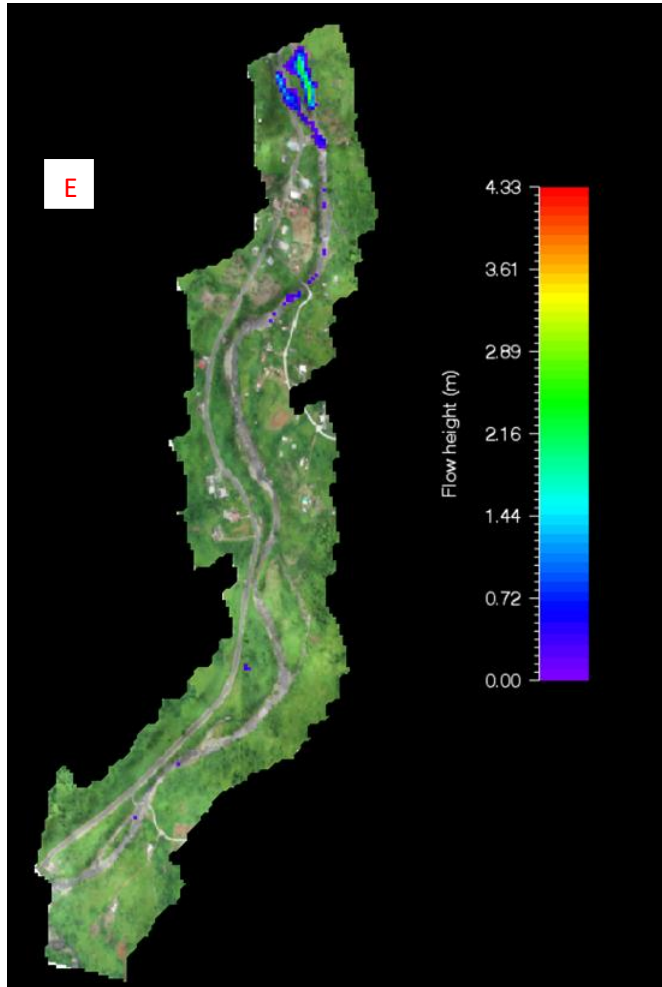


Figure 6.7: Results of RAMMS debris flow simulation of Pagua (Dominica), (E) flow deposition (in m³) and (F) flow momentum (in m/s) over the whole drainage area.

6.2.5 Pointe Michel South Debris Flows Simulation

Figure 6.8 and Table 6.10 report the results of RAMMS debris flow modelling of the point Michel South region of Dominica. Flow height of simulation was high throughout the channel, mainly within the channel-bed. Low flow heights were recorded at both channel banks and inland (Figure 6.8 A). The highest velocity was recorded at the flow release area and lowest velocity was recorded at the flow deposition area. Flow velocity direction of the velocity was north-west of the channel (Figure 6.8 B). High pressure areas were at the upper part of the channel, specifically the right bank of the channel. Most of the impact pressures were around the channel banks with some inland (Figure 6.8 C).

Channel Parts	Flow Distance (m)	Flow Height (m)	Flow Velocity (m/s)	Flow Pressure (Pa)
Upper channel	811	2.2 – 4.0	5.4 – 9.4	59.3 – 178
Middle Channel	402	1.3 – 2.2	2 – 5.4	29.9 – 60
Lower channel	501	0.1 – 1.3	0.01 - 2	0.01 – 30

Table 6.10: Pointe Michel South RAMMS simulation results showing runout distance, flow heights, flow velocities and flow pressure of various areas of the channel.

Entrainment volume after the simulation was 9458 m³ and entrainment basically occurred throughout the channel from flow release area to flow deposition area (Figure 6.8 D). Entrainment was high in the channel-bed from upstream to downstream. The channel contained sand, gravels, cobbles and boulders coupled with tree debris.

Depositional volume of the simulation was 13737 m³ (Figure 6.8 E). That is a decrease of 3212 m³ from the total flow volume of 16948 m³ representing 82% of the flow volume. Flow direction was north-west of the channel. Most of the flow went under the bridge and deposited downstream into the Caribbean Sea. Some of the flow was deposited behind the bridge and top

of the bridge as a result of debris blocking the bridge. The rest of the flow was deposited around the inland buildings, north-west of the channel.

There was a rise and fall of the flow momentum from the initiation area to the transition area and this decreased steadily to the deposition zone (Figure 6.8 F). Flow volume was 8158 m³ at 0.1s. Flow volume then increased rapidly from the point of initial to the transition point and relatively remaining at same level to the point of deposition.

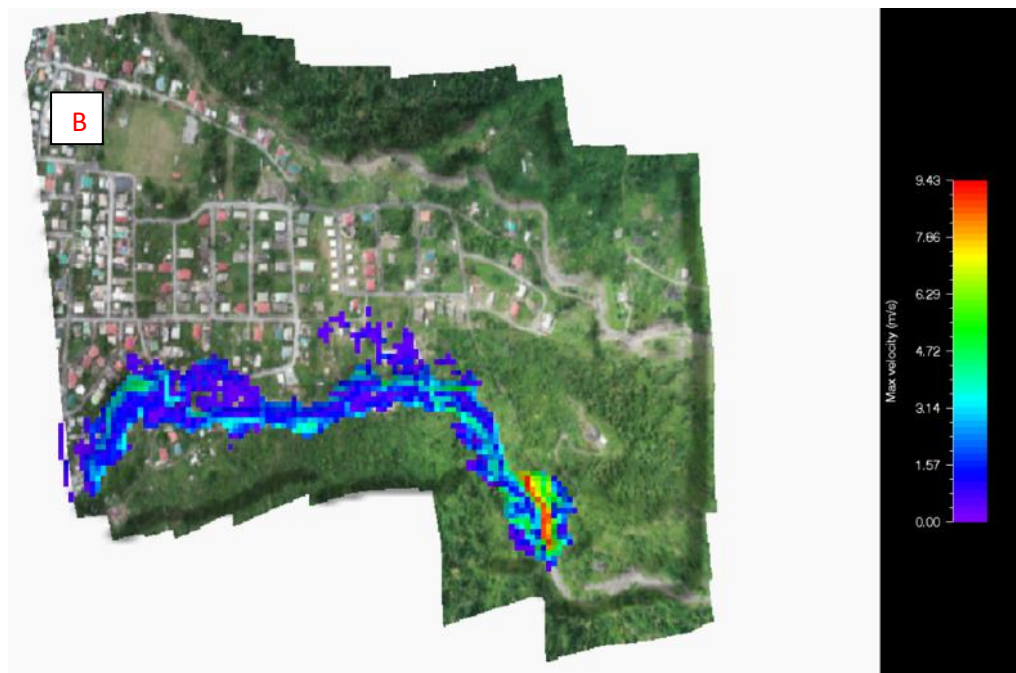
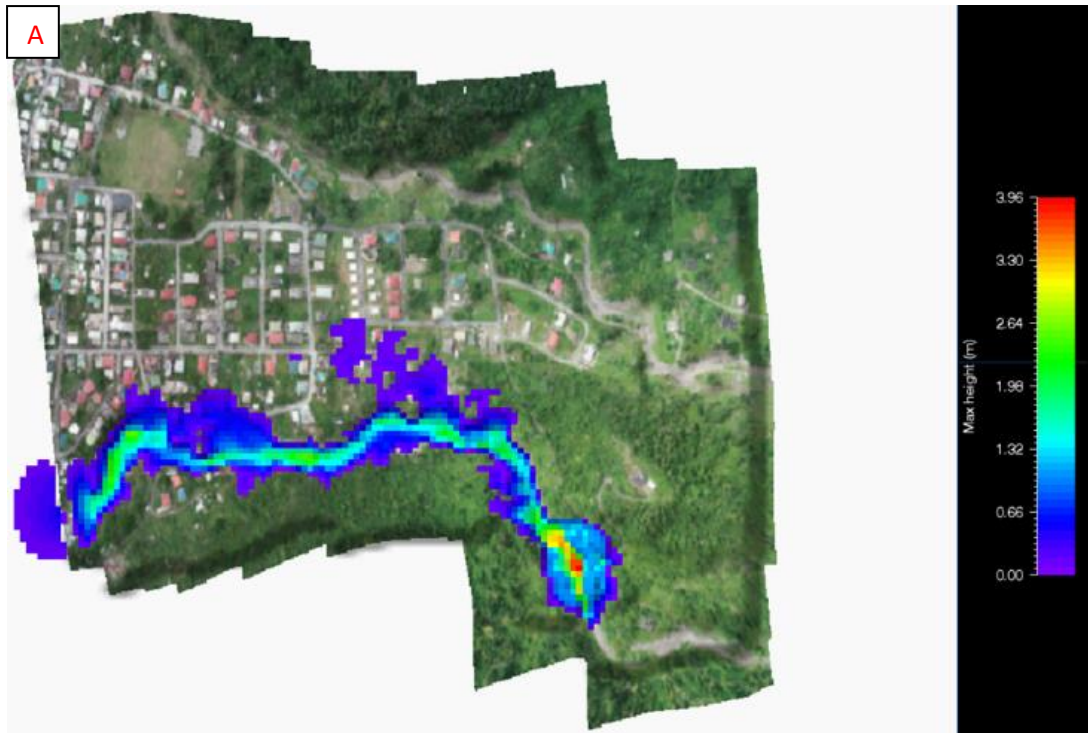


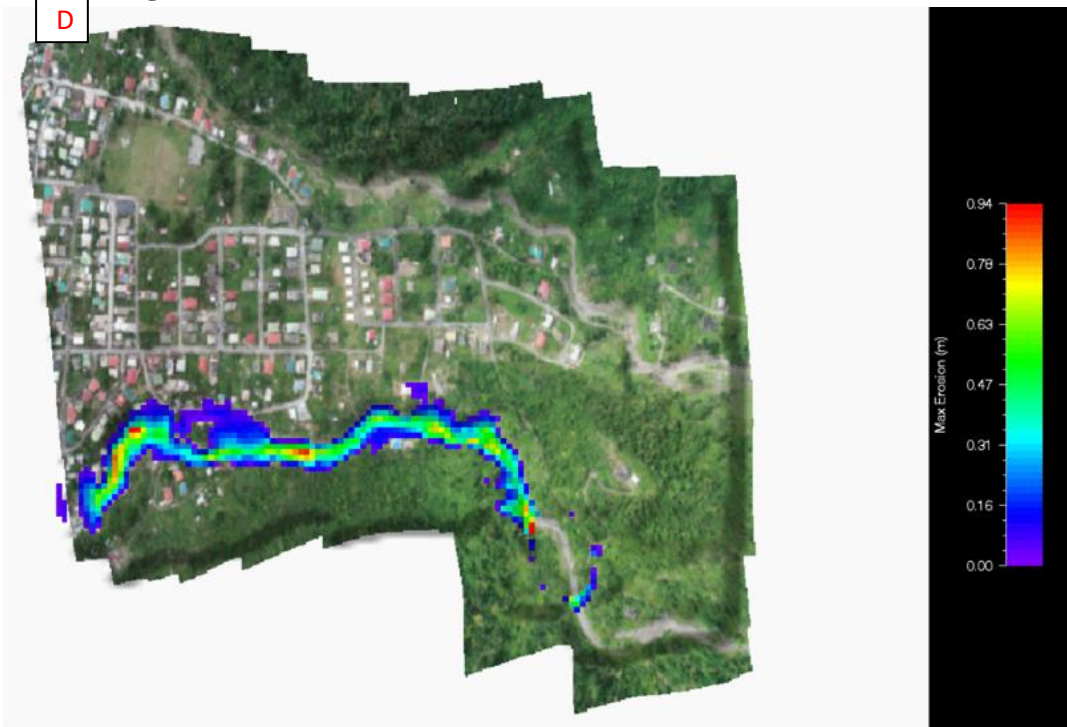
Figure 6.8 : RAMMS debris flow simulation of Pointe Michel South (Dominica), (A) Variations in flow height (in m); (B) flow velocity (in m/s) over the whole drainage area.

C



Figure 6.8: RAMMS debris flow simulation of Pointe Michel South

D



(Dominica); (C) flow pressure (in Pa), (D) flow entrainment (in m^3) over the whole drainage area.

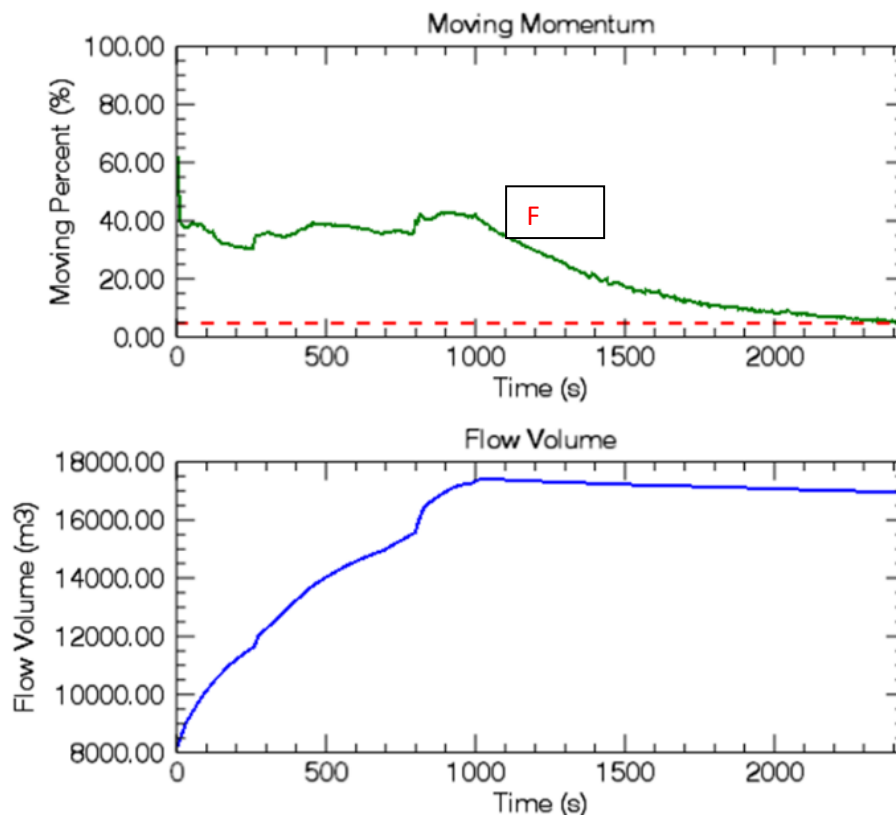


Figure 6.8: RAMMS debris flow simulation of Pointe Michel South (Dominica), (E) flow deposition (in m³) and (F) flow momentum (in m/s) over the whole drainage area.

6.2.6 Pointe Michel North Debris Flows Simulation

All results for the debris flow simulation of Point Michel North are shown in Figure 6.9 and Table 6.11. Flow height of simulation was high throughout the channel, mainly within the channel-bed. Low flow heights were recorded at both channel banks and inlands (Figure 6.9 A). Highest velocity was recorded at the flow release area and lowest velocity was recorded at the flow deposition area. There was variation of flow velocities throughout the channel and velocity was mainly active within the channel-bed (Figure 6.9 B). The direction of the flow velocity was north-west of the channel (Figure 6.9 B). High pressure areas were at the upper part of the channel. The highest values of the impact pressures were within the channel bed with activities at both banks and inland (Figure 6.9 C).

Channel Parts	Flow Distance (m)	Flow Height (m)	Flow Velocity (m/s)	Flow Pressure (Pa)
Upper channel	802	1.2 – 2.9	4.4 – 7.3	46.4 – 106.2
Middle Channel	551	1.0 – 1.2	1.8 – 4.4	20.8 – 46.4
Lower channel	300	0.1 – 1.0	0.01 – 1.8	0.01 – 20.8

Table 6.11: Pointe Michel North RAMMS simulation results showing runout distance, flow heights, flow velocities and flow pressure of various areas of the channel.

Entrainment volume after the simulation was 6168 m³ and entrainment basically occurred throughout the channel from flow release area to flow deposition area (Figure 6.9 D). Entrainment was highest in the channel-bed from upstream to downstream. The channel contained sand, gravels, cobbles and boulders coupled with tree debris. Total depositional

volume of the simulation was 12932 m³ (Figure 6.9 E), thus a decrease of 1,925 m³ from the total flow volume of 14857 m³ representing 87% of the flow volume.

Flow direction was north-west of the channel. Most of the material was deposited downstream into the settlements (Figure 6.9 E). The rest of the flow was deposited around the inland buildings south-west of the channel. Momentum of the flow was approximately the same from the initiation area to the transition area and increased slightly to the deposition area (Figure 6.9 F). There was a gradual increase of flow volume from the initiation area to the deposition area.

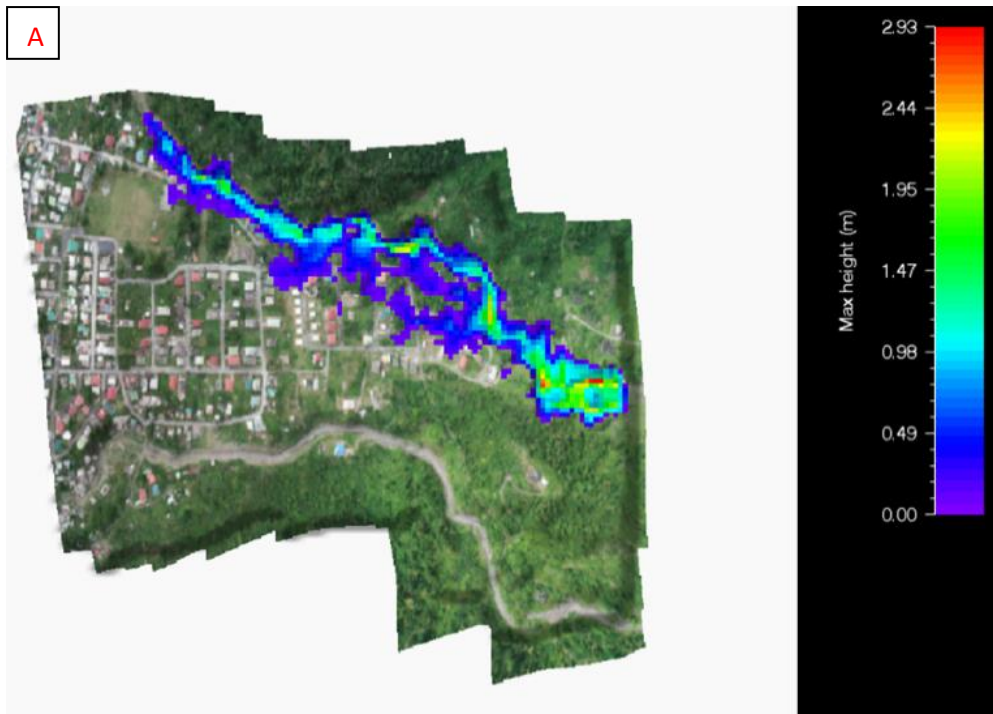


Figure 6.9: RAMMS debris flow simulation of Pointe Michel North (Dominica), (A) Variations in flow height (in m); (B) flow velocity (in m/s) over the whole drainage area.



Figure 6.9: RAMMS debris flow simulation of Pointe Michel North (Dominica), (C) flow pressure (in Pa), (D) flow entrainment (in m³) over the whole drainage area.

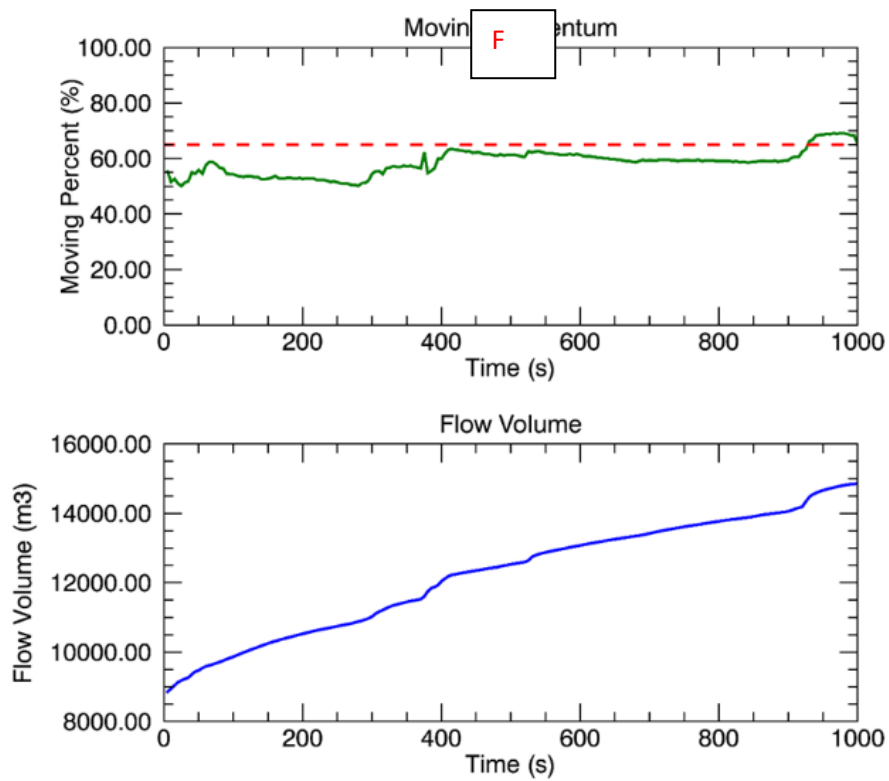


Figure 6.9: RAMMS debris flow simulation of Pointe Michel North (Dominica), (E) flow deposition (in m³) and (F) flow momentum (in m/s) over the whole drainage area.

6.2.7 Soufriere Debris Flows Simulation

For Soufriere, the results of the debris flow simulations are given in Figure 6.10 and Table 6.12. Flow height of simulation was maximum at the flow release area in the upper part of the channel, and the height of flow decreased down the channel (Figure 6.10 A). The highest velocity occurred at the flow release area and lowest was recorded at the flow deposition area. Flow velocity was most active in the upper part of the channel and direction of the velocity was south-west of the channel (Figure 6.10 B). High pressure areas were at the upper part of the channel, specifically within the channel-bed. The highest impact pressures were within the channel-bed with activities on both banks and inlands (Figure 6.10 C).

Channel Parts	Flow Distance (m)	Flow Height (m)	Flow Velocity (m/s)	Flow Pressure (kPa)
Upper channel	225	5.2 – 12.6	6.2 – 12.8	108.9 – 326.9
Middle channel	3950	2.5 – 5.2	2.9 – 6.2	43.7 – 108.9
Lower channel	200	0.1 – 2.5	0.01 – 2.9	0.01 – 43.7

Table 6.12: Soufriere RAMMS simulation results showing runout distance, flow heights, flow velocities and flow pressure of various areas of the channel.

Eroded volume after the simulation was 15536 m³ and entrainment predominantly occurred 225 m from the flow release area (Figure 6.10 D). Entrainment activities occurred at the middle and the lower part of the channel. The channel contained sand, gravels, cobbles and boulders coupled with tree debris. Depositional volume of the simulation was 11000 m³ (Figures 6.10 E). That is a decrease of 19933 m³ from the total flow volume of 30933 m³ representing 36% of the flow volume. Flow direction was south-west of the channel. Most of the flow was deposited downstream into the settlements and roads (Figures 6.10 E). Some of the flow was deposited upstream in the channel-bed as a result of debris blocking the flow. Momentum of

the flow dropped rapidly and then steadily from point of initiation to point of deposition (Figure 6.10 F). Flow volume increased sharply and then decreased steadily to the point of deposition.

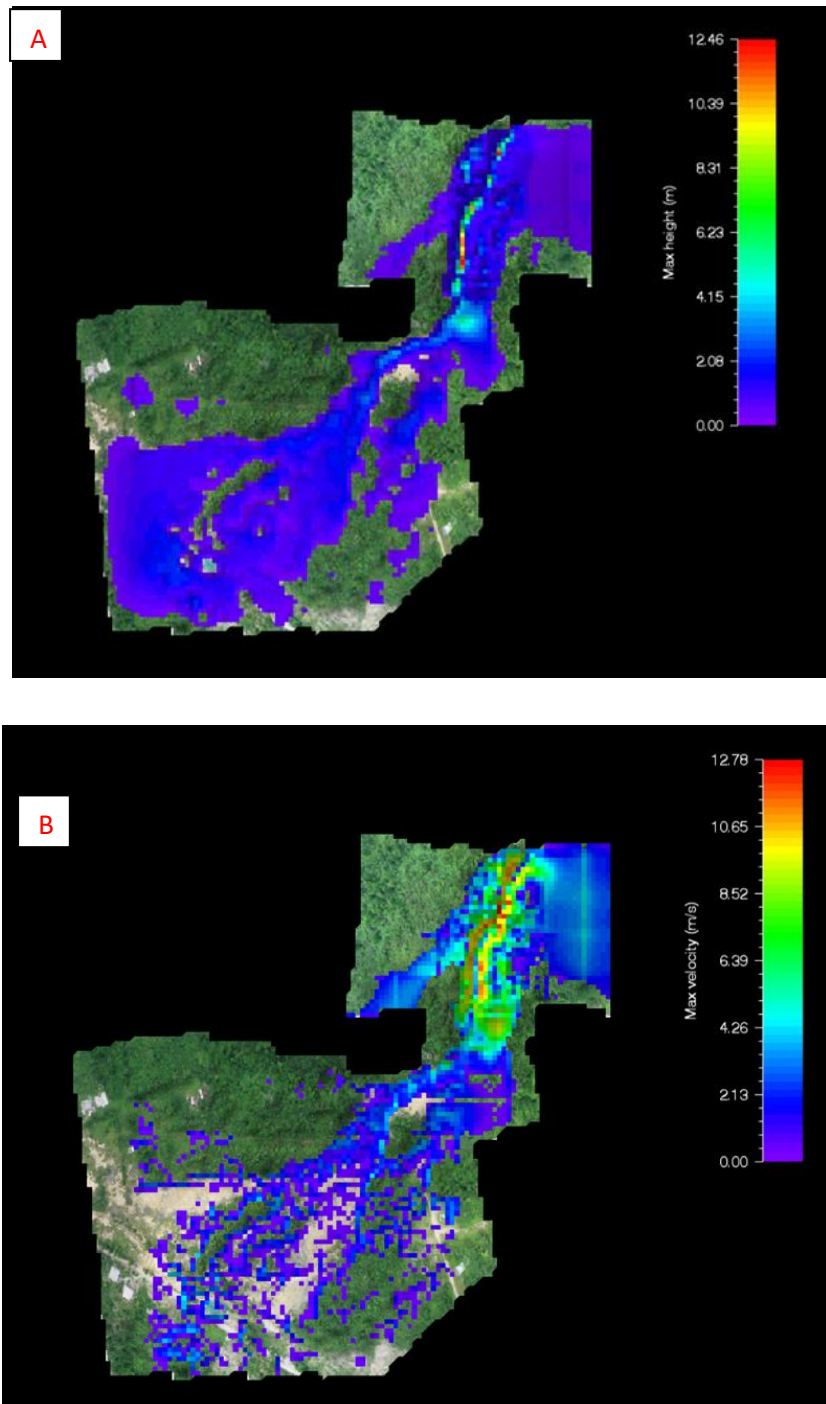


Figure 6.10: Results of RAMMS debris flow simulation of Soufriere (Dominica), (A) variations in flow height (in m); (B) flow velocity (in m/s) over the whole drainage area.

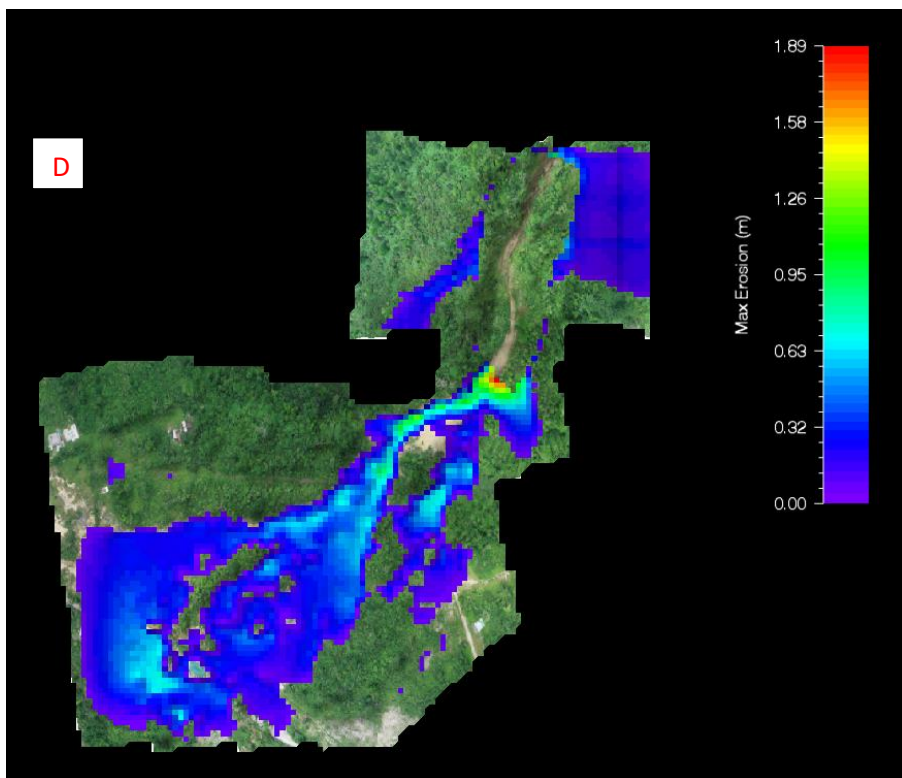
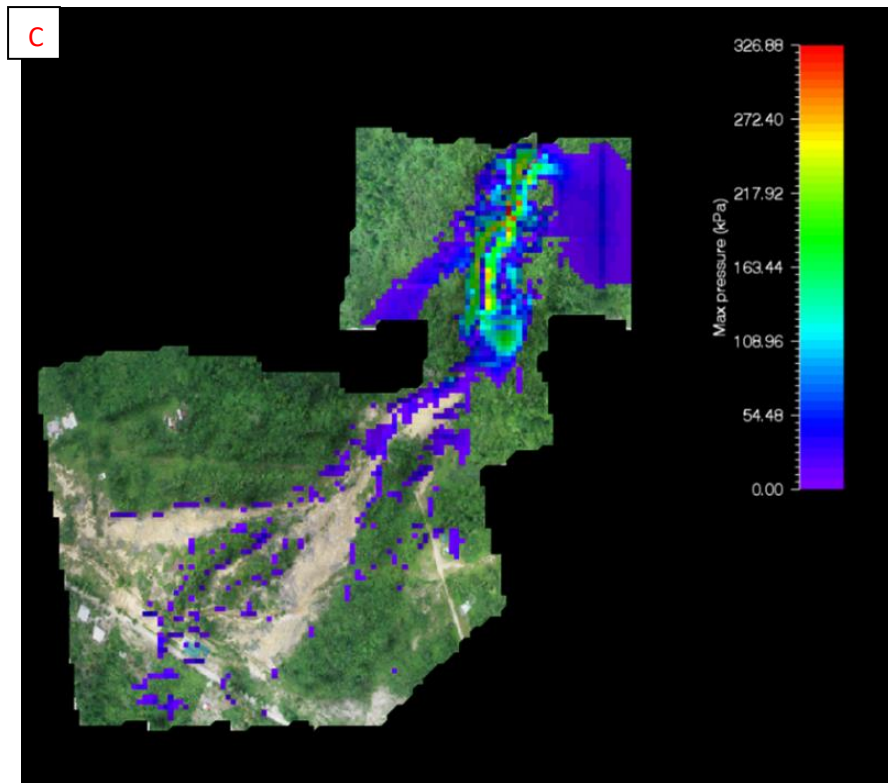


Figure 6.10: Results of RAMMS debris flow simulation of Soufriere (Dominica), (C) flow pressure (in Pa), (D) flow entrainment (in m³) over the whole drainage area.

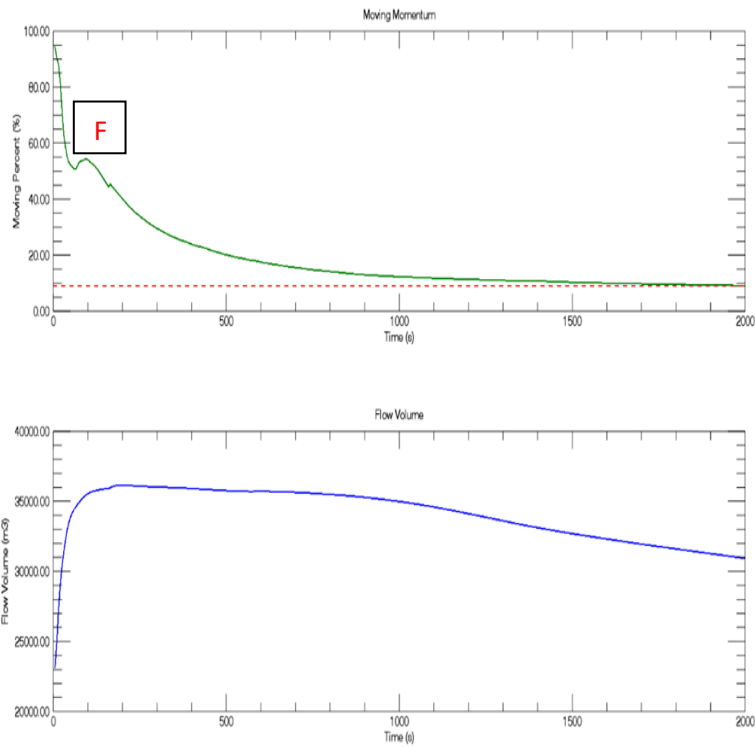
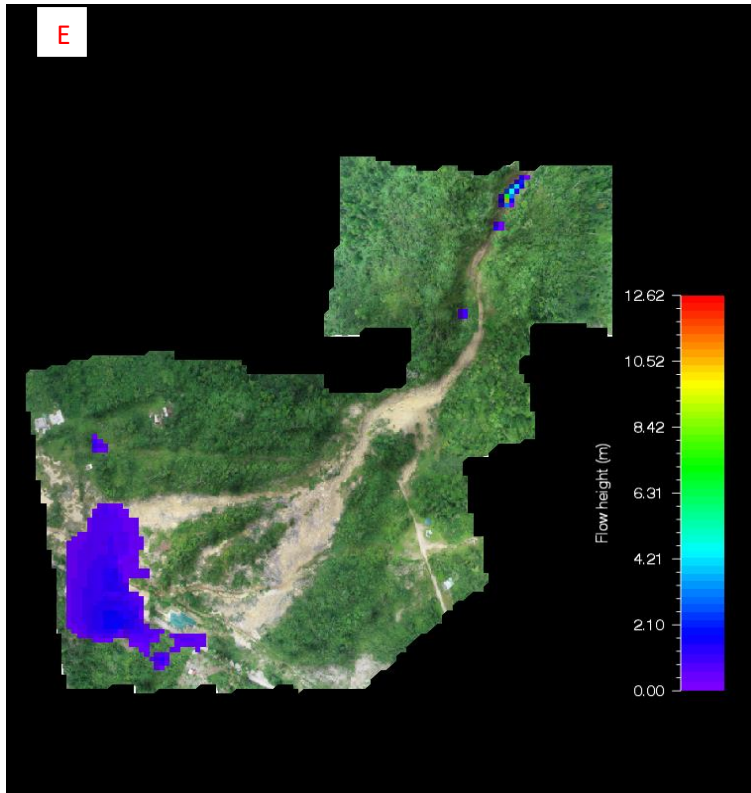


Figure 6.10: Results of RAMMS debris flow simulation of Soufriere (Dominica), (E) flow deposition (in m³) and (F) flow momentum (in m/s) over the whole drainage area.

6.2.8 Ribeira Domingo Santo Debris Flows Simulation

All of the results for the Ribeira Domingo Santo (Fogo) RAMMS modelling are given in Figure 6.11 and Table 6.13. Flow height of simulation was maximum at the flow release area which is the upper part of the channel. Height of flow decreased down the channel (Figure 6.11 A). The highest velocity was recorded at the flow release area and lowest velocity was recorded at the flow deposition area (Figure 6.11 B). Flow velocity was highest within the channel-bed and direction of the velocity was south-east of the channel. High pressure areas were at the upper part of the channel, specifically within the bed of the channel (Figure 6.11 C). Most of the impact pressures were within the channel bed with activities at both banks and inland.

Channel Parts	Flow Distance (m)	Flow Height (m)	Flow Velocity (m/s)	Flow Pressure (kPa)
Upper channel	1767	3.3 – 7.0	4.4 – 11.6	96 – 268.8
Middle Channel	2000	2.6 – 3.3	2.0 – 4.4	33.8 – 96
Lower channel	947	0.1 – 2.6	0.01 – 2.0	0.01 – 33.8

Table 6.13: Ribeira Santo Domingo (Fogo) RAMMS simulation results showing runout distance, flow heights, flow velocities and flow pressure of various areas of the channel.

Entrainment volume after the simulation was 87945 m³ and erosion predominantly occurred at the flow transition area (Figure 6.11 D). Entrainment occurred mainly in the channel bed and at the middle part of the channel. The channel contained sand, gravels, cobbles and boulders coupled with tree debris.

Depositinal volume of the simulation was 13,057 m³ (Figures 6.11 E). That is a decrease of 197,013 m³ from the total flow volume of 210070 m³ representing 6.2% of the flow volume. Flow direction was south-east of the channel. Most of the flow was deposited at the middle part of the channel. The rest of the flow were deposited 1500 m away from the flow release area. Momentum of the flow was high at the flow initiation area and then decreased steadily to

the deposition area (Figure 6.11 F). Flow volume increased gradually from the initiation area to the transition area and remained at approximately the same volume to the deposition area.

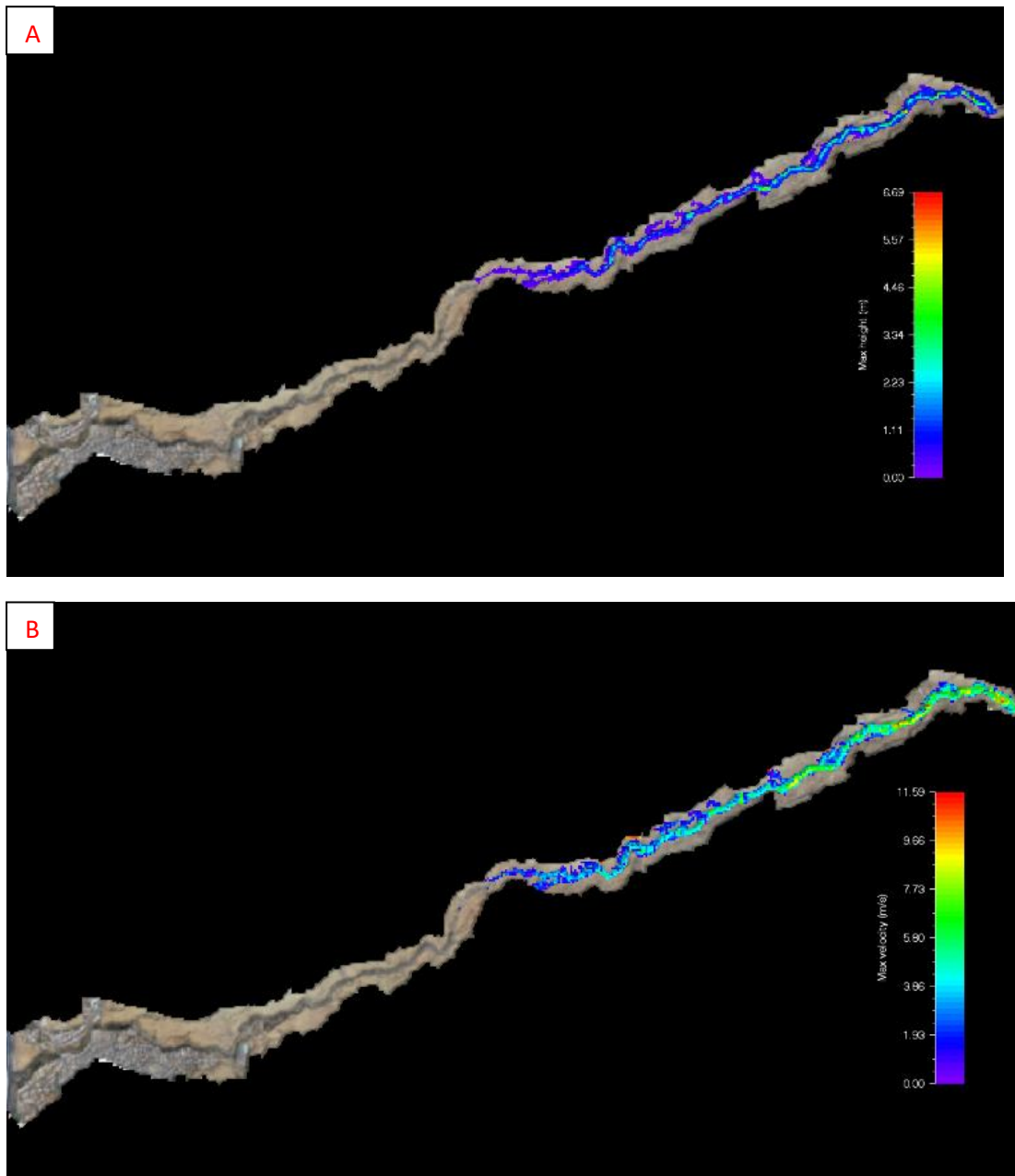


Figure 6.11: RAMMS debris flow simulation of Ribeira Santo Domingo (Fogo), (A) Variations in flow height (in m); (B) flow velocity (in m/s) over the whole drainage area.

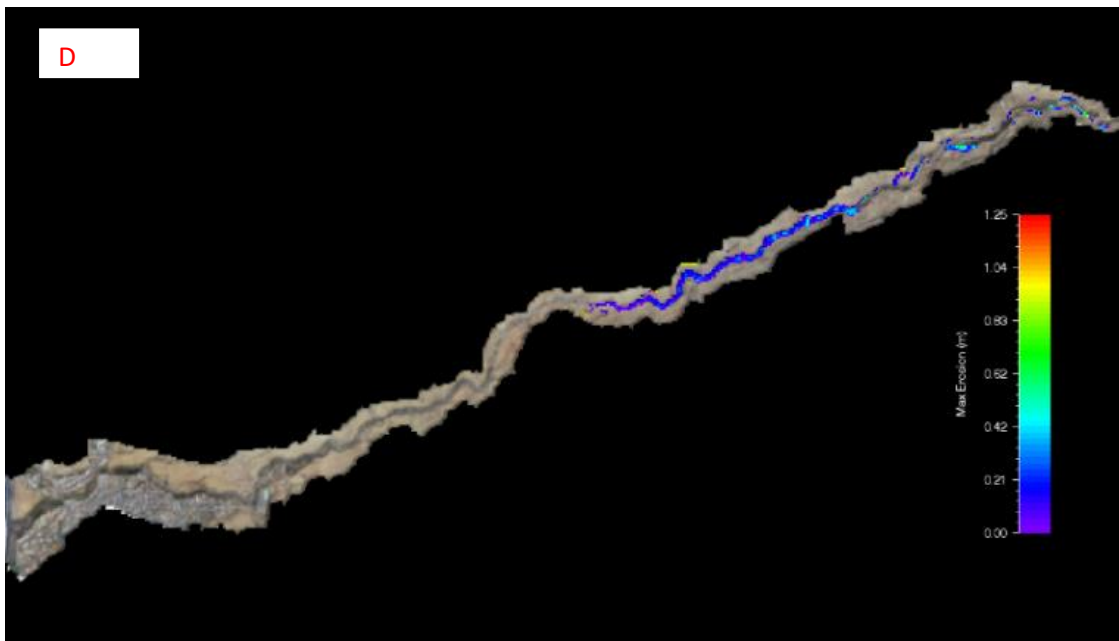
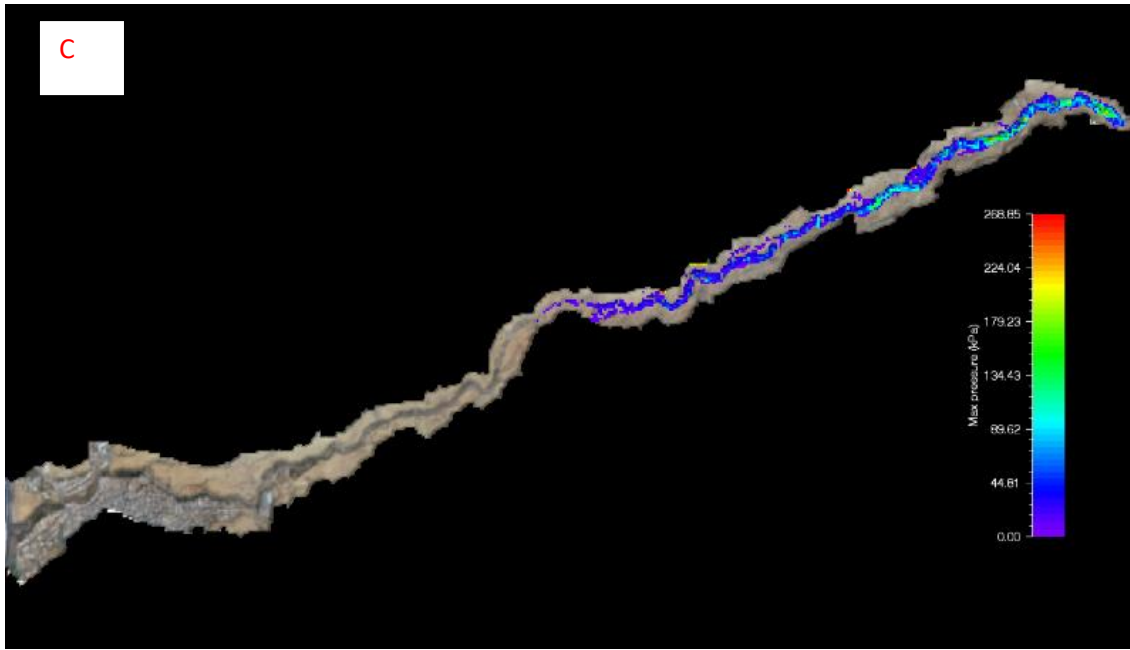


Figure 6.11: RAMMS debris flow simulation of Ribeira Santo Domingo (Fogo), (C) flow pressure (in Pa), (D) flow entrainment (in m³) over the whole drainage area.

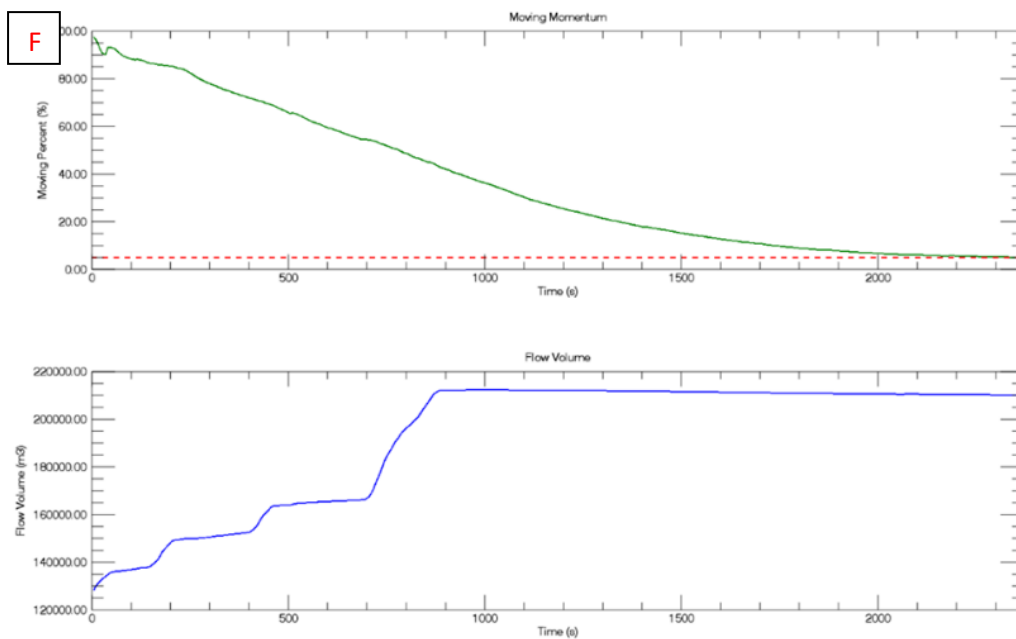
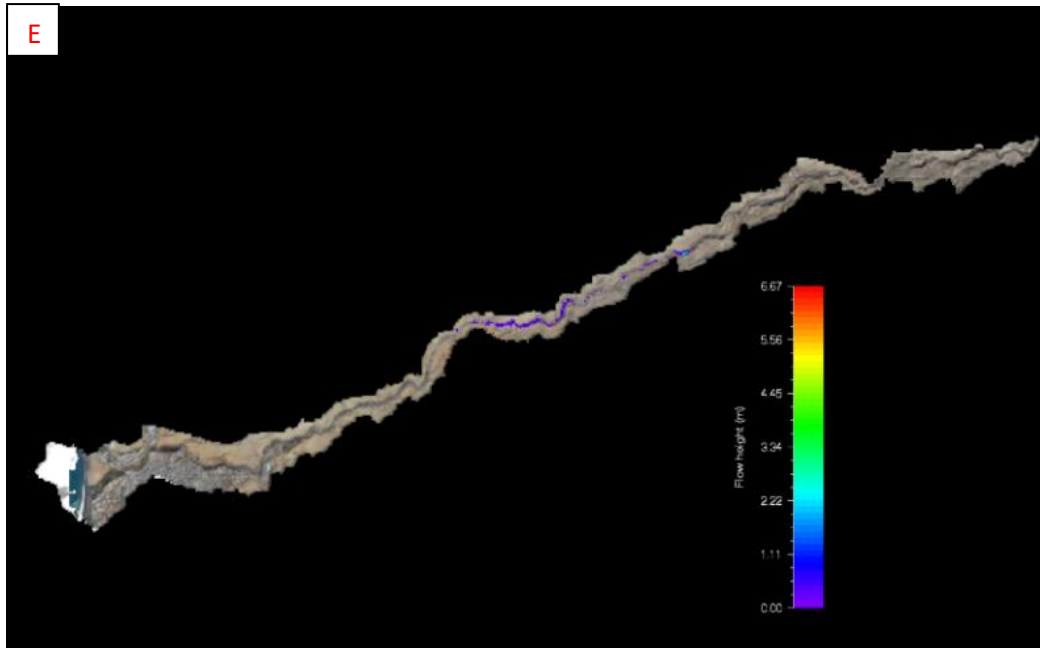


Figure 6.11: RAMMS debris flow simulation of Ribeira Santo Domingo (Fogo), (E) flow deposition (in m³) and (F) flow momentum (in m/s) over the whole drainage area.

6.3 HEC-RAS 2D Unsteady Flow Results

The results from 2D unsteady flow simulations for six localities in Dominica and one locality in Fogo, Cape Verde are presented in this section. Simulation was done using HEC RAS 2D model version 5.0.7. Outcomes of the modelling are presented as graphs and maps.

6.4 Model Calibration Results

Total area and DSM resolution for each locality are presented in Table 6.14. Results of the unsteady flow simulations are presented as maps and graphs showing flow depth, flow velocity and water surface elevation. HEC-RAS uses the United States of America’s customary “imperial” units system of measurement; hence outcomes of the simulations are presented as such. However, they will be converted to metric system in the text.

Locality	Coulibistrie	Delice	Layou	Pagua	Pointe Michel	Soufriere	Ribeira Santo Domingo
Area (km ²)	2.8	2.5	1.7	2.3	1.6	1.3	86.7
DSM Resolution (m)	5	2	3	7	7	6	15

Table 6.14: Total area and DSM resolution for each locality used for the unsteady flow simulation.

6.4.1. Coulibistre HEC-RAS 2D Unsteady Flow Simulation Results

Figure 5.1 shows the results of the unsteady flow simulation for Coulistrie. The simulation showed a maximum flood depth of 4.17 m and minimum flood depth of 0.0 m (Figure 6.12 A and B). Areas with high water depth were mainly along the main river channel into the Caribbean Sea and gradually spreading to the floodplains. This is due to the study area being in a rugged and high slope terrain, hence there is rapid flow of water from upstream to downstream causing inundation in the main river channel and floodplains. Variations of flood depth across the 2.8 km² of the modelled area are depicted in Figure 6.12 A and B.

From the simulation results there were variations in flow velocity across the whole drainage area (Figures 6.12 C and D). The highest velocity recorded after the simulation was 27342 m/s and the minimum velocity was 4 m/s (Figures 6.12 C and D) Surprisely, the flow velocity was approximately the same across most of the study area (Figure 6.12 C). High velocities were predominately recorded downstream as the flow entered the sea (Figure 6.12 C). This can be attributed to debris and boulders blocking the bridge downstream, creating an inundated dam and causing an increase in flow velocity.

Figures 6.12 E and F show the water surface elevation at which the terrain was inundated. From the simulation results, the minimum and maximum water surface elevation at which the area was inundated were -24 m and -11.1 m, respectively (Figures 6.12 E and F). The water surface elevation was high at the upper part of the terrain, gradually decreasing down the channel into the Caribbean Sea. This shows a correlation between the spatial distribution of the terrain's elevation, high slopes upstream and low-lying areas downstream.

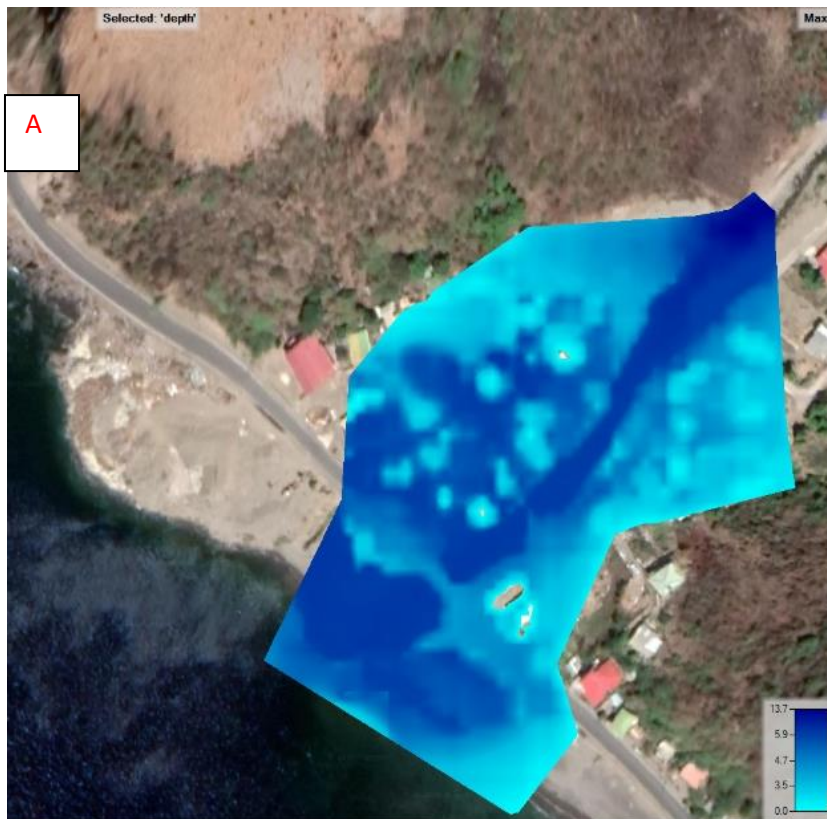


Figure 6.12 A: Results of HEC-RAS unsteady flow simulation for Coulibistrie (Dominica), showing variations in flow depth across the floodplain (in m)

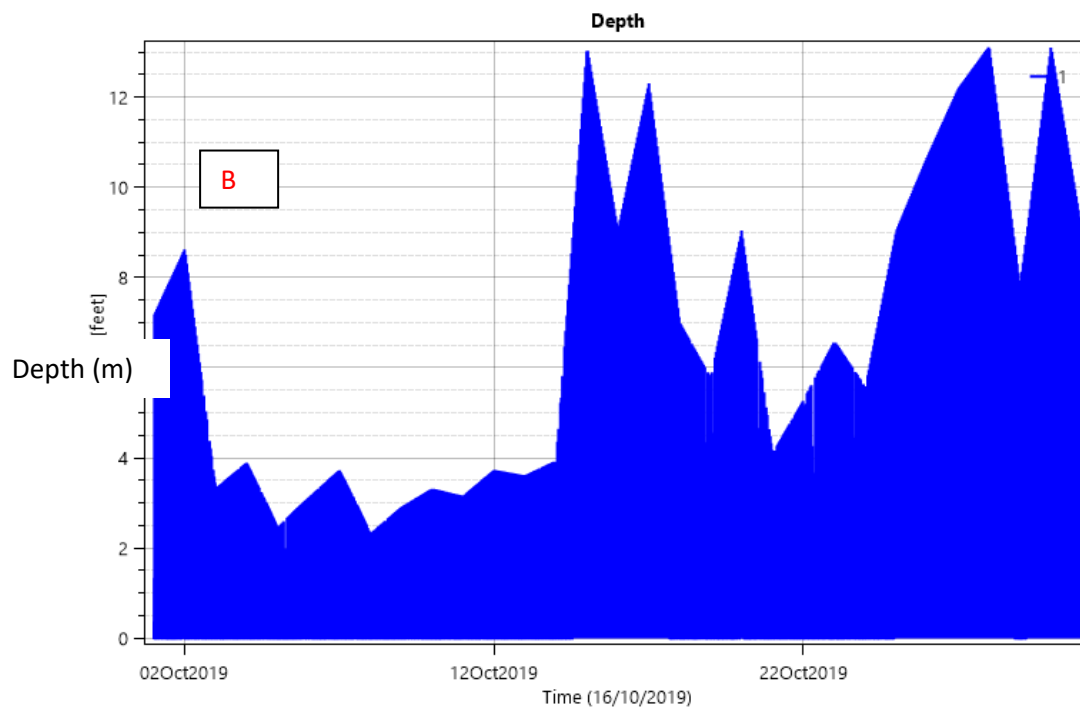


Figure 6.12 B: Results of HEC-RAS unsteady flow simulation for Coulibistrie (Dominica), showing variations in daily flow depth over a month (in m).

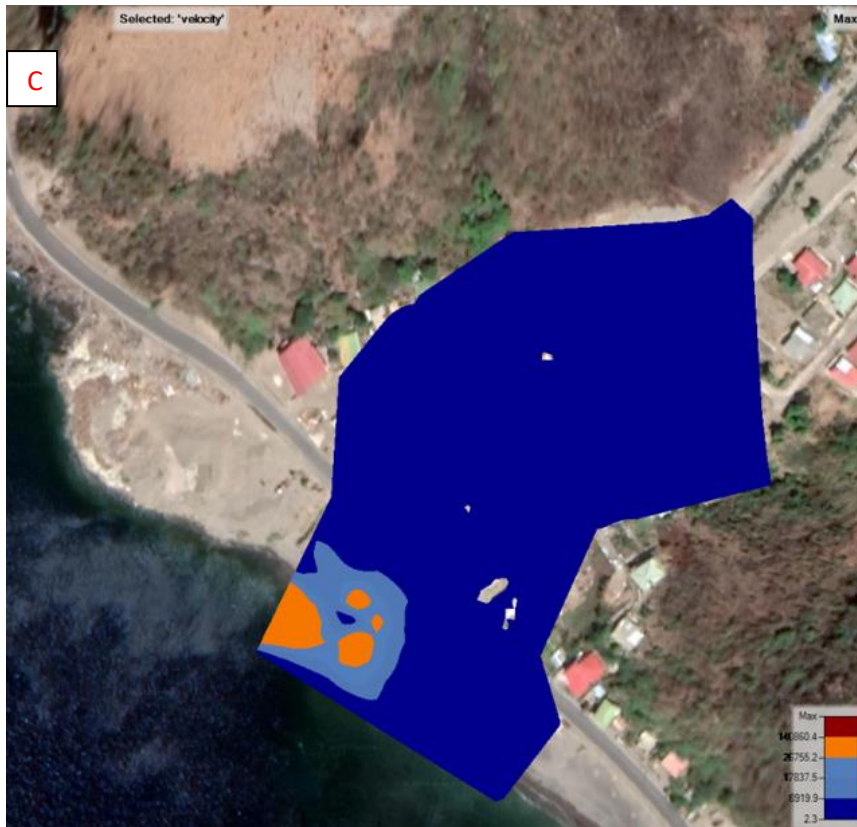


Figure 6.12 C: Results of HEC-RAS unsteady flow simulation for Coulibistrie (Dominica), showing variations in flow velocity across the floodplain (in m/s)

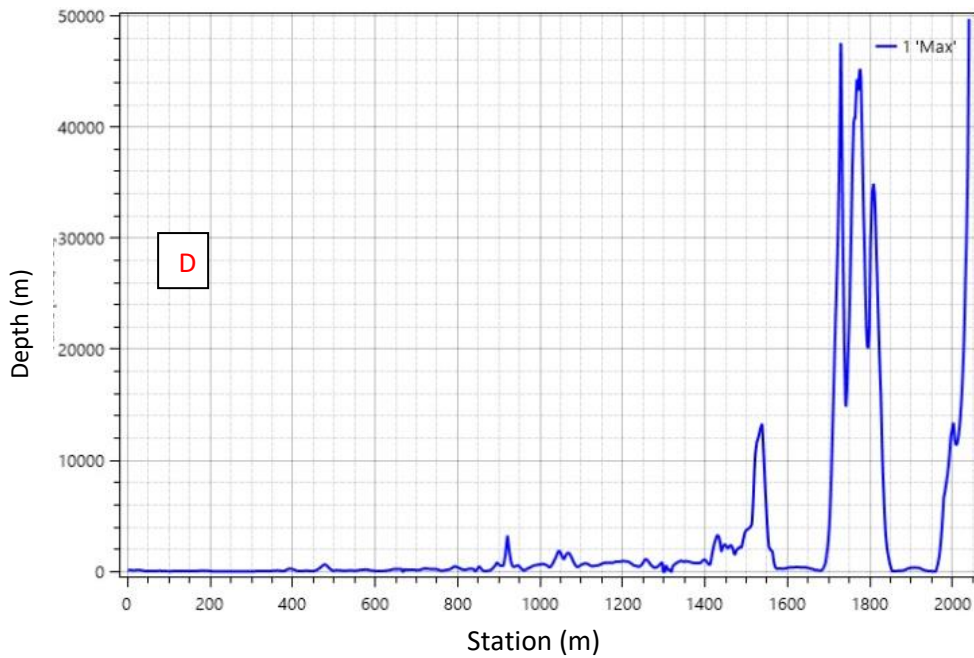


Figure 6.12 D: Results of HEC-RAS unsteady flow simulation for Coulibistrie (Dominica), showing variations in flow velocity along the channel (in m/s).

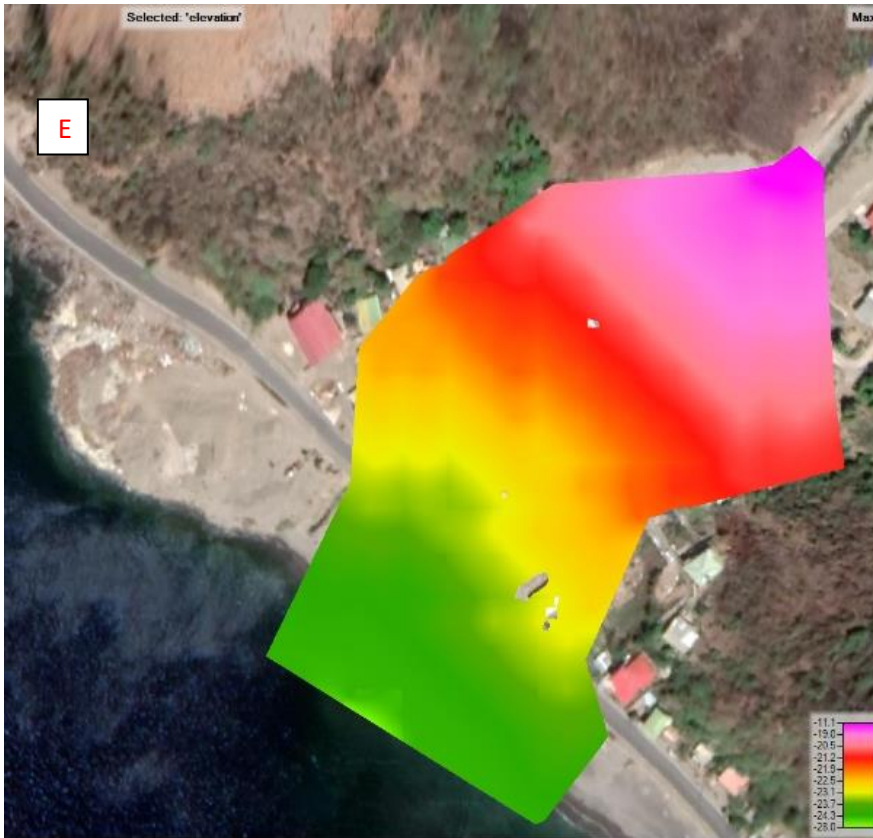


Figure 6.12 E: Results of HEC-RAS unsteady flow simulation for Coulibistrie (Dominica), showing variations in water surface elevation across the floodplain (in m).

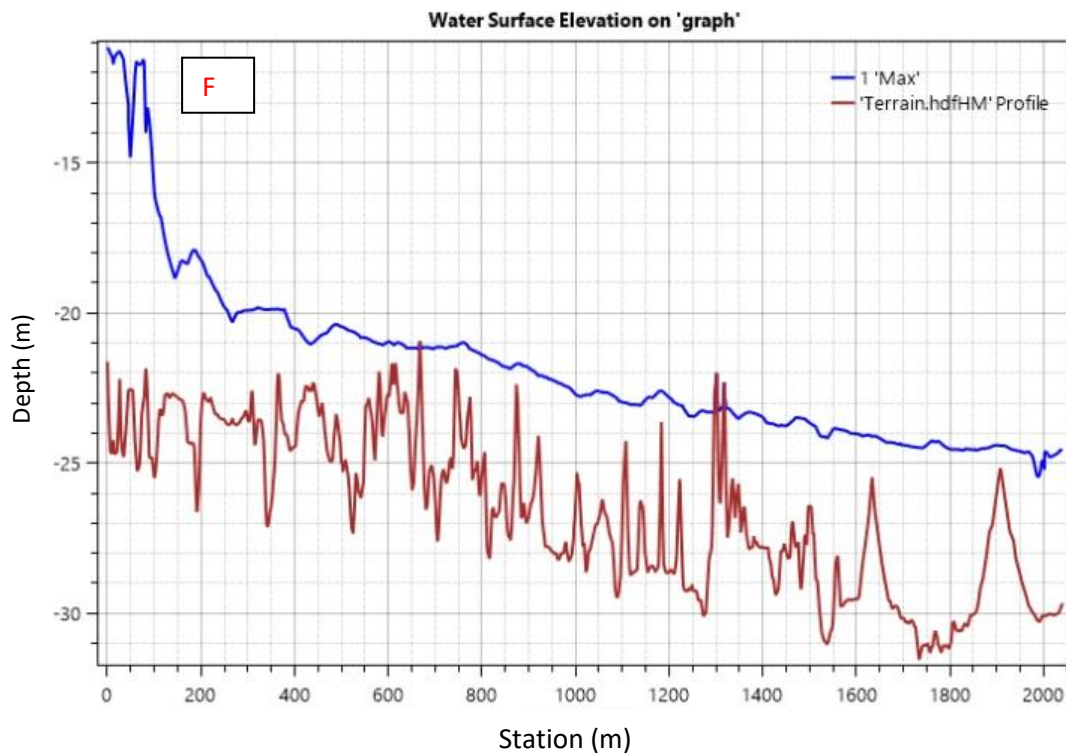


Figure 6.12 F: Results of HEC-RAS unsteady flow simulation for Coulibistrie (Dominica), showing comparison between water surface elevation and terrain elevation (in m).

6.4.2 Delice HEC-RAS 2D Unsteady Flow Simulation Results

Modelling results for Delice are presented in Figure 5.2 showing flow depth, flow velocity and water surface elevation. Maximum flow depth was 24 m whilst the minimum flow depth was 0.0 m after the simulation (Figures 6.13 A and B). Flow depth was high upstream and primarily within the main channel into the Atlantic Ocean. Low flow depths were recorded at the floodplains. This can be attributed to differences in elevation of the terrain, hence water flows rapidly from highlands into lowlands (Figure 6.13 A). Figure 6.13 B depicts variations of flow depth across the study area.

Flow velocity of the unsteady flow simulation for Delice is presented in figure 6.13 C and D. Almost the entire drainage area had similar velocities with the exception of the south-east and south-west corners. Force of the flow was very high to an extent that the maximum velocity recorded was 20726 m/s, whilst the minimum flow velocity was 14 m/s (Figures 6.13 C and D). High velocities were predominately recorded downstream into the Atlantic Ocean (Figures 6.13 C and D).

Water surface elevation results are presented in Figures 6.13 E and F. From the simulation results, the minimum surface elevation at which the terrain was inundated was -29 m and the maximum surface elevation where inundation occurred was -11 m (Figures 6.13 E and F). Based on the results Delice is very susceptible to flooding because it is situated in low-lying area. Just like Coulibistrie, the water surface elevation was high at the upper part of the terrain, steadily reducing down the channel into the Atlantic Ocean (Figures 6.13 E).

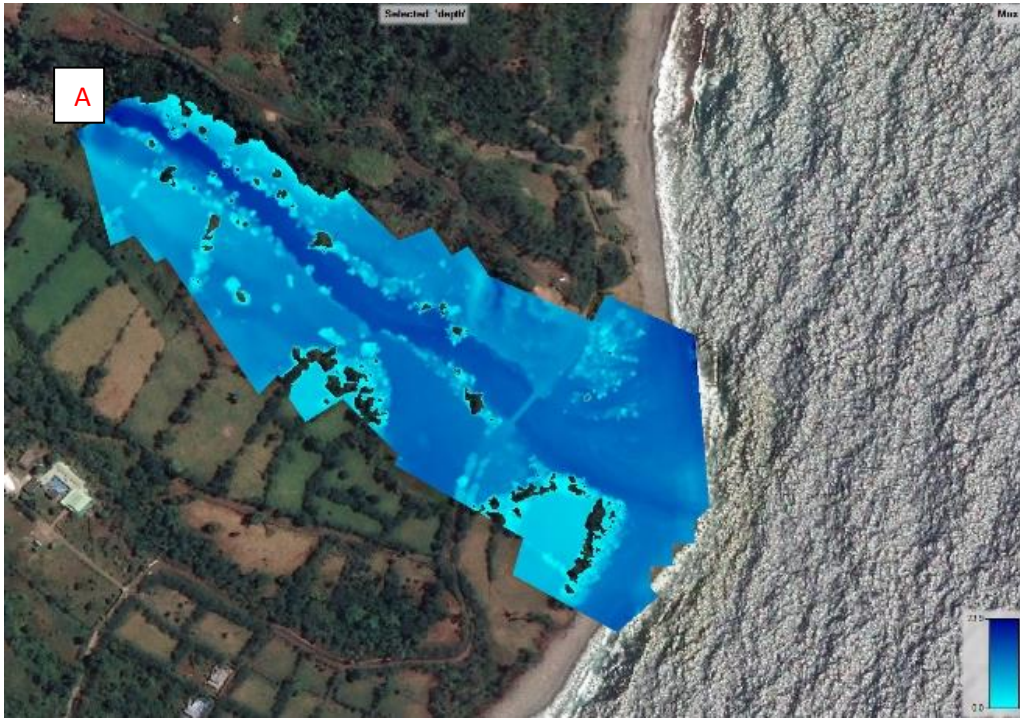


Figure 6.13 A: Results of HEC-RAS unsteady flow simulation for Delice (Dominica), showing variations in flow depth across the floodplain (in m)

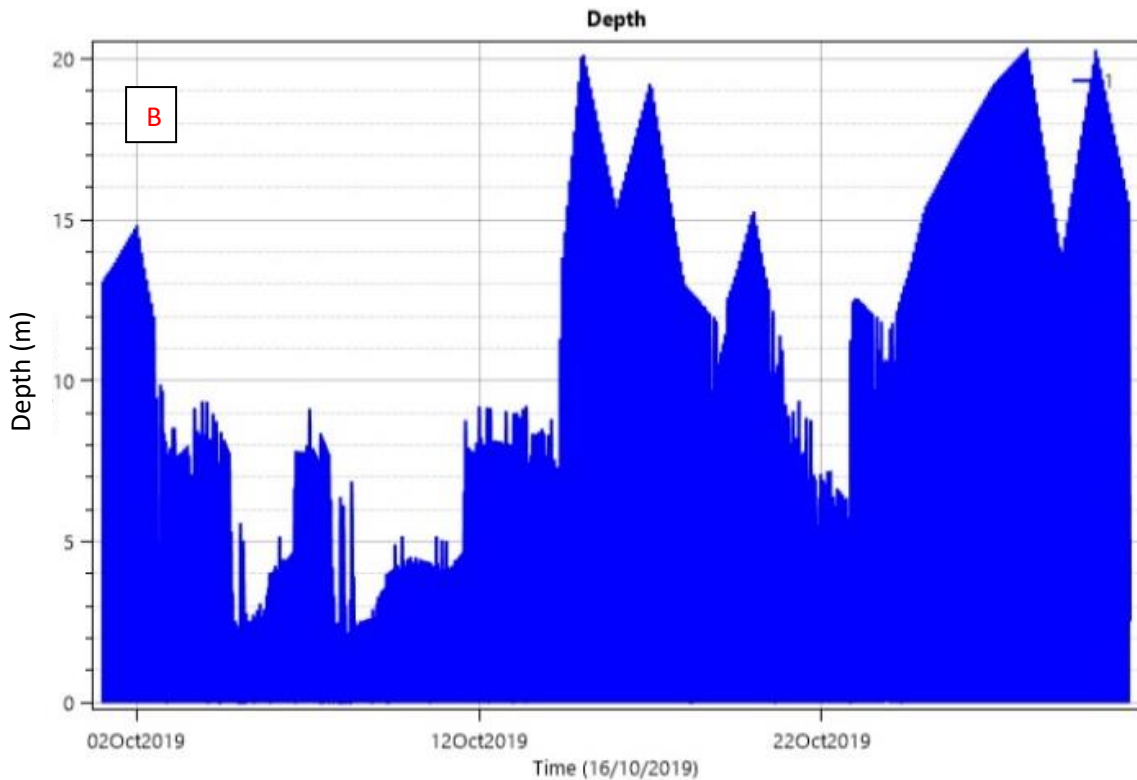


Figure 6.13 B: Results of HEC-RAS unsteady flow simulation for Delice (Dominica), showing variations in daily flow depth over a month (in m).

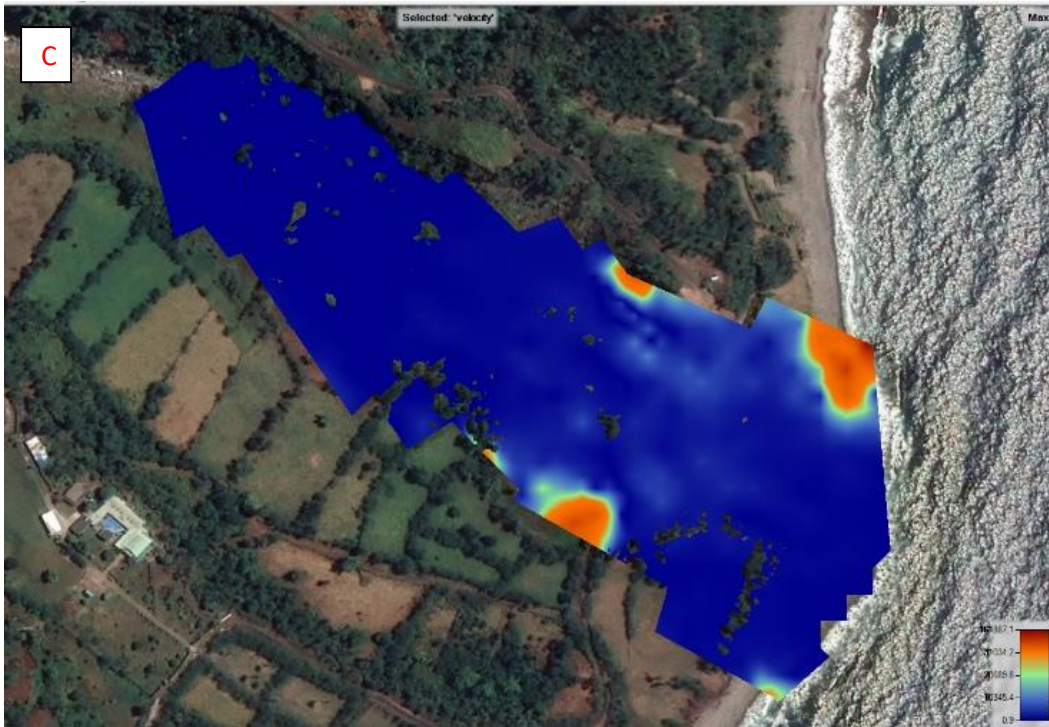


Figure 6.13 C: Results of HEC-RAS unsteady flow simulation for Delice (Dominica), showing variations in flow velocity across the floodplain (in m/s)

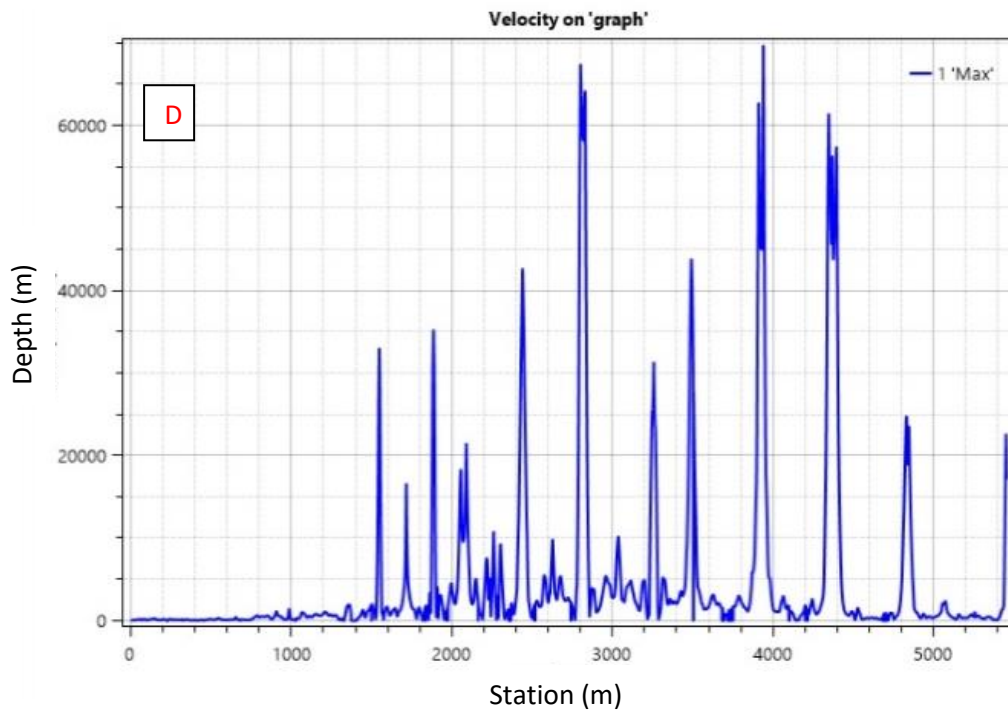


Figure 6.13 D: Results of HEC-RAS unsteady flow simulation for Delice (Dominica), showing variations in flow velocity along the channel (in m/s)

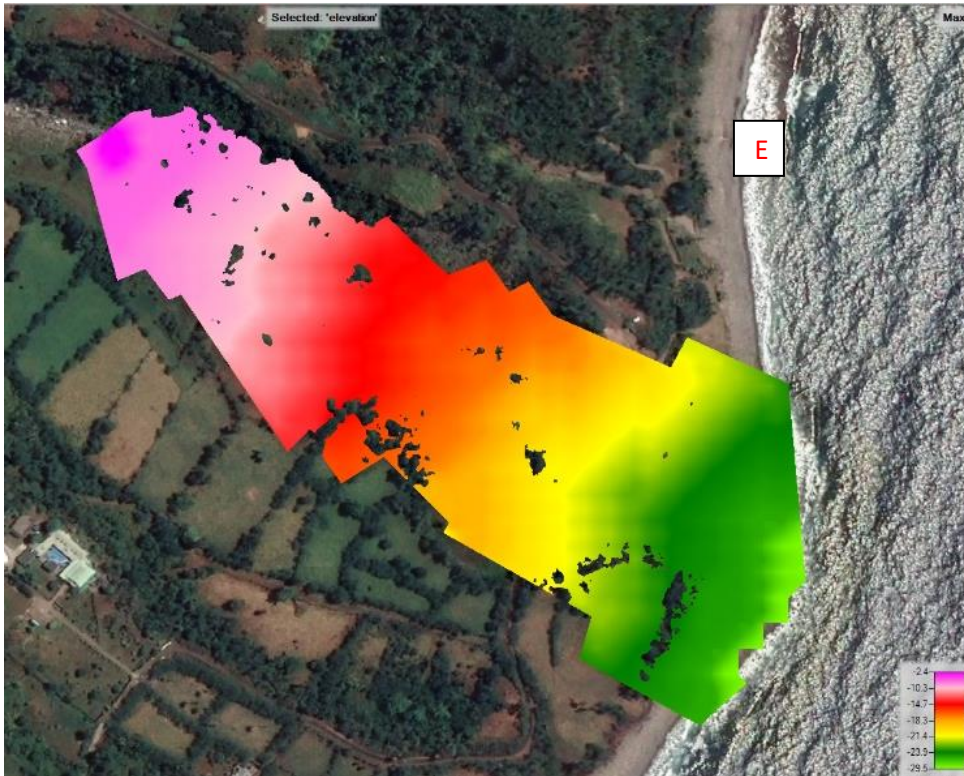


Figure 6.13 E: Results of HEC-RAS unsteady flow simulation for Delice (Dominica), showing variations in water surface elevation across the floodplain (in m)

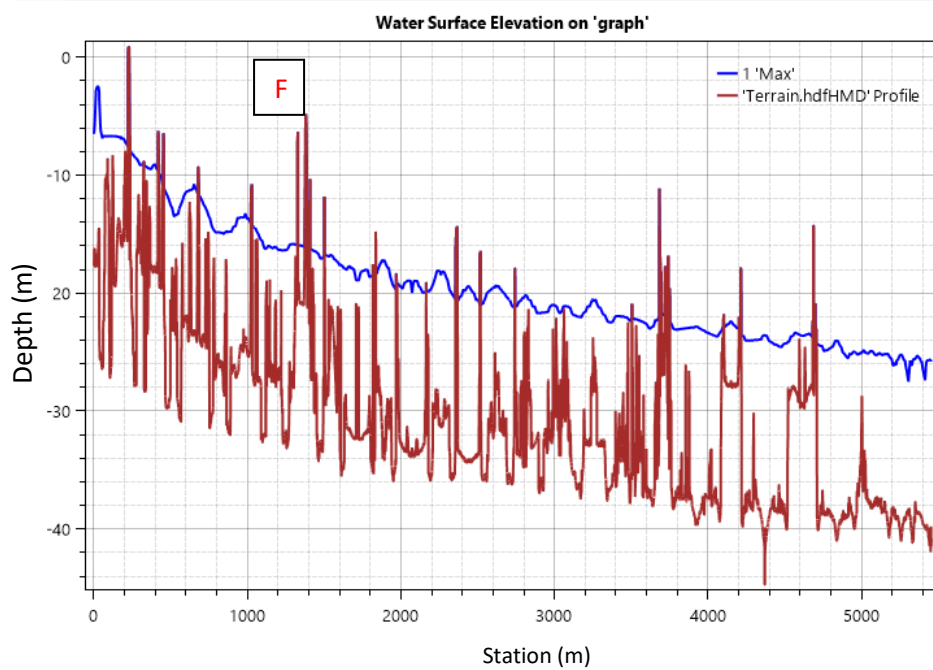


Figure 6.13 F: Results of HEC-RAS unsteady flow simulation for Delice (Dominica), showing comparison between water surface elevation and terrain elevation (in m)

6.4.3 Layou HEC-RAS 2D Unsteady Flow Simulation Results

Results of the unsteady flow simulation for Layou are presented in Figure 6.14. Highest flood depth recorded was 17.2 m and lowest flood depth recorded was 0.0 m (Figures 6.14 A and B). Maximum flood depth areas were mostly within the main channel whilst minimum flow depth areas were at the floodplains (Figure 6.14 A). Accumulation of flow from high slopes to low slope areas is the reason why flow depth is high within the main channel especially downstream (Figure 6.14 A). There were changes of flood depth across the drainage area throughout the month as depicted in Figure 6.14 B.

Figures 6.14 C and D shows the flow velocity results. Flow velocity was most active at the south-western parts of the drainage area. These areas are highlands, hence there was rapid flow of water down-slope into the channel (Figure 6.14 C). After the simulation, 8473.44 m/s was the maximum recorded flow velocity was and 10.6 m/s was the minimum recorded flow velocity (Figure 6.14 C and D). Most of the drainage area had similar flow velocity especially upstream and downstream of the channel (Figure 6.14 C).

Layou lies in a valley which makes the area very vulnerable to flood hazard. The water surface elevation results confirms that Layou is a low-lying area. The elevation at which the terrain was inundated are presented in Figures 6.14 E and F. From the modelling results, the maximum water surface elevation was -11.6 m and the minimum water surface elevation was -23.9 m respectively (Figures 6.14 E and F). Just like Coulibistrie and Delice, water surface elevation for Layou was also high at the upper part of the terrain and reduced steadily downstream of the channel.



Figure 6.14 A: Results of HEC-RAS unsteady flow simulation for Delice (Dominica), showing variations in flow depth across the floodplain (in m)

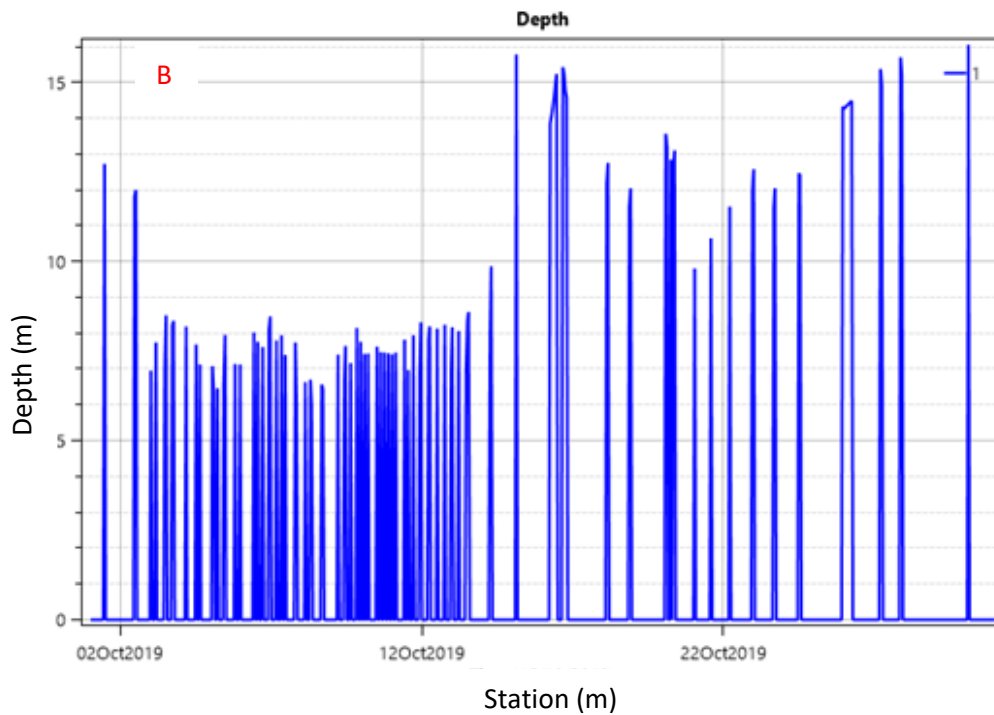


Figure 6.14 B: Results of HEC-RAS unsteady flow simulation for Layou (Dominica), showing variations in daily flow depth over a month (in m).

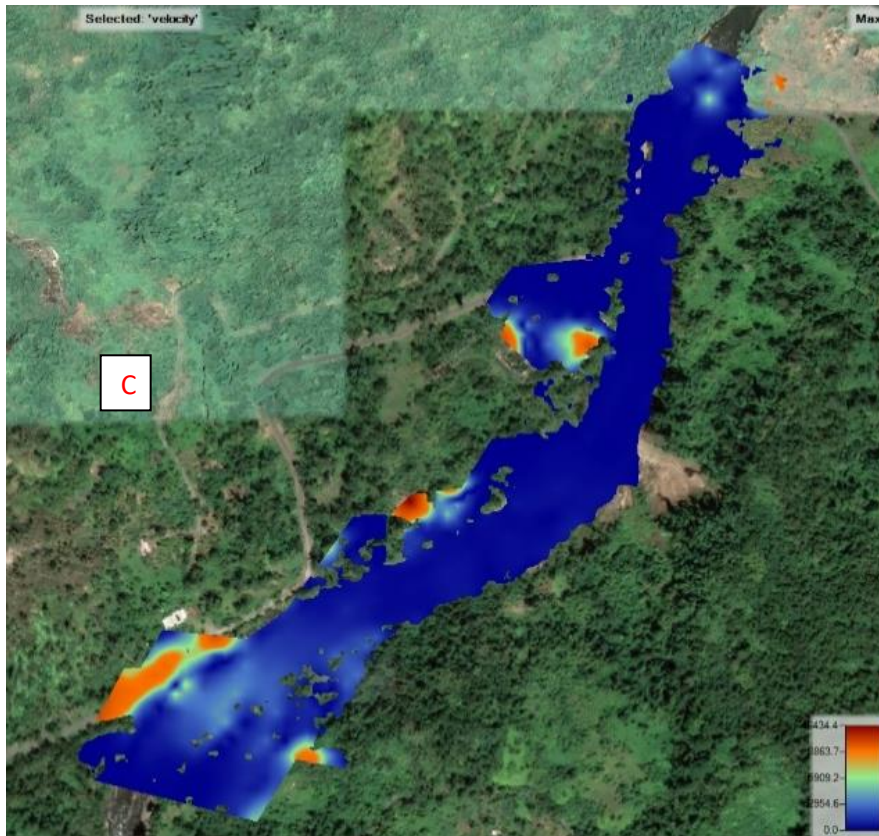


Figure 6.14 C: Results of HEC-RAS unsteady flow simulation for Layou (Dominica), showing variations in flow velocity across the floodplain (in m/s).

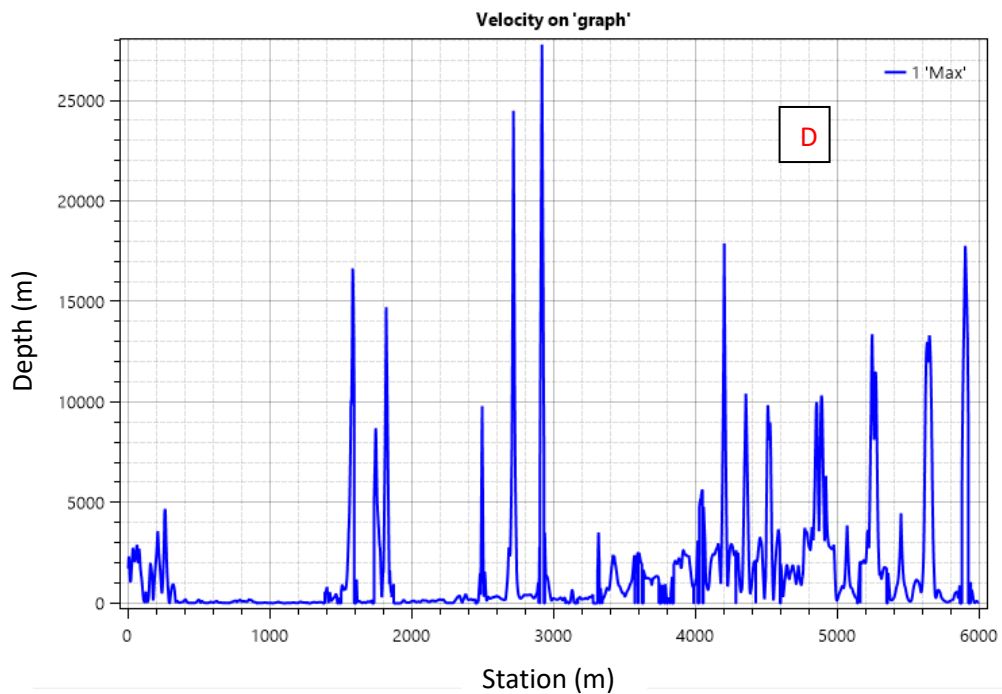


Figure 6.14 D: Results of HEC-RAS unsteady flow simulation for Layou (Dominica), showing variations in flow velocity along the channel (in m/s).

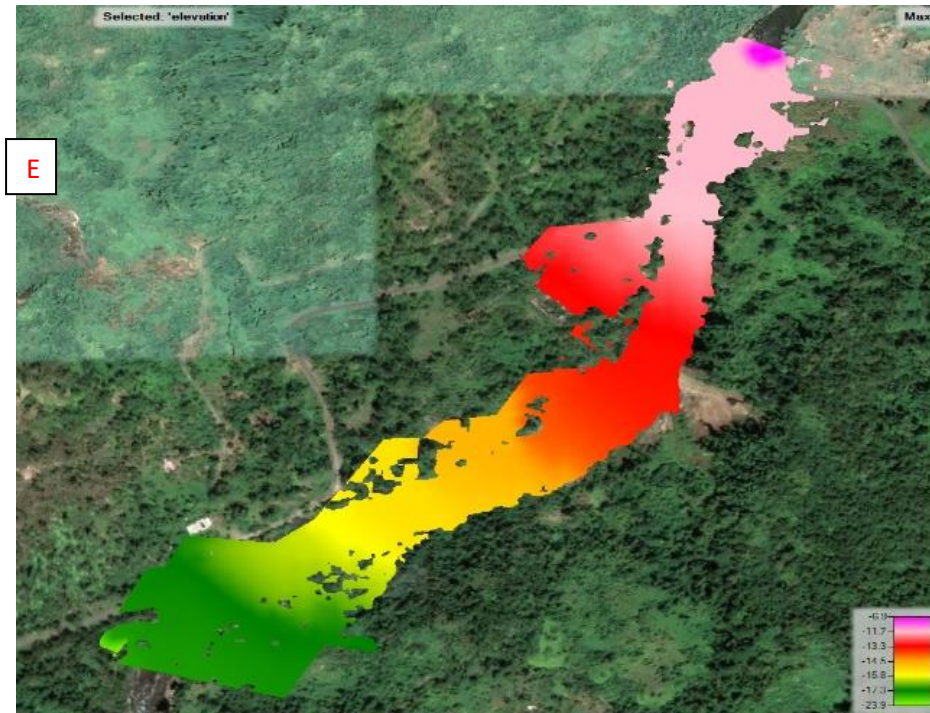


Figure 6.14 E: Results of HEC-RAS unsteady flow simulation for Layou (Dominica), showing variations in water surface elevation across the floodplain (in m)

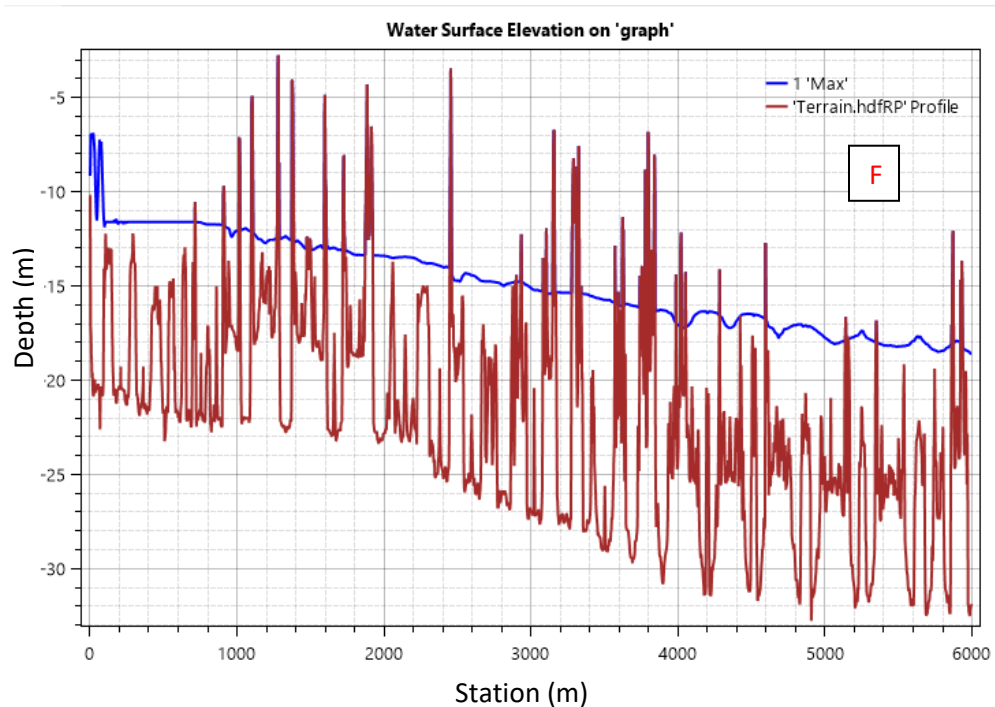


Figure 6.14 F: Results of HEC-RAS unsteady flow simulation for Layou (Dominica), showing comparison between water surface elevation and terrain elevation (in m)

6.4.4 Pagua HEC-RAS 2D Unsteady Flow Simulation Results

A maximum flow depth of 20.3 m and minimum flow depth of 0.0 m was recorded after the simulation (Figure 6.15 A and B). Flow depth was high within the main channel and low in the floodplains (Figure 6.15 A). Variation in the terrain's elevation is factor influencing high flow depth in the channel and low flow depth in the floodplains. This is because of the rapid flow of water from high grounds to low grounds water such as the main channel. Flow depth was relative high mid-November in comparison to the beginning of November (Figure 6.15 B).

Figures 6.15 C and D shows the flow velocity results after the simulation. Maximum flow velocity recorded was 4511 m/s and the minimum flow velocity recorded was 5 m/s. Similar flow velocities were recorded across the whole drainage area (Figure 6.15 C). Flow velocity was predominately high at the eastern corner of the channel within the flow transition zone (Figure 6.15 C). This can be attributed to debris jamming behind the extremely giant boulders, forming an inundated dam and diverting direction of water flow rapidly and causing an increase in flow velocity.

Figures 6.15 E and F shows both the water surface elevation at which the terrain was inundated and terrain's elevation above sea level. From the simulation results, the recorded maximum water surface elevation was 22 m against the terrain's highest elevation of 15 m and minimum water surface elevation at which the area was inundated were -6 m (Figures 6.15 E and F). Just like the other localities, water surface elevation was high at the upper part of the terrain and reduced in elevation gradually down the channel into the Atlantic Ocean. This indicates that most of the headstreams of these drainage areas begins at high slopes whilst the channel mouths are found in low-lying areas.

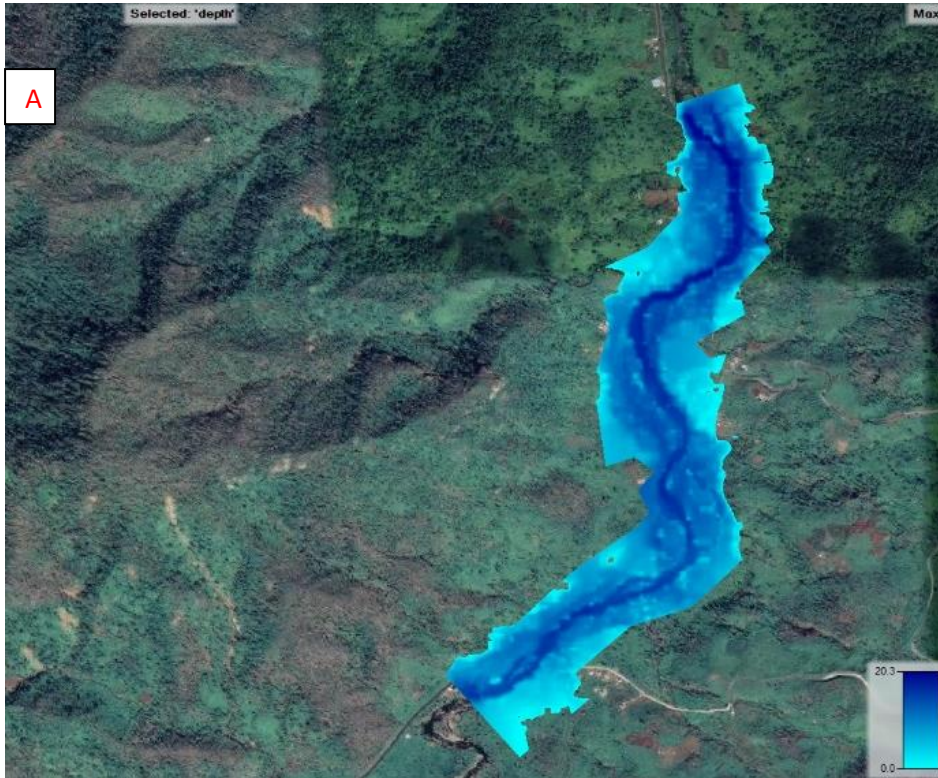


Figure 6.15 A: Results of HEC-RAS unsteady flow simulation for Pagua (Dominica), showing variations in flow depth across the floodplain (in m).

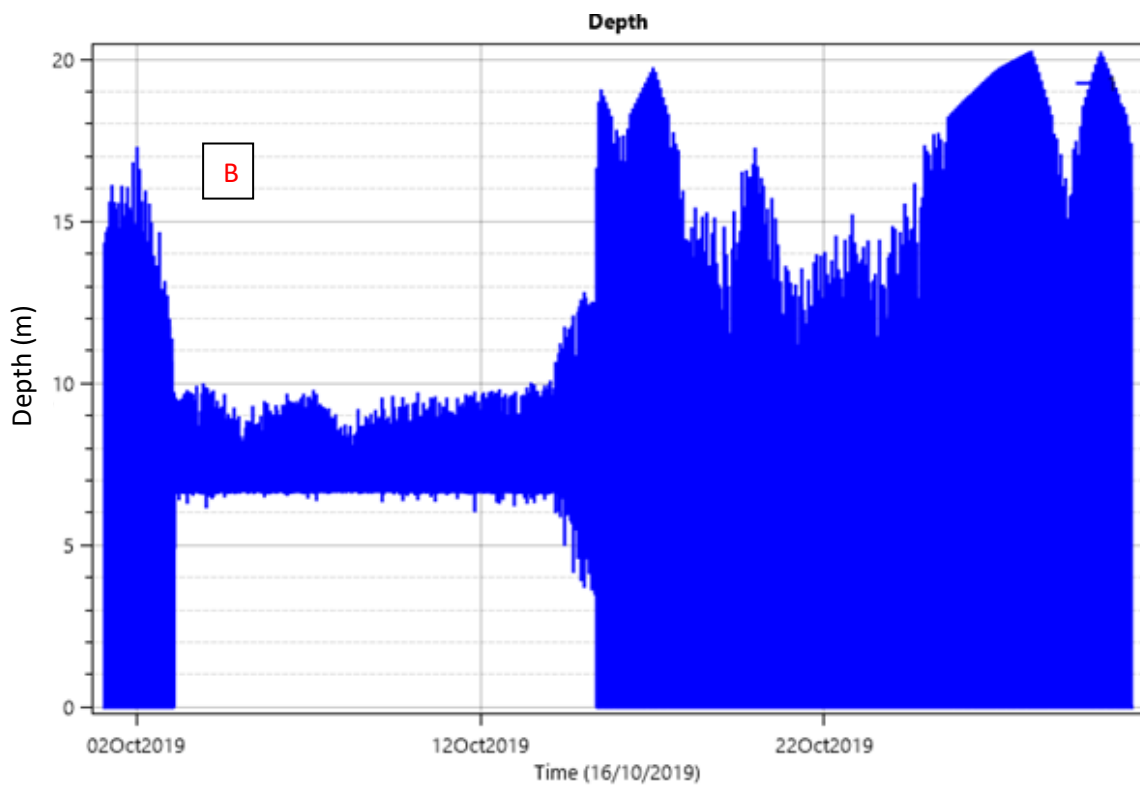


Figure 6.15 B: Results of HEC-RAS unsteady flow simulation for Pagua (Dominica), showing variations in daily flow depth over a month (in m).



Figure 6.15 C: Results of HEC-RAS unsteady flow simulation for Pagua (Dominica), showing variations in flow velocity across the floodplain (in m/s).

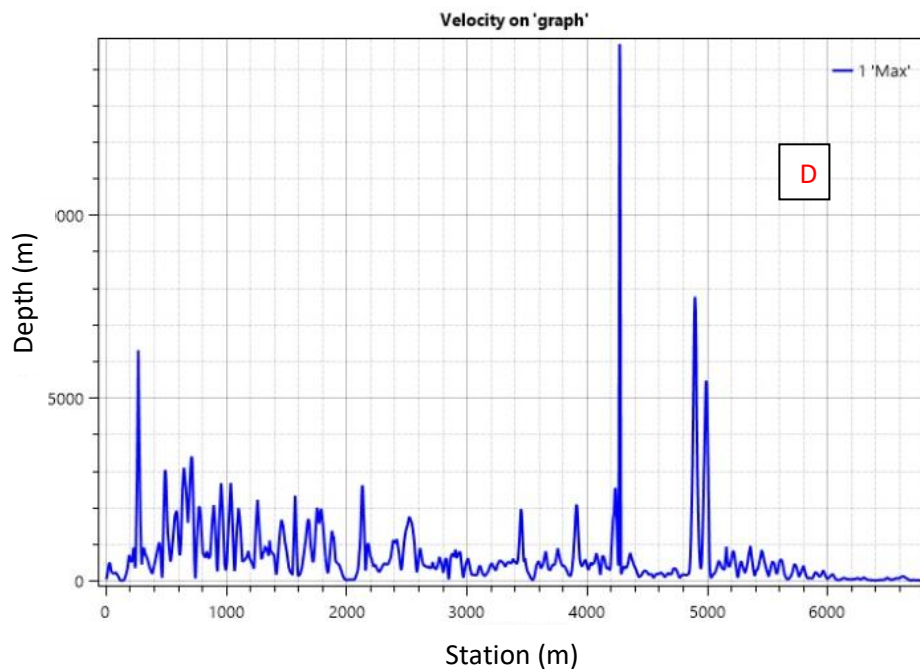


Figure 6.15 D: Results of HEC-RAS unsteady flow simulation for Pagua (Dominica), showing variations in flow velocity along the channel (in m/s).

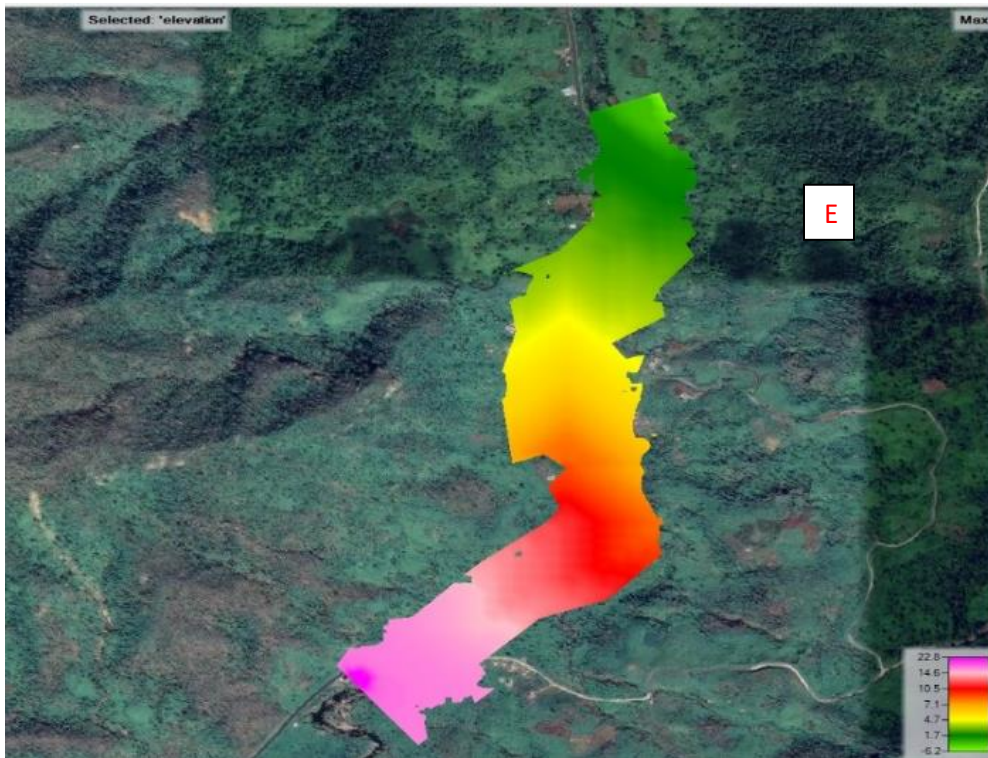


Figure 6.15 E: Results of HEC-RAS unsteady flow simulation for Pagua (Dominica), showing variations in water surface elevation across the floodplain (in m)

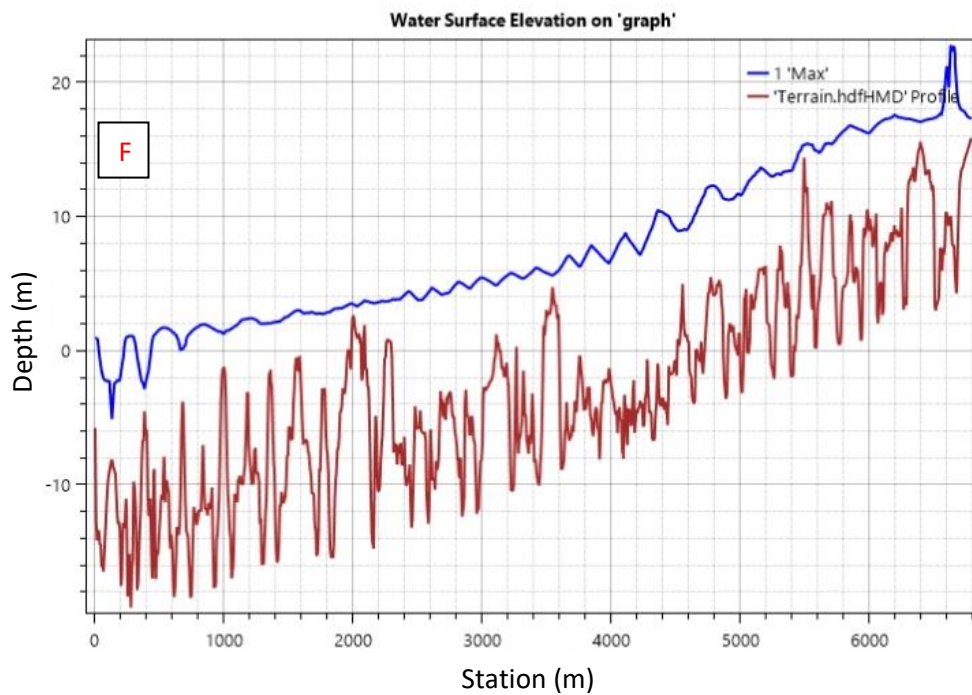


Figure 6.15 F: Results of HEC-RAS unsteady flow simulation for Pagua (Dominica), showing comparison between water surface elevation and terrain elevation (in m).

6.4.5 Pointe Michel HEC-RAS 2D Unsteady Flow Simulation Results

Pointe Michel's unsteady flow results are presented in Figure 6.16. After the modelling, the recorded maximum flow depth was 61.2 m and the minimum flow depth of 0.0 m (Figure 6.16 A and B). Areas with high water depth were mainly at the headstreams and within the main channel into the Caribbean Sea (Figure 6.16 A). Upper parts of the settlement sandwiched between the two channels also had relatively high flow depth (Figure 6.16 A). Low flow depths were recorded at floodplains of the north channel (Figure 6.16 A). Due to the ruggedness of the terrain, there was rapid flow of water from high slopes upstream to low slopes downstream into the Caribbean Sea.

Maximum flow velocity recorded was 17983 m/s whilst the minimum flow velocity recorded was 30 m/s (Figure 6.16 C and D). Just like the other localities, Pointe Michel recorded relatively the same across the entire drainage area. However, high flow velocities were recorded at the extreme ends of both the south and north channels (Figure 6.16 C). This can be attributed to debris and boulders blocking the bridges downstream hence creating an inundated dam and causing increase in flow velocity.

From the simulation results, the minimum and maximum water surface elevation at which the area was inundated were 6 m and 152 m respectively (Figures 6.16 E and F). Figures 6.16 E and F shows the water surface elevation at which the terrain was inundated and the terrain's elevation above sea level. From upstream to downstream, the water surface elevation decreased steadily down the channel into the Caribbean Sea (Figures 6.16 E).

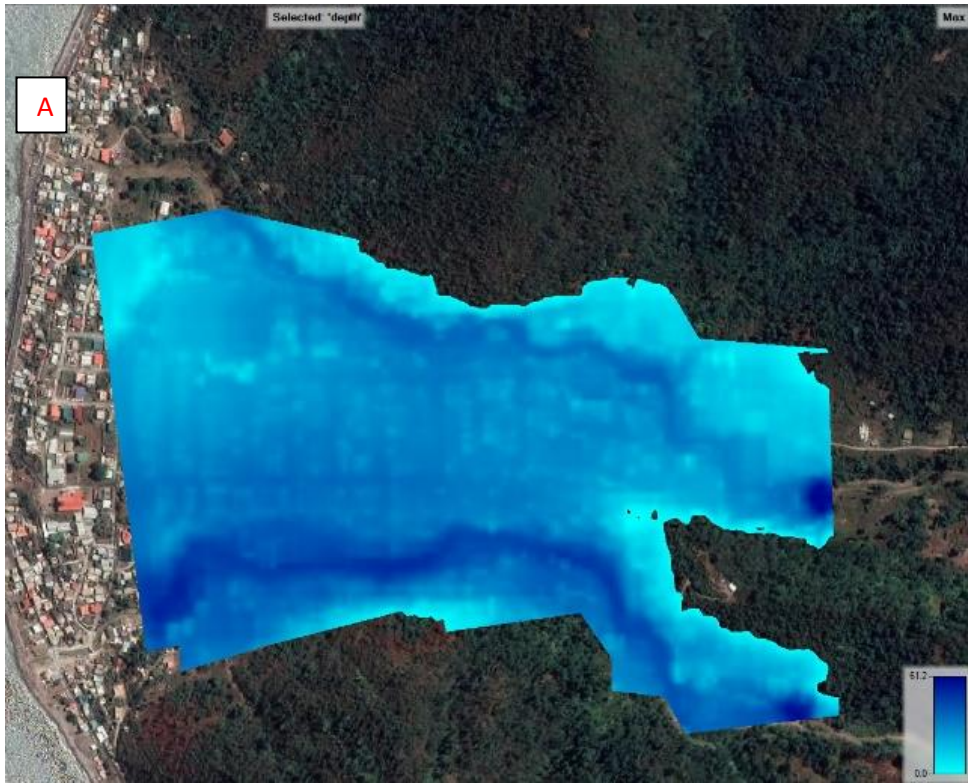


Figure 6.16 A: Results of HEC-RAS unsteady flow simulation for Pointe Michel (Dominica), showing variations in flow depth across the floodplain (in m).

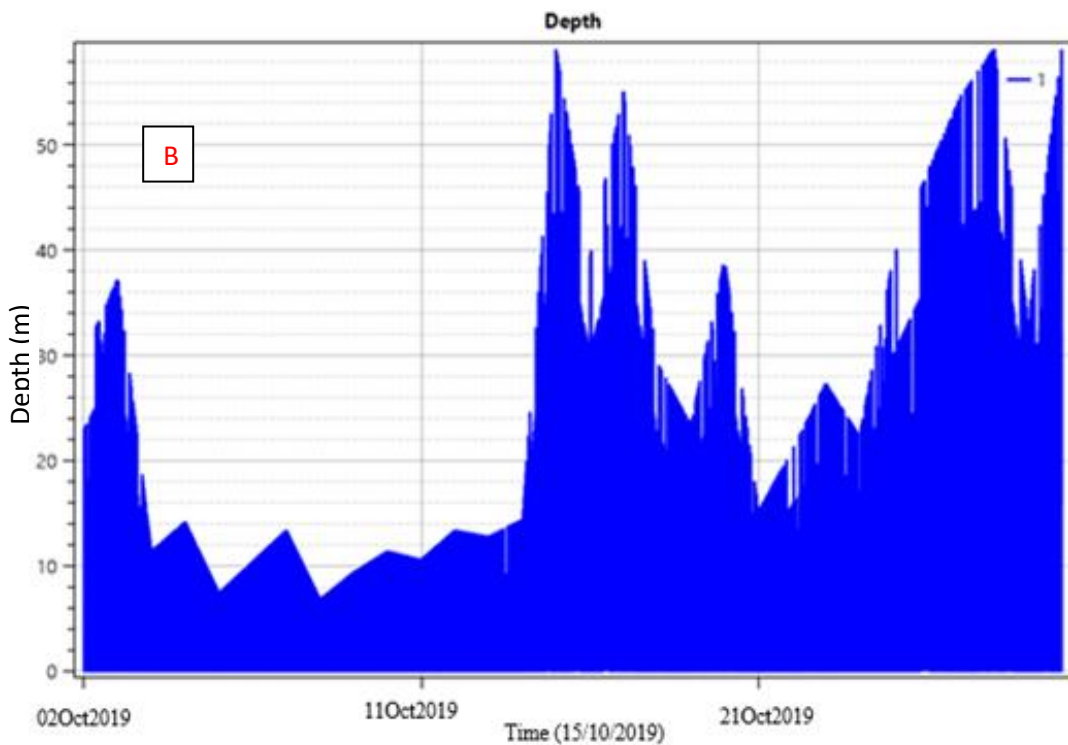


Figure 6.16 B: Results of HEC-RAS unsteady flow simulation for Pointe Michel (Dominica), showing variations in daily flow depth over a month (in m).



Figure 6.16 C: Results of HEC-RAS unsteady flow simulation for Pointe Michel (Dominica), showing variations in flow velocity across the floodplain (in m/s)

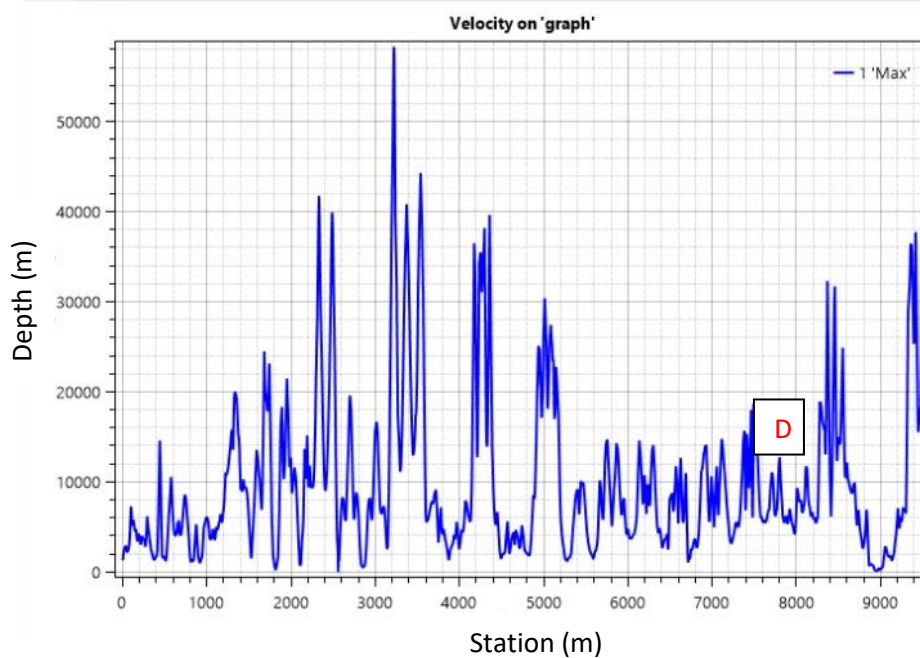


Figure 6.16 D: Results of HEC-RAS unsteady flow simulation for Pointe Michel (Dominica), showing variations in flow velocity along the channel (in m/s).

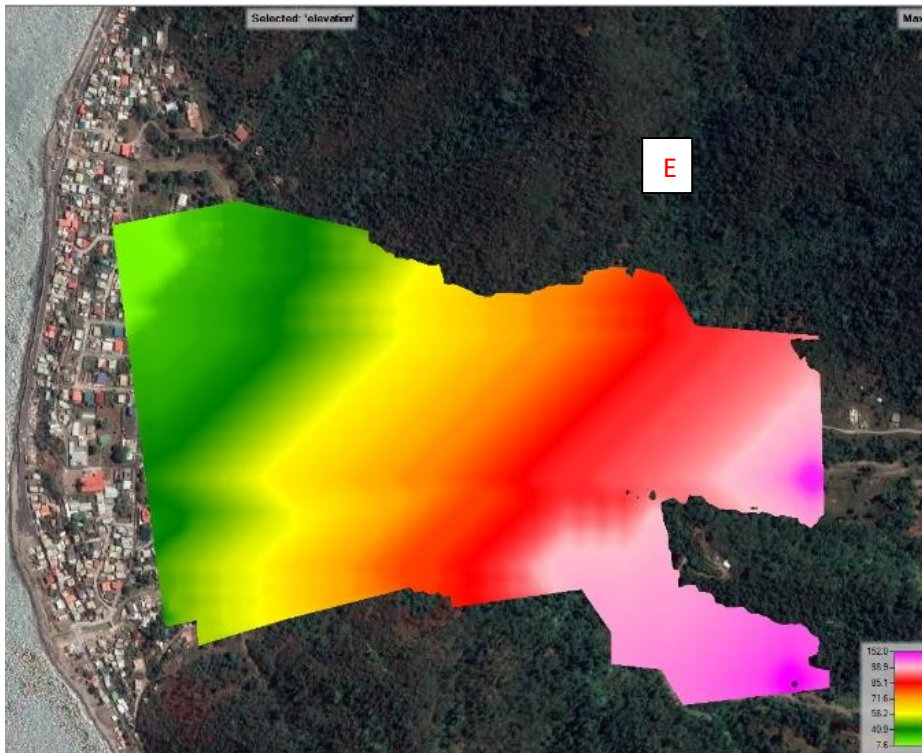


Figure 6.16 E: Results of HEC-RAS unsteady flow simulation for Pointe Michel (Dominica), showing variations in water surface elevation across the floodplain (in m).

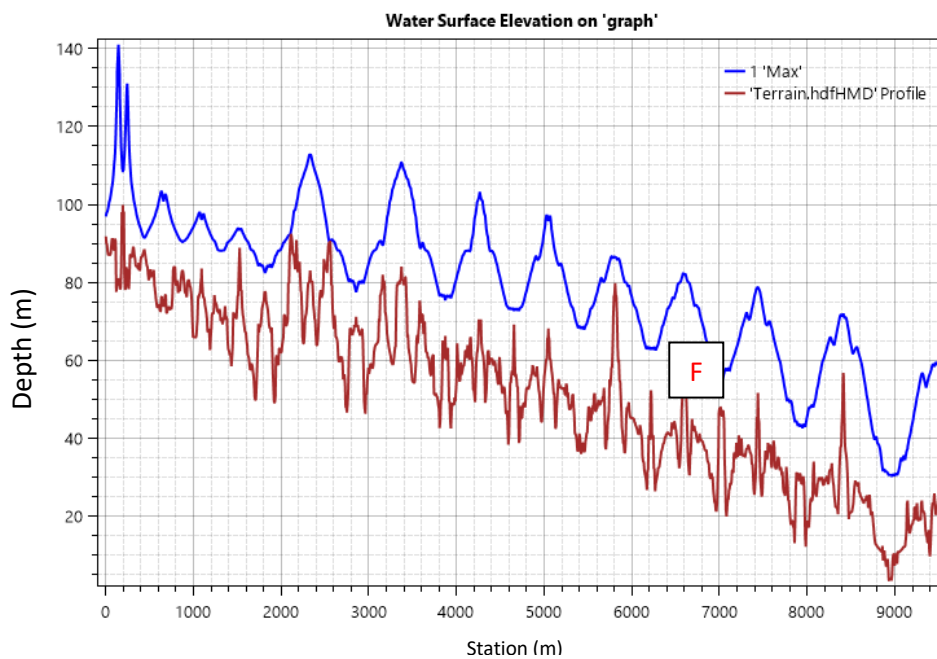


Figure 6.16 F: Results of HEC-RAS unsteady flow simulation for Pointe Michel (Dominica), showing comparison between water surface elevation and terrain elevation (in m).

6.4.6 Soufriere HEC-RAS 2D Unsteady Flow Simulation Results

Modelling results for Soufriere are presented in Figure 6.17. Flow depth was high mainly at the headstream and reduced steadily downstream (Figure 6.17 A). Flow depth was low downstream and across most of the drainage area because the area showed little elevation change. Outcome of the unsteady flow simulations showed a maximum flood depth of 36.8 m and minimum flow depth of 0.0 m (Figure 6.17 A and B). The sharp and extremely high slope caused by landslide means that there is rapid flow from highlands to lowlands.

Flow velocity results are presented in figures 6.17 C and D. Flow velocity did not change across most of the study area. The maximum velocity recorded after the simulation was 1189 m/s and the minimum velocity was 30 m/s (Figures 6.17 C and D). High velocities were predominately recorded at the north-east corner of the drainage area (Figure 6.17 C). This is as a result of the sharp slopes there, causing rapid flow of water hence high velocities occurred.

Figures 6.17 E and F shows the water surface elevation at which the terrain was inundated. From the simulation results, the minimum and maximum water surface elevation at which the area was inundated were 33 m and 160 m respectively (Figures 6.17 E and F). The water surface elevation was high at the upper part of the terrain, gradually decreasing down the channel into the settlement.



Figure 6.17 A: Results of HEC-RAS unsteady flow simulation for Soufriere (Dominica), showing variations in flow depth across the floodplain (in m).

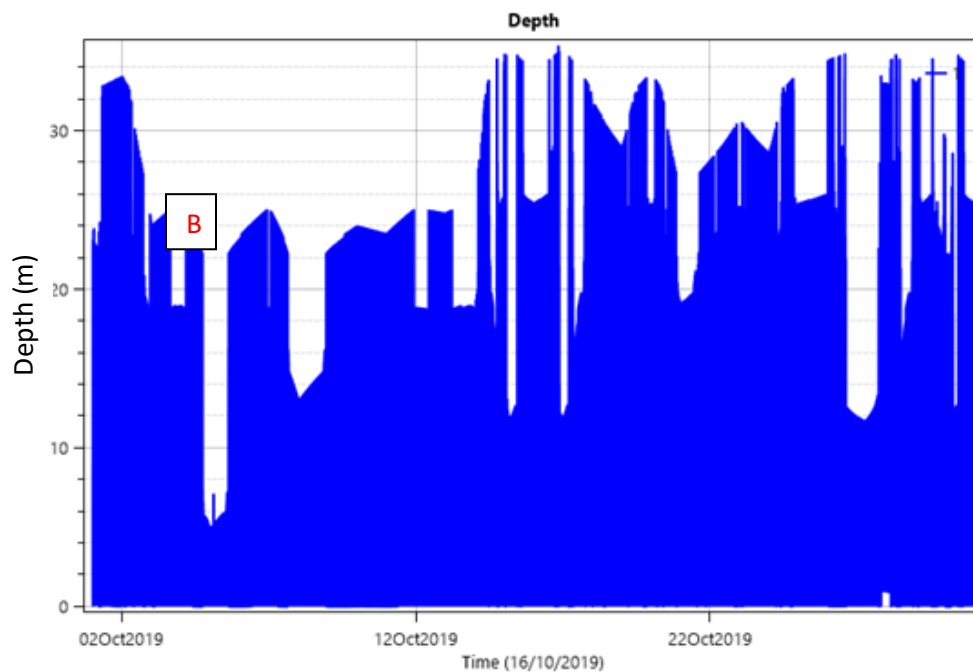


Figure 6.17 B: Results of HEC-RAS unsteady flow simulation for Soufriere (Dominica), showing variations in daily flow depth over a month (in m).



Figure 6.17 C: Results of HEC-RAS unsteady flow simulation for Soufriere (Dominica), showing variations in flow velocity across the floodplain (in m/s).

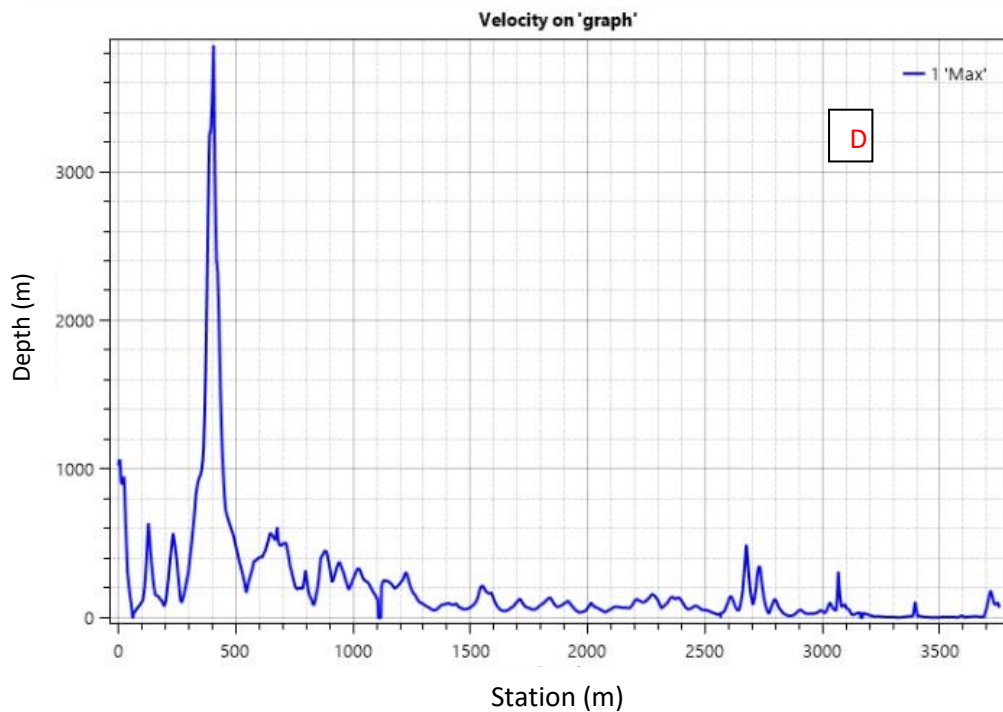


Figure 6.17 D: Results of HEC-RAS unsteady flow simulation for Soufriere (Dominica), showing variations in flow velocity along the channel (in m/s).

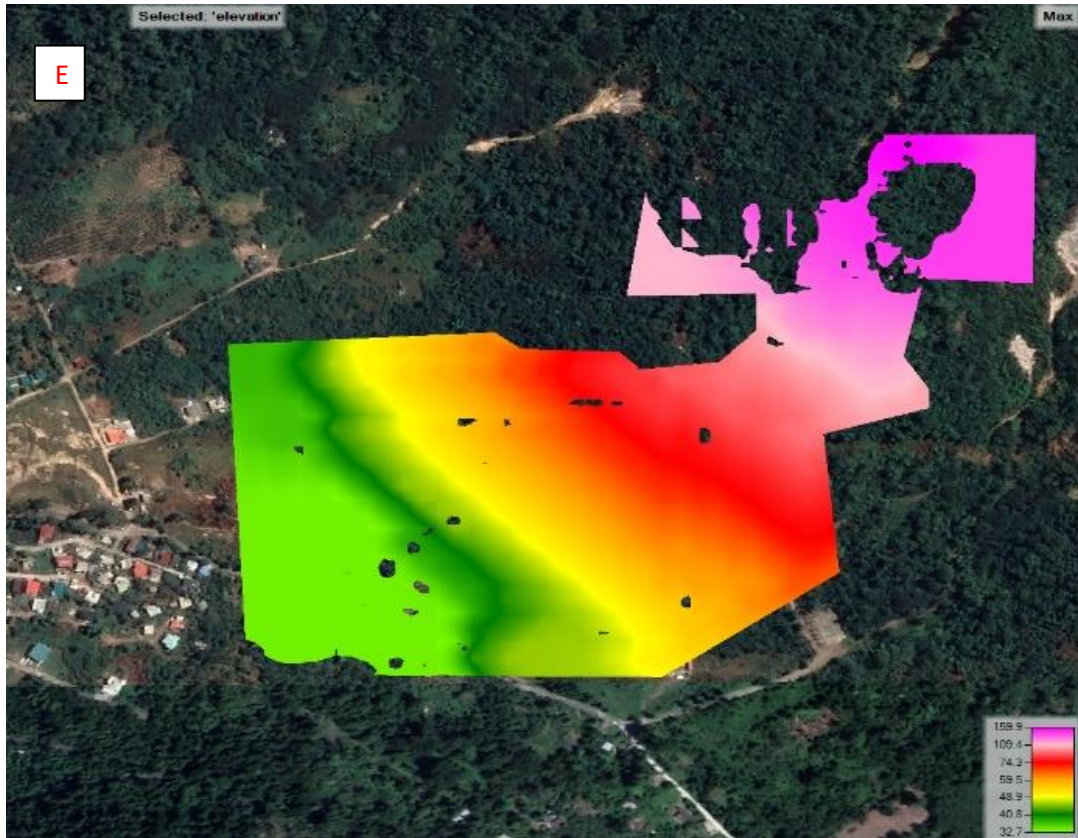


Figure 6.17 E: Results of HEC-RAS unsteady flow simulation for Soufriere (Dominica), showing variations in water surface elevation across the floodplain (in m).

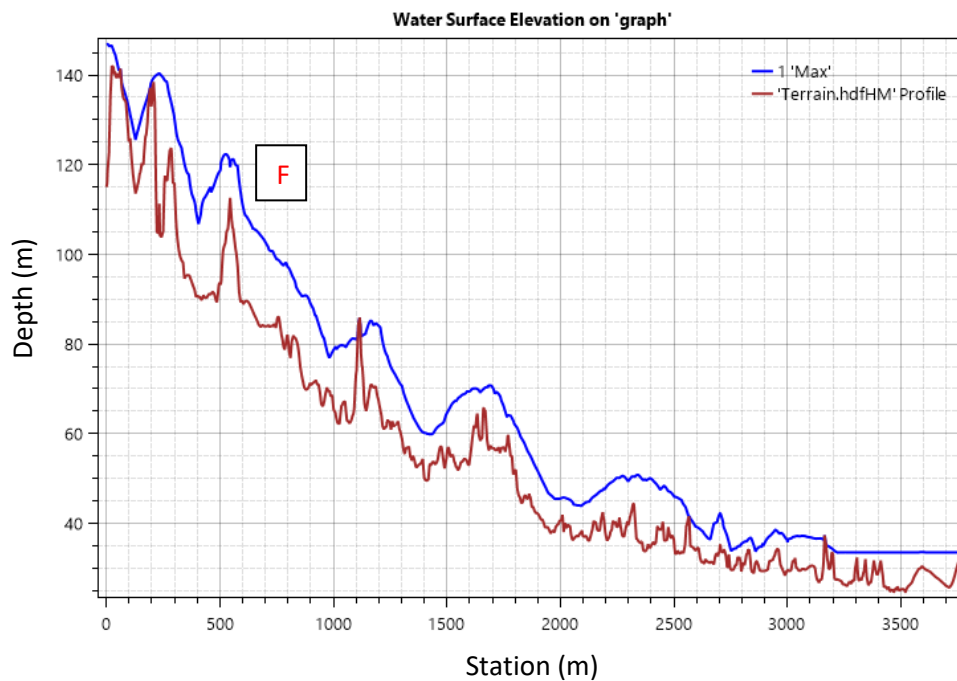


Figure 6.17 F: Results of HEC-RAS unsteady flow simulation for Soufriere (Dominica), showing comparison between water surface elevation and terrain elevation (in m).

6.4.7 Ribeira Santo Domingo HEC-RAS 2D Unsteady Flow Simulation Results

Simulation results of Ribeira Santo Domingo are presented in figure 6.18. Flow depth was high mainly at the channel mouth into the Atlantic Ocean (Figure 6.18 A). Flow depth was low upstream and over most of the floodplains because the elevation was relatively high hence quick flow of water into lowlands. Results of the unsteady flow modelling showed a maximum flow depth of 37.6 m and minimum flow depth of 0.0 m (Figure 6.18 A and B).

Flow velocity results are presented in Figures 6.18 C and D. Maximum flow velocity recorded after the simulation was 27342 m/s and the minimum flow velocity recorded was 4 m/s (Figure 6.18 C and D). Flow velocity was approximately the same over most of the study area (Figure 6.18 C). High velocities were predominately recorded at certain intervals along the drainage area (Figure 6.18 C). This is as a result of the variation of slopes across the terrain causing rapid rise and fall of flow as water went down the channel.

Water surface elevation results are presented in Figures 6.18 E and F showing the elevation at which the terrain was inundated. From the simulation results, the minimum flow and maximum water surface elevations at which the area was inundated were 64 m and 916 m, respectively (Figures 6.18 E and F). The water surface elevation was high at the upper part of the terrain, gradually decreasing down the channel into the Atlantic Ocean.



Figure 6.18 A: Results of HEC-RAS unsteady flow simulation for Ribeira Domingo Santo (Fogo), showing variations in flow depth across the floodplain (in m).

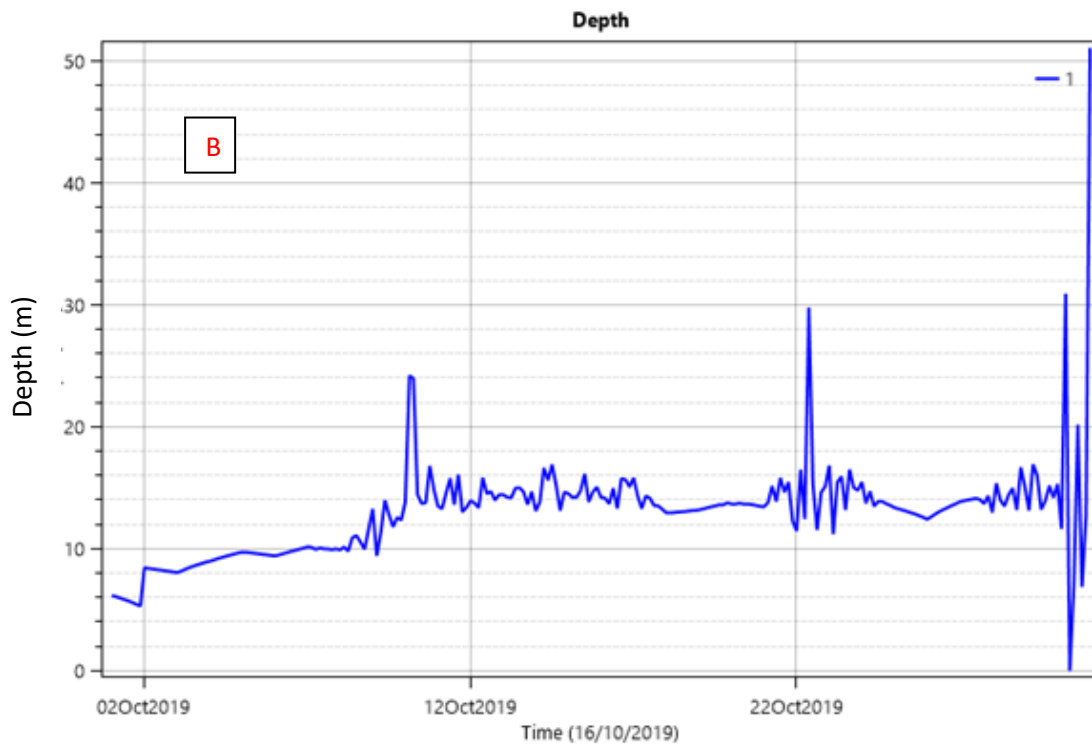


Figure 6.18 B: Results of HEC-RAS unsteady flow simulation for Ribeira Domingo Santo (Fogo), showing variations in daily flow depth over a month (in m).

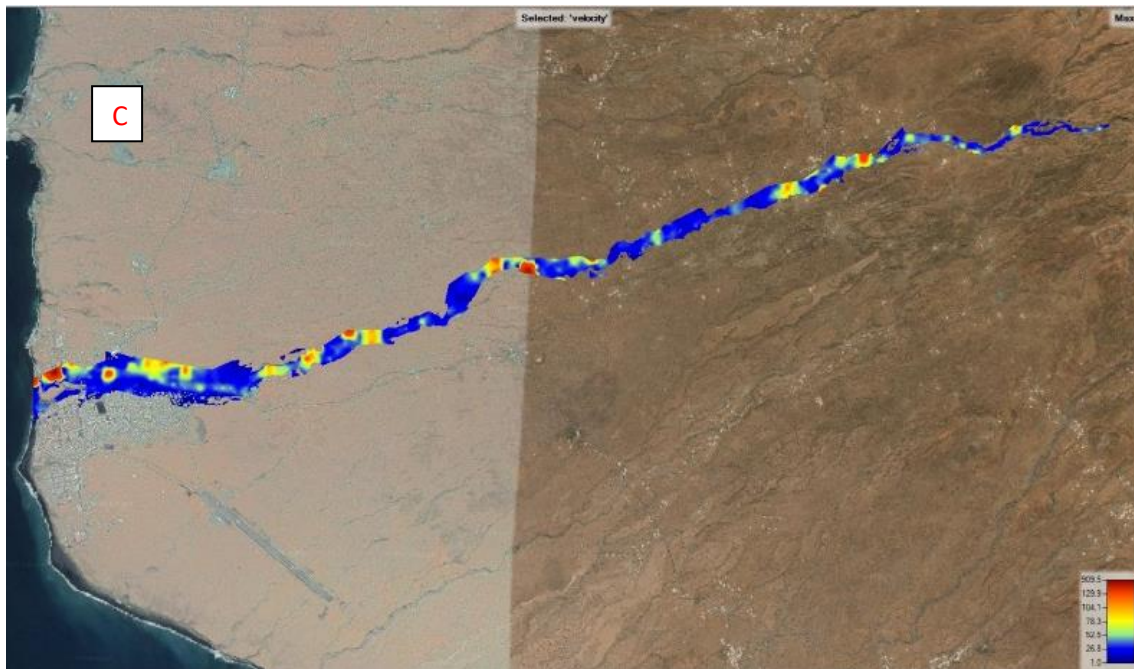


Figure 6.18 C: Results of HEC-RAS unsteady flow simulation for Ribeira Domingo Santo (Fogo), showing variations in flow velocity across the floodplain (in m/s).

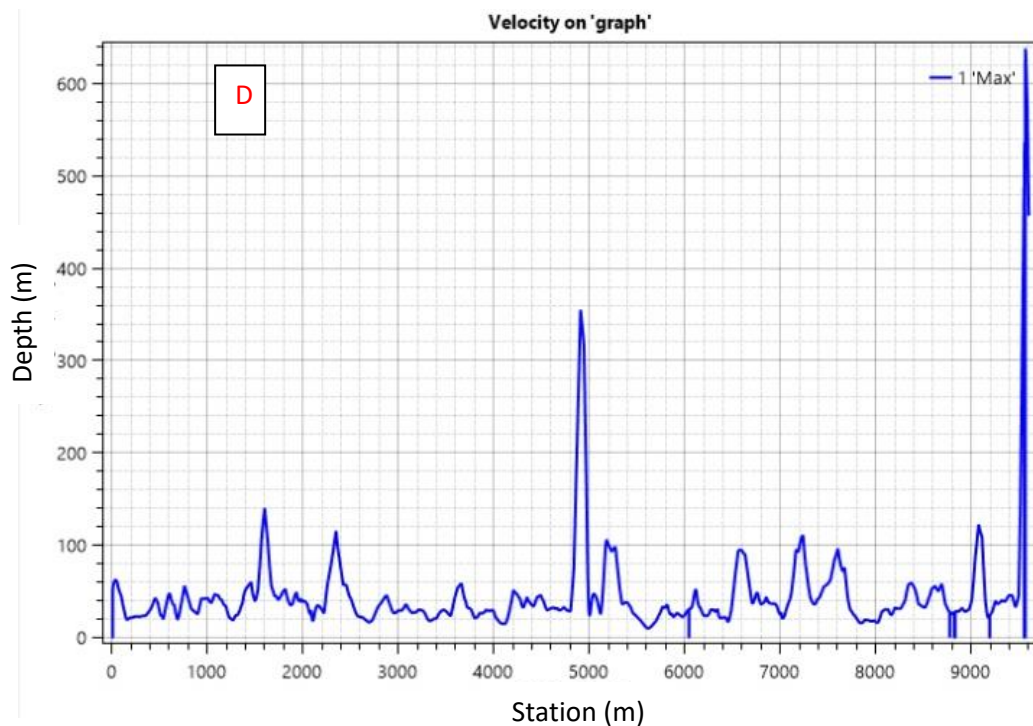


Figure 6.18 D: Results of HEC-RAS unsteady flow simulation for Ribeira Domingo Santo (Fogo), showing variations in flow velocity along the channel (in m/s).



Figure 6.18 E: Results of HEC-RAS unsteady flow simulation for Ribeira Domingo Santo (Fogo), showing variations in water surface elevation across the floodplain (in m).

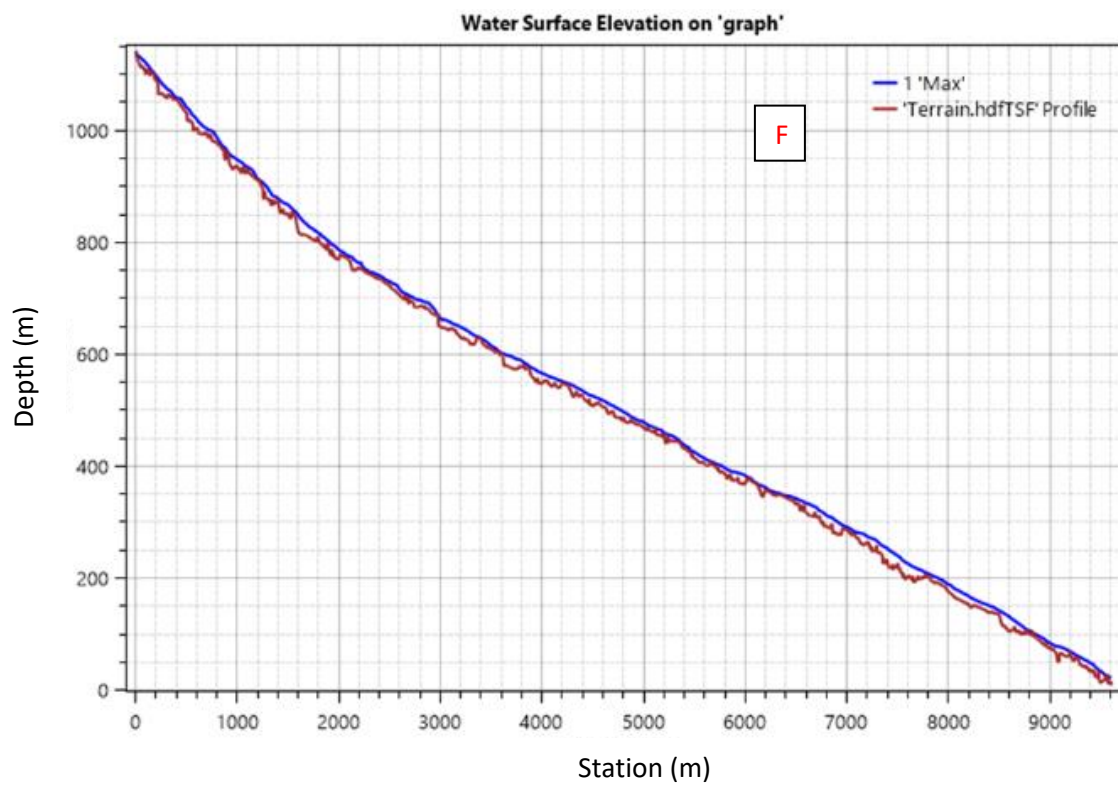


Figure 6.18 F: Results of HEC-RAS unsteady flow simulation for Ribeira Domingo Santo (Fogo), showing comparison between water surface elevation and terrain elevation (in m).

CHAPTER SEVEN

Discussion

7.0 Introduction

Chapter seven presents a discussion and interpretation of the results and modelling presented in Chapters four, five and six. It will concentrate on the main features of geohazards experienced during Hurricane Maria in Dominica and vulnerability of Dominica to geohazards. Also, implication of research work for managing geohazards in other SIDS and limitations of research work are discussed in this chapter.

7.1 Main Features of Geohazards Experienced During Hurricane Maria in Dominica

The category 5 Hurricane Maria with over 172 miles per hour wind speed caused severe devastation to Dominica in September 2017. Almost every sector of the island was affected by the events of Hurricane Maria. It triggered landslides, debris flows, flooding, erosion, destruction of vegetation, buildings, road networks and other infrastructure. Almost all the study areas experienced the same level of devastation except Pointe Michel where many fatalities and injuries were recorded. Comparison of Google Earth images from before and after Hurricane Maria, fieldwork observations and eye-witness evidence revealed the destruction caused at the six study areas.

Water supply services were disrupted during and after Hurricane Maria at all study localities (Figures 5.1-5.6). Water production and distribution pipelines were damaged and filled with debris and sediment, leaving residents of these areas with no water supplies (Figures 5.1-5.6). This affected livelihood, production and other economic activities. Approximately 90% of the country's buildings and infrastructures were destroyed and people had to seek shelter in

unaffected public buildings (Figures 5.1 - 5.6). Most roofs of buildings were completely blown away and had to be temporarily covered in tarpaulin (Figures 5.1 - 5.6).

Supply of electricity was completely cut off during Hurricane Maria because most power generation sites, transformers, electrical poles and wires were damaged (Figures 5.1 - 5.6).

Destruction of telecommunication systems meant that Dominica was cut off from the rest of the world and made it difficult for emergency rescue agencies to evacuate people on time.

Emergency services such as fire, police and ambulance services were all affected and had to be relocated. All stations and gadgets for monitoring hydro-meteorological and activities were completely wiped away.

Transportation networks such as roads, bridges ports, ferry terminals and airport were damaged during Hurricane Maria (Figures 5.1 - 5.6). Roads and bridges in the study localities were covered in landslide-induced debris flow sediments and debris, which made the roads inaccessible to evacuate people from severely affected areas (Figures 5.1 - 5.6).

Events of Hurricane Maria caused significant changes to the geomorphology of Dominica, channels were widened, vegetation and wood were blown away by the strong winds (Figures 5.1 - 5.6). With wind speeds of over 172 miles per hour, woodlands and vegetation of the study areas were destroyed (Figures 5.1 - 5.6). Torrential rainfall coupled with unstable slopes caused landslides, debris flows and erosion which resulted in major alterations in the landscape and geomorphology of these study areas (Figures 5.1 - 5.6). For example, landslide-triggered debris flows in Coulibistrie, Delice, Layou, Pagua, Pointe Michel and Soufriere caused expansion of existing channels and creation of new channels (Figures 5.1 - 5.6).

Events of Hurricane Maria caused significant changes to the geomorphology of Dominica, channels were widened, vegetation and wood were blown away by the strong winds (Figures 5.1 - 5.6). With wind speeds of over 172 miles per hour, woodlands and vegetation of the study areas were destroyed (Figures 5.1 - 5.6). Torrential rainfall coupled with unstable slopes caused landslides, debris flows and erosion which resulted in major alterations in the landscape and geomorphology of these study areas (Figures 5.1 - 5.6). For example, landslide-triggered debris flows in Coulibistrie, Delice, Layou, Pagua, Pointe Michel and Soufriere caused expansion of existing channels and creation of new channels (Figures 5.1 - 5.6).

Events of Hurricane Maria caused significant changes to the geomorphology of Dominica, channels were widened, vegetation and wood were blown away by the strong winds (Figures 5.1 - 5.6). With wind speeds of over 172 miles per hour, woodlands and vegetation of the study areas were destroyed (Figures 5.1 - 5.6). Torrential rainfall coupled with unstable slopes caused landslides, debris flows and erosion which resulted in major alterations in the landscape and geomorphology of these study areas (Figures 5.1 - 5.6). For example, landslide-triggered debris flows in Coulibistrie, Delice, Layou, Pagua, Pointe Michel and Soufriere caused expansion of existing channels and creation of new channels (Figures 5.1 - 5.6).

Events of Hurricane Maria caused significant changes to the geomorphology of Dominica, channels were widened, vegetation and wood were blown away by the strong winds (Figures 5.1 - 5.6). With wind speeds of over 172 miles per hour, woodlands and vegetation of the study areas were destroyed (Figures 5.1 - 5.6). Torrential rainfall coupled with unstable slopes caused landslides, debris flows and erosion which resulted in major alterations in the landscape and geomorphology of these study areas (Figures 5.1 - 5.6). For example, landslide-triggered debris flows in Coulibistrie, Delice, Layou, Pagua, Pointe Michel and Soufriere caused expansion of existing channels and creation of new channels (Figures 5.1 - 5.6).

Events of Hurricane Maria caused significant changes to the geomorphology of Dominica, channels were widened, vegetation and wood were blown away by the strong winds (Figures 5.1 - 5.6). With wind speeds of over 172 miles per hour, woodlands and vegetation of the study areas were destroyed (Figures 5.1 - 5.6). Torrential rainfall coupled with unstable slopes caused landslides, debris flows and erosion which resulted in major alterations in the landscape and geomorphology of these study areas (Figures 5.1 - 5.6). For example, landslide-triggered debris flows in Coulibistrie, Delice, Layou, Pagua, Pointe Michel and Soufriere caused expansion of existing channels and creation of new channels (Figures 5.1 - 5.6).

Events of Hurricane Maria caused significant changes to the geomorphology of Dominica, channels were widened, vegetation and wood were blown away by the strong winds (Figures 5.1 - 5.6). With wind speeds of over 172 miles per hour, woodlands and vegetation of the study areas were destroyed (Figures 5.1 - 5.6). Torrential rainfall coupled with unstable slopes caused landslides, debris flows and erosion which resulted in major alterations in the landscape and geomorphology of these study areas (Figures 5.1 - 5.6). For example, landslide-triggered debris flows in Coulibistrie, Delice, Layou, Pagua, Pointe Michel and Soufriere caused expansion of existing channels and creation of new channels (Figures 5.1 - 5.6).

Events of Hurricane Maria caused significant changes to the geomorphology of Dominica, channels were widened, vegetation and wood were blown away by the strong winds (Figures 5.1 - 5.6). With wind speeds of over 172 miles per hour, woodlands and vegetation of the study areas were destroyed (Figures 5.1 - 5.6). Torrential rainfall coupled with unstable slopes caused landslides, debris flows and erosion which resulted in major alterations in the landscape and geomorphology of these study areas (Figures 5.1 - 5.6). For example, landslide-triggered debris flows in Coulibistrie, Delice, Layou, Pagua, Pointe Michel and Soufriere caused expansion of existing channels and creation of new channels (Figures 5.1 - 5.6).

were moved during Hurricane Maria. According to the locals in Pagua, the boulders have not been moved for a long time, not even during Hurricane Maria. This was evident during the fieldwork because there were no signs of landslides and only sediments in the channels and trees debris were moved and deposited behind the weathered deep-seated in-situ boulders. In other study areas such as Coulibistrie, Delice, Layou, Pointe Michel and Soufriere majority of the boulders found were moved during Hurricane Maria based on eyewitness accounts. Some residents in these areas gave accounts of how their houses were damaged by boulders moving down slope. Nevertheless, some of the boulders were in-situ boulders that have dug up during the excavation works post Hurricane Maria from field observations and eyewitnesses. Analysis of boulders helped to know the size of boulders moved that caused damages to livelihood, the built and natural environment in each locality during Hurricane Maria (Figures 5.7–5.18). Most buildings in Soufriere and Coulibistrie were destroyed by movement of these giant boulders. Bridges and roads in Coulibistrie, Delice, Layou, Pagua, Soufriere and Pointe Michel were destroyed by boulders jammed under the bridges and displaced on the roads. The only fatality caused by movement of boulders was recorded in Pointe Michel. The extremely giant boulders were found in Pagua, measuring up to 10 m in size (Figure 5.9). Most boulders found in other study areas ranged from 0.3 m to 7.3 m in size (Figures 5.7-5.18). Most the boulders in all study areas were sharp and angular in shape which indicated recent movement. Most boulders in all localities were mainly andesite and dacite with dark-grey and pale-grey colours respectively. Only boulders in Soufriere and some boulders in Delice were hydrothermally altered by the hot springs and appeared brown-yellowish in colour. Although boulder movement analysis was not conducted in Ribeira Domingo Santo in Fogo, due to time constraints and capability of ImageJ, nevertheless field observations (Figure 5.19) showed the risk that movement of boulders poses to infrastructure in Sao Filipe, the main settlement on the island of Fogo.

7.2 Vulnerability of Dominica to Geohazards

7.2.1 Validation of Models

To determine the accuracy of the models used in this study for debris flow and flood simulation, the outcomes had to be compared with real-life events. Model validation is very essential because it helps to know how realisable and consistent the data and models are. Unfortunately, a detailed validation of models was not conducted for this study due to the lack of original data for real-life debris flow and flood events for all study areas. All the original debris flow data was cleared prior to the fieldwork, all debris was excavated after Hurricane Maria as the government made it a priority to get back to normality after Hurricane Maria. There was basically no trace of flood data after the events of Hurricane Maria. There are no past database of flood and debris flood inventories which could have been used to validate the models. This study is therefore novel since this the first time that drone-derived DSMs are applied in HEC-RAS and RAMMS to model flood and debris flow hazards in Dominica and Cape Verde.

However, notwithstanding the lack of original data to validate the accuracy and reliability of HEC-RAS 2D unsteady flow and RAMMS debris flow models. When the debris flow and unsteady flow simulated results (Figures 6.5-6.18) were overlain on orthophotographs and Google Earth maps of all the study areas, it can be seen all these areas were affected by real-life debris flow and flood events during Hurricane Maria. This was validated by comparing the simulated results (Figures 6.5-6.18) with the Google Earth images from after Hurricane Maria (Figures 4.1C-4.6C). Fieldwork observations and judgement confirmed the accuracy and reliability of the models. This is because the channels flow directions at all study areas observed during the field survey was the same as the simulated results. These observations and comparisons of results with Google Earth images after Hurricane Maria thus gives some credibility to RAMMS and HEC-RAS models even though there were errors and uncertainty with the data and input parameters.

7.2.2 Comparison of RAMMS Debris Flow Model Results with Google Earth Images.

RAMMS debris flow simulation results and post-Hurricane Maria Google Earth images for all study areas were compared to determine accuracy of the modelling. Not only will the comparison validate the accuracy and reliability of the model but also the applicability of the model to other SIDS. However, there was no information about flow height, flow volume, runout distance and velocity due lack of original data from the observed debris flow event.

Comparison of the RAMMS debris flow result for Coulibistrie (Figure 7.1A) and Google Earth image (Figure 7.2B) of the observed debris flow deposits post-Hurricane Maria shows some similarities. Buildings on the left side of channel were less affected by the debris flow than those on the right side (Figure 7.1A and B). The bridge was destroyed and covered in debris in both images and the flow channel and buildings nearby were completely covered in debris.

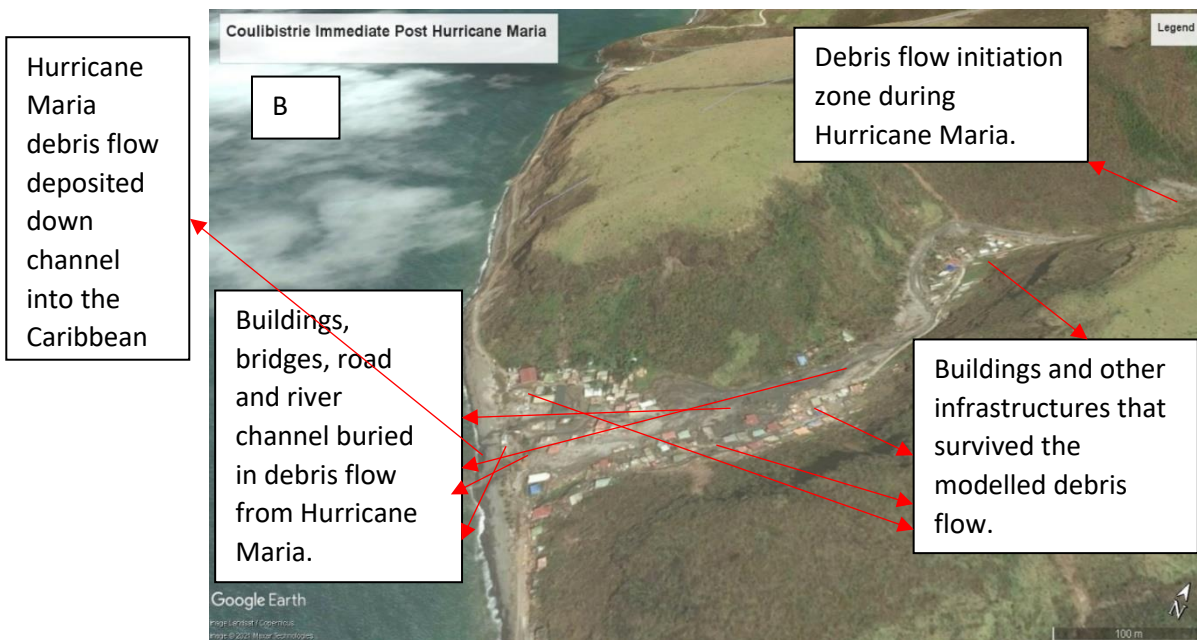
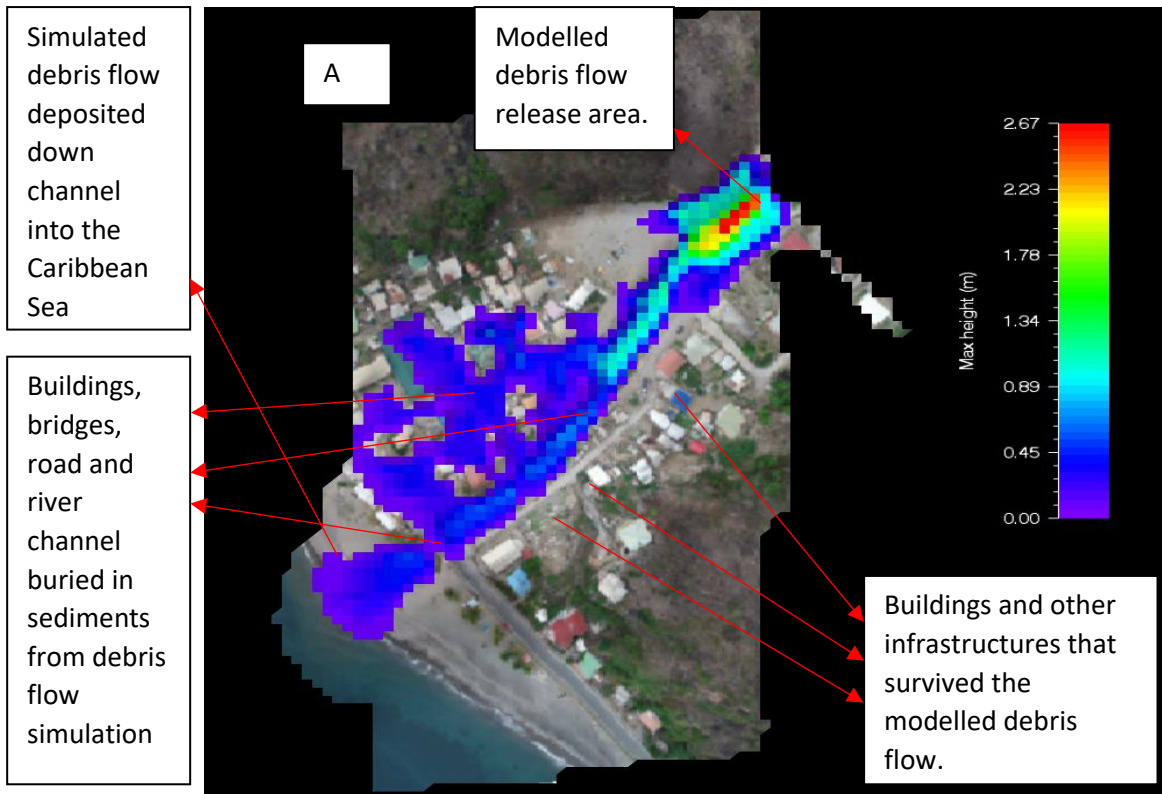


Figure 7.1 A and B: Comparison of RAMMS debris flow simulation result and Google Earth image of observed debris flow deposits from Hurricane Maria for Coulibistrie (Dominica).

Delice is less inhabited than Coulibistrie, so buildings were not so strongly affected by the debris flows in both the observed situation and RAMMS simulation (Figure 7.2A and B). However, road networks and farmlands were affected by the debris flow. Even though the post-Hurricane Maria Google Earth image (Figure 7.2B) is not very clear, there are similarities when compared with the simulated debris flow result (Figure 7.2A). Debris was mainly confined within the flow channel. Farmland on both sides of upper part of the channel were covered in debris (Figure 7.2A and B). The main road and bridge that links Delice with other southern towns were completely buried. Also, debris was deposited downstream into the Atlantic Ocean in both images. The only visible difference in the images is the destroyed vegetation in the Google Earth image and the growing vegetation in the simulated image.

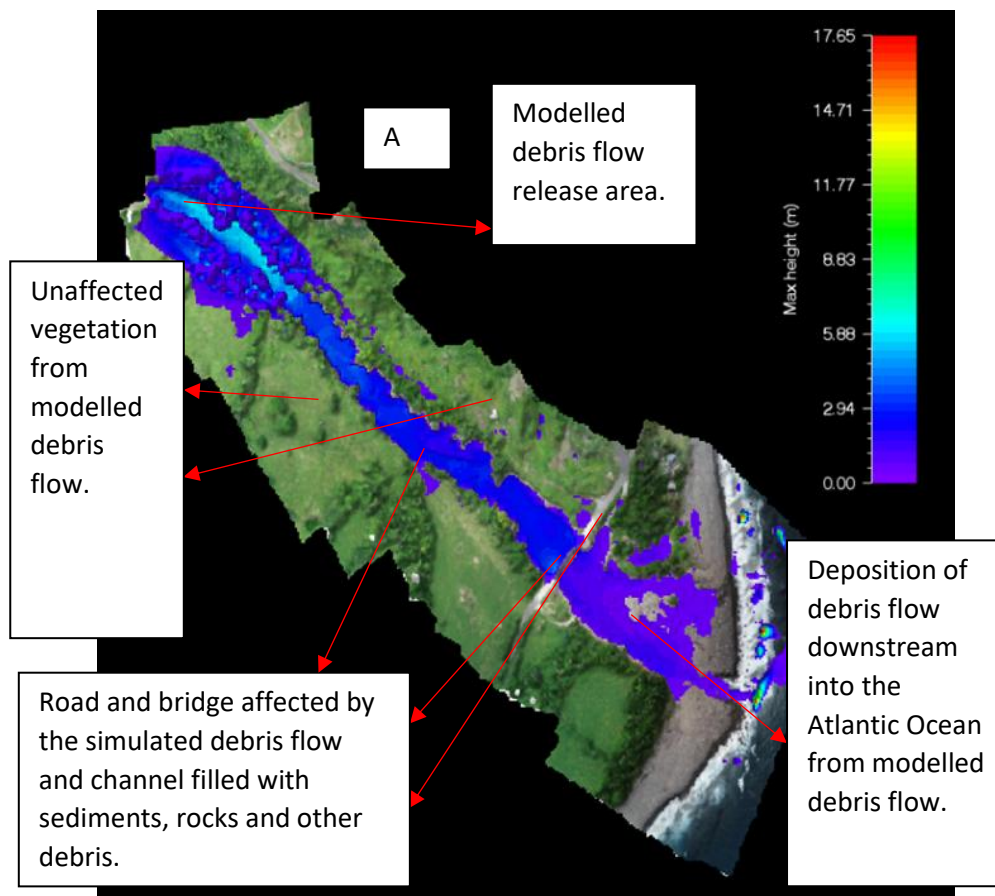




Figure 7.2 A and B: Comparison of RAMMS debris flow simulation and Google Earth image of observed debris flow event after Hurricane Maria for Delice (Dominica).

Just like Delice, there were not many buildings in Layou as seen in the simulation result (Figure 7.3A) and Google Earth image (Figure 7.3B). Comparison between the debris flow simulation and observed debris flow revealed some similarities. In both images, the debris flow was mainly within the flow channel. The road and bridge were partially covered in debris (Figure 7.3A and B) with extensive deposition of debris behind the bridge, possibly as a result of boulders and other debris jammed under the bridge.

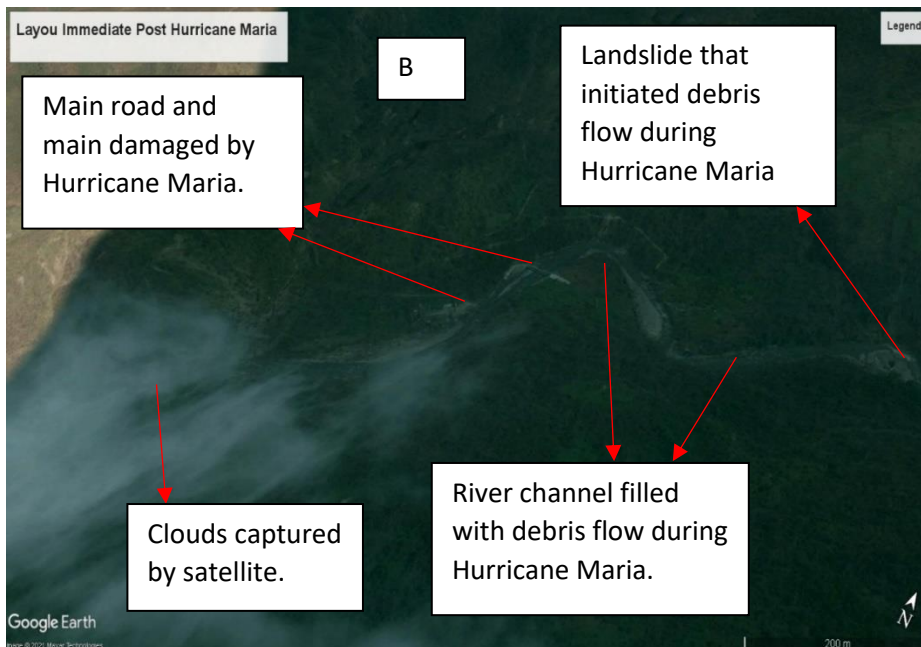
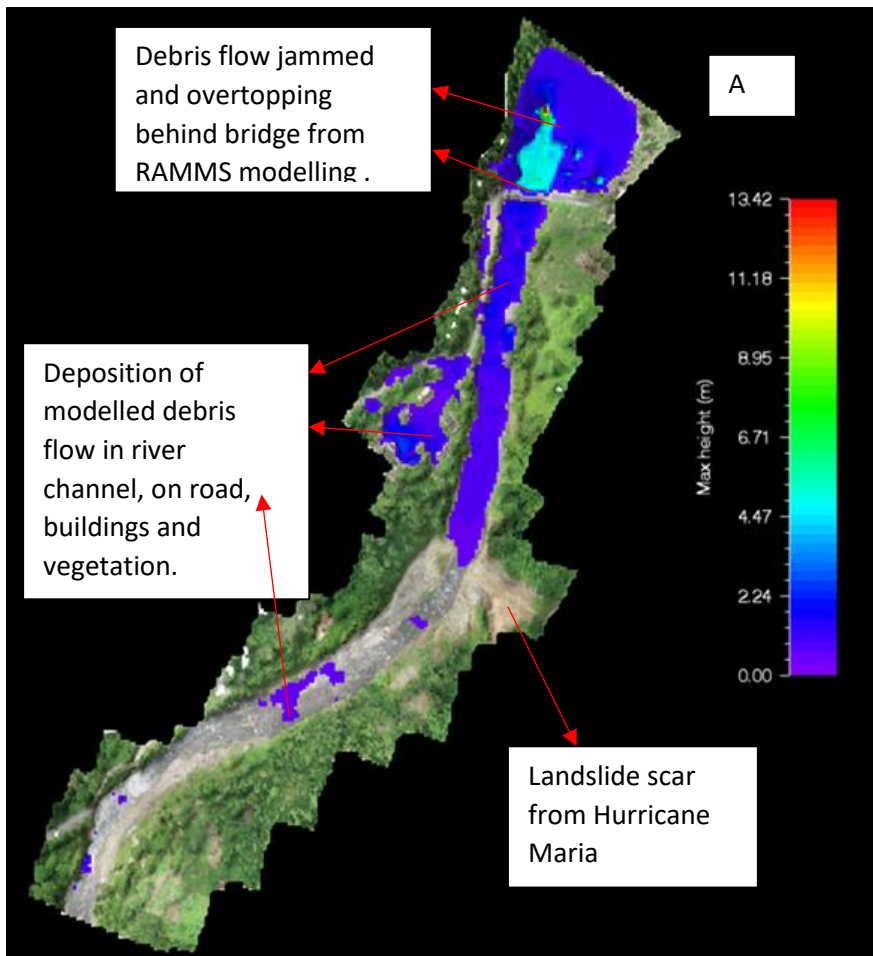
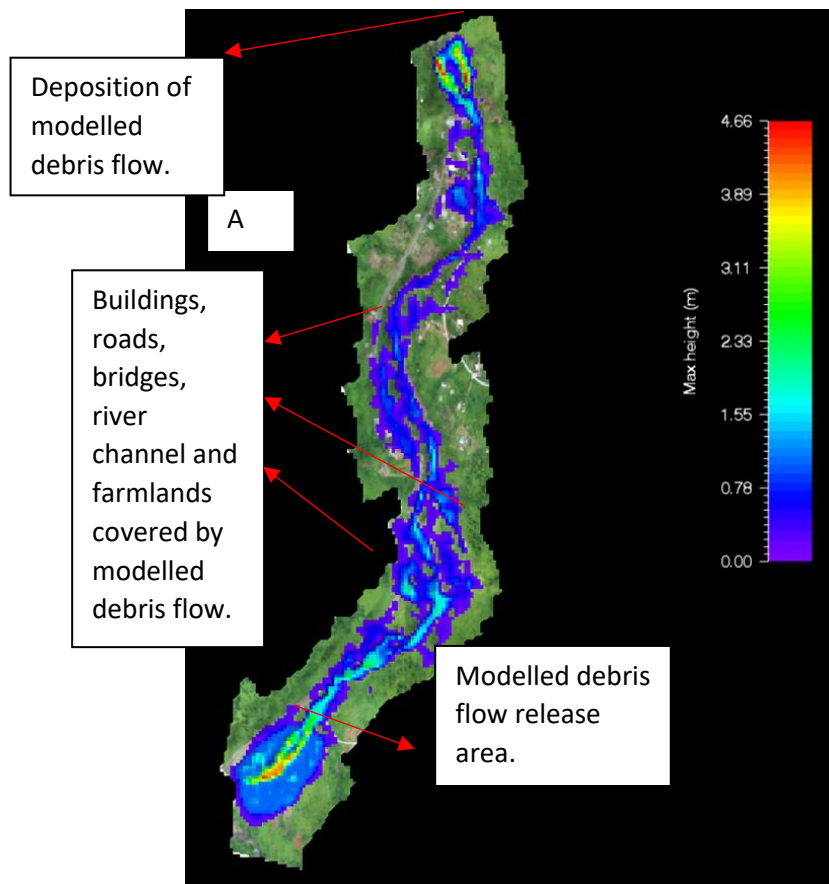


Figure 7.3 A and B: Comparison of RAMMS debris flow simulation result and Google Earth image of observed debris flow event post-Hurricane Maria for Layou in Dominica.

Pagua was least affected by debris flow during Hurricane Maria as is evident in the Google Earth image (Figure 7.4B) but was more affected by flooding and strong winds which destroyed the vegetation (Figure 7.4B). Therefore, it was not possible to determine the accuracy of the simulated debris flow result for Pagua (Figure 7.4A) because there was no debris in the Google Earth image to compare with the simulated result as in the other study areas. Nevertheless, the simulation can predict the susceptibility of Pagua to debris flow hazard. Based on the simulation outcome (Figure 7.4A), Pagua is highly vulnerable to debris flow hazards.



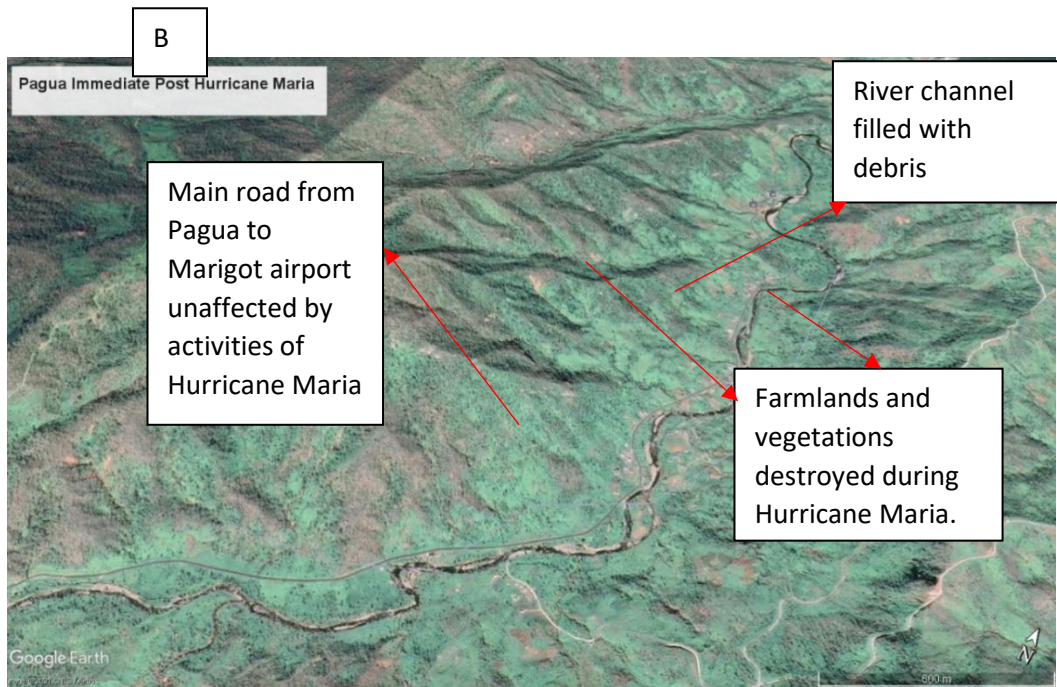
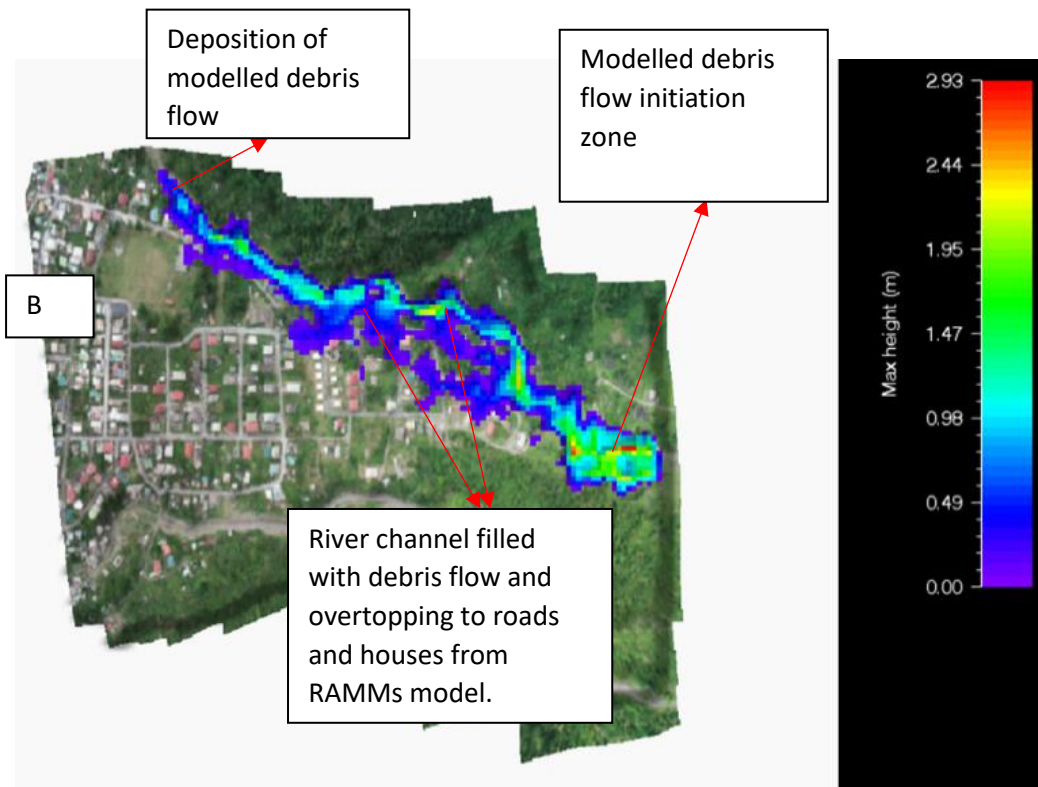
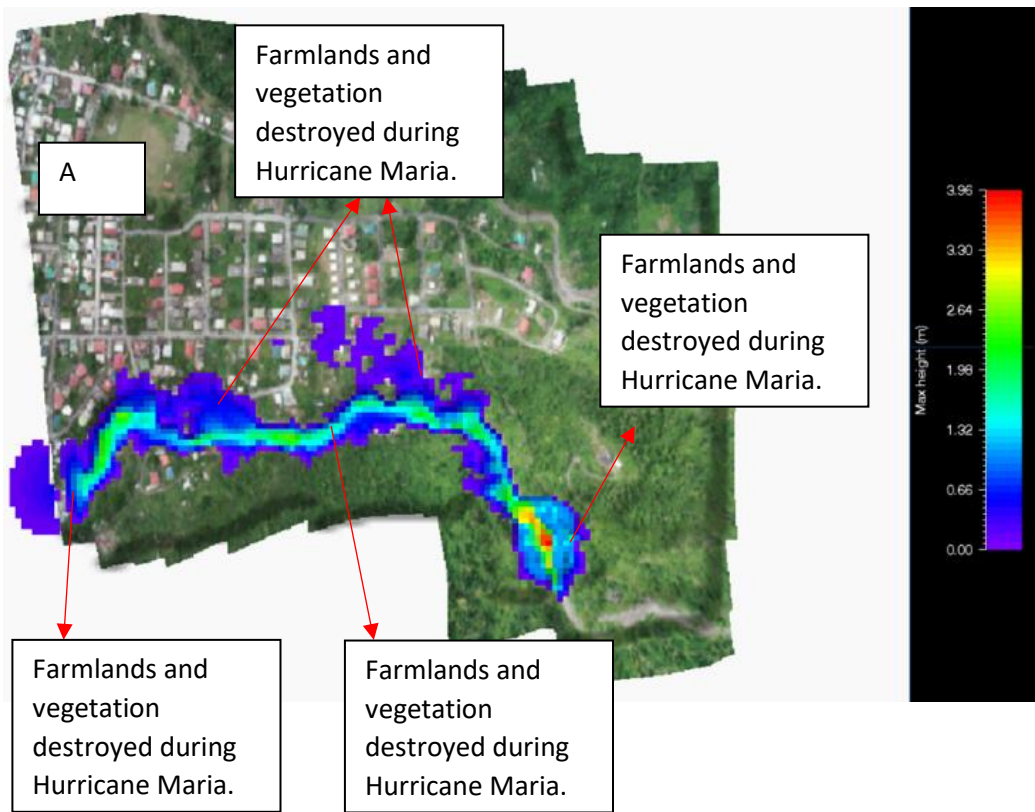


Figure 7.4 A and B: Comparison of RAMMS debris flow simulation result and Google Earth image from post-Hurricane Maria for Pagua (Dominica).

Pointe Michel is one of the study areas where the debris flow simulation results (Figures 7.5A and B) were almost a replica of the observed debris flow (Figure 7.5C). Simulation was conducted for both the north and south channels in Pointe Michel (Figures 7.5A and B). A comparison between the simulation debris flow results and the Google Earth image of post-Hurricane Maria debris flow shows great similarities. The debris flow was mainly within the north and south channels, and only buildings closer to the channels were affected by debris movement (Figure 7.5A, B and C). Also, buildings at the deposition point downstream were covered in debris, whereas buildings, roads and vegetation between the channels were hardly affected by debris flow (Figure 7.5A, B and C).



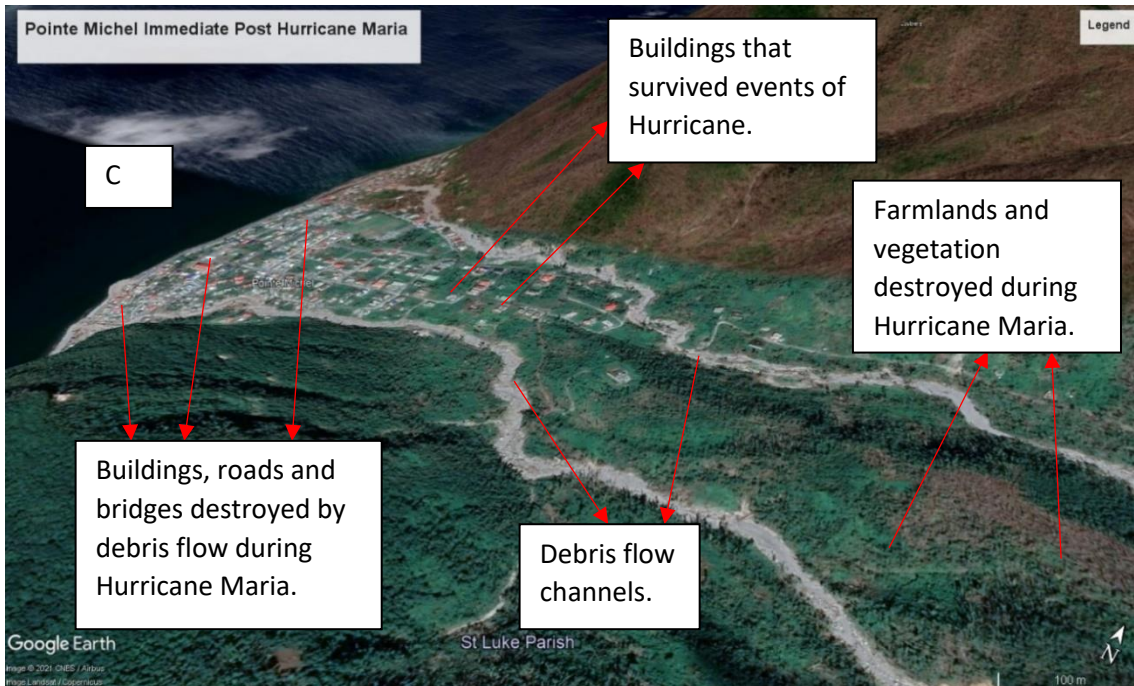


Figure 7.5 A and B: Comparison of RAMMS debris flow simulation result and Google Earth image of real-life debris flow event post-Hurricane Maria for Pointe Michel in Dominica.

In Soufriere, the debris flow simulation also reproduced a similar scenario to the observed debris flow (Figures 7.6A, B). Simulation results for Pointe Michel and Soufriere were quite similar to the observed events in comparison to the other study areas (Figures 7.1A, B to Figure 7.5A, B). Triggered by landslide from an unstable hillside during Hurricane Maria, the debris flow moved down-hill rapidly forcing creation of new channels (Figure 7.6 A, B). Vegetation and woodland in the way of the debris flow were completely destroyed and covered in debris while some buildings and roads were also covered in debris (Figure 7.6 A, B).

The comparison of RAMMS debris flow model results and observed events of debris post-Hurricane Maria in all study areas revealed some similarities. These similarities in both images serves as evidence that the model results are accurate and reliable even though there were

uncertainties and errors with the input data and parameters. Therefore, with the correct input data and parameters, the model can be applied in other SIDS to predict debris flow hazards.

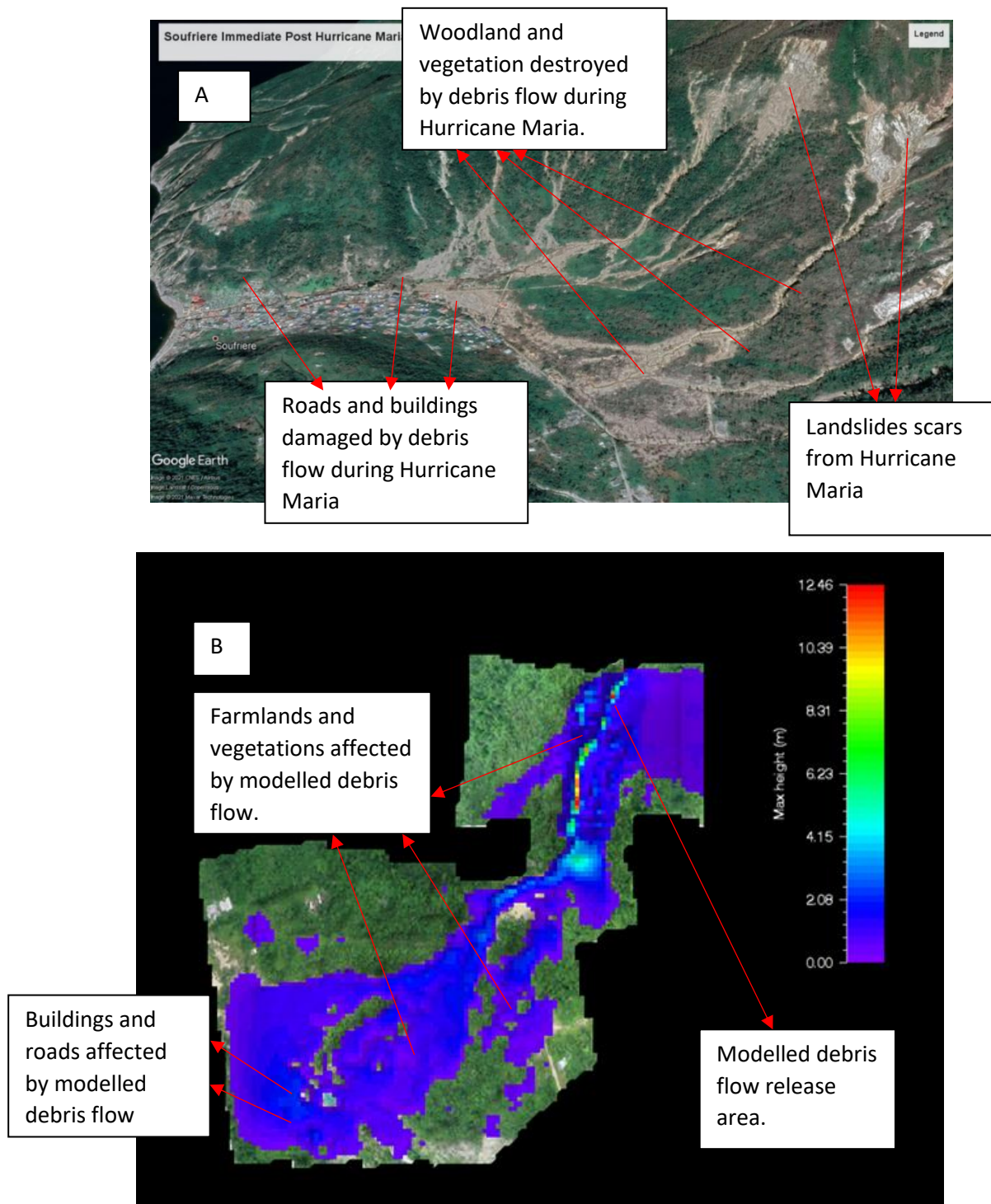


Figure 7.6 A and B: Comparison of RAMMS debris flow simulation result and Google Earth image of observed debris flow event post-Hurricane Maria for Soufriere in Dominica.

7.2.3 Analysis of Results

All the results from the debris flow modelling and unsteady flow simulation indicated that study localities in Dominica and Fogo are highly susceptible to flood and debris flow. The boulder size distribution and movement results also showed the risks the study areas in Dominica were exposed to during Hurricane Maria. Drone-derived high-resolution DSMs are up to date and more accurate than satellite-derived DSMs, so they are suitable for both unsteady flow and debris flow simulation because they present a more accurate representation of the study terrains (Jarihani et al, 2015; Farooq et al, 2019).

The success of HEC-RAS 2D modelling (Gain et al, 2015; Elfeki et al, 2016; Haltas et al, 2016; Papaionnou et al, 2016) and RAMMS debris flow module (Hussin, 2011; Simoni et al, 2012; Jarsve, 2018) in other research works was the main rationale for using these models for this study. Drone-derived DSM and 2D numerical flow models such as HEC-RAS and RAMMS have been demonstrated to be a good combination for assessing debris flow hazards (Hussin, 2011; Simoni et al, 2012; Jarsve, 2018) and flood hazards (Farooq et al, 2019; Yalcin et al, 2020). This is due to the ability of the models to accurately represent complex features of a terrain such as river channels, floodplains, bridges, roads and other man-made structures (Farooq et al, 2019; Yalcin et al, 2020). Hydraulic and rheological behaviour of a channel is well captured by HEC-RAS 2D model (Farooq et al, 2019; Yalcin et al, 2020) and RAMMS (Hussin, 2011; Simoni et al, 2012; Jarsve, 2018). Although initially developed for medical image analysis, the results from boulders analysis indicated that ImageJ is can be used to analyse geoscience images as well. There is no numerical model or software which is absolutely flawless (Box and Daper, 1987), yet they are very useful and RAMMS debris flow module, HEC-RAS and ImageJ are no exception.

7.2.4 HEC-RAS 2D Unsteady Flow and Hydraulic Modelling

The unsteady flow simulation was calibrated using Hurricane Maria rainfall data recorded for Puerto Rico published by the US National Hurricane Centre (Pasch et al, 2019). This is because all the Hurricane Maria rainfall data for Dominica were completely destroyed. Unsteady flow analysis results were presented in the form of quantitative variables such as flow depth, water surface elevation and flow velocity.

7.2.4.1 Flow Depth

Simulated flow depth recorded in Coulibistrie was relatively low at beginning of October and steadily falling and rising (Figure 6.12B). In mid-October, there was rapid rise in flow depth but declined from 20th October to 24th October (Figure 6.12B). Flow depth increased sharply again towards the end of October (Figure 6.12B). In Delice flow depths were high in mid-October, at the end of October and relatively low at the beginning October (Figure 6.13B). Flow depth was relatively at the same level within the first two weeks in October and increased from mid-October to end of October (Figure 6.13B). Just like Coulibistrie and Delice, flow depth in Layou low at the beginning of October but increased steadily from mid-October to the end of the month (Figure 6.14B). Result of flow depth in Pagua was a bit different other study areas. Figure 6.15B revealed that from 4th October to mid-October flow depth was at a constant level. There was a rise, a decline and rise again from mid-October to end of October (Figure 6.15B). Similar to Coulibistrie, Delice and Layou, flow depth in Pointe Michel was also low from start of October to mid-October (Figure 6.16B). However, from mid-October to end of October the depth of flow increased (Figure 6.16B). Although there were fluctuations with flow depth throughout October in Soufriere, majority of depths were at the same level (Figure 6.17B). Starting at low depth at the beginning of October, flow depth steadily increased to mid-October and declined again from mid-October to 21st October in Ribeira Domingo Santiago (Figure 6.18B). There was a rapid increase in flow depth and sharp drop from 21st October to 25th October (Figure 6.18B). Flow depth was fairly at the same level to the end of October

(Figure 6.18B). A critical look at the simulation results revealed discontinuities in flow in all study areas which indicates difference in elevation of the terrain. In all study areas, flow depth was high in low-lying areas whilst in the highlands flow depth was low (Figures 6.12A-6.18A). This could be due to the rapid flow of water from high slopes to low slopes.

7.2.4.2 Flow Velocity

Flow velocity in Coulibistrie was relatively the same for a distance of 0.4 km from upstream, this can be attributed to the fact that this section of the terrain was on same elevation (Figure 6.12C). There was a drastic change in flow velocity downstream which was due to the steepness of river-beds downstream (Figure 6.12D). In Delice, flow velocity was quite the same across the terrain (Figure 6.13D). High flow velocities were recorded at the north and southern corners of the channel, which can be attributed to the steep tributaries joining the main channel (Figure 6.13C). Layou experienced variation in flow velocity with constant rise and fall along the channel (Figure 6.14D). Areas that experienced rapid flow of water from high slopes into the channel had high flow velocities as shown in Figure 6.14C. In Pagua flow velocity was somewhat similar across the area with the exception of the middle corner of the channel (Figure 6.15D). This section was a steep slope, where water flowing into the channel was rapid in comparison any parts of Pagua (Figure 6.15D). Figure 6.16D showed that flow velocity was only high at points where the north and south channels connect with the bridges in Pointe Michel. This could be attributed to the fact that the bridges were blocked by debris, hence forcing flow diversion rapidly to the floodplains (Figure 6.16D). Just like most of the study areas, flow velocity in Soufriere was similar across the terrain except a section at the upper part of the channel (Figure 6.17D). The sharp steep slope was caused by a landslide during Hurricane Maria which transported water rapidly downstream (Figure 6.17D). There were variations in flow velocities in Ribeira Domingo Santo in comparison to the study areas in Dominica (Figure 6.18C). This is due the meandering nature of Ribeira Domingo Santo channel

coupled with steep river-beds (Figure 6.18C). These factors accelerate and decelerate flow downstream hence causing velocity to increase and decrease within a short period.

7.2.4.3 Water Surface Elevation

Simulated water surface elevation was compared with the actual terrain elevation of Coulibistrie to determine the level at which inundation occurred (Figure 6.12E). Water surface elevation was high upstream and gradually decreased downstream as seen in Figure 6.11F with the colour changes. The water surface elevation results were in negative values, indicating the terrain is below sea level (Figure 6.12F). Even though Coulibistrie is in low-lying area of Dominica, the negative values of water surface elevation are highly questionable. Just like Coulibistrie, the simulated water surface elevation for Delice also had negative values indicating the terrain is below sea level (Figure 6.13F). Situated in a valley, Layou also had negative values for the water surface elevation, also indicating inundation occurred below sea level (Figure 6.14F). With the exception of a low-lying area in Pagua, most water surface elevation results were above sea level (Figure 6.15F). Pointe Michel was one of the study areas where the elevation at which flooding occurred was above sea level (Figure 6.16F). Soufriere study area is a highland so there is no surprise that the elevation at which flooding occurred was above sea level (Figure 6.17F). Similar to Pagua, Pointe Michel and Soufriere, water surface elevation occurred above sea level because all the values were more than zero (Figure 6.18F). In comparison with the terrain's elevation, inundation occurred mainly within the channel and few metres into the floodplains. From the simulation results, Ribeira Domingo Santo is relatively less susceptible to flooding than study localities in Dominica. All water surface elevation values in Pointe Michel were positive. This could be due to an error in DSMs of Coulibistrie, Delice and Layou which has affected the outcomes of the simulation. This problem was known to the researcher but could not be rectified even after several attempts of reprocessing and correcting the DSM.

7.2.5 Assessment of Debris Flow and Flood Hazards in Study Localities

Results of the calibrated simulation for all the study localities in Dominica and Cape Verde revealed how susceptible these areas are to debris flow hazards. Orthophotographs for all study locations were wrapped over debris flow simulation results. Also, unsteady flow simulation results for all study areas were overlaid on Google Satellite. This was done to get a better visual understanding of the threat of debris flow and flood hazards to these localities. Knowing how susceptible these areas are to debris flow and flood hazards will help to put measures in place to mitigate the impact of these hazards.

7.2.5.1 Debris Flow Hazard Assessment

Figure 5.4 A showed how vulnerable Coulibistrie is to debris flow hazards. Approximately 40% of Coulibistrie was covered in debris flow from the simulation (Figure 6.4A). Buildings on the north side of the channel were more vulnerable to debris flow than the south side (Figures 6.4A). Some of the buildings were buried in debris on the north side of the channel (Figure 6.4A). Most of the debris flow were deposited downstream, covering the main bridge and into the Caribbean Sea (Figure 6.4A). The bridge which is the main link for transport network between southern and northern Dominica was affected by debris flow (Figure 6.4A).

Fortunately, there were not many buildings in Delice, however there were many farmlands which are prone to debris flow hazards. As shown in Figure 6.5A, the whole channel was filled with debris and overflowing into the farmlands on both sides of the channel. Another hazard posed by the debris flow was blockage of the bridge with debris and subsequently covering the whole bridge (Figure 6.5A). Just like the bridge in Coulibistrie, the bridge in Delice is the main link for transport network between Delice and other southern towns such Petite Savannah, Fond St. Jean, Dubuc and Berekua.

Simulation results for Layou revealed that flow was mainly within the channel (Figure 6.6A). However, some of flow were deposited as a result of the bridge being blocked by debris (Figure

6.6A). The bridge was partially covered by debris, making the road impassable. Some buildings on the left side of channel were buried in debris (Figure 6.6A).

Approximately 80% of Pagua was covered in debris flow (Figure 6.7A), from the simulation results, Pagua was the most vulnerable area to debris flow hazards. Most buildings and farmlands were covered in debris flow (Figure 6.7A). The whole road which leads to the national airport was completely buried in debris flow (Figure 6.7A).

In Pointe Michel, simulation was conducted at the north and south channels. In comparison to Pagua, Pointe Michel was less susceptible to debris flow hazard. Road network and farmlands at the upper parts of the channels were damaged by debris flows (Figures 6.8A and 6.9A). Buildings at the flow transition zone to deposition zone were covered in debris flow (Figures 6.8A and 6.9A). Buildings and other infrastructures situated in the middle of the study areas were not affected by activities of debris movements (Figures 6.8A and 6.9A).

Soufriere's debris flow simulation results indicated that, the thick woodland and buildings were at high risk of rapid mass movement (Figure 6.10A). Movement of debris flow down the channel, completely wiped away approximately 65% of the woodland (Figure 6.10A). This can expose the area to deforestation and erosion. Buildings and roads at the flow deposition zone were buried in debris (Figure 6.10A).

Ribeira Domingo Santo was the area which was least susceptible to debris flow hazards. This is because most of the flow was within the channels without any overflow over the banks (Figure 6.11A). This is due to the fact that, the channels at Ribeira Domingo Santo were very deep with depths ranging from 10 m to over 50 m approximately. Hence nearby farmlands and buildings were not at risk of debris flow hazards. However, some road networks were affected since most roads are constructed across the channels.

7.2.5.2 Flood Hazard Assessment

Flood is one of the major geohazards that cause severe destruction to livelihood, the built and natural environment particularly in suburban and urban areas along floodplains. It is therefore necessary to assess flood risk and implement strategic measures to mitigate its impact.

Assessing the vulnerability of all study localities to flood hazards from HEC-RAS unsteady results indicated that most areas are very susceptible to flood. Flow depth results (Figures 6.12A-18A) for all study were used for flood hazard assessment, which showed how vulnerable each area was to flood. All study localities in Dominica were more susceptible to flood than the study locality in Cape Verde, as presented in Figures 6.12A-18A.

All study areas in Dominica were almost completely flooded and flow depth was high in the channels and low-lying areas, decreasing in highlands. This posed risk to livelihood, the built and natural environment. In contrast to Dominica, Ribeira Domingo Santo was less susceptible to flood hazard. This is because the unsteady flow was mainly within the channel and approximately 3 m to the floodplains (Figure 6.18A). Even the densely populated and heavily urbanized township of Sao Felipe, which is south of Ribeira Domingo Santo, was barely affected by the flood (Figure 6.18A). However, there was still risk of collapse of buildings, destruction of roads and bridges. This is simply because most of the roads and bridges run across the flooded channels and most buildings were built on the floodplains of unstable slopes of the Ribeira Domingo Santo channel banks. Farmlands and livestock are also at risk of flooding.

Generally, Dominica is rugged terrain with many unstable slopes which experiences Storms, Hurricanes and torrential rainfall on practically every year. This makes the Island prone to flooding, landslides and debris flow hazards whenever these catastrophic events occur. The main cause of flooding across the island during Hurricane Maria was the intensive rainfall coupled with poor drainage systems and lack of proper settlement planning. As discussed in

section 7.1 the main factors that caused landslides and debris flow during Hurricane Maria across the island were excessive rainfall coupled unstable slopes and geotechnical properties of the soil and rocks. Debris flow and landslides during Hurricane Maria caused fatalities and severe damages to buildings and other infrastructures in the study areas. This is because most of the buildings were situated either on unstable slopes or extremely close to landslide prone areas without any mitigation measures in place. The lack proper evacuation plans also resulted in many casualties in areas such as Pointe Michel and Soufriere where 15 people were recorded dead and 5 people severely injured.

7.3 Implication of Research Work for Managing Geohazards in Other SIDS

7.3.1 Fogo, Cape Verde Example

One of the reason of the aims of this research work is to apply the developed methodology for debris flow and flood hazards modelling in other volcanic SIDS. To address this aim of the study the developed methodology was applied in Fogo, Cape Verde for pre-disaster planning. Making use of the post disaster knowledge from Dominica for pre-disaster planning and management in Fogo. Foreknowledge of any geohazard is very important for evaluating the level of risk that an area is exposed to and how to manage the risk. Although Fogo is less rugged and vegetated in comparison to Dominica, both islands are SIDS with limited resources and lack of technological development. Also, Dominica and Cape Verde are situated along the Atlantic Hurricane Line which makes them prone to hydro-meteorological hazards such as flood, landslides and debris whenever there is a storm or hurricane.

Results of both unstable flow in HEC-RAS and RAMMS debris flow showed that Fogo is susceptible to both flood and debris flow hazards especially the capital town (Sao Filipe) as seen in Figures 6.11 and 6.18). The simulation revealed that during intensive the Sao Filipe

township where majority of people in Fogo live is at high risk of flooding due to increase in surface runoff and poor drainage systems (Figure 6.18). Most houses are built on landslide prone areas where there are unstable slopes and on the edges of river-banks that undergoes constant erosion which them susceptible to debris flow hazards. As evident in the debris flow debris flow modelling results (Figure 6.11) most buildings in Sao Filipe, roads, bridges and other infrastructures are exposed to debris flow risks. Based on the modelling results (Figures 6.11 and 6.18) disaster reduction managers, policy makers and other stakeholders in Fogo, Cape Verde can put strategic measures in place to mitigate the impact of future geohazards. This can be done creating awareness among the locals through media outlets such as newspapers, radio stations, television stations and even schools. Relocating of people at high risk of flood and debris hazards, constructing proper drainage systems to management occurrence of floods and change in land use so that houses, roads and other infrastructures are not built on or close to unstable slopes where there is high chance of landslides and debris flow occurrence. The results will also help people responsible for disaster management and reduction in Fogo to put effective disaster response and evacuation plans to easily reach and evacuate affected people in case of any future disasters.

7.3.2 Evaluation of Usefulness of Drones.

Use of low-cost but high-resolution remote sensing data for flood and debris flow hazards modelling and mapping was the main objective of this research work. Application of UAV in the acquisition of aerial images provided the opportunity to produce 3D models such as DSMs and orthophotographs. Drones play a major role in the scale of observations between terrestrial field mapping and satellite methods of capturing remote sensing data. This method of acquisition of remote sensing data helps to collect a large amount of data within a short period of time. Drones provides a less expensive alternative means of collecting high resolution

geospatial remote sensing data before, during and after the occurrence of catastrophic phenomena. DEMs and orthophotographs generated from drone aerial images help planning and development stakeholders to plan on future constructions and infrastructures. Live images from drones helps disaster responders to identify which areas are of high risk and should be responded to first and how to get to such areas. The DJI Phantom 4 PRO V2.0 drone used for this study could capture data from inaccessible and unsafe areas. The portability, low-cost and ability to capture high-resolution aerial photos to generate DSMs and orthophotographs for geohazard modelling and mapping made application of a UAV in this research work very useful.

Generally, the cost of using unmanned aerial vehicles to capture remote sensing data is relatively less expensive in comparison to satellite imagery. However, acquiring drones are certainly not free of charge or cheap, well-equipped drones for mapping can cost anything from £1000 to £10,000. Drones are some of the useful technological inventions in the 21st century but they have not been utilised widely enough in geoscience research works. The most popularly used drone for aerial surveys is the Da-Jiang Innovations (DJI) Phantom 4 Pro V2.0 which was used for this research work and it costs £2751 including all necessary accessories. The cost of the Phantom 4 Pro V2.0 drone alone was £1589, ten low-noise propellers cost £10, three battery safe bags cost £27, two Micro Secure Digital Cards cost £62, six intelligent flight batteries cost £845, six wrap packs for the batteries cost £23, two batteries charging hubs cost £142, one 100 W battery charger cost £49 and one 100 W alternating current power adaptor cable cost £4.

Drones are only capable of capturing aerial images hence a different software is required to process these images into useful and interpretable georeferenced orthophotographs and DEMs. To convert the drone aerial images into georeferenced orthophotographs and DEMs, a photogrammetry software. For this research work, Agisoft Metashape Professional was used

because of its affordability and effectiveness in comparison to other photogrammetry softwares such as Pix4D and DroneDeploy. Agisoft Metashape Professional is a licensed software which means a purchase is required to use the software. The educational license version of Agisoft Metashape Professional which was used for this study cost £400 and it is a one-off purchase. The non-educational version of Agisoft Metashape Professional is more expensive and it cost £2543.

The system requirements for using Agisoft Metashape Professional is very high hence a powerful computer with high specifications is needed. Processing of images in Agisoft requires a large Random Access Memory (RAM) where data is stored for the processor. A small size RAM slows down or freezes the computer, so the minimum RAM size required for Agisoft is 32 gigabyte to 128 gigabyte. Central Processing Unit (CPU) is also an important requirement of the computer for using Agisoft because it determines the speed of the computer. Central Processing Unit with high-speed multiple cores is required to construct the geometry algorithms of the aerial images in Agisoft. Therefore, the central processing unit of computer with at least 6 to 24 intel cores and minimum speed of 3.0 GHz required. DEMs and orthophotographs generated in Agisoft are usually within 1 gigabyte to 100 gigabyte hence a computer with at least 3 terabyte storage size is required. For this study a Fujitsu Core i9 Windows 10 Pro desktop computer with 64 gigabyte RAM, 4 terabyte Solid State Drive and 10 intel cores Central Processing Unit with speed of 3.5 GHz was used.

The time it takes to survey an area with drone is not directly proportional to the size of the area. Weather conditions, permission to fly, suitable take-off and landing spots and ruggedness of the terrain can influence duration of surveys. A typical example is comparison of days it took to survey study areas in Dominica and days it took to survey study area in Cape Verde. It took approximately three weeks to survey a total area of 14 km² in Dominica and two weeks to survey a total area of 87 km² in Cape Verde. Although the area surveyed in Cape Verde was

six times bigger than the area surveyed in Dominica, it took less days to capture drone aerial images. This is because, the ruggedness of Dominica made it difficult accessing certain areas and finding vantage points to fly and land the drone. It was windier and rainier in Dominica than Cape Verde, so flights were abandoned on certain days and also it was difficult getting permission to fly the drone. In contrast to the days in the field, the post fieldwork data processing in Agisoft is directly proportional to the size of the area. It took approximately two months to process aerial images of a total area of 14 km² in Dominica and almost four months to process an area of 87 km² in Cape Verde. It is difficult to quantify the cost of drone survey per km² because this was not a commercial project. However, the total cost of drone survey for this study was approximately £10,000 which includes hardware, software and travel expenses for a total area of 101km² of all study localities.

Despite all the advantages of using a UAV for this research work, there were some challenges. Each battery of the drone used for this study only last for half an hour per flight and even with six batteries, this was not enough to conduct substantial survey in a single day. There was no possibility of re-charging the batteries on site as location of study areas were very remote and, even if there was a way to re-charge batteries on site, it takes about 3 hours to charge a battery.

Weather conditions also affected the smooth operations of the UAV during the fieldwork survey especially in Dominica where the weather is unstable and unpredictable. The weather conditions in Fogo were relatively stable and drone work was fairly smooth in comparison to Dominica. The drone could not be flown when it was raining and when the wind speed was above 20 mph, as it could be damaged by water or blown away by the wind.

Also, the ruggedness of Dominica topography coupled with thick forest made drone operations difficult in comparison to Fogo where the topography is less rugged without no thick forest or woodlands. Based on experience of operating the drone in these two countries, it was more

difficult to find take-off and landing spots in study areas in Dominica than in Fogo due to rugged and unstable nature of the terrain. Also, it was difficult to spot the drone in motion even with a spotter because the thick forest and woodlands coupled with the rugged topography had an adverse impact on visibility.

Lastly, DJI has incorporated flight restrictions in all drones they produced and DJI Phantom 4 PRO V2.0 drone was no exception. This meant survey works could not be carried out in areas under flight restriction zones without permission from the country's aviation authority. This was problematic in Roseau, the capital of Dominica, and in Sao Filipe in Fogo. However, permission was granted by authorities of Sao Filipe Airport which was then sent to DJI to deactivate the restriction. Regardless of all these challenges, application of DJI Phantom 4 PRO V2.0 drone for this research work still proved to be a good value for money and effective due to its time and cost efficiency.

Using the Agisoft Metashape Professional photogrammetry software, the drone-derived aerial images for all study areas were processed into high resolution and quality 3D models such as DSMs and orthophotographs. The processed DSMs and orthophotographs were the main input data for this research (Figures 5.20-5.32). DSMs for each study area were used in RAMMS and HEC-RAS 2D to model both debris flow and flood hazards respectively for all study localities. Orthophotographs generated for all study areas were used to assess devastation caused by Hurricane Maria and to analyse movements of boulders during Hurricane Maria with ImageJ. The results revealed there were issues of alignment of images due to inadequate images overlapping at some study areas during the photogrammetric processing. This affected the elevation accuracy of the DSMs for these areas which subsequently affected the results of water surface elevation from the HEC-RAS 2D simulation. The computer requirement for Agisoft Metashape Professional software meant it was impossible to process the result on site to identify any issues with the image-processing outcomes. This makes it impossible to detect

these errors and possibly to undertake another survey. Nevertheless, with just a laptop, images were processed to a certain stage overnight to detect some of these issues in some study areas. Unfortunately, this was not possible in other areas because the capacity of the laptop did not match the software and eventually stopped working.

Despite all these limitations, application a UAV to acquire low-cost remote sensing data for geohazard research works in SIDS is the best option. Results of the processed DSMs and orthophotographs together with results of debris flow and flood simulations showed the usefulness and effectiveness of applying UAV for modelling, mapping and monitoring geohazards in SIDS.

7.3.3 Recommendations for Geohazards Risk Management

Past knowledge of geohazards that a terrain is susceptible is very essential for risk assessment for the future (Lina et al, 2018; Jakob, 2021; Zhang et al, 2021). The level to which occurrence of debris flow can cause destructions to livelihood, the built and natural environment is debris flow risk assessment (Lina et al, 2018; Jakob, 2021; Zhang et al, 2021). Over the last decade, substantial efforts have been made by geoscientists, policy makers and other stakeholders to assess debris flow hazards and risks and how to mitigate its impacts (Lina et al, 2018; Jakob, 2021; Zhang et al, 2021). Different methods have been adopted by geoscientists to study the behaviour of earth materials, past debris flows events of a terrain and outcomes of numerical modelling of debris flows are used to assess risks of debris flows (Lina et al, 2018; Jakob, 2021; Zhang et al, 2021). Assessing the risks of debris flow hazard to the study areas are very important in the efforts to put mitigation strategies in place to control its impacts. Assessed debris flow hazard risks serves as an essential for tool for development planners and policy

makers in study areas for infrastructures planning, making policies on land use, developing and implementing debris flow hazard monitoring and control measures.

The fundamentals of undertaking debris flow risk assessment in the study areas involved understanding the factors that trigger its occurrence in an area. Examining how exposed the study areas were to debris flow hazard was another important aspect debris flow risk assessment that was considered. This helped to know the level of risk that occurrence of debris flow posed to the study areas and what control measures should be put in place to mitigate its effects. Based on field observations, local eyewitnesses accounts and debris flow modelling results in Dominica, torrential rainfall, slope gradient and geotechnical properties of the earth materials caused the occurrence of landslides and subsequently debris flows during Hurricane Maria.

The intensive rainfall saturated the slopes in the study areas which affected the stability of the slopes because the shear strength of the slope materials was weakened due to increase in shear stress and gravitational force. Hence, it caused landslides to occur and debris were moved down hillslope creating new channels and expanding old channels in the form debris flow. The debris flow moved down slope filling up and overtopping river channels into roads and were deposited downstream where most buildings and bridges were buried in debris. Most buildings and other infrastructures in the study areas were constructed on top of unstable slopes, at base of unstable slopes or at the path of a potential debris flow. This is because the planning restrictions in Dominica is less strict and development policies are poorly regulated. Therefore, everyone can basically put up a structure where they deem fit because they own the land. This increases the level of debris flow hazard risks they are exposed to which was evident during and Hurricane Maria. Figure 7.7 is a diagrammatic illustration of the triggering factors of debris flow and the related hazards it poses to any terrain.

ANATOMY OF A DEBRIS FLOW

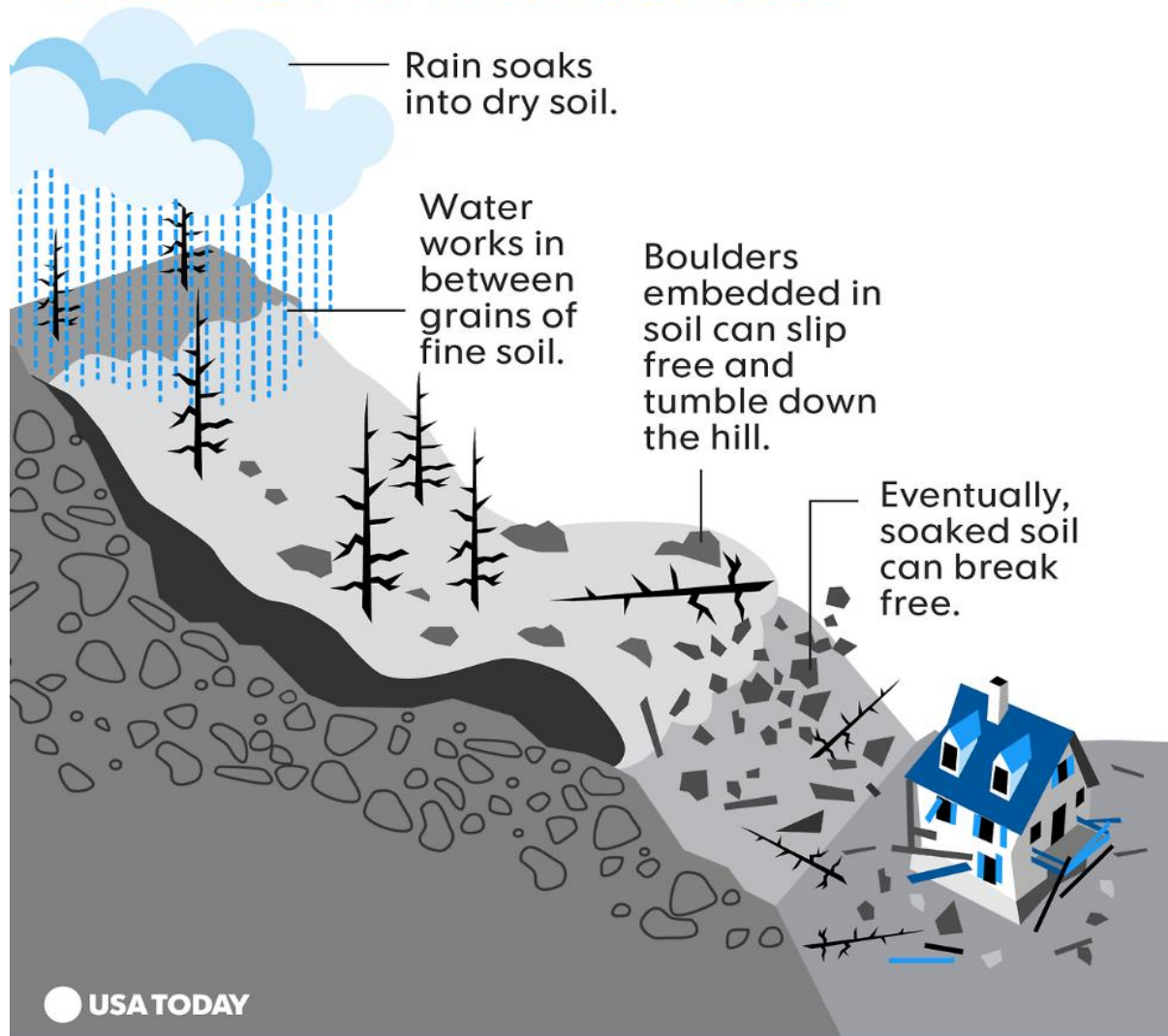


Figure 7.7: Diagrammatic presentation of factors that trigger debris flow and related hazards (USGS).

This study will be made available to policy makers, development planners and other governmental bodies responsible for monitoring, managing and mitigating disasters in Dominica and Cape Verde. Relocating the settlements in the debris flow hazard risk zones to relatively flat areas with stable slopes in St. Peter Parish by the government will be step in the right direction. This will be a difficult task because the people feel attached to area that their ancestors have been living for ages and also because of their farmlands as most of them are farmers. Therefore, to make the area appealing for the people to relocate, the government must plan the new settlement well with lot of social amenities and job opportunities for the people. Also, the government should provide the people with farming equipment and other incentive to help them continue their agricultural activities at the new place.

Educating and warning the people about the dangers that debris flow and flood hazards pose to them will help convince them to relocate to safer grounds with their families. Creating public disaster awareness and enlightenment by communicating to the general public on geohazards and involving them in disaster reduction activities at local, regional and national levels. Understanding the risk that geohazards such as flood and debris flow pose to them make willing to cooperate will policy makers in the efforts to mitigate the impacts of these disasters. This will also help manage disasters at local level by the people themselves without always waiting for the government make decisions for them.

SIDS such as Dominica and Cape Verde are situated in the Atlantic Ocean and completely surrounded by water. This makes it difficult for disaster relief and other humanitarian agencies such as Red Cross Society to reach them in time during and immediately after occurrence of a geohazard. It is very important for SIDS to make efforts be disaster self-sufficient so that they will not be over-dependent of foreign aids. They can use resources and funds donated by UN and other countries to make development towards becoming disaster resilient and self-sufficient when a catastrophic event such as Hurricane Maria occurs.

It is fundamental in any disaster risk reduction programme to have a clear and consistent plan for responding, evacuating and sheltering the and endangered and post disaster recovery plan. Disaster risk managers in Dominica and Cape Verde should put effective measures in place to quickly respond, evacuate and shelter people when storms and hurricanes strike. In the events of floods affected people should be evacuated with lifeboats to higher grounds or safe shelters. Although an area is likely to get flooded during torrential rainfall even with good drainage systems, it is still important to have good drainage systems as they help alleviate the impact of floods.

Areas with slope angles above 35° and less vegetation or trees to hold the soil together are classified as unstable slopes because they are likely to fail during torrential rainfall. Early assessment of slope stability by looking for features such as slope angles and vegetation cover will help to know areas which have unstable slopes. Figure 7.7 is typical example of slope failure from high slope angle area with less trees and vegetation which resulted in debris flow hazard. This also help to relocate people from potential landslides and debris flow areas to relatively safe environs. In certain situation, resettlement of people is not a possibility hence landslides and debris flow defence structures must be constructed to divert the flow path to protect livelihood, buildings and roads. Unlike floods, it is difficult to evacuate people in the events of debris flow hence early risk assessment is essential to the process of relocating people at high risk.

Attention must be paid to people or areas that severely affected post any disaster. Providing shelter for people who have been displaced and made homeless by floods and debris flow is the first to the recovery process. All affected roads, bridges, infrastructures and utility networks such as pipelines, electricity lines must be reconstructed as soon as possible because they are vital to reviving the economy and livelihood. Government must provide financial aid to affected individuals and communities to rebuild their homes and get their life back on track.

Aside providing financial help to the affected people, they must be offered post disaster mental health support. After catastrophic events such as Hurricane Maria, many people suffer psychological stress, anxiety, depression, post-traumatic stress disorder and substance abuse among others. Hence, mental health and psychological support must be provided to affected people to help them recover.

7.4 Limitations of Research Work

7.4.1 Uncertainties and Errors

Most academic research work has to consider uncertainties and errors (Box and Daper, 1987), this research work is not an exception. Even though a thorough desk-study, ground truthing and field data collection was undertaken, there were still many uncertainties with this study. The uncertainties and errors associated with this research work were due to time constraints, limited resources, lack of accessibility and other circumstances beyond the researcher's control.

Remote sensing data in the form of DSMs and orthophotographs were the main data used for this research work. Data were collected using a drone in the form of aerial photos and processed into DSMs and orthophotographs using Agisoft Metashape Professional photogrammetry software. Although remote sensing data acquisition with the drone is relatively easy, quick and time-efficient, nevertheless there were still some difficulties that affected the accuracy of the data. There were inadequate overlapping images in some study localities such as Coulibistrie and Layou in Dominica. This was due to some areas being inaccessible and therefore it was unsafe to operate the drone. Also, the drone batteries only last for 30 minutes per flight and there was no means to charge them in the field, hence making it impossible to capture sufficient perfectly overlapping images in a short period of time. Lack of a powerful computer to process the images quickly enough to identify the overlapping errors during the fieldwork also contributed to the problem. All these problems affected the data after processing which undermines the accuracy of the results. Nevertheless, using drone-derived DSMs was a better option than the outdated, erroneous and low-resolution ASTER and ALOS PALSAR DSMs.

There were basically no Hurricane Maria rainfall data for Dominica because all the rain gauges on the island were destroyed. Therefore, Hurricane Maria rainfall data recorded in Puerto Rico and published by United States of America Hurricane Centre (USHC) were used for the unsteady flow simulation in HEC-RAS. Just like Dominica, the rainfall data of Tropical Storm

Fran in Cape Verde was not well documented and data published in other research works (Clark, 1984) were used. Although not a bad practice, utilization of actual ground data would have resulted in more correct outcomes for both study areas. The justification for using rainfall data recorded in Puerto Rico during Hurricane Maria for the Hydraulic and unsteady flow simulation was based on the fact that both islands are SIDS. Also, both Dominica and Puerto Rico were the most affected SIDS in the Caribbean by the catastrophic events of Hurricane Maria. The level of devastations and fatalities recorded during Hurricane Maria in Puerto Rico and Dominica were relatively higher in comparison to other SIDS in the Caribbean and Central America. Although Hurricane Maria rainfall data from the closest islands to Dominica such as Guadeloupe in the north and Martinique in the south could have been used for the study, these islands were barely affected by events of Hurricane Maria. Therefore, it was only rational to use the rainfall data recorded in Puerto Rico for unsteady flow modelling in Dominica. This is because it helped to replicate the real-life flooding and level of destructions that occurred during Hurricane Maria in Dominica.

In mass movement, debris flow occurs when there is rapid movement of sediments, rocks, debris (organic and inorganic matter) and water downslope under gravitational force (Iverson, 1997; Regmi et al, 2015). Flows with about 60% sediments of all sizes and shapes are considered as debris flows whilst flows with 10% to 40% sediments concentration are classified as hyperconcentrated flows (Pierson, 2005). Most debris flows are cascading effects of rainfall induced landslides which was the case of Dominica during the 2017 Hurricane Maria. However, there are other types of debris flows which are not as a result of occurrence of landslides but due to other geomorphological processes (Iverson et al, 1997; Zhuang et al, 2013).

During torrential rainfall, the pore water pressure increases and adds weight to unstable slopes and eventually increasing the shear stress acting on the unstable slope hence reducing the shear

strength of the slope materials (Iverson et al, 1997; Zhuang et al, 2013) (Figure 7.8). This causes the occurrence of landslides and the mass moved downslope are mobilised from the point of initiation through the transition zone to the point of deposition (Figure 7.8 and 7.9) in the form of debris flow (Iverson et al, 1997; Zhuang et al, 2013). This type of debris flow is considered as landslide sourced debris flow (Zhuang et al, 2013).

Channel-bed failure and erosion are other geomorphic processes that cause debris flows aside landslides (Figure 7.9) (Gregoretti et al, 2008; Zhuang et al, 2013; Shen et al, 2018). During intensive rainfall or dam breach, cohesionless sediments in the channel bed are eroded and transported downstream as channelised debris flow (Figure 7.9) (Gregoretti et al, 2008; Zhuang et al, 2013; Shen et al, 2018). Also, erosion and hydrodynamic forces affect stability of the channel banks slopes because the materials supporting the unstable slopes are eroded during dam breach or torrential rainfall (Figure 7.9) (Gregoretti et al, 2008; Zhuang et al, 2013; Shen et al, 2018). This results in collapse of channel banks into the channel bed forming a landslide-dam which eventually breaks and moves downstream as debris flow by surface runoff. (Gregoretti et al, 2008; Zhuang et al, 2013; Shen et al, 2018).

Landslide-triggered debris flows are characterised by rapid movements, large flow volume, long distance coverage, channelised and unchannelised (Gregoretti et al, 2008; Zhuang et al, 2013; Shen et al, 2018). Various materials ranging from soil, rocks, tree debris and other inorganic debris such as plastics and metals of all shape and sizes are found in landslide sourced debris flows (Gregoretti et al, 2008; Zhuang et al, 2013; Shen et al, 2018). On the other hand, channel-bed failure sourced debris flows are relatively less rapid, small volume, covers a short distance and flow path is channelised (Gregoretti et al, 2008; Zhuang et al, 2013; Shen et al, 2018). This type of debris flow usually contains sediments and rock particles such as cobbles (Gregoretti et al, 2008; Zhuang et al, 2013; Shen et al, 2018).

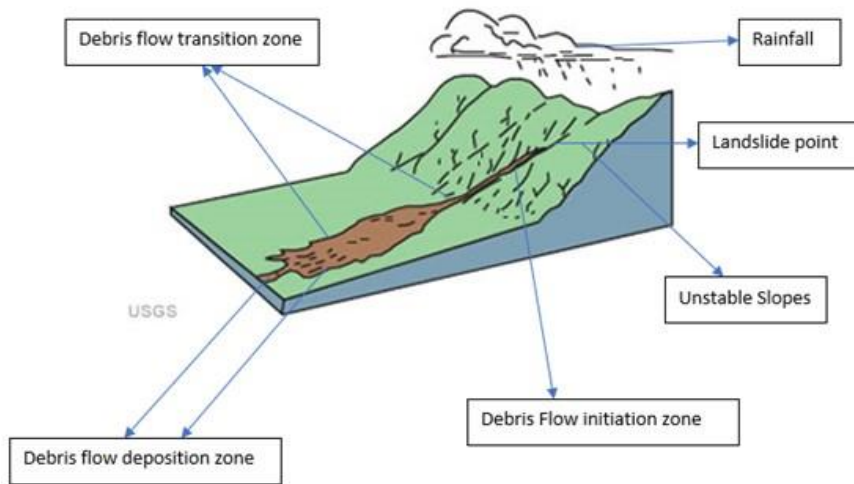


Figure 7.8: Diagrammatic presentation of rainfall-induced landslide sourced debris flow (USGS)

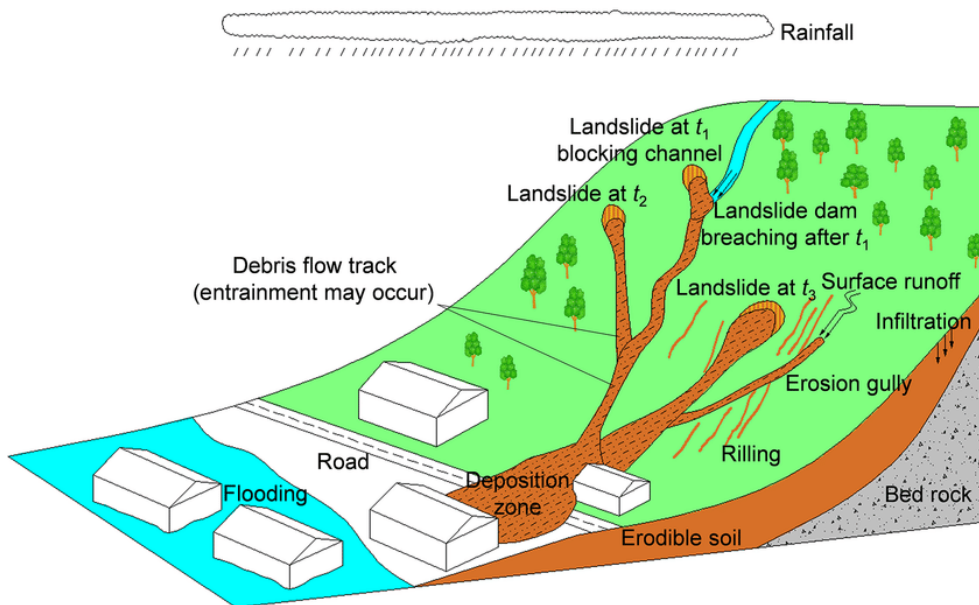


Figure 7.9: Diagrammatic presentation of landslide initiated debris flow, and channel-bed failure and erosion initiated debris flow (Shen et al, 2018).

The type of debris flow that occurred in Dominica during the 2017 Hurricane Maria was landslide-initiated debris flow. The intensive rainfall saturated many unstable slopes which increased pore water pressure, shear stress and decreasing shear strength of the slope materials. This resulted in occurrence of many landslides across the island, sediments, rocks and tree debris were mobilised and transported down slope as debris flow which caused many destructions. Knowing the type of debris flow that occurred during Hurricane helped in deciding what input parameters to use for the modelling.

When undertaking any debris flow modelling, it is important to know the earth materials of the terrain. Availability of geotechnical data of the study area helps to choose appropriate input parameters for the debris flow simulation. Data about slope angles and aspects of the study area are also integral aspects in debris flow modelling because they influence the occurrence of mass movement. Unfortunately, the geotechnical data of Dominica is not well documented so it was difficult to choose accurate input parameters such as friction coefficient (μ), turbulent coefficient (ξ) and earth pressure (Λ).

With RAMMS, slope gradients and aspects are automatically computed from the DEMs of each study area. However, input parameters such as friction coefficient (μ), turbulent coefficient (ξ) and earth pressure (Λ) are chosen by default in RAMMS. In order to determine which parameters are suitable for the terrain, a sensitivity analysis must be undertaken and results must be compared with real-life event data.

This is the first research that has applied RAMMS debris flow module for simulation of debris flows in tropical volcanic islands of Dominica and Cape Verde. Hence random input parameter values were used for the simulation based on the model's calibration. Using these random input parameters to determine the flow height, distance, volume, velocity, pressure and entrainment probably does not represent accurate and realistic events in the study localities. Also, the flow

initiation volume for all localities was based on an assumption according to the size of the DSMs as the flow initiation volumes of the 2017 debris flows are unknown. Hence, the accuracy of the simulation results is questionable. Furthermore, RAMMS was developed and primarily used in Switzerland where debris flows are typically composed of many angular blocks of rock and little fine-grained matrix. This is in contrast with volcanic terrains such as Dominica and Cape Verde where debris flows are composed of a variety of blocky materials and a large amount of fine-grained muddy materials.

As image analysis software, ImageJ can be used to analyse different types of images. However, ImageJ was ideally made for analysing medical images but not geoinformatics images. Therefore, there is a degree of uncertainty with the accuracy of the outcomes because there is a huge difference between images of human tissues and boulders. Nevertheless, sizes of boulders from the ImageJ analysis results matched the size of boulder measured during the fieldwork which was used as scale for analysing all the boulders in each study locality. It would have been good practice to measure all boulders in all study areas or at least one study area during the field work and compare the data with the image analysis results. However, due to circumstances beyond control such as time constraints and limited resource, the idea of measuring all boulders during the fieldwork was not pursued.

7.4.2 Problems Associated with SRTM and ALOS PALSAR DEMs.

A desk study was conducted with SRTM and ALOS PALSAR DEMs in ArcGIS prior to the fieldwork in Dominica. This was done in order to understand the terrain in terms of its geomorphology, geology and hydrology. For this work, a 30 m SRTM DEM and 12.5 m ALOS PALSAR DEM were used. The desk study analysis revealed very important information about both SRTM and ALOS PALSAR DEMs.

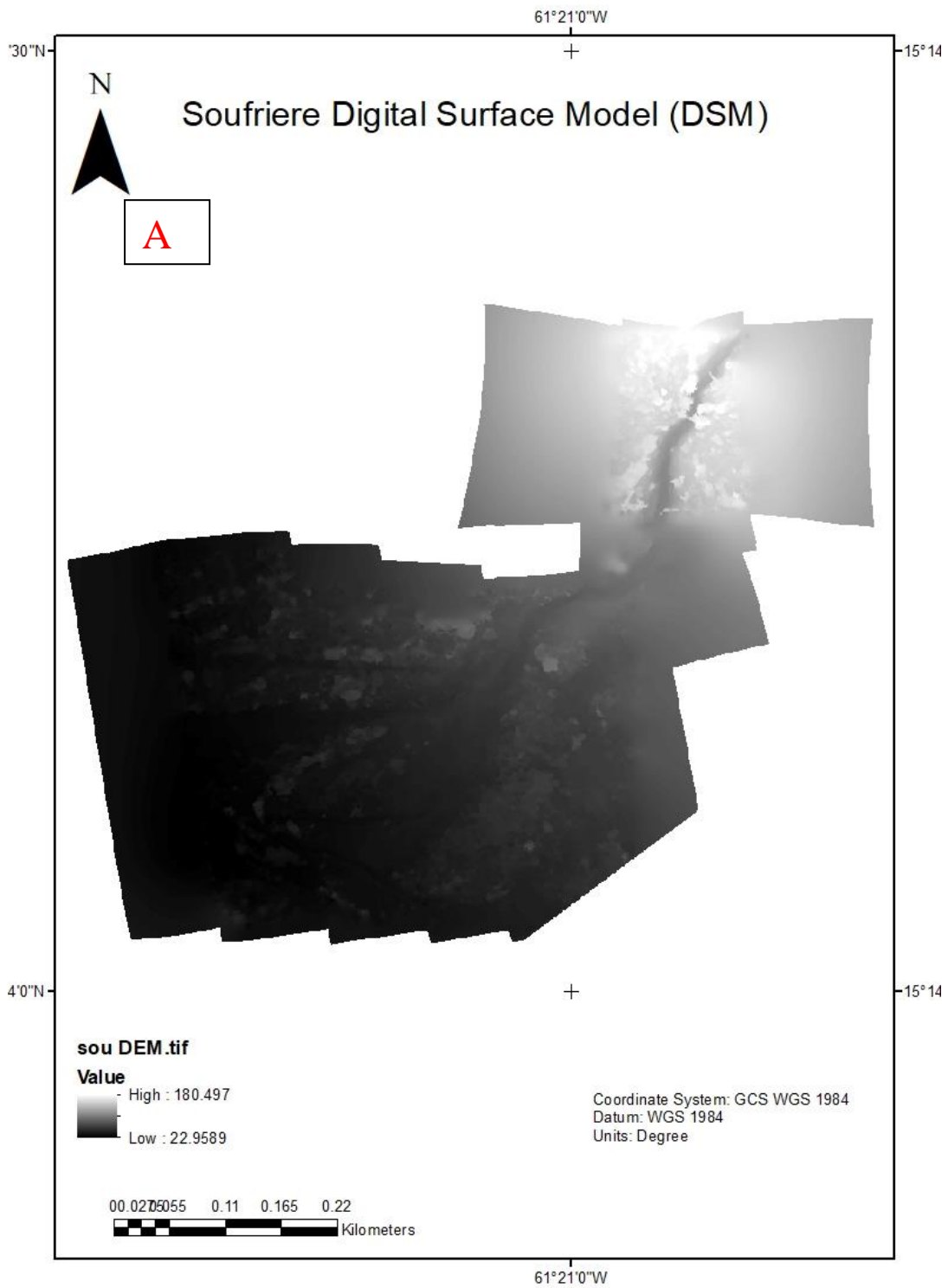
There were problems associated with both SRTM and ALOS PALSAR DEMs. One of the main problems was incorrect presentation of elevation of the terrain. Many cells above sea-level in the DEMs had negative backscatter values which means the raster surface areas were below sea-level. Also, many cells in both DEMs were completely void which meant those raster surface areas had no backscatter values. This had to be reprocessed and corrected by merging the two DEMs into one (Figure 4.1). Looking at the corrected DEM, all cells raster surfaces had backscatter values without any voids. Although all cells now had backscatter values above at sea-level or above, there were still issues with the elevation of some raster surface areas. Also, orientation (aspect) of the terrain's slopes were incorrect even after reprocessing of the DEM's. There were also discontinuities in drainage channels even after several attempts of reprocessing of the DEMs.

Aside from the backscatter and elevation problems identified in the DEMs, another major concern about the SRTM and ALOS PALSAR DEMs was that the data were outdated for this study. This is because the most recent freely available SRTM and ALOS PALSAR DEMs dates back to 2011 which is almost a decade old. The data pre-dates Hurricane Maria, also the terrain has undergone several geomorphological changes since 2011. Hence the processed SRTM and ALOS PALSAR DEM do not represent the current state of the terrain.

Also, another problem with the corrected SRTM and ALOS PALSAR DEM was it was too general with low resolution. The DEM was too generic as it represented the whole island and

not specific to the study areas. Working with such data is difficult unless the project is about the whole island not selected study areas. Resolution of the corrected SRTM and ALOS PALSAR DEM was relatively low in comparison to the drone-derived DEMs. Therefore, even though the data was freely available, it was not suitable for this study. This is because using such data for this research work would have produced inaccurate and unrealistic results and would undermined the aim of this research work. Figure 7.10A and B shows comparison between high resolution and detailed drone-derived DSM of one of the study areas (Soufriere) with erroneous low resolution and outdated SRTM DEM of Dominica

Nevertheless, the terrain analysis (Figure 4.2-4.5 and drainage network analysis (Figures 4.6-4.7) conducted during the desk study were very useful. The results gave an insight about the terrain prior to the fieldwork. They also helped to choose the selected study areas for the study. The decision to use drone-derived DEMs and orthophotographs for this research work was greatly influenced by these identified problems associated with the SRTM and ALOS PALSAR DEMs.



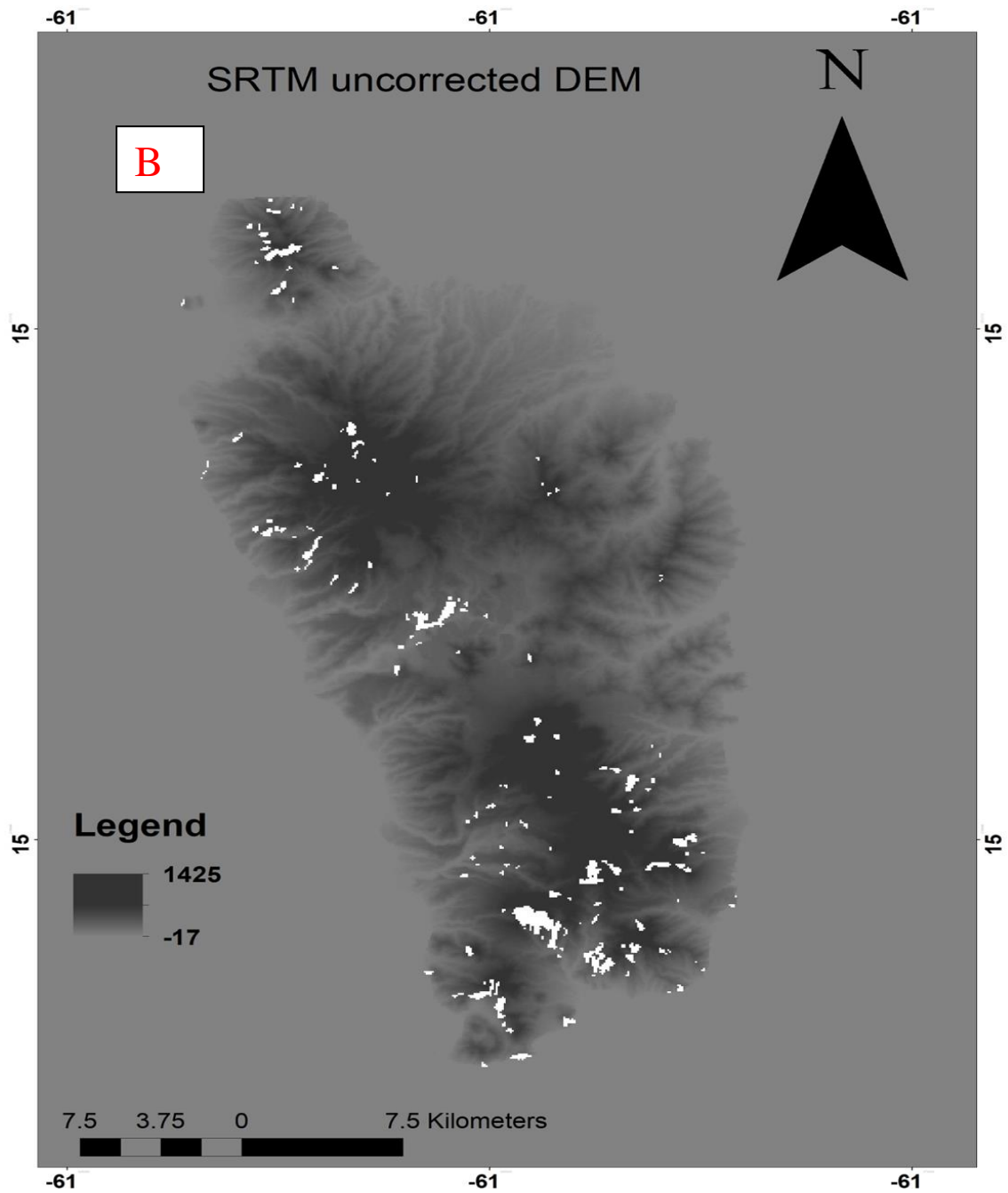


Figure 7.10 A and B: (A) Comparison of high resolution and up to date drone-derived DSM of Soufriere with (B) erroneous slow resolution and outdated SRTM DEM of Dominica.

7.4.3 Sensitivity Analysis of RAMMS Debris Flow Module

Just like most numerical models, sensitivity analysis was conducted on the RAMMS debris flow model used for this study. Results of the analysis showed how an input variables can influence output variables of the model and its ability to predict debris flow hazard in different scenarios. Also, outcomes of the sensitivity analysis revealed the input parameters that features of debris flow such as flow height, velocity, volume and runout distance are most sensitive to.

Using only the default input parameters of RAMMS to model real-life debris flow events that occurred during Hurricane Maria would have been a disservice to this research work. This is because RAMMS has never been applied in volcanic island such as Dominica and Cape Verde to model debris flow hazards hence input parameters that are suitable for such terrains are not known. Therefore, it was essential to conduct sensitivity analysis to determine not only how sensitive the model is to a change in input parameters but also what input parameters suits volcanic terrains such Dominica and Cape Verde. Outcomes of the sensitivity analysis showed the behave of the debris flow in relation to the changes in input parameters and revealed input parameters replicated the real-life debris flow during Hurricane Maria are probably suitable for a volcanic terrain.

Outcomes of the sensitivity analysis indicated that the RAMMS debris flow module was very sensitive to changes of the input parameters. A change in input parameters such as turbulent coefficient (ξ), friction coefficient (μ) and earth pressure (Lambda) resulted in a significant change in flow height, volume and runout distance (Figures 6.1-6.3). An increase in turbulent coefficient (ξ) caused an increase in the runout distance of the flow, volume of flow and height of flow (Figure 6.1). Also, a decrease in flow height, volume and runout distance is as a result of decrease in turbulent coefficient (ξ) (Figure 6.1).

Unlike the turbulent coefficient (ξ), an increase friction coefficient (μ) automatically resulted in a decrease in the flow runout distance, volume and height (Figure 6.2). And a decrease in friction coefficient (μ) caused an increase in runout distance, height and volume of the flow (Figure 6.2). A reduction in earth pressure (Lambda) resulted in an increase in flow runout distance, height and volume and lateral spread of flow (Figure 6.3). However, flow moved thinly and reduced in runout distance, height and volume when earth pressure (Lambda) was increased (Figure 6.1).

Also, the velocity of the flow increased when there was an increased in turbulent coefficient (ξ) and decreased when there was an increase in friction coefficient (μ) and vice versa.

Turbulent coefficient (ξ) is considered as a velocity dependent coefficient (Hurlimann et al, 2008; Hussin, 2011). This is because it behaves as a drag force which influences momentum and velocity of the flow (Hurlimann et al, 2008; Hussin, 2011). These findings (Figures 6.1-6.3) indicated that the RAMMS debris flow model is very sensitive to a change input parameters such as turbulent coefficient (ξ), friction coefficient (μ) and earth pressure (Lambda).

Evaluation of sensitivity analysis results indicated that flow height and runout distance were most sensitive to friction coefficient (μ), whilst flow velocity was most sensitive to turbulent coefficient (ξ) and flow volume was more sensitive to earth pressure (Lambda) (Figures 6.1-6.3). Based on sensitivity analysis results, 0.05 friction coefficient (μ), 800 turbulent coefficient (ξ) and 1 earth pressure (Lambda) produced similar debris flow like the real-life event even though the original data had been tampered with by clean-up works. Understanding the debris flow runout route, distribution pattern, volume, height and velocity of possible future events helps to define areas that are at risk of debris flow hazards in a vulnerability assessment.

7.4.4 Further Work

Results of RAMMS debris flow module, HEC-RAS unsteady flow simulations and ImageJ boulder analysis are not hundred percent accurate just like most models, thus is a potential for further works. Factors such as errors and uncertainties associated with input data and parameters contributed to the inaccuracy of the results. Even though the data were not wholly erroneous, the minor errors in the data made the results not 100% reliable.

Fieldwork was undertaken for this research work to validate desk study and collect current data of the study areas. However, due to time constraints and factors beyond control, there was not enough coverage and overlaps of aerial images taken at Coulibistrie, Delice and Layou. This affected the outcome of the processed DSMs data even after several reprocessing and corrections. This is why the water surface elevation results for these areas had negative values, indicating flooding occurred below sea level. There was no Hurricane Maria rainfall data for Dominica because all rain gauges were wiped away during events of Hurricane Maria. Therefore, hydrograph data for HEC-RAS unsteady flow analysis was taken from US Hurricane Centre for neighbouring Lesser Antilles countries that were also affected by Hurricane Maria. Although not a bad practise, results would have been more credible if data were from rain gauges in Dominica.

Also, while ImageJ have been to analyse images from all disciplines, it was mainly developed to analyse medical images. Although it was relatively good for analysing the orthophotographs, in cooperating plugins for analysing geoscience images would make the results more reliable. Prior to this study, RAMMS debris flow module has not been applied in tropic volcanic terrains such as Dominica and Cape Verde. Developed in Switzerland, it has mainly been used to simulate debris flow in Switzerland, Italy and France which are completely different terrains to Dominica and Cape Verde. Updating RAMMS input parameters to suit volcanic terrains

such as Dominica and Cape Verde would make the results more accurate. Developers HEC-RAS 2D recognises there are some limitations of the model which they are currently working. At the moment hydraulic structures cannot be added in a 2D flow area and bridge modelling is not possible in 2D flow areas. Also, it is not possible to analyse water quality, sediment transport and depositions in the current version of HEC-RAS 2D. When all these issues are addressed in the future version as confirmed the HEC-RAS developers, the results will be more accurate and reliable.

Nevertheless, when all these issues are addressed in future and with correct data, these methodologies can be applied in other SIDS and areas such as Santo Antao in Cape Verde and Roseau in Dominica to model and map geohazards.

CHAPTER EIGHT

Conclusion

8.0 Conclusion

This research work utilized low-cost remote sensing data in RAMMS, HEC-RAS 2D and ImageJ to model, map and monitor flood, debris flow and boulder movement hazards in the SIDS of Dominica and Cape Verde. Even though SRTM and ALOS PALSAR DEMs are available freely, they are not suitable for conducting any current research work. This is because not only are they outdated, but they are also erroneous with low quality resolution and the results they produce are not realistic. Devastations caused by the 2017 Hurricane Maria event in Dominica were also analysed using pre- and post-Hurricane Maria Google Earth images. The modelling of floods, debris flow and analysis of movements of boulders was done to understand the vulnerability of these areas to such geohazards and how to mitigate their effects on livelihood, the built and natural environment.

DSMs and orthophotographs which were the principal data used for this research work were acquired from processed drone aerial images by Agisoft Metashape Professional. Pre- and post-Hurricane Maria data were acquired from Google Earth Pro. Rainfall data during events of Hurricane Maria were taken from literature and landcover data for Dominica and Cape Verde were obtained from <http://www.charim-geonode.net/> and USGS respectively.

DSMs and orthophotographs were applied in RAMMS to simulate debris flow, DSMs, orthophotographs together with landcover and rainfall data were used in HEC-RAS 2D to model flooding. ImageJ analysed orthophotographs to determine the size of boulders moved during Hurricane Maria. Assessment of devastation caused by Hurricane Maria was done using Google Earth images of pre- and post-Hurricane Maria events.

Analysis results clearly showed that study areas in Dominica were severely damaged by events of Hurricane Maria. There were many fatalities, injuries, displacement of people and loss of homes

in all the study areas and Dominica as a whole. Most buildings, transportation networks, crops, livestock, water and electricity supplies were all damaged. Most boulders found in study areas were moved during Hurricane Maria except few giant boulders in Pagua. Movement of boulders caused damages to buildings, bridges, farmlands and the vegetation.

Results of the simulations revealed that all study localities in Dominica are susceptible to debris flow and flood hazards. Ribeira Domingo Santo in Fogo was less susceptible to both hazards in comparison to Coulibistrie, Delice, Layou, Pagua, Pointe Michel and Soufriere in Dominica. Most study localities were completely flooded and covered in debris which clearly showed how vulnerable to debris flow and flood hazards should there be another event like Hurricane Maria. This is because most buildings, roads other infrastructures were situated in hazard prone areas.

There were errors and uncertainties associated with the input data and parameters used in this research work. The simulation results were not validated due to lack of both historic and original flood and debris flow data for study localities. These challenges made the accuracy and reliability of the simulation results doubtful. Despite these problems and limitation, the models are good for predicting debris flow and flood hazards with the right input data and parameters. Therefore, the application of low-cost drone-derived remote sensing data in ImageJ, RAMMS and HEC-RAS for modelling, mapping and monitoring boulder movements, debris flow and flood hazards. This approach can be applied to other SIDS for hazard monitoring, safety assessment and development planning. This is because it is cost and time-effective for SIDS with lack of technological development, limited human and capital resources to tackle these geohazards.

To mitigate the threat posed by these hazards to livelihood, the built and natural environment, awareness must be created at local, regional and national levels. Government should create about geohazards awareness at all levels through media outlets such as newspapers, social

media, radio and television stations. The general public should be educated on geohazards through community and regional forums and seminars. Debris flow, flow and other hazards maps should be produced and distributed freely to areas that are at high risk to serve as warning signs to populace. If possible, the government must relocate or rehouse people who live in geohazard prone areas. Emergency evacuation routes must be created at areas susceptible to geohazards to enable easy rescue operations should there be an unexpected disaster. There should be incorporation of strategic measures in the process of development planning by policy makers and development planners at all levels. Acknowledging the vulnerability of an area to hazards in development planning and policy making will help to control and mitigate their effects on livelihood, the built and natural environment.

REFERENCES

(<http://ndl.ethernet.edu.et/bitstream/123456789/24698/1/1.pdf.pdf>)

(http://uwiseismic.com/Downloads/Dominica_VHA.pdf)

(<https://reliefweb.int/sites/reliefweb.int/files/resources/dominica-pdna-maria.pdf>)

(<https://trid.trb.org/view/281932>)

Ahmadi, F.F. and Ebadi, H., 2009. An integrated photogrammetric and spatial database management system for producing fully structured data using aerial and remote sensing images. *Sensors*, 9(4), pp.2320-2333.

Amelung, F. and Day, S., 2002. InSAR observations of the 1995 Fogo, Cape Verde, eruption: Implications for the effects of collapse events upon island volcanoes. *Geophysical Research Letters*, 29(12), pp.47-1.

Anderson, D.L., Tanimoto, T. and Zhang, Y.S., 1992. Plate tectonics and hotspots: the third dimension. *Science*, 256(5064), pp.1645-1651.

ASF DAAC (<http://www.asf.alaska.edu>) 2014

Assessing the U.S. Climate in 2018". National Centers for Environmental Information (NCEI). Retrieved February 9, 2019.

Ave-Lallemant, H.G., Sisson, V.B., 2005. Caribbean-South American plate interactions, Venezuela. *Geol Soc America Spec Pap* 394:1-353

Baioni, D., 2011. Human activity and damaging landslides and floods on Madeira Island. *Natural Hazards and Earth System Sciences*, 11(11), pp.3035-3046.

Balenović, I., Marjanović, H., Vuletić, D., Paladinić, E., Sever, O., Zorana, M. and Indir, K., 2016. Quality assessment of high-density digital surface model over different land cover classes. *Periodicum Biologorum*, 117(4), pp.459-470.

Barboriak, D.P., Padua, A.O., York, G.E. and MacFall, J.R., 2005. Creation of DICOM—aware applications using ImageJ. *Journal of Digital Imaging*, 18(2), pp.91-99.

Barclay, J., Haynes, K., Mitchell, T., Solana, C., Teeuw, R., Darnell, A., Crossweller, S., Cole, P., Pyle, D., Lowe, C., Fearnley, C., and Kelman, I., 2008. Framing volcanic risk communication within disaster risk reduction: finding ways for the social and physical sciences

to work together. In: *Communicating Environmental Geoscience*, Vol. 305, 163–177. Eds: Liverman, D., Pereira, C., and Marker, B., Special Publications, Geological Society, London.

Bartelt, P., Buehler, Y., Christen, M., Deubelbeiss, Y., Graf, C., McArdell, B., Sals, M. and Schneider, M., 2013. RAMMS: Rapid Mass Movement Simulation: A numerical model for debris flows in research and practice, User Manual v1. 5 Debris Flow. Swiss Institute for Snow and Avalanche Research SLF, Birmensdorf.

Baugh, C.A., Bates, P.D., Schumann, G. and Trigg, M.A., 2013. SRTM vegetation removal and hydrodynamic modeling accuracy. *Water Resources Research*, 49(9), pp.5276-5289.

Bell, F.G., 1999. *Geological Hazards. Their Assessment, avoidance and mitigation*, vol. 1. <https://www.routledge.com/Geological-Hazards-Their-Assessment-Avoidance-and-Mitigation/Bell/p/book/9780415318518>

Bellon, H., 1988. Chronological recognition of the first two phases of volcanic activity in Dominica (Lesser Antilles). *Proceedings of the Academy of Sciences. Series 2, Earth Sciences*, 306 (20), pp.1487-1492.

Bellon, H., Pelletier, B. and Westercamp, D. 1974. Geochronometric data on Martinican volcanism. *C.R. Acad. Sc. Paris*, 279 (series D), pp. 457-460.

Benson, C. and Clay E.J, 2000. ‘Developing Countries and the Economic Impacts of Natural Disasters’. In: *Managing Disaster Risk in Emerging Economies*. Eds. Kreimer A and Arnold M. Disaster Risk Management Series 2. Washington, D.C.: World Bank. pp11-21.

Bessette-Kirton, E.K., Cerovski-Darriau, C., Schulz, W.H., Coe, J.A., Kean, J.W., Godt, J.W., Thomas, M.A. and Hughes, K.S., 2019. Landslides triggered by Hurricane Maria: Assessment of an extreme event in Puerto Rico. *GSA Today*, 29(6), pp.4-10.

Bhandari, M., Nyaupane, N., Mote, S.R., Kalra, A. and Ahmad, S., 2017. 2D Unsteady Flow Routing and Flood Inundation Mapping for Lower Region of Brazos River Watershed. In: *World Environmental and Water Resources Congress 2017* (pp. 292-303).

Blaikie, P., Cannon, T., Davis, I. and Wisner, B., 2005. *At risk: natural hazards, people's vulnerability and disasters*. Routledge.

Blaschke, T., Lang, S. and Hay, G. eds., 2008. *Object-based image analysis: spatial concepts for knowledge-driven remote sensing applications*. Springer Science & Business Media.

Bommer, J.J. and Rodríguez, C.E., 2002. Earthquake-induced landslides in Central America. *Engineering Geology*, 63(3-4), pp.189-220.

Bouysse, P., 1988. Opening of the Grenada back-arc basin and evolution of the Caribbean Plate during the Mesozoic and early Paleogene. *Tectonophysics*, 149(1-2), pp.121-143.

Box, G.E. and Draper, N.R., 1987. *Empirical model-building and response surfaces* (Vol. 424). New York: Wiley.

Cape Verde Islands dry forests. *Terrestrial Ecoregions*. World Wildlife Fund. Retrieved 3 April 2019.

Cape Verde: Plant and animal life". *Encyclopædia Britannica*. Retrieved, April 2019.

Centre for Research on the Epidemiology of Disasters – CRED 2018, *Natural Disaster annual report*.

CEPAL, 1999. *Central America: Assessment of the Damage Caused by Hurricane Mitch, 1998. Implications for Economic and Social Development and for the Environment*, 41pp. At <http://www.cepal.org.mx/>.

Cesca, M. and d'Agostino, V., 2008. Comparison between FLO-2D and RAMMS in debris-flow modelling: a case study in the Dolomites. *W.I.T Transactions on Engineering Sciences*, 60, pp.197-206.

Christen, M., Bartelt, P., Kowalski, J. and Stoffel, L., 2008. Calculation of dense snow avalanches in three-dimensional terrain with the numerical simulation program RAMMS. In: *Proceedings of the 2008 International Snow Science Workshop*, p. 709.

Christen, M., Kowalski, J. and Bartelt, P., 2010. RAMMS: Numerical simulation of dense snow avalanches in three-dimensional terrain. *Cold Regions Science and Technology*, 63, pp.1-14.

Collins, F.E.K. and Asare, M.Y., *River Inundation and Hazard Mapping—a Case Study of Susan River—Kumasi*.

Collins, Tony J. 2007. ImageJ for microscopy. *Biotechniques* 43, no. S1: S25-S30.

Comfort, L., Wisner B., Cutter S. et al. 1999. "Reframing Disaster Policy: The Global Evolution of Vulnerable Communities." *Environmental Hazards* 1:39-44.

Cozzens, T. Volcanic GIS: Mapping and imaging the Kilauea eruption. <http://geospatial-solutions.com/volcanic-gis-mapping-and-imaging-the-kilauea-eruption/>

Dabove, P., Manzano, A.M. and Taglioretti, C., 2015. The DTM accuracy for hydrological analysis. *Geam-Geoingegneria Ambientale E Mineraria-Geam-Geoengineering Environment And Mining*, 144, pp.15-22.

Das, A., Agrawal, R. and Mohan, S., 2015. Topographic correction of ALOS-PALSAR images using InSAR-derived DEM. *Geocarto International*, 30(2), pp.145-153.

Day, S.J., Da Silva, S.H. and Fonseca, J.F.B.D., 1999. A past giant lateral collapse and present-day flank instability of Fogo, Cape Verde Islands. *Journal of Volcanology and Geothermal Research*, 94(1-4), pp.191-218.

Day, S.J., Heleno da Silva, S.I.N. & Fonseca, J.F.B.D., 1999. A past giant lateral collapse and present-day flank instability of Fogo, Cape Verde Islands. *J. Volc. Geotherm. Res.*, 94, 191-218, doi:10.1016/S0377-0273(99)00103-1.

De Graff, J. V. 1987. Landslide hazards on Dominica West Indies - Final Report. Washington, D.C.: Organization of American States.

De Graff, J. V. et al. 1989. Landslides: Their Extent and Significance in the Caribbean. In: *Landslides: Extent and Economic Significance*. Ed. Brabb E.E. and Harrod. Rotterdam B.L.: Balkema, A.A. pp51-80.

Del Soldato, M., Riquelme, A., Bianchini, S., Tomás, R., Di Martire, D., De Vita, P., Moretti, S. and Calcaterra, D., 2018. Multisource data integration to investigate one century of evolution for the Agnone landslide (Molise, southern Italy). *Landslides*, 15(11), pp.2113-2128.

Demange, J., Leborne, H., Traineau, H. and Westercamp, D., 1985. Volcano-structural History of the Southern Region of Dominica. Bureau of Geological and Mining Research (BRGM), Joint Institute for Geothermal Research, Report, 85.

Deng, Y., Wilson, J.P. and Gallant, J.C., 2008. Terrain analysis. *The handbook of geographic information science*, pp.417-435.

Dikshit, A., Satyam, N. and Pradhan, B., 2019. Estimation of rainfall-induced landslides using the TRIGRS model. *Earth Systems and Environment*, 3(3), pp.575-584.

Dilley, M., Chen, R.S., Deichmann, U., Lerner-Lam, A.L. and Arnold, M., 2005. Natural disaster hotspots: a global risk analysis. The World Bank.

Dominica News Online. [Archived](#) from the original on June 16, 2018. IFRCRCS

Dominica: Hurricane Maria (PDF) (Information Bulletin). International Federation of Red Cross and Red Crescent Societies. September 25, 2017. Retrieved September 26, 2017.

Dominica: The impact of Hurricane Maria - Disaster Profile – January 2018". ReliefWeb. Assessment Capacities Project.

Dragičević, S., Lai, T. and Balram, S., 2015. GIS-based multicriteria evaluation with multiscale analysis to characterize urban landslide susceptibility in data-scarce environments. *Habitat International*, 45, pp.114-125.

Earle K. W 1928. Geological notes on the island of Dominica, BWI. *Geological Magazine* 65:169–187

Economic Commission for Latin America and the Caribbean (ECLAC). 2009. "Caribbean Development Report."

Edgar, N.T., Ewing, J.I. and Hennion, J., 1971. Seismic refraction and reflection in Caribbean Sea. *AAPG Bulletin*, 55, pp.833-870.

Eisele, S., Reißig, S., Freundt, A., Kutterolf, S., Nürnberg, D., Wang, K.L. and Kwasnitschka, T., 2015. Pleistocene to Holocene offshore tephrostratigraphy of highly explosive eruptions from the southwestern Cape Verde Archipelago. *Marine Geology*, 369, pp.233-250.

Farooq, M., Shafique, M. and Khattak, M.S., 2019. Flood hazard assessment and mapping of River Swat using HEC-RAS 2D model and high-resolution 12-m TanDEM-X DEM (WorldDEM). *Natural Hazards*, 97, pp.477-492.

Fischer, L., Purves, R.S., Huggel, C., Noetzli, J. and Haeberli, W., 2012. On the influence of topographic, geological and cryospheric factors on rock avalanches and rockfalls in high-mountain areas. *Natural Hazards and Earth System Sciences*, 12, p.241.

Florinsky, I., 2016. *Digital terrain analysis in soil science and geology*. Academic Press.

Foeken J., Day S. and Stuart F. 2009. Cosmogenic ³He exposure dating of the Quaternary basalts from Fogo, Cape Verdes: implications for rift zone and magmatic reorganisation. *Quat Geochronol* 4:37-49.

Fonseca, J.F.B.D. et al., 2003. Multiparameter monitoring of Fogo Island, Cape Verde, for volcanic risk mitigation, *J. Volc. Geotherm. Res.*, 125, 39–56, doi:10.1016/S0377 0273(03)00088-X.

Førllie, OA, 2019. 2D numerical modeling of Manndalselva to ensure flood protection (Master's thesis, NTNU).

Forsee, W.J. and Ahmad, S., 2011. Evaluating urban storm-water infrastructure design in response to projected climate change. *Journal of Hydrologic Engineering*, 16, pp.865-873.

Fournier, N., Witham, F., Moreau-Fournier, M. and Bardou, L., 2009. Boiling Lake of Dominica, West Indies: High-temperature volcanic crater lake dynamics. *Journal of Geophysical Research: Solid Earth*, 114(B2) pp.1-4.

Fragoso, M., Trigo, R.M., Pinto, J.G., Lopes, S., Lopes, A., Ulbrich, S. and Magro, C., 2012. The 20 February 2010 Madeira flash-floods: synoptic analysis and extreme rainfall assessment. *Natural Hazards and Earth System Sciences*, 12(3), pp.715-730.

Frey, H., Huggel, C., Bühler, Y., Buis, D., Burga, M.D., Choquevilca, W., Fernandez, F., Hernández, J.G., Giráldez, C., Loarte, E. and Masias, P., 2016. A robust debris-flow and GLOF risk management strategy for a data-scarce catchment in Santa Teresa, Peru. *Landslides*, 13(6), pp.1493-1507.

Gabriel Elizondo (September 25, 2017). Hurricane Maria turns Dominica into 'giant debris field'. Al Jazeera.

Gaillard, J.C and Kelman, I. 2012. Framing Disasters: Theories and Stories Seeking to Understand Hazards, Vulnerability and Risk. Pp. 18-33 In: *The Routledge Handbook of Hazards and Disaster Risk Reduction*, Eds: Wisner, B., Gaillard, J.C. and Kelman, I., London: Routledge.

Gaillard, J.C, 2010. "Introduction to Neglected Disasters." *Jamba: Journal of Disaster Risk Studies* 2(3):151-8.

Gaillard, J.C., Wisner, B., Benouar, D et al. 2010. "Alternatives pour une réduction durable des risques de catastrophe." *Human Geography* 3:66-88.

Garbrecht, J. and Martz, L.W., 2000. Digital elevation model issues in water resources modeling. *Hydrologic and hydraulic modeling support with geographic information systems*, pp.1-28. Environmental Systems Research Institute (esri.com)

Garmon, W.T., Allen, C.D. and Groom, K.M., 2017. Geologic and tectonic background of the Lesser Antilles. In: *Landscapes and Landforms of the Lesser Antilles*, pp. 7-15. Springer, Cham.

Gesch, D.B. and Maune, D., 2007. Digital elevation model technologies and applications: the DEM users' manual. In: American Society for Photogrammetry and Remote Sensing, 2, pp. 99-118.

Gilbert B. Clark (1984). Tropical Storm Fran Preliminary Report (GIF) (Report). National Hurricane Center. p. 1. Retrieved March 11, 2020.

Girvan, N. 2006. Caribbean Dependency Thought Revisited. Caribbean Journal of Development Studies 27(3):329-352.

Global Assessment of Disaster Risk Reduction 2011. Geneva: UNISDR. 2009. Global Assessment of Disaster Risk Reduction. Geneva: UNISDR 2009b. "Terminology". Last <<http://www.unisdr.org/we/inform/terminology>>.

GoCD. 1999. Statistical Digest: 21st Anniversary of Independence Publication. Roseau: Central Statistical Office, Ministry of Finance, Industry and Planning, Government of the Commonwealth of Dominica.

Goff, J., Liu, P.L., Higman, B., Morton, R., Jaffe, B.E., Fernando, H., Lynett, P., Fritz, H., Synolakis, C. and Fernando, S., 2006. Sri Lanka field survey after the December 2004 Indian Ocean tsunami. Earthquake Spectra, 22(S3), pp.155-172.

Gomes, C., 2014. The case of small island developing states of the Caribbean: The challenge of building resilience. Published by cepal.org

Gregoretti, C. and Fontana, G.D., 2008. The triggering of debris flow due to channel-bed failure in some alpine headwater basins of the Dolomites: Analyses of critical runoff. Hydrological Processes: An International Journal, 22(13), pp.2248-2263.

Grevemeyer, I. et al., 2004. Cruise report No. M62-3 of the German research vessel METEOR, http://www.dfg-ozean.de/fileadmin/DFG/Berichte/M62_3_opt.pdf, University Hamburg.

Guarnieri, A., Masiero, A., Vettore, A. and Pirotti, F., 2015. Evaluation of the dynamic processes of a landslide with laser scanners and Bayesian methods. Geomatics, Natural Hazards and Risk, 6(5-7), pp.614-634.

Gudmundsson, M.T., Pedersen, R., Vogfjörð, K., Thorbjarnardóttir, B., Jakobsdóttir, S. and Roberts, M.J., 2010. Eruptions of Eyjafjallajökull Volcano, Iceland. Eos, Transactions American Geophysical Union, 91(21), pp.190-191.

Guerrero, F.J.D.T., Hinojosa-Corona, A. and Kretzschmar, T.G., 2016. A comparative study of NDVI values between North-and South-Facing slopes in a semiarid mountainous region. *IEEE Journal of Selected Topics in Applied Earth Observations and Remote Sensing*, 9(12), pp.5350-5356.

Gurenko, A.A., Trumbull, R.B., Thomas, R. and Lindsay, J.M., 2005. A melt inclusion record of volatiles, trace elements and Li–B isotope variations in a single magma system from the Plat Pays Volcanic Complex, Dominica, Lesser Antilles. *Journal of Petrology*, 46, pp.2495-2526.

Guth, P.L., 2006. Geomorphometry from SRTM. *Photogrammetric Engineering & Remote Sensing*, 72(3), pp.269-277.

Halama, R., Boudon, G., Villemant, B., Joron, J.L., Le Friant, A. and Komorowski, J.C., 2006. Pre-eruptive crystallization conditions of mafic and silicic magmas at the Plat Pays volcanic complex, Dominica (Lesser Antilles). *Journal of Volcanology and Geothermal Research*, 153, pp.200-220

Hancock, G.R., Martinez, C., Evans, K.G. and Moliere, D.R., 2006. A comparison of SRTM and high-resolution digital elevation models and their use in catchment geomorphology and hydrology: Australian examples. *Earth Surface Processes and Landforms: The Journal of the British Geomorphological Research Group*, 31, pp.1394-1412.

Headquarters for Earthquake Research Promotion 2011: Evaluation of the 2011 off the Pacific Coast of Tohoku Earthquake. http://www.jishin.go.jp/main/chousa/11mar_sanriku-oki2/index.htm (in Japanese)

Heidarzadeh, M., Teeuw, R., Day, S. and Solana, C., 2018. Field survey of the damage to infrastructures due to the September 2017 Hurricane Maria in Dominica. In: *EGU General Assembly Conference Abstracts* (p. 10742).

Heleno, S.I.N. & Fonseca, J.F.B.D., 1999. A seismological investigation of the Fogo Volcano, Cape Verde, *Volc. Seism.* 20, 199–217.

Holm, P.M., Grandvuinet, T., Friis, J., Wilson, J.R., Barker, A.K. and Plesner, S., 2008. An ^{40}Ar - ^{39}Ar study of the Cape Verde hot spot: Temporal evolution in a semistationary plate environment. *Journal of Geophysical Research: Solid Earth*, 113(B8).

Holm, P.M., Wilson, J.R., Christensen, B.P., Hansen, L., Hansen, S.L., Hein, K.M., Mortensen, A.K., Pedersen, R., Plesner, S. and Runge, M.K., 2006. Sampling the Cape Verde mantle

plume: evolution of melt compositions on Santo Antão, Cape Verde Islands. *Journal of Petrology*, 47(1), pp.145-189.

Houston, D., Werrity, A., Bassett, D., Geddes, A., Hoolachan, A. and McMillan, M., 2011. Pluvial (rain-related) flooding in urban areas: the invisible hazard. (<https://eprints.gla.ac.uk/>)

<https://weather-and-climate.com/average-monthly-Rainfall-Temperature-Sunshine,sao-filipe-fogo-cv,Cape-Verde,2020>.

<https://www.climatestotravel.com/climate/cape-verde,2020>.

<https://www.hec.usace.army.mil/confluence/rasdocs/r2dum/latest/steady-vs-unsteady-flow-and-1d-vs-2d-modeling/1d-vs-2d-hydraulic-modeling>

Hu, T. and Smith, R.B., 2018. The impact of Hurricane Maria on the vegetation of Dominica and Puerto Rico using multispectral remote sensing. *Remote Sensing*, 10(6), p.827.

Hu, T. and Smith, R.B., 2018. The impact of Hurricane Maria on the vegetation of Dominica and Puerto Rico using multispectral remote sensing. *Remote Sensing*, 10(6), p.827.

Hürlimann, M., Rickenmann, D., Medina, V. and Bateman, A., 2008. Evaluation of approaches to calculate debris-flow parameters for hazard assessment. *Engineering Geology*, 102, pp.152-163.

Hurricane Maria: Dominica – Situation Report No. 1 (PDF) (Report). United Nations. September 25, 2017.

Hussin, H.Y., 2011. Probabilistic run-out modeling of a debris flow in Barcelonnette, France (Master's thesis, University of Twente).

Hussin, H.Y., Quan Luna, B., Van Westen, C.J., Christen, M., Malet, J.P. and Van Asch, T.W., 2012. Parameterization of a numerical 2-D debris flow model with entrainment: a case study of the Faucon catchment, Southern French Alps. *Natural Hazards and Earth System Sciences*, 12, pp.3075-3090.

Hutchinson, M. and Gallant, J., 2000. Digital elevation models. *Terrain Analysis: Principles and Applications*; John Wiley & Sons: New York, NY, USA, pp.29-50.

Ikromi, A.I. and Wardhana, P.N., 2020. Hydrodynamic simulation of a dam breach of Cipanas Dam using HEC-RAS 5.0. 5. In *IOP Conference Series: Earth and Environmental Science*, 437, No. 1, p. 012052. IOP Publishing.

International Federation of Red Cross and Red Crescent Societies. September 25, 2017

Issler, D., Jenkins, J.T. and McElwaine, J.N., 2018. Comments on avalanche flow models based on the concept of random kinetic energy. *Journal of Glaciology*, 64(243), pp.148-164.

Iverson, R.M., 1997. The physics of debris flows. *Reviews of geophysics*, 35(3), pp.245-296.

Iverson, R.M., 2015. Scaling and design of landslide and debris-flow experiments. *Geomorphology*, 244, pp.9-20.

Iverson, R.M., Reid, M.E. and LaHusen, R.G., 1997. Debris-flow mobilization from landslides. *Annual Review of Earth and Planetary Sciences*, 25(1), pp.85-138.

Jakob, M., 2021. Debris-Flow Hazard Assessments: A Practitioner's View. *Environmental & Engineering Geoscience*, 27(2), pp.153-166.

Jakubowski, M., Li, W., Guo, Q. and Kelly, M., 2013. Delineating individual trees from LiDAR data: A comparison of vector-and raster-based segmentation approaches. *Remote Sensing*, 5(9), pp.4163-4186.

Jarsve, K.T., 2018. Uncertainties of Simulating Rockfalls and Debris Flows Using RAMMS (Master's thesis). University of Oslo

Javernick, L., Brasington, J. and Caruso, B., 2014. Modeling the topography of shallow braided rivers using Structure-from-Motion photogrammetry. *Geomorphology*, 213, pp.166-182.

Jenkins, S.F., Day, S.J., Faria, B.V.E. and Fonseca, J.F.B.D., 2017. Damage from lava flows: insights from the 2014–2015 eruption of Fogo, Cape Verde. *Journal of Applied Volcanology*, 6(1), pp.1-17.

Johnson, D. M. 2012. The role of multidisciplinary research and collaboration for improving the resilience of communities to volcanic risk *Journal of Applied Volcanology*, 1, 1, doi:10.1186/2191-5040-1-1.

Jordan, B.R., 2015. A bird's-eye view of geology: The use of micro drones/UAVs in geologic fieldwork and education. *GSA today*, 25(7), pp.50-52.

Joyce, K.E., Samsonov, S.V., Levick, S.R., Engelbrecht, J. and Belliss, S., 2014. Mapping and monitoring geological hazards using optical, LiDAR, and synthetic aperture RADAR image data. *Natural hazards*, 73(2), pp.137-163.

Julea, A., Méger, N. and Trouvé, E., 2006. Sequential patterns extraction in multitemporal satellite images. In 17th European Conference on Machine Learning and the 10th European Conference on Principles and Practice of Knowledge Discovery in Databases (ECML/PKDD) (pp. 96-99).

Kelman, I., 2008. Addressing the root causes of large-scale disasters. Large scale disasters: Prediction, control, and mitigation, pp.94-119. Cambridge University Press

Kerr, A. C., White, R. V., Thompson, P. M. E., Tarney, J. and Saunders, A. D., 2003. No oceanic plateau— no Caribbean plate? The seminal role of an oceanic plateau in Caribbean plate evolution. In: Bartolini, Buffler R. T., and Blickwede J., (Eds)., The Circum-Gulf of Mexico and the Caribbean: Hydrocarbon habitats, basin formation, and plate tectonics: AAPG Memoir 79, p. 126–168.

Kerr, A.C., Tarney, J., Marriner, G.F., Nivia, A., Klaver, G.T. and Saunders, A.D., 1996. The geochemistry and tectonic setting of late Cretaceous Caribbean and Colombian volcanism. *Journal of South American Earth Sciences*, 9(1-2), pp.111-120.

Kingsland, K., 2020. Comparative analysis of digital photogrammetry software for cultural heritage. *Digital Applications in Archaeology and Cultural Heritage*, 18, p.e00157.

Knebl, M.R., Yang, Z.L., Hutchison, K. and Maidment, D.R., 2005. Regional scale flood modeling using NEXRAD rainfall, GIS, and HEC-HMS/RAS: a case study for the San Antonio River Basin Summer 2002 storm event. *Journal of Environmental Management*, 75, pp.325-336.

Kowalski, J., 2008. Two-phase modeling of debris flows. ETH Zurich.

Laporte-Fauret, Q., Marieu, V., Castelle, B., Michalet, R., Bujan, S. and Rosebery, D., 2019. Low-cost UAV for high-resolution and large-scale coastal dune change monitoring using photogrammetry. *Journal of Marine Science and Engineering*, 7(3), p.63.

Lastilla, L., Belloni, V., Ravanelli, R. and Crespi, M., 2021. DSM Generation from Single and Cross-Sensor Multi-View Satellite Images Using the New Agisoft Metashape: The Case Studies of Trento and Matera (Italy). *Remote Sensing*, 13(4), p.593.

Le Friant, A., Boudon, G., Komorowski, JC and Deplus, C., 2002. The island of Dominica, at the origin of the largest volcano debris avalanches of the Lesser Antilles arc. *Rendus Geoscience Accounts*, 334 (4), pp.235-243.

- Lee, C.T., 2012, April. Characteristics of earthquake-induced landslides and differences compared to storm-induced landslides. In EGU General Assembly Conference Abstracts (p. 6937).
- Lee, J.S., 1980. Digital image enhancement and noise filtering by use of local statistics. *IEEE Transactions on Pattern Analysis & Machine Intelligence*, (2), pp.165-168.
- Lee, J.S., Papathanassiou, K.P., Ainsworth, T.L., Grunes, M.R. and Reigber, A., 1998. A new technique for noise filtering of SAR interferometric phase images. *IEEE Transactions on Geoscience and Remote Sensing*, 36(5), pp.1456-1465.
- Leidig, M., Teeuw, R.M., Day, S., Solana, C., Heidarzadeh, M. and Schaefer, M., 2019, Infrastructure as both hazard victim and hazard multiplier on Dominica, during and after Hurricane Maria. In: AGU Fall Meeting Abstracts (Vol. 2019, pp. NH11B-0776).
- Levander, A., Schmitz, M., Avé Lallemand, H.G., Zelt, C.A., Sawyer, D.S., Magnani, M.B., Mann, P., Christeson, G., Wright, J.E., Pavlis, G.L. and Pindell, J., 2006. Evolution of the southern Caribbean plate boundary. *Eos, Transactions American Geophysical Union*, 87(9), pp.97-100.
- Li, Z., Zhu, C. and Gold, C., 2004. *Digital terrain modeling: principles and methodology*. CRC Press.
- Lina, X.U., Zhu, L. and Guo, X., 2018, October. Review Study on the Risk Assessment of Debris Flow. In *IOP Conference Series: Materials Science and Engineering* (Vol. 423, No. 1, p. 012021). IOP Publishing.
- Lindsay, J.M. (Ed.), 2005. *Volcanic hazard atlas of the Lesser Antilles*. Seismic Research.
- Loew, A. and Mauser, W., 2007. Generation of geometrically and radiometrically terrain corrected SAR image products. *Remote Sensing of Environment*, 106(3), pp.337-349.
- Macdonald, R., Hawkesworth, C.J. and Heath, E., 2000. The Lesser Antilles volcanic chain: a study in arc magmatism. *Earth-Science Reviews*, 49(1-4), pp.1-76.
- Madeira, J., Brum da Silveira, A., Torres, PC, Réffega, A., Figueiredo, MO, Silva, LC, Costa, FL, Mendes, MH, Silva, TP and Correia, E., 1995. Apparent contradiction between the final volumes of spills and the estimation of effusion rates: The case of the 1995 eruption of Fogo. In: *Simposio Internacional on the volcanic eruption of Fogo* (pp. 153-163).

Madjid, M.Y.A., Vandeginste, V., Hampson, G., Jordan, C.J. and Booth, A.D., 2018. Drones in carbonate geology: Opportunities and challenges, and application in diagenetic dolomite geobody mapping. *Marine and Petroleum Geology*, 91, pp.723-734.

Maidment, D.R. and Djokic, D. eds., 2000. *Hydrologic and hydraulic modeling support: with geographic information systems*. ESRI, Inc.

Maidment, D.R. and Morehouse, S., 2002. *Arc Hydro: GIS for water resources*. ESRI, Inc.

Malfait, B.T. and Dinkelman, M.G., 1972. Circum-Caribbean tectonic and igneous activity and the evolution of the Caribbean plate. *Geological Society of America Bulletin*, 83(2), pp.251-272.

Mani, P., Chatterjee, C. and Kumar, R., 2014. Flood hazard assessment with multiparameter approach derived from coupled 1D and 2D hydrodynamic flow model. *Natural hazards*, 70(2), pp.1553-1574.

Mann, P., 1999. Caribbean sedimentary basins: Classification and tectonic setting from Jurassic to present. In: *Sedimentary Basins of the World*, 4, pp. 3-31.

Martin-Kaye, P.H.A (1960) Preliminary notes on the geological map of Dominica. Unpublished progress reports of the Government Geologist, Dominica

Mata-Lima, H., Alvino-Borba, A., Pinheiro, A., Mata-Lima, A. and Almeida, J.A., 2013. Impacts of natural disasters on environmental and socio-economic systems: What makes the difference? *Ambiente & Sociedade*, 16(3), pp.45-64.

Matthew Weaver; Claire Phipps; Sam Levin (September 20, 2017). "Hurricane Maria makes landfall on Puerto Rico – live updates". *The Guardian*.

McIver, L., Kim, R., Woodward, A., Hales, S., Spickett, J., Katscherian, D., Hashizume, M., Honda, Y., Kim, H., Iddings, S. and Naicker, J., 2016. Health impacts of climate change in Pacific Island countries: a regional assessment of vulnerabilities and adaptation priorities. *Environmental health perspectives*, 124(11), pp.1707-1714.

Méheux, K, Dominey-Howes, D. and Lloyd, K. 2007. Natural Hazard Impacts in Small Islands Developing States: A Review of Current Knowledge and Future Research Needs. *Natural Hazards* 40:429-446.

- Meunier, P., Hovius, N. and Haines, A.J., 2007. Regional patterns of earthquake-triggered landslides and their relation to ground motion. *Geophysical Research Letters*, 34(20).
- Mimura, N., L. Nurse, R.F. McLean *et al.* 2007. Small Islands. *Climate Change 2007: Impacts, Adaptation and Vulnerability*. Pp. 687-716 in *Contribution of Working Group II to the Fourth Assessment Report of the Intergovernmental Panel on Climate Change*, Eds: M.L. Parry, O.F. Canziani, J.P. Palutikof, P.J. van der Linden, and C.E. Hanson. Cambridge University Press.
- Mitchell, J.G., Le Bas, M.J., Zielonka, J. and Furnes, H., 1983. On dating the magmatism of Maio, Cape Verde islands. *Earth and Planetary Science Letters*, 64(1), pp.61-76.
- Monjaret, MC, 1985. Contribution to the study of the arch of the Lesser Antilles. Volcanism of Dominica. Chronological, mineralogical and geochemical data. Unpublished thesis, University of Western Brittany.
- Mora C, S., 1995. The impact of natural hazards on socio-economic development in Costa Rica. *Environmental & Engineering Geoscience*, 1(3), pp.291-298.
- Mora, S., 2007. The nature of disasters: reflections on their causes and consequences in Latin America and the Caribbean (LAC). In: *Proceedings of the 1st North American Landslide Conference* (pp. 1-30).
- National Meteorology and Geophysics Institute United Nations Framework Convention on Climate Changes, 2007
- NDRRMC. NDRRMC Update: SitRep No. 13 re Magnitude 6.1 Earthquake in Castillejos, Zambales (PDF). Retrieved May 1, 2019
- Newmark, N.M., 1965. Effects of earthquakes on dams and embankments. *Geotechnique*, 15(2), pp.139-160.
- O'Brien, K and Leichenko, R., 2000. Double Exposure: Assessing the Impacts of Climate Change within the Context of Economic Globalization. *Global Environmental Change* 10(3):221-232.
- Parihar, N., Nathawat, M.S., Das, A. and Mohan, S., 2011. Accuracy assessment of DEMs derived from multi-frequency SAR images. In *3rd International Asia-Pacific Conference on Synthetic Aperture Radar (APSAR)* (pp. 1-4). IEEE.

Pasch et al 2019 National Hurricane Center Tropical Cyclone report Hurricane Maria AL152017 (https://www.nhc.noaa.gov/data/tcr/AL152017_Maria.pdf)

Peace Corps. April 2006. "The Peace Corps Welcomes You to Cape Verde" (PDF). Archived from the original (PDF) on 27 April 2017.

Pelling, M., 2012. Hazards, risk and urbanization. In: *The Routledge Handbook of Hazards and Disaster Risk Reduction*, pp.145-155.

Piciullo, L., Calvello, M. and Cepeda, J.M., 2018. Territorial early warning systems for rainfall-induced landslides. *Earth-Science Reviews*, 179, pp.228-247.

Pickles, J. ed., 1995. *Ground truth: The social implications of geographic information systems*. Guilford Press.

Pierson, T.C., 2005. Distinguishing between debris flows and floods from field evidence in small watersheds (No. 2004-3142). US Geological Survey.

Pike, R. J., Evans I. S., Hengl T. 2008. *Geomorphometry: a Brief Guide*. In: Hengl, T. and Reuter, H.I. (Eds), *Geomorphometry: Geomorphometry: Concepts, Software, Applications*. *Developments in Soil Science*, vol. 33, Elsevier, 1-28 pp.

Pim, J., Peirce, C., Watts, A.B., Grevemeyer, I. and Krabbenhöft, A., 2008. Crustal structure and origin of the Cape Verde Rise. *Earth and Planetary Science Letters*, 272(1-2), pp.422-428.

Piras, M., Taddia, G., Forno, M.G., Gattiglio, M., Aicardi, I., Dabove, P., Russo, S.L. and Lingua, A., 2017. Detailed geological mapping in mountain areas using an unmanned aerial vehicle: application to the Rodoretto Valley, NW Italian Alps. *Geomatics, Natural Hazards and Risk*, 8(1), pp.137-149.

Plesner, S., Holm, P.M. and Wilson, J.R., 2003. ^{40}Ar - ^{39}Ar geochronology of Santo Antão, Cape Verde Islands. *Journal of Volcanology and Geothermal Research*, 120(1), pp.103-121.

Post-Disaster Needs Assessment Hurricane Maria September 18, 2017. Resilient Caribbean Caricom. November 15, 2017

Pyka, K., 2017, June. Comparison of quality of metric photos relative orientation in Micmac and PhotoScan. In: *2017 Baltic Geodetic Congress (BGC Geomatics)* (pp. 126-131). IEEE.

Rahmes, M., Karp, J., Smith, A. and Connetti Jr, S., Harris Corp, 2006. Method and apparatus for enhancing a digital elevation model (DEM) for topographical modeling. U.S. Patent 7,142,984.

Ramalho, R., Helffrich, G., Cosca, M., Vance, D., Hoffmann, D. and Schmidt, D.N., 2010. Episodic swell growth inferred from variable uplift of the Cape Verde hotspot islands. *Nature Geoscience*, 3(11), pp.774-777.

Ramalho, R., Helffrich, G., Schmidt, D.N. and Vance, D., 2010. Tracers of uplift and subsidence in the Cape Verde Archipelago. *Journal of the Geological Society*, 167, pp.519-538.

Rauste, Y., Lonqvist, A., Molinier, M., Henry, J.B. and Heme, T., 2007, July. Orthorectification and terrain correction of polarimetric SAR data applied in the ALOS/Palsar context. In 2007 IEEE International Geoscience and Remote Sensing Symposium (pp. 1618-1621). IEEE.

Regmi, N.R., Giardino, J.R., McDonald, E.V. and Vitek, J.D., 2015. A review of mass movement processes and risk in the critical zone of Earth. *Developments in Earth Surface Processes*, 19, pp.319-362.

Ribeiro, O., 1960. *a Ilha do Fogo e as suas erupções*, Memórias, serie geografica I. Publ. Junta de Investigações do Ultramar, Ministerio do Ultramar, 2nd edn. Lisbon, Portugal.

Richter, N., Favalli, M., Zeeuw-van Daltsen, E.D., Fornaciai, A., Silva Fernandes, R.M.D., Pérez, N.M., Levy, J., Victória, S.S. and Walter, T.R., 2016. Lava flow hazard at Fogo Volcano, Cabo Verde, before and after the 2014–2015 eruption. *Natural Hazards and Earth System Sciences*, 16(8), pp.1925-1951.

Robson, J.R., 1966. Catalogue of the active volcanoes and solfatara fields of the West Indies. *Catalogue of the Active Volcanoes of the World*. (<https://ci.nii.ac.jp/naid/10006218514/>)

Rodríguez-Morata, C., Villacorta, S., Stoffel, M. and Ballesteros-Cánovas, J.A., 2019. Assessing strategies to mitigate debris-flow risk in Abancay province, south-central Peruvian Andes. *Geomorphology*, 342, pp.127-139.

Roobol, M.J. and Smith, A.L., 2004. Geological map of Dominica, West Indies. Geology Department, University of Puerto Rico at Mayaguez.

Roobol, M.J. and Stasiuk, M.V, Lindsay, J M and Smith AL, 2000. Volcanic hazards atlas.

Routledge Handbook of Hazards and Disaster Risk Reduction, 2011. Eds: Wisner, B, Gaillard, J.C. and Kelman I. London: Routledge. "Urban Governance and Disaster Risk Reduction in the Caribbean: The Experiences of Oxfam GB." *Environment and Urbanization*

Rowley, K., 1992. 'Volcanic Geology of the Lesser Antilles and Volcanic Hazards in Eastern Caribbean'. *Journal of the Geological Society of Jamaica*. Special issue 12. Natural Hazards in the Caribbean. Ed. Rafi A., Kingston. pp26–33.

Salm, B., 1993. Flow, flow transition and runout distances of flowing avalanches. *Annals of Glaciology*, 18, pp.221-226. http://uwiseismic.com/Downloads/Dominica_VHA.pdf

Salvacion, A.R., 2016. Terrain characterization of small island using publicly available data and open-source software: a case study of Marinduque, Philippines. *Modeling Earth Systems and Environment*, 2(1), p.31.

Schaefer, M., Teeuw, R., Day, S., Zekkos, D., Weber, P., Meredith, T. and Van Westen, C.J., 2020. Low-cost UAV surveys of hurricane damage in Dominica: automated processing with co-registration of pre-hurricane imagery for change analysis. *Natural Hazards*, pp.1-30.

Schillaci, C., Braun, A. and Kropáček, J., 2015. Terrain analysis and landform recognition. *Geomorphological Techniques*, 2, pp.1-18.

Schläpfer, D. and Richter, R., 2002. Geo-atmospheric processing of airborne imaging spectrometry data. Part 1: parametric orthorectification. *International Journal of Remote Sensing*, 23(13), pp.2609-2630.

Schneider, C.A., Rasband, W.S. and Eliceiri, K.W., 2012. NIH Image to ImageJ: 25 years of image analysis. *Nature Methods*, 9(7), pp.671-675.

Scott, K.M., Macías, J.L., Naranjo, J.A., Rodríguez, S. and McGeehin, J.P., 2001. Catastrophic debris flows transformed from landslides in volcanic terrains: mobility, hazard assessment, and mitigation strategies (No. 1630). US Department of the Interior, US Geological Survey.

Sechin, A.Y., 2014. Digital Photogrammetric Systems. *GeoInformatics*, 17(4), p.32.

Shen, P., Zhang, L., Chen, H. and Fan, R., 2018. EDDA 2.0: integrated simulation of debris flow initiation and dynamics considering two initiation mechanisms. *Geoscientific Model Development*, 11(7), pp.2841-2856.

- Shultz, J.M., Cohen, M.A., Hermosilla, S., Espinel, Z. and McLean, A., 2016. Disaster risk reduction and sustainable development for small island developing states. *Disaster Health*, 3(1), pp.32-44.
- Sierra Leone: Mudslides - Area and Infrastructure Affected - August 2017" (PDF). International Federation of Red Cross and Red Crescent Societies. Retrieved August 21, 2017.
- Sigurdsson, H. and Carey, S.N., 1991. Caribbean volcanoes: a field guide to Martinique, Dominica and St. Vincent. Geological Association of Canada, Toronto, pp.1-101.
- Sigurdsson, H., 1972. Partly-welded pyroclast flow deposits in Dominica, Lesser Antilles. *Bulletin Volcanologique*, 36(1), pp.148-163.
- Simoni, A., Mammoliti, M. and Graf, C., 2012. Performance Of 2D debris flow simulation model RAMMS. In: Annual International Conference on Geological and Earth Sciences GEOS. (https://www.researchgate.net/profile/Alessandro_Simoni2/publication/268459030)
- Sinha, S., Jeganathan, C., Sharma, L.K. and Nathawat, M.S., 2015. A review of radar remote sensing for biomass estimation. *International Journal of Environmental Science and Technology*, 12(5), pp.1779-1792.
- Smith, A.L., Roobol, M.J. and Gunn, B.M., 1980. The Lesser Antilles—a discussion of the island arc magmatism. *Bulletin Volcanologique*, 43(2), pp.287-302.
- Smith, A.L., Roobol, M.J., Mattioli, G.S., Fryxell, J.E., Daly, G.E. and Fernandez, L.A., 2013. The volcanic geology of the mid-arc Island of Dominica. *Geological Society of America* (Vol. 496), pp. 9-25
- Solomon, C. and Breckon, T., 2011. *Fundamentals of Digital Image Processing: A practical approach with examples in Matlab*. John Wiley & Sons.
- Soria, F.A., Sawamoto, M. and Kazama, S., 2008. Sensitivity analysis to evaluate the effect of land use change on discharge rate. *From Headwaters to the Ocean: Hydrological Change and Water Management-Hydrochange 2008*, 1-3 October 2008, Kyoto, Japan, p.203.
- Sovilla, B., Burlando, P. and Bartelt, P., 2006. Field experiments and numerical modeling of mass entrainment in snow avalanches. *Journal of Geophysical Research: Earth Surface*, 111(F3), pp.9

Sowter, A., 2010. Orthorectification and interpretation of differential InSAR data over mountainous areas: a case study of the May 2008 Wenchuan Earthquake. *International Journal of Remote Sensing*, 31(13), pp.3435-3448.

Stillman, C.J., Furnes, H., LeBas, M.J., Robertson, A.H.F. and Zielonka, J., 1982. The geological history of Maio, Cape Verde islands. *Journal of the Geological Society*, 139(3), pp.347-361.

Sun, G., Ranson, K.J. and Kharuk, V.I., 2002. Radiometric slope correction for forest biomass estimation from SAR data in the Western Sayani Mountains, Siberia. *Remote Sensing of Environment*, 79(2-3), pp.279-287.

Tarboton, D.G., 1997. A new method for the determination of flow directions and upslope areas in grid digital elevation models. *Water resources research*, 33(2), pp.309-319.

Teeuw, R., 2007. Applications of remote sensing for geohazard mapping in coastal and riverine environments. *Geological Society London Special Publications*, 283, pp.93-106.

Teeuw, R.M. (Ed.), 2007. Mapping hazardous terrain using remote sensing. *Geological Society of London Special Publication* 283.

Teves, A.S.G., 2018. Escoadas de lava históricas do Vulcão do Fogo (Cabo Verde): cartografia e análise geomorfológica (Doctoral dissertation).

The Office of Disaster Management (ODM) and the Caribbean Disaster Emergency Management Agency (CDEMA) reference. (<https://www.cdema.org/>)

Thomas, A., Pringle, P., Pflleiderer, P. and Schleussner, C.F., 2017. Tropical Cyclones: Impacts, the link to Climate Change and Adaptation. *Climate Analytics*. Available online at: <http://climateanalytics.org/publications/2017/tropical-cyclones-impactsthe-link-to-climate-change-and-adaptation>.

Tobler, W.R., 1969. An analysis of a digitalized surface. *A Study of the Land Type*, 86, pp.59-76. ([researchgate.net](https://www.researchgate.net)).

Tomlinson, R. F. 1962. "Computer Mapping: An Introduction to the use of Electronic Computers in the Storage, Compilation and Assessment of Natural and Economic Data for the Evaluation of Marginal Lands." Report presented to the National Land Capability Inventory Seminar held under the direction of the Agricultural Rehabilitation and Development Administration of the Canada Department of Agriculture, Ottawa

Tomlinson, R. F., 1967. "An Introduction to the Geo-Information Systems of the Canada Land Inventory", Department of Forestry and Rural Development, Ottawa 9. In: Tomlinson, Roger F., 1968. "A Geographic Information System for Regional Planning"

Tomlinson, R., 1963. "Feasibility Report of Computer Mapping System." Report to Agricultural Rehabilitation Development Administration, Department of Agriculture, Government of Canada

Toppe, R., 1987. Terrain models: a tool for natural hazard mapping. Avalanche formation, movement and effects, IAHS Publ, 162, pp.629-638.

Torres, P.C., Madeira, J., Silva, L. C., Silveira, A. B., Serralheiro, A. & Gomes, A. M. (1997) -- Carta geológica das erupções históricas da ilha do Fogo: revisão e actualização. Simp. Int. "A erupção vulcânica de 1995 na ilha do Fogo, Cabo Verde" IICT, 119--132.

Torres, PC, Silva, LC, Serralheiro, A., Tassinari, CCG and Munhá, J., 2002. Geochronological framework by the K / Ar method of the main volcano-stratigraphic sequences of Ilha do Sal-Cabo Verde. Garcia de Orta. Geology Series, 18 (1/2), pp.9-13.

Turner, D., Lucieer, A. and Watson, C., 2012. An automated technique for generating georectified mosaics from ultra-high resolution unmanned aerial vehicle (UAV) imagery, based on structure from motion (SfM) point clouds. Remote Sensing, 4(5), pp.1392-1410.

Udden, J.A., 1914. Mechanical composition of clastic sediments. Bulletin of the Geological Society of America, 25(1), pp.655-744.

Ullman, S., 1979. The interpretation of structure from motion. Proceedings of the Royal Society of London. Series B. Biological Sciences, 203(1153), pp.405-426.

UN Department of Humanitarian Affairs (October 12, 1984). Cape Verde - Heavy Rains/Floods Sep 1984 UNDR0 Situation Reports 1-2 (HTML) (Report). ReliefWeb. Retrieved March 11, 2020.

United Nations Strategy for Disaster Reduction Secretariat (UNISDR). 2012. "Safe Schools and Hospitals." <<http://www.unisdr.org/we/campaign/schools-hospitals>>.

United Nations, 2011. Small Island developing states: Small Islands big (ger) stakes. Office of the High Representative for the Least Developed Countries, Landlocked Developing Countries and Small Island Developing States, United Nations, New York, NY.

United Nations, 2013. Small Island Developing States: Small Islands Big (ger) Stakes. New York: United Nations, August.

United States Agency for International Development (July 29, 1993). Country: Cape Verde Is (PDF) (Report). Retrieved March 11, 2020.

UNICEF, 2019. Massive flooding in Mozambique, Malawi and Zimbabwe <https://www.unicef.org/stories/massive-flooding-malawi-mozambique-and-zimbabwe>

Vacca, G., Furfaro, G. and Dessì, A., 2018. The use of the UAV images for the building 3D model generation. In: Free and Open Source Software for Geospatial Conference, FOSS4G 2018 (Vol. 42, No. 4W8, pp. 217-223). International Society for Photogrammetry and Remote Sensing.

Vallance, James W.; Iverson, Richard M. (2015), "Chapter 37 - Lahars and Their Deposits", in Sigurdsson, Haraldur (ed.), *The Encyclopedia of Volcanoes (Second Edition)*, Amsterdam: Academic Press, pp. 649–664, ISBN 978-0-12-385938-9

Varnes, D.J., 1984. Landslide hazard zonation: a review of principles and practice (No. 3).

Voellmy, A. (1955) On the Destructive Power of Avalanches. Swiss construction newspaper, year 73. Issue 12, 159 - 162, 15, 212 - 217, 17, 246 - 249, 19, 280-285.

Volcanic Hazards & Prevention: Landslides, Lahars & Tsunamis. (2013, November 21). Retrieved from <https://study.com/academy/lesson/volcanic-hazards-prevention-landslides-lahars-tsunamis.html>.

Wadge, G., 1985. Morne Patates volcano, southern Dominica, Lesser Antilles. *Geological Magazine*, 122(3), pp.253-260.

Wentworth, C.K., 1922. A scale of grade and class terms for clastic sediments. *The Journal of Geology*, 30(5), pp.377-392.

Westoby, M.J., Brasington, J., Glasser, N.F., Hambrey, M.J. and Reynolds, J.M., 2012. ‘Structure-from-Motion’ photogrammetry: A low-cost, effective tool for geoscience applications. *Geomorphology*, 179, pp.300-314.

Wieczorek, G.F. and Snyder, J.B., 2009. Monitoring slope movements. *Geol. Monit.*, vol.1 pp.245-271.

Wieczorek, G.F., 1996. Landslides: investigation and mitigation. Chapter 4-Landslide triggering mechanisms. Transportation Research Board Special Report, (247).

Williams, D.K., 2018 <https://sciencing.com/differences-between-north-southfacing-slopes-8568075.html>

Wilson, J.P., 2012. Digital terrain modeling. *Geomorphology*, 137(1), pp.107-121.

Wise, S., 2011. Cross-validation as a means of investigating DEM interpolation error. *Computers & Geosciences*, 37(8), pp.978-991.

World Bank & United Nations, 2010. Natural hazards, unnatural disasters: the economics of effective prevention. Washington, DC: The International Bank for Reconstruction and Development/The World Bank

Yalcin, E., 2020. Assessing the impact of topography and land cover data resolutions on two-dimensional HEC-RAS hydrodynamic model simulations for urban flood hazard analysis. *Natural Hazards*, 101(3), pp.995-1017.

Yuliya Talmazan (September 22, 2017). Hurricane Maria Damages Dominica's Main Hospital, Leaves 'War Zone' Conditions. (https://en.wikipedia.org/wiki/Hurricane_Maria)

Zahibo, N., Pelinovsky, E., Okal, E., Yalçiner, A., Kharif, C., Talipova, T. and Kozelkov, A., 2005. The earthquake and tsunami of November 21, 2004 at Les Saintes, Guadeloupe, Lesser Antilles. *Science of Tsunami Hazards*, 23(1), p.25.

Zakerinejad, R. and Märker, M., 2014. Prediction of gully erosion susceptibilities using detailed terrain analysis and maximum entropy modelling: a case study in the Mazayejan Plain, Southwest Iran. *Geogr Fis Din Quat*, 37(1), pp.67-76.

ZHANG, M. and LI, T., 2011. Triggering factors and forming mechanism of loess landslides. *Journal of Engineering Geology*, 19(4), pp.530-540.

Zhang, Y., Chen, J., Wang, Q., Tan, C., Li, Y., Sun, X. and Li, Y., 2021. GIS-models with fuzzy logic for Susceptibility Maps of debris flow using multiple types of parameters: A Case Study in Pinggu District of Beijing, China. *Natural Hazards and Earth System Sciences Discussions*, pp.1-23.

Zhou Q and Zhu, A. X. 2013. The recent advancement in digital terrain analysis and modelling. *International Journal of Geographical Information Science*, 27:7, 1269-1271.

Zhuang, J.Q., Cui, P., Peng, J.B., Hu, K.H. and Iqbal, J., 2013. Initiation process of debris flows on different slopes due to surface flow and trigger-specific strategies for mitigating post-earthquake in old Beichuan County, China. *Environmental earth sciences*, 68(5), pp.1391-1403.